University of Cyprus

DEPARTMENT OF PHYSICS

SEARCHES FOR SIGNATURES OF A HEAVY PSEUDOSCALAR A BOSON IN THE TWO-HIGGS-DOUBLET MODEL

DOCTOR OF PHILOSOPHY DISSERTATION

AIMILIOS IOANNOU

2020

University of Cyprus

DEPARTMENT OF PHYSICS

SEARCHES FOR SIGNATURES OF A HEAVY PSEUDOSCALAR A BOSON IN THE TWO-HIGGS-DOUBLET MODEL

AIMILIOS IOANNOU

A Dissertation Submitted to the University of Cyprus in Partial Fulfillment of the Requirements for the Degree of Doctor of Philosophy

May 2020

VALIDATION PAGE

Doctoral Candidate: Aimilios Ioannou

Doctoral Thesis Title: Searches for signatures of a heavy pseudoscalar A boson in the Two-Higgs-Doublet Model

The present Doctoral Dissertation was submitted in partial fulfillment of the requirements for the Degree of Doctor of Philosophy at the ***Department of Physics*** *and was approved on the 20/05/2020 by the members of the* ***Examination Committee****.*

Examination Committee:

Research Supervisor: Panos Razis (Prof. Dep. Of Physics, UCY)

Committee Member: Andreas Othonos (Prof. Dep. Of Physics, UCY)

Committee Member: Fotios Ptochos (Associate Prof. Dep. Of Physics, UCY)

Committee Member: Spyros Tzamarias (Prof. Dep. Of Physics, AUTH)

Committee Member: Aristotelis Kyriakis (Senior Researcher, NCSR DEMOKRITOS Institute of Nuclear & Particle Physics)

DECLARATION OF DOCTORAL CANDIDATE

The present doctoral dissertation was submitted in partial fulfillment of the requirements for the degree of Doctor of Philosophy of the University of Cyprus. It is a product of original work of my own, unless otherwise mentioned through references, notes, or any other statements.

Aimilios Ioannou

Περίληψη

Η παρούσα Διδακτορική Διατριβή επικεντρώνεται στην αναζήτηση ενός βαρύτερου ψευδοβαθμωτού μποζονίου Higgs, CP-odd Higgs A μποζόνιο, που μπορεί να διασπαστεί με ενδιάμεσες καταστάσεις στο μποζόνιο Z ($m_Z = 91$ GeV) αλλά και στο μποζόνιο Higgs ($m_h = 125$ GeV) του Καθιερωμένου Προτύπου, με τελικές καταστάσεις δύο λεπτόνια ($e^+e^-,\ \mu^+\mu^-$) και ένα ζεύγος b κουαρκς ($b\bar{b}$), όπως προβλέπεται από τη θεωρία Two-Higgs-Doublet Model. Επίσης, γεγονότα με τελικές καταστάσεις ενός ζεύγους b κουαρκς και της ελλειμματικής εγκάρσιας ενέργειας που οφείλεται στην παρουσία των μη ανιχνεύσιμων νετρίνων ($\nu\bar{\nu}$) λαμβάνονται υπόψη πρώτη φορά για το κανάλι $A \to Zh$.

Το κανάλι $A \to Zh$ έχει μελετηθεί για τις περιπτώσεις όπου στα γεγονότα οι τελικές καταστάσεις είναι ένα ζεύγος λεπτονίων και ένα ζεύγος b κουάρκς ($A \to Zh \to \ell^+\ell^- b\bar{b}$) αλλά και για την περίπτωση γεγονότων όπου υπάρχει ελλειμματικό ισοζύγιο ενέργειας (MET) και ένα ζεύγος b κουάρκς που προέρχεται από το μποζόνιο Higgs ($A \to Zh \to \nu\bar{\nu} b\bar{b}$). Τα δύο αυτά κανάλια έχουν εξεταστεί και για τις δύο μεθόδους παραγωγής του A μποζονίου (gluon-gluon fusion και b-quark associated production), για μάζες από 225 GeV μέχρι 1 TeV. Εννέα περιοχές σήματος ($1,\ 2,\ 3\ b-tags$ και $0\ell,\ 2e,\ 2\mu$) έχουν καθοριστεί χρησιμοποιώντας το βέλτιστο παράθυρο μάζας του ζέυγους των b κουάρκς ($100 < m_{b\bar{b}} < 140$ GeV) και κάνοντας χρήση τριών μεταβλητών διαχωρισμού (discriminating variables), που χρησιμοποιούνται για να μειώσουν τυχόν συνεισφορά των πιθανών υποβάθρων στην περιοχή του σήματος. Επιπρόσθετα, πέντε περιοχές υποβάθρων έχουν εξεταστεί και εκτιμηθεί όπου η κάθε περιοχή αντιστοιχεί και σε μια κύρια πηγή υποβάθρου ($Z + Jets,\ Z + b,\ Z + b\bar{b},\ W + Jets,\ t\bar{t}$). Αυτό γίνεται για ένα καλύτερο έλεγχο των δειγμάτων MC με τα πραγματικά γεγονότα που χρησιμοποιήθηκαν στην ανάλυση.

Πέντε εκτιμήσεις υποβάθρων (background scale factors) έχουν υπολογιστεί για τις πέντες περιοχές και έχουν εφαρμοστεί στα δείγματα MC για καλύτερη περιγραφή των πραγματικών γεγονότων. Ανώτατα όρια εμπιστοσύνης 95% της ενεργού διατομής του ψευδοβαθμωτού μποζονίου A έχουν υπολογιστεί και για τους δύο μηχανισμούς παραγωγής. Περίσσεια γεγονότων και για τους δύο μηχανισμούς παραγωγής δεν έχει παρατηρηθεί πάνω από το όριο του προβλεπόμενου υποβάθρου, με

αποτέλεσμα όρια αποκλεισμού στην ενεργό διατομή του A μποζονίου να τίθονται και να αποκλείονται οι διατομές από 1 pb για μάζες του A μποζονίου κοντά στην περιοχή $m_h + m_Z \lesssim m_{\mathcal{A}} \lesssim 2 \cdot m_t$ και 0.02 pb για μεγαλύτερες μάζες (μέχρι 1 TeV) στο όριο εμπιστοσύνης 95%. Επίσης, τα όρια αποκλεισμού έχουν ερμηνευτεί στα πλαίσια της θεωρίας 2HDM και για τα τέσσερα είδη Τύπων. Τα αποτελέσματα παρουσιάζονται στο επίπεδο της μεταβλητής $tan\beta$ συναρτήσει της μεταβλητής $cos(\beta-\alpha)$ και της μάζας του μποζονίου A, m_A. Από τα αποτελέσματα παρατηρείται ότι μια μεγάλη περιοχή τιμών των τριών μεταβλητών ($tan\beta$, $cos(\beta-\alpha)$, και m_A) έχει αποκλειστεί από την ανάλυση αυτή, θέτοντας πιο αυστηρά όρια για το συγκεκριμένο κανάλι διάσπασης.

Abstract

The current thesis is dedicated to the study of the search for a heavy pseudoscalar Higgs boson, A, which could decay either to Z boson ($m_Z = 91$ GeV) or to the SM Higgs boson ($m_h = 125$ GeV) as predicted by the Two-Higgs-Doublet Model (2HDM) theory. Final products of such decay mode ($A \to Zh$) are a pair of leptons (e^+e^- and $\mu^+\mu^-$) and a pair of b-quarks ($b\bar{b}$). Additionally, events with missing transverse energy (MET) and a pair of b-quarks as final states are considered too. The analysis of the $A \to Zh \to \nu\bar{\nu}b\bar{b}$ decay channel is pioneered and presented elaborately in this thesis.

The $A \to Zh \to \ell^+\ell^- b\bar{b}$ and $A \to Zh \to \nu\bar{\nu}b\bar{b}$ channels have been searched for the gluon-gluon fusion and b-quark associated production. Thirteen A mass points have been generated in a mass range between 225 GeV and 1 TeV in order to extract results for the four types of the 2HDM theory. Nine signal regions (SRs) have been determined by using the most optimal SM Higgs mass window (100 GeV $< m_{b\bar{b}} <$ 140 GeV) and applying three discriminating variables (kinematic, angular and event shape discriminants) for reducing a possible contribution of the background sources in the signal region.

Five control regions (CRs) for $Z+Jets$, $Z+b$ $Z+b\bar{b}$, $W+Jets$, $t\bar{t}$ background sources were also examined and their background scale factors were computed in order to have the best consistency between MC samples and data. No excess of data over the background prediction is observed and the upper limits are set at 95% confidence level on the product of the A boson production cross sections times the branching ratios $\sigma_A \times Br(A \to Zh) \times Br(h \to b\bar{b})$ for the two Higgs production modes, which exclude 1 pb to 0.02 pb in the 225-1000 GeV mass range of A. The findings of the analysis are interpreted in the 2HDM theory; observed and expected exclusion limits for Type-I, Type-II, Flipped and Lepton-specific Types are presented in the planes $tan\beta$ versus $cos(\beta - \alpha)$ and $tan\beta$ versus m_A, reducing considerably the allowed parameter space for extensions of the Standard Model.

Acknowledgements

My journey in the magic of the Experimental Particle Physics world is going to be finished soon and it would not fair to me to not refer to people who helped and supported me to complete this doctoral thesis.

First of all, I would like to express my deepest and sincerest gratitude to my supervisor Professor Panos Razis, who had given me the opportunity to become his PhD student. He has supervised and guided me to complete this research work sharing his enormous knowledge with me. He was always willing to help me providing a solution of any obstacle that I had encountered even it was one or two o'clock in the morning. As the most expert on High Energy Physics he has always inspired me in any meeting that we had together. I am very grateful for his continuum guidance and the huge amount of scientific knowledge that I had adopted from him. It was an honour for me to have him as my supervisor. I really really thank Prof. Panos Razis for everything that you gave me in these years. I could continue writing for hours expressing my feelings for him but even though, I wouldn't manage to find a suitable word to express my thankfulness.

Second, I would like to thank Mr Charalambos Nicolaou and Dr. Jehad Mousa for their great support and patient guidance. Dr. Jehad Mouse was also willing to teach me how to program and perform any kind of CMS analysis or search. We have spent a lot of his precious time in his office by programming and debugging codes. He is a distinguished scientist and I was very lucky to work with him. Also, Mr. Charalambos Nicolaou did not stop giving me his support and valuable advices in these years. I really appreciate all that things that he has done for me and I really express my deepest gratitude to him.

Third, I would like to give special thanks to Dr. Alberto Zucchetta from University of Zurich who was my colleague in this journey. We worked hardly together to finish this study presenting our findings at many CMS meetings and workshops. With his guidance and expertise I finally completed my PhD thesis, acquiring a great knowledge from him.

Also, I want to thank my parents, Prodromos and Panayiota, for their endless love and support.

Without them I would achieve nothing. Everything that I have done was because of them and their love.

Last but not least I could not forget to thank my lovely wife Emily for everything that she has done for me. My PhD thesis is dedicated to her for her support that gave me all these years. Without her presence I could not finish my dissertation and any successful goals would not be achievable. She always is there for me and she was my travel buddy in my postgraduate studies by caring me all the time. She never complains and with her positive energy I managed to write this doctoral thesis. I am very extremely lucky to have such wonderful wife who can trust me and support me for everything. I really appreciate all that things that she has done for me and a small thing that I should do is to dedicate my dissertation to her.

List of Publications

1. The CMS Collaboration, "Search for a heavy pseudoscalar boson decaying to a Z and a Higgs boson at $\sqrt{s} = 13$ TeV", *Eur. Phys. J. C* **79**, 564 (2019), https://doi.org/10.1140/epjc/s10052-019-7058-z

Contents

List of Figures

List of Tables

Introduction

In 2012, the ATLAS and CMS Collaborations observed a particle with mass 125 GeV which could literally be the Higgs boson of the Standard Model (SM). Indeed, this particle with mass 125 GeV is now considered to carry the properties of the Higgs boson which is predicted by the Standard Model theory, that was remaining unobservable for many decades. By the discovery of the Higgs boson, the SM was established as the most remarkable theory in High Energy Physics. However, despite the fact that the SM is consistent with the experimental data, it cannot sufficiently explain some features, thus exhibiting some problems, such as the hierarchy problem, the lag of unification of couplings, the lifetime of proton and so on. Therefore, new theories were proposed to address the shortcomings of the SM, such as the Two-Higgs-Doublet Model (2HDM) [1].

The Two-Higgs-Doublet Model is the simplest extension of the SM and can predict five physical states of the Higgs boson, by introducing an additional scalar doublet. Taking advantage of the one physical state of the Higgs boson to be the SM Higgs particle (h), the 2HDM becomes the most promising theory beyond the SM which can address many issues and problems of the SM [2]. The remaining physical states are two charged Higgs bosons ($H^{\pm}$), a CP-even Higgs boson (H), and a heavy CP-odd Higgs boson (A) which could have masses at or below the TeV scale, which is a regime accessible to the Large Hadron Collider (LHC) physics program.

As mentioned, 2HDM is a theory which contains two scalar Higgs doublets. The advantages of this kind of model is that the additional doublet can cancel any anomalies which arise from the scalars in chiral multiplets together with chiral spin $-1/2$ (a case of supersymmetry) and the second doublet is also able to give mass to the charge $2/3$ and $-1/3$ quarks, simultaneously. Moreover, the other motivation comes from Axion models [3] in which a CP-violating term in the QCD Lagrangian can be rotated away if the Lagrangian contains a global U(1) symmetry which can be only imposed if there are two Higgs doublets. Another advantage of the two-Higgs-doublet model is the generation of a baryon asymmetry in the Universe of sufficient size due to the flexibility of the scalar mass spectrum of the 2HDM theory and the existence of additional

sources of CP violation. The 2HDM model could have two independent CP-violating phases which could account for the matter-antimatter imbalance.

Four different Types which are separated by the coupling of fermions to scalar doublets are included in the 2HDM theory. In Type-I all fermions couple to the Higgs fields in the second scalar doublet. In Type-II, down-type quarks and charged leptons couple to the Higgs field of the first scalar doublet and up-type quarks couple to the second one. In the Flipped Type, up-type quarks and charged leptons couple to the second scalar doublet, however, down-type quarks couple to the first scalar doublet. Finally, in the Lepton-specific Type, all quarks couple to the Higgs field of the second doublet and charged leptons couple to the first doublet.

The cross sections and branching fractions of the five physical states of the Higgs bosons are affected by the Type of 2HDM. However, the production cross section of the heavy pseudoscalar Higgs boson, A, has less impact than the other Higgs bosons and the primary decay mode is the $A \to Zh$ channel in any 2HDM Type when the mass of A lies between the sum of the Higgs and the Z boson masses and two times the top mass [1].

The heavy pseudoscalar Higgs boson, A, might be produced by two Higgs production modes: gluon-gluon fusion and b-quark associated production mode. The production cross section for the pseudoscalar boson A depends on the value of $tan\beta$ which is defined as the fraction of the two vacuum expectation values of the two higgs doublets and on the mass of the A boson. In the gluon-gluon fusion, the cross section for the A boson is dominant for centre-of-mass energy 13 TeV ($\sigma_{ggA} \approx 10^6$ fb as presented in Chapter 5.2.1) for the lowest value of $tan\beta$ ($tan\beta = 0.1$) and for the range of the A mass between 250 and 350 GeV. However, the production cross section in the b-quark associated production is dominant for the highest value of $tan\beta$ in Type-II and the Flipped Type only as described in Chapter 5.2.1. Additionally, the branching ratio of the decay mode $A \to Zh$ is similar among the four Types of 2HDM and decreases sharply at about $m_A \simeq 2 \cdot m_{top}$ because of the opening of the $A \to t\bar{t}$ channel in all Types of 2HDM.

In fact, the $A \to Zh$ channel is the primary decay mode, in particular when the Z boson decays leptonically and the SM Higgs boson decays into a pair of b-quarks. The $h \to b\bar{b}$ channel is the most preferable decay mode from any other mode, due to its large branching ratio ($\sim 58\%$). In addition, when the Z boson decays into a pair of leptons ($e^{\pm}$ or $\mu^{\pm}$), the background processes might be easily suppressed due to the clean final states of the Z decays.

Considering that the $A \to Zh \to \ell^+\ell^- b\bar{b}$ decay mode is favoured in all Types of 2HDM, the ATLAS and CMS Collaborations have carried out searches for signatures of the heavy pseudoscalar A boson in 2HDM. The latest results relevant with this channel are shown in Fig. 1, which shows the 95% CL exclusion limits for the $A \to ZH \to \ell^+\ell^- b\bar{b}$ channel in the m_H

vs. $tan\beta$ plane in two 2HDM scenarios of Type-I and Type-II. As it is shown in the figure, the parameter space of the $A \to ZH \to \ell^+\ell^- b\bar{b}$ decay mode, which is excluded by the CMS analyses, is small and therefore a rich parameter space is still unexamined. The channel was investigated for the lowest values of $tan\beta$ up to 3 and for the A mass up to 350 GeV. Additionally, exclusion limits for three additional decay modes ($H \to WW/XX$, $A/H/h \to \tau\tau$, and $A \to ZH \to \ell\ell\tau\tau$) are computed and presented in the same contour plot. As we know from the 2HDM theory, the $A \to Zh \to \ell^+\ell^- b\bar{b}$ could be produced for larger values of $tan\beta$ and m_A; also, it could be presented in the Flipped and Lepton-specific Types too. As a consequence, it would be wise if the $A \to ZH \to \ell^+\ell^- b\bar{b}$ is investigated further.

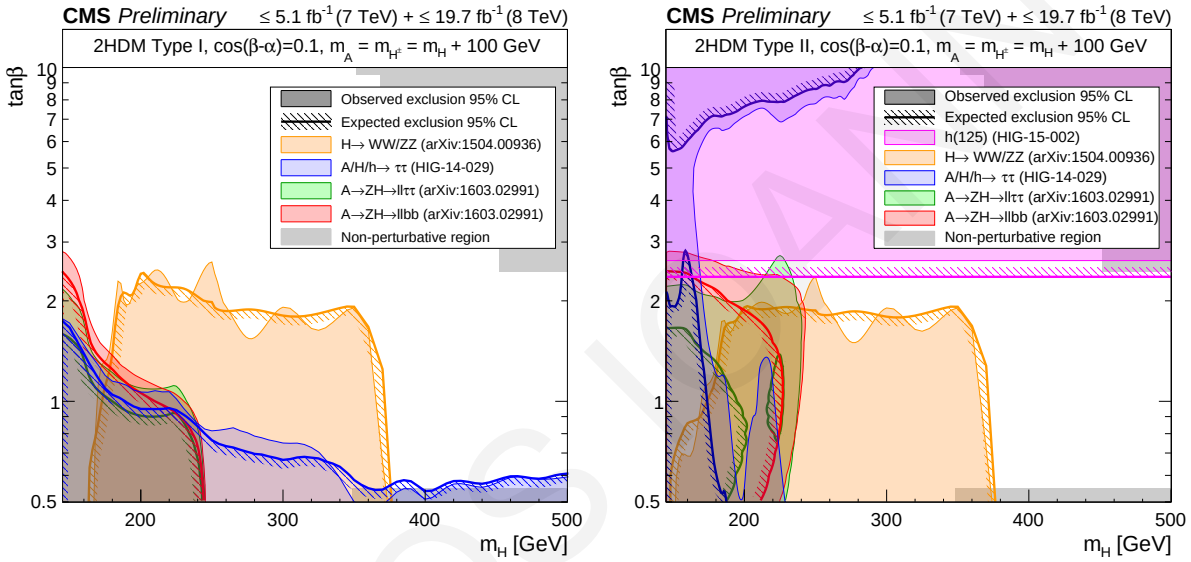

Figure 1: 95% CL exclusion limits, in two 2HDM scenarios of (left) Type-I and (right) Type-II as obtained by CMS analyses that have been performed on the LHC run-1 dataset. Taken from Ref. [4].

This thesis is dedicated to the search for signatures of a heavy CP-odd Higgs boson via the decay mode: $A \to Zh \to \ell^+\ell^-(\nu\bar{\nu})b\bar{b}$, by using data of integrated luminosity 35.9 fb^{-1} which were collected in 2016 by the CMS experiment at $\sqrt{s} = 13$ TeV. The analysis is performed by searching two same type and opposite charged leptons (e^+e^-, $\mu^+\mu^-$) or a pair of neutrinos with a pair of b-quarks as final states. The channel is examined in the Type-I, Type-II, Flipped and Lepton-specific Types and our findings are finally interpreted in the 2HDM theory.

In Chapter 1, a brief description of the SM and the Higgs sector are presented. In addition, the latest results relevant with the SM Higg decay modes are shorty described. The most important problems which should be addressed by theories beyond the SM are reported at the beginning of Chapter 2. Moreover, the 2HDM theory is presented in detail and mass matrices and wave

functions of the five physical Higgs states are derived, covering the Higgs sector of 2HDM. Furthermore, Higgs decays and branching ratios are highlighted by emphasising the $A \to Zh$ decay mode and the corresponding branching fractions. Chapter 3 and Chapter 4 describe the Large Hadron Collider and the CMS experiment, respectively.

The entire analysis of $A \to Zh \to \ell^+\ell^-(\nu\bar{\nu})b\bar{b}$ decay mode is presented in Chapter 5. This chapter describes the analysis strategy followed to reconstruct the Z, h and A boson candidates from the visible decay products or the missing energy reconstructed in the events. Thirteen signal samples of A mass points between 225 GeV and 1 TeV are produced for the gluon-gluon fusion and b-quark associated production. The mass range is extended up to 1 TeV for covering also the regions where the $A \to Zh$ decay channel is less dominant as predicted by 2HDM [1].

Furthermore, in Chapter 5, we describe the way how to identify and select the best b-quarks which reconstruct the Higgs candidate. Two jets with the highest-scoring Combine Secondary Vertex (CSV) algorithm [5] in the event are selected to reconstruct the Higgs candidate. The b-tagging of our analysis is highly accurate and only 3% of the events have not correctly-associated jets. Additionally, various techniques are used to suppress the background processes as much as possible by increasing the signal sensitivity. Six different CSV working points and eleven Higgs mass windows are defined and examined in order to choose the most optimal scenarios. Three discriminating variables are utilised to get rid of the irreducible backgrounds. The first one exploits the fact that the masses of the h and Z bosons are known by improving the A mass resolution by $1 \sim 2\%$. The second discriminating variable is an angular discriminator which is a combination of helicity variables and helps discriminate the signal against the $Z + b\bar{b}$ background. Finally, the event discriminator is constructed by a combination of the Z mass and the missing energy of the event aiming to reject the $t\bar{t}$ background.

Nine different signal regions are defined (1, 2, or 3 b-tags and 0ℓ, $2e$, 2μ) in this analysis and the final signal efficiency ranges between 10% and 20%. On the other hand, five control regions for the most important background sources, such as $Z + jets$, $Z + b$, $Z + b\bar{b}$, $W + jets$, $t\bar{t}$, are defined in order to check and validate the Monte Carlo prediction. These regions are used to constrain the main background normalisations.

Chapter 5 ends with the presentation of the results of the $A \to Zh$ analysis. Before determining the 95% confidence-level limit on the signal contribution in the data, background scale factors are derived by performing a background-only fit with the signal regions blinded. The consistency between data and SM backgrounds is very good given that the scale factors are approximately equal to unit for each background source. Finally, no excess of data over the background prediction is observed and the upper limits are set at 95% confidence level on the product of the

A boson production cross sections and the branching ratios $\sigma_A \times Br(A \to Zh) \times Br(h \to b\bar{b})$, which exclude 1 to 0.02 pb in the 225-1000 GeV mass range. All possible systematic uncertainties are included to the calculation of the results and are highlighted in this channel. The thesis concludes with an interpretation of the result in term of Two-Higgs-Doublet Models. Observed and expected exclusion limits for Type-I, Type-II, Flipped and Lepton-specific models as a function of $cos(\beta - \alpha)$ and $tan\beta$ (m_A and $tan\beta$) are presented.

Part I

Theoretical Background

Chapter 1

The Standard Model And The Discovery Of The Higgs Boson

Everything in the Universe is built from a few ingredients, called fundamental particles, which are governed by four forces. Electromagnetic, strong, weak forces and gravity play an essential role in the whole Universe. The first three forces are described by a unique and powerful theory, called "The Standard Model" (SM), providing a successful explanation of the interactions among the known particles with a remarkably high precision. The SM provides a sufficient clarification on how the mediator vector fields of weak interaction gain masses through the mechanism of Spontaneous Symmetry Breaking (SSB), called the Higgs Mechanism. For many decades, this prospective theory was remaining unverified due to the lack of sufficiently high energies, suitable detectors and accelerators. The Higgs boson is the evidence that completed the puzzle of the Standard Model; in 2008, the Large Hadron Collider (LHC) was constructed to collide high energy proton beams. With the help of the CMS and the ATLAS experiments which collected data, scientists discovered an evidence for the existence of the Higgs boson, confirming the SM. This Chapter describes the Standard Model, the Higgs Mechanism and experimental searches for the discovery of the Higgs boson.

1.1 The Standard Model

The *Standard Model (SM)* is a theory which describes the electromagnetic, weak and strong interactions with a simple structure and classifies all known fundamental particles. It is a unified description in terms

of gauge theories of all interactions of known particles, with the absence of gravity.

Additionally, the SM is described by the field theory of $SU(3)_C \otimes SU(2)_L \otimes U(1)_Y$, which is a combination of three symmetry groups. The $SU(3)_C$ group corresponds to the gauge theory called *Quantum Chromo-Dynamics (QCD)*, which describes the interactions between quarks of different colours. In this theory the quarks occupy an internal property called *"colour"* and its gauge bosons are named *"gluons"* which play the role of the mediators of the strong interaction. There are eight massless spin-one gauge bosons in the $SU(3)_C$ symmetry group.

The $SU(2)_L \otimes U(1)_Y$ group was studied in detail by Glashow [6], Salam[7] and Weinberg [8], who combined the electromagnetic interactions with the Weak Interactions. This symmetry group is spontaneously broken into the $U(1)_{em}$ subgroup of *Quantum Electrodynamics (QED)* through the *Higgs Mechanism* and the $SU(2)_L$ subgroup of the Weak Interactions. The Higgs Mechanism is the procedure through which the mediators of the weak interactions, $W^{\pm}$ and Z gain masses. On the other hand, the electromagnetic interactions are described by the $U(1)_{em}$ symmetry group in which a massless and electrically-neutral photon (γ) plays the role of the mediator. The mediators of the three interactions as well as their quantum numbers (J^P), their charge (Q) and their Isospin (I_3), are reported in Tab.1.1.

Mediator	Interaction	Mass	J^P	Q	I_3
Photon (γ)	Electromagnetic	-	1^-	0	0
Z^0	Weak	$91.18 GeV/c^2$	1	0	0
$W^{\pm}$	Weak	$80.40 GeV/c^2$	1	$\pm e$	± 1
8 gluons (g)	Strong	-	1^-	0	0

Table 1.1: The three interactions and their mediators.

In 1964, Gell-Mann and Zweig independently postulated that the SM could be constituted by fundamental particles which could be used to describe a large number of the observed particles at the time. These fundamental particles are named quarks which are fermions with $\frac{1}{2}\hbar$-spin and fractional charge. Overall, the SM has six flavours of quarks (u, d, s, c, b, t) and six leptons $(e, \mu, \tau, \nu_e, \nu_\mu, \nu_\tau)$ together with their corresponding anti-particles. As mentioned, the SM is based on the symmetry group $SU(3)_C \otimes SU(2)_L \otimes U(1)_Y$, and the left- and right-handed components of the quark and lepton fields are assigned to different representations of the group due to the chiral structure of the weak interactions. Moreover, quarks and leptons are divided into three generations, in doublets and singlets of a representation of the $SU(2)$ symmetry group. The content of the SM and their quantum numbers are shown in Tab. 1.2.

The fundamental particles of the SM can be found in Tab. 1.2 without the presence of the mediators and the Higgs boson. As reported from Tab. 1.2, the leptons have integer electric charges in contrast to the quarks that they have electric charges which are not integer multiple of the electron charge e. The

Fermions	First	Second	Third	Q	$U(1)_Y$	$SU(2)_L$	$SU(3)_C$
Leptons	$\begin{pmatrix}\nu_e\\ e\end{pmatrix}_L$	$\begin{pmatrix}\nu_\mu\\ \mu\end{pmatrix}_L$	$\begin{pmatrix}\nu_\tau\\ \tau\end{pmatrix}_L$	0 -1	-1/2	2	1
	$\nu_e R$	$\nu_\mu R$	$\nu_\tau R$	0	0	1	1
	e_R	μ_R	τ_R	-1	-1	1	1
Quarks	$\begin{pmatrix}u\\ d\end{pmatrix}_L$	$\begin{pmatrix}c\\ s\end{pmatrix}_L$	$\begin{pmatrix}t\\ b\end{pmatrix}_L$	$+2/3$ -1/3	$+1/6$	2	3
	u_R	c_R	t_R	$+2/3$	$+2/3$	1	3
	d_R	s_R	b_R	-1/3	-1/3	1	3

Table 1.2: The quantum numbers of the SM fermions under the $SU(3) \times SU(2)_L \times U(1)_Y$ symmetry for the left- and right-handed particles.

electric charge for the up-type quarks is $+\frac{2}{3}e$ and $-\frac{1}{3}e$ for down-type quarks. Quarks are met in the Universe either as a combination of two or three. Their products built by a quark and an anti-quark ($q\bar{q}$), are called *mesons* and the other kind of their products are *baryons*, which consist of three quarks qqq or three anti-quarks $\bar{q}\bar{q}\bar{q}$. Mesons and baryons are named *hadrons* in the physics language.

Whatever we mentioned up to now, fundamental particles, mediators and interactions among them can be mathematically described by a compact and unique Lagrangian, as follows [9]:

$$\begin{aligned}\mathcal{L}_{\mathcal{SM}} = &-\frac{1}{4}W_{\mu\nu}\cdot W^{\mu\nu} - \frac{1}{4}B_{\mu\nu}B^{\mu\nu}\\ &+\bar{L}\gamma^\mu\left(i\partial_\mu - g\frac{1}{2}\tau\cdot W_\mu - g'\frac{Y}{2}B_\mu\right)L + \bar{R}\gamma^\mu\left(i\partial_\mu - g'\frac{Y}{2}B_\mu\right)R\\ &+\left|\left(i\partial_\mu - g\frac{1}{2}\tau\cdot W_\mu - g'\frac{Y}{2}B_\mu\right)\phi\right|^2 - V(\phi)\\ &-\left(G_1\bar{L}\phi R + G_2\bar{L}\phi_c R + \text{hermitian conjugate}\right)\end{aligned} \tag{1.1}$$

- $-\frac{1}{4}W_{\mu\nu}\cdot W^{\mu\nu} - \frac{1}{4}B_{\mu\nu}B^{\mu\nu}$: $W^\pm, Z, \gamma$ kinetic energies and self-interactions.
- $+\bar{L}\gamma^\mu\left(i\partial_\mu - g\frac{1}{2}\tau\cdot W_\mu - g'\frac{Y}{2}B_\mu\right)L + \bar{R}\gamma^\mu\left(i\partial_\mu - g'\frac{Y}{2}B_\mu\right)R$: lepton and quark kinetic energies and their interactions with $W^\pm, Z, \gamma$.
- $+\left|\left(i\partial_\mu - g\frac{1}{2}\tau\cdot W_\mu - g'\frac{Y}{2}B_\mu\right)\phi\right|^2 - V(\phi)$: $W^\pm, Z, \gamma$, and Higgs masses and couplings.
- $-\left(G_1\bar{L}\phi R + G_2\bar{L}\phi_c R + \text{hermitian conjugate}\right)$: lepton and quark masses and couplings to the Higgs.

where $\boldsymbol{L}$ denotes a left-handed fermion (lepton or quark) doublet, $\boldsymbol{R}$ denotes a right-handed fermion singlet, $\boldsymbol{W^\mu}$ represents the three vector bosons and $\boldsymbol{B^\mu}$ is related to a fourth vector boson field. In

addition, generators of the SU(2) group of gauge transformation are represented by $\boldsymbol{T}$ and they can be replaced by the isospin version of the Pauli matrices $\boldsymbol{\tau}$, as follows:

$$\boldsymbol{T} = \frac{\boldsymbol{\tau}}{\mathbf{2}} \tag{1.2}$$

and $\boldsymbol{\Upsilon}$ signifies a generator of the $U(1)_Y$ group, named *hypercharge*. A deep study of the SM Lagrangian reveals that four Dirac γ matrices are used and g indicates the coupling of $SU(2)_L$ symmetry, g' is the coupling of $U(1)$ symmetry and finally, eight gauge fields are represented by G, corresponding to the gluons. This Lagrangian describes the entire Standard Model theory.

1.2 THE ELECTROWEAK INTERACTION AND SYMMETRY BREAKING

As reported in Chapter 1.1, massless, massive particles and their interactions are included in the SM Lagrangian by an elegant way. However, how can particles acquire a mass and they appear in the Lagrangian? The question can be addressed by *Electroweak Symmetry Breaking* which is responsible for the appearance of massive gauge bosons in the SM Lagrangian. Without Electroweak Symmetry Breaking, massive bosons would not exist in the Lagrangian and its form would be completely different due to the absence of mass terms. If there was no symmetry breaking, mass terms for fermions and gauge bosons would not appear in the SM Lagrangian because only singlets could gain a mass with an interaction of $m^2\phi^\dagger\phi$ without breaking the gauge invariance in the $SU(3)_C \times SU(2)_L \times U(1)_Y$ symmetry. Fortunately, the symmetry breaking occurs in the SM and its Lagrangian consists of mass terms and interactions, implying massive gauge bosons.

1.2.1 ELECTROWEAK INTERACTION

Glashow tried to unify Electromagnetic and Weak interactions based on the $SU(2)_L \times U(1)_Y$ symmetry group, named Electroweak theory or Electroweak interaction, at the end of the 1960s [10]. The Electroweak theory includes electromagnetic and weak interactions with neutral currents (NC) and charged currents (CC). In this theory photons and massive vector bosons ($W^\pm, Z^0$) are introduced together as gauge massless fields. However, the Electroweak interaction must be broken to be consistent with experimental findings such as massive vector bosons and massless photons.

The Electromagnetic theory and the weak interaction theory are connected by the following equation:

$$Y = 2(Q - I_3) \tag{1.3}$$

where Y is the weak hypercharge for the $U(1)_Y$ group and I is referred to as the weak isospin charge

for $SU(2)_L$ group and both are linked to the charge Q. In addition, I_3 is the third component of the weak isospin in Eq. 1.3.

In order to unify the electromagnetic interaction with the weak interaction a new conserved current has to be introduced. In the weak interaction there are three conserved currents [11], $J_\mu^\pm$ and J_μ^3. The two charged currents $J_\mu^\pm$ interact only with left-handed particles or right-handed antiparticles and, the weak isospin current, J_μ^3, couples only to left-handed fermions.

In general, charged currents, J_μ^{CC}, can connect leptons in the same or different generations and may also link quarks of different generations as described in the Cabibbo-Kobayashi-Maskawa matrix (CKM). In the case of the neutral current interaction, J_μ^{NC}, the neutral current does not change the flavour of a lepton, which participates in the reaction. However, when fermions are quarks, it appears an anomaly (*Flavour Changing Neutral Currents* -FCNC-), where the neutral current changes the strangeness flavour, connecting strange and down quarks. Fortunately, this anomaly is strongly suppressed at the tree level by the Glashow-Iliopoulos-Maiani (GIM) mechanism [12].

Additionally, the weak neutral currents (J_μ^{NC}) have a right-handed component and consequently, the weak isospin current cannot be identified as weak neutral current because it couples only to left-handed fermions. Also, the electromagnetic current is a neutral current with right- and left-handed components and therefore, a new conserved current, j_μ^Y, should be introduced in order to achieve the electroweak unification. The new conserved current is included together with J_μ^3 in the definition of the electromagnetic current, as follows:

$$j_\mu^{em} = J_\mu^3 + \frac{1}{2} j_\mu^Y \tag{1.4}$$

The j_μ^Y is called the weak hypercharge current and it is given by:

$$j_\mu^Y = \bar{\psi} \gamma_\mu Y \psi \tag{1.5}$$

where the weak hypercharge Y is defined by Eq. 1.3, ψ is the wavefunction of a particle and γ_μ the gamma matrices.

Despite the fact that Eq. 1.4 practically achieves the unification of the electromagnetic and weak interactions, the symmetry requires that W and Z bosons and all fermions are massless, which it is not consistent with the experimental findings. Experimental data indicate that the Z and $W^\pm$ bosons are massive, with masses 91.1876 ± 0.0021 GeV and 80.385 ± 0.015 GeV, respectively [13]. Fortunately, a solution of this inconsistency, called *Spontaneous Symmetry Breaking (SSB)*, can resolve the problem of massless and massive particles and it is presented in the following section.

1.2.2 ELECTROWEAK SYMMETRY BREAKING

As mentioned, the invariance of the Lagrangian of the three interactions implies that their mediators are massless. However, this statement is inconsistent with the fact that W, Z bosons, and fermions are not massless.

The inconsistency is solved by assuming a spontaneous breaking of the gauge theory. In a spontaneous breakdown, the lowest energy state (the physical vacuum) is not a zero but it is a member of a set of physically equivalent states. This degeneracy of the vacuum induces scalar fields, having vacuum expectation values different from zero.

Indeed, in 1961, Goldstone proved that the spontaneous breaking of a symmetry leads to massless scalar bosons, when the symmetry is not explicitly broken. Scalar bosons can be generated by the spontaneous breaking as many as the symmetry group allows. Three years later, Englert & Brout [14], and Higgs [15] showed independently that the Goldstone boson becomes unphysical if the symmetry group of the Lagrangian is extended from global to local transformations by introduction the coupling of a vector gauge field.

In Quantum Field Theory (QFT), a system is described by its Lagrangian which is the difference between kinetic and potential energy densities. In the case of the Electroweak theory, which is described by the $SU(2) \times U(1)$ symmetry group, the spontaneous breaking occurs when a potential density $V(\Phi)$ is included in the terms of Lagrangian consisting of a scalar complex field Φ, which is an isospin doublet:

$$\Phi = \begin{pmatrix} \phi^+ \\ \phi^0 \end{pmatrix} = \begin{pmatrix} \phi_1^+ + i\phi_2^+ \\ \phi_3^0 + i\phi_4^0 \end{pmatrix} \tag{1.6}$$

By adding the scalar complex field, the potential of the Lagrangian is:

$$V(\Phi) = \frac{1}{2}\mu^2\Phi^2 + \frac{1}{4}\lambda\Phi^4 \tag{1.7}$$

where Φ^2 is defined, as follows:

$$\Phi^2 \equiv \Phi^+\Phi = (\phi^{*-}\phi^{*0})\begin{pmatrix} \phi^+ \\ \phi^0 \end{pmatrix} \tag{1.8}$$

As it is highlighted, the potential contains two terms where the first one is proportional to Φ^2 and the second term corresponds to $\frac{1}{4}\lambda\Phi^4$. If the potential was described by a term proportional to Φ^2 only, the potential energy density would correspond to scalar particles with mass μ. However, the presence of the term proportional to Φ^4 indicates the self-interactions among scalar fields.

When Φ is real, the potential is minimized by taking the first partial derivative of Φ and setting a

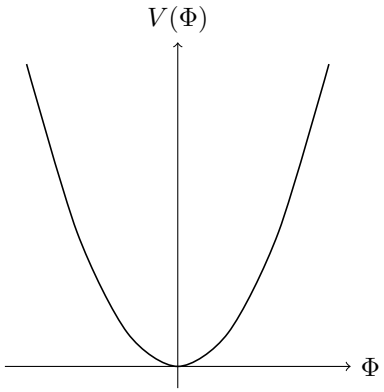

Figure 1.1: The shape of potential $V(\Phi)$ where $\mu^2 > 0$ and $\lambda > 0$.

consequent equation to be equal to zero:

$$\frac{\partial V}{\partial \Phi}\Big|_{\Phi_{min}} = \Phi(\mu^2 + \lambda\Phi^2) = 0 \tag{1.9}$$

As it is easily noticed from Eq. 1.9, choosing the parameter μ^2 to be greater than zero ($\mu^2 > 0$), the vacuum corresponds to $\Phi_{min} = 0$. By taking into account the zero as the vacuum, the potential is minimized at zero ($V(\Phi_{min}) = 0$), as expected. The field and the potential are zero in the minimum energy state as shown in Fig. 1.1.

On the other hand, if the parameter μ^2 is set to be negative ($\mu^2 < 0$) and the parameter λ is still positive, the minimum of the potential is not zero and the choice of the ground state is arbitrary. The system state is not symmetric anymore under $SU(2)$ group, and the chosen coordinate is not invariant under transformation in the (ϕ^+, ϕ^0) space; this is known as the *Spontaneous Symmetry Breaking (SSB)*. The shape of the scalar potential $V(\Phi)$ is sketched in Fig. 1.2 where the choice of $\Phi = 0$ is not a minimum of the potential.

By taking into account μ imaginary $\mu^2 < 0$, Eq. 1.9 will have two solutions, as follows:

$$\Phi_{min} = \pm\sqrt{\frac{-\mu^2}{\lambda}} \equiv \pm\upsilon \tag{1.10}$$

In addition, it is important to note that considering μ imaginary, there will be no physical objects with imaginary mass. The solutions of Eq. 1.10 are called vacuum expectation values (VEVs) and by replacing them to the potential Eq. 1.8, one will find that the potential density has the same value in both minima, as shown in Fig. 1.2.

$$V(\Phi_{min}) = -\frac{1}{4}\frac{\mu^4}{\lambda} = -\frac{\lambda}{4}\upsilon^4 \tag{1.11}$$

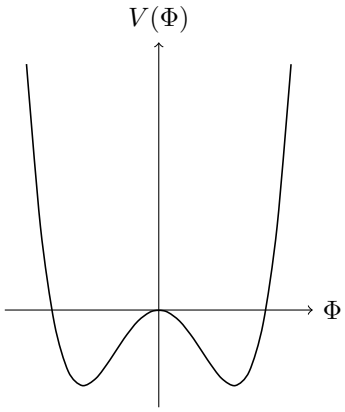

Figure 1.2: The shape of potential $V(\Phi)$ where $\mu^2 < 0$ and $\lambda > 0$.

1.3 THE HIGGS MECHANISM

Despite the fact that massless particles appear in the terms of the potential according to the Goldstone theorem, the mass problem remains unsolved. Indeed, it makes the problem worse since it requires massive states instead of massless particles. Fortunately, the mass problem was solved by a formation of massive particles cased by the Higgs Mechanism.

Consider the following doublet:

$$\Phi = \begin{pmatrix} \phi^+ \\ \phi^0 \end{pmatrix} \equiv \begin{pmatrix} \frac{1}{\sqrt{2}}(\phi_1 + i\phi_2) \\ \frac{1}{\sqrt{2}}(\phi_3 + i\phi_4) \end{pmatrix} \tag{1.12}$$

The doublet is called the Higgs boson field and is written in $SU(2)_L$ group symmetry with two scalar components. The Higgs' Lagrangian includes kinetic and potential terms, as follows:

$$\mathcal{L}_{Higgs} = (D^\mu \Phi)^\dagger D_\mu \Phi - V(\Phi) = (D^\mu \Phi)^\dagger D_\mu \Phi - \mu^2 \Phi^\dagger \Phi - \lambda(\Phi^\dagger \Phi)^2 \tag{1.13}$$

By requiring μ imaginary and λ positive, the potential is very similar to the potential arisen from the breaking of symmetry, as seen in Fig. 1.3. In addition, the doublet can be simplified by setting the positive component zero and the other one equal to the vacuum expectation value of the symmetry breakdown, as follows:

$$\Phi = \frac{1}{\sqrt{2}} \begin{pmatrix} 0 \\ \upsilon \end{pmatrix} \tag{1.14}$$

where

$$\upsilon^2 = \frac{-\mu^2}{\lambda} \tag{1.15}$$

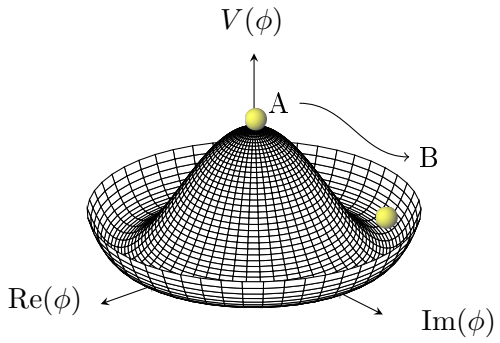

Figure 1.3: The Higgs potential and the symmetry breakdown

In the Higgs mechanism, one can consider fluctuations around the vacuum expectation value:

$$\Phi = \frac{1}{\sqrt{2}}\begin{pmatrix} 0 \\ \upsilon + H(x) \end{pmatrix} \tag{1.16}$$

where $H(x)$ describes the fluctuations around the Higgs minimum value. Thanks to the Higgs mechanism, after the symmetry breakdown, three bosons acquire mass $(W^{\pm}, Z)$, and one remains massless (γ), solving the mass problem which is described in Electroweak Symmetry Breaking. By taking into account the Higgs related-terms and the sector related to the gauge fields, the Lagrangian is written:

$$\begin{aligned} \mathcal{L}_{GH} &= \mathcal{L}_{gauge} + \mathcal{L}_{Higgs} \\ &= -\frac{1}{4}W_i^{\mu\nu}W^i_{\mu\nu} - \frac{1}{4}B^{\mu\nu}B_{\mu\nu} + (D^{\mu}\Phi)^{\dagger}D_{\mu}\Phi - \mu^2\Phi^{\dagger}\Phi - \lambda(\Phi^{\dagger}\Phi)^2 \end{aligned} \tag{1.17}$$

where D_{μ}:

$$D\mu = \partial_{\mu} - igW^{\alpha}_{\mu}T_{\alpha} - ig'\frac{Y}{2}B_{\mu} \tag{1.18}$$

The covariant derivative acts on field Φ, by giving the following results:

$$\begin{aligned} (D^{\mu}\Phi)^{\dagger}D_{\mu}\Phi =& \frac{1}{2}\partial^{\mu}H\partial_{\mu}H \\ &+ \frac{1}{8}(\upsilon + H)^2 g^2 (W^{1\mu} + iW^{2\mu})(W^1_{\mu} - iW^2_{\mu}) \\ &+ \frac{1}{8}(\upsilon + H)^2 (g'B^{\mu} - gW^{3\mu})(g'B_{\mu} - gW^3_{\mu}) \end{aligned} \tag{1.19}$$

where

$$W_3^\mu = sin\theta_W A^\mu + cos\theta_W Z^\mu \tag{1.20a}$$
$$B^\mu = cos\theta_W A^\mu - sin\theta_W Z^\mu \tag{1.20b}$$
$$\tag{1.20c}$$

or, equivalently:

$$Z^\mu = -sin\theta_W B^\mu + cos\theta_W W_3^\mu \tag{1.21a}$$
$$A^\mu = cos\theta_W B^\mu + sin\theta_W W_3^\mu \tag{1.21b}$$
$$W_\mu^\pm = \frac{1}{\sqrt{2}}(W_\mu^1 \pm iW_\mu^2) \tag{1.21c}$$

The angle of the above equations is the mixing angle θ_W known as Weinberg angle and defined as follows:

$$cos\theta_W = \frac{g}{\sqrt{g^2 + g'^2}} \qquad sin\theta_W = \frac{g'}{\sqrt{g^2 + g'^2}} \tag{1.22}$$

Gathering all formulas and mathematical definitions together, the Lagrangian can be written as:

$$\begin{aligned}\mathcal{L}_{GH} = & \frac{1}{2}\partial^\mu H \partial_\mu H - \mu^2 H^2 \\ & - \frac{1}{4}(\partial_\mu W_{1\nu} - \partial_\nu W_{1\mu})(\partial_\mu W_1^\nu - \partial_\nu W_1^\mu) + \frac{1}{8}g^2\upsilon^2 W_{1\mu}W_1^\mu \\ & - \frac{1}{4}(\partial_\mu W_2\nu - \partial_\nu W_{2\mu})(\partial_\mu W_2^\nu - \partial_\nu W_2^\mu) + \frac{1}{8}g^2\upsilon^2 W_{2\mu}W_2^\mu \\ & - \frac{1}{4}(\partial_\mu Z_\nu - \partial_\nu Z_\mu)(\partial_\mu Z^\nu - \partial_\nu Z^\mu) + \frac{1}{8}(g^2 + g'^2)\upsilon^2 Z_\mu Z^\mu \\ & - \frac{1}{4}(\partial_\mu A_\nu - \partial_\nu A_\mu)(\partial_\mu A^\nu - \partial_\nu A^\mu)\end{aligned} \tag{1.23}$$

The Higgs mass term and massive gauge bosons appear from nowhere in the formula and simultaneously, a massless particle is presented, satisfying the symmetry $U(1)_{em}$. The second term in Eq. 1.23 represents the mass of the Higgs boson:

$$m_H = \sqrt{2\mu} = \sqrt{2\lambda}\upsilon \tag{1.24}$$

At this point, it is worth noting that the parameter υ is related to the *Fermi constant*, G_F, by the relation:

$$\upsilon^2 = \frac{1}{\sqrt{2}G_F} \simeq (246\ \text{GeV})^2 \tag{1.25}$$

The G_F was written by Enrico Fermi in 1933 when he wrote down the effective Lagrangian for the

low-energy weak interactions, proportional to positive and negative currents:

$$\mathcal{L} = -2\sqrt{2}G_F \times J^-_\mu J^{+\mu} \tag{1.26}$$

where G_F is equal to:

$$G_F = \frac{1}{4\sqrt{2}}\frac{g_2^2}{M_W^2} \tag{1.27}$$

and can be precisely defined by the measured muon lifetime (τ_μ) [16]. The forth and sixth terms of the Higgs's Lagrangian stand for the mass of the $W^\pm$ bosons, determined as follows:

$$m_{W^\pm} = \frac{1}{2}g\upsilon \tag{1.28}$$

Additionally, it is clear that the eighth term of Eq. 1.23 represents the mass of the Z boson and is equal to:

$$m_Z = \frac{1}{2}\upsilon\sqrt{g^2 + g'^2} = \frac{m_{W^\pm}}{cos\theta_W} \tag{1.29}$$

Finally, as it can be shown, the last term is related to the photon which remains massless as it is consistent with the unbroken symmetry $U(1)_{em}$.

To sum up, gauge bosons acquire mass thanks to the Higgs Mechanism and the mediator of the electromagnetic force remains massless, generating a new boson called Higgs particle. Consequently, the mass problem which appears in the *Spontaneous Symmetry Breaking* can be avoided by the Higgs mechanism. In addition, it explains accurately how the gauge bosons become massive and the photon remains massless.

1.4 THE HIGGS BOSON

As reported in the previous section, the Higgs Mechanism predicts not only the masses of the mediators, but also all the couplings of the Higss boson, which are defined as follows:

$$g_{Hf\bar{f}} = \frac{m_f}{\upsilon} \tag{1.30a}$$

$$g_{HVV} = \frac{2m_V^2}{\upsilon} \tag{1.30b}$$

$$g_{HHVV} = \frac{2m_V^2}{\upsilon} \tag{1.30c}$$

$$g_{HHH} = \frac{3m_H^2}{\upsilon} \tag{1.30d}$$

$$g_{HHHH} = \frac{3m_H^2}{\upsilon^2} \tag{1.30e}$$

where m_f is the mass of fermions, m_V is the vector boson masses. The corresponding vertices of each coupling are illustrated in Fig.1.4:

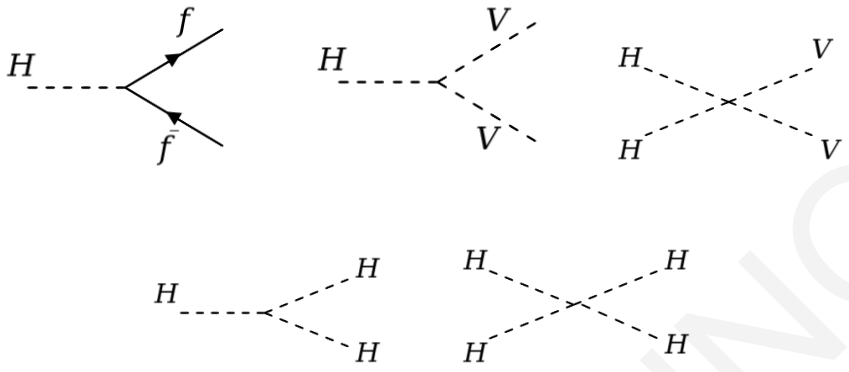

Figure 1.4: The vertices of the Higgs boson.

As shown from Eq. 1.24, the Higgs boson mass depends on the vacuum expectation value (υ) and on the field self-coupling constant λ. Nevertheless, a possible prediction of the Higgs mass was not achievable for many decades due to the lack of determination of the λ which must be defined experimentally. Luckily, due to the rapid development of the accelerating science and more accurate detector systems, the Higgs boson can be produced and observed at the *Large Hadron Collider* (LHC) via the most dominant production modes:

1. gluon-gluon fusion (ggH),
2. vector boson fusion (VBF),
3. associated production with a vector boson (VH),
4. association with a pair of top quarks $(t\bar{t}H)$.

Generally speaking, the Higgs boson is more possible to be generated via gluon-gluon fusion than the other production mechanisms because this has the largest cross section. However, it could be also observed in the other production modes but with lower probability. Second, the vector boson fusion (VBF) produces the Higgs boson with associated quarks which are hadronised to jets as final states. These jets can be observed to a forward direction or they can be easily identified from their large invariant mass, making the VBF production attractive to Higgs hunters. The third Higgs production mode is the associated production with a vector boson (VH), which is well-known as *Higgs Strahlung*. The Higgs boson might be emitted by a virtual W or Z boson, given that it carries sufficient energy which

allows the emission. This process is the third largest contribution in the Higgs production from proton-proton collisions. The last process is the assosiation with a pair of top quarks ($t\bar{t}H$) which has the lowest cross section by far from the other productions. In this production, two pairs of heavy quark-antiquark will be produced by two colliding gluons and the Higgs boson will be generated by the combination of a quark in the one pair and an antiquark of the other pair, as shown in Fig. 1.5.

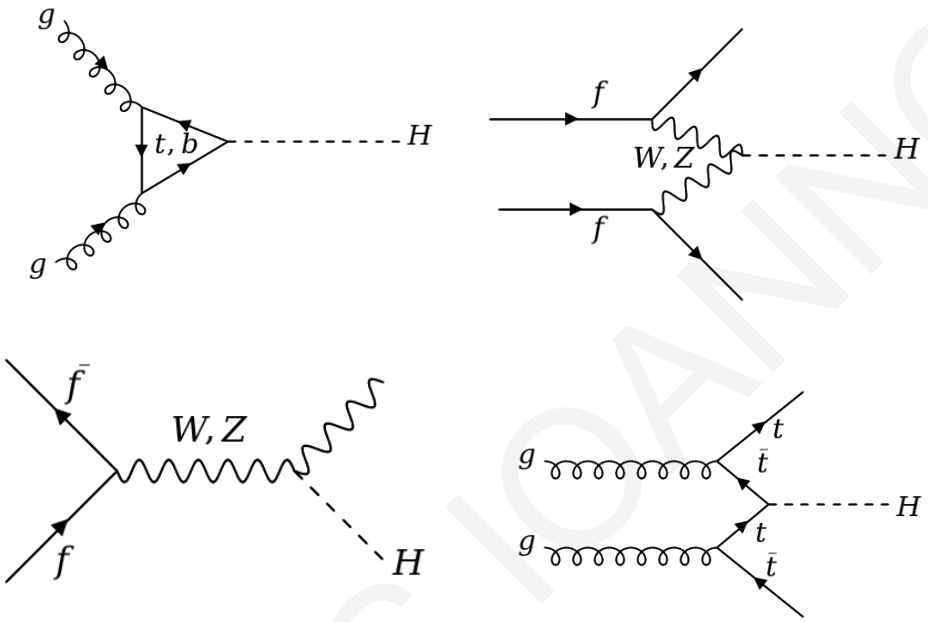

Figure 1.5: The Feynmann diagrams of the four Higgs production mechanisms at the LHC. Top left: gluon-gluon fusion. Top right: vector boson fusion. Bottom left: Higgs Strahlung. Bottom right: top fusion.

The corresponding cross sections of each Higgs production mode at a centre-of-mass energy of 13 TeV (top left plot) and 14 TeV (top right plot) as a function of Higgs mass are indicated in Fig. 1.6. The dependence of the cross section on a centre-of-mass energy is also included (bottom plot).

As shown in Fig 1.6, Next-to-Leading Order (NLO), Quantum ChromoDynamics (QCD), Electroweak (EW), and Next-to-Next-to-Leading (NNLO) orders are taken into account to the calculations of the cross sections. It is clearly seen that the main Higgs production mode is the gluon-gluon fusion with its cross section roughly 50 pb to 60 pb for $\sqrt{s} = 13, 14$ TeV. Moreover, Fig. 1.6 shows the cross section of the production of the SM Higgs boson associated with bottom quarks which includes 4-flavour-scheme (4FS) and 5-flavour-scheme (5FS). In the 4FS scheme the Higgs boson is built by an interaction of two gluons and the Higgs boson is associated with two bottom quarks generated by collided ingredients of proton particles. On the other hand, in 5FS scheme the Higgs boson is built by two massless bottom quarks and they gain mass after their interaction, associating the Higgs boson.

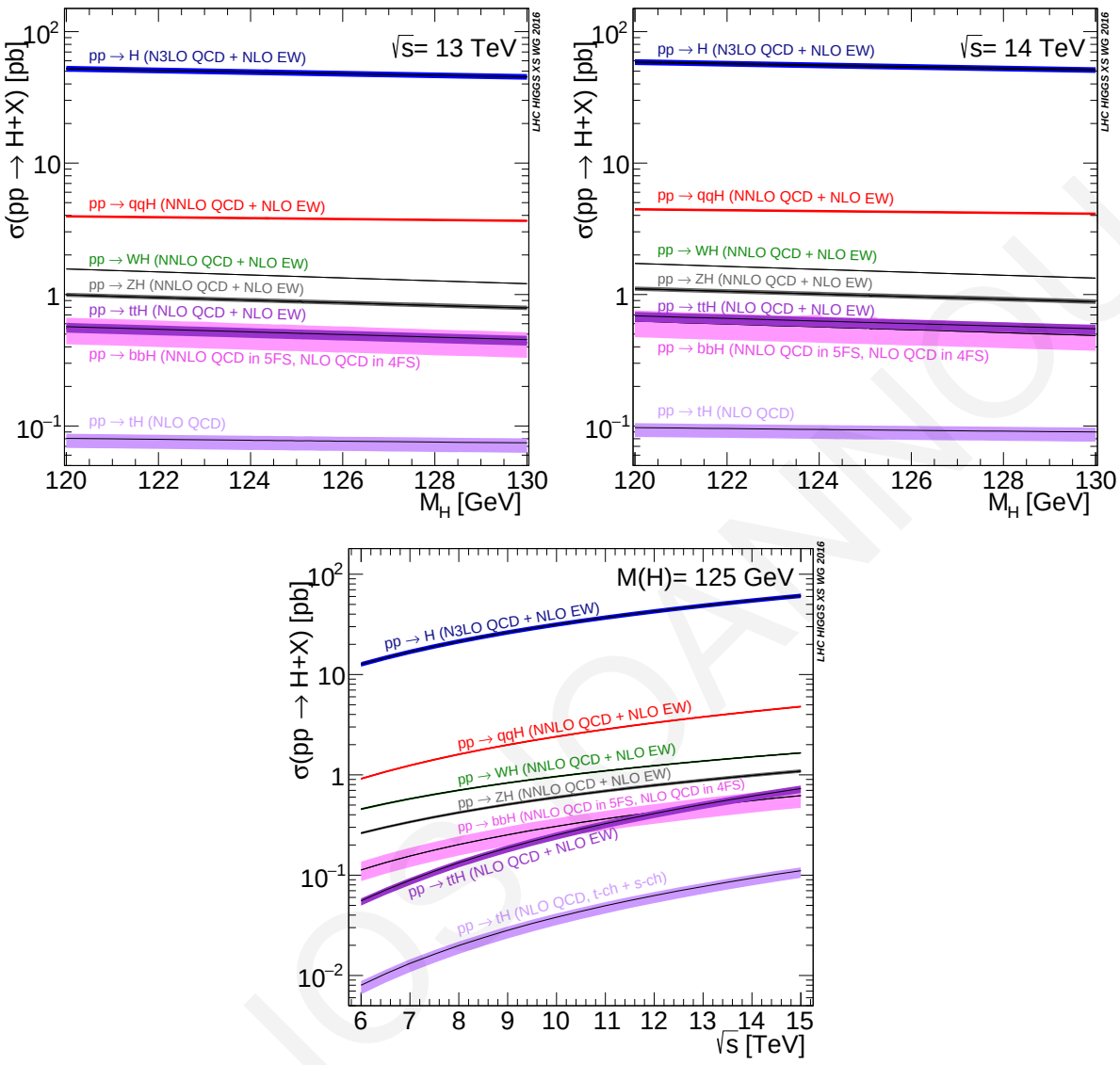

Figure 1.6: Cross sections of Standard Model (SM) Higgs boson production at centre-of-mass $13TeV$ (top left plot) and $14TeV$ (top right plot) as a function of Higgs mass, and the cross section of SM Higgs boson production as a function of centre-of-mass for Higgs mass of $125GeV$ (bottom plot). Taken from Ref. [17].

Up to now we presented the cross section of each Higgs production mode but we do not say anything about how to observe the Higgs particle. As we know, the Higgs boson cannot be observed directly but we might detect a combination of fundamental SM particles which come from the Higgs boson decay, with a particular probability. The Higgs boson can decay into fundamental SM particles with certain probability named *Branching Ratio* ($\mathcal{B}r$). The Branching Ratios give the probability of the Higgs boson to decay into specific SM particles and can be obtained mathematically by dividing the partial width of

the decay channel with that of all possible decays of the Higgs boson, as follows:

$$\mathcal{B}r(H \to XX) = \frac{\Gamma(H \to XX)}{\sum_{\text{all chanells}} \Gamma(H \to XX)} \tag{1.31}$$

In order to compute the Br for each possible decay channel, we have to firstly derive the partial width of each process. The Higgs particle can decay into leptons, quarks, photons and vector bosons. Firstly, let us take the case where the Higgs boson can decay into charged leptons; the partial decay width of this channel is:

$$\Gamma(H \to l^+l^-) = \frac{G_F m_l^2}{4\pi\sqrt{2}} m_H \beta_l^3 \tag{1.32}$$

where $\beta_l = \sqrt{1 - 4m_l^2/m_H^2}$ is the lepton velocity. Eq.1.32 is very similar with the partial decay width of quark-antiquark pair (a second Higgs decay mode), however, there are three important differences. The first difference is related to the colour and it contains a factor of three, the second one is due to the running of the quark mass and the last difference exists due to QCD corrections as taken into account in Eq. 1.33:

$$\Gamma(H \to q\bar{q}) = \frac{3G_F m_q^2(m_H)}{4\pi\sqrt{2}} m_H \beta_q^3 \tag{1.33}$$

When the Higgs boson is kinematically allowed, it can also decay into a pair of vector bosons W^+W^- or ZZ with partial widths:

$$\Gamma(H \to W^+W^-) = \frac{G_F m_H^3}{8\pi\sqrt{2}} \left(1 - \frac{4m_W^2}{m_H^2}\right)^{1/2} \left[1 - 4\left(\frac{m_W^2}{m_H^2}\right) + 12\left(\frac{m_W^2}{m_H^2}\right)^4\right] \tag{1.34}$$

and

$$\Gamma(H \to ZZ) = \frac{G_F m_H^3}{8\pi\sqrt{2}} \left(1 - \frac{4m_Z^2}{m_H^2}\right)^{1/2} \left[1 - 4\left(\frac{m_Z^2}{m_H^2}\right) + 12\left(\frac{m_Z^2}{m_H^2}\right)^4\right] \tag{1.35}$$

It is important to note that these decays into vector bosons can occur when the condition $m_H > 2m_W$ or $m_H > 2m_Z$ is satisfied, respectively. However, below this threshold, a vector boson channel might be observed if one boson is real and the other is virtual, but the partial width decreases rapidly, making an observation unlikely.

Once all partial decay widths have been calculated within the Standard Model theory, the total partial width of the Higgs boson is obtained by summing them. The $\mathcal{B}$r for each possible decay channel of the SM Higgs can be derived by Eq.1.31 and the branching ratio of each channel as a function of the Higgs boson mass is illustrated in Fig.1.7.

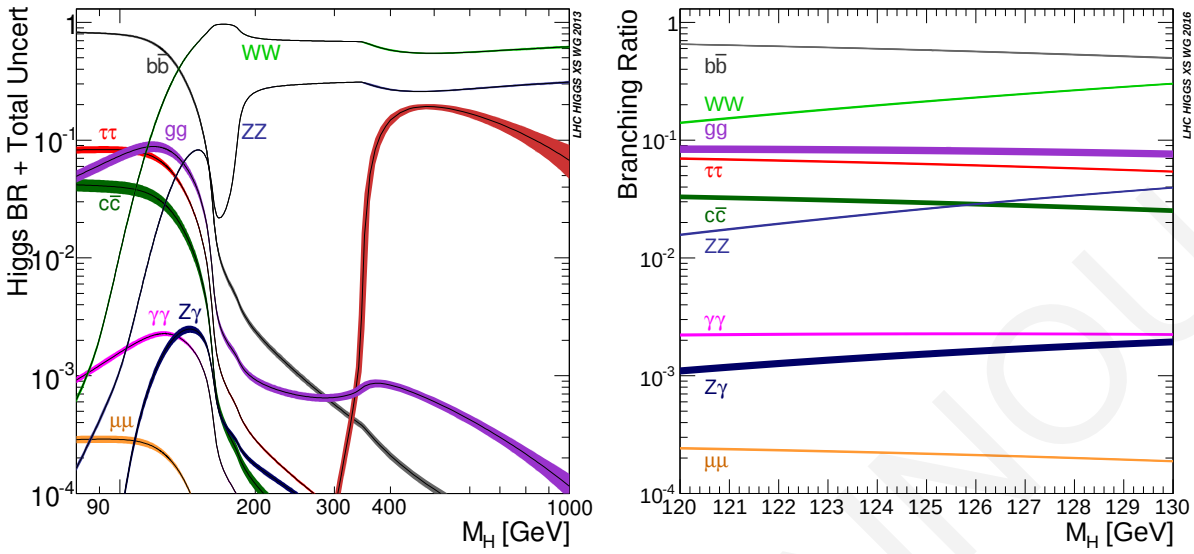

Figure 1.7: The Higgs branching ratios as functions of m_H. Taken from Ref. [17].

1.5 THE DISCOVERY OF THE HIGGS BOSON

The first breakthrough for the Higgs boson came in the summer of 2012 after four years of the LHC operation. CMS and ATLAS experiments announced simultaneously the observation of a new boson with a mass close to 125 GeV, with a statistical significance 5σ. The two experiments collected data 5 fb^{-1} at $\sqrt{s} = 7\ TeV$ in 2011 and 5 fb^{-1} at $\sqrt{s} = 8\ TeV$ in 2012. Analysing these data, they observed an excess of events in different channels at the mass close to 125 GeV. The observed CMS significance 4.9σ [18, 19] and the ATLAS' announcement for the discovering of a new boson with observed significance 6σ [20] pushed CERN to publicly announce the discovery of a new particle on July 4, 2012.

Another significant discovery came six years later, after the first Long Shutdown (LS1) and during the Run-II. CMS and ATLAS experiments announced the observation of ttH production on April 8, 2018. The third and last breakthrough did not take a long time to be announced, two months later, fulfilling another expectation of CERN before finishing the Run-II for the second Long Shutdown (LS2). Again, both experiments announced the observation of Higgs bosons which decay into bottom quarks on August 28, 2018. The remarkable outcome of such discovery is that the Higgs boson is not only produced by gluon-gluon fusion, but also it is generated by associated production with a vector boson.

1.5.1 THE $H \to \gamma\gamma$ DECAY CHANNEL

The $h \to \gamma\gamma$ decay channel was the first channel where the Higgs boson was discovered, although its branching ratio is about 0.1%. The decay is quite rare and a possible signal of Higgs boson overlaps with the large background from non-resonant QCD di-photon production or single photon production in association with jets. The two energetic isolated high transverse momentum photons provide a clear reconstruction of a signature of an invariant di-photon mass. In such decay channel, an evidence of a new boson can be confirmed by a narrow peak over a smoothly-falling continuum of the invariant mass spectrum which is the most discriminant variable against QCD and fake photon backgrounds. The enhancement of the sensitivity of the analysis has been achieved by using multivariate techniques, dividing events into exclusive categories, making the peak of the di-photon invariant mass more visible.

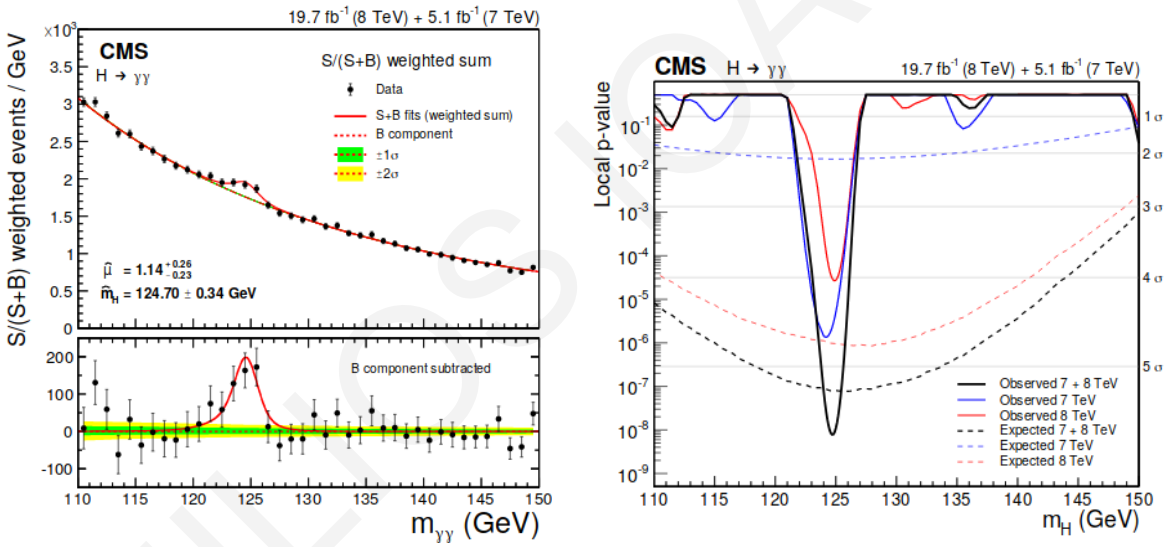

Figure 1.8: Left: Di-photon mass spectrum weighted by the ratio $S/(S+B)$ in each event. Right: Local p-values as a function of m_H for the 7 TeV, 8 TeV and the combined dataset. Taken from Ref. [21].

The di-photon mass spectrum (left plot) and its local significance of the observed excess (right plot) are shown in Fig.1.8, by weighing the events with the ratio of the signal S and the sum of the signal plus calculated background, $S+B$. The excess of events is for $m_{\gamma\gamma} = 124.7 \pm 0.34\ GeV$ and has a local significance 5.2σ. In addition, the ratio between the measured cross section and the expectation of the SM, $\mu = \sigma/\sigma_{SM}$, named signal strength, is $\mu = 1.14^{+0.26}_{-0.23}$.

1.5.2 THE $H \to ZZ^*$ DECAY CHANNEL

The $H \to ZZ^* \to 4l$ channel, named as *golden channel*, is well-studied due to its reducible background. In this channel at least one of the two Z is off the mass shell (Z^*) and Z bosons decay into pairs of electrons and muons. This channel is attractive to be investigated due to an easy identification of four isolated leptons with high transverse momentum. Furthermore, another important advantage of the $H \to ZZ^* \to 4l$ channel is that the four leptons can be reconstructed with high accuracy, and all kinematic information of the decay in the reconstructed final state is completely recovered. The analysis strategy is to search for a narrow peak in the invariant mass of the four-lepton above a small continuous background. Two isolated, same flavour and opposite charge leptons (electors, $e^{\pm}$, or muons, $\mu^{\pm}$) are selected with high transverse momentum in order to reconstruct an on-shell or off-shell Z mass. A peak for this decay channel appeared also at about 126 GeV, corresponding to the Higgs boson mass.

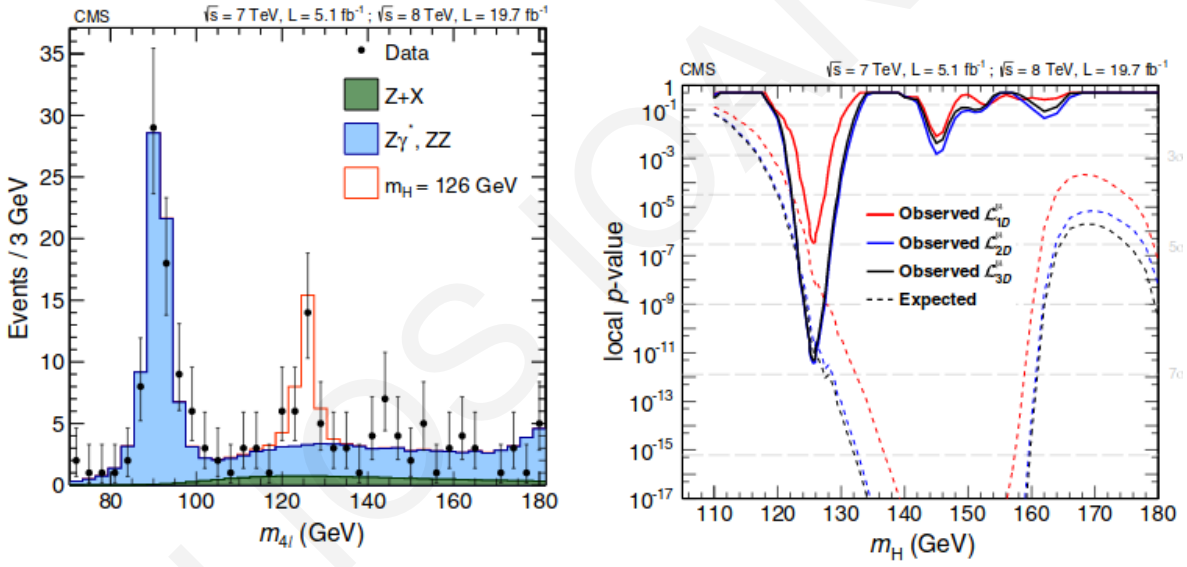

Figure 1.9: Left: Distribution of the four-lepton reconstructed mass for the sum of the $4e, 4\mu, 2e2\mu$ channels. Right: Significance of the local excess with respect to the SM background expectation as a function of the Higgs boson mass for one ($\mathcal{L}^{\mu}_{1D}$), two ($\mathcal{L}^{\mu}_{2D}$), and three ($\mathcal{L}^{\mu}_{3D}$) dimensional likelihood functions. Taken from Ref. [22].

Fig. 1.9 illustrates the Higgs boson with mass 126 GeV on left plot and its statistical significance 6.8σ on the right plot. It is important to note that the right plot of Fig. 1.9 shows the local significance of the peak for three different models fitted by likelihood functions [Appendix A.1.2]. The best-fit value is given for $3D$ model with local significance 6.8σ. In addition, the channel is divided into three decay channels for further investigations of the Higss boson. The negative log likelihood function is scanned as a function of the SM Higgs boson mass for each of the three channels separately and the combination of the three when the $3D$ model is used.

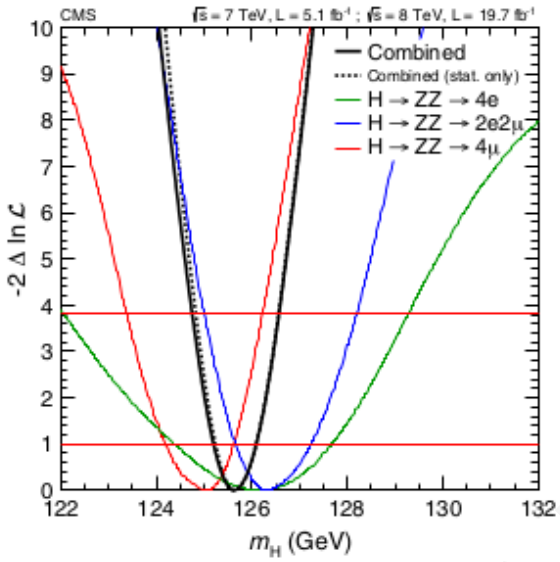

Figure 1.10: Scan of the negative log likelihood $-2\Delta ln\mathcal{L}$ vs the SM Higgs boson mass, m_H, for each of the three channels separately and the combination of the three, when using the $3D$ model, only. Taken from Ref. [22].

In addition, Fig. 1.10 shows the scan of the negative log likelihood $-2\Delta ln\mathcal{L}$ of the three channels as a function of the SM Higgs mass. The measured Higgs mass for the $H \to ZZ^* \to 4e$ is $126.2^{+1.5}_{-1.8}$, for the $H \to ZZ^* \to 2e2\mu$ is $126.3^{+0.9}_{-0.7}$, and for the $H \to ZZ^* \to 4\mu$ channel is $125.1^{+0.6}_{-0.9}$. The combination of the three channels gives a measured Higgs mass of $125.6 \pm 0.4(stat.) \pm 0.2(syst.)$, with a measured signal strength $0.93^{+0.26}_{-0.23}\ (stat.)^{+0.13}_{-0.09}(syst.)$.

1.5.3 THE $H \to WW \to 2l2\nu$ DECAY CHANNEL

The $H \to WW \to 2l2\nu$ decay channel has a very large branching ratio, $\mathcal{B}r = 21.5 \pm 0.9\%$. However, it is not the most sensitive channel for a search of the Higgs boson due to the presence of two undetected neutrinos in the final state (events cannot be completely reconstructed). Despite of the non-precise mass determination, the channel is useful for investigation of the Higgs coupling to the vector boson. The background of the channel might be easily suppressed due to the small electroweak processes, coming from mainly $t\bar{t}$ di-leptonic decays and the presence of the irreducible WW di-bosons production can be exploited for investigating Higgs couplings.

1.5.4 THE $H \to \tau^{\pm}\tau^{\mp}$ DECAY CHANNEL

An observation of the Higgs boson decay into tau pairs is extremely important because the Yukawa couplings of the Higgs boson to leptons can be directly investigated. Its $\mathcal{B}r$ of 5% to 8% makes the decay of the Higgs boson to be the fourth most preferable decay. Searches of the Higgs boson focus on four di-tau final states: $e\tau_h,\ \mu\tau_h,\ e\mu$ and $\mu\mu$, where τ_h represents hadronic decays of τ particle.

To perform such searches, events are divided into three different categories according to the final state topology. The first is a VBF category which includes events with two leading jets at large rapidity separation. The second one is a boosted category in which at least one hadronic jet is required and the last category is the zero-jet which is characterized by larger event yields with lower purity due to the contribution of the $Z \to \tau^{\pm}\tau^{\mp}$ background.

Despite the fact that the resolution of the Higgs boson invariant mass is worse than other channels, an excess of data is observed at mass 125.09 GeV ($m_H = 125.09$ GeV) with local significance 4.9σ. Additionally, the corresponding value for the signal strength, μ, is $1.09^{+0.27}_{-0.26}$ at $m_H = 125.09$ GeV. The invariant mass of the Higgs boson for the three different categories is shown in Fig. 1.11.

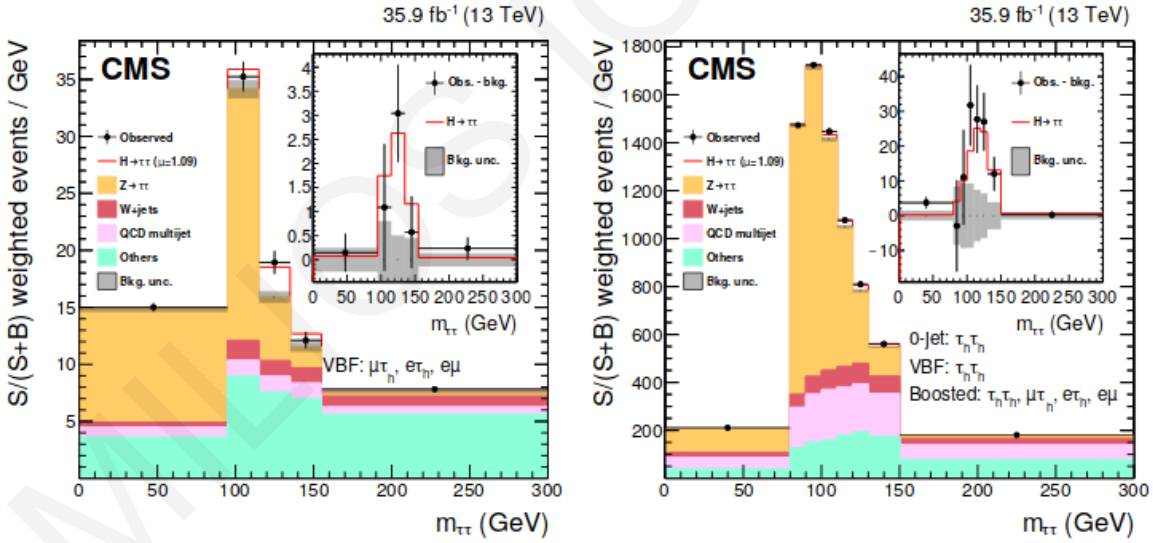

Figure 1.11: Left: The invariant mass of τ pairs for the VBF category of the $\mu\tau_h, e\tau_h$ and $e\mu$ channels. Right: The invariant mass of τ pairs for all other channels. Taken from Ref. [23].

1.5.5 OBSERVATION OF $t\bar{t}H$ PRODUCTION

As mentioned in Chapter 1.4, the Higgs boson can be produced via the fusion of a top quark-antiquark pair or through radiation from a top quark, as illustrated from Feynman diagrams in Fig. 1.12.

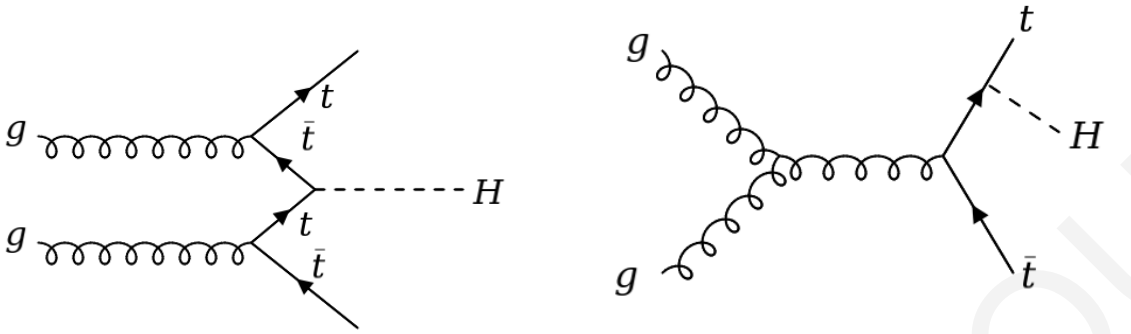

Figure 1.12: Left diagram: The Higgs boson production in the fusion of a top quark-antiquark pair. Right diagram: The Higgs boson production through radiation from a top quark.

A possible observation of this production mechanism is vital because a top-Higgs coupling is directly confirmed. Discovering the Higgs boson via the association with top quarks production mode, it is a direct probe of the Higgs coupling to the top quark.

The CMS experiment has collected all data at the centre-of-mass energies 7, 8 and 13 TeV, with the Higgs boson decaying into pairs of Z, W bosons, photons, τ-particles, and has combined them for maximising the sensitivity, extracting significant results. The search of the observation of $t\bar{t}H$ production has revealed an excess of events with a significance 5.2σ, confirming the tree-level coupling of the Higgs boson to the top quark. This measurement was published by CERN on April 8, 2018, putting another missing piece in the puzzle of the SM completeness.

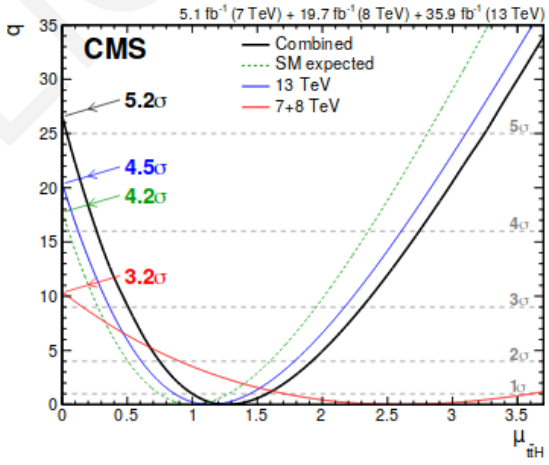

Figure 1.13: The test statistic q [Appendix A.1.7] as a function of $\mu_{t\bar{t}H}$ for all decay modes at 7, 8 and 13 TeV. Taken from Ref. [24].

1.5.6 Observation Of VH Production And The $H \to b\bar{b}$ Decay Channel

Before Run-II ending, another two breakthroughs were recorded, confirming the SM again. The associated Higgs production with a W or Z boson (VH) was observed and the Higgs boson decay into a pair of bottom quarks was reported simultaneously [25].

According to Fig. 1.7, the $\mathcal{B}r$ of the $H \to b\bar{b}$ decay channel has the largest percentage ($\sim 58\%$) from the rest decay channels, however, its discovery had delayed due to an enormous background. The analysis strategy such decay channel is based on five distinct final states $Z(\nu\nu)H$, $W(\mu\nu)H$, $W(e\nu)H$, $Z(\mu\mu)H$, $Z(ee)H$, corresponding to three channels with 0, 1, or 2 charged leptons from the vector boson decay by suppressing significantly background processes. The productions of W and Z bosons in association with jets ($V + jets$), production of top quark pairs ($t\bar{t}$) and single top quarks (t), diboson (WW, WZ, ZZ)) and multijet (QCD) events are dominant in this analysis. An efficient identification of b-jets is used to suppress the main backgrounds. In addition, the usage of multivariate discriminant techniques provide a better and clear separation of signal from background.

Following the above techniques, this analysis strategy yields an excess of events at $m_H = 125.09$ GeV with a significance 4.8σ, publishing the Higgs production with associated W or Z boson (VH). The corresponding measured signal strength is $\mu = 1.01 \pm 0.22$. Furthermore, a combination of three Higgs production modes (gluon-gluon fusion, VBF and association with top quarks) yields an increase of the significance 5.6σ for the $H \to b\bar{b}$ decay channel.

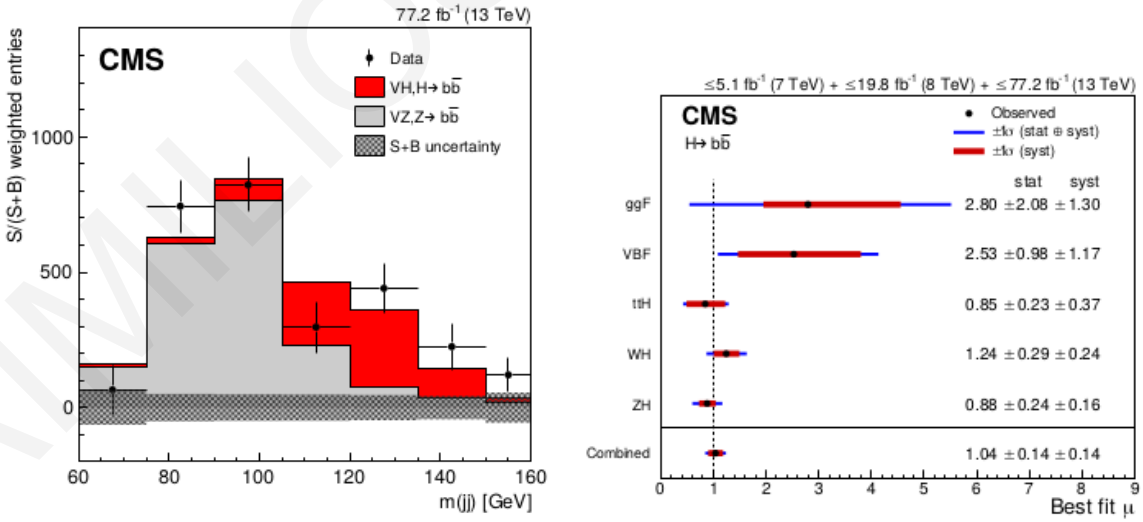

Figure 1.14: Left: Dijet invariant mass distribution for events weighted by $S/(S+B)$ in all channels combined in the 2016 and 2017 data sets. Right: Best-fit value of the $H \to b\bar{b}$ signal strength with its 1σ systematic (red) and total (blue) uncertainties for the five individual production modes. Taken from Ref. [25].

Overall, Fig. 1.14 shows the observation of the Higgs boson mass (left plot) at $m_H = 125.09$ GeV which decays into a pair of bottom quarks with local significance 5.6σ. The right plot of Fig. 1.14 is the signal strength for each process as well as the combined signal strength, μ reaches at 1.04 ± 0.20. This result confirms the observation of the Higgs boson which is produced through VH production mode and the discovery of the $H \to b\bar{b}$ channel.

Chapter 2

Beyond The Standard Model

The recent breakthroughs of the discovery of the Higgs boson as well as confirmations of the Higgs production mechanisms render the SM as a remarkably successful theory. However, there are strong theoretical and experimental motivations which suggest that there are alternative theories beyond the Standard Model. Several theories have been proposed by extending the SM in order to overcome issues which cannot be explained and predicted by the SM such as the unification of the four forces, the prediction of the neutrino masses, the hierarchy problem and so on. In this chapter, the motivations to extend the SM are briefly described. The Chapter focuses on the theory beyond the SM which is called "Two-Higgs-Doublet-Model" (2HDM), concentrating on the phenomenology of its Higgs sector.

2.1 The Problems Of The Standard Model

Despite the fact that the SM is a remarkably successful theory, including the introduction of the Higgs field and the discovery of its corresponding particle, it is unfortunately an incomplete theory because it is not able to address vital issues. The *hierarchy problem*, its failure to predict the neutrino masses, the matter - antimatter imbalance are such problems which make the SM inappropriate theory to overcome the issues, creating a need for new physics beyond the SM.

As we know, the SM has many free parameters which cannot be sufficiently explained by the current SM theory. One can see that the minimal version of the SM has at least nineteen free parameters. It has nine free fermion masses $(m_e, m_\mu, m_\tau, m_u, m_d, m_c, m_s, m_t, m_b)$, three Cabibbo-Kobayashi-Maskawa (CKM) mixing angles ($\theta_{12},\ \theta_{23},$ and θ_{13}) and one CP-violating phase (δ_{13}), and three coupling con-

stants: one electromagnetic (g'), one weak (g), and one strong (g_s); it has also one QCD vacuum angle (Θ_3) and the parameter of the vacuum expectation value (υ). Finally, the Higgs potential coupling constant λ is also taken as a free parameter in the SM.

2.1.1 THE HIERARCHY PROBLEM

A major problem of the flawed SM is the hierarchy problem which is related to the huge energy difference between the weak and the Planck scale [26]. The weak scale is approximately equal to 246 GeV, given by the vev of the Higgs field, $\upsilon = \frac{1}{\sqrt{\sqrt{2}G_F}} = 2M_W/g \simeq 246$ GeV. However, the SM might be valid up to the Planck mass, M_P, due to the radiative corrections to the scalar boson squared mass, originating from its couplings to fermions and gauge boson as well as its self-couplings as shown in Fig. 2.1. These corrections are quadratically proportional to the ultraviolet momentum cutoff Λ_{UV}. By considering the SM to be a reliable theory up to the Planck scale, the most affected boson is the Higgs boson mass which receives the quantum correction of thirty orders of magnitude larger than m_H^2. This is well-known as the *naturalness problem* of the H boson mass.

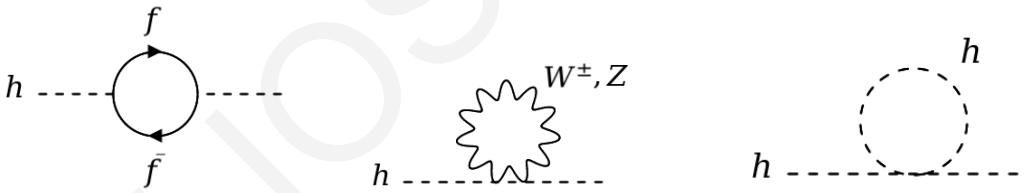

Figure 2.1: 1-loop radiative corrections to the Higgs boson mass.

The radiative contributions to the Higgs mass via 1-loop diagrams (Fig. 2.1) are shown in Eq. 2.1.

$$\delta m_h^2 \simeq \frac{3\Lambda_{UV}^2}{8\pi^2\upsilon^2}\left(2m_W^2 + m_Z^2 + m_h^2 - 4m_t^2\right) \tag{2.1}$$

It is clear that cancellations between the bare mass, $m_{h,bare}^2$, and the correction δm_h^2 must be applied in order to extract the observed Higgs mass of 125 GeV. For this major reason, Beyond Standard Models (BSM) were proposed to avoid this fine-tuning, by introducing new scalar particles at the TeV scale which are coupled to the scalar bosons, cancelling the Λ_{UV}^2 divergence.

2.1.2 NEUTRINO MASSES

Another important issue of the SM is the presence of massless, left-handed neutrinos. SM predicts left-handed neutrinos with null mass, however, experimental measurements of neutrino flavour oscillations [27, 28] indicate that neutrinos are not massless particles but they are massive objects with very small mass values. From the experiments, it is well-established that the neutrinos can oscillate, implying that they have masses and they can change their flavour in flight.

2.1.3 SUPPRESSION OF FLAVOUR CHANGING NEUTRAL CURRENTS (FCNCS)

The effect of the *Flavour Changing Neutral Currents* (FCNCs) is a problem which cannot be significantly suppressed in the SM. The SM suffers from many accidental symmetries and features in which proton decays are forbidden; lepton numbers and lepton family number are preserved for vanishing neutrino masses and the $K^+ \to \pi^+ \nu\bar{\nu}$ decay is suppressed at the tree-level. Moreover, the accidental symmetries lead to suppressed electric dipole moments for the e^-, n, atoms, etc. and make the SM unable to explain such phenomena.

2.1.4 FERMION PROBLEM

As it is well-known, there are three families of fermions: (ν_e, e^-, u, d) is denoted as the first family, (ν_μ, μ^-, c, s) as the second, and the third family contains the following fermions: (ν_τ, τ^-, t, b). The second and the third families of fermions are heavier than the first family with no obvious reason. As a result, the SM cannot give a sufficient explanation of the existence of these heavier families and the worst is, it cannot provide a prediction of the fermion masses.

2.1.5 GAUGE PROBLEM

The Standard Model consists of three subgroups $SU(3) \times SU(2) \times U(1)$, with particular gauge couplings for each subgroup. However, it cannot provide a good explanation about the chirality of the electroweak part (parity-violating). Also, it does not explain why all particles have charges which are multiples of $e/3$ (charge quantization). Moreover, the structure of the SM suggests a unification of the couplings of the three interactions, however, these coupling constants are never unified in the framework of the Standard Model. In the SM, weak and electromagnetic interactions can be combined together, by creating the electroweak interaction, but the coupling constant of the strong interaction does never meet the other two, achieving the unification.

2.1.6 VACUUM STABILITY

After the discovery of the Higgs boson with mass 125 GeV, another cosmological problem which doubts the consistency of the SM, is the vacuum stability [29]. By solving the following equation for the Higgs self-coupling λ:

$$\beta_\lambda = \frac{1}{(4\pi)^2}\left[24\lambda^2 - 6y_t^4 + \frac{3}{8}\left(2g^4 + (g^2 + g'^2)^2\right) + (-9g^2 - 3g'^2 + 12y_t^2)\lambda\right] \quad (2.2)$$

and taking the mass of the Higgs boson ($m_H = 125$ GeV) and the top mass of 173.2 GeV into account, λ becomes negative at higher scales as shown in Fig. 2.2 (left plot). This effect has an impact on the stability of the Higgs potential, making the potential unstable at the higher scale, establishing the Standard Model defective. Recent measurements for stability, instability and meta-stability regions, revealed that the meta-stability region is more natural according to the Higgs boson mass and pole top mass.

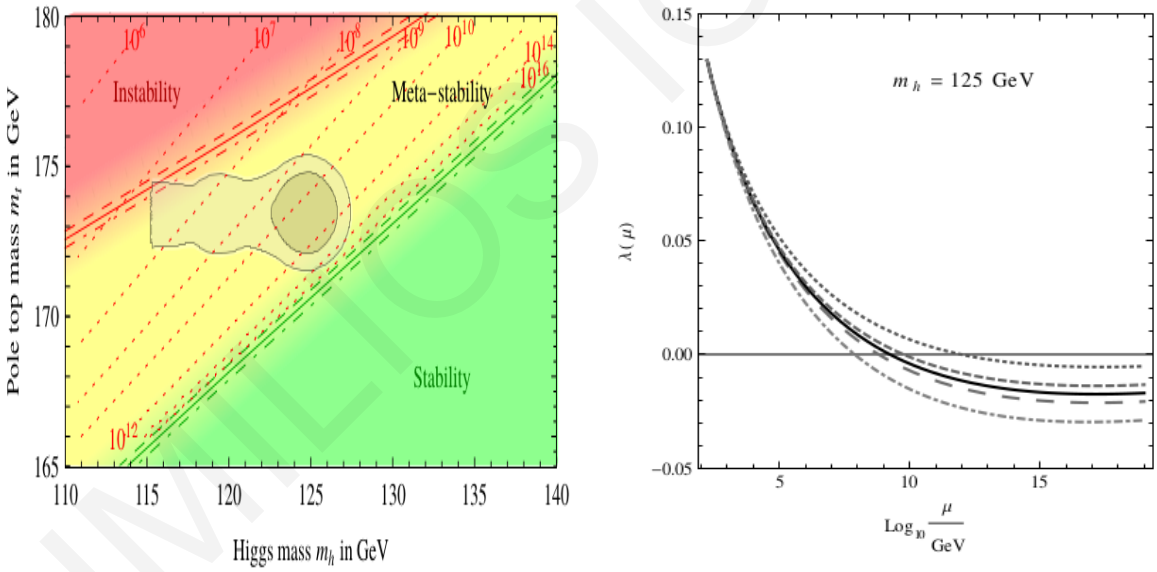

Figure 2.2: Left: Stability, instability and meta-stability regions in the m_H vs m_t plane [29]. Right: Higgs self-coupling constant $\lambda(\mu)$ for different top masses in Standard Model. Black solid line is for $m_t = 173.2GeV$ and $a_s(M_Z) = 0.1184$. Dotted lines is for $m_t = 171.4GeV$ and Dot-Dashed lines represents the case of $m_t = 175.0GeV$. The lines closer to the solid one, are for $a_s(M_Z) = 0.1198$ (dashed line) and $a_s(M_Z) = 0.1170$ (long dashed line). Taken from Ref. [30].

2.1.7 MATTER AND ANTIMATTER ASYMMETRY

The SM has not a sufficient mechanism to explain the observed asymmetry between baryons and anti-baryons in the Universe [31]. However, new mechanisms such as the minimal see-saw model [32], can involve the out of equilibrium decays of superheavy Majorana right-handed neutrinos [33]. Other possibilities which can explain matter anti-matter asymmetry, are the first order electroweak phase transition (electroweak baryogenesis [34]) which is met in the Minimal Supersymmetric extension (MSSM); the decay of a coherent scalar field like a scalar quark or lepton in supersymmetry theory or CPT violation. Finally, it is not reasonable to reject the possibility that the asymmetry is due to an initial condition of the Big Bang, but on the other hand, this possibility will not exist if the Universe underwent a period of rapid inflation.

2.2 TWO-HIGGS-DOUBLET MODEL (2HDM)

The *two-Higgs-doublet model (2HDM)* is the simplest possible extension of the SM [1]. In general, this model contains two scalar doublets instead of one scalar doublet like in the Standard Model. 2HDM provides a wide range of motivations due to the second scalar Higgs doublet, making the model attractive to be investigated. The best known motivation is *supersymmetry* [35]. As we know, in supersymmetry the scalar particles belong to chiral multiplets and their conjugates belong to multiplets of the opposite chirality and, therefore, multiplets of different chiralities cannot couple together in the Lagrangian. As a consequence, they cannot acquire mass. However, the addition of the second Higgs doublet gives mass to the charge $2/3$ and charge $-1/3$ quarks, simultaneously. Also, the second Higgs doublet provides cancellation of anomalies which are caused by the scalars in chiral multiplets together with chiral spin $-1/2$.

Moreover, the second Higgs doublet can provide to the QCD Lagrangian a global $U(1)$ symmetry in which possible CP-violating terms can be rotated away. This symmetry happens in axion models, in which variations with singlets at a higher scale are acceptable and the effective low-energy theory for those models still requires two Higgs doublets [1].

Another motivation for 2HDM is the fact that the 2HDM theory can partially explain the baryon asymmetry of the Universe, in contrast of the SM which is unable to do so. 2HDM could justify the matter-antimatter imbalance due to the flexibility of their scalar mass spectrum and the existence of additional sources of CP violation. 2HDM provides two additional independent CP-violating phases which could be accounted for matter-antimatter asymmetry.

Overall, the 2HDM model is particularly attractive because it predicts new phenomena, such as additional physical Higgs bosons (up to seven physical states of Higgs bosons), FCNCs' suppression (if appropriate Higgs-fermion couplings are chosen) [36], and the compatibility with parameter ρ[1]. The parameter ρ is very useful variable in the $SU(2) \otimes U(1)$ gauge theory because it is one critical piece of evidence about the scalar structure. Experimentally, ρ is very close to one and this is a strong evidence that the 2HDM model could be the extension of the SM because both $SU(2)$ singlets with $Y = 0$ and $SU(2)$ doublets with $Y = \pm 1$ give $\rho = 1$, since they both have $I(I+1) = \frac{3}{4}Y^2$ [1].

[1] $\rho = \dfrac{\sum_{i=1}^{n}[I_i(I_i+1) - \frac{1}{4}Y_i^2]v_i}{\sum_{i=1}^{n}\frac{1}{2}Y_i^2 v_i} = \frac{m_W^2}{m_Z^2 cos^2\theta_W}$

2.2.1 THE 2HDM LAGRANGIAN

The Lagrangian of the 2HDM theory can be written as follows:

$$\mathcal{L}_{2HDM} = \mathcal{L}_{\phi} + \mathcal{L}_{Yukawa} + \mathcal{L}_{SM} \tag{2.3}$$

$\mathcal{L}_{SM}$ describes the SM interactions of gauge bosons and fermions, $\mathcal{L}_{Yukawa}$ describes the Yukawa interactions of fermions with Higgs scalars. The Higgs scalar Lagrangian $\mathcal{L}_{\phi}$ is similar with the SM Higgs Lagrangian, however, the new Higgs potential consists of two Higgs doublets instead of one doublet.

$$\mathcal{L}_{\phi} = \sum_{i=1,2} (D_{\mu}\Phi_i)^{+}(D^{\mu}\Phi_i) - V_H(\Phi_1, \Phi_2) \tag{2.4}$$

The covariant derivative, D_{μ} is exactly the same that one finds in the SM Eq. 1.18, $\Phi_{i=1,2}$ is two Higgs doublets, and V_H stands for the Higgs potential which will be described in the next Chapter 2.2.2.

2.2.2 SPONTANEOUS SYMMETRY BREAKING

The vacuum structure of 2HDM is very rich. The most general scalar potential contains fourteen parameters and might have CP-conserving, CP-violating and charge-violating minima. By introducing two doublets Φ_1 and Φ_2 of the $SU(2)$ subgroup, which contain complex scalar fields with hypercharge equal to unity, the most general Higgs doublets can be given as follows:

$$\Phi_1 = \begin{pmatrix} \phi_1^+ \\ \phi_1^0 \end{pmatrix} = \frac{1}{\sqrt{2}} \begin{pmatrix} \phi_1 + i\phi_2 \\ \phi_3 + i\phi_4 \end{pmatrix} \quad \Phi_2 = \begin{pmatrix} \phi_2^+ \\ \phi_2^0 \end{pmatrix} = \frac{1}{\sqrt{2}} \begin{pmatrix} \phi_5 + i\phi_6 \\ \phi_7 + i\phi_8 \end{pmatrix} \tag{2.5}$$

And the most general potential $V(\Phi_1\Phi_2)$ can be written:

$$\begin{aligned} V_H = {} & m_{11}^2 \Phi_1^{\dagger}\Phi_1 + m_{22}^2 \Phi_2^{\dagger}\Phi_2 - \left(m_{12}^2 \Phi_1^{\dagger}\Phi_2 + h.c. \right) \\ & + \frac{1}{2}\lambda_1 (\Phi_1^{\dagger}\Phi_1)^2 + \frac{1}{2}\lambda_2 (\Phi_2^{\dagger}\Phi_2)^2 + \lambda_3 (\Phi_1^{\dagger}\Phi_1)(\Phi_2^{\dagger}\Phi_2) + \lambda_4 (\Phi_1^{\dagger}\Phi_2)(\Phi_2^{\dagger}\Phi_1) \\ & + \left[\frac{1}{2}\lambda_5 (\Phi_1^{\dagger}\Phi_2)^2 + \lambda_6 (\Phi_1^{\dagger}\Phi_1)(\Phi_1^{\dagger}\Phi_2) + \lambda_7 (\Phi_2^{\dagger}\Phi_2)(\Phi_1^{\dagger}\Phi_2) + h.c. \right] \end{aligned} \tag{2.6}$$

where "h.c" corresponds to the Hermitian conjugate. The parameters m_{11}^2, m_{22}^2 and $\lambda_{1,2,3,4}$ are real, while the remaining parameters m_{12}^2 and $\lambda_{5,6,7}$ are complex. Overall, the general 2HDM has 14 free parameters.

By minimising the general potential, one can find that the vacuum structure of 2HDM is much richer than that of the SM. First of all, there are three different types of vacua in 2HDM:

- "Normal" vacua, with vacuum expectation values (v.e.v.) which do not include any complex relative phase and can be real:

$$\langle\Phi_1\rangle = \begin{pmatrix} 0 \\ \frac{\upsilon_1}{\sqrt{2}} \end{pmatrix}, \quad \langle\Phi_2\rangle = \begin{pmatrix} 0 \\ \frac{\upsilon_2}{\sqrt{2}} \end{pmatrix} \tag{2.7}$$

  where $\upsilon = \sqrt{\upsilon_1^2 + \upsilon_2^2} = 246\ GeV$ and one can define $tan\beta = \frac{\upsilon_2}{\upsilon_1}$.

- CP breaking vacua, where the vevs contain a relative complex phase:

$$\langle\Phi_1\rangle = \begin{pmatrix} 0 \\ \frac{\bar{\upsilon_1}}{\sqrt{2}} e^{i\theta} \end{pmatrix}, \quad \langle\Phi_2\rangle = \begin{pmatrix} 0 \\ \frac{\bar{\upsilon_2}}{\sqrt{2}} \end{pmatrix} \tag{2.8}$$

  where $\bar{\upsilon_1}$ and $\bar{\upsilon_2}$ are real. The complex phase is not a guarantee of spontaneous CP-violation.

- Charge breaking vacua, in which one of the vacuum expectation values carries electric charge:

$$\langle\Phi_1\rangle = \begin{pmatrix} \frac{\alpha}{\sqrt{2}} \\ \frac{\upsilon_1'}{\sqrt{2}} \end{pmatrix}, \quad \langle\Phi_2\rangle = \begin{pmatrix} 0 \\ \frac{\upsilon_2'}{\sqrt{2}} \end{pmatrix} \tag{2.9}$$

  where $\upsilon_1',\ \upsilon_2',\ \alpha$ are real numbers. However, these vacua present an important problem. Due to the vev in the upper component (charged) of the fields, the vacuum breaks electric charge conservation and the photon acquires mass.

To avoid any unpleasant result, such as massive photons, one must ignore the Charge breaking vacua and the CP breaking vacua. The difference between normal vacua and CP breaking vacua is the complex phase $(e^{i\theta})$ between the expectation values of the two doublets. Assuming $\theta = 0$, the CP breaking vacua transform to the normal vacua without the complex phase, avoiding the CP-violation. In addition, FCNC suppressions can be achieved by applying the $\mathbb{Z}_2$ discrete symmetry for the invariance of the potential:

$$\Phi_1 \to -\Phi_1, \Phi_2 \to \Phi_2 \quad or \quad \Phi_1 \to \Phi_1, \Phi_2 \to -\Phi_2 \tag{2.10}$$

If the above recommendations are not considered, the minimisation of the potential cannot be solved analytically. However, once one adopts the above recommendations, the equations $\partial V/\partial\upsilon_1 = 0$ and $\partial V/\partial\upsilon_2 = 0$ are used to estimate the parameters m_{11} and m_{22}, respectively. By taking the first partial derivative of the Higgs potential for each vev, the results are shown below:

$$m_{11}^2\upsilon_1 - Re(m_{12}^2)\upsilon_2 + \frac{\lambda_1}{2}\upsilon_1^3 + \frac{1}{2}\upsilon_1\upsilon_2^2(\lambda_3 + \lambda_4 + Re(\lambda_5)) = 0 \tag{2.11a}$$

$$m_{22}^2\upsilon_2 - Re(m_{12}^2)\upsilon_1 + \frac{\lambda_2}{2}\upsilon_2^3 + \frac{1}{2}\upsilon_2\upsilon_1^2(\lambda_3 + \lambda_4 + Re(\lambda_5)) = 0 \tag{2.11b}$$

2.2.3 THE HIGGS SECTOR

Taking the assumptions from the previous Chapter 2.2.2 (applying $\mathbb{Z}_2$ discrete symmetry, using the normal vacua and setting $\lambda_{6,7} = 0$) into account, the general scalar Higgs potential for two doublets Φ_1 and Φ_2 is:

$$\begin{aligned} V = {} & m_{11}^2 \Phi_1^\dagger \Phi_1 + m_{22}^2 \Phi_2^\dagger \Phi_2 - m_{12}^2 (\Phi_1^\dagger \Phi_2 + \Phi_2^\dagger \Phi_1) + \frac{\lambda_1}{2} (\Phi_1^\dagger \Phi_1)^2 + \frac{\lambda_2}{2} (\Phi_2^\dagger \Phi_2)^2 \\ & + \lambda_3 \Phi_1^\dagger \Phi_1 \Phi_2^\dagger \Phi_2 + \lambda_4 \Phi_1^\dagger \Phi_2 \Phi_2^\dagger \Phi_1 + \frac{\lambda_5}{2} \left[(\Phi_1^\dagger \Phi_2)^2 + (\Phi_2^\dagger \Phi_1)^2 \right] \end{aligned} \tag{2.12}$$

Following the same procedure as in spontaneous symmetry breaking, by taking the first partial derivative of the 2HDM Higgs potential for each vev, ($\partial V/\partial \upsilon_1 = 0$ and $\partial V/\partial \upsilon_2 = 0$), the minimisation of the Higgs potential gives:

$$\langle \Phi_1 \rangle = \begin{pmatrix} 0 \\ \frac{\upsilon_1}{\sqrt{2}} \end{pmatrix}, \quad \langle \Phi_2 \rangle = \begin{pmatrix} 0 \\ \frac{\upsilon_2}{\sqrt{2}} \end{pmatrix} \tag{2.13}$$

Now, considering two complex scalar $SU(2)$ doublets, there are eight fields:

$$\Phi_\alpha = \begin{pmatrix} \phi_\alpha^+ \\ (\upsilon_\alpha + \rho_\alpha + i\eta_\alpha)/\sqrt{2} \end{pmatrix}, \quad \alpha = 1, 2 \tag{2.14}$$

Three of them are used to give mass to $W^\pm$ and Z bosons and the remaining five fields are physical scalar Higgs fields. There are two neutral scalars (CP even), H, h, one pseudoscalar (CP odd), A, and two charged scalar Higgs states, $H^\pm$. In order to derive the mass of each Higgs physical state, one should compute the eigenvalues of the mass matrix.

The squared mass for the charged Higgses is given by the eigenvalues of a 2×2 matrix whose elements are computed by:

$$\left[M_{H^\pm}^2 \right]_{ij} = \frac{\partial^2 V_H}{\partial \phi_i^+ \partial \phi_j^-} \tag{2.15}$$

Calculating the eigenvalues of mass matrix Eq. 2.15, overall there are four degrees of freedom. Two zero eigenvalues correspond to the Goldstone bosons ($G^\pm$) which give mass to the $W^\pm$ bosons and the other two eigenvalues are related to the charged Higgs state, as follows:

$$m_{H^\pm}^2 = \left[\frac{m_{12}^2}{\upsilon_1 \upsilon_2} - \frac{1}{2}(\lambda_4 + \lambda_5) \right] \upsilon^2 \tag{2.16}$$

The elements of the 2×2 pseudo-scalar mass matrix can be derived from the second derivatives of the imaginary parts of the neutral components:

$$\left[M_A^2 \right]_{ij} = \frac{1}{2} \frac{\partial^2 V_H}{\partial Im(\phi_i^0) \partial Im(\phi_j^0)} \tag{2.17}$$

Again, there is a zero eigenvalue which corresponds to the Goldstone boson (G^0) which gives mass to the Z boson, and the pseudoscalar squared mass is determined:

$$m_A^2 = m_{H^\pm}^2 + \frac{1}{2}[\lambda_4 - \lambda_5]v^2 = \left[\frac{m_{12}^2}{v_1 v_2} - \lambda_5\right](v_1^2 + v_2^2) \tag{2.18}$$

Note that, when the parameter $m_{12} = 0$ and $\lambda_5 = 0$ the CP-odd Higgs boson becomes massless. This happens when there is an additional global $U(1)$ symmetry which is spontaneously broken. Finally, the masses of CP-even Higgs bosons can be derived from the eigenvalues of the symmetric 2×2 matrix, given by:

$$[M_h^2]_{ij} = \frac{1}{2}\frac{\partial^2 V_H}{\partial Re(\phi_i^0)\partial Re(\phi_j^0)} = \begin{pmatrix} m_{11}^2 + \frac{3}{2}\lambda_1 v_1^2 + \frac{\lambda_{345}}{2}v_2^2 & -m_{12}^2 + \lambda_{345}v_1 v_2 \\ -m_{12}^2 + \lambda_{345}v_1 v_2 & m_{22}^2 + \frac{3}{2}\lambda_2 v_2^2 + \frac{\lambda_{345}}{2}v_1^2 \end{pmatrix} \tag{2.19}$$

where $\lambda_{345} = \lambda_3 + \lambda_4 + \lambda_5$. The physical masses for the two CP-even Higgs bosons are equal to:

$$m_{h,H}^2 = \frac{1}{2}\left[a_{11} + a_{22} \mp \sqrt{(a_{11} - a_{22})^2 + 4a_{12}^2}\right] \tag{2.20}$$

where

$$a_{11} = m_{11}^2 + \frac{3}{2}\lambda_1 v_1^2 + \frac{\lambda_{345}}{2}v_2^2 \tag{2.21a}$$

$$a_{12} = -m_{12}^2 + \lambda_{345}v_1 v_2 \tag{2.21b}$$

$$a_{21} = -m_{12}^2 + \lambda_{345}v_1 v_2 \tag{2.21c}$$

$$a_{22} = m_{22}^2 + \frac{3}{2}\lambda_2 v_2^2 + \frac{\lambda_{345}}{2}v_1^2 \tag{2.21d}$$

The mass eigenstate of each physical Higgs state can be obtained by performing the following orthogonal transformations:

$$\begin{pmatrix}\rho_1 \\ \rho_2\end{pmatrix} = R(\alpha)\begin{pmatrix}H \\ h\end{pmatrix} \tag{2.22a}$$

$$\begin{pmatrix}\eta_1 \\ \eta_2\end{pmatrix} = R(\beta)\begin{pmatrix}G^0 \\ A\end{pmatrix} \tag{2.22b}$$

$$\begin{pmatrix}\phi_1^\pm \\ \phi_2^\pm\end{pmatrix} = R(\beta)\begin{pmatrix}G^\pm \\ H^\pm\end{pmatrix} \tag{2.22c}$$

The rotation matrices have the following form:

$$R(\theta) = \begin{pmatrix} cos\theta & -sin\theta \\ sin\theta & cos\theta \end{pmatrix} \tag{2.23}$$

where h stands for a neutral light CP-even, H corresponds to a neutral heavy CP-even, A is for a neutral

CP-odd Higgs boson and $H^{\pm}$ is for two charged Higgs bosons, as before. The existence of massless pseudo-Nambu-Goldstone bosons $G^{\pm}$ and G^0 is due to the longitudinal components of the massive gauge bosons [37], $W^{\pm}$ and Z boson, respectively. The mixing angle β as referred before, can be expressed through the ratio of the two vevs, as follows:

$$tan\beta = \frac{v_2}{v_1} \tag{2.24}$$

Moreover, the mixing angle α can be extracted from the elements of the CP-even scalar mass matrix in Eq.2.19.

$$tan2\alpha = \frac{2\alpha_{12}}{a_{11} - a_{22}} \tag{2.25}$$

Finally, the eigenstates of each five states of Higgs as a function of the mixing angle α and ϕ_1^0 and ϕ_2^0 are:

$$H = -cos\alpha Re(\phi_1^0) - sin\alpha Re(\phi_2^0) \tag{2.26a}$$

$$h = sin\alpha Re(\phi_1^0) - cos\alpha Re(\phi_2^0) \tag{2.26b}$$

$$A = sin\beta Im(\phi_1^0) + cos\beta Im(\phi_2^0) \tag{2.26c}$$

$$H^{\pm} = sin\beta\phi_1^{\pm} + cos\beta\phi_2^{\pm} \tag{2.26d}$$

To sum up, there are three degrees of freedom which are absorbed by the longitudinal components of the massive gauge bosons, $W^{\pm}$ and Z, when they become massive and the remaining five degrees of freedom lead to the presence of the five physical states of Higgs boson:

- 2 charged bosons, $H^{\pm}$, with quantum numbers $J^P = 0^+$
- 2 neutral Higgs bosons, h and H, with quantum numbers $J^{CP} = 0^{++}$
- and 1 pseudoscalar boson, A, with quantum numbers $J^{CP} = 0^{+-}$

It is worth mentioning that the "modified" 2HDM model has seven free parameters, instead of only one λ parameter as the SM. The parameters of the 2HDM can be expressed by:

$$m_{H^{\pm}}, \quad m_H, \quad m_h, \quad m_A, \quad tan\beta, \quad m_{12}^2, \quad sin(\beta - \alpha) \tag{2.27}$$

2.2.4 HIGGS-GAUGE BOSON COUPLINGS

The examination of the couplings of the five physical Higgs bosons to vector bosons is presented in this section. The Higgs-gauge boson couplings are very important for a possible observation of a non-SM

Higgs boson because they impact on productions and decays of the Higgs boson. Couplings of the Higgs to a vector boson can be understandable by examining the J^{PC}[2] quantum numbers to all bosons of the theory. Table 2.1 shows the J^{PC} quantum numbers of each Higgs and vector boson for two cases. The first case is when C and P are separately conserved and the second one is when C and P are violated but CP is conserved.

Particle	J^{PC}		J^P
When C and P are separately conserved			
γ	1^{--}	$W^{\pm}$	1^-
Z	1^{--}	$H^{\pm}$	0^+
H^0	0^{++}		
h^0	0^{++}		
A^0	0^{+-}		
When C and P are violated but CP is conserved			
γ	1^{--}	$W^{\pm}$	$1^-, 1^+$
Z	$1^{--}, 1^{++}$	$H^{\pm}$	$0^+, 0^-$
H^0	$0^{++}, 0^{--}$		
h^0	$0^{++}, 0^{--}$		
A^0	$0^{+-}, 0^{-+}$		

Table 2.1: Quantum numbers of Higgs and gauge bosons [38].

At first glance, the J^{PC} quantum numbers of A^0 are weird because A^0 might be a C-odd and CP-odd boson as indicated in Table 2.1, however, the existence of the ZH^0A^0 vertex can justify this behaviour. The existence of the ZH^+H^- vertex implies that Z is a 1^{--} vector boson and the presence of the $H^0h^0h^0$ vertex requires H^0 scalar boson with 0^{++} quantum numbers [38]. Therefore, due to the existence of the ZH^0Z^0 vertex, A^0 should be both C-odd and CP-odd. The absence of $A^0W^+W^-$ and A^0ZZ couplings can be sufficiently explained by looking at the bosonic sector of the Lagrangian in which the certain terms are missing.

Furthermore, in any model of electroweak symmetry breaking, the couplings must satisfy the requirement that partial amplitudes ($V_LV_L \to V_LV_L$ and $f_+\bar{f}_+ \to V_LV_L$) do not violate unitarity bounds. In any gauge theory, the partial wave amplitude cannot grow with energy and this condition could be achieved by requiring cancellations among Feynman diagrams. For instance, in $WW \to WW$ scattering, the cancellation which avoids the growing energy terms is applied in the Standard Model by the tree-level relation $g_{\phi^0WW} = gm_W$, where g is the gauge coupling [38]. However, in models with more than one doublet, this cancelation cannot guarantee the treatment of the unitarity problems. In order to

[2] J:total spin, P:Parity, C:Charge conjugate

ensure unitarity, the couplings must obey the following sum rules:

$$\sum_i g^2_{h^0_i VV} = g^2_{\phi^0 VV} \tag{2.28}$$

and

$$\sum_i g_{h^0_i VV} g_{h^0_i f\bar{f}} = g_{\phi^0 VV} g_{\phi^0 f\bar{f}} \tag{2.29}$$

where i labels are for the neutral Higgs bosons of the extended Higgs sector, and ϕ^0 corresponds to the SM Higgs. For the case of 2HDM, the sum rule becomes:

$$g^2_{h^0 VV} + g^2_{H^0 VV} = g^2_{\phi^0 VV} \tag{2.30}$$

and V is for W or Z boson. Moreover, the couplings can be defined in terms of the angles α and β as follows:

$$\frac{g_{h^0 VV}}{g_{\phi^0 VV}} = sin(\beta - \alpha) \quad \frac{g_{H^0 VV}}{g_{\phi^0 VV}} = cos(\beta - \alpha) \tag{2.31}$$

Here, it is worthwhile to note that the absence of the coupling $A^0 VV$ is noticeable. Only V-V-Higgs couplings are shown so far, while it is vital to define the V-Higgs-Higgs couplings in the two-doublet model too. By using an analogous definition for V-Higgs-Higgs couplings, the $A^0 ZH$ coupling can be written:

$$g^2_{H^+ W^- h^0} + g^2_{H^+ W^- H^0} = [g^2_{A^0 Z h^0} + g^2_{A^0 Z H^0}] cos^2\theta_W = g^2/4 \tag{2.32}$$

Additionally, by following a similar procedure as before, the V-Higgs-Higgs couplings are related to the mixing angles α and β.

$$g_{h^0 A^0 Z} = \frac{g}{2cos\theta_W} cos(\beta - \alpha) \tag{2.33a}$$

$$g_{H^+ W^- h^0} = \frac{g}{2} cos(\beta - \alpha) \tag{2.33b}$$

$$g_{H^0 A^0 Z} = \frac{g}{2cos\theta_W} sin(\beta - \alpha) \tag{2.33c}$$

$$g_{H^+ W^- H^0} = \frac{g}{2} sin(\beta - \alpha) \tag{2.33d}$$

As can be seen, due to the existence of five Higgs bosons in 2HDM, there is a large number of possible couplings of the Higgs bosons to the particles of the model. Table 2.2 shows the couplings that are either proportional to $cos(\beta - \alpha)$ and $sin(\beta - \alpha)$ or angle-independent.

$cos(\beta-\alpha)$	$sin(\beta-\alpha)$	Angle-independent
HW^+W^-	hW^+W^-	-
HZZ	hZZ	-
ZAh	ZAH	$ZH^+H^-,\ \gamma H^+H^-$
$W^\pm H^\mp h$	$W^\pm H^\mp H$	$W^\pm H^\mp A$
$ZW^\pm H^\mp h$	$ZW^\pm H^\mp H$	$ZW^\pm H^\mp A$
$\gamma W^\pm H^\mp h$	$\gamma W^\pm H^\mp H$	$\gamma W^\pm H^\mp A$
-	-	$VV\phi\phi,\ VVAA,\ VVH^+H^-$

Table 2.2: Couplings between Higgs bosons and vector fields. Here $\phi = h, H$ and $VV = W^+W^-, ZZ, Z\gamma, \gamma\gamma$.

2.2.5 YUKAWA COUPLINGS IN THE 2HDM MODEL

In this section, we discuss the various Yukawa couplings in the Two-Higgs-Doublet model. Four different 2HDM types arise from the couplings of the Higgs doublets to the fermions and leptons by assuming the CP-conservation in the extended Higgs sector:

- ***Type-I***: all fermions are coupled to the Higgs fields in the Φ_2 doublet, and discrete symmetry is applied in Type-I: $\Phi_1 \to -\Phi_1$
- ***Type-II***: up-type quarks are coupled to the Φ_2 doublet, down-type quarks and charged leptons couple to the Higgs field in the Φ_1 doublet.
- ***Flipped***: up-type quarks and charged leptons are coupled to the Φ_2 doublet, down-type quarks are coupled to Φ_1.
- ***Lepton-specific***: all quarks are coupled to the Higgs field in the Φ_2 doublet, and charged leptons are coupled to Φ_1.

Table 2.3 summarises the four different types of 2HDM where up- and down-quarks are coupled to different Higgs fields for the various types of 2HDM.

Models	u_R^i	d_R^i	e_R^i
Type-I	Φ_2	Φ_2	Φ_2
Type-II	Φ_2	Φ_1	Φ_1
Flipped	Φ_2	Φ_1	Φ_2
Lepton-specific	Φ_2	Φ_2	Φ_1

Table 2.3: The four types of the 2HDM and the couplings between up-down quarks and Higgs fields.

As we can see from Tab. 2.3, there is no reference to the neutrinos because they do not couple to any Higgs boson in 2HDM.

In order to examine the Yukawa couplings, one can derive the couplings of the five physical Higgs bosons to the leptons and quarks by examining the Lagrangian of Yukawa in terms of mass eigenstates of the Higgs bosons as [37]:

$$\begin{aligned}\mathcal{L}_{Yukawa}^{2HDM} = &- \sum_{f=u,d,\ell} \frac{m_f}{\upsilon}\left(\xi_h^f \bar{f} f h + \xi_H^f \bar{f} f H - i\xi_A^f \bar{f}\gamma_5 f A\right) \\ &+ \left\{\frac{\sqrt{2}V_{ud}}{\upsilon}\bar{u}\left(m_u \xi_A^u P_L + m_d \xi_A^d P_R\right) d H^+ + \frac{\sqrt{2}m_\ell \xi_A^\ell}{\upsilon}\bar{\upsilon}_L \ell_R H^+ + h.c.\right\}\end{aligned} \tag{2.34}$$

where P_L and P_R are the left and right handed projective operations, respectively, the VEV $\upsilon = \sqrt{\upsilon^1 + \upsilon^2} \simeq 246$ GeV, V_{ud} represents the element of CKM matrix and γ_5 is the fifth Dirac matrix. Parameters ξ correspond to the couplings of the five Higgs bosons to quarks and leptons. As can be observed, there are couplings which are referred to the fermions, up- and down-quarks and leptons, but not to the couplings which correspond to the neutrinos and any Higgs boson in the Lagrangian. The factors ξ are presented in Table 2.4 in which the Yukawa couplings of up-, down-quarks and leptons to all physical Higgs states in the four models of 2HDM are included.

Couplings	Type-I	Type-II	Flipped	Lepton-specific
ξ_h^u	$cos\alpha/sin\beta$	$cos\alpha/sin\beta$	$cos\alpha/sin\beta$	$cos\alpha/sin\beta$
ξ_h^d	$cos\alpha/sin\beta$	$-sin\alpha/cos\beta$	$-sin\alpha/cos\beta$	$cos\alpha/sin\beta$
ξ_h^ℓ	$cos\alpha/sin\beta$	$-sin\alpha/cos\beta$	$cos\alpha/sin\beta$	$-sin\alpha/cos\beta$
ξ_H^u	$sin\alpha/sin\beta$	$sin\alpha/sin\beta$	$sin\alpha/sin\beta$	$sin\alpha/sin\beta$
ξ_H^d	$sin\alpha/sin\beta$	$cos\alpha/cos\beta$	$cos\alpha/cos\beta$	$sin\alpha/sin\beta$
ξ_H^ℓ	$sin\alpha/sin\beta$	$cos\alpha/cos\beta$	$sin\alpha/sin\beta$	$cos\alpha/cos\beta$
$\xi_{H^\pm}^u$	$cot\beta$	$cot\beta$	$cot\beta$	$cot\beta$
$\xi_{H^\pm}^d$	$cot\beta$	$-tan\beta$	$-tan\beta$	$cot\beta$
$\xi_{H^\pm}^\ell$	$cot\beta$	$-tan\beta$	$cot\beta$	$-\tan\beta$
ξ_A^u	$cot\beta$	$cot\beta$	$cot\beta$	$cot\beta$
ξ_A^d	$-cot\beta$	$tan\beta$	$tan\beta$	$-cot\beta$
ξ_A^ℓ	$-cot\beta$	$tan\beta$	$-cot\beta$	$tan\beta$

Table 2.4: Yukawa couplings of υ, d, ℓ to the neutral Higgs bosons h, H, A, $H^\pm$ in the four different types of the 2HDM model.

2.2.6 THE DECOUPLING AND ALIGNMENT LIMITS IN THE 2HDM MODEL

Many BSM theories might converge to the SM under suitable conditions. Such theory is the 2HDM model in which the SM-like Higgs boson (h_{SM}) can arise in the *alignment limit* [39] or in the *decoupling limit* [40].

The *decoupling limit* of 2HDM corresponds to the case in which one of the two Higgs doublets receives a very large mass and is therefore decoupled from the theory. It can be satisfied when $cos(\beta - \alpha)$ converges to the limit of 0 ($cos(\beta - \alpha) \rightarrow 0$). This is equivalent to $(\beta - \alpha) \rightarrow \pi/2$ given that $0 \leq \beta \leq \pi/2$. In the decoupling limit, the mass of h can have the mass of the SM-like Higgs boson, while the remaining masses ($H, H^{\pm}, A$) are much larger. Indeed, if the theory is characterised by two mass scales, m_S and m_L and the former mass scale is much greater than the latter scale, $m_S >> m_L$, the effective field theory such as 2HDM, if it exists, can correspond to the SM because the one of the Higgs doublets is integrated out. In the decoupling limit the m_h is approximately equal to the mass scale m_L, $m_h \simeq m_L$, and the remaining masses tend to be equal to the mass scale m_S, $m_H, m_H^{\pm}, m_A \simeq m_S$.

The *alignment limit* is the limit in which the one of the two neutral CP-even Higgs bosons aligns with the direction of the scalar field vacuum expectation values, $m_h \simeq v$ or $m_H \simeq v$, disappearing the mixing between the h and H states. The alignment limit corresponds either to the limit of $cos(\beta - \alpha) \rightarrow 0$, if h is identified as the SM-like Higgs boson, or to the limit of $sin(\beta - \alpha) \rightarrow 0$, if H is identified as the SM-like Higgs boson. The alignment limit is clearly independent of the choice of basis for the two Higgs doublets and is more general case than the decoupling limit [41]. It is important to note that it is not necessary that the H, A, and $H^{\pm}$ bosons are heavy.

2.2.7 WRONG-SIGN YUKAWA COUPLING IN THE 2HDM MODEL

The *wrong-sign Yukawa coupling* [42] is the region of 2HDM where at least one of the couplings of h to down-type and up-type fermions pairs is opposite in sign to the corresponding coupling of h to vector-vector boson pairs. On the contrary, in the SM, the couplings of h to fermion pairs and to VV pairs have the same positive sign.

Tab. 2.4 shows that the Type-I 2HDM and Lepton-specific models have the same couplings of the h to up-type quarks and to down-type quarks. At first glance, there is no-negative sign, however, both the ξ_h^u and ξ_h^d couplings can be conveniently rewritten in the following form:

$$\frac{cos\alpha}{sin\beta} = sin(\beta - \alpha) + cos(\beta - \alpha)cot\beta \tag{2.35}$$

In order to normalise ξ_h^u and ξ_h^d to be equal to -1, $sin(\beta - \alpha)$ should be -1, which is only possible if $tan\beta < 1$. However, $tan\beta < 1$ is phenomenologically constraint from B physics observables and from the $R_b \equiv \Gamma(Z \rightarrow b\bar{b})/\Gamma(Z \rightarrow hadrons)$ measurements.

It is clear (see Tab. 2.4) that the wrong sign exists in the Type-II 2HDM and in the Flipped type.

Similarly, rewriting both couplings ξ_h^u and ξ_h^d as follows:

$$\xi_h^d : -\frac{sin\alpha}{cos\beta} = -sin(\beta+\alpha) + cos(\beta+\alpha)tan\beta \tag{2.36}$$

$$\xi_h^u : \frac{cos\alpha}{sin\beta} = sin(\beta+\alpha) + cos(\beta+\alpha)cot\beta \tag{2.37}$$

it is highly visible that the ξ_h^d coupling is equal to -1 in the case of $sin(\beta+\alpha) = 1$, whereas the ξ_h^u coupling is $+1$. The wrong-sign of ξ_h^d coupling can be achieved for values of $tan\beta > 1$ when $sin(\beta-\alpha) = -cos2\beta$. On the other hand, the ξ_h^u coupling takes the wrong-sign when $sin(\beta-\alpha) = cos2\beta$ which implies the forbidden case from B physics observables and from R_b measurements, where $tan\beta$ must be less than 1.

Overall, to have the wrong-sign Yukawa couplings, $tan\beta$ must be greater than 1 when $sin(\beta-\alpha) = -cos2\beta$ and it occurs only in the Type-II 2HDM and in the Flipped type.

2.2.8 HIGGS PRODUCTION IN THE 2HDM MODEL

The production of the Higgs boson of the SM is studied in detail. Calculations of two-loop corrections, including next-to-next-to-leading order calculations and soft-gluon resummations, have all been analysed in detail. Therefore, if the 2HDM model is valid, five physical Higgs states are predicted by the theory, having their own production modes. This section covers the production modes of all five Higgs bosons.

2.2.8.1 GLUON-GLUON FUSION

In the SM, at the parton lever, the cross section of the Higgs mass from gluon-gluon fusion is $\hat{\sigma}_{LO} = m_h^2\delta(\hat{s}-m_h^2)\sigma_o$, where:

$$\sigma_o = \frac{G_\mu \alpha_s^2}{512\sqrt{2}\pi}\left|\sum_q A_{1/2}^h(\tau_q)\right|^2 \tag{2.38}$$

G_F stands for the Fermi constant from muon decay, α_s is the strong coupling constant, and:

$$A_{1/2}^h(\tau_q) = 2[\tau_q + (\tau_q-1)f(\tau_q)]/\tau_q^2, \quad \tau_q = \frac{m_h^2}{4m_q^2}, \quad q : \text{quark} \tag{2.39}$$

where

$$f(\tau_q) = \begin{cases} arcsin^2(\sqrt{\tau_q}), & \text{when } \tau_q \le 1, \\ -\frac{1}{4}\left(log\frac{1+\sqrt{1-1/\tau_q}}{1-\sqrt{1-1/\tau_q}} - i\pi\right)^2, & \text{when } \tau_q > 1 \end{cases} \tag{2.40}$$

The delta-function ($\delta(\hat{s} - m_h^2)$) in the leading order cross section ensures that the Higgs particle is on-shell and that the Higgs mass is related to the proton-proton centre-of-mass energy, S as follows [43]:

$$\hat{s} = x_1 x_2 S = m_h^2 \tag{2.41}$$

The production cross section of each Higgs boson can be calculated in the 2HDM model when one can simply multiply the SM cross section by a factor which is related to the coupling of a specific state to quarks. Each of the five physical Higgs states can be generated by gluon-gluon fusion with a particular cross section.

For instance, the production cross section of the light Higgs boson, h, through gluon-gluon fusion is the SM cross section multiplied by the factor $(cos\alpha/sin\beta)^2$ in the Type-I or the Lepton-specific 2HDM type. In the Type-II or the Flipped 2HDM type where the b-quark loop plays a dominant role, the cross section of h is somehow different. The contribution of the top quark is also multiplied by $(cos\alpha/sin\beta)^2$, and additionally, the b-loop contribution to the amplitude is multiplied by $-tan\alpha tan\beta$.

In the case of the heavy CP-even Higgs boson, H, the results are similar with that of the light Higgs boson. In the Type-I or the Lepton-specific 2HDM type, the cross section of the CP-even Higgs boson is the SM cross section multiplied by the factor $(sin\alpha/sin\beta)^2$. In the Type-II or the Flipped 2HDM type, where the b-quark loop can contribute significantly to the cross section, the b-loop contribution is multiplied by $cot\alpha tan\beta$ and the top quark contribution is multiplied by $(sin\alpha/sin\beta)^2$.

For the gluon-gluon fusion production of the (pseudoscalar) CP-odd Higgs, A, the cross section does not only receive trivial factors by multiplying them by the top and b-quark contributions, but also, the factor $A_{1/2}^h$ (Eq. 2.39) is replaced by the simpler form $2f(\tau_q)/\tau_q$, which in the limit $m_t >> m_A$ is 2 instead of $4/3$. In the Type-I 2HDM or the Lepton-specific 2HDM type, the production cross section of the CP-odd Higgs is also multiplied by a total factor of $(9/4)cot^2\beta$, however, this factor is replaced by $tan^2\beta$ in the Type-II or the Flipped 2HDM type.

2.2.8.2 VECTOR BOSON PRODUCTION PROCESSES

The light and heavy CP-even neutral Higgs bosons can be produced through vector boson production processes such as $W^* \to WH$, $Z^* \to ZH$, $WW \to H$ and $ZZ \to H$, where H can be either the light or the heavy neutral Higgs. In all 2HDM types, the cross section of the light CP-even Higgs boson, h, is the SM cross section multiplied by the factor $sin^2(\alpha - \beta)$.

Additionally, the cross section of the heavy Higgs boson, H is also the SM cross section multiplied by the $cos^2(\alpha - \beta)$. On the other hand, the CP-odd Higgs boson, A, cannot be generated via this production mode, given that there are no W^+W^-A and ZZA vertices.

2.2.8.3 ASSOCIATED $t\bar{t}X$ PRODUCTION

This process always has a smaller rate than gluon-gluon fusion, however, it is an interesting production mode due to a clear signal if one can tag on a lepton from the decay of the top or antitop quark. In all 2HDM models, the cross section of light Higgs, h, can be multiplied by the factor $(cos\alpha/sin\beta)^2$. The cross section of the heavy neutral Higgs is multiplied by the factor $(sin\alpha/sin\beta)^2$ and the cross section of the pseudoscalar Higgs boson is multiplied by the factor $cot^2\beta$.

2.2.8.4 ASSOCIATED $b\bar{b}X$ PRODUCTION

This mechanism might be significant for large β values in the Type-II, when the Higgs coupling to b-quark pairs becomes strong enough. The rate of the production cross section for each five physical state of Higgs is negligible for the Type-I and the Lepton-specific type because there is no contribution from b-quark loops. Alternatively, in the Type-II or the Flipped 2HDM type, the associated $b\bar{b}X$ production can be important for very large values of β. The production cross section of h is multiplied by the factor $(sin\alpha/cos\beta)^2(m_b/m_t)^2$ whereas the cross section of the heavy scalar Higgs is proportional to $(cos\alpha/cos\beta)^2$. In the case of heavy CP-odd Higgs boson, A, the cross section is multiplied by $tan\beta$ and therefore, the production increases significantly when $tan\beta$ receives large values.

2.2.9 HIGGS DECAYS AND BRANCHING RATIOS IN THE 2HDM MODEL

In the 2HDM model, branching fractions do not exclusively depend on masses, but they are affected by mixing angles α and β. This makes calculations of $\mathcal{B}r$ complicated and a possible analysis of each Higgs state is more difficult. Table 2.5 summarises all possible decay channels of the five physical Higgs states in the 2HDM model, however, some of them are suppressed and some others are dramatically dominant due to the Higgs' couplings to quarks, leptons, or vector bosons.

Higgs bosons	Decay	Channels in 2HDM	Final States
$h,\ H,\ A$	H_iH_i	$H \to AA, hh$	$(bb/\tau\tau/WW/ZZ/\gamma\gamma)(bb/\tau\tau/WW/ZZ/\gamma\gamma)$
	H_iZ	$H \to AZ, A \to HZ, hZ$	$(bb/\tau\tau/WW/ZZ/\gamma\gamma)(\ell\ell/qq/\nu\nu)$
	$H^\pm H^\mp$	$H \to H^\pm H^\mp$	$(tb/\tau\nu/cs)(tb/\tau\nu/cs)$
	$H^\pm W^\mp$	$H/A \to H^\pm W^\mp$	$(tb/\tau\nu/cs)(\ell\nu/qq)$
charged Higgs $H^\pm$	$H_iW^\pm$	$H^\pm \to hW^\pm, HW^\pm, AW^\pm$	$(bb/\tau\tau/WW/ZZ/\gamma\gamma)(\ell\nu/qq)$

Table 2.5: Summary of all possible decay modes for non-SM Higgs bosons in the 2HDM model, where $H_i = h, H, A$.

In general, the branching fractions of any channel can increase or decrease due to a multiplied factor.

For instance, in the Type-I 2HDM, the coupling of the light neutral Higgs to fermions is the same as in the SM but multiplied by $cos\alpha/sin\beta$, while the light Higgs boson's couplings to WW and ZZ are multiplied by $sin(\alpha-\beta)$. Moreover, the coupling of the heavy CP-even Higgs boson to WW is multiplied by $sin\alpha/sin\beta$, while the coupling of the H to ZZ is multiplied by $cos(\alpha-\beta)$ [1].

As mentioned, there are some special cases where the suppression of the mixing angles α and β is interesting. If $sin(\alpha-\beta)$ ($cos(\alpha-\beta)$) vanishes, then the h (H) field is gauge-phobic and it does not couple to WW and ZZ. If $cos\alpha$ ($sin\alpha$) vanishes, then the h (H) is fermiophobic and the $\gamma\gamma$ decay can become dominant. In addition, the light Higgs boson can decay to ZA ($h \to ZA$), if the pseudoscalar mass, m_A, is less than $m_h - m_Z$. The width of the $h \to ZA$ decay channel is given by:

$$\Gamma(h \to ZA) = \frac{g^2 m_h^3 cos^2(\alpha-\beta)}{64\pi m_W^2}\left[(1-(m_Z^2-m_A^2)/m_h^2)^2 - 4m_Z^2 m_A^2/m_h^4\right]^{3/2} \quad (2.42)$$

The width takes the maximum value when $cos^2(\alpha-\beta)=1$, making the channel dominant. In addition, if pseudoscalars were lighter than h ($h \to AA$), the light Higgs boson, h, could decay to a pair of pseudoscalar Higgs boson.

Now, examining the decay channels of the heavier neutral scalar, H, it is clear that it couples to fermions proportionally to $sin\alpha/sin\beta$ and to vector bosons proportionally to $cos(\alpha-\beta)$. The H is a gauge-phobic at $\alpha = -\pi/4$ and the fermion's decay becomes dominant. On the other hand, the fermiophobic point is $\alpha = 0$ and the $H \to hh$ and $H \to AA$ decays may be kinematically allowed:

$$\Gamma(H \to hh) = \frac{g^2 m_Z^2}{128\pi m_H cos^2\theta_W}\left[cos2\alpha cos(\beta+\alpha) - 2sin2\alpha sin(\beta+\alpha)\right]^2\left(1-\frac{4m_h^2}{m_H^2}\right)^{1/2} \quad (2.43)$$

$$\Gamma(H \to AA) = \frac{g^2 m_Z^2}{128\pi m_H cos^2\theta_W}\left[cos2\beta cos(\beta+\alpha)\right]^2\left(1-\frac{4m_A^2}{m_H^2}\right)^{1/2} \quad (2.44)$$

Finally, the couplings of the CP-odd Higgs boson (A) to fermions are multiplied by $cot\beta$ and as reported before, there are no couplings to a pair of vector bosons. The branching fractions of the A related-channels will be independent of α and β and they will be derived from fermion mass ratios and phase space. For the pseudoscalar Higgs boson, there is an interesting scenario which is reasonable to be investigated where the CP-odd Higgs boson mass is greater than $m_h + m_Z$ but below 350 GeV. A possible decay mode of this scenario is the $A \to Zh$ decay channel. This decay channel dominates below 350 GeV due to the coupling of $t\bar{t}$. Over this point, the pseudoscalar Higgs boson decays to $t\bar{t}$, making the $A \to t\bar{t}$ a dominant channel, while the $\mathcal{B}r(A \to Zh)$ falls down dramatically. The

corresponding width is given by:

$$\Gamma(A \to Zh) = \frac{g^2 \left[(m_A^2 + m_h^2 - m_Z^2)^2 - 4m_A^2 m_h^2 \right]^{3/2} cos^2(\beta - \alpha)}{64\pi m_Z^2 m_A^3 cos^2\theta_W} \tag{2.45}$$

Comparing the decay modes of Type-II 2HDM and Type-I 2HDM, minor differences are observed. As shown in the previous Chapter 2.2.5, the coupling of h to fermions depends on the fermion charge. The coupling of the up-type quarks is the same as in Type-I (the SM coupling is multiplied by $cos\alpha/sin\beta$). Alternatively, the coupling of the down-type quarks and leptons are multiplied by $-sin\alpha/cos\beta$. For large $tan\beta$ values, these couplings are much larger than the couplings of the down-type quarks and leptons in Type-I. Unlike the Type-I 2HDM, all possible branching ratios are strongly dependent on $tan\beta$ and can drastically affect the Higgs phenomenology.

In Lepton-specific 2HDM type, the $\mathcal{B}r(h \to \tau^+\tau^-)$ is much larger than $\mathcal{B}r(h \to b\bar{b})$, and it grows as $tan^2\beta cot^2\alpha$. In the Lepton-specific type, the b-phobic value of α is $\pm\pi/2$ and the τ-phobic value of α is zero. When $\alpha = \pm\pi/2$, the $\tau^+\tau^-$ mode is dominant than other modes, however, when $\alpha = 0$, the $b\bar{b}$ mode replaces the $\tau^+\tau^-$ channel.

In Flipped 2HDM type, the τ-coupling is forbidden to have a huge improvement because it would also enhance the top-quark coupling, and a possible improvement of the latter would cause vital issues with perturbation theory and unitarity. The branching ratios of the light scalar h are similar with the Type-II ratios, however, the branching fraction of $\tau^+\tau^-$ mode is greater than that of the $b\bar{b}$ decays. In addition, the branching ratios of the other physical states of Higgsses (H, $H^\pm$ and A) are very similar to that of the Type-II.

Part II

Experimental Infrastructure

Chapter 3

The Large Hadron Collider Machine

Many colliders were built during the past decades but never one like the Large Hadron Collider (LHC). The LHC was built to outreach energy limits that previous accelerators could not achieve them. The LHC covers absolutely wider range of searches, including searches for supersymmetry and dark matter. The primary target of LHC was to discover the Higgs boson which was achieved on the 4^{th} July, 2012. The Higgs boson was discovered by using the data of RUN-I collected by the main detectors of LHC. This chapter is dedicated to the functionality of the LHC and describes various parts of the machine.

3.1 HISTORICAL DETAILS

The Large Hadron Collider (LHC) is located at the European Organisation for Nuclear Research (CERN) near Geneva, Switzerland, and it is a forceful machine for high energy physics experiments. It was constructed to collide heavy ion or proton beams with a centre-of-mass energy 14 TeV and luminosity $\simeq 10^{34}$ cm^{-2}s^{-1}. LHC is a two-ring-superconducting-hadron accelerator which replaced the Large Electron-Positron Collider (LEP) machine in the existing 27 Km circular tunnel. The tunnel is constructed around 45 m to 175 m underground and has a diameter of 3.7m. The particle collider requires to have two rings with counter-rotating beams, in contrast to particle-antiparticle colliders that can have both beams

Figure 3.1: The location of CERN.

in a single ring. For this reason, it is needed to exist two separate proton rings in the tunnel. The insufficient place in the tunnel did not allow the installation of two separate rings. Therefore, an alternative suggestion was proposed to solve the problem of space. The twin-bore magnet patent was proposed by John Blewett at the Brookhaven laboratory in 1971 [44] and the LHC was finally born.

3.2 LHC GOALS

Beyond the discovery of the Higgs at 125 GeV, the LHC aims to establish physics beyond the Standard Model with centre of mass collision energies of up to 14 TeV. Every second of the operation of the LHC will produce an extraordinary number of events (40 million events per second), computed by the following relation:

$$N_{event} = \mathcal{L}\sigma_{event} \tag{3.1}$$

where σ_{event} is the cross section for the event channel under study and $\mathcal{L}$ stands for the machine *luminosity*. The machine luminosity is proportional to the beam parameters, as follows:

$$\mathcal{L} = \frac{N_b^2 n_b f_{rev} \gamma_r}{4\pi\epsilon_n \beta^*} F \tag{3.2}$$

where N_b is the number of particles per bunch, n_b is the number of bunches per beam, f_{rev} the revolution frequency, γ_r the relativistic gamma factor, ϵ_n the normalized transverse beam emittance, β^* is the beta function at the collision point, and F the geometric luminosity reduction factor due to the crossing angle at the interaction point (IP):

$$F = \left(1 + \left(\frac{\theta_c \sigma_z}{2\sigma^*}\right)^2\right)^{-1/2} \tag{3.3}$$

where θ_c is the full crossing angle at the IP, σ_z the RMS bunch length and σ^* is the transverse RMS beam size at the IP. The LHC is designed to provide a luminosity $L = 10^{34}\text{cm}^{-2}\text{s}^{-1}$ for proton operation.

The machine parameters relevant for the operation of LHC detectors are listed in Tab. 3.1.

3.3 PARTS OF LHC

The LHC is not only a ring with diameter 27 Km, but it is a complex of accelerators. Protons are produced through the ionization of hydrogen gas in a duo-plasmatron and go through a set of accelerators before injecting in the LHC. An electric field is used to break down hydrogen atoms into protons and electrons. After that, they are sent to a radio frequency quadrupole, reaching the energy 750 KeV. The

Description	Symbol	proton-proton collision	Unit
Energy per nucleon	E	7	TeV
Dipole field at 7 TeV	B	8.33	T
Design Luminosity	$\mathcal{L}$	10^{34}	$\mathrm{cm}^{-2}\mathrm{s}^{-1}$
Bunch separation		25	ns
Number of bunches	k_B	2808	
Number of particles per bunch	N_p	1.15×10^{11}	
Collision			
$\beta-$value at IP	β^*	0.55	m
RMS beam radius at IP	σ^*	16.7	μm
Luminosity lifetime	τ_L	15	hr
Number of collisions/crossing	n_c	$\simeq 20$	

Table 3.1: The LHC parameters relevant for the LHC detectors.

first accelerator of the LHC is the LINAC2, where the protons acquire energy 50 MeV. Then, they are injected in the first circular accelerator, BOOSTER, until their energy becomes about 1.4 GeV, before entering the Proton Synchrotron (PS). In the PS ring, protons are accelerated at an energy 25 GeV. The last "small" accelerator is the Super Proton Synchrotron (SPS) where protons increase their energy to 470 GeV before injected in the LHC ring. Finally, in the LHC, protons are accelerated to their final energy 7 TeV for each beam. In the LHC, protons are divided into two different beams with opposite direction and they are collided at certain collision points.Fig. 3.2 illustrates the complex of accelerators at CERN.

3.4 FOUR EXPERIMENTS

Four collision points are located along the LHC ring. Four experiments are installed at the four collision points in the LHC:

1. CMS (Compact Muon Solenoid) [46].
2. ATLAS (A Toroidal LHC ApparatuS) [47]
3. LHCb (Large Hadron Collider beauty) [48]
4. ALICE (A Large Ion Collider Experiment) [49]

CMS is one of the largest and vital experiments in the LHC, which consists of a variety of detectors, giving the possibility to investigate a widespread range of physics objectives. The main purpose of CMS is to detect the SM scalar Higgs boson as well as supersymmetric particles including some candidates

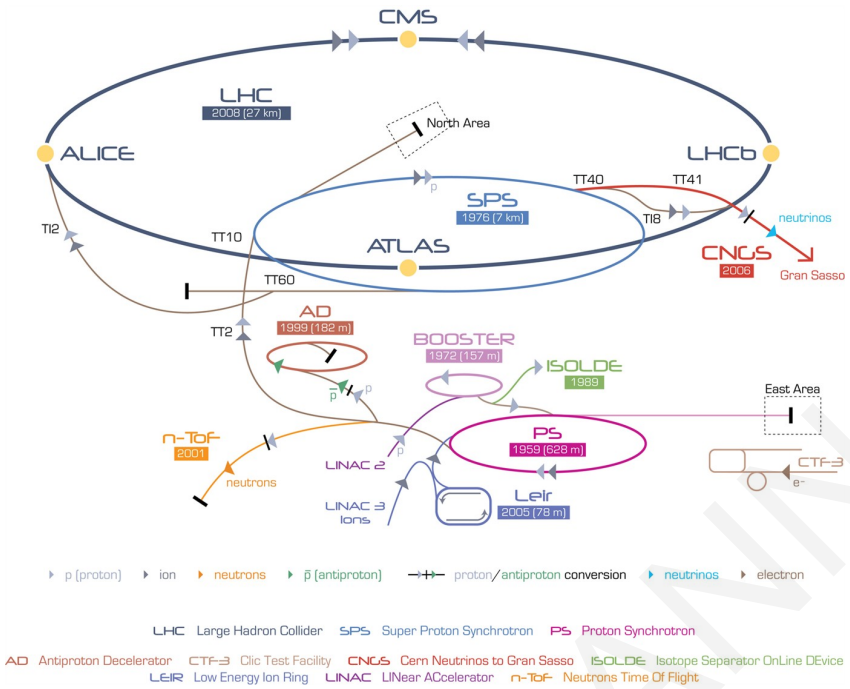

Figure 3.2: Overview of the CERN accelerator complex. Taken from Ref. [45].

of dark matter. The next Chapter is completely dedicated to the CMS experiment in which each detector of the experiment is described in detail.

ATLAS is the second largest experiment in the LHC. It has the same physics goals as CMS, however, it uses different subdetector/choices. The remaining experiments of LHC, are smaller than CMS and ATLAS but they play an important role to the detection of new physics too. LHCb was designed to study CP-violation as well as rare decays of b-quarks. ALICE is a heavy-ion detector which aims to examine strong interactions in high energy densities where a new phase of matter is expected to be formed, the *quark-gluon plasma*.

3.5 OPERATION OF LHC

LHC was designed to start operating in 2008, however, a faulty electrical connection between two magnets caused a loss of approximately six tonnes of liquid helium, damaging a total of 53 magnets. Finally, LHC went live on 20 November 2009 and successfully operated for four and half years completing RUN-I by delivering luminosity 30 fb^{-1}. In 2013, its operation stopped for replacing damaged detector components with new ones. The first *Long Shut Down* (LS1) took place in 2013 and lasted for two years. After that, LHC started operating again, accelerating the beam protons at a centre-of-mass energy 13 TeV and delivering an overall integrated luminosity 150 fb^{-1} in RUN-II. Again, it stopped circulating

the beams at the end of 2018 for the big upgrade of the four experiments and the accelerator machine. During Long Shut Down 2 (LS2) the PS Booster and the SPS will receive the most major upgrades. In addition, the CMS experiment will also receive new subdetectors and upgraded electronics. Gas Electron Multiplier (GEM) superchambers will be installed into the CMS endcap as part of the newest CMS muon subsystem and the CMS Muon Cathode Strip Chamber (CS) subsystem will have upgraded electronics. The LS2 is expected to be completed in 2021 and then LHC will be ready for RUN-III. RUN-III will last for three entire years, delivering an integrated luminosity 300 fb^{-1} before stopping again for the biggest upgrade. During Long Shut Down 3 (LS3), the particle accelerator chain will be entirely renovated and the experiments will replace numerous components, even whole subdetectors in order to be efficient for high luminosity runs (an integrated luminosity of about 3000 fb^{-1}). A new Electromagnetic Calorimeter called High-Granularity Calorimeter (HGCAL) will replace the current electromagnetic calorimeter in order to cope with the new environment and retain a good physics performance up to 3000 fb^{-1}. The CMS HGCAL consists of an electromagnetic part called Endcap Electromagnetic EE and two hadronic parts called Front Hadronic (FH) and Back Hadronic (BH) calorimeters. Layers of silicon pad sensors as active elements with lead in a stainless steel envelope as absorber are used in the electromagnetic part. The two hadronic parts consist of steel absorbers and silicon as active elements are used in the high $|\eta|$ regions and scintillating tiles with Silicon Photomultipliers (SiPM) readout in the lower $|\eta|$ regions [50]. In addition, a new H^- Linac (Linac4) will be installed as a new part of LHC, the PS Booster, and PS and SPS synchrotrons will also receive massive upgrades in order to operate smoothly in the high-luminosity LHC (HL-LHC) era [51].

The LHC accelerator between 2010 and 2018 delivered an overall integrated luminosity 180 fb^{-1}. Fig. 3.3 illustrates the delivered luminosity for these years, indicating the corresponding centre-of-mass energy.

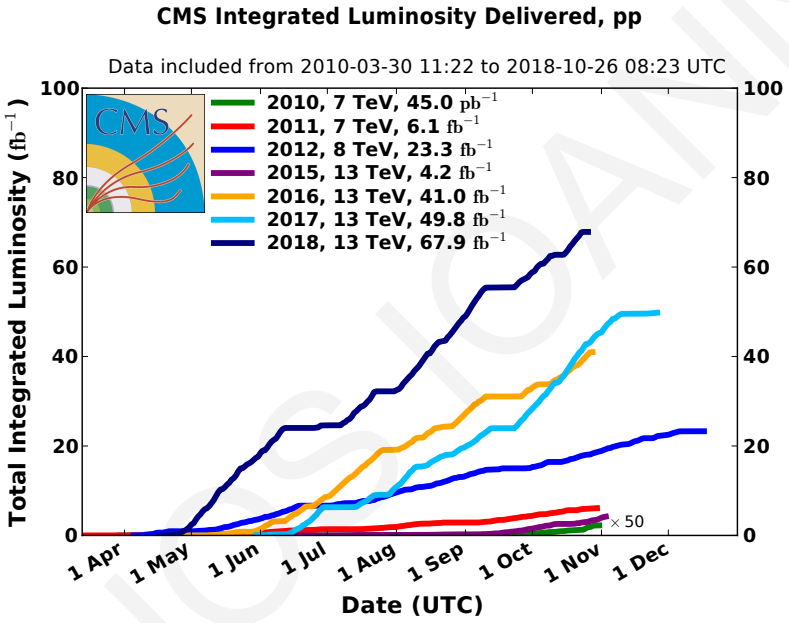

Figure 3.3: Delivered luminosity as a function of time for 2010-2012 (RUN I) and 2015-2018 (RUN II). Taken from Ref. [52].

Chapter 4

Compact Muon Solenoid Experiment

The LHC is just an accelerator; it does not record any data, it just circulates and collides two opposite proton beams. In order to record events, a complex of detectors must be placed at the collision points of LHC. The Compact Muon Solenoid (CMS) experiment is one of these detectors. This Chapter is referred to the CMS Experiment by describing its detectors, one by one, revealing their power to identify any unknown particles.

4.1 CMS IN A NUTSHELL

The Compact Muon Solenoid (CMS) apparatus has a primary target to precisely identify muon particles thanks to its state-of-the-art muon system. In addition, it is designed to study a wide range of particles and their properties which are created by high energy collisions. CMS is able to identify muons, electrons, photons, and hadrons by measuring their energy accurately. Furthermore, CMS can indirectly measure the *Missing Transverse Energy* (MET or $\not{E}_T$) of neutrinos by using powerful algorithms which are able to reconstruct the energy of neutrinos. To summarise, CMS consists of, from the outermost to the innermost part:

(a) **Muon system**: for identifying muon particles.

(b) **Superconducting Magnet**: for providing a 3.8 Tesla magnetic field parallel to the beam axis to bend the tracks of all charged particles.

(c) **Hadronic Calorimeter (HCAL)**: for measuring energies and directions of hadrons and jets as well as calculating the missing transverse energy of events.

(d) **Preshower Detector**: placed in front of Endcap ECAL helping to discriminate between single photons and neutral pions (π^0).

(e) **Electromagnetic Calorimeter (ECAL)**: for measuring energies and directions of electrons, positrons and photons. ECAL has a very good energy resolution, better than 0.5%.

(f) **Tracker Detector**: for determining momentum of particles, primary and secondary vertices of charged particles. The Tracker Detector records the trajectories of produced particles from high energy collisions.

(g) **Trigger**: for recording only the interesting events by reducing the huge amount of data produced in the proton-proton collisions.

Fig. 4.1 shows the whole complex of CMS detectors and its dimensions. CMS weighs 14 000 tons, is 28.7m long and has a diameter of 15.0 m. In addition, the coordinate system adopted by CMS is shown in Fig. 4.1 and it has the origin centred at the nominal collision point. The x-axis is pointing radially inward toward the centre of the LHC and the y-axis is pointing vertically upward. The z-axis points along the beam direction toward the Jura mountains from LHC Point 5.

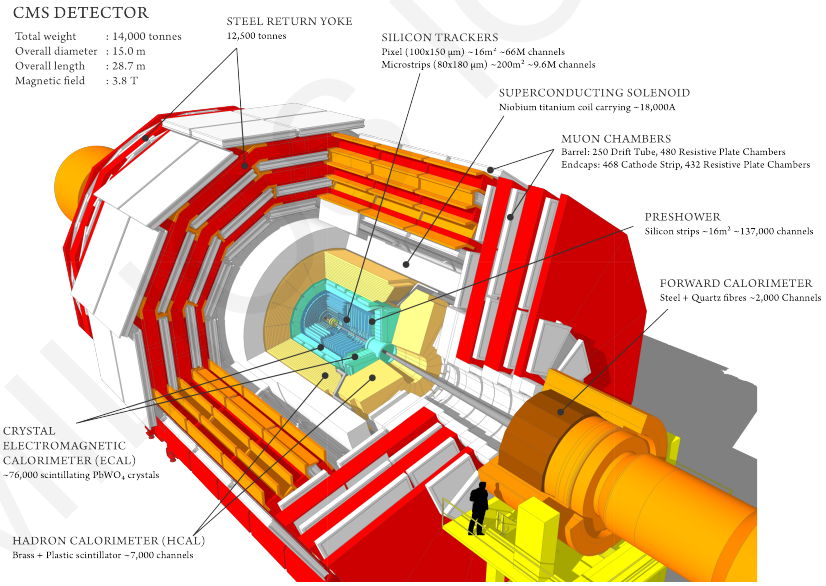

Figure 4.1: The Compact Muon Solenoid experiment.

The azimuthal angle ϕ is measured from the x-axis in the x-y plane and the polar angle θ from the z-axis. In high energy experiments, a new variable, *pesudorapidity* (η), is introduced instead of the polar angle. Pseudorapidity is defined in terms of the polar angle, as follows:

$$\eta = -\ln \tan(\theta/2) \tag{4.1}$$

When pseudorapidity of a particle is equal to zero ($\eta = 0$), its movement is perpendicular to the beam direction and, additionally, the beam direction itself has pseudorapidity $\pm\infty$ in the z-direction. Another useful variable similar to pseudorapidity, is the rapidity, y, defined as:

$$y = \frac{1}{2}\ln\left(\frac{E + p_z}{E - p_z}\right) \tag{4.2}$$

and it is equivalent to the pseudorapidity for massless particles. The transverse momentum of particles, denoted by p_T, is computed from the x- and y-components. Similarly, the energy measured transverse to the beam direction, is defined as $E_T = E\sin\theta$, and the imbalance of energy in the transverse plane is called *Missing Transverse Energy* (MET), denoted by $\not{E}_T$ or E_T^{miss}. Additionally, the distance between two particles recorded by detectors can be measured in a third Lorentz-invariant variable, called ΔR, and it is equal:

$$\Delta R = \sqrt{\Delta\eta^2 + \Delta\phi^2} \tag{4.3}$$

where $\Delta\eta$ and $\Delta\phi$, are the differences of pseudorapidity and azimuthal angle between two particles, respectively.

4.2 MAGNET

CMS was built providing the strongest superconducting magnet ever built. The Collaboration selected a large superconducting solenoid magnet for achieving its primary goal, which is the measurement of 1 TeV muon momentum with 10% resolution and bending the tracks of charged particles by a magnetic field 3.8 Tesla. The magnet is 12.9 m long and has an inner diameter of 5.9 m. 2168 turns were needed to cover the entire magnet, carrying a 19.5 kA current. The superconducting solenoid magnet can produce roughly 3.8 Tesla in extremely low temperature, achievable by cooling down the magnet with liquid helium.

4.3 TRACKING SYSTEM

The inner tracking system of CMS provides a precise and efficient measurement of the tracks of charged particles as well as a precise reconstruction of secondary vertices for jet identification. It has a length of 5.8 m and a diameter 2.5 m, surrounding the entire interaction point. Furthermore, the tracking detector requires a high granularity and fast response due to the large number of particles and tracks for each proton-proton interaction, which occurs every 25 ns. The tracking system can be damaged by radiation interactions due to the intense particle flux and therefore, the main challenge was to develop a system able to operate in this harsh environment. The inner tracking system, based on silicon detector

technology, provides a system with high granularity, speed and radiation hardness.

The CMS tracker consists of a pixel detector with 3 barrel layers placed close to the interaction vertex, where the particle flux is the highest, and silicon microstrip detectors with 10 barrel detection layers, located in the intermediate and outermost regions where the particle flux is sufficiently dropped. The difference between two regions is that silicon microstrip detectors with a minimum cell size of 10 cm $\times$ 80 μm are used in the intermediate region, while larger-pitch silicon microstrips with maximum cell size of 25 cm $\times$ 180 μm are placed in the outermost region. Besides, the forward region is equipped with 2 pixel and 9 microstrip layers in each of the 2 Endcaps. The barrel part is separated into an Inner and an Outer Barrel, where the inner barrel is shorter than the outer barrel for avoiding excessively shallow track crossing angles. The gap area between them is covered by placing three additional inner disks. The pixel detector covers an area of 1 m^2, whilst the silicon detectors' coverage is 200 m^2 [53, 54]. The CMS inner tracking system is composed of 1440 pixel and 15 148 strip detector modules.

A drawing of the whole CMS tracking system is shown in Fig. 4.2. Three cylindrical layers of pixel detector modules surround the interaction point at the positions $r = 4.4,\ 7.3,\ 10$ cm, respectively. Two discs of pixel modules on each side complete the pixel detector by covering an area of about 1 m^2 and having 66 million pixels, ready to detect any charged particle trajectory at the interaction point.

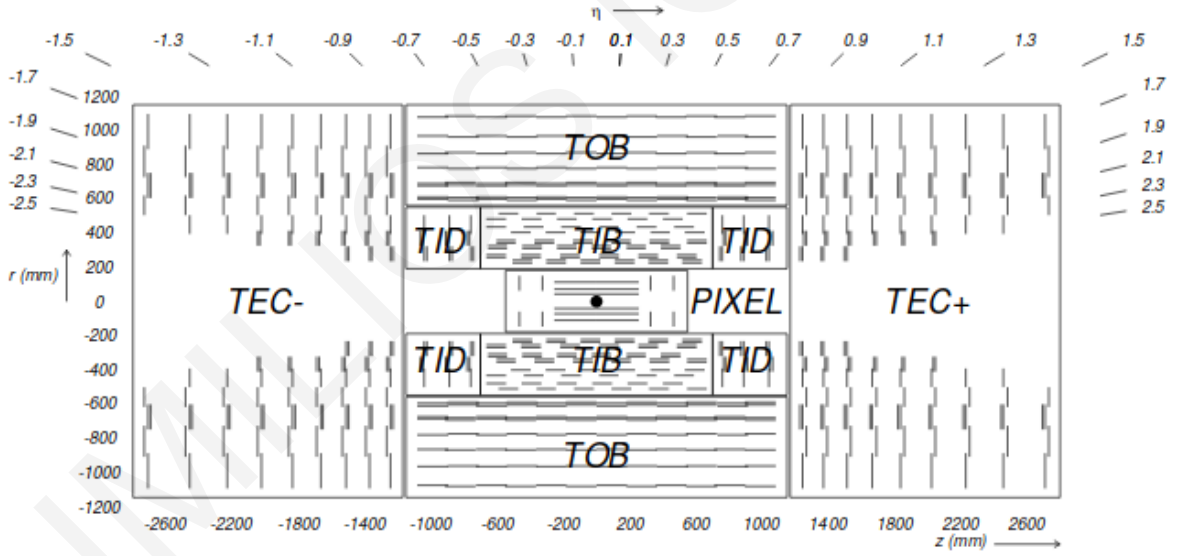

Figure 4.2: The CMS tracker. Each line corresponds to a detector module. Each area has own name and symbol. TOB: Tracker Outer Barrel, TEC-: Tracker Endcap Minus, TEC+: Tracker Endcap Plus, TID: Tracker Inner Disk, TIB: Tracker Inner Barrel. Taken from Ref. [55].

The silicon strip detector covers the radial region between 20 cm and 116 cm. The *Tracker Inner Barrel* and *Disks* (TIB/TID) reach at radius of 55 cm and consist of 4 barrel layers, supplemented by 3 disks at each end. The *Tracker Outer Barrel* (TOB) surrounds the TIB/TID, and has a radius of 116 cm and is

composed of 6 barrel layers of microstrip detectors. The *Tracker EndCaps* (TEC+/TEC-) consist of 9 disks, carrying up to 7 rings of silicon microstrip detectors. TEC+/TEC- are placed in the direction of the z-axis.

The material budget of the CMS tracker in units of radiation lengths and hadronic interaction length is shown in Fig. 4.3, as estimated from simulation [56]. The figure illustrates the tracker material budget with an accuracy better than 10%, as was established by measuring the distribution of reconstructed nuclear interactions and photon conversions in the tracker.

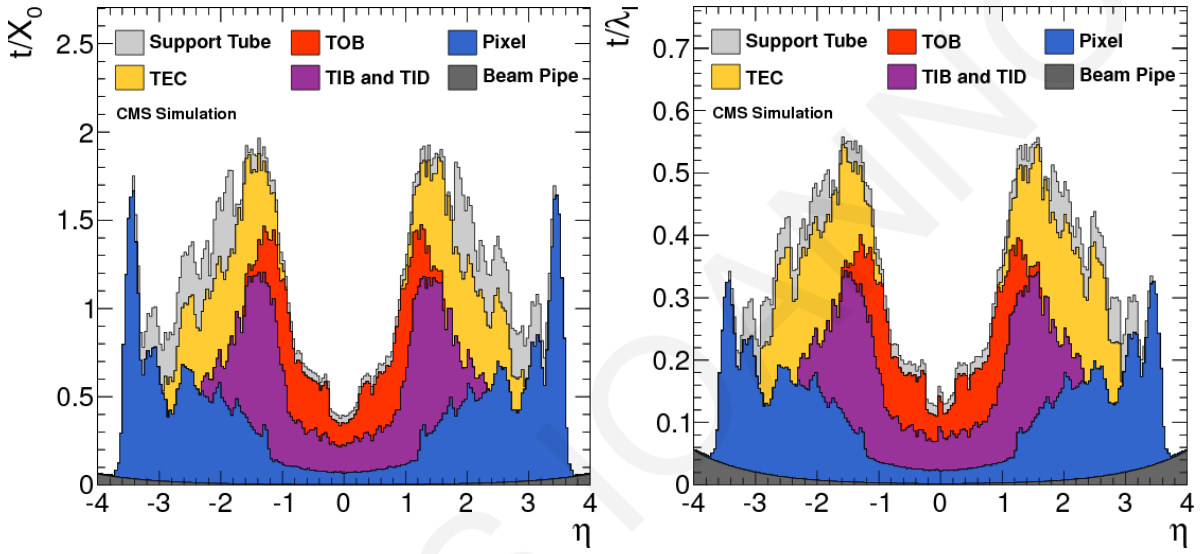

Figure 4.3: Right: Radiation length t/X_0 of the tracker material as a function of pseudorapidity η for the different sub-detectors of the tracker. Left: Hadronic interaction length t/λ_I of the tracker material as a function of pseudorapidity η for the different sub-detectors of the tracker. Taken from Ref. [56].

4.3.1 PIXEL DETECTOR

The pixel system is the innermost part of the CMS tracking system and surrounds the interaction region. It provides a precise measurement of the tracking points in $r-\phi$ and x directions and is responsible for a good secondary vertex reconstruction. It has the leading role for the reconstruction of tracks and vertices. In order to achieve a good track resolution in both $r-\phi$ and z directions, the pixel system consists of pixel cell sizes of 100×150 μm^2. By taking advantage of the small size of pixel cells, it can easily reconstruct a 3D vertex which will be important for secondary vertices. Moreover, the pixel system provides a good position resolution and can well separate signal and noise hits as well as to identify large hit clusters from overlapping tracks.

The pixel detector is extended from pseudorapidity -2.5 to 2.5 ($-2.5 < \eta < 2.5$) and consists of three

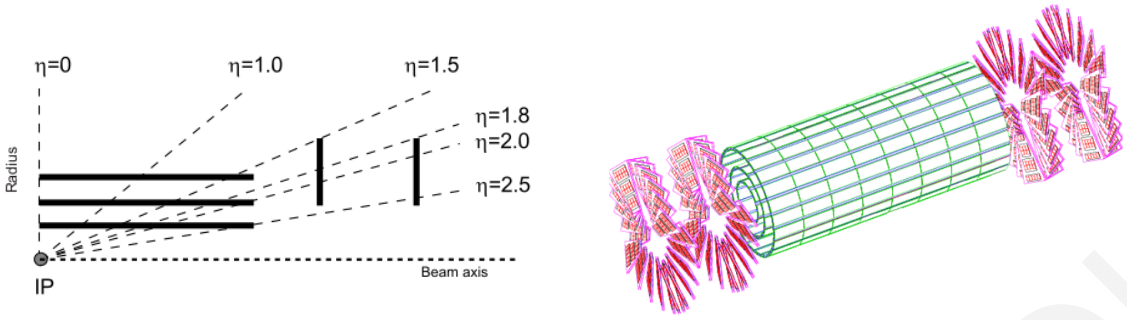

Figure 4.4: Geometrical layout of the pixel detector.

barrel layers (BPix) and two endcap disks (FPix), as shown in Fig. 4.4. BPix contains 48M pixels covering a total area of 0.78 m^2, and FPix includes 18 million pixels in a total area of 0.28 m^2. The arrangement of the three barrel layers and the two pixel disks on each side ensures 3 tracking hits over almost the full η-range. The pixel detector is exposed to a strong radiation produced by proton-proton collisions and, as a result, it must have a radiation tolerant design. A very important feature of the pixel detector is to have a very good resolution because the pixel detector is very close to the interaction point which implies a very high track rate. The current technology of the pixel detector can achieve a spatial resolution in the range of 15-20 μm. Finally, it is worthwhile mentioning that the endcaps disks are assembled in a turbine-like geometry, titled at 20^0 to induce charge-sharing, which is a phenomenon caused by the geometric effect of particles entering the detector at an average angle of 20^0 away from normal incidence [57]. The charge-sharing effect is more intense at the presence of the magnetic field, in particular of 3.8 Tesla and is enhanced by the $\vec{E} \times \vec{B}$ drift.

4.3.2 SILICON STRIP DETECTOR

The silicon strip detector surrounds the pixel detector and is positioned to the intermediate and outermost regions. It is divided into two parts as mentioned in the previous Sec. 4.3: the TIB and the TOB. The TIB consists of four layers and covers up to $|z| < 65$ cm using silicon sensors with a thickness of 320 μm. The strip pitch varies from 80 to 120 μm and is placed between two sequential silicon sensors. The first two layers host double sided modules with a strip pitch of 80 μm, while the outer two layers comprise single sided modules with a strip pitch of 120 μm. This assembly of the TIB provides a measurement in both $r - \phi$ and $r - z$ coordinates. The TOB is made of six layers with a half-length of $|z| < 110$ cm. Silicon sensors with a thickness of 500 μm which are used as the radiation levels, are smaller in the outermost region. The thicker silicon sensors can maintain a good signal-to-noise (S/N) ratio for longer strip length and for wider strip pitch, which varies from 120 to 180 μm. Similarly, the first two layers of TOB are instrumented with double sided modules and the last two layers with single sided microstrip

modules.

The endcaps are divided into the Tracker EndCap (TEC) and Tracker Inner Disks (TID). Each TEC is made of nine disks, covering the region 120 cm $< |z| <$ 280 cm. Each TID comprises three small disks which fill the gap between the TIB and the TEC. The TEC and TID modules are arranged in rings, centred on the beam line. As the first two layers of TIB and TOB, the first two rings of the TID and the innermost 2 rings and the fifth ring of the TEC comprise double sided modules, while the remaining rings are equipped with single sided modules. The sensors of the TID and the 3 innermost rings of the TEC have a thickness of 320 μm and the rest of the TEC has a thickness of 500 μm.

The whole silicon strip detector is made of 15400 modules and operates in a cold environment of -20^0C.

4.4 ELECTROMAGNETIC CALORIMETER

The CMS *Electromagnetic Calorimeter* (ECAL) [58, 59] is a hermetic, homogeneous calorimeter and covers the pseudorapidity region from -3 to 3 ($-3 < \eta < 3$), as shown in Fig. 4.5. The purpose of ECAL is to measure precisely energies and directions of photons and electrons and for this reason 61200 lead tungstate ($PbWO_4$) crystals were chosen to be installed in the central barrel region, closed by 7324 crystals in each of the 2 endcaps.

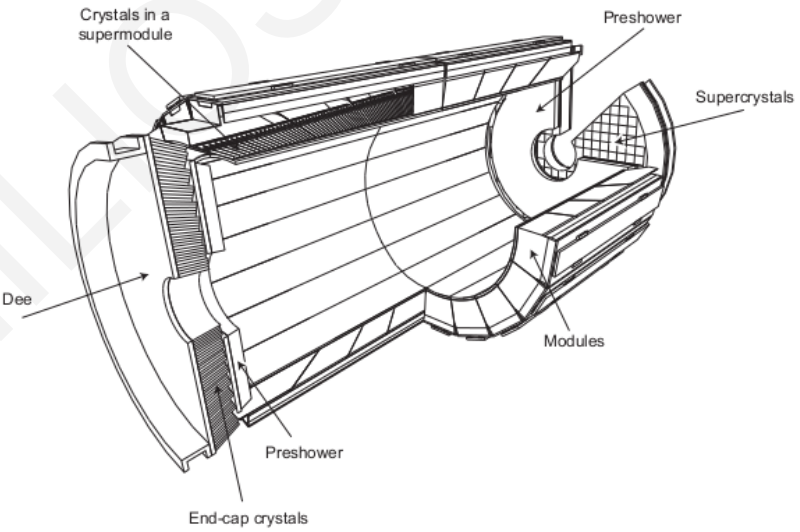

Figure 4.5: Layout of the ECAL, showing the barrel supermodules, the two endcaps and the preshower detectors. Taken from Ref. [58].

Taking advantage of the previous knowledge and experience on calorimeters, ECAL has been con-

structed with using lead tungstate ($PbWO_4$) scintillating crystals because of their short radiation ($X_0 = 0.89$ cm). Furthermore, these crystals have a very fast response (80% if the light is emitted within 25 ns). On the other hand, a lead tungstate crystal has the disadvantage of the low light yield ($30\gamma/MeV$), but fortunately, this can be fixed by using photodetectors with intrinsic gain that can operate in a magnetic field. There are two types of photodetectors; silicon avalanche photodiodes (APDs) [60], used in the barrel region and vacuum phototriodes (VPTs) [61], used in the endcaps. The diversity of photodetectors in the two regions is due to the radiation level. In the endcap regions, the radiation levels are much higher and special photodetectors, such as vacuum phototriodes, are required. Both crystals and photodetectors are sensitive to the changes of temperature and a temperature stability (around 0.1^0C) is required for accuracy. The main advantages of using $PbWO_4$ crystals are the fast production of the crystals (one lead tungstate crystal per two days), the fine granularity and their radiation hardness.

The barrel section (EB) has an inner radius of 129 cm and is made of 36 supermodules (each supermodule has 4 modules [62]), 18 in each half barrel, each covering 20^0 in ϕ. The 36 supermodules of the barrel section cover the pseudorapidity range $|\eta| < 1.479$. The endcaps (EE) cover a pseudorapidity range of $1.479 < |\eta| < 3.0$. The distance between the interaction point and the edge of the endcap is 3144 mm. The endcap consists of 5×5 crystals (supercrystals, or SCs) and is divided into 2 halves, named *Dees*. Each Dee includes 3662 crystals. These crystals are grouped into 138 standard SCs and 18 special partial supercrystals on the inner and outer circumference. Fig. 4.6 shows a transverse section through ECAL where the barrel (EB) and endcap (EE) sections are pointed out.

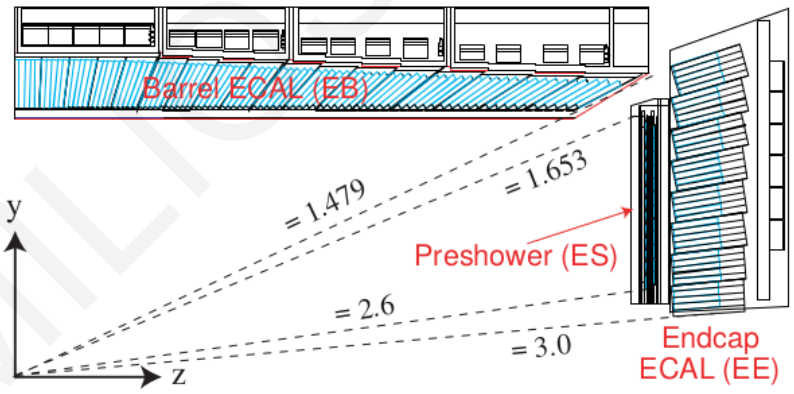

Figure 4.6: Transverse slice of ECAL, showing geometrical features. Taken from Ref. [62].

The energy resolution can be obtained by fitting a Gaussian function to the reconstructed energy distributions and can be parameterised as a function of energy, as follows:

$$\left(\frac{\sigma}{E}\right)^2 = \left(\frac{S}{\sqrt{E}}\right)^2 + \left(\frac{N}{E}\right)^2 + C^2 \tag{4.4}$$

where S stands for the stochastic term which includes contributions from the shower containment, the number of photoelectrons and fluctuations. It was determined to be 2.8%. N is for the noise term, equal to 12% at 1 GeV and originates from the electronics and digitization. C is the constant term, equal to 0.3%, which includes the energy resolution for high energy electron and photon showers and the leak of energy outside the calorimeter. ECAL can measure precisely the energy of photons and electrons with an energy resolution, σ/E, better than 0.5%, as shown in Fig. 4.7.

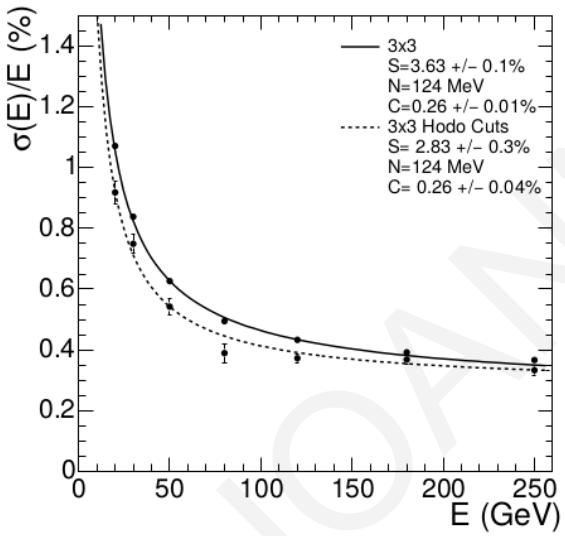

Figure 4.7: ECAL energy resolution, σ/E, as a function of electron energy as measured from a beam test as well as the corresponding values of stochastic, noise, and constant terms. Taken from Ref. [62].

4.4.1 PRESHOWER DETECTOR

The CMS Preshower detector (ES) is placed in front of EE to discriminate between single photons and neutral pions in the region of $1.653 < |\eta| < 2.6$. Additionally, it enhances the position determination of electrons and photons. The ES is a sampling calorimeter, consisting of two detector layers one after the other. Each detector layer is composed by a lead radiator plane followed by the Silicon Strip sensor plane. The first radiator plane is 2 X_0 (radiation lengths), whilst the second is 1 X_0. The splitting in two planes instead of one with 3 X_0 was done to improve the spatial resolution.

A neutral pion is created in the proton-proton collisions, and will immediately decay into two closely-spaced photons. The main feature of these photons is the angle between them, which is small for pions directed towards the endcaps, and depends on the energy of the pion and its direction. The granularity of EE is not sufficient to be able to recognise the energy of a photon or the energy of a pion (decayed into two closely-spaced photons) and, therefore, the usage of ES is mandatory.

4.5 HADRONIC CALORIMETER

The Hadronic Calorimeter (HCAL) as sampling calorimeter, is able to measure jets' energies as well as the missing transverse energy ($\not{E}_T$). It is located inside the magnet coil and just outside ECAL, divided into four parts: the hadron barrel part (HB), the hadron endcap part (HE), the hadron forward part (HF) and the hadron outer (HO) part which is placed outside the magnet coil for absorbing a possible remaining energy of hadrons, as illustrated in Fig. 4.8.

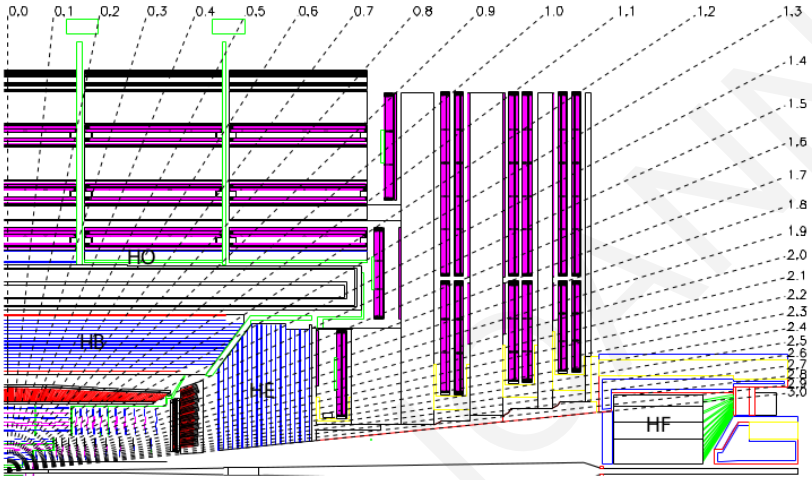

Figure 4.8: Longitudinal view of the CMS detector in which the locationf of the hadron barrel (HB), endcap (HE), outer (HO), and forward (HF) calorimeters are indicated. Taken from Ref. [46].

HCAL uses brass as absorber material with a reasonably short interaction length. It consists of plastic scintillator tiles read out by embedded wavelength-shifting (WLS) fibres [46]. The HB is a sampling calorimeter which consists of 32 towers and covers the pseudorapidity region $-1.4 < \eta < 1.4$. It is divided into two half barrel sections (HB+ and HB-) in which 15 brass plates are instrumented, each with a thickness of 5 cm, plus 2 external stainless steel plates for mechanical strength. The first and the last scintillator plates of HB are 9 mm length instead of 3.7 mm of the other plates and the light collected by the first layer is optimised to be a factor of 1.5 higher than the other scintillator plates. For the former, the purpose is to sample hadronic showers developing in the inert material between EB and HB and for the latter, its larger thickness serves to correct for late developing showers leaking out the back of HB.

The hadron outer detector (HO) is made of scintillators with a thickness of 10 mm, located outside the magnet coil, as shown in Fig. 4.9, covering the pseudorapidity region $-1.26 < \eta < 1.26$. The main priority of HO is to record the energy from hadron showers which leak through the rear of the

calorimeters, ensuring that no other particle escapes from the detectors except from muon particles, which are detected from the muon system. The HO behaves like *tail-catcher* and by increasing the thickness of the hadron calorimeter to over 10 interaction lengths, it achieves the reduction of the tails in the energy resolution function and improves the $\not{E}_T$ resolution of the calorimeter.

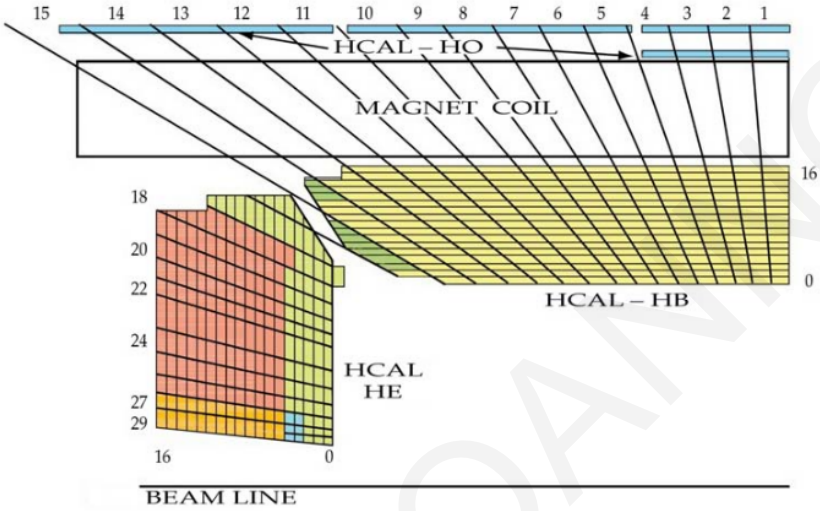

Figure 4.9: The HCAL tower segmentation in the r, z plane. The position of the HO is clearly pointed out outside the magnet coil. Taken from Ref. [46].

Furthermore, there are two hadron endcaps (HE+ and HE-) that each one consists of 14 η towers with $5^0\phi$ segmentation. Each HE covers the pseudorapidity region $1.3 < |\eta| < 3.0$. The total number of HE towers is 2304, ensuring a good measurement of hadron showers directed in the endcap regions.

Fig. 4.8 indicates another detector which covers the pseudorapidity region $3.0 < |\eta| < 5.0$. The hadron forward calorimeter (HF) was built to be in charge of the detection of particles that travel directly in the forward regions. The HF is a steel/quartz fibre calorimeter with a thickness of its absorber 1.65 m and distance from the interaction point 11.2 m. It detects Cerenkov light emitted in the quartz fibres and then transferred to photomultipliers. The absorber structure is made of 1 mm square grooves into steel plates. The quartz fibres, with diameter 0.6 mm, run parallel to the beam line and are inserted into grooves, creating 2 effective longitudinal samplings. The 2 HF modules have 900 towers and 1800 channels. The HCAL energy resolution is parametrised, as follows:

$$\frac{\sigma}{E} \simeq \frac{\alpha}{\sqrt{E}} + b \tag{4.5}$$

where $\alpha \simeq 65\%$ in the barrel, 85% in the endcaps and 100% in the HF, while b is 5% over the full η range.

4.6 MUON SYSTEM

The CMS provides a powerful detector dedicated to the detection of muons. The CMS muon system is based on three types of gaseous detectors used to identify and measure the momentum of muons: *Drift tube chambers* (DT), *cathode strip chambers* (CSC) and *resistive plate chambers* (RPC) are used to assemble the CMS muon subdetector system.

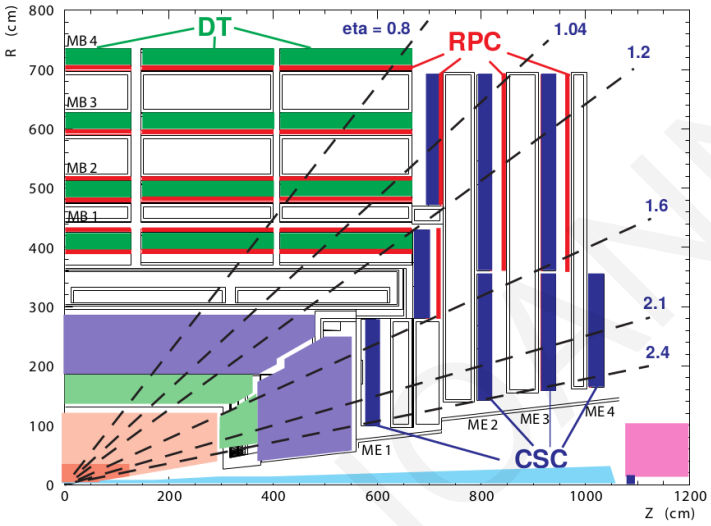

Figure 4.10: Layout of one quarter of the CMS muon system. The three types of gaseous detectors are also illustrated and highlighted. The Drift Tubes (DT), the Cathode Strip Chambers (CSC) and the Resistive Plate Chambers (RPC). Taken from Ref. [63].

In the barrel region the drift tubes are used, covering the pseudorapidity region $|\eta| < 1.2$. Drift tube chambers were chosen for maximising their efficiency in the regions where the neutron background is small, the muon rate is low and the magnetic field in the chambers is also low. On the other hand, in the 2 endcaps, the choice of cathode strip chambers (CSC) is mandatory due to the intensity of magnetic field and the neutron background. The CSCs are placed in the 2 endcaps, covering the pseudorapidity region up to $|\eta| < 2.4$, as shown in Fig. 4.10. Finally, the last detector of the CMS muon system is positioned in both regions. Resistive plate chambers (RPC) were chosen for ensuring good operation at high rates in the barrel and endcap areas. The usage of RPC, in the barrel and endcap regions provides a fast response with better time resolution than the DTs or CSCs. In a few words, the muon system is divided into 4 stations of detectors in the Muon Barrel (MB) region with the iron yoke. Each MB region contains 5 wheels of the yoke along the beam direction (labeled YB-2 for the farthest wheel in $-z$ and YB+2 for the farthest in $+z$). The CSCs and RPCs placed in the endcaps are arranged in 4 disks, 3 rings in the innermost station and 2 in the outermost station. Overall, the muon system is made of 25000 m^2 active detection planes. The muon system can provide a resolution of about 10% for muons without

information of the tracker system.

4.6.1 DRIFT TUBE CHAMBERS

In the barrel region, 250 DTs are organised in 4 layers (MB1, MB2, MB3, and MB4) inside the magnet return yoke, which is divided into five wheels. Each wheel is divided into 12 sectors. There are 12 chambers in each of the 3 inner layers, whereas only 2 chambers are included in the fourth layer, thus leading to a total of 14 chambers per wheel in MB4. The MB1, MB2 and MB3 are made of 12 planes of aluminium drift tubes; 4 $r-\phi$ measuring planes in each of the 2 outermost *superlayers* separated by about 20 cm and sandwiching a z-superlayer comprising 4 z-measuring planes. The MB4 station does not contain the z-measuring planes.

In stations MB1 and MB2, DT chamber is placed between 2 RPCs, while the MB3 and MB4 consist of 1 DT and 1 RPC, which is positioned in the innermost side of the station. Thus, a high-p_T muon crosses up to 6 PRCs and 4 DT chambers, producing up to 44 measured points in the DT system from which a muon track candidate can be reconstructed.

4.6.2 CATHODE STRIP CHAMBERS

Cathode strip chambers (CSCs) are placed in the Muon Endcap (ME) system. There are 468 CSCs in the 2 endcaps and each CSC is trapezoidal in shape and comprises 6 gas gaps. Each gap has a plane of radial cathode strips and a plane of anode wires running almost perpendicularly to the strips. Additionally, there are 18 chambers in the innermost ring (ME1/1) and 36 chambers in each other rings of a muon station (ME2/1, ME3/1, and ME4/1) as shown in Fig. 4.10 (the four innermost blue planes). The gas ionization and electron avalanche are caused by a charged particle traversing each plane of a chamber, producing a charge on the anode wire and an image charge on a group of cathode strips. The signal of these detectors is fast and a precise position measurement consists of the determination of the centre-of-gravity of the charge distribution induced on te cathode strips. The spatial resolution is about 200 μm and the angular resolution is of the order 10 mrad.

4.6.3 RESISTIVE PLATE CHAMBERS

The CMS resistive plates' system consists of gaseous parallel-plate detectors which are placed in both the barrel and the endcap regions. Size layers of RPC chambers are installed in the barrel iron yoke, 2 located in each of the first and second muon stations and 1 in each of the 2 last stations. In the endcap region, RPCs are placed only in 3 layers up to $\eta = 1.6$.

The CMS RPC is a double-gap module consisting of 2 gaps, referred to up and down gaps in which strips are installed. The total signal is the sum of the 2 single-gap signals which provide the possibility to operate at lower high voltage. Moreover, the CMS RPCs combine the spatial resolution with a time resolution comparable to that of scintillators, which can achieve a good measurement and reconstruction of muon-track candidate.

4.7 THE CMS TRIGGER

The LHC collides bunches of two opposite proton beams every 25 ns, achieving a beam crossing frequency of 40 MHz, which corresponds to about 10^9 interactions per second. Since the huge amount of data produced by the collisions are not simply feasible to be stored, a rate reduction has to be achieved. The CMS trigger system aims to reduce this high event rate by selecting only events that have a physical interest; events with high transverse momentum of particles. The reduction of the high rate of events is performed in two steps called *Level-1 Trigger* (L1) [64] and *High-Level Trigger* (HLT) [65], respectively. The difference between the L1 and High-Level triggers is that L1 is made of largely programmable electronics, whereas HLT is a software system implemented in a filter farm of a thousand commercial processors. By operating together, L1 and HLT are designed to achieve at least a rate reduction of a factor of 10^6. The L1 trigger uses information from the calorimeters and the muon system by achieving an output rate of 100kHz. The HLT works slightly different from the L1. The CMS HLT can use the complete read-out data by performing complex calculations similar to those made in the offline analysis. The data rate can decrease significantly by taking advantage of the combination of L1 and HLT, reaching about 300 Hz before data storage.

4.7.1 LEVEL-1 TRIGGER

The Level-1 trigger formed by custom hardware processors must take a decision very fast and accurately. It uses information from different subdetectors, such as the calorimeters and the muon system, as well as some correlation of information between these systems. The L1 decision is based on the so-called *trigger primitive* objects, such as electrons, muons, photons and jets above a set E_T or p_T threshold. In addition, it uses information from the global sums of E_T and $\not{E}_T$. The L1 trigger is designed to reduce the data rate from 40 MHz to 100kHz, keeping only events with physics interest. All the high-resolution data is kept in pipelined memories during the Level-1 decision making period.

4.7.2 HIGH-LEVEL TRIGGER

After the performance of Level-1 trigger, the data from the pipelines are transferred to front-end readout bufffers for more investigation and rate reduction. The high-level trigger software code is performed by each processor which contains data from a given event with a size of about 1.5 MB (pp interactions). This procedure reduces the Level-1 output rate of 100 kHz to 100 Hz for mass storage. The development of the HLT code is based on various strategies which reconstruct only the objects and regions of the detectors that are actually needed, leading to a partial reconstruction.

Part III

Physics Analysis Channel

Chapter 5

Search For The Heavy Pseudo-Scalar A Boson via $A \to Zh \to (\ell^+\ell^-/\nu\bar{\nu})b\bar{b}$

After the discovery of the SM Higgs boson in 2012, more and more Beyond Standard Model approaches have being considerably studied. A need to cross the borders of the SM theory is mandatory due to its shortcomings. Searches for additional Higgs states can be performed either by measuring deviations in the expected values of the couplings of the discovered h boson to other SM particles, or through direct searches in final states disfavoured by the SM. Thanks to the mass of the SM Higgs boson, new physics may be detected by searching bosons that decay into final states which contain the Higgs boson whose mass has already been measured at 125 GeV. This Chapter describes the search for a heavy pseudoscalar A boson that decays into a Z and h boson, with the Z boson decaying further into a pair of leptons (electrons or muons) or a pair of neutrinos, and the h boson into a pair of b-quarks in $\sqrt{s} = 13$ TeV collisions. The A boson is predicted by the 2HDM theory and generated through gluon-gluon fusion and in association with b-quarks. These two mechanisms are studied in this Chapter in detail.

5.1 Methodology And Analysis Strategy

This search for a heavy pseudoscalar boson, A, decaying through a Z boson and a light h boson into a pair of leptons (electrons or muons) or a pair of neutrinos and a pair of b-quarks, is performed on 35.9 fb^{-1} of data collected by CMS during 2016 [66]. The analysis strategy is to reconstruct the Z, h, and A boson candidates from the visible decay products or the missing energy reconstructed in the event. The signal

would manifest itself as a peak in the four-body invariant mass ($m_{\ell^+\ell^-b\bar{b}}$) or transverse mass ($m^T_{\nu\bar{\nu}b\bar{b}}$) spectrum over the expected SM continuum. Irreducible backgrounds correspond to Z boson production with two accompanying b quark jets, and $t\bar{t}$ events in the di-leptonic final state. These backgrounds are evaluated and normalized directly using appropriate control regions in data. The h boson produced in association with a Z boson provides a contribution to the background, but it differs from the signal because the $m_{\ell^+\ell^-b\bar{b}}$ mass does not contain a resonant peak. Signal sensitivity is improved by exploiting the known value of the h boson mass, using it to rescale the jet momenta to match the value expected in the di-jet invariant mass. Additionally, optimal signal efficiency and background rejection is achieved using multivariate discriminators. Upper limits are presented on the product of the total cross section and the $A \to Zh$ and $h \to b\bar{b}$ branching fractions for a pseudoscalar boson, and interpreted within the 2HDM model.

5.2 SIGNAL, BACKGROUND AND DATA SAMPLES

All Monte Carlo samples belong to the *RunIISummer16MiniAODv2* campaign, and are generated simulating the Pile-up conditions, using the *PUMoriond17_80X_mcRun2_asymptotic_2016* PU scenario. Parton showering and hadronization processes are performed in PYTHIA [67] with the CUETP8M1 underlying event tune [68, 69]. A full detector simulation and event reconstruction has been performed with Geant4 [70] and CMSSW [71]. The CUETP8M2T4 tune is used for top quark pair production [72]. The signal is simulated using MADGRAPH5_AMC NLO using the NNPDF30_lo_as_0130_nf_4 [73] parton on distribution functions (PDFs).

5.2.1 SIGNAL SAMPLES

With respect to the SM case, a heavy pseudoscalar A boson cannot be generated via Higgs-strahlung from the W, Z production mode because of not sufficient energy of W or Z boson to create an additional Higgs physical state. Vector Boson Fusion (VBF) production mode is also forbidden, given that there are not $W^{\pm}W^{\mp}A$ and ZZA vertices, as mentioned in Chapter 2.2.8. Hence, a heavy pseudoscalar A boson could be produced by the two remaining production modes, gluon-gluon fusion and b-quark associated, which strongly depend on the BSM model parameters. At moderate $tan\beta \lesssim 3$ values, the dominating mode is the gluon fusion process, and associated production (especially with b-quarks) plays a role only for $tan\beta \gtrsim 4$ and low masses. Since it is possible to have both production modes simultaneously, two separate signal samples are produced. The newly-discovered SM-like Higgs boson by ATLAS [20] and CMS [18] is interpreted as the lightest scalar in general two Higgs Doublet Models, the others A, $H^{\pm}$ being heavier than h, and allowing to know the mass of the second resonance in the searched decay

chain, thus adding an additional constraint to the kinematic of the event. In the generated signal samples the light Higgs has a fixed mass $m_h = 125.0$ GeV.

The general 2HDM phenomenology is present in MadGraph in the dedicated model *2HDMt_II_NLO* [74], which can simulate the full top and bottom quark loops of the gluon-gluon fusion process though the NLO capabilities for the MadGraph generator. However, inspite exploiting the NLO capabilities, the signal is still generated at LO with up to one additional parton in the final state. The b-quark associated production is also produced at LO, with no additional jets in the final state (besides at least two b-quarks from the hard process) with the 4F scheme. Diagrams of such a process are shown in Fig. 5.1.

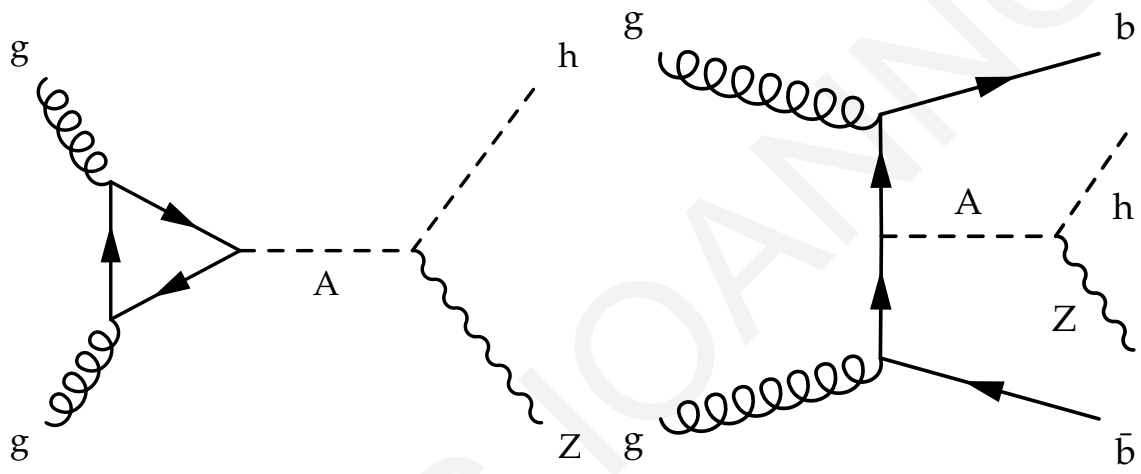

Figure 5.1: Feynman diagrams of the production within the 2HDM model of a pseudoscalar A boson through gluon-gluon fusion (left) and with accompanying b quarks (right).

In both mechanisms, the A boson is forced to decay into an on-shell Z and a light Higgs h. The former is then forced to decay into electron, muon or τ-lepton pairs (or alternatively, in a pair of neutrinos), and the latter is forced to decay into $b\bar{b}$ quark pairs.

For a large fraction of the 2HDM parameter space, the $A \to Zh$ channel has its maximum sensitivity in a restricted interval of m_A masses, ranging from $m_A \approx m_Z + m_h$ where the Z boson becomes on-shell, to about $m_A \approx 2 \cdot m_{top}$, where the branching ratio $\mathcal{B}r(A \to Zh)$ sharply decreases because of the opening of the $A \to t\bar{t}$ channel. In this mass interval, a total of six signal samples were produced, each separated by about 25 GeV. Additionally, since in some scenarios the A coupling with top-like quarks are suppressed, other mass points are generated in 100 GeV steps to estimate the sensitivity of the channel to higher masses. In summary, thirteen mass points are available: 225, 250, 275, 300, 325, 350, 400, 500, 600, 700, 800, 900, 1000 GeV.

The production cross section for the heavy pseudoscalar A boson in the gluon-gluon fusion and b-quark associated production were calculated by using the SuSHi 1.6.1 [75] for a given $cos(\beta - \alpha) = 0.1$.

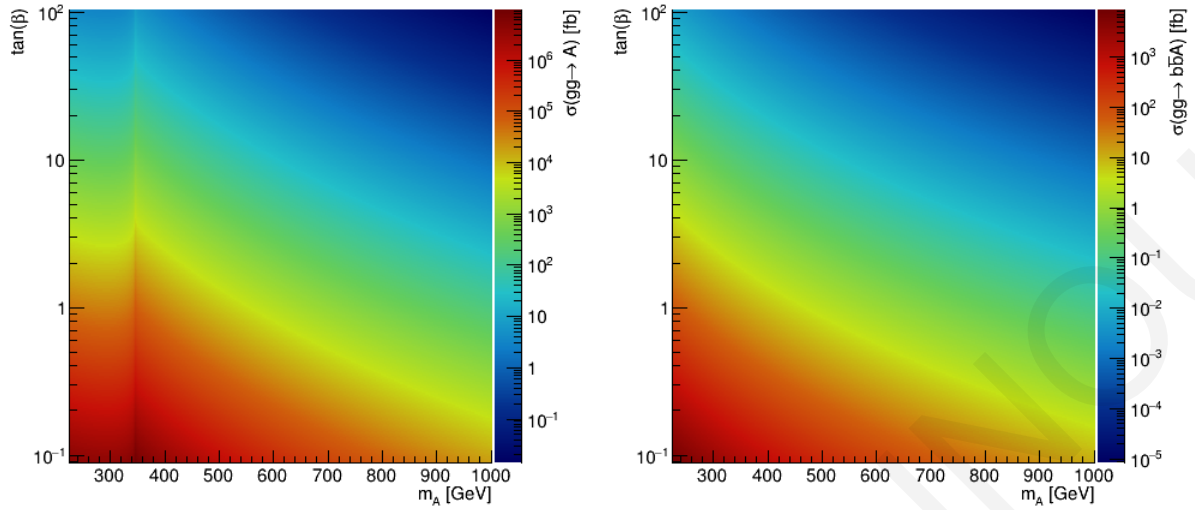

Figure 5.2: The production cross section for the pseudo-scalar boson A in the gluon-gluon fusion (left) and b-quark associated production (right) in the plane m_A versus $tan\beta$, for Type-I 2HDM, for $cos(\beta - \alpha) = 0.1$.

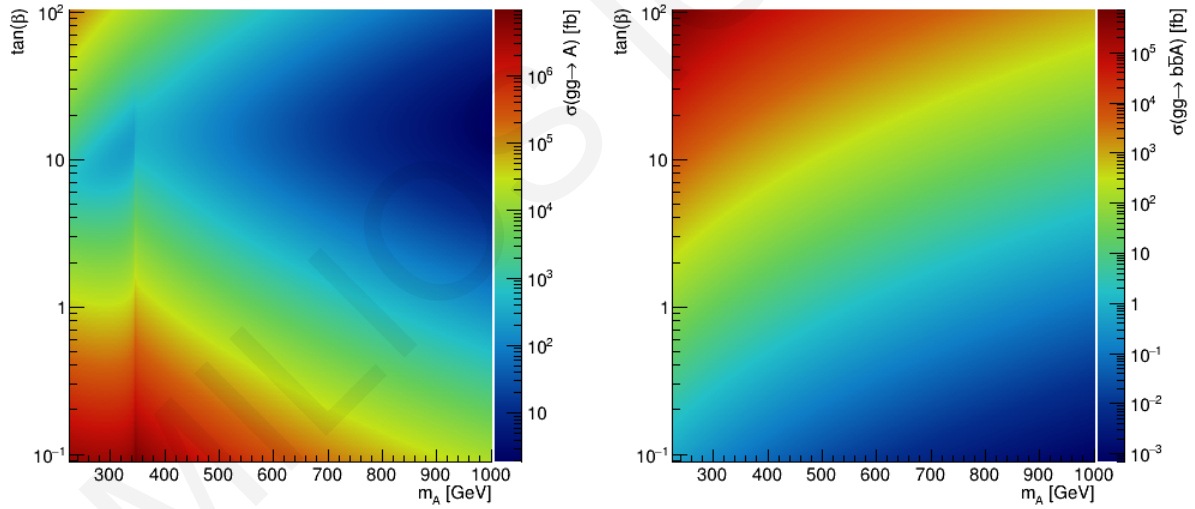

Figure 5.3: The production cross section for the pseudo-scalar boson A in the gluon-gluon fusion (left) and b-quark associated production (right) in the plane m_A versus $tan\beta$, for Type-II 2HDM, for $cos(\beta - \alpha) = 0.1$.

The specific value (0.1) of the $cos(\beta - \alpha)$ is chosen to be close at the *alignment limit* $cos(\beta - \alpha) \to 0$, as indicated in Chapter 2.2.6. As mentioned, the two production modes of the heavy pseudoscalar A boson vanish at the alignment limit, and the only survived Higgs physical state is the SM Higgs boson in which the Standard Model theory is dominant for $cos(\beta - \alpha) = 0$. The cross section for the heavy

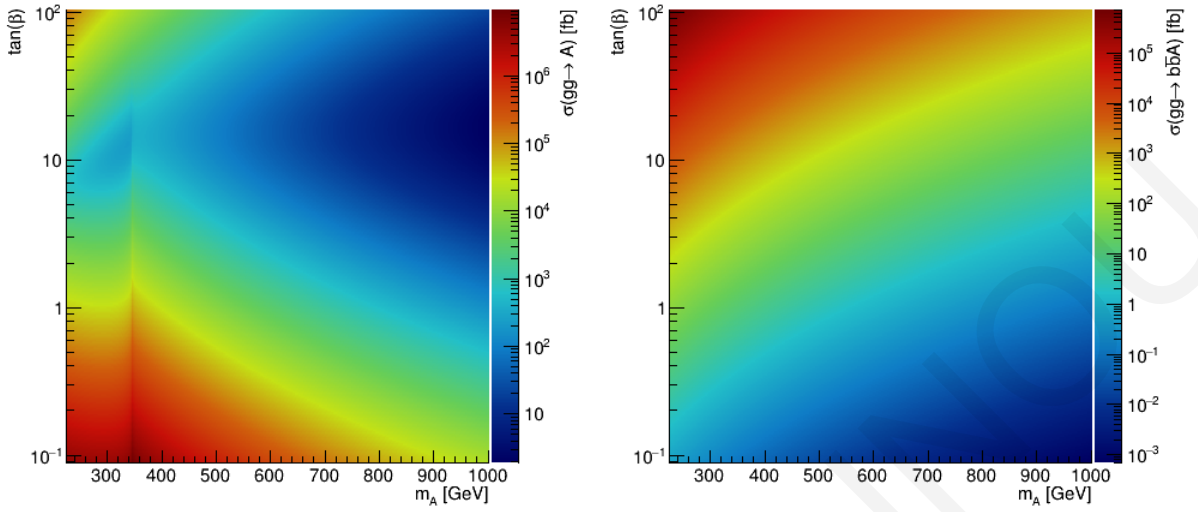

Figure 5.4: The production cross section for the pseudo-scalar boson A in the gluon-gluon fusion (left) and b-quark associated production (right) in the plane m_A versus $tan\beta$, for Flipped 2HDM, for $cos(\beta - \alpha) = 0.1$.

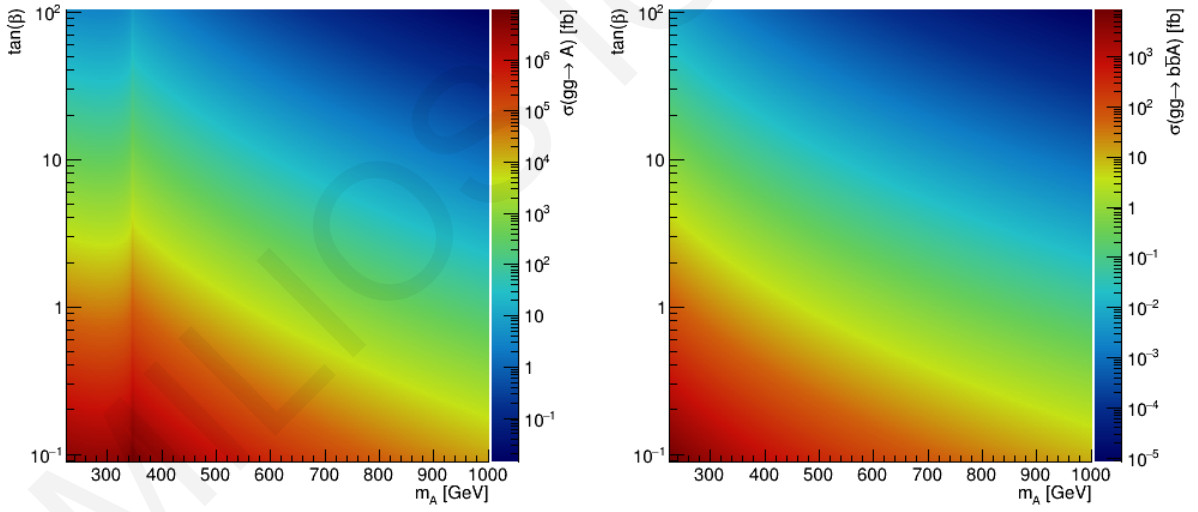

Figure 5.5: The production cross section for the pseudo-scalar boson A in the gluon-gluon fusion (left) and b-quark associated production (right) in the plane m_A versus $tan\beta$, for Lepton-specific 2HDM, for $cos(\beta - \alpha) = 0.1$.

pseudoscalar A boson in the gluon-gluon fusion and b-quark associated production is presented in plane m_A versus $tan\beta$ for the four different types of 2HDM. In Type-I, the cross sections of the gluon-gluon fusion and b-quark associated production depend on the m_A and the value of $tan\beta$, as shown in Fig. 5.2, due to the dependence on $cot\beta$. The cross section is dominant for low $tan\beta$ and small values of A mass

for both mechanisms. A similar behaviour of the production cross section (for both mechanisms) shows up in the Lepton-specific 2HDM, as shown in Fig. 5.5, where the quarks couple to Higgs field in the second Higgs doublet (Φ_2), similarly, in Type-I, the fermions couple to the Higgs field in the second Higgs doublet too. Nevertheless, in Type-II and Flipped 2HDM models, where up-type quarks couple to Φ_2 doublet, while down-type quarks couple to Φ_1, the cross sections for both mechanisms have the same behaviour in these two models, as shown in Fig. 5.3 and Fig. 5.4, respectively. The cross section of the gluon-gluon fusion is negligible for higher values of $tan\beta$, however, it increases significantly for lower values of β ($tan\beta \leq 1$). The cross section is dominant for lower $tan\beta$ due to the dependence of top-quark coupling which is proportional to $\sim 1/tan\beta$. On the contrary, the b-quark associated production cross section for both A production mechanisms has a significant increase when $tan\beta$ climbs at higher values due to the dependence of b-quark with $tan\beta$ parameter in particular for lower mass values.

Not only is the production cross section affected, but also the $\mathcal{B}r(A \rightarrow Zh)$ is changed due to the various couplings between quarks and the Higgs doublets. The branching fraction of the $A \rightarrow Zh$ channel differs for each type of 2HDM, as shown in Fig. 5.6.

The branching ratio $\mathcal{B}r(A \rightarrow Zh)$ is calculated by 2HDMC 1.7.0 [76]. Clearly, it decreases sharply at about $m_A \approx 2 \cdot m_{top}$ because of the opening of the $A \rightarrow t\bar{t}$ channel, for all types of 2HDM. After that critical mass value $m_A \approx 2 \cdot m_{top}$, the branching ratio $\mathcal{B}r(A \rightarrow Zh)$ gradually increases, in particular, for large $tan\beta$. The branching fraction of the $A \rightarrow Zh$ channel is large for lower values of $tan\beta$ given that the A boson mass is less than $2 \cdot m_{top}$.

Furthermore, a scan of the cross section of gluon-gluon fusion and b-quark association is performed in plane $cos(\beta - \alpha)$ versus $tan\beta$, keeping the m_A fixed. The value of m_A is selected to be close to the opening of the $A \rightarrow t\bar{t}$ channel in which the $A \rightarrow Zh$ is dominant. The scan is performed for each type of 2HDM and only for $m_A = 300$ GeV. Fig. 5.7 shows the cross section of gluon-gluon fusion (right plot) and b-quark associated production (left plot) for $m_A = 300$ GeV in the plane $cos(\beta - \alpha)$ - $tan\beta$, for the Type-I 2HDM.

At the alignment limit a potential heavy pseudo-scalar A boson vanishes and only the SM Higgs boson could exist. However, for different $cos(\beta - \alpha)$ and at lower values of $tan\beta$, an A boson could be generated by both production modes. Additionally, at $tan\beta > 5$, the cross section of b-quark associated production disappears because of no contribution from b-quark loops, making this production mode forbidden, but for the gluon-gluon fusion, its cross section is small but non-existent.

In the Type-II 2HDM model (Fig. 5.8), where the b-quark coupling is proportional to $tan\beta$ values, the cross section of b-quark associated production is dominant at largest values of $tan\beta$ and, at lowest values, its cross section is again zero. A noticeable fluctuation in the production cross section of the A boson for the gluon-gluon fusion is due to the factor $tan^2\beta$ which takes place in the calculations.

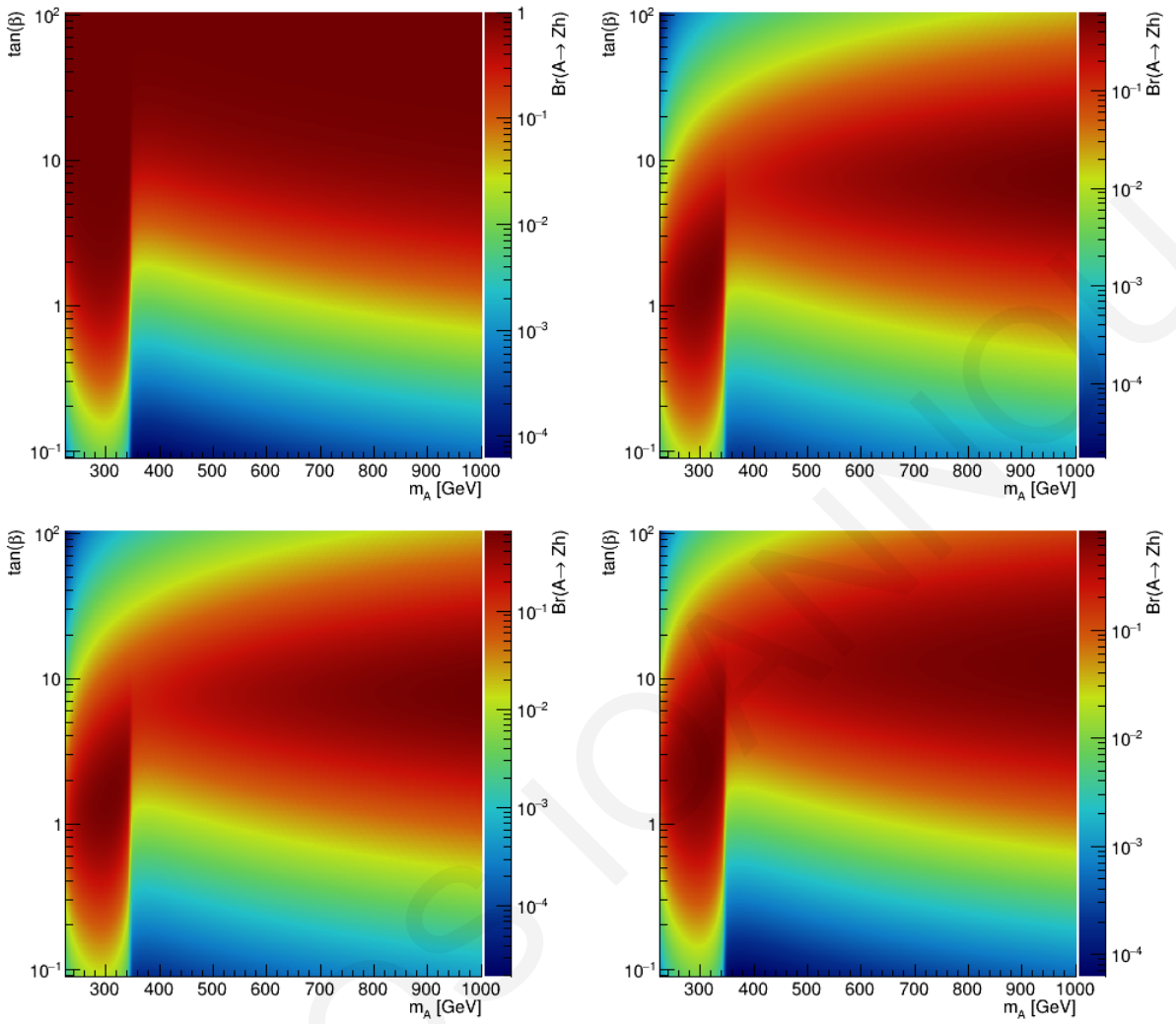

Figure 5.6: **Top left**: $\mathcal{B}r(A \to Zh)$ for Type-I 2HDM. **Top right**: $\mathcal{B}r(A \to Zh)$ for Type-II 2HDM. **Bottom left**: $\mathcal{B}r(A \to Zh)$ for Flipped 2HDM. **Bottom right**: $\mathcal{B}r(A \to Zh)$ for Lepton-specific 2HDM.

Similarly, production cross sections of the Flipped 2HDM model are shown in Fig. 5.9, where cross sections of both production modes are similar with that in Type-II 2HDM due to the same multiplied factor $tan^2\beta$. Finally, the cross sections for the Lepton-specific 2HDM model are illustrated in Fig. 5.10 in the plane $cos(\beta - \alpha)$ versus $tan\beta$. As mentioned in Chapter 2.2.8, the cross section of gluon-gluon fusion behaves like Type-I 2HDM because the production cross section of A boson is multiplied by the factor $cot^2\beta$. Besides, the cross section of b-quark associated production is negligible because there is no contribution from b-quarks loops.

Tables A.4 and A.5 of Appendix C.3 report the names of the signal samples as published in the CMS Data Aggregation System (DAS). For each mass point, 100 000 events have been generated.

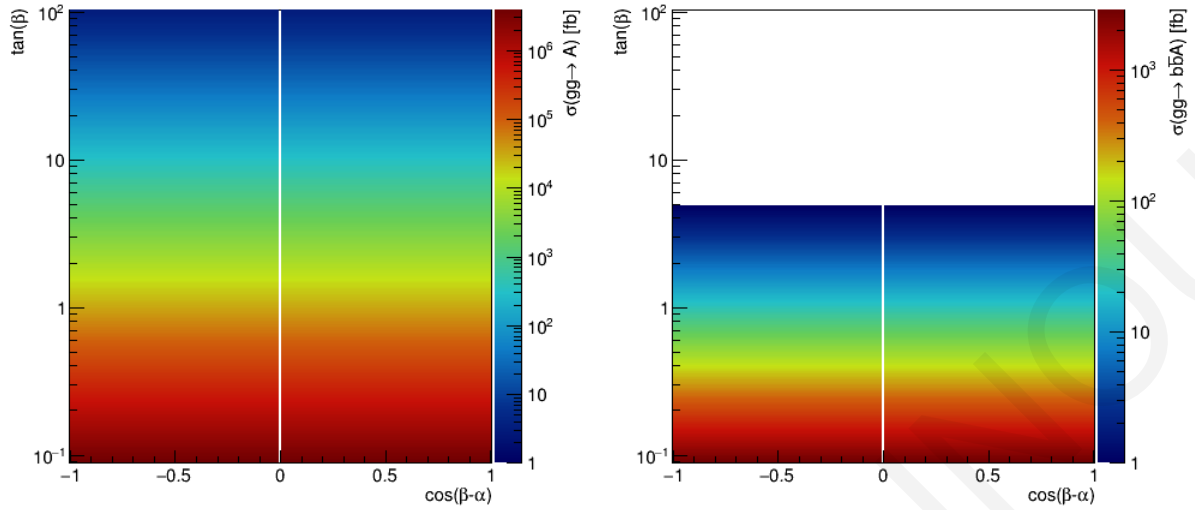

Figure 5.7: The production cross section for the pseudo-scalar boson A in the gluon-gluon fusion (left) and b-quark associated production (right) in the plane $cos(\beta-\alpha)$ versus $tan\beta$, for Type-I 2HDM, for $m_A = 300$ GeV.

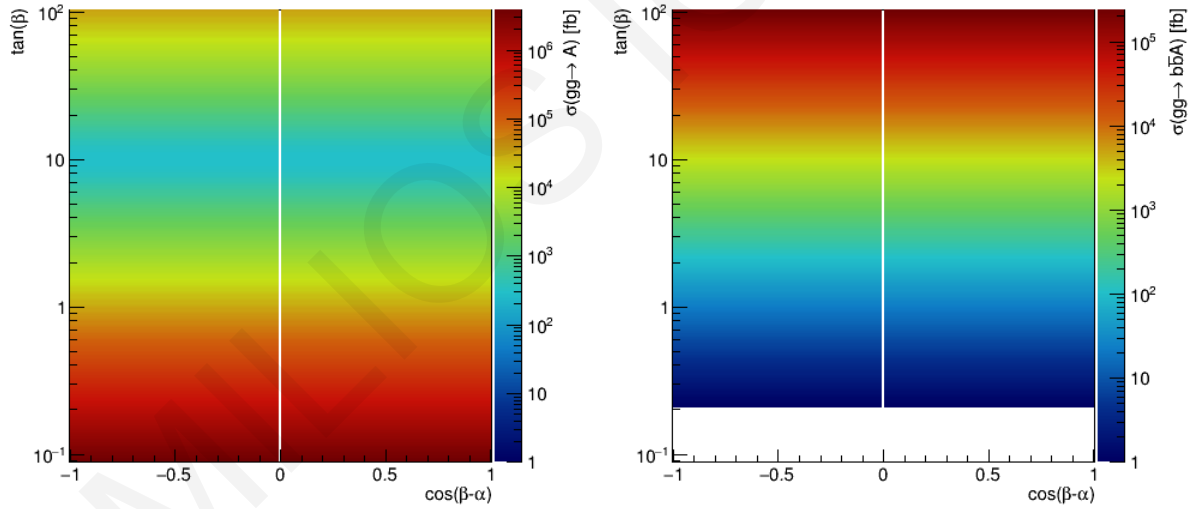

Figure 5.8: The production cross section for the pseudo-scalar boson A in the gluon-gluon fusion (left) and b-quark associated production (right) in the plane $cos(\beta-\alpha)$ versus $tan\beta$, for Type-II 2HDM, for $m_A = 300$ GeV.

5.2.1.1 *A* BOSON WIDTH

Other than its mass, another important property of the pseudoscalar A boson is its width. Generally speaking, it fully depends on the model considered and its parameters. However, since A does not decay

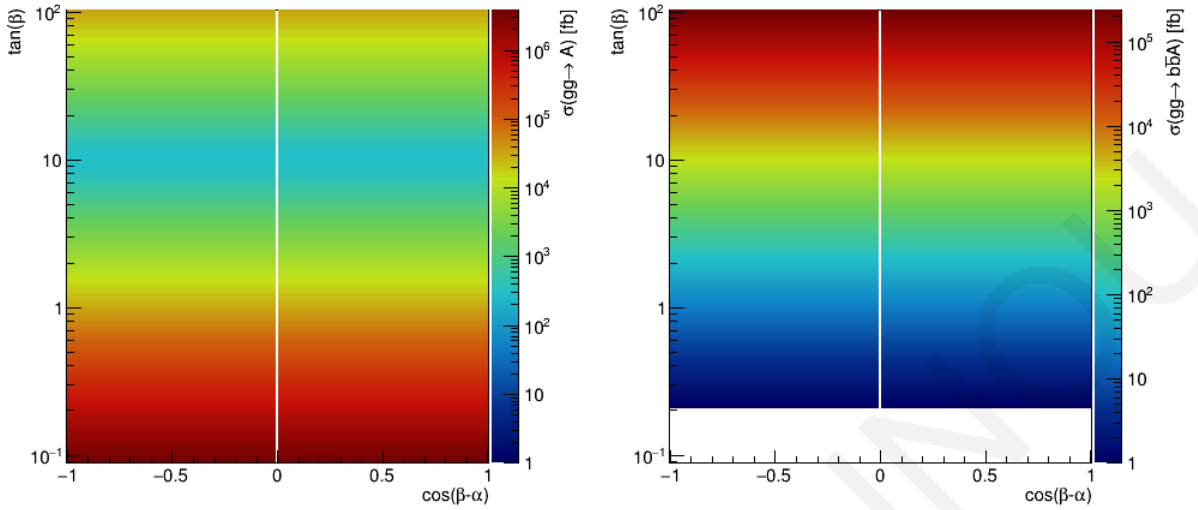

Figure 5.9: The production cross section for the pseudo-scalar boson A in the gluon-gluon fusion (left) and b-quark associated production (right) in the plane $cos(\beta-\alpha)$ versus $tan\beta$, for Flipped 2HDM, for $m_A = 300$ GeV.

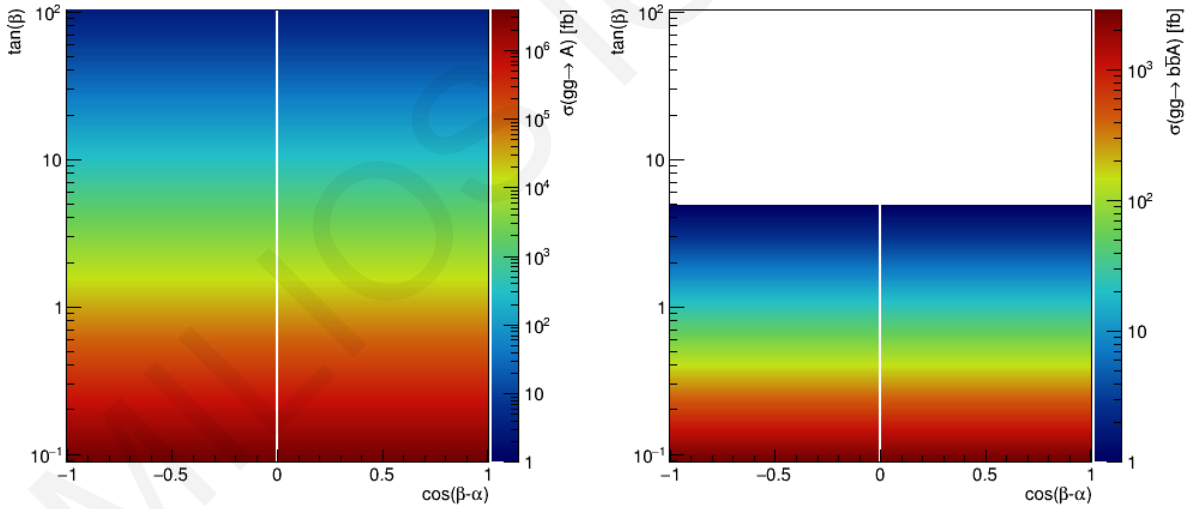

Figure 5.10: The production cross section for the pseudo-scalar boson A in the gluon-gluon fusion (left) and b-quark associated production (right) in the plane $cos(\beta-\alpha)$ versus $tan\beta$, for Lepton-specific 2HDM, for $m_A = 300$ GeV.

into vector bosons, the width of the pseudoscalar is generally much lower than the one of the scalar Higgs(es), even for higher masses, at least until the top quark decay threshold. In this case, a strong dependence on the model parameters is present. For $m_A \lessapprox 2m_{top}$, the typical A width ranges from some MeV to a few GeV. For this reason, and to provide as much as possible model-independent result,

the A is considered in the *narrow width approximation*, and its generation width is kept fixed to a mean value $\Gamma_A = 0.1$ GeV.

If the A boson natural width is smaller than the experimental resolution, the exclusion upper limit does not directly depend on the width of the resonance. In order to check the validity of this assumption, a scan of the width Γ_A is performed within Type-I, Type-II, Flipped, and Lepton-specific 2HDM parameter space. The result is that for $m_A < 2m_{top}$ the width is smaller than the experimental resolution ($\approx$ few GeV) for almost any parameter of the theory. For $m_A > 2m_{top}$, with the accessibility of the $A \to t\bar{t}$ channel, Γ_A shows sharp variations near the kinematical threshold.

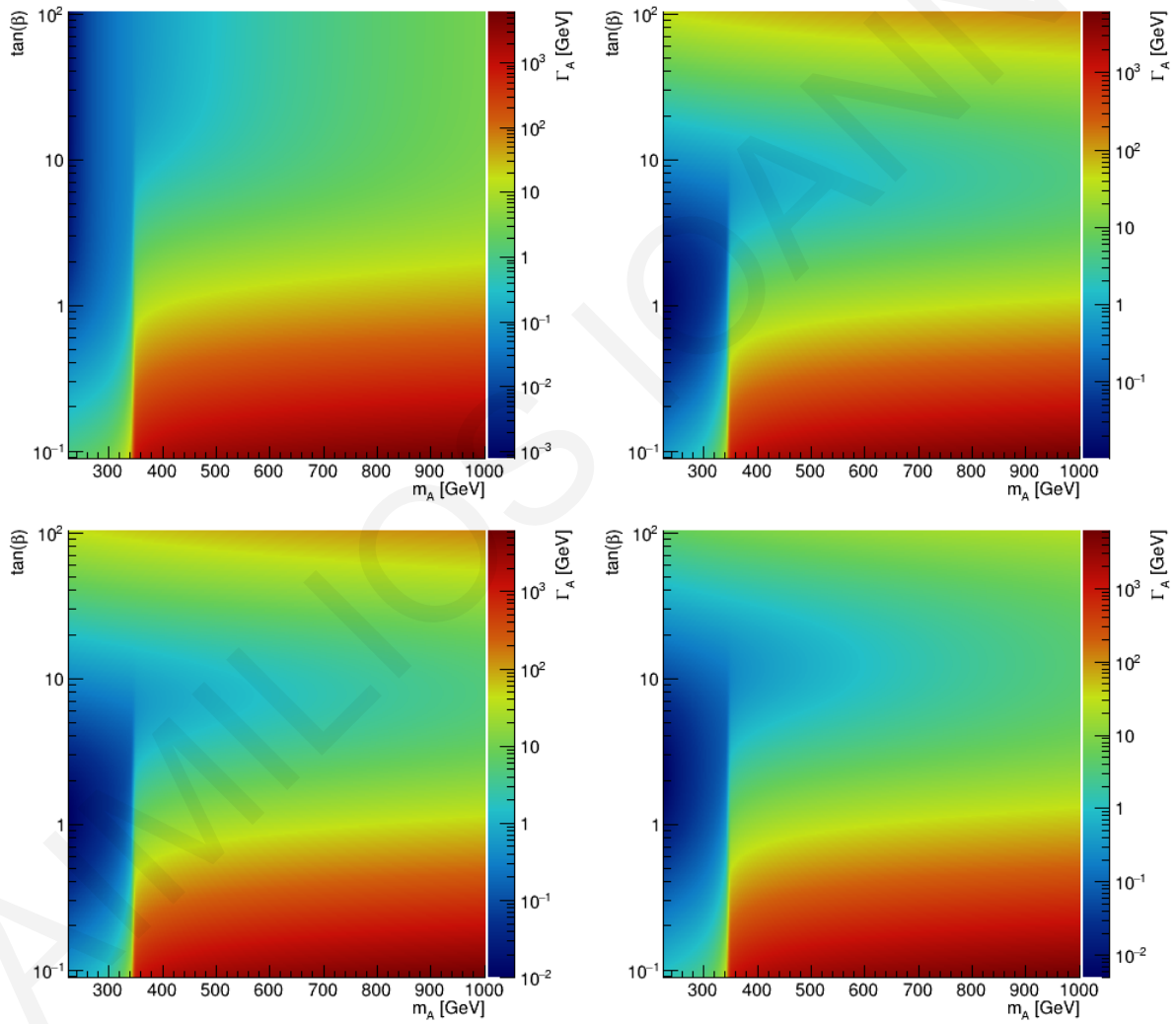

Figure 5.11: **Top left**: Γ_A for Type-I 2HDM. **Top right**: Γ_A for Type-II 2HDM. **Bottom left**: Γ_A for Flipped 2HDM. **Bottom right**: Γ_A for Lepton-specific 2HDM.

5.2.1.2 ASSOCIATED PRODUCTION

As mentioned, a heavy pseudoscalar A boson could be also produced by the associated production mode which is deeply investigated in the current thesis too. The p_T and η distributions of b-quarks produced from the SM Higgs boson at generation level are reported in Fig. 5.12, and Fig. 5.13 for the leading b-quark as well as Fig. 5.14, and Fig. 5.15 for the sub-leading b-quark, respectively.

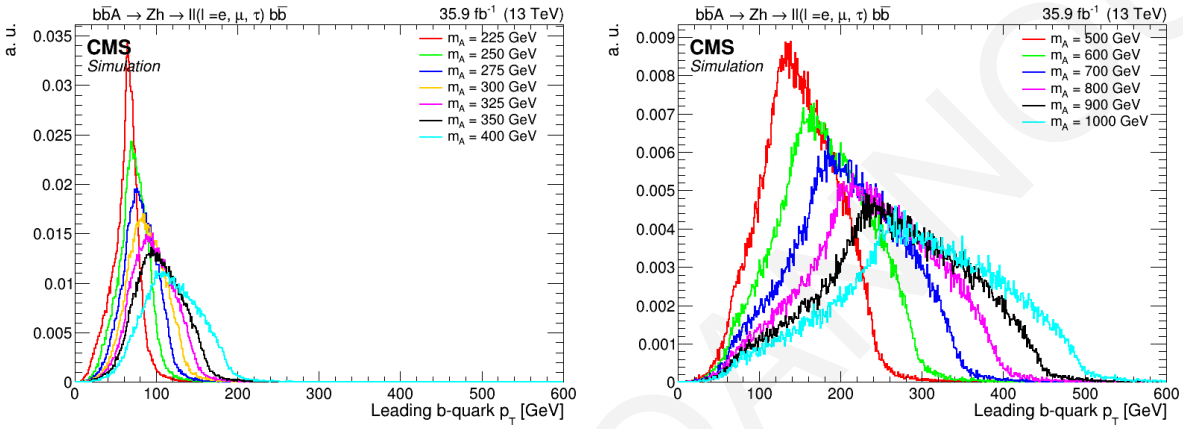

Figure 5.12: The p_T distribution for leading b-quark produced from SM Higgs boson for each mass point of A boson.

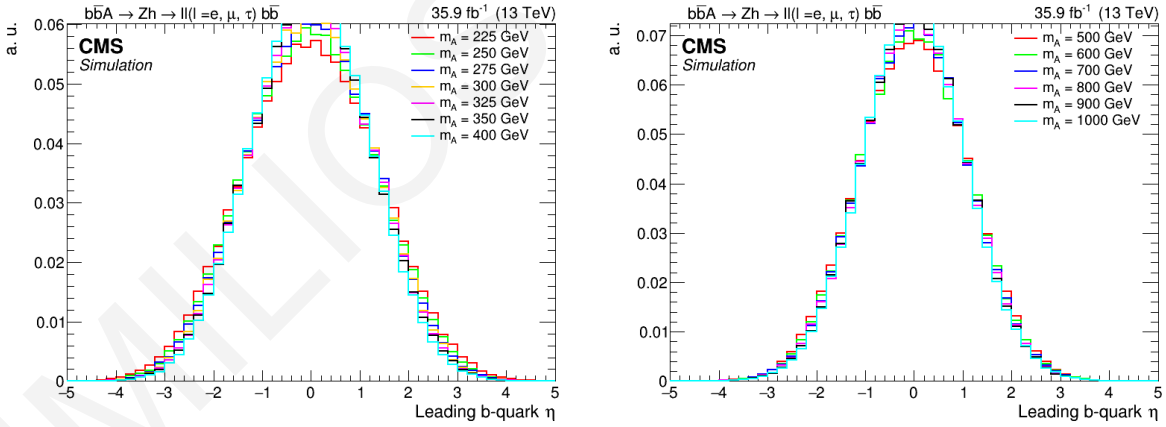

Figure 5.13: The η distribution for leading b-quark produced from SM Higgs boson for each mass point of A boson.

In the associated production mode, there are two additional b-quarks which accompany a possible heavy pseudoscalar A boson which are presented in the final states. The final states of each event of that production mode have four b-quarks (two come from the Higgs decay and the other two originate in the gluon gluon fusion) and a pair of leptons or neutrinos which are the final products of Z boson. The p_T and η distributions of associated b-quarks at generation level are illustrated in Fig. 5.16 and Fig. 5.17,

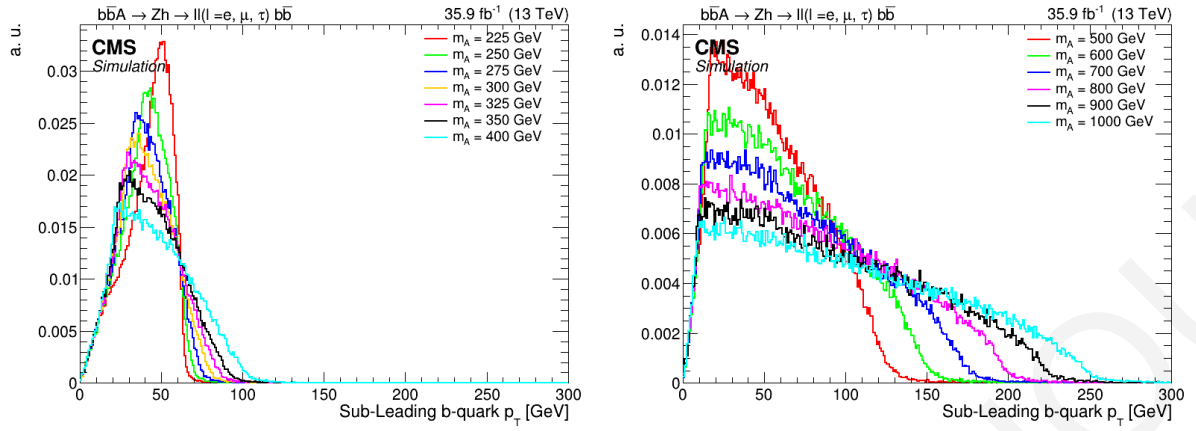

Figure 5.14: The p_T distribution for sub-leading b-quark produced from SM Higgs boson for each mass point of A boson.

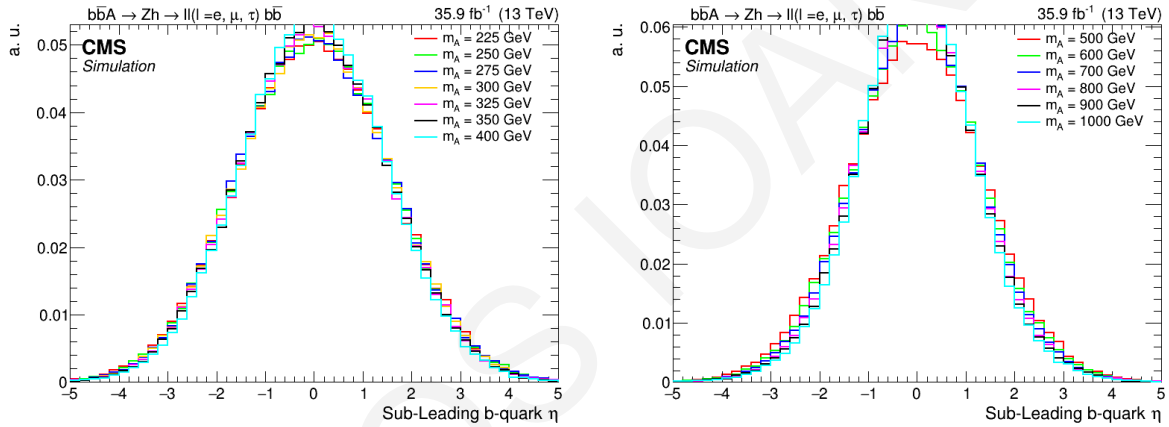

Figure 5.15: The η distribution for sub-leading b-quark produced from SM Higgs boson for each mass point of A boson.

respectively.

The plots indicate that the associated b-quarks are generally produced with a softer p_T spectrum and at higher pseudo-rapidity than the b-quarks which are generated by the SM Higgs decay. Only in a small fraction of events the associated b-quarks are above the kinematic and geometrical thresholds, implying that in the majority of the events the additional b-jets can not even be reconstructed or identified.

5.2.2 BACKGROUND SAMPLES

All physics processes yielding final states with one or two leptons and a large missing transverse momentum in association with one or two b-quarks have to be considered as possible sources of background

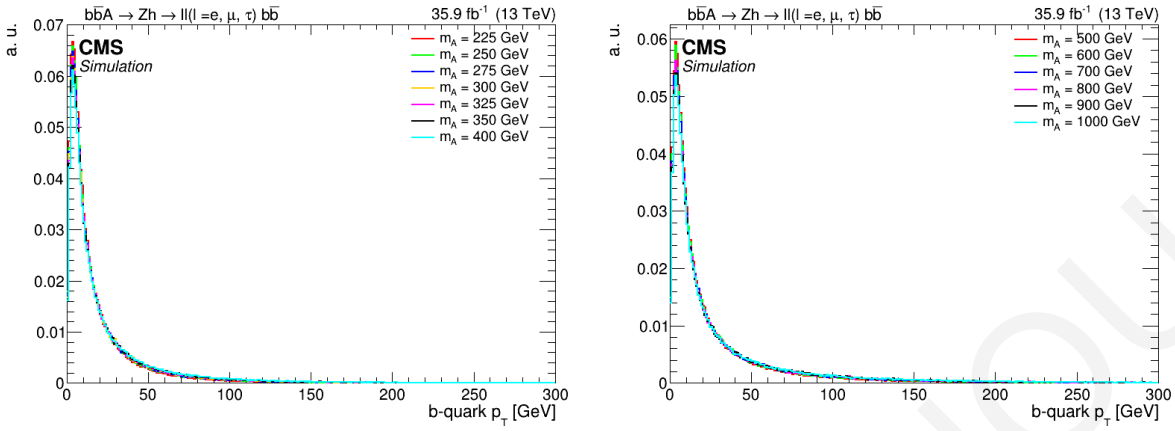

Figure 5.16: The p_T distribution for associated b-quarks for each mass point of A boson.

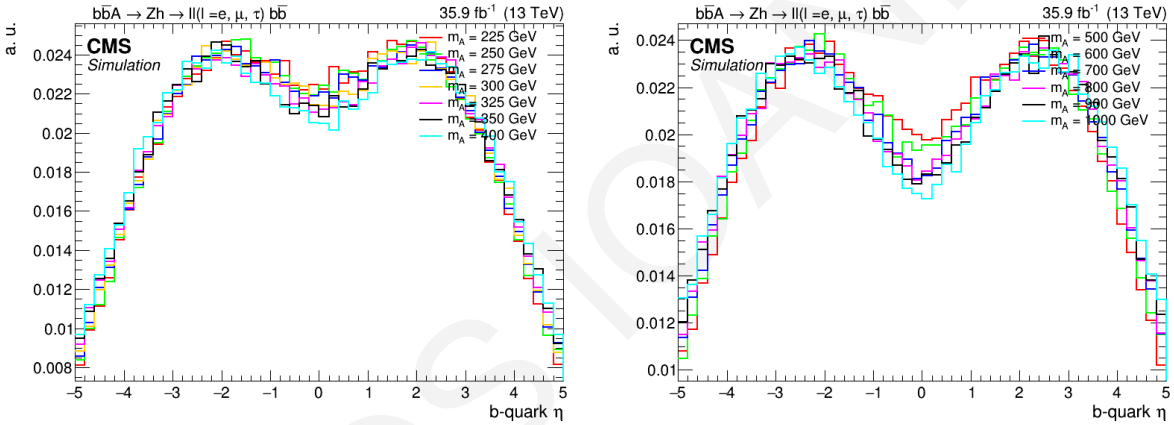

Figure 5.17: The η distribution for associated b-quarks for each mass point of A boson.

for the analysis. The complete list of background datasets considered is presented in Table B.6 and Table B.7 in Appendix D.4. The cross section used to normalise SM backgrounds are derived from the generators or calculations with dedicated softwares reported in Ref. [77], and/or calculated at (N)NLO by the Standard Model Cross section Working Group [78]. For all MC background samples, the hard scattering process uses the NNPDF 3.0 [73] parton distribution functions (PDFs).

5.2.2.1 Z + Jets

This process represents the main irreducible background for the signal in the 0- and 2-lepton final states given the large missing transverse momentum or the presence of two resonating leptons in the final state, respectively. The production of single Z/γ^* bosons in association with one or more partons or gluons in the final state is topologically similar to the searched signal, but its final state quarks feature a

generally softer p_T spectrum, a non-resonant and rapidly falling di-jet mass distribution, and other less distinctive characteristics (effective spin and colour radiation) that should theoretically distinguish it from the signal. Before b-quark tagging, the contribution for *udscg* (light) partons dominates, while after the application of b-tagging the primary contribution in the signal region is from $Z + b(b)$. This Z+jets background is produced with the MADGRAPH5_aMC@NLO generator at LO in QCD, and normalised to the next-to-next-to-leading-order (NNLO) cross section, computed using FEWZ V3.1 [79]. The V boson p_T spectra are corrected to account for next-to-leading-order (NLO) QCD and EW contributions [80]. In addition to an inclusive sample, exclusive samples are produced in several bins of HT (the sum of the p_T of the hadrons at Les Houches Accords (LHE) level [81]) starting from 100 GeV, or for 1, 2, 3, or 4 additional partons in the final state of the hard process.

5.2.2.2 W + JETS

The leptonic decay of a W boson can be an irreducible background in the single-lepton channel, or in the zero-lepton channel in the case the charged lepton escapes undetected (e.g. outside the detector acceptance) or fails the lepton identification requirements. The production of a W boson has a cross section larger by an order of magnitude with respect to the Z, and this makes the W+jets a relevant background also when a lepton veto is applied. Analogously to the Z+jets samples, an inclusive $W(\rightarrow \ell\nu)$ sample has been produced with MADGRAPH5_aMC@NLO at LO in QCD in HT-binned samples. Similarly to the Z+jets, also the W+jets backgrounds are reweighted to account for next-to-leading-order (NLO) QCD and EW contributions [80]. Exclusive samples are produced in several bins of HT (the sum of the p_T of the hadrons at LHE level) starting from 70 GeV.

5.2.2.3 $t\bar{t}$

The production of $t\bar{t}$ pairs represents a particularly challenging background at the LHC, given its large production cross section. These events always contain two energetic b-jets and two W bosons which may decay to high p_T, isolated leptons. The primary handles to reduce the $t\bar{t}$ background are topological, such as its larger jet multiplicity and the azimuthal opening angle between the vector boson and the di-jet system, which is more broadly distributed in top pair production than in signal events. In the di-lepton final state, the most important cut to reduce $t\bar{t}$ is the candidate Z p_T. In $t\bar{t}$ production the di-lepton p_T spectrum is sharply falling, given the absence of a di-lepton resonance. The main sample considered is generated at NLO in QCD with the POWHEG 2.0 [82, 83, 84] generator, and the cross section is computed with TOP++v2.0 [85] at next-to-next-to-leading order.

5.2.2.4 SINGLE-TOP

Inclusive single top samples have been produced at NLO in QCD with the MADGRAPH5_aMC@NLO generator using the FXFX merging scheme [86], including all the possible decays of the W bosons. The s-channel and t-channel single-top samples are produced in the 4-flavour scheme, while tW-channel is produced in the 5-flavour scheme.

5.2.2.5 DI-BOSON

The production of two vector bosons in the SM is a rare process, with a similar kinematics to that of the signal. Furthermore, the boost of the bosons could be large. The main handle to discriminate against VV backgrounds is a tight cut on the jet mass. The SM Higgs boson production (VH) instead, is virtually indistinguishable from the signal except for the mass resonance itself. However, the SM Higgs production cross section is much smaller than the one of the other di-boson processes. All the di-boson production processes (WW, WZ, ZZ, WH, ZH) and their corresponding (semi)-leptonic decay modes are considered, including those involving one or more neutrinos. These backgrounds are simulated at NLO in QCD with the MADGRAPH5_aMC@NLO generator.

5.2.2.6 MULTIJET (QCD)

Despite its enormous cross section at LHC, the probability to produce final states with prompt, isolated leptons or large missing transverse momentum is very low. HT binned samples are generated at LO with the MADGRAPH5_aMC@NLO generator.

5.2.3 CORRECTIONS ON V BOSON MOMENTUM

5.2.3.1 NLO QCD

In Run-II, the usage of next-to-leading order generator, such as a MADGRAPH5_aMC@NLO, allowed to have a much better description of the vector bosons (Z, W) with respect to Run-I, when only leading order generators were available. This is confirmed by data/simulation comparison. Unfortunately, NLO generators have not been used to generate large exclusive samples with the high statistics needed for analyses in the high-p_T regime. Instead, exclusive MADGRAPH5_aMC@NLO samples are available. In these, the p_T spectra of the W and Z bosons are known to be non-perfectly described, compared to data and the inclusive MADGRAPH5_aMC@NLO samples, as shown in Fig. 5.18 (left plot).

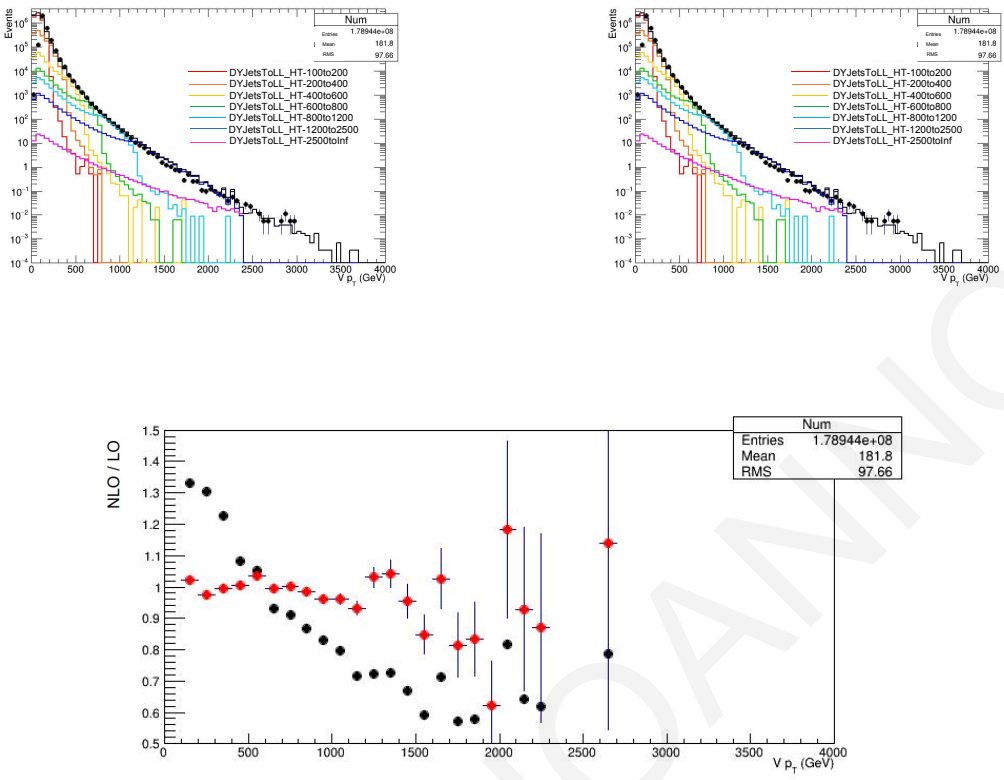

Figure 5.18: The p_T spectrum for the exclusive NLO (back dots) and exclusive LO (solid lines) samples for the $Z \to \ell\ell$ process before (left) and after (right) the fit and the k-factor application. The bottom plot shows the NLO/LO ratio before (black points) and after the fit (red points).

Multiplicative scale factors, applied to each exclusive LO samples, and hence called QCD k-factors, are derived from official Z/W+jets samples generated at NLO. Instead of an iterative approach [87], starting from the largest HT sample, the k-factors are derived through a simultaneous fit. The fit is performed by excluding the low mass region ($Vp_T < 100$ GeV) not described by the exclusive samples. The reference distribution to be matched is represented by the NLO exclusive samples, which are generated with the same generator and parameters as the inclusive NLO sample, but in different ranges of vector boson p_T and allow a much more accurate determination of the k-factors at large HT. In Figs. 5.18, 5.19, and 5.20 show the distributions before and after the fit, with the LO exclusive samples rescaled. The ratio plot before/after the fit can be seen too.

The same procedure is repeated to derive the k-factors for the exclusive LO Drell-Yan samples with 1, 2, 3, or 4 additional partons in the final state. The list of the new cross sections for the LO samples, accounting for the NLO QCD correction factors, is reported in Table 5.1. Since the statistical uncertainty of the k-factors is negligible, it is not accounted for as a systematic uncertainty.

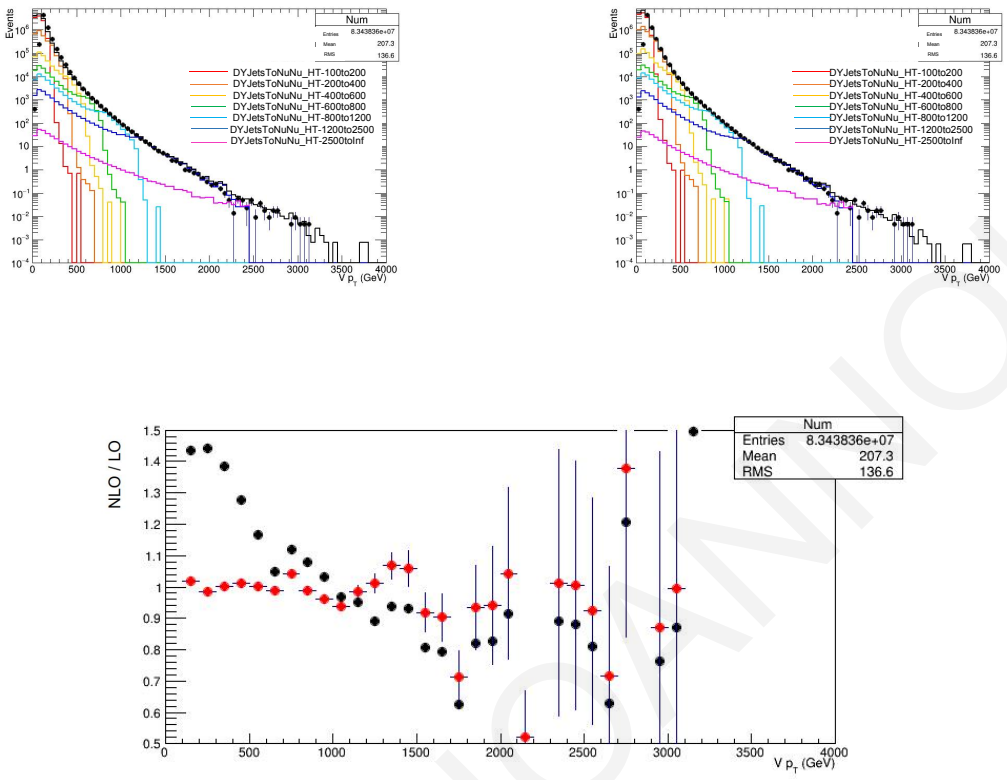

Figure 5.19: The p_T spectrum for the exclusive NLO (back dots) and exclusive LO (solid lines) samples for the $Z \to \nu\nu$ process before (left) and after (right) the fit and the k-factor application. The bottom plot shows the NLO/LO ratio before (black points) and after the fit (red points).

5.2.3.2 NLO Electroweak

Further corrections to the Vp_T spectrum comes from NLO electroweak contributions that become more and more important with the transverse momentum. These corrections, applied on top of the k-factors, are effectively applied on a per-event basis, depending on the p_T of the vector boson at generation level. The calculation of these contributions is explained in Ref. [80]. Fig. 5.21 shows the correction for the W and Z bosons as a function of their p_T. The full variation of the correction is taken as systematic uncertainty.

5.2.4 Top Momentum Reweighting

The top quark p_T is known to be mismodeled in simulation when compared to data [88]. To correct this effect, a dedicated correction is recommended by the TOP group based on the p_T of the two top quarks

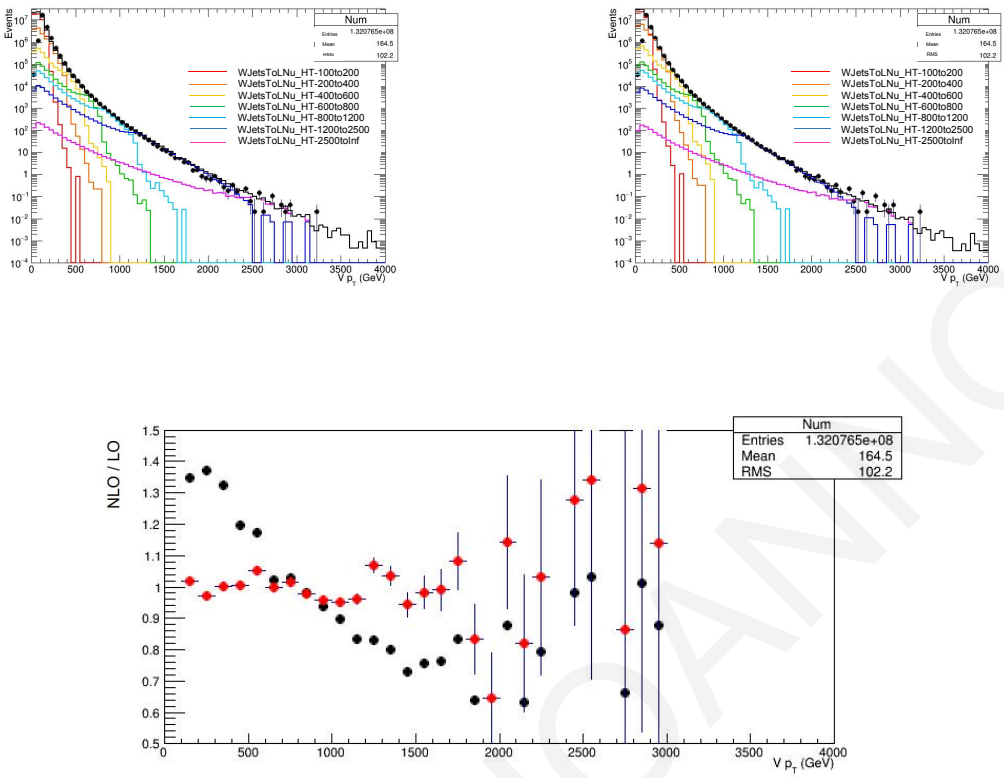

Figure 5.20: The p_T spectrum for the exclusive NLO (back dots) and exclusive LO (solid lines) samples for the $W \to \ell\nu$ process before (left) and after (right) the fit and the k-factor application. The bottom plot shows the NLO/LO ratio before (black points) and after the fit (red points).

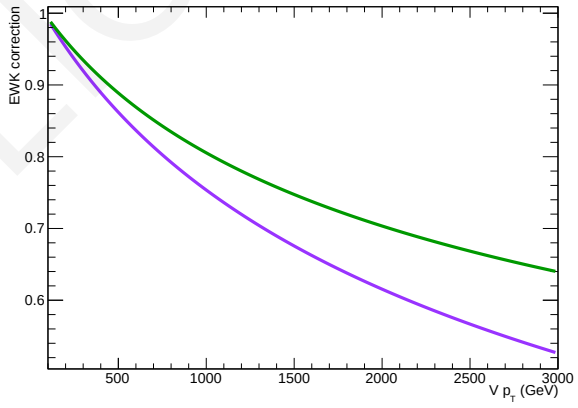

Figure 5.21: Electroweak corrections for the Z (green line) and W boson (purple line) as a function of the transverse momentum [80].

at generation level:

$$SF(p_T) = e^{0.0615 - 0.0005 \cdot p_T} \tag{5.1}$$

Dataset	cross section (pb)	QCD NLO k-factor
DYJetsToLL_M-50_HT-100to200	213.4	1.45
DYJetsToLL_M-50_HT-200to400	65.42	1.60
DYJetsToLL_M-50_HT-400to600	7.31	1.29
DYJetsToLL_M-50_HT-600To800	1.49	1.10
DYJetsToLL_M-50_HT-800To1200	0.661	1.05
DYJetsToLL_M-50_HT-1200To2500	0.119	0.79
DYJetsToLL_M-50_HT-2500ToInf	0.00280	0.79
DY1JetsToLL_M-50	1016	0.272
DY2JetsToLL_M-50	331.4	0.041
DY3JetsToLL_M-50	96.36	0.056
DY4JetsToLL_M-50	51.4	0.041
ZJetsToNuNu_HT-100To200	384.1	1.37
ZJetsToNuNu_HT-200To400	118.1	1.52
ZJetsToNuNu_HT-400To600	14.7	1.37
ZJetsToNuNu_HT-600To800	3.35	1.04
ZJetsToNuNu_HT-800To1200	1.68	1.14
ZJetsToNuNu_HT-1200To2500	0.316	0.88
ZJetsToNuNu_HT-2500ToInf	0.00722	0.88
WJetsToLNu_HT-100To200	1695.	1.26
WJetsToLNu_HT-200To400	532.4	1.48
WJetsToLNu_HT-400To600	61.6	1.26
WJetsToLNu_HT-600To800	12.4	1.03
WJetsToLNu_HT-800To1200	5.77	1.05
WJetsToLNu_HT-1200To2500	1.023	0.77
WJetsToLNu_HT-2500ToInf	0.0248	0.77

Table 5.1: Exclusive LO QCD k-factors derived with the fit method. Due to the lack of statistics in the exclusive NLO samples, the k-factors for the 1200To2500 and 2500ToInf samples are taken to be equal. The relative cross sections correspond to a centre-of-mass energy 13 TeV.

where p_T is taken at matrix element level and an overall weight is calculated per-event, as follows:

$$w = \sqrt{SF(t) \cdot SF(\bar{t})} \tag{5.2}$$

The effect of the corrections have been tested in our signal depleted $t\bar{t}$ control regions, finding an improved data/simulation agreement. Therefore, the reweighting procedure is applied consistently to the $t\bar{t}$ samples for all signal and control regions throughout the analysis. The recommended uncertainties are then propagated accordingly.

5.2.5 DATA SAMPLES

Data events have been collected during the 2016 data taking, at a centre-of-mass energy of 13 TeV, with leptonic and $\not{E}_T$ triggers. The MET primary dataset is used when requiring missing energy triggers, and the *SingleMuon* and *SingleElectron* are used for data selected with a single muon and electron trigger, respectively. The MET triggers are also used to recover part of the efficiency lost due to muon trigger issues.

The full list of datasets used is shown in Tab. 5.2. Data belong to the *03Feb2017ReMiniAOD* campaign which is processed by the *CMSSW_8_0_26_patch1* release. Runs and lumisections (a fixed time period in data taking, approximately 24 seconds) are taken into account according to the latest available Golden JSON file[1] that includes all the runs certified as valid for all CMS subsystems. The integrated luminosity amounts to 35.867 fb^{-1} as illustrated in Fig. 5.22.

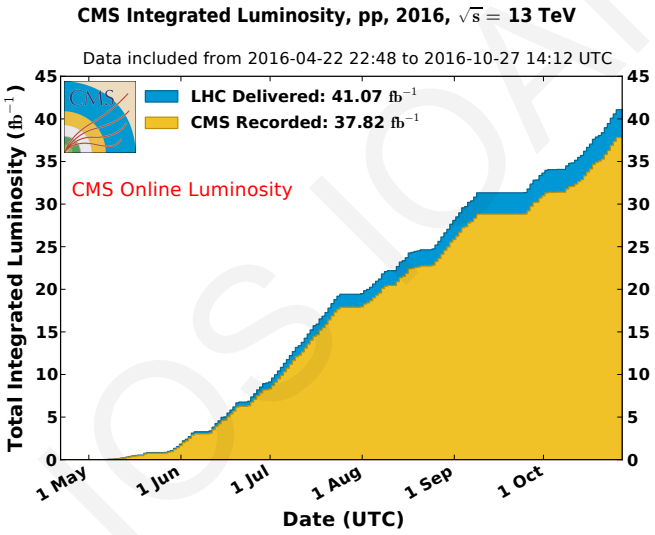

Figure 5.22: Cumulative luminosity versus day delivered to (blue), and recorded by CMS (orange) during stable beams and for pp collisions at 13 TeV centre-of-mass energy in 2016. The delivered luminosity accounts for the luminosity delivered from the start of stable beams until the LHC requests CMS to turn off the sensitive detectors to allow a beam dump or beam studies. Given is the luminosity as determined from counting rates measured by the luminosity detectors.

5.2.6 TRIGGER

Events are selected on-line by the two stage trigger system. The Level-1 (L1) trigger (described in Chapter 4.7.1) consists of hardware processors that perform a very basic selection and counting of

[1] The latest available Golden JSON file is the *Cert_271036-284044_13TeV_23Sep2016ReReco_Collisions16_JSON.txt*

Dataset	Int. lumi (fb^{-1})
MET/Run2016B-03Feb2017-v2	5.9
MET/Run2016C-03Feb2017-v1	2.6
MET/Run2016D-03Feb2017-v1	4.4
MET/Run2016E-03Feb2017-v1	4.1
MET/Run2016F-03Feb2017-v1	3.2
MET/Run2016G-03Feb2017-v1	7.7
MET/Run2016H-03Feb2017-v2 MET/Run2016H-03Feb2017-v3	8.9
SingleMuon/Run2016B-03Feb2017-v2	5.9
SingleMuon/Run2016C-03Feb2017-v1	2.6
SingleMuon/Run2016D-03Feb2017-v1	4.4
SingleMuon/Run2016E-03Feb2017-v1	4.1
SingleMuon/Run2016F-03Feb2017-v1	3.2
SingleMuon/Run2016G-03Feb2017-v1	7.7
SingleMuon/Run2016H-03Feb2017-v2 SingleMuon/Run2016H-03Feb2017-v3	8.9
SingleElectron/Run2016B-03Feb2017-v2	5.9
SingleElectron/Run2016C-03Feb2017-v1	2.6
SingleElectron/Run2016D-03Feb2017-v1	4.4
SingleElectron/Run2016E-03Feb2017-v1	4.1
SingleElectron/Run2016F-03Feb2017-v1	3.2
SingleElectron/Run2016G-03Feb2017-v1	7.7
SingleElectron/Run2016H-03Feb2017-v2 SingleElectron/Run2016H-03Feb2017-v3	8.9

Table 5.2: Datasets used for 2016.

physics objects, and reduce the rate from 40 MHz down to 100 kHz. Events passing the L1_decision are acquired by the DAQ system and a complete and more accurate reconstruction is performed by the High Level Trigger (HLT) which exploits similar but faster variations of the same algorithms used in the offline event reconstruction. A trigger path is a string that identifies a list of selections performed at HLT (further information in Chapter 4.7.2).

Events are considered if they fire a specific set of triggers, in both data and Monte Carlo. Single lepton triggers requiring at least one, non-isolated lepton, have been used to select events for the one and two-lepton categories. The efficiencies are derived separately in both data and MC and scale factors, defined as $SF = \epsilon_{data}/\epsilon_{MC}$, are applied consistently to simulated events in order to correct for potential discrepancies.

The orthogonality of the primary dataset is guaranteed by the fact that for every channel/selection, only the corresponding primary dataset (the one containing the trigger corresponding to the channel) is used. As a general cross check, a scan on the event number, lumisection number and run number is made, to

check for duplicate events.

5.2.6.1 ELECTRON TRIGGER

Electrons are selected by requiring two types of electron trigger to ensure an optimal efficiency over the whole p_T range. Due to the relatively high threshold of the single electron non-isolated triggers (115 GeV), the most efficient way to collect events with low boost is to use a single electron, isolated trigger, with a logical *OR* statement with the usual non-isolated triggers to maintain the efficiency in the boosted regime. The logical "OR" is used to get the best possible trigger efficiency by combining several triggers. In order to compute the combined efficiency of N different uncorrelated triggers, the following mathematical equation is used:

$$\epsilon_{combined} = 1 - \prod_{i=1}^{N}(1 - \epsilon_i) \tag{5.3}$$

where $\epsilon_{combined}$ is the combined trigger efficiency and ϵ_i are the efficiencies of the base triggers. The single electron triggers are reported in Tab. 5.3.

HLT paths	L1 seeds
HLT_Ele105_CaloIdVT_GsfTrkIdT	L1_SingleEG30–40
HLT_Ele115_CaloIdVT_GsfTrkIdT	OR
	L1_SingleJet170–200
HLT_Ele27_WPTight_Gsf	OR
HLT_Ele32_WPTight_Gsf	L1_SingleTau100–120er

Table 5.3: Single electron HLT trigger paths used in the analysis.

The single electron trigger efficiency (Fig. 5.23) is evaluated with the *tag and probe package* [89], similarly with the method used for muons, exploiting electrons arising from Z decays. The full available statistics used in the analysis has been employed to derive the efficiency for data, while the full statistics of an inclusive NLO DY sample is used for evaluating the trigger efficiency in MC. The tag electron is matched to low-pt-eta-restricted *HLT_Ele27_eta2p1_WPTight_Gsf_v** trigger, while the trigger efficiency is measured for probe electrons passing the Loose cut-based ID requirements, considering the OR of all HLT paths. The electron trigger scale factors are applied to all the MC samples used in the analysis and the next section (Chapter 5.2.6.2) is dedicated to the determination of the electron trigger scale factors.

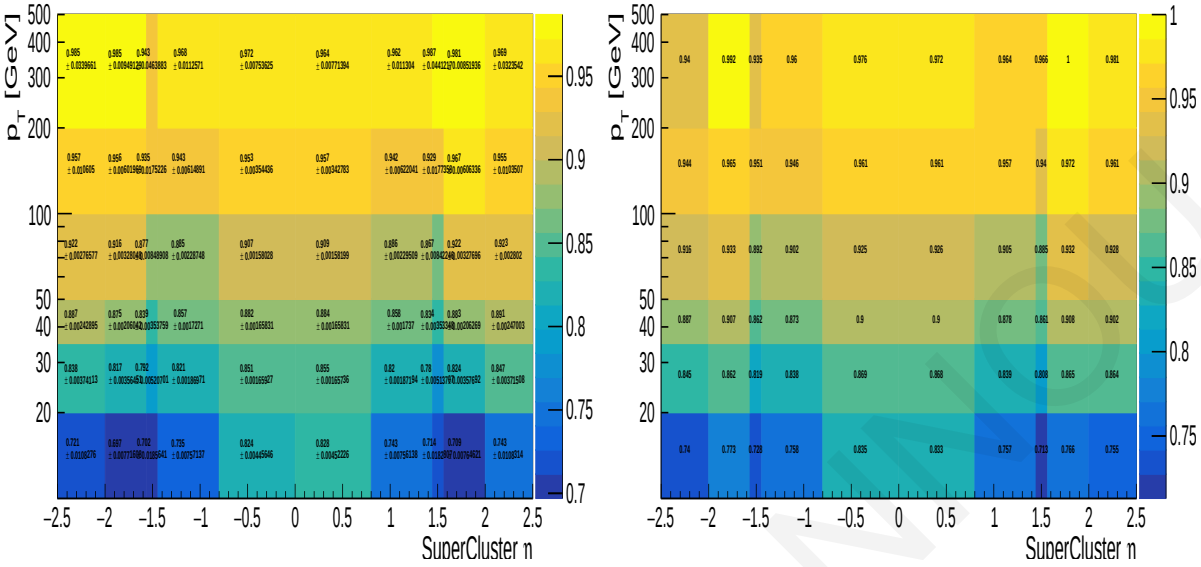

Figure 5.23: HLT_Ele*_WPTight_Gsf OR HLT_Ele*_CaloIdVT_GsfTrkIdT efficiencies on data (left) and MC (right) as a function of the η and p_T of the electron. The efficiency is extracted with the tag and probe method.

5.2.6.2 Electron Trigger Scale Factors

To compute electron scale factors, the *tag and probe method* was used. This method provides an elegant way to estimate trigger efficiencies with only small statistical uncertainties and without a bias. The method selects events which contain a well-known physics process that its final state is two physics objects of the same flavour.

This method is used to determine muon trigger or electron trigger efficiencies by finally calculating the electron or muon scale factors. It uses events in which a Z boson is produced and decays into two electrons. The one reconstructed electron is so-called *tag electron* and is an object which fires the trigger. In general, the *tag electron* is an object which passes a set of very tight selection criteria [90]. It is chosen to be a very tight criterion, ensuring the isolation of the required electron candidate. The other reconstructed electron is called *probe electron* and belongs to the loose selections [90]. This electron has to pass a set of loose selection criteria and additionally, it is classified as *passing probe* and *failing probe*. Table 5.4 records the selection criteria that the two electron candidates have to pass.

Given that the first electron is defined as *tag* and the second one as *probe*, the invariant mass of two is required to be compatible with the Z invariant mass peak. A mass of tag and probe pairs has to range from 50 GeV to 130 GeV that is the Z mass window which is determined by *tag and probe method*.

Based on these selection criteria events may be classified as TT, TP and TF, where T corresponds to tag

	Tag	Probe
Super cluster position	$\|\eta\| \leq$ 2.1	-
Super cluster η	$\|\eta\| \leq$ 1.44, 1.56 $\leq \|\eta\| \leq$ 2.5	$\|\eta\| < 2.5$
Transverse momentum of electron	$p_T \geq$ 30 GeV	–
Transverse energy of super cluster	$E_T > 5$ GeV	$E_T > 5$ GeV

Table 5.4: The tag and probe selection criteria.

electron, P referred as a passing probe and F related to a failing probe. The single electron efficiency is calculated taking into account the events which are classified as TT, TP and TF, as follows:

$$\epsilon(TnP) = \frac{2N_{TT} + N_{TP}}{2N_{TT} + N_{TP} + N_{TF}} \tag{5.4}$$

where N_{TT}, N_{TP} and N_{TF} are the events in which tag and probe electrons have been observed. The factor of 2 is used in order to avoid double counting of the events where both electrons pass the tag criteria. Equation 5.4 gives the efficiency of data and/or of MC samples.

Scale factors are calculated by using the following formula:

$$scale\ factor = \frac{\epsilon(TnP)_{Data}}{\epsilon(TnP)_{MC}} \tag{5.5}$$

The statistical uncertainty of the *scale factor* (SF) is determined by propagation of the $\Delta_{\epsilon(TnP)}$ in data and MC events. The statistical uncertainty of the efficiency (ϵ) is calculated as follows:

$$\Delta\epsilon(TnP) = \frac{\epsilon(1-\epsilon)}{N} \tag{5.6}$$

where ϵ corresponds to the efficiency of data or MC and N is related to the whole number of events. Finally, the statistical uncertainty of the scale factor can be derived by:

$$\Delta SF = SF\sqrt{\left(\frac{\Delta\epsilon^{Data}}{\epsilon^{Data}}\right)^2 + \left(\frac{\Delta\epsilon^{MC}}{\epsilon^{MC}}\right)^2} \tag{5.7}$$

Given that efficiencies may depend on the kinematics, the calculations are performed in two dimensional bins of transverse momentum (p_T) and pseudorapidity ($|\eta|$) of the electrons. The pseudorapidity ranges from -2.5 to 2.5 and is divided by ten regions in the following way:

$$|\eta| : \ [0.0 - 0.8,\ 0.8 - 1.444,\ 1.444 - 1.566,\ 1.566 - 2.0,\ 2.0 - 2.5] \tag{5.8}$$

Additionally, efficiencies of the data and MC, as well as the scale factors, are calculated for specific

areas of the transverse momentum. The regions of p_T are the following:

$$p_T \text{ (GeV)} : \ [10-20,\ 20-35,\ 35-50,\ 50-100,\ 100-200,\ 200-500] \tag{5.9}$$

Four electron HLT trigger paths are used in this analysis and their scale factors are derived by using the *tag and probe method* which is described in detail. The results, the efficiencies and the scale factors in bins of $p_T \times \eta$ for the trigger paths are summarised in Tab. 5.5, Tab. 5.6, Tab. 5.7 and Tab. 5.8. In addition, their scale factors and uncertainties are graphically presented in Fig. 5.24, Fig. 5.25, Fig. 5.26 and Fig. 5.27.

		$p_T \in (10,20)$ (GeV)	$p_T \in (20,35)$ (GeV)	$p_T \in (35,50)$ (GeV)	$p_T \in (50,100)$ (GeV)	$p_T \in (100,200)$ (GeV)	$p_T \in (200,500)$ (GeV)
$\eta \in (-2.5,-2.0)$	ϵ_{data}	0.722 ± 0.003	0.838 ± 0.001	0.887 ± 0.001	0.923 ± 0.001	0.957 ± 0.004	0.985 ± 0.011
	ϵ_{MC}	0.740 ± 0.006	0.845 ± 0.002	0.887 ± 0.001	0.915 ± 0.002	0.943 ± 0.010	0.940 ± 0.034
	SF	0.976 ± 0.014	0.992 ± 0.004	1.000 ± 0.003	1.009 ± 0.004	1.015 ± 0.011	1.048 ± 0.036
$\eta \in (-2.0,-1.566)$	ϵ_{data}	0.698 ± 0.003	0.816 ± 0.001	0.875 ± 0.001	0.916 ± 0.001	0.956 ± 0.003	0.985 ± 0.006
	ϵ_{MC}	0.773 ± 0.005	0.845 ± 0.002	0.907 ± 0.001	0.932 ± 0.001	0.965 ± 0.005	0.992 ± 0.008
	SF	0.903 ± 0.010	0.947 ± 0.004	0.965 ± 0.002	0.983 ± 0.003	0.991 ± 0.006	0.993 ± 0.009
$\eta \in (-1.566,-1.444)$	ϵ_{data}	0.701 ± 0.008	0.792 ± 0.002	0.839 ± 0.001	0.876 ± 0.002	0.935 ± 0.008	0.943 ± 0.024
	ϵ_{MC}	0.729 ± 0.014	0.819 ± 0.004	0.863 ± 0.002	0.892 ± 0.004	0.950 ± 0.015	0.935 ± 0.044
	SF	0.962 ± 0.026	0.967 ± 0.006	0.972 ± 0.004	0.982 ± 0.009	0.984 ± 0.019	1.009 ± 0.050
$\eta \in (-1.444,-0.8)$	ϵ_{data}	0.735 ± 0.002	0.820 ± 0.001	0.857 ± 0.001	0.884 ± 0.001	0.943 ± 0.002	0.968 ± 0.005
	ϵ_{MC}	0.758 ± 0.004	0.838 ± 0.001	0.873 ± 0.001	0.902 ± 0.001	0.946 ± 0.004	0.962 ± 0.010
	SF	0.970 ± 0.010	0.979 ± 0.002	0.982 ± 0.002	0.980 ± 0.002	0.997 ± 0.007	1.006 ± 0.012
$\eta \in (-0.8,0.0)$	ϵ_{data}	0.825 ± 0.002	0.852 ± 0.001	0.882 ± 0.001	0.907 ± 0.001	0.953 ± 0.002	0.972 ± 0.004
	ϵ_{MC}	0.835 ± 0.003	0.869 ± 0.001	0.900 ± 0.001	0.925 ± 0.001	0.961 ± 0.003	0.975 ± 0.007
	SF	0.988 ± 0.005	0.980 ± 0.002	0.980 ± 0.002	0.981 ± 0.002	0.992 ± 0.004	0.997 ± 0.008
$\eta \in (0.0,0.8)$	ϵ_{data}	0.827 ± 0.002	0.855 ± 0.001	0.885 ± 0.001	0.909 ± 0.001	0.957 ± 0.001	0.964 ± 0.004
	ϵ_{MC}	0.834 ± 0.003	0.868 ± 0.001	0.900 ± 0.001	0.926 ± 0.001	0.961 ± 0.003	0.972 ± 0.007
	SF	0.992 ± 0.005	0.985 ± 0.002	0.983 ± 0.002	0.982 ± 0.002	0.996 ± 0.004	0.992 ± 0.008
$\eta \in (0.8,1.444)$	ϵ_{data}	0.743 ± 0.001	0.820 ± 0.001	0.858 ± 0.001	0.886 ± 0.001	0.942 ± 0.002	0.962 ± 0.005
	ϵ_{MC}	0.757 ± 0.004	0.839 ± 0.001	0.878 ± 0.001	0.905 ± 0.001	0.958 ± 0.004	0.964 ± 0.010
	SF	0.982 ± 0.010	0.977 ± 0.002	0.977 ± 0.002	0.979 ± 0.002	0.983 ± 0.007	0.998 ± 0.012
$\eta \in (1.444,1.566)$	ϵ_{data}	0.713 ± 0.008	0.780 ± 0.002	0.834 ± 0.001	0.867 ± 0.002	0.930 ± 0.009	0.983 ± 0.005
	ϵ_{MC}	0.715 ± 0.014	0.809 ± 0.004	0.861 ± 0.002	0.885 ± 0.004	0.938 ± 0.016	0.964 ± 0.035
	SF	0.997 ± 0.026	0.964 ± 0.006	0.969 ± 0.004	0.980 ± 0.009	0.991 ± 0.019	1.020 ± 0.046
$\eta \in (1.566,2.0)$	ϵ_{data}	0.709 ± 0.003	0.824 ± 0.001	0.883 ± 0.001	0.921 ± 0.001	0.967 ± 0.003	0.980 ± 0.007
	ϵ_{MC}	0.766 ± 0.005	0.865 ± 0.001	0.908 ± 0.001	0.932 ± 0.001	0.974 ± 0.005	1.000 ± 0.001
	SF	0.926 ± 0.010	0.953 ± 0.004	0.972 ± 0.002	0.988 ± 0.003	0.993 ± 0.006	0.980 ± 0.008
$\eta \in (2.0,2.5)$	ϵ_{data}	0.742 ± 0.003	0.847 ± 0.001	0.891 ± 0.001	0.923 ± 0.001	0.955 ± 0.004	0.969 ± 0.013
	ϵ_{MC}	0.755 ± 0.005	0.864 ± 0.001	0.902 ± 0.001	0.928 ± 0.002	0.961 ± 0.008	0.981 ± 0.019
	SF	0.983 ± 0.014	0.980 ± 0.004	0.988 ± 0.003	0.995 ± 0.004	0.994 ± 0.011	0.988 ± 0.033

Table 5.5: Single electron trigger efficiencies for data and Monte Carlo together with scale factors for trigger path HLT_Ele27_WPTight_Gsf.

5.2.6.3 Double Electron Trigger Efficiency

Double electron trigger and single electron trigger have been examined and compared with each other for deciding which trigger is the most optimal in this analysis. The study is performed for the double electron trigger path HLT_Ele23_Ele12_CaloIdL_TrackIdL_IsoVL_DZ and for the single electron trigger path HLT_Ele27_WPTight_Gsf. The goal is to examine their efficiency for each mass point and whether the double electron trigger yields better results than the single electron trigger.

To compute the efficiency, electron candidates have to pass selection criteria and trigger. The efficiency

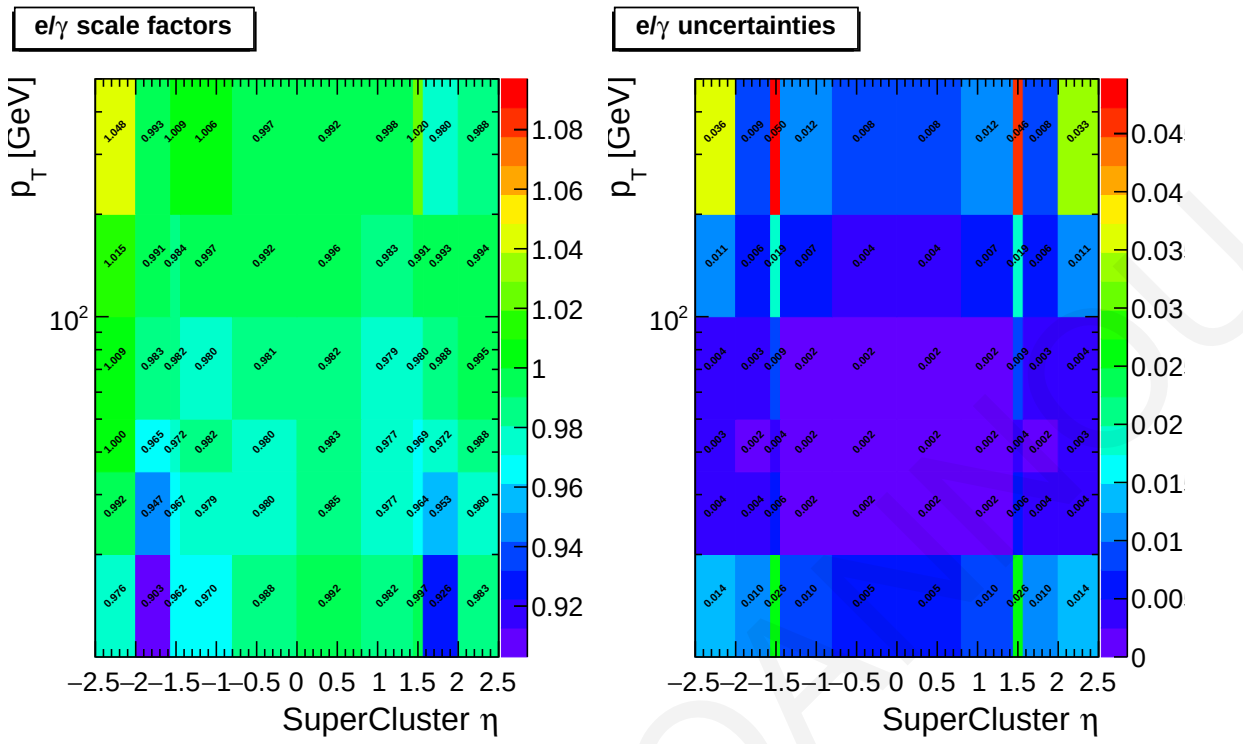

Figure 5.24: Scale factors and their uncertainties for trigger path HLT_Ele27_WPTight_Gsf.

		$p_T \in (10,20)$ (GeV)	$p_T \in (20,35)$ (GeV)	$p_T \in (35,50)$ (GeV)	$p_T \in (50,100)$ (GeV)	$p_T \in (100,200)$ (GeV)	$p_T \in (200,500)$ (GeV)
$\eta \in (-2.5,-2.0)$	ϵ_{data}	0.721 ± 0.004	0.838 ± 0.001	0.887 ± 0.001	0.922 ± 0.001	0.957 ± 0.004	0.985 ± 0.011
	ϵ_{MC}	0.740 ± 0.006	0.845 ± 0.002	0.887 ± 0.001	0.916 ± 0.002	0.944 ± 0.010	0.940 ± 0.034
	SF	0.974 ± 0.015	0.992 ± 0.004	1.000 ± 0.003	1.007 ± 0.003	1.014 ± 0.011	1.048 ± 0.036
$\eta \in (-2.0,-1.566)$	ϵ_{data}	0.697 ± 0.003	0.817 ± 0.001	0.875 ± 0.001	0.916 ± 0.001	0.956 ± 0.003	0.985 ± 0.007
	ϵ_{MC}	0.773 ± 0.005	0.862 ± 0.001	0.907 ± 0.001	0.933 ± 0.001	0.965 ± 0.005	0.992 ± 0.008
	SF	0.902 ± 0.010	0.948 ± 0.004	0.965 ± 0.002	0.982 ± 0.004	0.991 ± 0.006	0.993 ± 0.010
$\eta \in (-1.566,-1.444)$	ϵ_{data}	0.702 ± 0.007	0.792 ± 0.002	0.839 ± 0.001	0.877 ± 0.002	0.935 ± 0.009	0.943 ± 0.024
	ϵ_{MC}	0.728 ± 0.014	0.819 ± 0.004	0.862 ± 0.002	0.892 ± 0.004	0.951 ± 0.014	0.935 ± 0.044
	SF	0.964 ± 0.026	0.967 ± 0.006	0.973 ± 0.004	0.983 ± 0.010	0.983 ± 0.018	1.009 ± 0.050
$\eta \in (-1.444,-0.8)$	ϵ_{data}	0.735 ± 0.002	0.821 ± 0.001	0.857 ± 0.001	0.885 ± 0.001	0.943 ± 0.002	0.968 ± 0.005
	ϵ_{MC}	0.758 ± 0.004	0.838 ± 0.001	0.873 ± 0.001	0.902 ± 0.001	0.946 ± 0.004	0.960 ± 0.010
	SF	0.970 ± 0.010	0.980 ± 0.002	0.982 ± 0.002	0.981 ± 0.003	0.997 ± 0.006	1.008 ± 0.012
$\eta \in (-0.8,0.0)$	ϵ_{data}	0.824 ± 0.001	0.851 ± 0.001	0.882 ± 0.001	0.907 ± 0.001	0.953 ± 0.002	0.972 ± 0.004
	ϵ_{MC}	0.835 ± 0.003	0.869 ± 0.001	0.900 ± 0.001	0.925 ± 0.001	0.961 ± 0.003	0.976 ± 0.006
	SF	0.987 ± 0.005	0.979 ± 0.002	0.980 ± 0.002	0.981 ± 0.002	0.992 ± 0.004	0.996 ± 0.008
$\eta \in (0.0,0.8)$	ϵ_{data}	0.828 ± 0.002	0.855 ± 0.001	0.884 ± 0.001	0.909 ± 0.001	0.957 ± 0.001	0.964 ± 0.004
	ϵ_{MC}	0.833 ± 0.003	0.868 ± 0.001	0.900 ± 0.001	0.926 ± 0.001	0.961 ± 0.003	0.972 ± 0.007
	SF	0.994 ± 0.005	0.985 ± 0.002	0.982 ± 0.002	0.982 ± 0.002	0.996 ± 0.004	0.992 ± 0.008
$\eta \in (0.8,1.444)$	ϵ_{data}	0.743 ± 0.002	0.820 ± 0.001	0.858 ± 0.001	0.886 ± 0.001	0.942 ± 0.002	0.962 ± 0.005
	ϵ_{MC}	0.757 ± 0.004	0.839 ± 0.001	0.878 ± 0.001	0.905 ± 0.001	0.957 ± 0.004	0.964 ± 0.010
	SF	0.982 ± 0.010	0.977 ± 0.002	0.977 ± 0.002	0.979 ± 0.003	0.984 ± 0.006	0.998 ± 0.012
$\eta \in (1.444,1.566)$	ϵ_{data}	0.714 ± 0.008	0.780 ± 0.002	0.834 ± 0.001	0.867 ± 0.002	0.929 ± 0.009	0.987 ± 0.009
	ϵ_{MC}	0.713 ± 0.014	0.808 ± 0.004	0.861 ± 0.002	0.885 ± 0.004	0.940 ± 0.016	0.966 ± 0.034
	SF	1.001 ± 0.026	0.965 ± 0.006	0.969 ± 0.004	0.980 ± 0.010	0.988 ± 0.019	1.022 ± 0.046
$\eta \in (1.566,2.0)$	ϵ_{data}	0.709 ± 0.003	0.824 ± 0.001	0.883 ± 0.001	0.922 ± 0.001	0.967 ± 0.003	0.981 ± 0.007
	ϵ_{MC}	0.766 ± 0.005	0.865 ± 0.001	0.908 ± 0.001	0.932 ± 0.001	0.972 ± 0.005	1.000 ± 0.001
	SF	0.926 ± 0.010	0.953 ± 0.004	0.972 ± 0.002	0.989 ± 0.004	0.995 ± 0.006	0.981 ± 0.009
$\eta \in (2.0,2.5)$	ϵ_{data}	0.743 ± 0.003	0.847 ± 0.001	0.891 ± 0.001	0.923 ± 0.001	0.955 ± 0.004	0.969 ± 0.013
	ϵ_{MC}	0.755 ± 0.005	0.864 ± 0.001	0.902 ± 0.001	0.928 ± 0.002	0.961 ± 0.008	0.981 ± 0.019
	SF	0.984 ± 0.014	0.980 ± 0.004	0.988 ± 0.003	0.995 ± 0.003	0.994 ± 0.011	0.988 ± 0.033

Table 5.6: Single electron trigger efficiencies for data and Monte Carlo together with scale factors for trigger path HLT_Ele32_WPTight_Gsf.

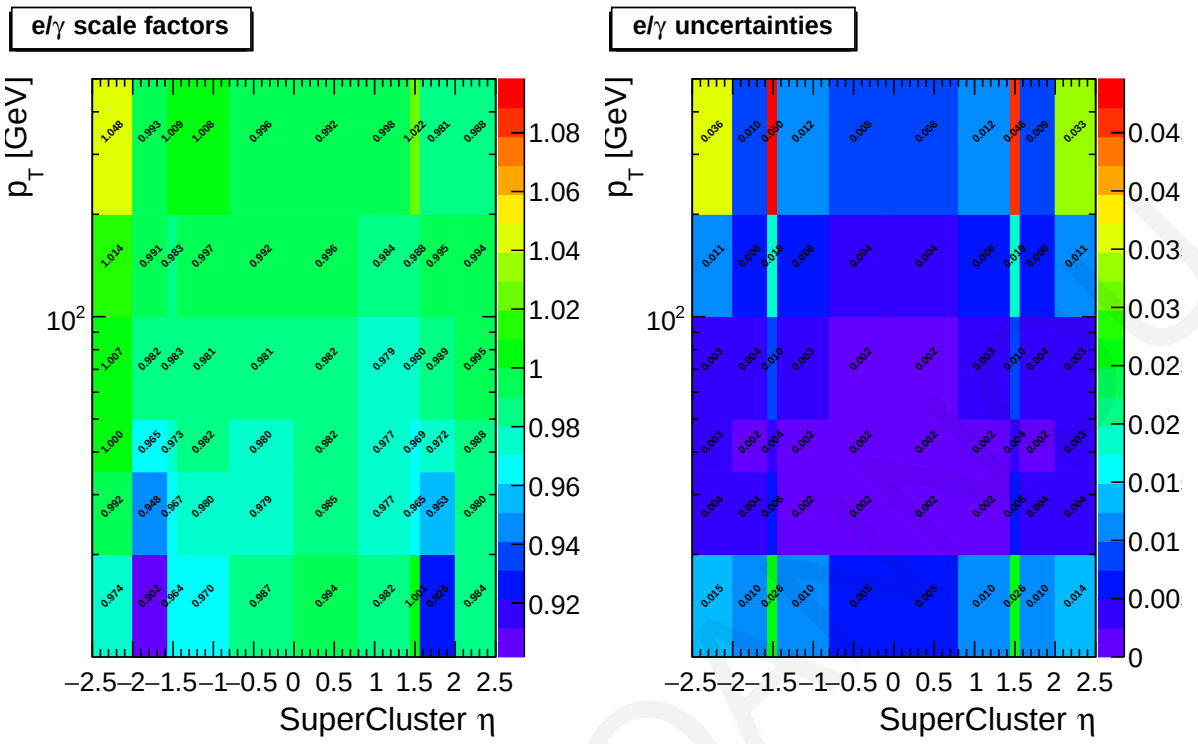

Figure 5.25: Scale factors and their uncertainties for trigger path HLT_Ele32_WPTight_Gsf.

		$p_T \in (10,20)$ (GeV)	$p_T \in (20,35)$ (GeV)	$p_T \in (35,50)$ (GeV)	$p_T \in (50,100)$ (GeV)	$p_T \in (100,200)$ (GeV)	$p_T \in (200,500)$ (GeV)
$\eta \in (-2.5,-2.0)$	ϵ_{data}	0.721 ± 0.004	0.838 ± 0.001	0.887 ± 0.001	0.922 ± 0.001	0.957 ± 0.004	0.985 ± 0.011
	ϵ_{MC}	0.740 ± 0.006	0.845 ± 0.002	0.887 ± 0.001	0.916 ± 0.002	0.944 ± 0.010	0.940 ± 0.034
	SF	0.974 ± 0.015	0.992 ± 0.004	1.000 ± 0.003	1.007 ± 0.003	1.014 ± 0.011	1.048 ± 0.036
$\eta \in (-2.0,-1.566)$	ϵ_{data}	0.697 ± 0.003	0.817 ± 0.001	0.875 ± 0.001	0.916 ± 0.001	0.956 ± 0.003	0.985 ± 0.007
	ϵ_{MC}	0.773 ± 0.005	0.862 ± 0.001	0.907 ± 0.001	0.933 ± 0.001	0.965 ± 0.005	0.992 ± 0.008
	SF	0.902 ± 0.010	0.948 ± 0.004	0.965 ± 0.002	0.982 ± 0.004	0.991 ± 0.006	0.993 ± 0.010
$\eta \in (-1.566,-1.444)$	ϵ_{data}	0.702 ± 0.007	0.792 ± 0.002	0.839 ± 0.001	0.877 ± 0.002	0.935 ± 0.009	0.943 ± 0.024
	ϵ_{MC}	0.728 ± 0.014	0.819 ± 0.004	0.862 ± 0.002	0.892 ± 0.004	0.951 ± 0.014	0.935 ± 0.044
	SF	0.964 ± 0.026	0.967 ± 0.006	0.973 ± 0.004	0.983 ± 0.010	0.983 ± 0.018	1.009 ± 0.050
$\eta \in (-1.444,-0.8)$	ϵ_{data}	0.735 ± 0.002	0.821 ± 0.001	0.857 ± 0.001	0.885 ± 0.001	0.943 ± 0.002	0.968 ± 0.005
	ϵ_{MC}	0.758 ± 0.004	0.838 ± 0.001	0.873 ± 0.001	0.902 ± 0.001	0.946 ± 0.004	0.960 ± 0.010
	SF	0.970 ± 0.010	0.980 ± 0.002	0.982 ± 0.002	0.981 ± 0.003	0.997 ± 0.006	1.008 ± 0.012
$\eta \in (-0.8,0.0)$	ϵ_{data}	0.824 ± 0.001	0.851 ± 0.001	0.882 ± 0.001	0.907 ± 0.001	0.953 ± 0.002	0.972 ± 0.004
	ϵ_{MC}	0.835 ± 0.003	0.869 ± 0.001	0.900 ± 0.001	0.925 ± 0.001	0.961 ± 0.003	0.976 ± 0.006
	SF	0.987 ± 0.005	0.979 ± 0.002	0.980 ± 0.002	0.981 ± 0.002	0.992 ± 0.004	0.996 ± 0.008
$\eta \in (0.0,0.8)$	ϵ_{data}	0.828 ± 0.002	0.855 ± 0.001	0.884 ± 0.001	0.909 ± 0.001	0.957 ± 0.001	0.964 ± 0.004
	ϵ_{MC}	0.833 ± 0.003	0.868 ± 0.001	0.900 ± 0.001	0.926 ± 0.001	0.961 ± 0.003	0.972 ± 0.007
	SF	0.994 ± 0.005	0.985 ± 0.002	0.982 ± 0.002	0.982 ± 0.002	0.996 ± 0.004	0.992 ± 0.008
$\eta \in (0.8,1.444)$	ϵ_{data}	0.743 ± 0.002	0.820 ± 0.001	0.858 ± 0.001	0.886 ± 0.001	0.942 ± 0.002	0.962 ± 0.005
	ϵ_{MC}	0.757 ± 0.004	0.839 ± 0.001	0.878 ± 0.001	0.905 ± 0.001	0.957 ± 0.004	0.964 ± 0.010
	SF	0.982 ± 0.010	0.977 ± 0.002	0.977 ± 0.002	0.979 ± 0.003	0.984 ± 0.006	0.998 ± 0.012
$\eta \in (1.444,1.566)$	ϵ_{data}	0.714 ± 0.008	0.780 ± 0.002	0.834 ± 0.001	0.867 ± 0.002	0.929 ± 0.009	0.987 ± 0.009
	ϵ_{MC}	0.713 ± 0.014	0.808 ± 0.004	0.861 ± 0.002	0.885 ± 0.004	0.940 ± 0.016	0.966 ± 0.034
	SF	1.001 ± 0.026	0.965 ± 0.006	0.969 ± 0.004	0.980 ± 0.010	0.988 ± 0.019	1.022 ± 0.046
$\eta \in (1.566,2.0)$	ϵ_{data}	0.709 ± 0.003	0.824 ± 0.001	0.883 ± 0.001	0.922 ± 0.001	0.967 ± 0.003	0.981 ± 0.007
	ϵ_{MC}	0.766 ± 0.005	0.865 ± 0.001	0.908 ± 0.001	0.932 ± 0.001	0.972 ± 0.005	1.000 ± 0.001
	SF	0.926 ± 0.010	0.953 ± 0.004	0.972 ± 0.002	0.989 ± 0.004	0.995 ± 0.006	0.981 ± 0.009
$\eta \in (2.0,2.5)$	ϵ_{data}	0.743 ± 0.003	0.847 ± 0.001	0.891 ± 0.001	0.923 ± 0.001	0.955 ± 0.004	0.969 ± 0.013
	ϵ_{MC}	0.755 ± 0.005	0.864 ± 0.001	0.902 ± 0.001	0.928 ± 0.002	0.961 ± 0.008	0.981 ± 0.019
	SF	0.984 ± 0.014	0.980 ± 0.004	0.988 ± 0.003	0.995 ± 0.003	0.994 ± 0.011	0.988 ± 0.033

Table 5.7: Single electron trigger efficiencies for data and Monte Carlo together with scale factors for trigger path HLT_Ele105_CaloIdVT_GsfTrkIdT.

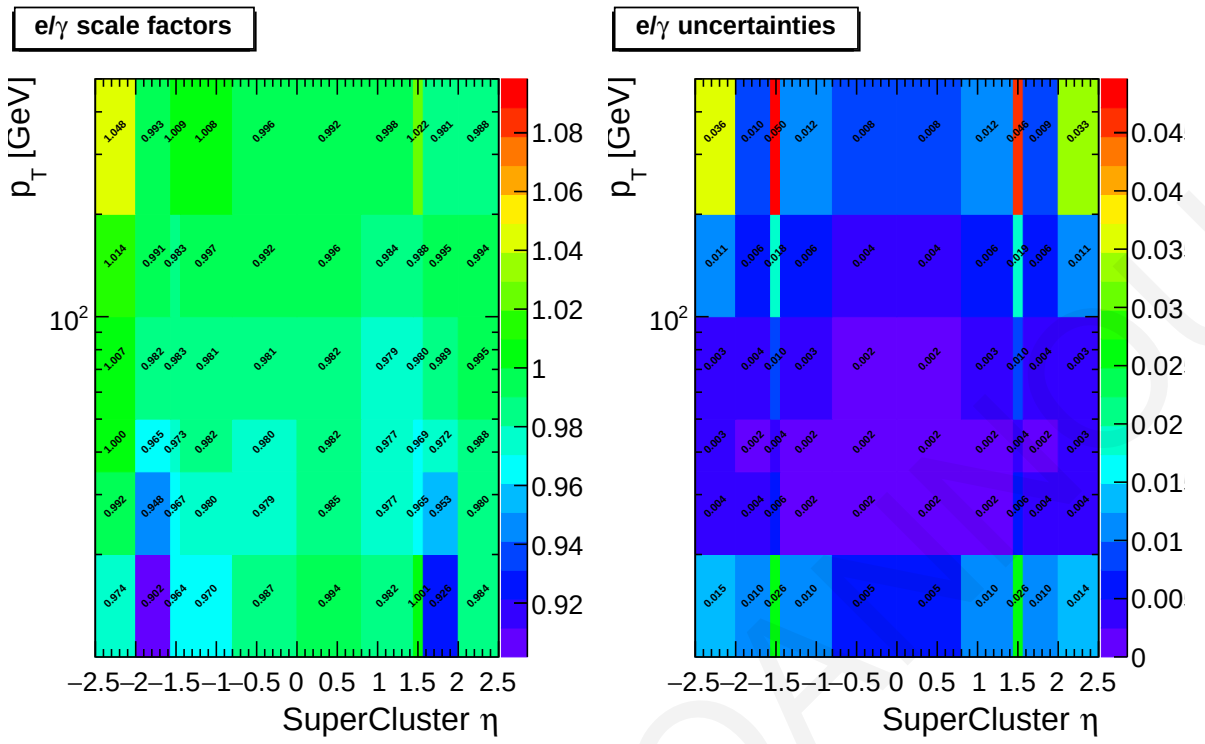

Figure 5.26: Scale factors and their uncertainties for trigger path HLT_Ele105_CaloIdVT_GsfTrkIdT.

is defined by calculating the events in which electrons candidates satisfy the selection criteria and the specific trigger path by the number of events which pass only the selection criteria:

$$Efficiency = \frac{N_{S+T}}{N_S} \tag{5.10}$$

where N_{S+T} is referred to events where electron candidates have passed the selection criteria and the trigger path; N_S corresponds to events where electrons have passed the selections without cut on the trigger.

In the case of the single electron trigger path HLT_Ele27_WPTight_Gsf, electron candidates have to satisfy the selection criteria which are summarized in Table 5.9 and in the case of the double electron trigger (HLT_Ele23_Ele12_CaloIdL_TrackIdL_IsoVL_DZ) the selection criteria are shown in Table 5.10.

The suggestions of criteria on electron candidates for single and double electron triggers are obtained from HLTPOG [91]. The efficiencies for single and double triggers are calculated for each mass point separately and they are presented in Fig. 5.28 and Fig. 5.29.

Fig. 5.28 and Fig. 5.29 show efficiencies of single and double electron triggers as a function of transverse momentum (p_T) of leading electrons. A significant difference between the two types of triggers is

		$p_T \in (10,20)$ (GeV)	$p_T \in (20,35)$ (GeV)	$p_T \in (35,50)$ (GeV)	$p_T \in (50,100)$ (GeV)	$p_T \in (100,200)$ (GeV)	$p_T \in (200,500)$ (GeV)
$\eta \in (-2.5,-2.0)$	ϵ_{data}	0.721 ± 0.004	0.838 ± 0.001	0.887 ± 0.001	0.922 ± 0.001	0.957 ± 0.004	0.985 ± 0.011
	ϵ_{MC}	0.740 ± 0.006	0.845 ± 0.002	0.887 ± 0.001	0.916 ± 0.002	0.944 ± 0.010	0.940 ± 0.034
	SF	0.974 ± 0.015	0.992 ± 0.004	1.000 ± 0.003	1.007 ± 0.003	1.014 ± 0.011	1.048 ± 0.036
$\eta \in (-2.0,-1.566)$	ϵ_{data}	0.697 ± 0.003	0.817 ± 0.001	0.875 ± 0.001	0.916 ± 0.001	0.956 ± 0.003	0.985 ± 0.007
	ϵ_{MC}	0.773 ± 0.005	0.862 ± 0.001	0.907 ± 0.001	0.933 ± 0.001	0.965 ± 0.005	0.992 ± 0.008
	SF	0.902 ± 0.010	0.948 ± 0.004	0.965 ± 0.002	0.982 ± 0.004	0.991 ± 0.006	0.993 ± 0.010
$\eta \in (-1.566,-1.444)$	ϵ_{data}	0.702 ± 0.007	0.792 ± 0.002	0.839 ± 0.001	0.877 ± 0.002	0.935 ± 0.009	0.943 ± 0.024
	ϵ_{MC}	0.728 ± 0.014	0.819 ± 0.004	0.862 ± 0.002	0.892 ± 0.004	0.951 ± 0.014	0.935 ± 0.044
	SF	0.964 ± 0.026	0.967 ± 0.006	0.973 ± 0.004	0.983 ± 0.010	0.983 ± 0.018	1.009 ± 0.050
$\eta \in (-1.444,-0.8)$	ϵ_{data}	0.735 ± 0.002	0.821 ± 0.001	0.857 ± 0.001	0.885 ± 0.001	0.943 ± 0.002	0.968 ± 0.005
	ϵ_{MC}	0.758 ± 0.004	0.838 ± 0.001	0.873 ± 0.001	0.902 ± 0.001	0.946 ± 0.004	0.960 ± 0.010
	SF	0.970 ± 0.010	0.980 ± 0.002	0.982 ± 0.002	0.981 ± 0.003	0.997 ± 0.006	1.008 ± 0.012
$\eta \in (-0.8,0.0)$	ϵ_{data}	0.824 ± 0.001	0.851 ± 0.001	0.882 ± 0.001	0.907 ± 0.001	0.953 ± 0.002	0.972 ± 0.004
	ϵ_{MC}	0.835 ± 0.003	0.869 ± 0.001	0.900 ± 0.001	0.925 ± 0.001	0.961 ± 0.003	0.976 ± 0.006
	SF	0.987 ± 0.005	0.979 ± 0.002	0.980 ± 0.002	0.981 ± 0.002	0.992 ± 0.004	0.996 ± 0.008
$\eta \in (0.0,0.8)$	ϵ_{data}	0.828 ± 0.002	0.855 ± 0.001	0.884 ± 0.001	0.909 ± 0.001	0.957 ± 0.001	0.964 ± 0.004
	ϵ_{MC}	0.833 ± 0.003	0.868 ± 0.001	0.900 ± 0.001	0.926 ± 0.001	0.961 ± 0.003	0.972 ± 0.007
	SF	0.994 ± 0.005	0.985 ± 0.002	0.982 ± 0.002	0.982 ± 0.002	0.996 ± 0.004	0.992 ± 0.008
$\eta \in (0.8,1.444)$	ϵ_{data}	0.743 ± 0.002	0.820 ± 0.001	0.858 ± 0.001	0.886 ± 0.001	0.942 ± 0.002	0.962 ± 0.005
	ϵ_{MC}	0.757 ± 0.004	0.839 ± 0.001	0.878 ± 0.001	0.905 ± 0.001	0.957 ± 0.004	0.964 ± 0.010
	SF	0.982 ± 0.010	0.977 ± 0.002	0.977 ± 0.002	0.979 ± 0.003	0.984 ± 0.006	0.998 ± 0.012
$\eta \in (1.444,1.566)$	ϵ_{data}	0.714 ± 0.008	0.780 ± 0.002	0.834 ± 0.001	0.867 ± 0.002	0.929 ± 0.009	0.987 ± 0.009
	ϵ_{MC}	0.713 ± 0.014	0.808 ± 0.004	0.861 ± 0.002	0.885 ± 0.004	0.940 ± 0.016	0.966 ± 0.034
	SF	1.001 ± 0.026	0.965 ± 0.006	0.969 ± 0.004	0.980 ± 0.010	0.988 ± 0.019	1.022 ± 0.046
$\eta \in (1.566,2.0)$	ϵ_{data}	0.709 ± 0.003	0.824 ± 0.001	0.883 ± 0.001	0.922 ± 0.001	0.967 ± 0.003	0.981 ± 0.007
	ϵ_{MC}	0.766 ± 0.005	0.865 ± 0.001	0.908 ± 0.001	0.932 ± 0.001	0.972 ± 0.005	1.000 ± 0.001
	SF	0.926 ± 0.010	0.953 ± 0.004	0.972 ± 0.002	0.989 ± 0.004	0.995 ± 0.006	0.981 ± 0.009
$\eta \in (2.0,2.5)$	ϵ_{data}	0.743 ± 0.003	0.847 ± 0.001	0.891 ± 0.001	0.923 ± 0.001	0.955 ± 0.004	0.969 ± 0.013
	ϵ_{MC}	0.755 ± 0.005	0.864 ± 0.001	0.902 ± 0.001	0.928 ± 0.002	0.961 ± 0.008	0.981 ± 0.019
	SF	0.984 ± 0.014	0.980 ± 0.004	0.988 ± 0.003	0.995 ± 0.003	0.994 ± 0.011	0.988 ± 0.033

Table 5.8: Single electron trigger efficiencies for data and Monte Carlo together with scale factors for trigger path HLT_Ele115_CaloIdVT_GsfTrkIdT.

BARREL CUTS		ENDCAP CUTS	
Electron P_T	>20 GeV	Electron P_T	> 20 GeV
full5x5_sigma|eta|eta	<0.00998	full5x5_sigma|eta|eta	<0.0292
|dEtaInSeed|	<0.00308	|dEtaInSeed|	<0.00605
|dPhiIn|	<0.0816	|dPhiIn|	<0.0394
H/E	<0.0414	H/E	<0.0641
Rel. comb. PF iso with EA corr.	<0.0588	Rel. comb. PF iso with EA corr.	<0.0571
|1/E - 1/p|	<0.0129	|1/E - 1/p|	<0.0129
expected missing inner hits	≤1	expected missing inner hits	≤1
pass conversion veto	yes	pass conversion veto	yes
d0 (cm)	<0.05	d0 (cm)	<0.05
dz (cm)	<0.10	dz (cm)	<0.20

Table 5.9: Selection criteria on electron candidates in the case of the single electron trigger [90].

noticeable. The efficiency of single electron trigger is absolutely better than the efficiency of the double trigger. It seems clearly that the single electron trigger is functioning better than the double trigger. Taking into account the results of efficiency's studies, the single electron trigger is used in the analysis due to a better efficiency as illustrated in the figures.

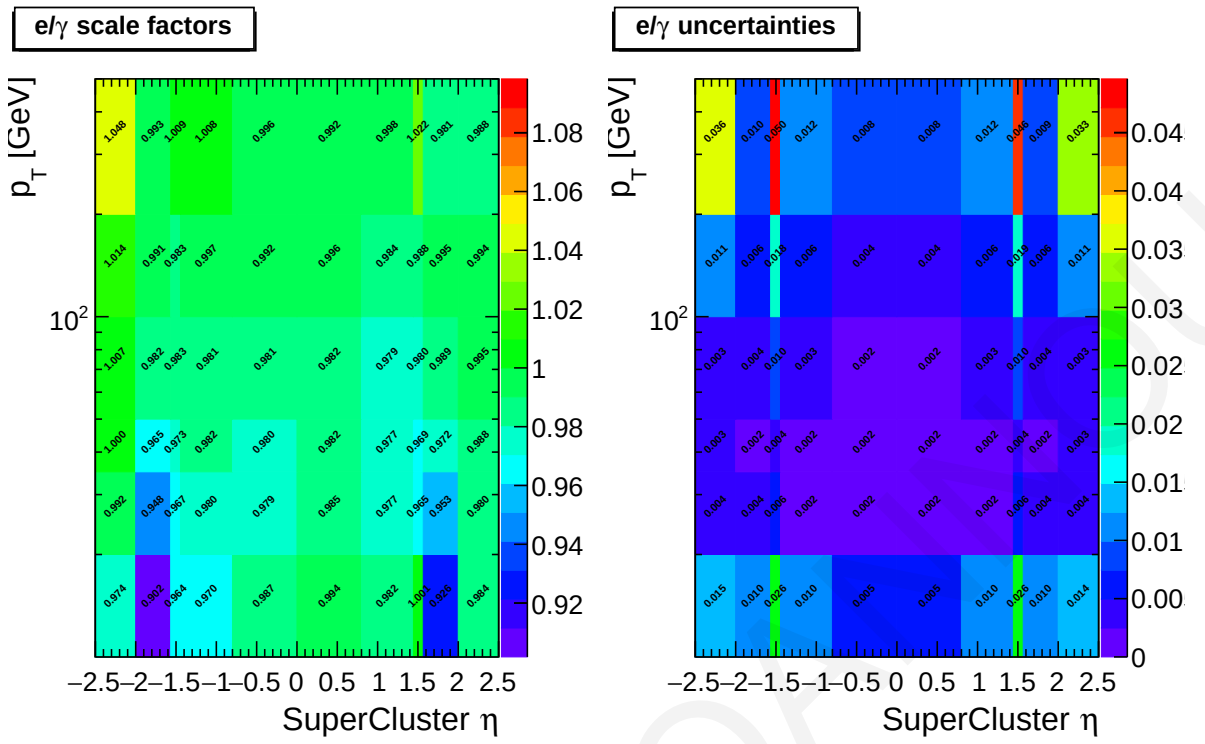

Figure 5.27: Scale factors and their uncertainties for trigger path HLT_Ele115_CaloIdVT_GsfTrkIdT.

BARREL CUTS		ENDCAP CUTS	
Electron P_T	>15 GeV	Electron P_T	> 15 GeV
full5x5_sigma|eta|eta	<0.00998	full5x5_sigma|eta|eta	<0.0292
|dEtaInSeed|	<0.00308	|dEtaInSeed|	<0.00605
|dPhiIn|	<0.0816	|dPhiIn|	<0.0394
H/E	<0.0414	H/E	<0.0641
Rel. comb. PF iso with EA corr.	<0.0588	Rel. comb. PF iso with EA corr.	<0.0571
|1/E - 1/p|	<0.0129	|1/E - 1/p|	<0.0129
expected missing inner hits	≤1	expected missing inner hits	≤1
pass conversion veto	yes	pass conversion veto	yes
d0 (cm)	<0.05	d0 (cm)	<0.05
dz (cm)	<0.10	dz (cm)	<0.20

BARREL CUTS		ENDCAP CUTS	
Electron P_T	>5 GeV	Electron P_T	> 5 GeV
full5x5_sigma|eta|eta	<0.011	full5x5_sigma|eta|eta	<0.0314
|dEtaInSeed|	<0.00477	|dEtaInSeed|	<0.00868
|dPhiIn|	<0.222	|dPhiIn|	<0.213
H/E	<0.298	H/E	<0.101
Rel. comb. PF iso with EA corr.	<0.0994	Rel. comb. PF iso with EA corr.	<0.107
|1/E - 1/p|	<0.241	|1/E - 1/p|	<0.14
expected missing inner hits	≤1	expected missing inner hits	≤1
pass conversion veto	yes	pass conversion veto	yes
d0 (cm)	<0.05	d0 (cm)	<0.05
dz (cm)	<0.10	dz (cm)	<0.20

Table 5.10: Selection criteria on leading electron candidates (left) and sub-leading electrons (right) in the case of the double electron trigger [90].

5.2.6.4 MUON TRIGGER

Events with muons are selected with single muon triggers that require no isolation, in order to avoid efficiency losses in case of very boosted $Z \to \mu^+\mu^-$ events, when the two muons are close to each other. In 2016, the non-isolated muon threshold was raised to 50 GeV. The two triggers adopted are listed in Tab. 5.11.

The trigger efficiency is then evaluated studying the lepton efficiency as a function of both p_T and η for both data and MC. The muon trigger scale factors are applied to the simulated events passing the trigger requirements in the analysis to match the trigger efficiency measured in data.

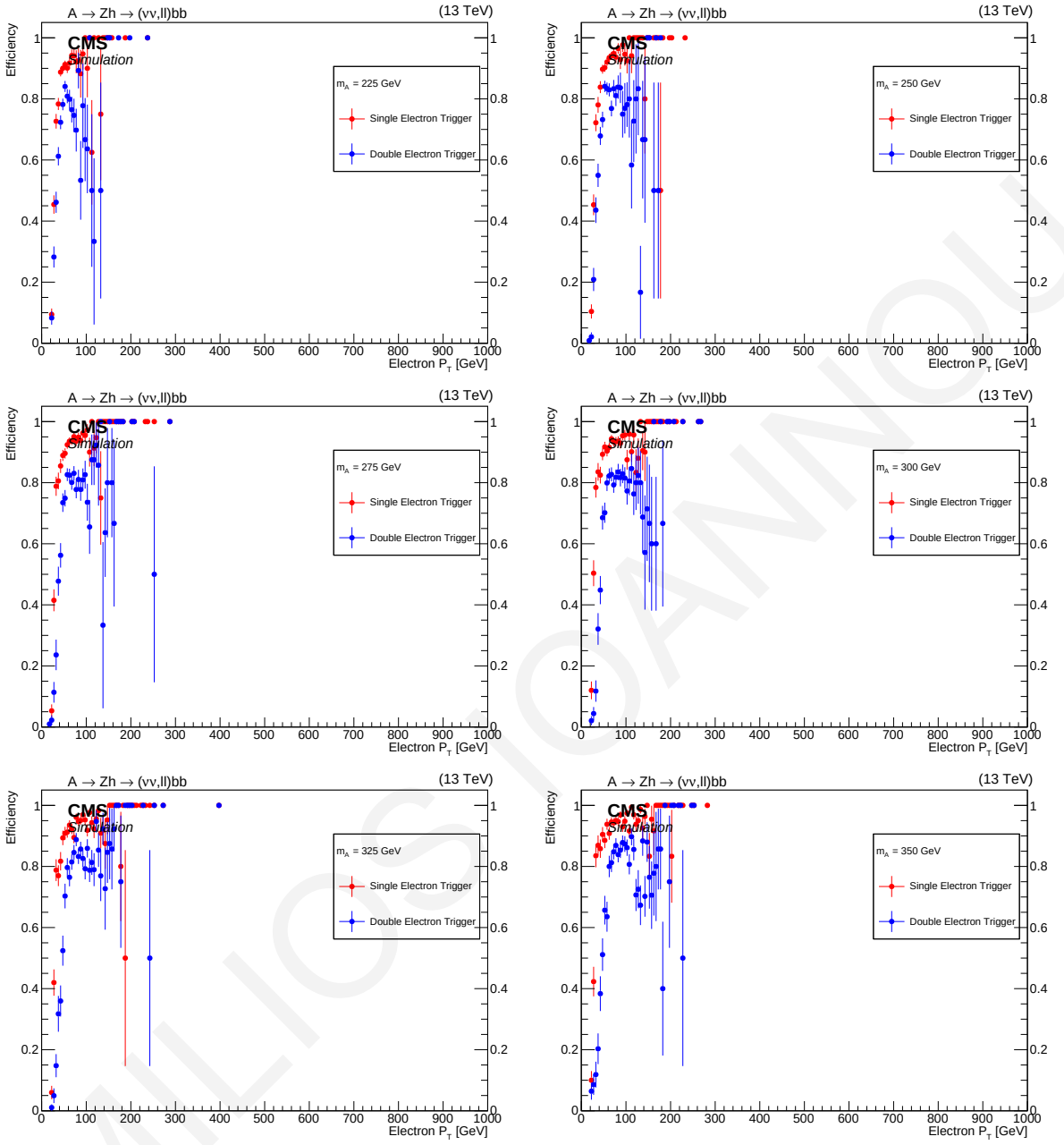

Figure 5.28: Single electron trigger efficiencies comparing double electron trigger efficiencies for mass range of $225 < m_A < 350$ GeV.

The efficiencies of the single muon triggers are provided centrally by the MuonPOG [92] with a tag and probe procedure by selecting $Z \to \ell^+\ell^-$ events. Tight lepton identification requirements [93] are applied to the probes. The trigger efficiency is then evaluated studying the tag lepton efficiency as a function of both p_T and η for both data and MC. The muon trigger efficiency are applied consistently to the simulation throughout the analysis.

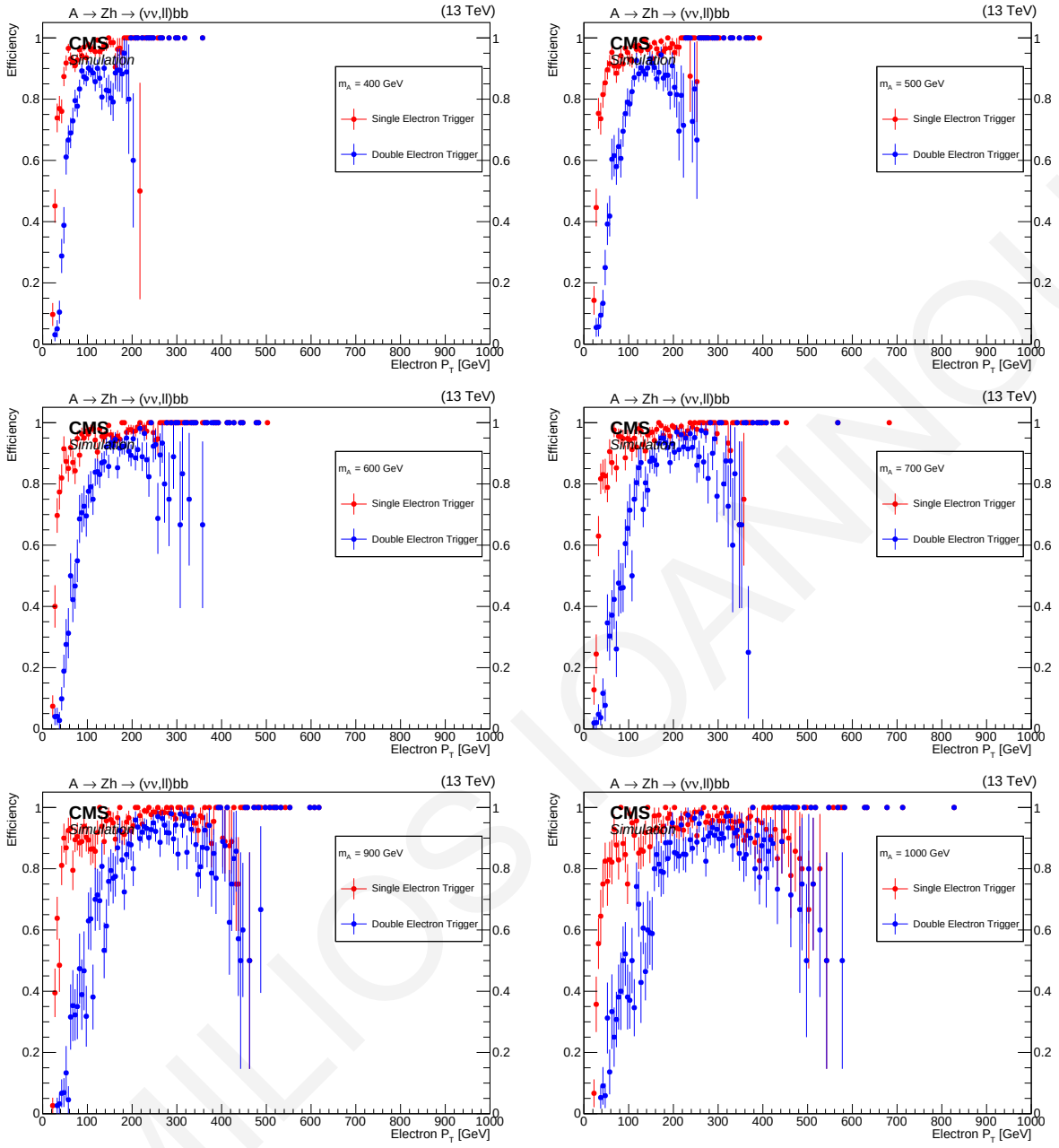

Figure 5.29: Single electron trigger efficiencies comparing double electron trigger efficiencies for the mass range of $400 < m_A < 1000$ GeV.

5.2.6.5 MISSING ENERGY TRIGGER

The $\not{E}_T$ triggers are the logic OR of different trigger quantities, with thresholds on both the MET and the missing transverse hadronic energy ($MHT = |-\sum_i^{jets} \vec{p}_{T,i}|$) computed using particle flow objects [94]. These HLT triggers are all seeded at L1 by *L1_ETM_50*, *L1_ETM_60*, *L1_ETM_70* which are the lowest unprescaled L1_trigger common to all the HLT $\not{E}_T$ paths. The list of triggers used is reported in

HLT paths	L1_seeds
HLT_IsoMu24 HLT_IsoTkMu24	L1_SingleMu22
HLT_IsoMu27 HLT_IsoTkMu27	L1_SingleMu22 OR L1_SingleMu25

Table 5.11: Single muon HLT trigger paths used in the analysis.

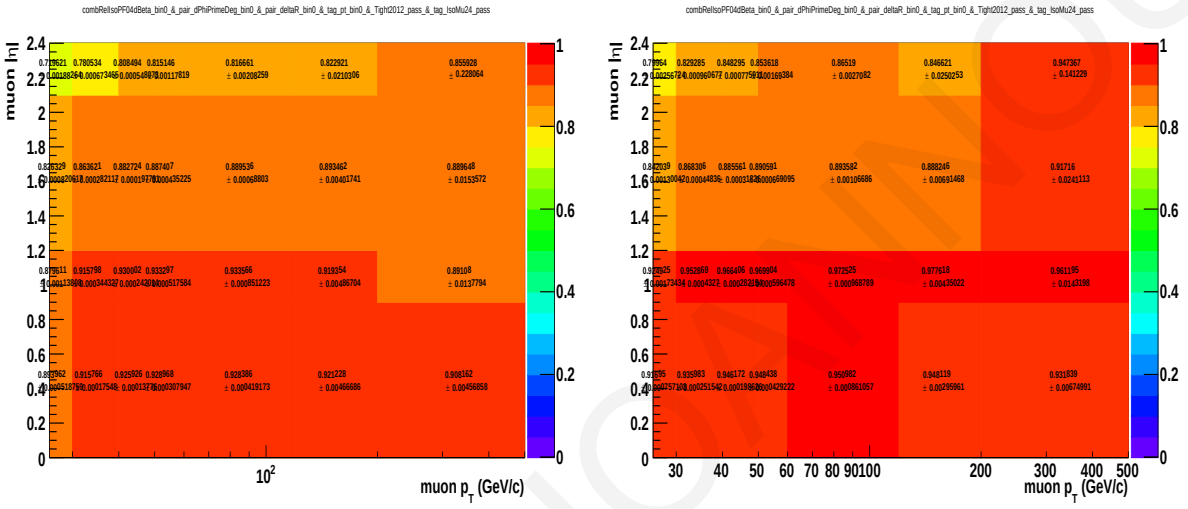

Figure 5.30: HLT_Mu24 OR HLT_TkMu24 efficiencies on data (left) and MC (right) as a function of the η and p_T of the muon. The efficiency is extracted with the tag and probe method, and provided by the Muon POG.

Tab. 5.12.

HLT paths	L1_seeds
HLT_PFMETNoMu90_PFMHTNoMu90_IDTight	
HLT_PFMETNoMu110_PFMHTNoMu110_IDTight	L1_ETM70
HLT_PFMETNoMu120_PFMHTNoMu120_IDTight	OR
HLT_PFMETNoMu90_JetIdCleaned_PFMHTNoMu90_IDTight	L1_DoubleJetC56_ETM60
HLT_PFMETNoMu120_JetIdCleaned_PFMHTNoMu120_IDTight	OR
HLT_PFMET110_PFMHT110_IDTight	L1_ETM50
HLT_PFMET120_PFMHT120_IDTight	
HLT_PFMET170_NoiseCleaned	L1_ETM60
HLT_PFMET170_HBHECleaned	OR
HLT_PFMET170_HBHE_BeamHaloCleaned	L1_ETM70

Table 5.12: Missing energy HLT trigger paths used in the analysis.

The efficiency of the $\not\!\!E_T$ triggers is measured selecting $W \to e\nu_e$ events in the SingleElectron primary dataset, on events that trigger the `HLT_Ele27_WPTight_Gsf_v*` OR `HLT_Ele32_WPTight_Gsf_v*`

path. These events have to have exactly one electron with $p_T > 30$ GeV, lying in the central region $|\eta| < 2.1$, passing tight identification and isolation requirements, and with a minimum separation in the azimuthal angle $\Delta\phi(e, \not{E}_T) > 0.5$. These events represent the denominator, and the numerator events are also required to fire at least one of the $\not{E}_T$ HLT trigger paths. Due to the different quantities considered at HLT level, the turn-on curve for the $\not{E}_T$ triggers (shown in Fig. 5.31) are calculated as a function of the minimum of the offline reconstructed missing transverse momentum ($\not{E}_T$), the $\not{E}_T$ after the subtraction of the muon momentum, and the hadronic missing transverse momentum ($\not{H}_T$). At the threshold value of 200 GeV, the trigger OR is 98% efficient in the SingleElectron dataset, and 99.8% efficient in the SingleMuon. The difference between the two values, a conservative 2% is considered as systematic uncertainty. The values from the SingleElectron dataset are used to reweight the MC depending on the minimum between the offline MET and MHT.

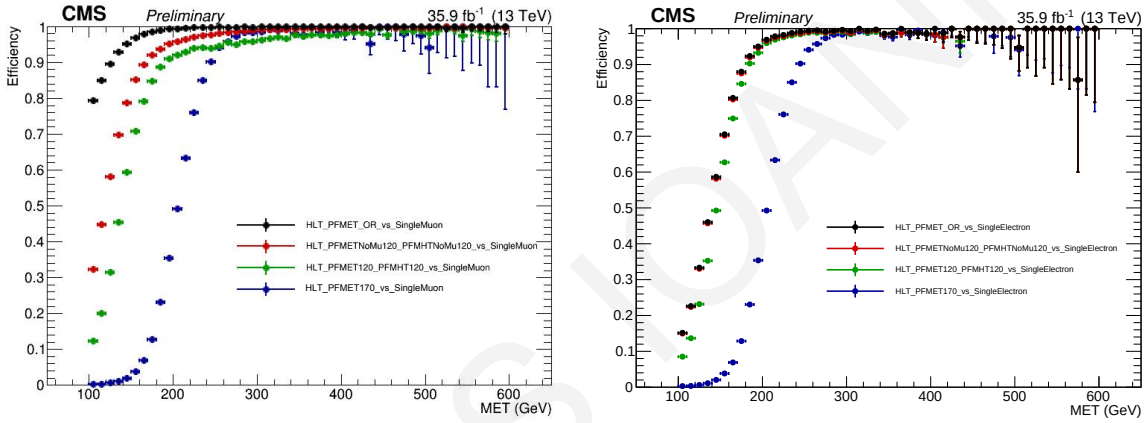

Figure 5.31: Trigger efficiency for the OR of the HLT_PFMETNoMu*_PFMHTNoMu*_IDTight, HLT_PFMET*_PFMHT*_IDTight, and HLT_PFMET170_* HLT paths as function of the minimum value between the offline reconstructed MET and MHT. The efficiencies are calculated from the SingleElectron (right) and SingleMuon (left) primary dataset.

5.3 PHYSICS OBJECTS

In this section, a list of the physics objects used in the analysis is presented, with performance and validation plots. The physics objects are selected according to the standard Run-II recommendations as described in Appendix B.2. Please note that the plots that follow in the next Chapters are referred to as CM Preliminary plots. Although, all the data collected in 2016, were analysed. This notation was kept until the corresponding publication was submitted to The European Physics Journal C.

5.3.1 PRIMARY VERTEX AND PILE-UP

Due to pile-up, several primary vertices are typically reconstructed in an event. The primary vertex of the events is chosen as the one with the highest sum of the p_T^2 of the associated clustered particles, identified leptons, and missing transverse momentum [95]. It has to fulfill the following conditions:

- number of associated tracks > 0
- number of degrees of freedom n_{dof}> 4
- vertex position along the beam pipe $|z_{vtx}| < 24$ cm
- vertex distance with respect to the beam pipe d_0 < 2 cm

where z_{vtx} and d_0 are the distance along and perpendicular to the beam line of the vertex with respect to the nominal interaction point (0, 0, 0).

The data sample contains a significant number of additional interactions per bunch crossing, an effect known as pileup (PU). Nevertheless, the MC PU description does not match exactly the conditions in data. Therefore, there is the need to reweigh the simulated events in order to improve the agreement with the data.

The MC samples are reweighted using the standard CMS PU reweighting technique [96, 97], assuming a total inelastic cross section of $\sigma_{in} = 69200\ \mu b$. The pileup distribution is shown in Fig. 5.32. The comparison between the distributions of primary vertices in data and MC after the PU reweighting is applied is shown in Fig. 5.33 after analysis preselections.

The comparison between the distributions of primary vertices in data and MC after the PU reweigting is applied is shown in Fig. 5.33 for two different event selections. A poor data/MC agreement is obvious after reweighting due to the strip tracker dynamic inefficiency related to the saturation effects in the pre-amplifier of the APV chip [98].

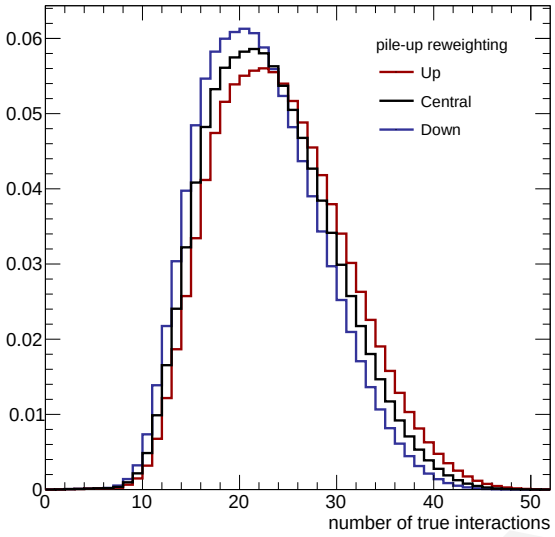

Figure 5.32: Pile-up distribution estimated form data assuming a total inelastic cross section of $\sigma_{in} = 69\,200\mu b$. The red and blue lines correspond to $\pm 5\%$ variation of the cross section value. The plot is referred to the number of true interaction in data samples.

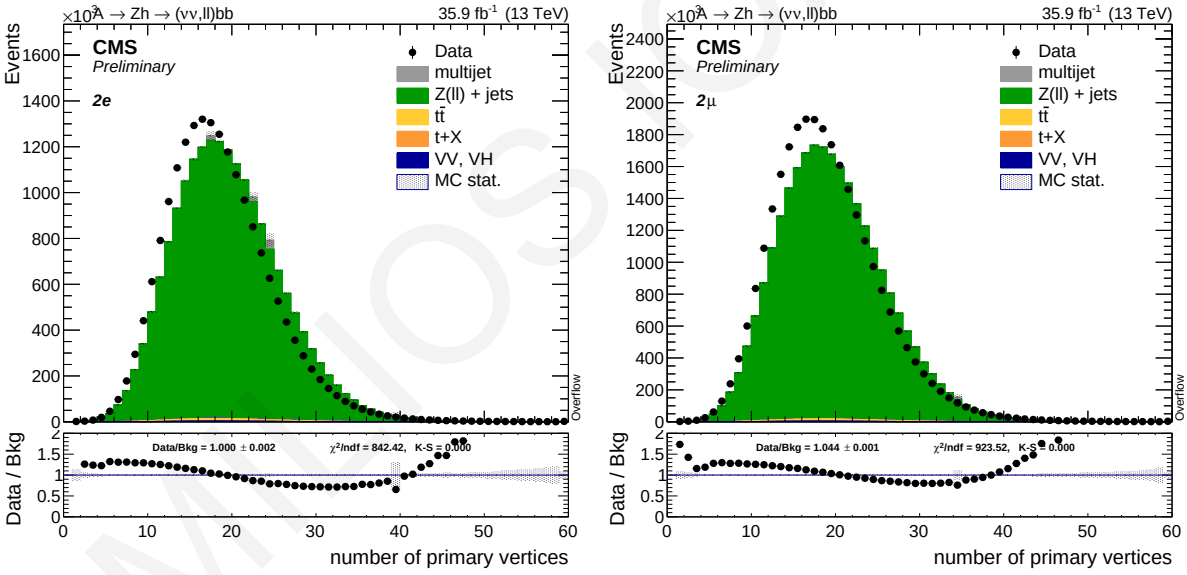

Figure 5.33: Primary vertices distributions after reweighting with the official recipe and $\sigma_{in} = 69\,200\mu b$, in the $2e$ (left) and 2μ selection (right). The poor data/simulation agreement is due to the dynamical tracker inefficiencies in part of the data taking period. $K - S$ corresponds to Kolmogorov-Smirnov test as described in Appendix A.1.5.

Fig. 5.34 shows the primary vertices distribution after reweighting in the 0ℓ selection. The data/simulation agreement is worse than the $2e$ and 2μ selections, due to the peculiarity of Z decays into a pair of neutrinos which cannot be recorded by any CMS subsystem as well as due to the tracker inefficiencies too.

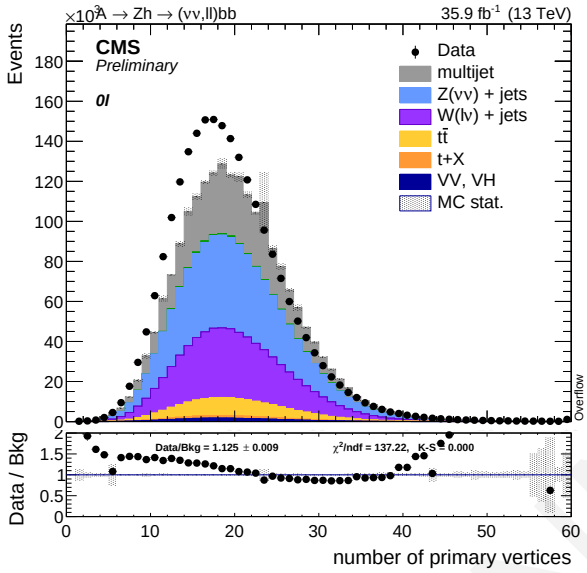

Figure 5.34: Primary vertices distribution after reweighting with the official recipe and $\sigma_{in} = 69\,200\mu b$, in the 0ℓ selection. The poor data/simulation agreement is due to the dynamical tracker inefficiencies in part of the data taking period and due to non-detection of neutrinos.

5.3.2 ELECTRONS

Electrons are reconstructed from energy deposits in the ECAL matched to tracks reconstructed in the silicon tracker, as well described in Chapter B.2.2.3. The electron trajectories are reconstructed using a dedicated modeling of the electron energy loss and fitted with a Gaussian Sum Filter (GSF) [99]. Electrons used in this analysis are required to pass the Particle Flow criteria, and to fall in the ECAL pseudorapidity fiducial range ($|\eta| < 2.5$).

The electron identification used in this analysis is based on the "cut-based" Id defined by [90]. Isolation cuts are already applied within the cut-based Id definitions, therefore no additional Isolation cut is required. In the isolation definition the effect of PU is considered by taking into account the energy deposits in the calorimeter, estimated through the so-called $\rho - area$ method, by subtracting the median energy density in the event ρ multiplied by electron effective area. The isolation value is computed in a ΔR cone of 0.3 centred along the lepton direction.

In this analysis, two different electron cut-based Ids are considered: *loose* and *tight* Ids. The detailed set of cuts are reported in Tab. 5.13.

$\Delta\eta_{in}^{seed}$ and $\Delta\phi_{in}$ are the difference in η and ϕ between the track position as measured in the inner layer, extrapolated to the interaction vertex and then extrapolated to the calorimeter and the η of the seed cluster or the ϕ of the supercluster, H/E is the ratio of the hadronic energy of the CaloTowers in a cone of radius 0.15 centred on the electron's position in the calorimeter to the electromagnetic energy of

Electrons		*loose*		*tight*	
		EB	EE	EB	EE
$\sigma_{i\eta i\eta}$	$<$	0.011	0.0314	0.00998	0.0292
$\Delta\eta_{in}^{seed}$	$<$	0.00477	0.00868	0.00308	0.00605
$\Delta\varphi_{in}$	$<$	0.222	0.213	0.0816	0.0394
H/E	$<$	0.298	0.101	0.0414	0.0641
relIso (EA)	$<$	0.0994	0.107	0.0588	0.0571
$1/E - 1/p$	$<$	0.241	0.14	0.0129	0.0129
missing hits	$\leq$	1	1	1	1
conversion veto		yes	yes	yes	yes
$\lvert d_0\rvert$	$<$	0.05	0.10	0.05	0.10
$\lvert d_z\rvert$	$<$	0.10	0.20	0.10	0.20

Table 5.13: Spring16 cut-based selection for 80X releases [90]. EB: barrel cuts ($|\eta_{\text{supercluster}}| \leq 1.479$); EE: endcap cuts ($|\eta_{\text{supercluster}}| > 1.479$)

the electron's supercluster, σ_{inin} is the spread in η in units of crystals of the electrons' energy in a 5×5 block of crystals centred on the seed crystal, and $1/E - 1/p$ is the difference of the inverse of the energy and the momentum. The relative isolation is defined as the ratio of the p_T sum of all charged and neutral particle-flow candidates (excluding other PF electrons and muons) in the event within a cone of a radius of $\Delta R = 0.3$ centred along the electron direction. Corrections in order to reduce the PU contamination are also applied, using the effective area method. Electrons in the current analysis are identified with the standard cut-based identification methods, and the *loose* or *tight* working points. The former is also used to count and identify electrons in all the leptonic categories.

Scale factors for the electron reconstruction, identification, isolation are derived by the EGammaPOG [90] through the tag-and-probe method on the $Z \rightarrow e^+e^-$ mass peak for all the working points separately, as a function of the p_T and η of the electrons, and are applied consistently in the analysis to account for the small data/simulation difference in the efficiencies of these selections.

Validation of the electron object is performed with an inclusive $Z \rightarrow e^+e^-$ selection, for events passing the electron triggers, and the leading (sub-leading) electron passing the *loose* Id, and a p_T threshold of 30 GeV (10 GeV).

The data/simulation comparison, after the application of all scale factors, is shown in Figures 5.35-5.37. Overall, a very good data/simulation agreement for the reconstructed Z mass is noticeable in Fig. 5.37. Furthermore, in Fig. 5.38, the best data/simulation agreement for the invariant mass of Z is when the Z invariant mass is reconstructed by two "barrel" electrons and the worst agreement when the leading and sub-leading electrons are detected in the endcap regions. As it is widely known, the electrons recorded by ECAL detectors located in the barrel region can be fully reconstructed due to the full deposit of their energy in the crystals. In the endcap region, preshower detector is positioned in front of EE and a full

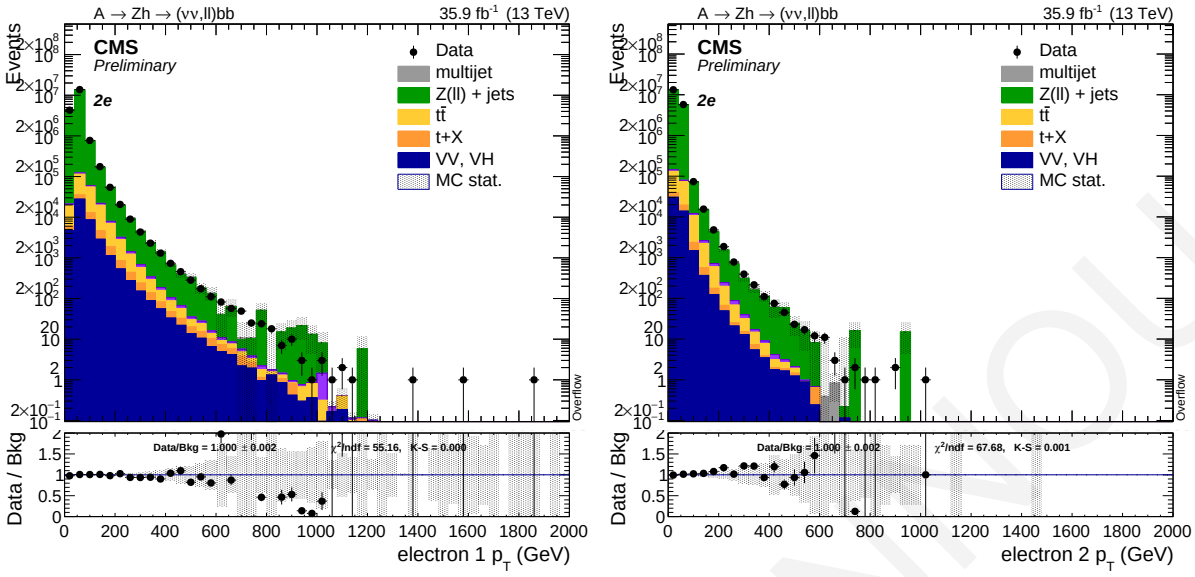

Figure 5.35: Leading (left) and sub-leading (right) electron p_T spectra after $Z \to e^+e^-$ pre-selections.

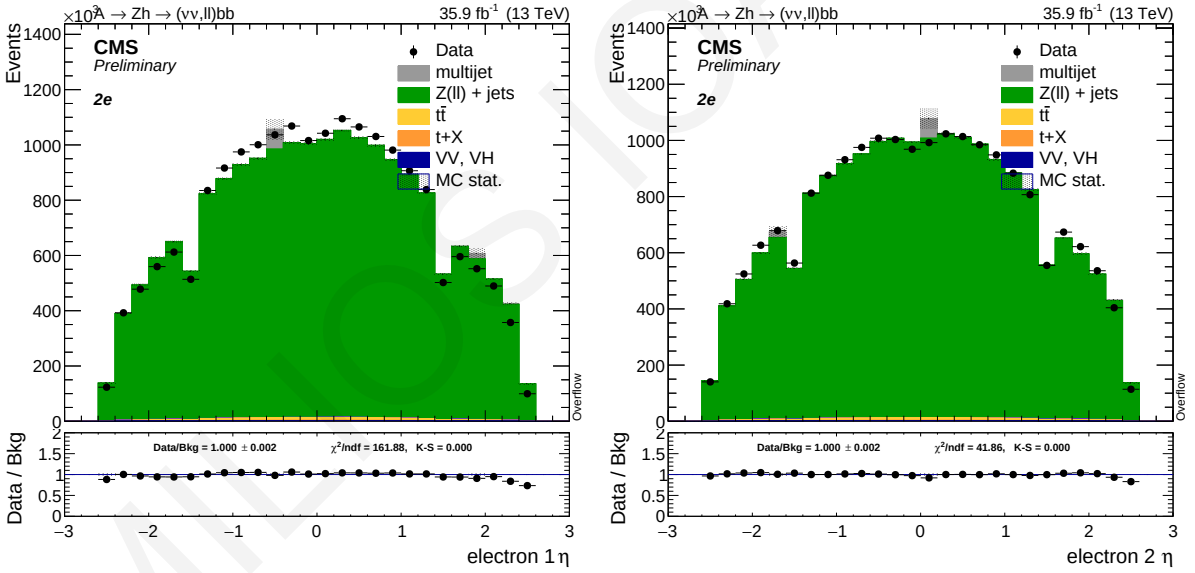

Figure 5.36: Leading (left) and sub-leading (right) electron η distribution after $Z \to e^+e^-$ pre-selections.

reconstruction of electron particle is not achievable due to its energy loss.

5.3.3 MUONS

Muons used in the present analysis are based on the *Particle Flow Muon* selection as described in Chapter B.2.2.4, considering Global Muon or a Tracker Muon candidates and by applying minimal

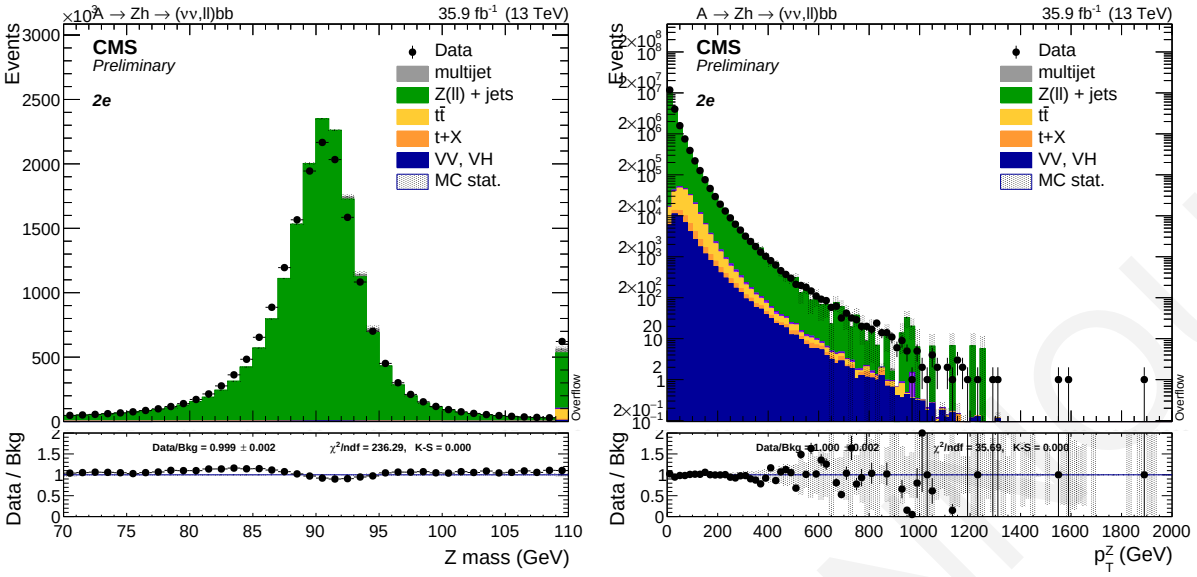

Figure 5.37: Reconstructed Z mass (left) and Z p_T (right) after the $Z \to e^+e^-$ pre-selections.

requirements on the track components in the muon system and taking into account a matching with small energy deposits in the calorimeters. In order to further increase purity, additional cuts are applied, matching the *Tight* identification working point defined by MuonPOG [93]. The list of quantity cuts are listed below. Scale factors, provided by the MuonPOG are applied as a function of the p_T and η of the muons to cope with the residual differences between data and simulation [92]. Tab. 5.14 lists the muon id criteria which are applied for selecting proper muon objects in the two-lepton channels:

Id criterion	Loose	Tight
isGlobalMuon	yes	yes
isPFMuon	yes	yes
normalizedChi2	-	< 10
numberOfValidMuonHits	-	> 0
numberOfMatchedStations	-	> 1
numberOfValidPixelHits	-	> 0
trackedLayersWithMeasurement	-	> 5
d_{xy}	-	<0.2
d_z	-	<0.5

Table 5.14: Muon Id criteria used in the analysis for two-lepton channels.

On the other hand, in the zero-lepton channel, different Id cuts are applied in order to have an effective veto (muons with p_T as low as 10 GeV are vetoed), a standard loose id is applied in this case:

- isPFMuon
- to be or Tracker or Global

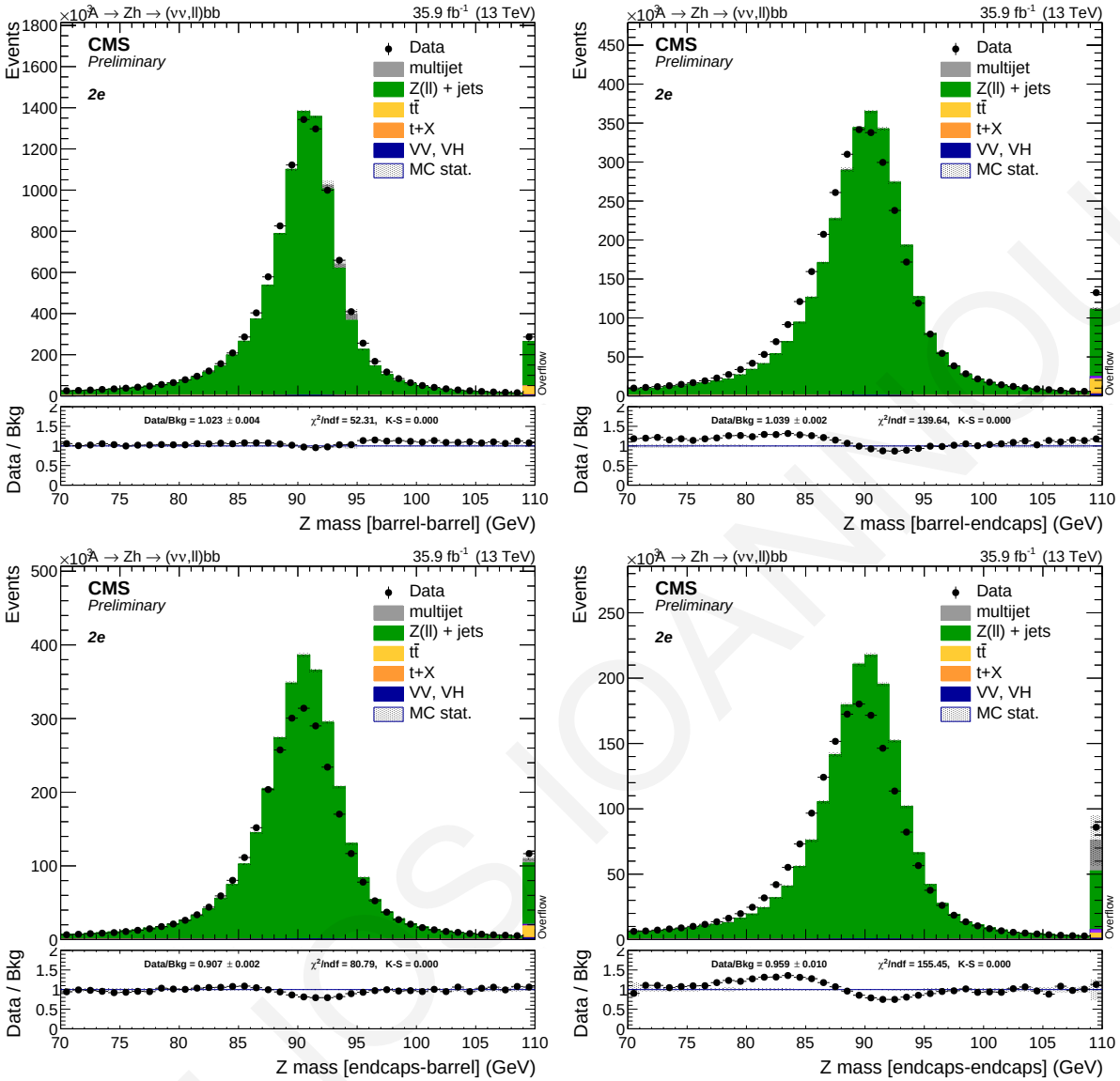

Figure 5.38: Reconstructed Z mass in different electron η regions after the inclusive $Z \to e^+e^-$ selections. Top left: both electrons in the barrel. Top right: leading electron in the barrel, subleading electron in the endcaps. Bottom left: leding electron in the endcaps, subleading electron in the barrel. Bottom right: both electrons in the endcaps.

For muons reconstructed using the PF algorithm, the standard muon isolation is defined as the ratio of the p_T sum of all charged and neutral particle-flow candidates in the event within a cone with a radius of $\Delta R = 0.4$ centred along the lepton direction. Corrections in order to reduce the PU contamination are also applied, using the $\delta\beta$ method [100]. This variable is defined by:

$$\delta\beta - Iso^{\mu^i} = \sum_{\Delta R(i,j)<0.4}^{CH-LV} p_T^i + max(0, \sum_{\Delta R(i,j)<0.4}^{NH} p_T^j + \sum_{\Delta R(i,j)<0.4}^{PH} p_T^j - \frac{1}{2}\sum_{\Delta R(i,j)<0.4}^{CH-PU} p_T^j) \quad (5.11)$$

where each sum runs over the particles with $\Delta R < 0.4$ of the muon, p_T^i is the transverse momentum of each surrounding particle, CH-LV and CH-PU are charged particles associated with leading vertex (LV) and pileup (PU) vertices, respectively, and NH and PH are neutral hadrons and photons reconstructed with the particle-flow algorithm.

Muons with $p_T > 10$ GeV identified with the loose id and passing the loose working point of the PFIsolation (<0.25) are used for muon counting and vetoed in the 0-lepton category.

Figure 5.39 and Figure 5.41 show the data/simulation comparison for the muons after the preselections, consisting of a p_T requirement for the leading (sub-leading) of 30 (10) GeV, tight (loose) Id and loose isolation.

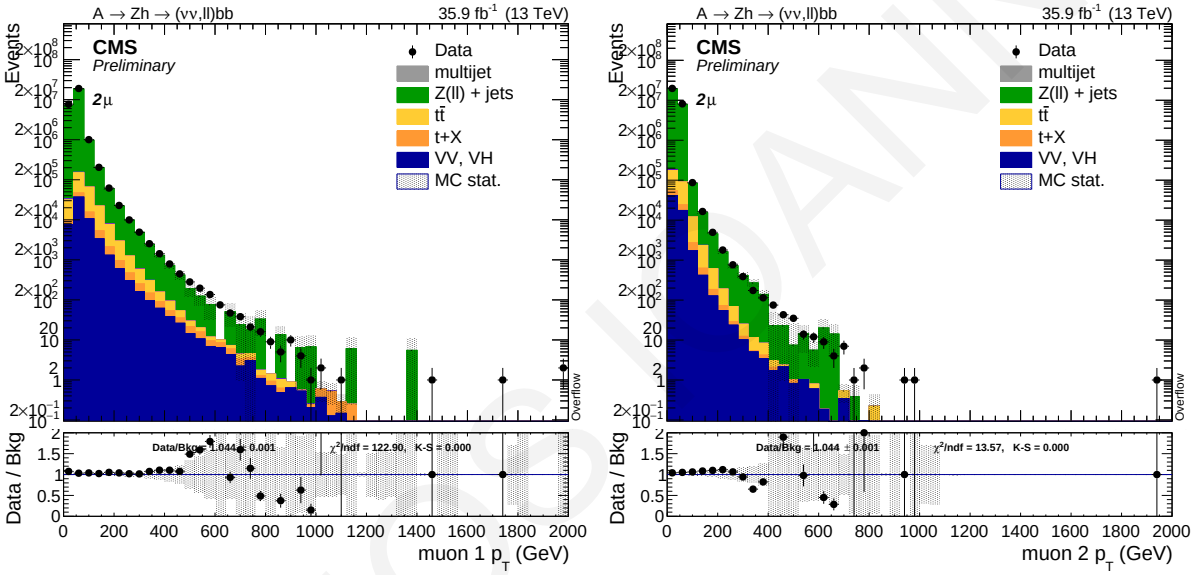

Figure 5.39: Leading (left) and sub-leading (right) muon p_T spectra after Z selections.

Figure 5.42 illustrates the invariant mass of Z boson reconstructed by two muons from different parts of the CMS muon system. Either the muons come from the barrel or the endcap or the combination of them, there is a good data/simulation agreement, and the simulation can well describe the Z boson mass distribution like real data. The Z boson mass can be precisely derived from any muon (barrel or/and endcap muons) with a very good data/simulation agreement due to the powerful Muon System provided by the CMS experiment.

5.3.4 TAUS

The presence of hadronically-decaying taus may be an indication of other electroweak bosons in the events, for instance from $t\bar{t}$ decays. Since hadronic tau decays are not targeted in this analysis, they only

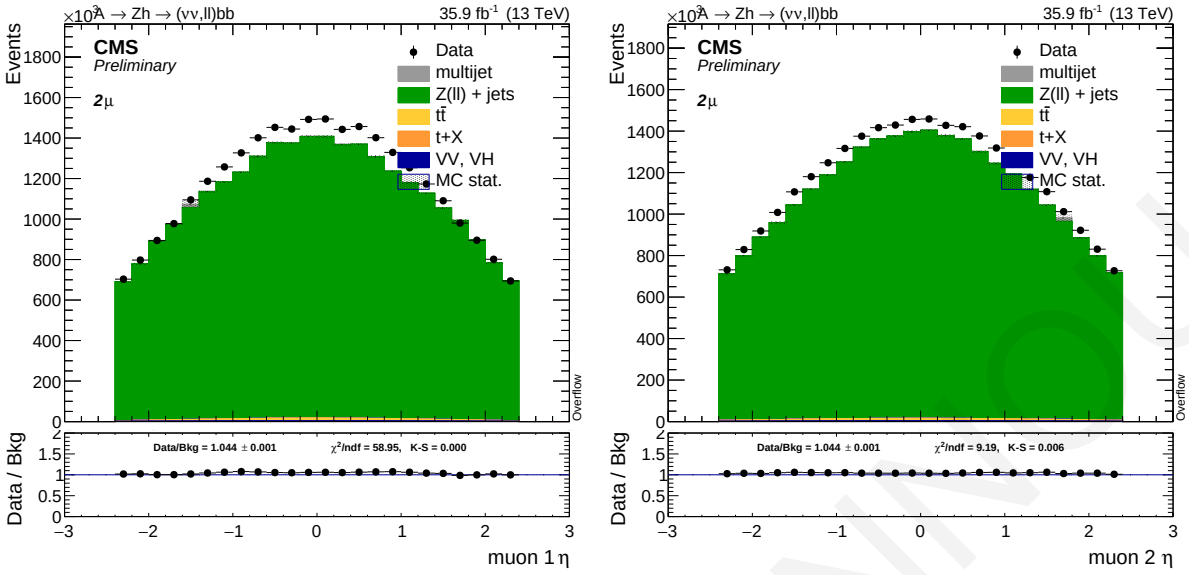

Figure 5.40: Leading (left) and sub-leading (right) muon η after Z selections.

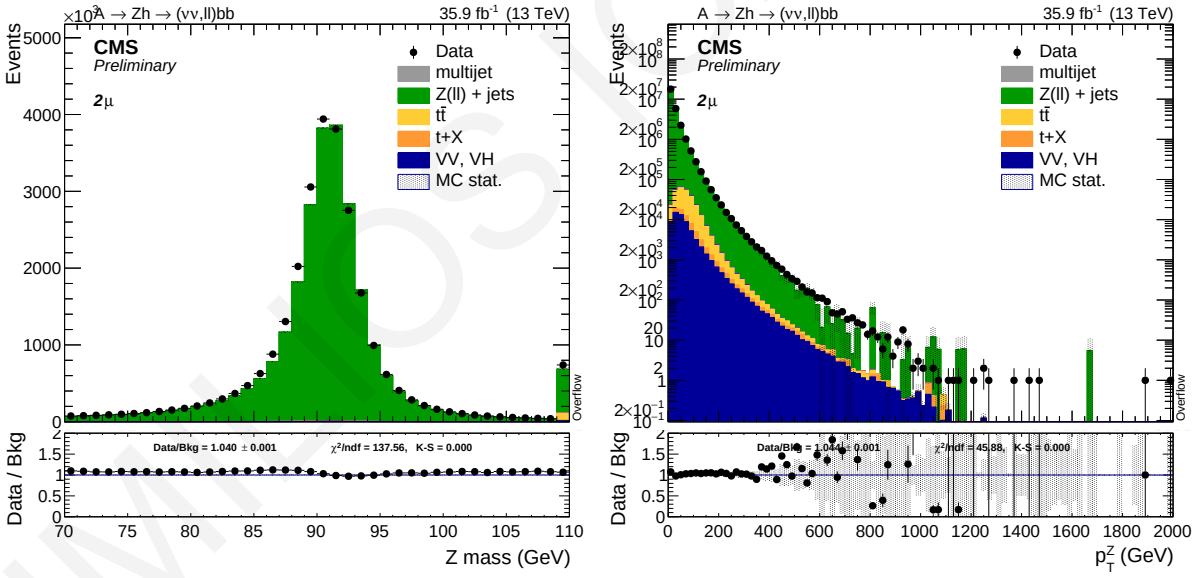

Figure 5.41: Reconstructed Z mass (left) and Z p_T (right) after the inclusive $Z \to \mu^+\mu^-$ selections.

act as veto for the events both in the signal and in the control regions. The selection criteria for taus are $p_T > 18$ GeV and $|\eta| < 2.3$, passing the *byVTightIsolationMVArun2v1PWnewDMwLT* identification [101], and being at least $\Delta R > 0.4$ far from other isolated electrons and muons. The $\tau^{\pm}$ multiplicity is generally well described in simulation for zero-lepton, and two-lepton categories, as shown in Fig. 5.43.

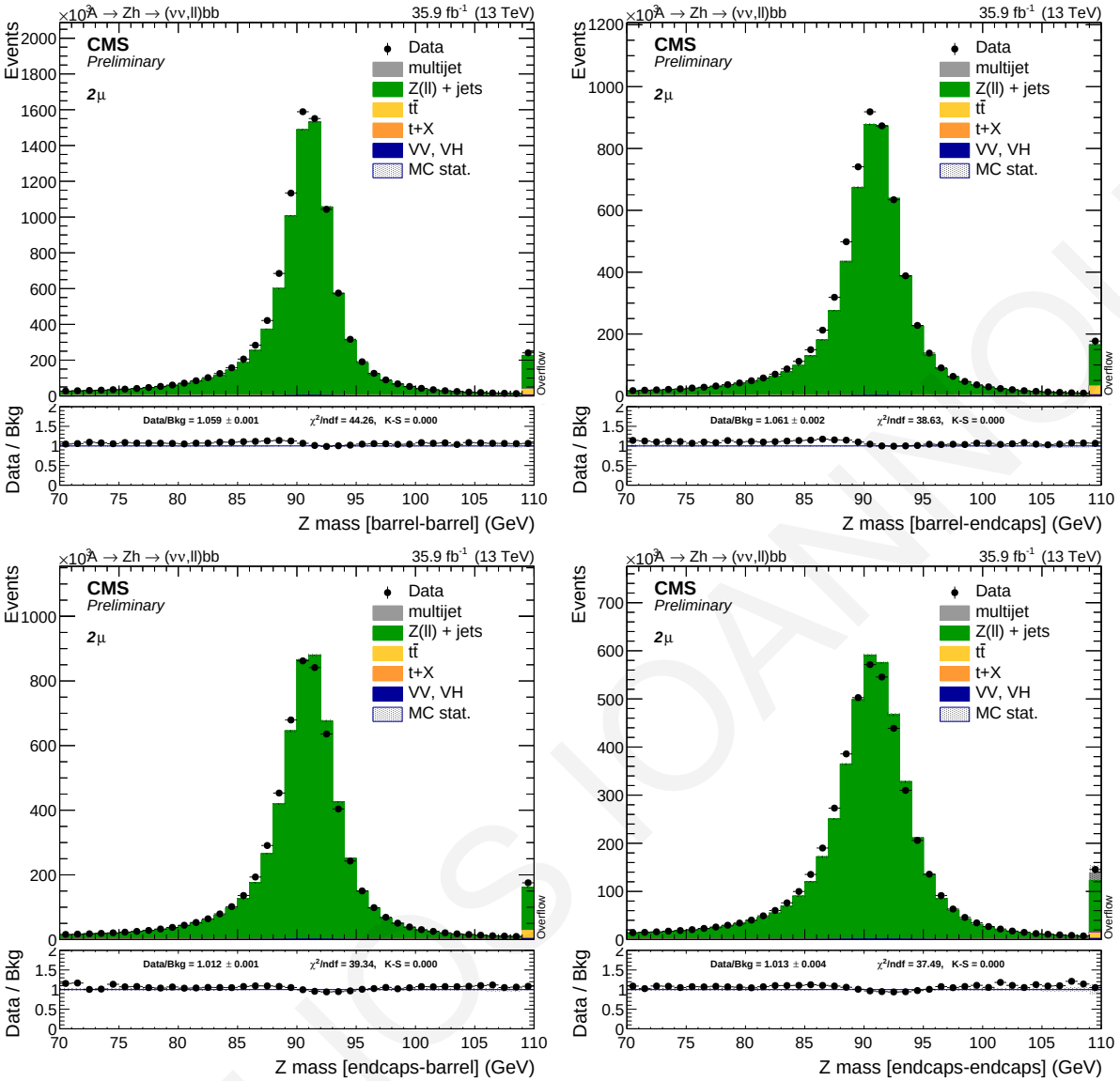

Figure 5.42: Reconstructed Z mass in different muon η regions after the inclusive $Z \to \mu^+\mu^-$ selections. Top left: both muons in the barrel. Top right: leading muon in the barrel, sub-leading muon in the endcaps. Bottom left: leading muon in the endcaps, sub-leading muon in the barrel. Bottom right: both muons in the endcaps.

5.3.5 JETS

Events in the CMS detector are reconstructed using the particle-flow algorithm as described in Appendix B.2.2.6, which combines information from all subdetectors in order to reconstruct stable particles. The charged hadron subtraction algorithm (CHS) removes candidates not associated to the primary vertex in order to remove contributions from pileup [102]. The remaining particles are used as input to jet clustering algorithms to reconstruct particle-flow jets. The jets are clustered using the FASTJET package

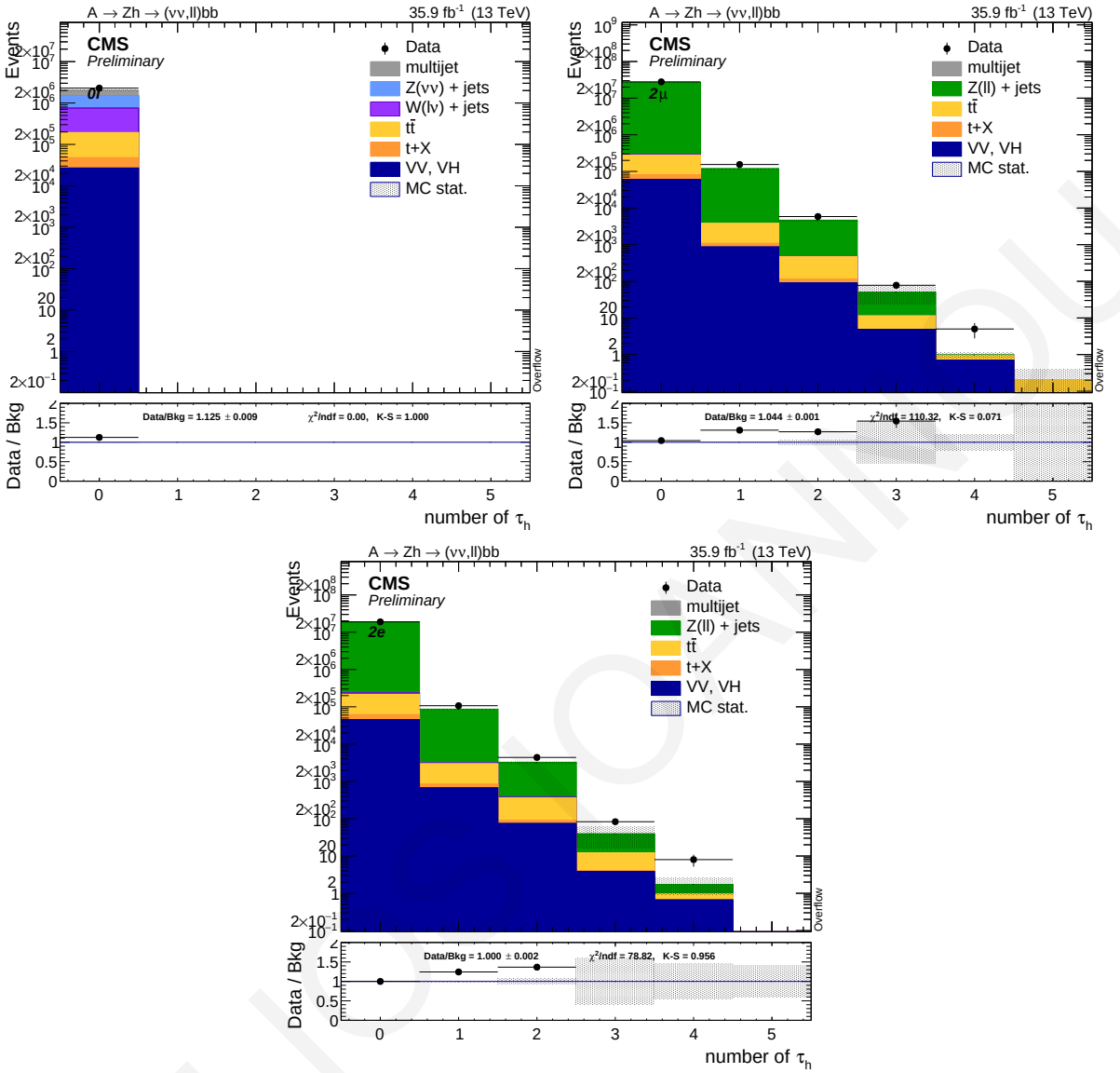

Figure 5.43: The $\tau^{\pm}$ multiplicity for the zero-lepton channel (top left), for the two-muons channel (top right) and for the two-electrons category (bottom centre).

[103] with the anti-k_T jet clustering algorithm, with the clustering parameters $R = 0.4$ (AK4 jets). Several levels of jet energy corrections are applied as reported in Appendix B.2.2.6.

The tags of the jet energy corrections are defined by the latest recommendations of Ref. [104] for data and simulation, respectively. In this analysis, jets are considered with p_T larger than 30 GeV and lie in the tracker acceptance ($|\eta| < 2.4$). Additionally, they are required to pass loose jet identification requirements defined by the JETMET POG for Run-II analyses [105], listed in Tab. 5.15.

The jet energy resolution (JER) measured on data is not the same as in MC. The impact of this difference,

PF Jet ID	*loose*	*tight*
Neutral Hadron Fraction	< 0.99	< 0.90
Neutral EM Fraction	< 0.99	< 0.90
Number of Constituents	> 1	> 1
Muon Fraction	-	-
Additionally, for $\|\eta\| < 2.4$		
Charged Hadron Fraction	> 0	> 0
Charged Multiplicity	> 0	> 0
Charged EM Fraction	< 0.99	< 0.99

Table 5.15: The *loose* and *tight* jet identification requirements for Run2.

and the subsequent systematic uncertainty is evaluated by smearing the jet energy in simulation. This procedure is suggested by the JETMET POG [106], and the smearing coefficients and their errors are reported in Tab. 5.16 for 2016 data. The uncertainties are evaluated by shifting the smearing value by its uncertainty and they are evaluated with respect to the smearing central value. The difference is propagated to the final selection of events and distributions, and it is taken as a systematic uncertainty.

η	0.0 – 0.5	0.5 – 0.8	0.8 – 1.1	1.1 – 1.3	1.3 – 1.7	1.7 – 1.9	1.9 – 2.1	2.1 – 2.3	2.3 – 2.5	2.5 – 2.8	2.8 – 3.0	3.0 – 3.2	3.2 – 5.0
SF	1.109 ± 0.008	1.138 ± 0.013	1.114 ± 0.013	1.123 ± 0.024	1.084 ± 0.011	1.082 ± 0.035	1.140 ± 0.047	1.067 ± 0.053	1.177 ± 0.041	1.364 ± 0.039	1.857 ± 0.071	1.328 ± 0.022	1.160 ± 0.029

Table 5.16: Smearing coefficients and JER uncertainties [106].

5.3.6 B-TAGGING

Several algorithms have been developed to tag jets from b-quarks. One of the best-performing algorithms, used throughout this analysis is the *Combined Secondary Vertex (CSVv2)*, as fully described in Appendix B.2.2.7. Three working points are usually defined for each algorithm, defining cuts in the discriminators based on the level of mis-tagging. The cut values of the CSVv2 and the corresponding mis-tagging for light-flavour jets relative to the CSVv2 algorithm are reported in Tab. 5.17.

Working point	Cut	ε_{light}
Loose	0.5426	$\sim 10\%$
Medium	0.8484	$\sim 1\%$
Tight	0.9535	$\sim 0.1\%$

Table 5.17: CSVv2 official working points.

It is known that b-tagging efficiency is not the same in data and MC. In order to take into account this shortcoming, the BTV POG [107] provides collections of b-tagging scale factors for b-jets and mis-tagged light jets, measured for different physics processes, for the supported tagging algorithms and the

three standard working points [108]. A weight is calculated on a per-event basis as a function of the b-tagging status and the flavour of the hadron that initiated the jet in the event, according to method 1a in Ref. [109].

Furthermore, in the analysis workflow, jets are ordered by decreasing CSV value. The two jets with the highest CSV value are used to reconstruct the Higgs boson candidate. Various combinations of CSV working points are studied for choosing the best reconstructed Higgs boson candidate as shown in the next Chapter 5.4.

5.3.7 MISSING ENERGY

The $\not{E}_T$ is defined as the imbalance in the transverse energy of all visible particles, and it is reconstructed with the particle flow algorithm as described in Appendix B.2.2.5. Particle flow MET with Type-1 corrections applied is currently the default one used by CMS physics analyses. In our analysis study, PF MET Type-1 corrections are also used for chasing an evidence of a heavy pseudoscalar A boson. Figure 5.44 shows the $\not{E}_T$ distribution for data and Monte Carlo after the correction for the three different Z decay categories.

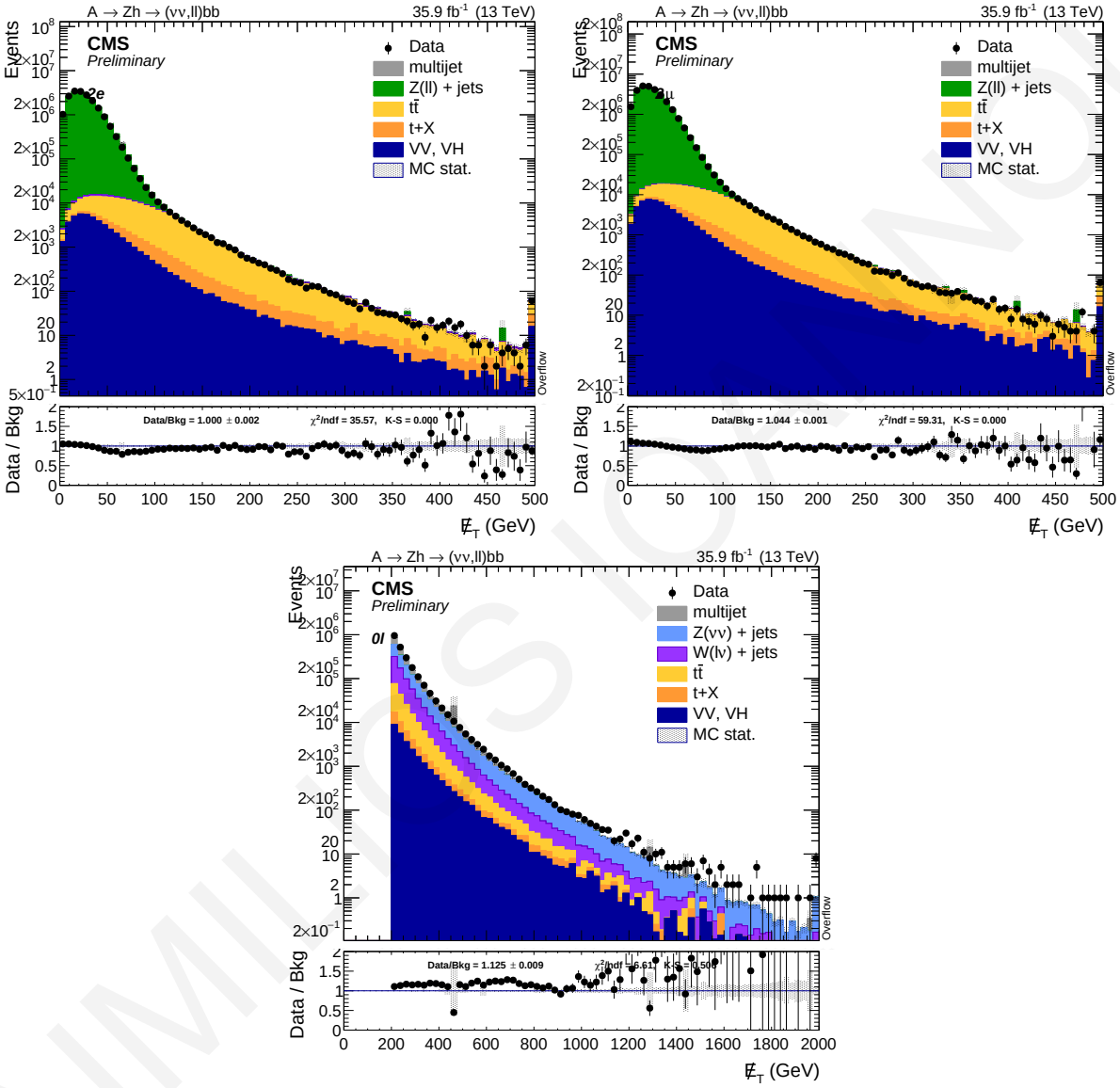

Figure 5.44: Type-1 corrected $\not{E}_T$ in $Z \to e^+e^-$ (top left), $Z \to \mu^+\mu^-$ (top right), and $Z \to \nu\bar{\nu}$ (bottom centre) events.

5.4 OPTIMISATION

In this section a method followed to choose a suitable selection for the CSV working point and for a Higgs mass window, is described. In this analysis workflow the Higgs candidate is reconstructed from the two highest-scoring CSV jets in the event, and the performances of the CSV selection and Higgs mass window are estimated using this association criteria. The fraction of jets initiated by a b-quark coming from the Higgs is shown in Fig. 5.45. Depending on the category, from 80% to 97% of the events have correctly-associated jets. This study performed in order to find out how many b-jets which satisfy the requirement of the medium CSV working point selection as defined in Tab. 5.17, come from the Higgs candidate. It is clear that when we apply 1 b-tag medium requirement, the possibility to have b-jets originated from the Higgs candidate ranges from 80% to 85%. However, when the 2 b-tag medium working point selection is applied, the percentage of the medium CSV b-jets originated from the Higgs candidate is $\sim 97\%$ at least. Consequently, by applying the 2 b-tag medium working point selection, the two b-jets are literally from the Higgs candidate by $95\% \sim 97\%$ as shown in the simulation study.

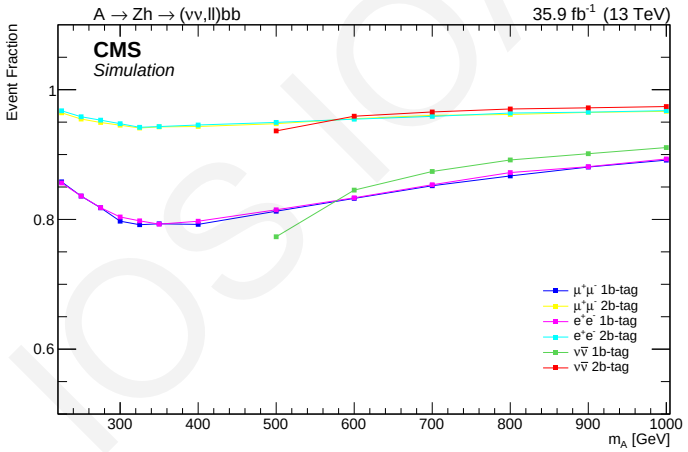

Figure 5.45: Fraction of events with jets correctly associated to reconstruct the Higgs boson.

This method takes advantage of results which are derived from the *Figure Of Merit (FOM)* to determine which selection could improve our signal efficiency. FOM is defined as follows:

$$FOM = \frac{S}{\sqrt{B+1}} \tag{5.12}$$

where S stands for signal events and B corresponds to background events. Equation 5.12 is used to quantise how well background events are rejected from the signal region while maintaining the signal, by calculating the number of signal events divided by the number of background events in the signal area. The signal area is defined as a region where a heavy pseudo-scalar A boson mass candidate could be located. For instance, for signal of $m_A = 300$ GeV, the signal area is the region with a window of

3% around the mass of 300 GeV. It is important to note that a background and signal which are taken into account in the calculation are those which fall into a window with 3% width at a signal region of each A mass point.

5.4.1 CSV WORKING POINT SELECTION

The CSV selection is vital for our analysis because two highest-scoring CSV jets are chosen to reconstruct the SM-like Higgs boson candidate with mass 125 GeV. As mentioned, three possible working point selections (*Loose, Medium, and Tight*) are investigated by calculating the figure of merit of each working point. A selection which increases the FOM for each mass point is considered as the best CSV working point selection and it can remove as much as possible background events from the signal area and at the same time, it does not affect the signal events.

From all the possible scenarios six of them can be chosen to reconstruct the SM-like Higgs boson and are listed in Table 5.18.

Scenario	$Jet_1\ CSV$	$Jet_2\ CSV$
1	Loose	Loose
2	Medium	Loose
3	Medium	Medium
4	Tight	Loose
5	Tight	Medium
6	Tight	Tight

Table 5.18: Six possible scenarios for CSV working point selection.

Their FOM is calculated for each mass point (thirteen mass points) and is shown in Fig. 5.46. The worst CSV working point selection is when the $Jet_1\ CSV$ and $Jet_2\ CSV$ are identified as *Loose*. This selection corresponds to the turquoise line in Fig. 5.46 and as we can see, it has the lowest FOM values. As a consequence, a significant number of interesting events is rejected by this working point selection.

On the other hand, the highest FOM value is given by *Tight and Medium* (blue line in Fig. 5.46) and *Medium and Medium* (green line in Fig. 5.46) working point selections. The differences between of two are negligible, with a slightly better efficiency when the *Tight and Medium* working point is selected, however, the *Medium and Medium* working point selection is chosen to reconstruct the SM-like Higgs boson candidate, avoiding the strictest choice of the CSV selection. In addition, Table 5.19 records the signal and background events that remain in the signal region after implementing the CSV working point selections.

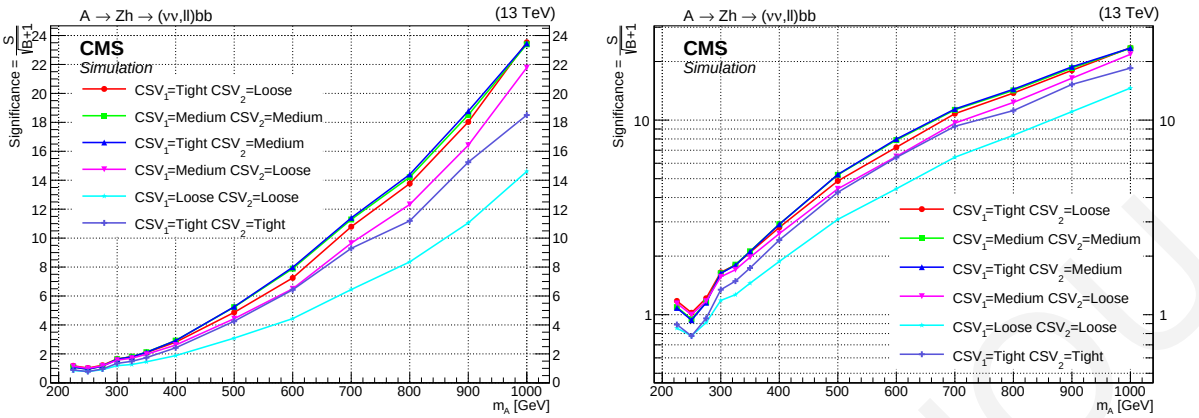

Figure 5.46: Significance plot comparing CSV working point selections for each mass point in linear scale (left) and logarithmic scale (right).

5.4.2 Higgs Mass Window

The Higgs mass window is another crucial variable to our analysis. A proper window has to be determined around the discovered Higgs mass by selecting two b-jets that originate from the Higgs boson candidate. An optimisation of a Higgs mass window is performed on eleven different windows. Higgs mass windows range from the lowest value of 85 GeV and they reach up to 150 GeV divided into eleven regions. The Higgs mass windows are listed in Table 5.20 and their FOM values are presented in Figure 5.47.

Figure 5.47 shows that the FOM values for all Higgs mass windows are roughly similar at the lowest A boson masses. However, at the highest A masses, the $100 < m_h < 140$ GeV window (black line in Fig. 5.47) has the best FOM value. The $100 < m_h < 140$ GeV Higgs mass window is chosen as the most optimal window which removes more background than signal events in the signal region. The remnant of the background and signal events for the various Higgs mass windows, are listed in Table 5.21.

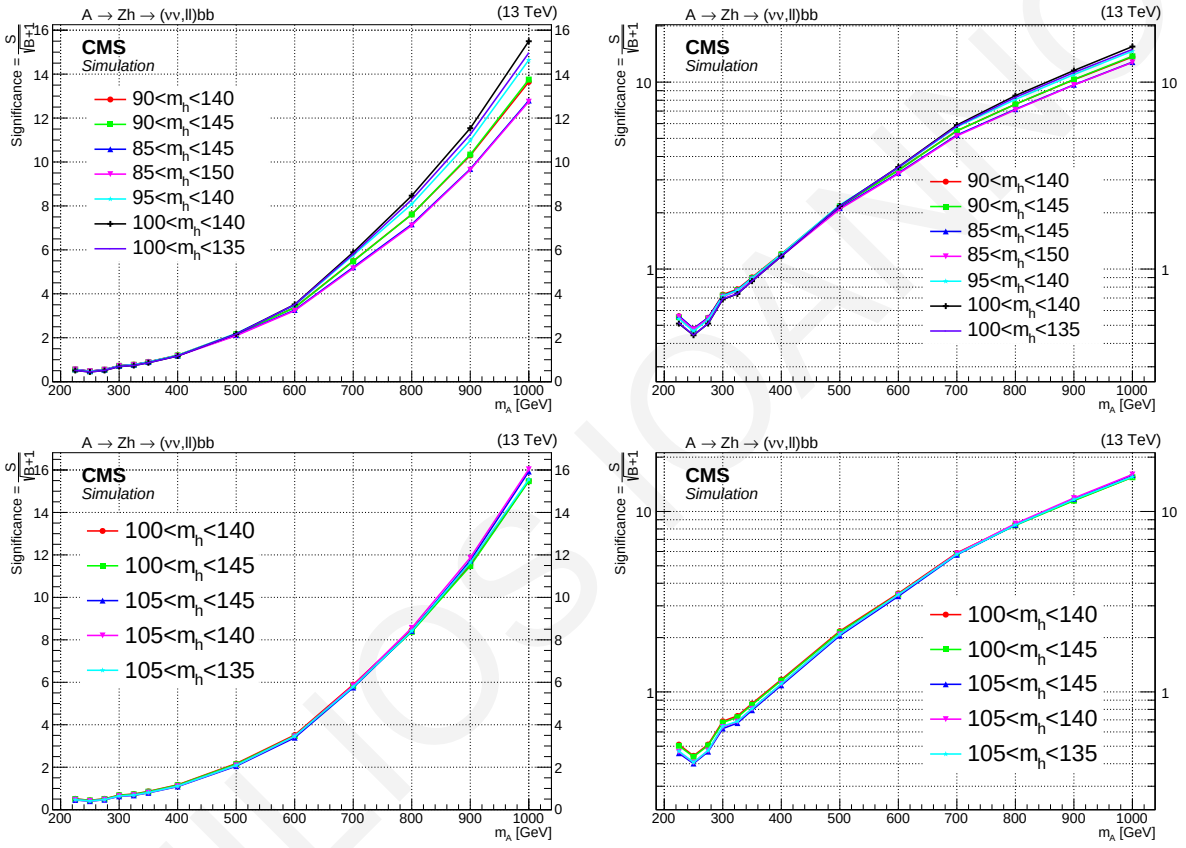

Figure 5.47: FOM plots comparing the different Higgs mass windows for each mass point in linear scale (left) and logarithmic scale (right). The bottom plots show the comparison among the $100 < m_h < 140$ GeV window and other tighter Higgs mass windows.

Mass point (GeV)	Samples	Events					
Working Points		L-L	M-L	M-M	T-L	T-M	T-T
225	Signal	150.10	140.87	85.84	122.30	80.98	50.33
	Background	30967.13	15191.42	6156.37	10791.72	5589.12	3197.36
250	Signal	183.17	170.87	102.36	147.70	96.18	59.95
	Background	55318.95	29184.48	11631.84	20834.97	10541.28	5947.71
275	Signal	198.66	186.03	112.75	160.61	105.96	65.98
	Background	47518.87	25133.91	9436.15	17483.76	8458.97	4749.10
300	Signal	190.86	179.47	111.19	156.10	105.09	64.96
	Background	25986.74	13141.66	4639.83	8935.69	4151.43	2335.35
325	Signal	222.18	208.11	128.16	180.57	120.19	74.27
	Background	30741.23	14949.87	5025.93	10048.14	4482.65	2490.56
350	Signal	237.18	222.59	136.56	192.44	127.98	78.00
	Background	26706.23	12737.09	4157.61	8490.86	3683.11	2014.35
400	Signal	261.72	245.78	151.87	212.82	142.31	86.59
	Background	19418.69	8869.63	2707.96	5738.65	2382.22	1280.28
500	Signal	308.76	290.91	181.68	251.08	169.96	100.67
	Background	9995.83	4305.07	1204.91	2661.35	1044.56	558.44
600	Signal	343.04	322.01	198.81	275.91	185.51	109.88
	Background	5974.29	2453.76	633.22	1447.77	538.77	291.30
700	Signal	373.39	349.71	212.04	296.66	196.88	114.12
	Background	3355.21	1312.60	351.94	755.50	297.49	149.81
800	Signal	393.76	367.61	219.88	308.87	202.92	115.04
	Background	2218.83	888.62	238.36	502.35	197.60	104.67
900	Signal	406.79	378.78	223.58	316.23	205.15	115.03
	Background	1353.81	531.42	144.89	306.75	118.40	55.91
1000	Signal	404.92	375.34	217.64	311.40	199.37	109.07
	Background	767.40	295.94	85.58	174.14	71.25	33.74

Table 5.19: Events in the window with 3% width at each signal area for different CSV working point selections. L: Loose, M: Medium and T: Tight.

Window	Higgs mass (GeV)
1	$90 < m_h < 140$
2	$90 < m_h < 145$
3	$85 < m_h < 145$
4	$85 < m_h < 150$
5	$95 < m_h < 140$
6	$100 < m_h < 140$
7	$100 < m_h < 135$

Tighter windows	
8	$100 < m_h < 145$
9	$105 < m_h < 145$
10	$105 < m_h < 140$
11	$105 < m_h < 135$

Table 5.20: Eleven Higgs mass windows range from 85 GeV to 150 GeV.

Higgs mass windows (GeV)	Samples	Events												
Mass point (GeV)		225	250	275	300	325	350	400	500	600	700	800	900	1000
$90 < m_h < 140$	Signal	170.23	202.23	215.64	209.18	238.39	253.03	279.77	331.72	371.96	408.63	436.00	452.66	451.08
	Background	92670.83	178457.84	154377.50	82075.98	93438.93	78520.54	53837.52	23194.97	12062.75	5533.42	3276.29	1932.09	1092.29
$90 < m_h < 145$	Signal	174.37	208.15	221.94	214.52	244.72	260.07	287.51	340.14	381.61	419.58	449.14	467.24	466.92
	Background	99534.29	192058.63	166220.24	88387.18	100637.55	84543.25	57767.13	24724.02	12835.16	5862.52	3479.32	2041.42	1151.82
$85 < m_h < 145$	Signal	186.08	220.99	235.51	225.79	258.71	274.59	301.32	354.02	393.82	430.94	457.46	473.49	472.06
	Background	109924.55	211582.86	183682.78	98138.93	112026.94	94363.25	64777.13	27960.05	14577.48	6846.67	4079.36	2392.35	1360.21
$85 < m_h < 150$	Signal	189.18	225.25	240.12	229.42	263.01	279.37	306.42	359.07	399.44	436.46	463.73	480.92	479.34
	Background	116472.09	224558.28	194726.71	103993.24	118701.14	99948.84	68523.79	29441.93	15266.98	7162.29	4251.40	2485.19	1413.53
$95 < m_h < 140$	Signal	155.06	185.24	198.07	193.21	220.23	234.62	260.73	311.91	354.11	391.14	422.37	441.10	441.95
	Background	82098.25	158331.18	137052.95	72683.64	82230.62	68854.62	47165.87	20073.70	10376.97	4615.15	2731.90	1613.47	910.19
$100 < m_h < 140$	Signal	136.44	164.59	176.88	173.21	196.84	210.69	236.22	285.04	328.82	365.91	401.01	421.62	426.35
	Background	71417.81	138404.45	119868.52	63455.02	71603.70	59820.02	40756.46	17217.15	8745.85	3859.25	2242.14	1334.34	756.01
$100 < m_h < 135$	Signal	130.25	156.19	167.65	165.06	186.79	199.82	224.02	270.38	311.31	344.55	375.24	391.80	393.22
	Background	64128.23	124139.00	107311.65	56700.94	64179.78	53748.75	36555.33	15540.51	7872.73	3515.87	2048.72	1211.06	689.46
$100 < m_h < 145$	Signal	140.58	170.51	183.17	178.54	203.16	217.73	243.96	293.46	338.48	376.87	414.15	436.21	442.19
	Background	78281.09	152005.02	131711.35	69765.21	78802.79	65844.33	44685.88	18746.24	9518.26	4188.35	2445.16	1443.67	815.54
$105 < m_h < 145$	Signal	118.86	145.60	157.92	154.18	175.53	188.87	213.45	260.07	304.58	341.98	381.99	407.43	416.95
	Background	67618.21	132063.76	114663.75	60591.74	68331.04	56971.46	38542.11	16093.42	8075.67	3535.74	2057.83	1204.24	684.47
$105 < m_h < 140$	Signal	114.72	139.68	151.63	148.84	169.20	181.83	205.71	251.64	294.92	331.02	368.84	392.85	401.11
	Background	60755.10	118463.96	102821.22	54280.58	61130.84	50947.22	34612.48	14564.36	7303.27	3206.64	1854.80	1094.91	624.94
$105 < m_h < 135$	Signal	108.53	131.28	142.40	140.69	159.15	170.95	193.52	236.99	277.41	309.66	343.07	363.03	367.98
	Background	53465.66	104198.46	90265.72	47527.34	53706.89	44875.71	30411.24	12887.73	6430.18	2863.26	1661.38	971.62	558.39

Table 5.21: The remaining events in the signal region after implementing the Higgs mass windows for each mass point.

5.5 DISCRIMINATING VARIABLES

The gluon-gluon fusion production of a heavy pseudoscalar and its decay $A \to Zh \to \ell^+\ell^- b\bar{b}$ yields a very characteristic signature even with respect to the irreducible backgrounds. The possibility to reject the latter relies almost exclusively in finding the most characteristic variables of the signal process.

Two approaches can be attempted: the first and most immediate one is to consider variables which are natural from an experimental point of view, such as the final objects transverse momenta, invariant masses, pseudorapidity and azimuthal separation, and many more. This can be thought of as a type of bottom-up parametrisation, and the full set of variables can be found in Chapter 5.7.

The alternative is a top-down parametrisation, motivated by the physical process. A good starting point are the variables that characterise the pseudoscalar production, such as the polar angle, and follow the decay chain up to the final objects (leptons and quarks) in their rest frame. This procedure is described in Chapter 5.5.2.

5.5.1 KINEMATICS

The present search has a final state with two resonant states of known mass, and both on shell ($m_Z = 91$ GeV $m_h = 125$ GeV): $Z \to \ell^+\ell^-$ (in the 2ℓ channel) and $h \to b\bar{b}$. The resolution of the two b-jets forming the latter state is not as good as the one of the leptons forming the Z, so the peak resolution of the A boson is dominated by the Higgs boson mass resolution. This is especially true at low m_A, because at high m_A the resolution of the A mass is dominated by the resolution of the Higgs p_T, rather than its mass. To improve the m_A resolution, and consequently increase the discovery potential, it is possible to exploit the fact that the mass of the h is known in order to correct the jets' four momenta. The largest factor in determining a jet 4 momentum is the determination of its p_T, which is intrinsically limited by the calorimetry non-linear response, low-p_T track reconstruction momentum determination and losses due to non-sensitive areas in the detector. In general, the η and ϕ of the jet have a smaller impact of the di-jet mass resolution and are usually well estimated by the jet reconstruction and clustering methods. These considerations motivate the focus on the correction of the p_T of the two jets used to reconstruct the Higgs candidate.

In the calculation of the best estimate of the A boson mass, the four momenta of the two jets are rescaled to match an invariant mass of $m_{jj} = 125$ GeV. The rescaling is not the same for the jet pair, but is proportional to the uncertainty on the jet energy scale (JES). In this way, the jet with the largest

JES uncertainty is corrected more that the other. The corrected jet p_T are:

$$p_T^{i'} = p_T^i \cdot \frac{m_h}{m_{jj}} \cdot w_i \tag{5.13}$$

where $w_i = 2 \cdot \frac{\sigma_i}{\sigma_1+\sigma_2}$, the index i runs on the jet number $(i = 1, 2)$, and σ_i is the JES uncertainty for the i-th jet.

A similar method is applied to leptons, if present in the final state. The mass of the Z boson is very well measured, and similarly to the jets, the lepton momenta are rescaled to match the expected Z boson invariant mass. In the lepton case, the scale uncertainties are much smaller than the ones of the jets, and the w_i are set to 1. Even if the effect on the A resolution is smaller that kinematic constrain on the jets, this additional constrain limits the impact of the lepton energy scale, and helps especially at low m_A where the peak is very narrow, improving the resolution by $1 \sim 2\%$.

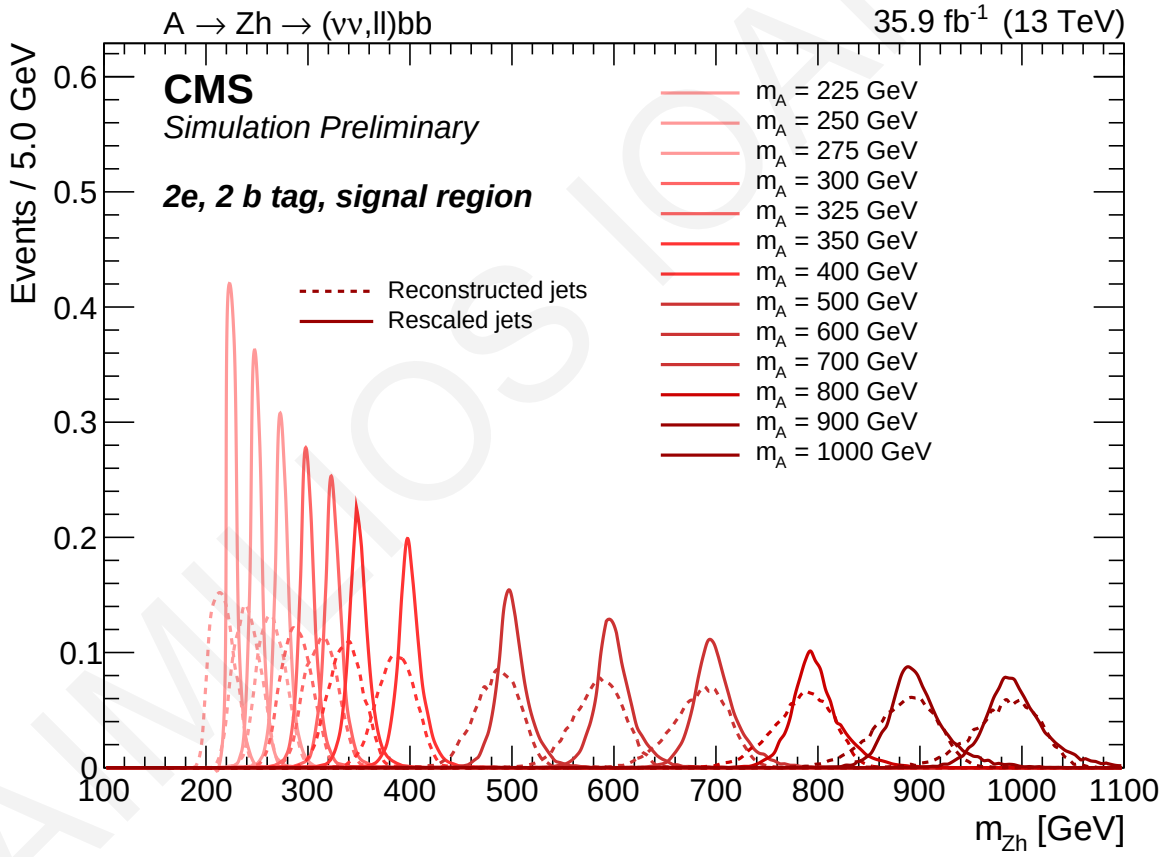

Figure 5.48: m_A before and after the kinematic constrain on the Z and h for the different signal mass points in the $2e$ category.

In 0ℓ final state, the situation is quite different: the final state cannot be reconstructed, and the transverse mass resolution is dominated by the $\not{E}_T$, whose true value is obviously unknown. Furthermore, this

		225	250	275	300	325	350	400	500	600	700	800	900	1000
No Kin	Mean (GeV)	217	241	265	289	313	337	386	484	583	682	780	879	977
	Width (GeV)	11.5	13.7	14.3	16.1	18.2	18.0	20.7	26.3	29.0	34.3	39.3	42.8	50.6
	Res (%)	0.053	0.057	0.054	0.056	0.058	0.053	0.054	0.054	0.050	0.050	0.050	0.049	0.052
Kin	Mean (GeV)	226	250	275	300	325	350	400	500	600	699	797	895	990
	Width (GeV)	6.0	8.7	9.5	11.3	14.5	13.3	16.3	22.3	25.2	31.1	37.3	41.0	48.2
	Res (%)	0.027	0.035	0.035	0.038	0.044	0.038	0.041	0.045	0.042	0.044	0.047	0.046	0.049

Table 5.22: Results of the kinematic constrain on the A mass peak in the $2e$ category, estimated from the RMS and mean of the histograms. The resolution is defined as RMS/mean.

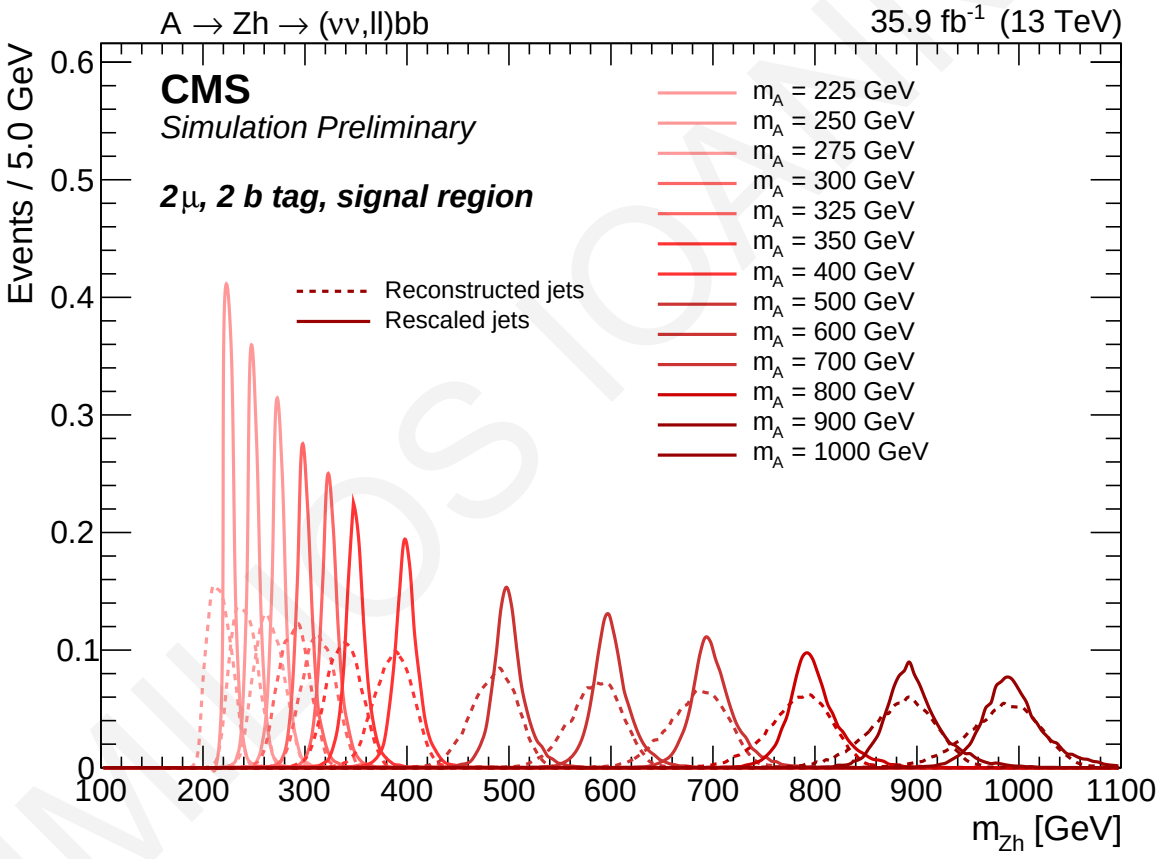

Figure 5.49: m_A before and after the kinematic constrain on the Z and h for the different signal mass points in the 2μ category.

channel is contributing at high mass, where the effectiveness of the kinematic constrain is intrinsically lower. Even if the gain in resolution is not large as in the di-leptonic final states, it is still visible, and retained in the estimation of the A boson transverse mass.

		225	250	275	300	325	350	400	500	600	700	800	900	1000
No Kin	Mean (GeV)	217	241	265	290	314	338	387	484	583	681	780	878	977
	Width (GeV)	11.4	14.3	14.9	17.4	17.8	18.6	22.2	25.6	30.7	35.6	39.9	45.5	50.4
	Res (%)	0.052	0.059	0.056	0.060	0.057	0.055	0.057	0.053	0.053	0.052	0.051	0.052	0.052
Kin	Mean (GeV)	226	250	275	300	325	350	400	500	600	699	797	895	991
	Width (GeV)	5.9	9.3	10.2	13.3	13.2	13.8	18.3	21.1	26.8	31.7	36.1	41.4	45.5
	Res (%)	0.026	0.037	0.037	0.044	0.041	0.039	0.046	0.042	0.045	0.045	0.045	0.046	0.046

Table 5.23: Results of the kinematic constrain on the A mass peak in the 2μ category, estimated from the RMS and mean of the histograms. The resolution is defined as RMS/mean.

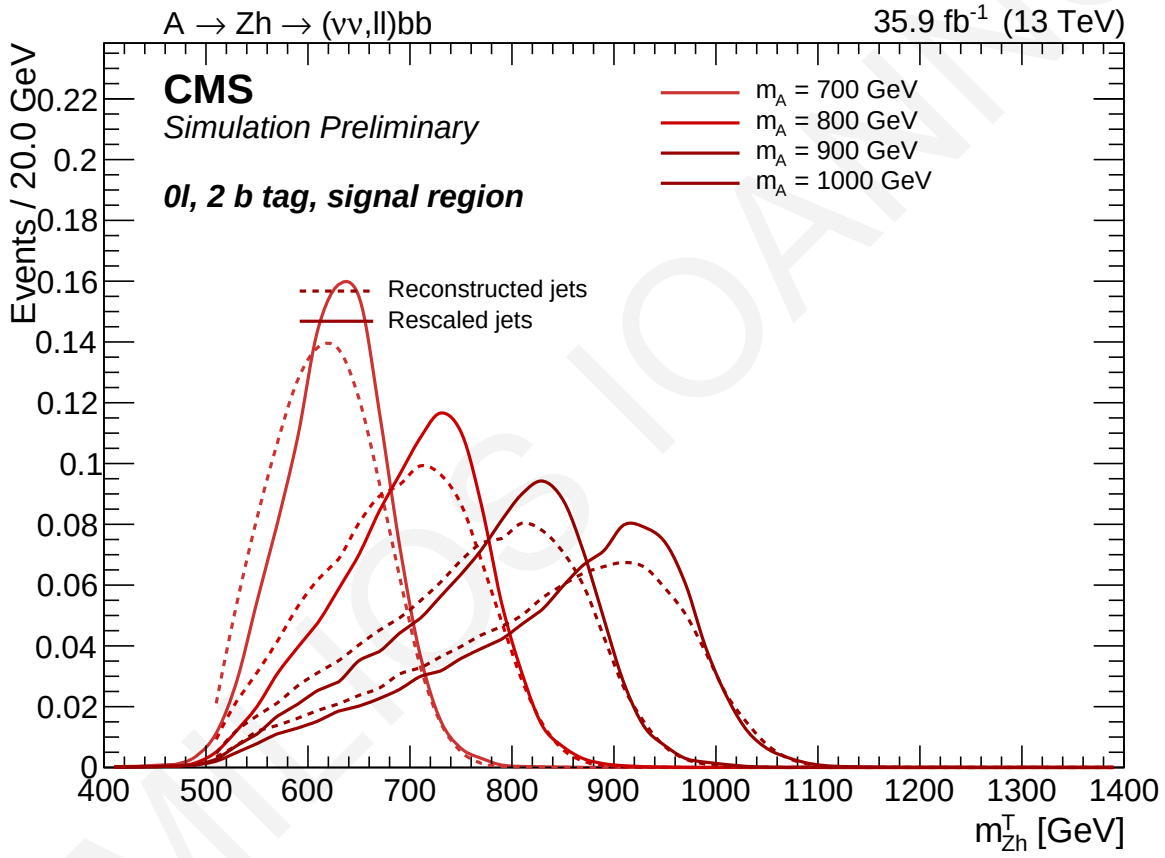

Figure 5.50: m_A before and after the kinematic constrain on the h for the different signal mass points in the 0ℓ category.

5.5.2 ANGULAR VARIABLES

There are several features in the signal $A \to Zh \to \ell^+\ell^- b\bar{b}$ decay kinematics which can help to discriminate the background. In fact, five helicity-dependent angular observables fully describe the kinematics in a $2 \to 1 \to 2 \to 4$ decay; they are independent on the three invariant masses of the

		700	800	900	1000
No Kin	Mean (GeV)	616	684	757	829
	Width (GeV)	52.1	75.8	99.8	123.4
	Res (%)	0.085	0.111	0.132	0.149
Kin	Mean (GeV)	627	698	771	842
	Width (GeV)	50.3	72.5	95.9	119.0
	Res (%)	0.080	0.104	0.124	0.141

Table 5.24: Results of the kinematic constrain on the A transverse mass peak in the 0ℓ category, estimated from the RMS and mean of the histograms. The resolution is defined as RMS/mean.

particles involved (A, Z, h) and on the longitudinal and transverse momenta but typically they have weaker discrimination power and rely on PDFs and process dynamics. These variables are largely uncorrelated and are more attractive to be used in a collective discriminator rather than independently.

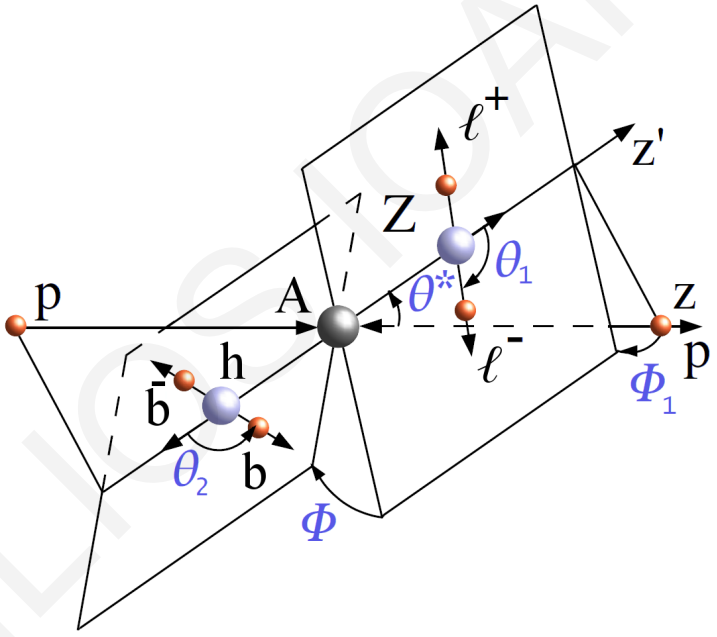

Figure 5.51: Diagram of the $A \to Zh \to \ell^+\ell^- b\bar{b}$ decay and the definition of the five helicity angles.

The five angles are sketched in Fig. 5.51; two of them are production angles (θ^*, Φ_1), the remaining three are decay angles $(\theta_1, \theta_2, \Phi)$. Their normalized distributions are shown in Fig. 5.52 and are defined as:

θ^*: angle between the A flight direction and the beam in the A rest frame

θ_1: angle between the negatively charged lepton and the Z flight direction in the Z rest frame

θ_2: same as θ_1, but for h and jets.

Φ: angle between the Z and h decay planes

Φ_1: angle between the Z decay plane and the plane where the Z and the beam directions lie

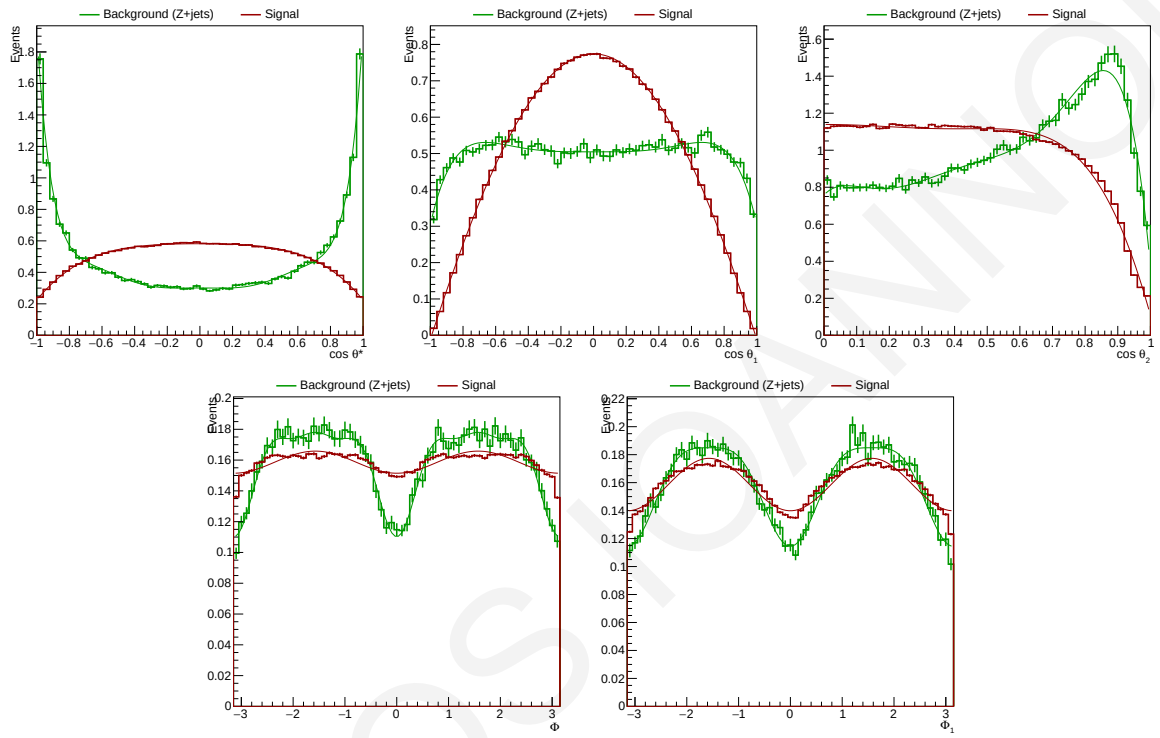

Figure 5.52: Signal (red) and background (green) probability distribution functions for the five angles. The signal is the sum of the signal samples, the green represents the Drell-Yan background. The distribution are obtained after the selection reported in Tab. 5.25.

5.5.2.1 LIKELIHOOD ANGULAR DISCRIMINANT

Since helicity variables are known to have generally low discriminating power, cutting on these would force to reject a significant fraction of signal events. However, they can be combined together using a multivariate discriminator. A Likelihood Discriminant is constructed starting from the signal and background probability distribution functions s_i and b_i. A likelihood has been chosen for its simplicity and robustness with respect to others multivariate methods. In addition, if the variables which construct the likelihood discriminant are uncorrelated, there is no degradation in performance and the discriminant gives the optimal separation between signal and background as described in Appendix A.1.14. The

likelihood ratio discriminator is defined as follows:

$$Discr = \frac{\prod_i s_i(x_i)}{\prod_i s_i(x_i) + \prod_i b_i(x_i)} \tag{5.14}$$

The training of the likelihood has been performed by selecting all the simulated events passing the pre-selections described in Chapter 5.6 and the selections in Tab. 5.25. The background distributions are taken exclusively from DY processes, weighted by their cross sections. The signal distributions are obtained from the sum of all signal samples, weighted with an unitary cross section. The list of cuts applied to backgrounds and signal is reported in Tab. 5.25.

In addition, the corresponding *Receiver Operating Characteristic* (ROC) curve is presented in Fig. 5.53. The point on the ROC curve represents the final selection of the Angular Likelihood Discriminator (AngularLD > 0.5). By applying this specific cut, the signal efficiency is 85% and the $Z + jets$ background rejection is 50%.

Variable	Cut
$m_{\ell^+\ell^-}$ (GeV)	$70 < m_{\ell^+\ell^-} < 110$
CSV_1	medium
CSV_2	medium
$m_{b\bar{b}}$ (GeV)	$100 < m_{b\bar{b}} < 140$
$\not{E}_T$ (GeV)	< 100

Table 5.25: Cut list for Likelihood training.

The five angular variables for background and signal samples are shown compared to data in Fig. 5.54; the final Angular Discriminator output is also shown in Fig. 5.55.

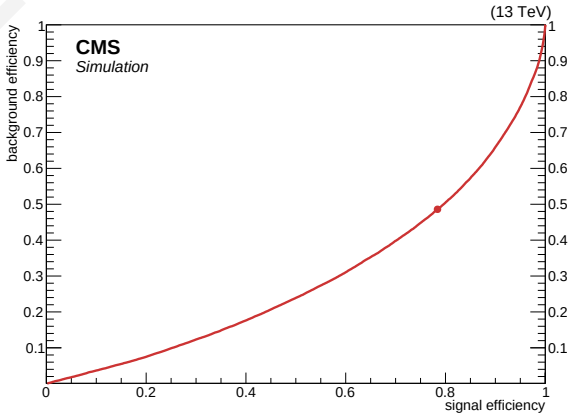

Figure 5.53: ROC curve of the Likelihood discriminant.

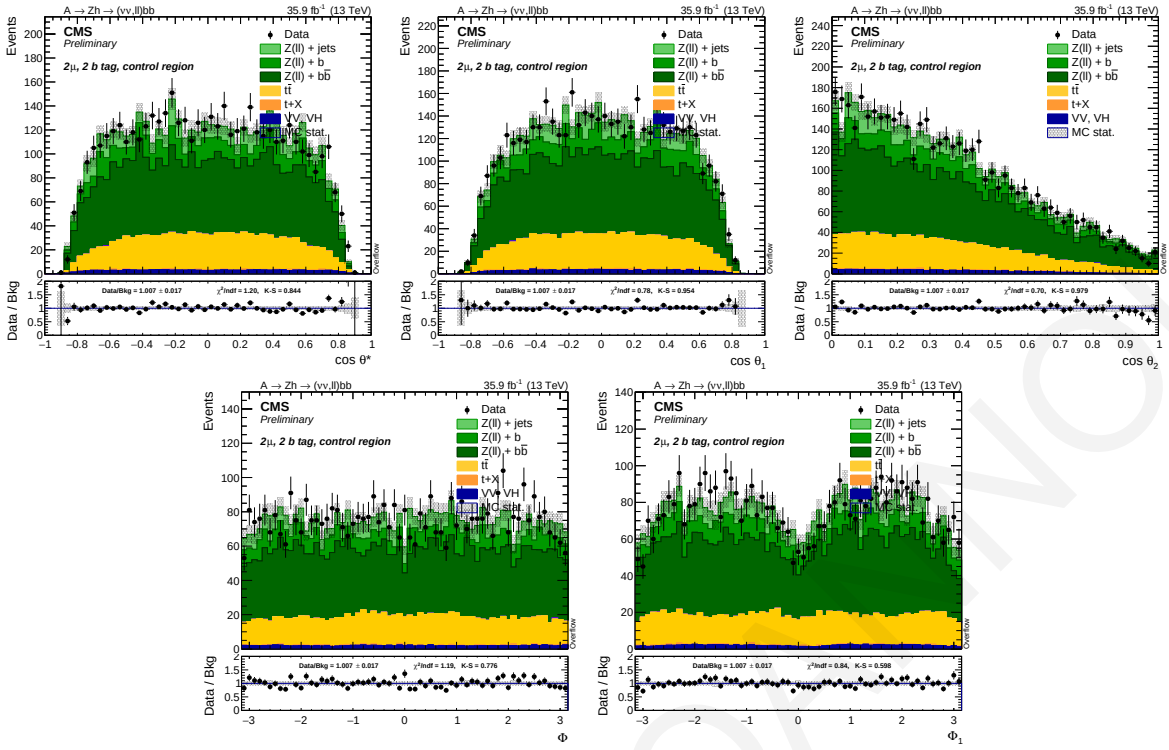

Figure 5.54: Data and MC comparison for the five angles after analysis preselections and after the implementation of the angular selection (AngularLD > 0.5).

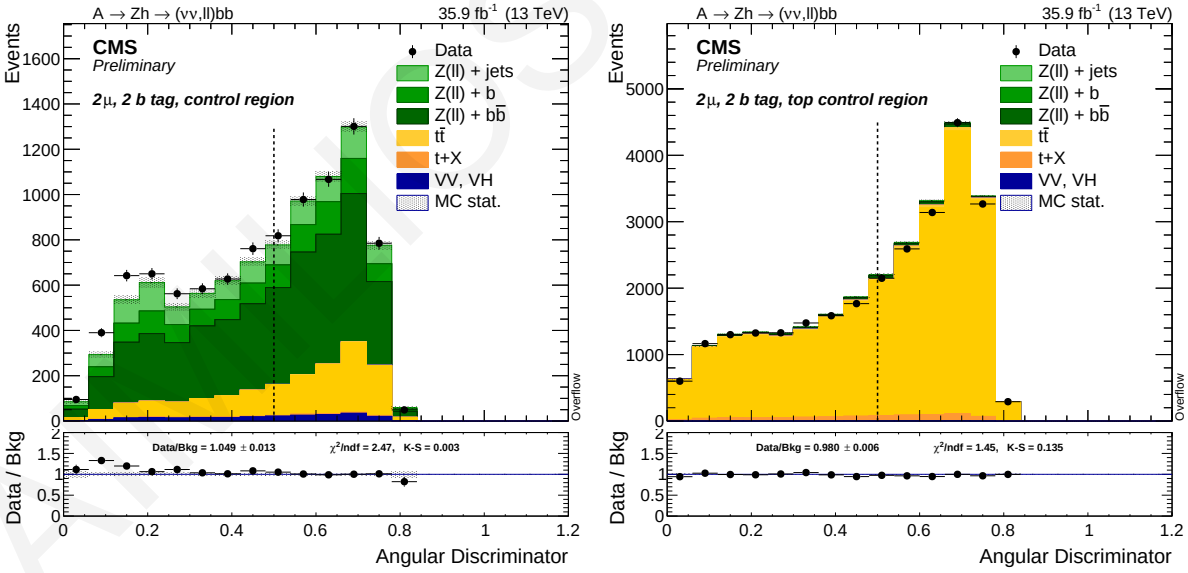

Figure 5.55: Angular Discriminant output in the $Z+b\bar{b}$ control region (left) and $t\bar{t}$ control region (right).

5.5.3 EVENT SHAPE

The angular discriminator is effective in discriminating the signal against the $Z + b\bar{b}$ background, but unfortunately the $t\bar{t}$ background behaves as a signal. In order to reduce its contribution in the *Signal Region (SR)* (and thus increasing the S/B ratio), a different set of discriminating variables can be used. These variables are physically motivated by the the different physics behind the $t\bar{t}$ production, the *Z mass* and the $\not{E}_T$. In the $t\bar{t}$ production, there is no real Z candidate, so the two leptons does not reconstruct the Z mass correctly, and the contribution is almost *flat* in the di-lepton invariant mass spectrum. The $Z + b\bar{b}$ and the signal have no intrinsic missing energy coming from neutrinos in the final state and it is expected that the $\not{E}_T$ distribution in $t\bar{t}$ background will be generally larger than the one in $Z + b\bar{b}$ and signal.

5.5.3.1 LIKELIHOOD EVENT DISCRIMINANT

Similarly to the angular discriminant, event discriminator can be trained to explicitly reject the $t\bar{t}$ background. In this case, the background definition in the training is just $t\bar{t}$. Figure 5.56 reports the normalised shapes of the signal and background, while Fig. 5.57 shows the ROC curve in the signal region. Fig. 5.58 displays the agreement between data and simulation in two of the most important control regions. The Event Shape discriminator's cut is shown on the ROC curve and corresponds to > 0.5 (Event Shape discriminator > 0.5). By implementing this particular cut, we remove approximately 75% $t\bar{t}$ background contamination and the signal loss is roughly 15%.

The list of cuts employed before the training is the same as the angular discriminator, reported in Tab. 5.25. Because of the small or null correlation between the input variables, the outputs of the two discriminators are also uncorrelated, as shown in Fig. 5.59.

5.6 EVENT SELECTION

Events considered in this analysis have to pass a certain number of selections before being considered as suitable signal candidates, identically in both data and simulation. The selections are reported below and in Table 5.26. The final signal efficiency is shown separately depending on the number and flavour of the leptons and b-tagged subjects in Figure 5.60 and 5.61 for both A boson production modes.

As shown in Fig. 5.60, the overall signal efficiency is 2-15% and the biggest loss is from the Higgs mass window. Better efficiency could be gained by the 1 b-tag category, however, the S/B ratio is worse due to much more background which has to be dealt with.

	$Z \to e^+e^-$	$Z \to \mu^+\mu^-$	$W \to e^\pm\nu_e$	$W \to \mu^\pm\nu_\mu$	$Z \to \nu\bar{\nu}$
Trigger	`HLT_Ele(27,32)` `HLT_Ele(105,115)`	`HLT_(Tk)Mu24`	`HLT_Ele(27,32)` or `HLT_Ele(105,115)`	`HLT_(Tk)Mu24`	`HLT_PFMET(NoMu)` or `HLT_PFMET170`
Lept Id	$2e$ *loose* WP	1μ tight, 1μ loose	$1e$ *tight*	1μ tight	e, μ, τ veto
Lept Iso	inc. in Id	loose PFIso	inc. in Id	tight PFIso	-
Lept p_T	$p_T > 30, 10$GeV	$p_T > 30, 10$GeV	$p_T > 30$GeV	$p_T > 30$GeV	$p_T < 10$GeV
Jets	AK4 PFJet, $p_T > 30$ GeV, *loose Id*				*tight Id*, $chf > 0.1$
H p_T	-	> 200GeV			> 200GeV
H mass	$100 < m_j < 140$ GeV (SR)				
H b-tag	1, 2, or 3 CSVv2 *medium* b-tagged				
V boson	$70 < m_{\ell^+\ell^-} < 110$GeV		$\not{E}_T/U > 200$GeV		$\not{E}_T > 200$GeV
Bkg rejection	$\not{E}_T < 100$GeV		-		min $\Delta\varphi_{j,\not{E}_T} > 0.4$
Event LD	> 0.5		-		
Angular LD	> 0.5		-		

Table 5.26: Summary of the selection cuts for all the five final states of the analysis.

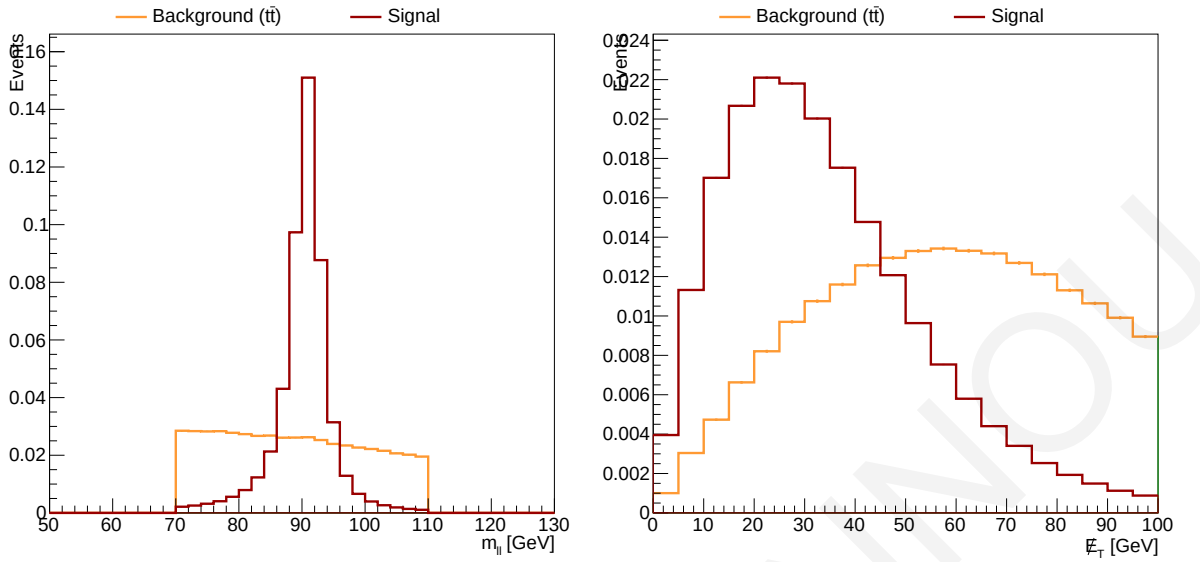

Figure 5.56: Signal (red) and background (orange) probability distribution functions for the $m_{\ell^+\ell^-}$ and $\not{E}_T$ variables. The signal is the sum of the signal samples, the orange represents the $t\bar{t}$ background.

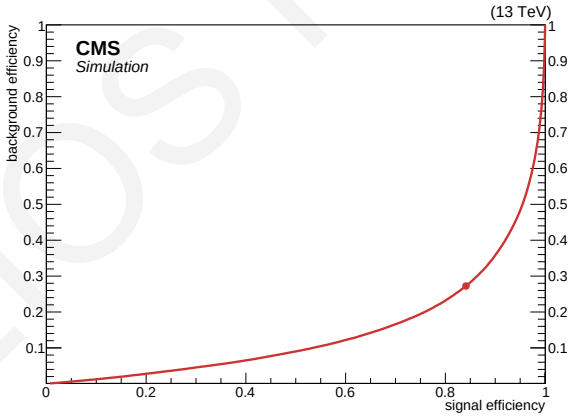

Figure 5.57: ROC curve and output distribution of the Event Shape discriminator.

On the other hand, in the associated b-quark production case (shown in Fig. 5.61), the signal efficiency is 1-12%. A non-negligible fraction of events has additional b-quarks in the final state, however, it is low dues to the small kinematical acceptance of the accompanying b-quarks. Only 20% of events which have 3 b-quarks can pass through kinematical acceptance and only 4% of events which have 4 b-quarks, can survive from the acceptance.

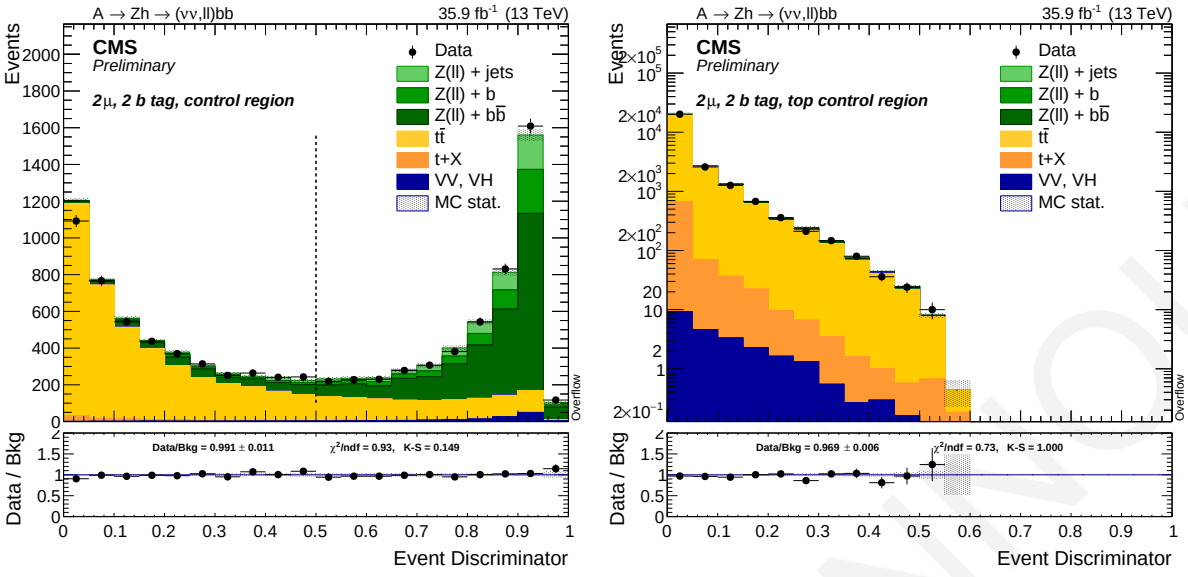

Figure 5.58: Event Discriminant output in the $Z + b\bar{b}$ control region (left) and $t\bar{t}$ control region (right).

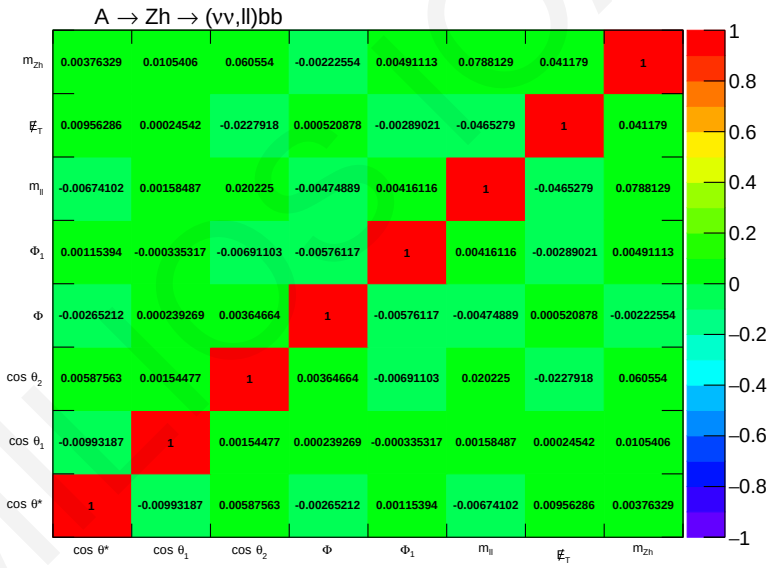

Figure 5.59: Correlation between the variables used in the two discriminators, and the four body invariant mass itself. The cross-correlation is always meant to be very small.

5.6.1 PRE-SELECTION CUTS

Events are classified into three independent categories (0ℓ, $2e$, and 2μ), based on the number and flavour of the reconstructed leptons. The pre-selection cuts for each categories are presented:

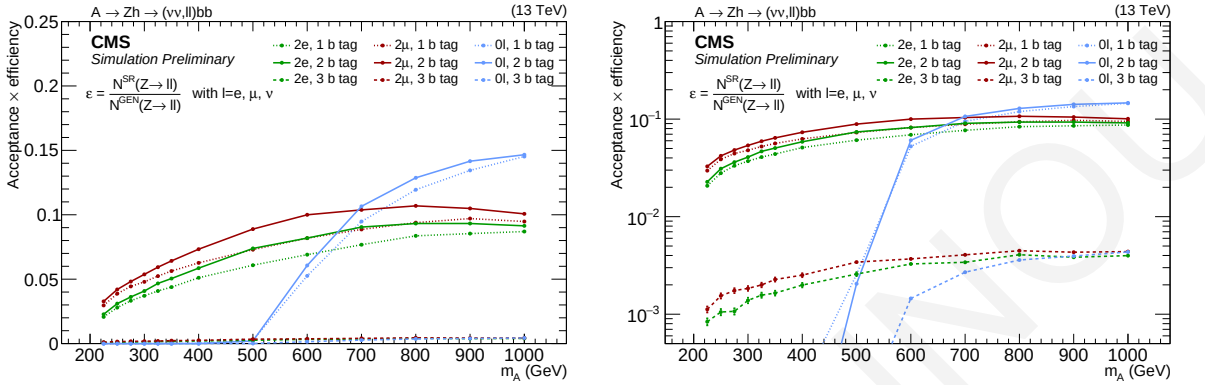

Figure 5.60: Signal efficiency separated by final state and b-tagging multiplicity after the signal region selections in the normal scale (left plot) and in the log scale (right plot). The efficiency is relative to the gluon fusion production mode.

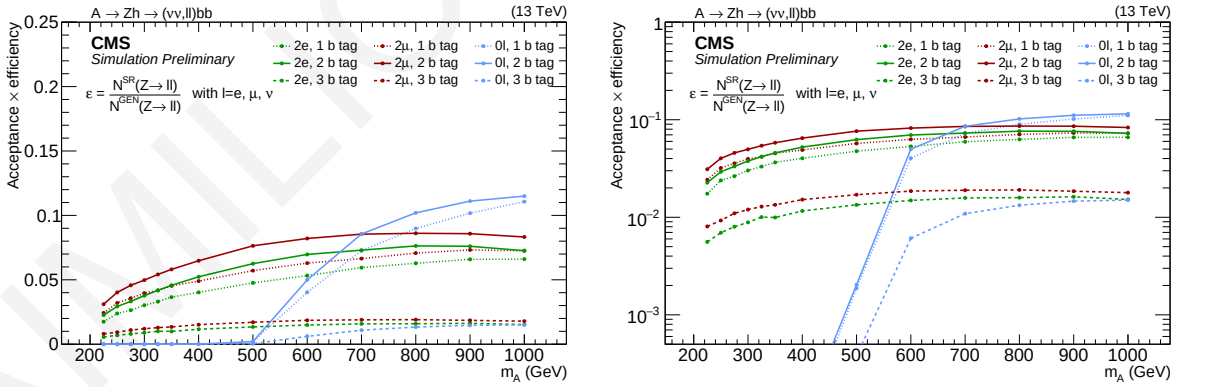

Figure 5.61: Signal efficiency separated by final state and b-tagging multiplicity after the signal region selections in the normal scale (left plot) and in the log scale (right plot). The efficiency is relative to the b-quark associated production mode.

Neutrino channel (0ℓ):

In the 0ℓ category, no isolated electron or muon with $p_T > 10$ GeV is allowed. Events containing isolated hadronic decays of the τ leptons with $p_T > 18$ GeV are vetoed as well. A selection is applied on the reconstructed $\not{E}_T$, which is required to be larger than 200 GeV, such that the trigger is at least 95% efficient.

- **Trigger:** $\not{E}_T$ triggers (Chapter 5.2.6.5)
- **MET:** Type-1 corrected missing energy $\not{E}_T > 200$ GeV
- **Leptons:** electrons, muons, and τ are vetoed

Di-electron channel ($2e$):

In the $2e$ category, events are required to have at least two isolated electrons within the detector geometrical acceptance. The p_T threshold is set to 30 GeV for the electron with highest p_T, and to 10 GeV for the electron with next-highest p_T. The Z boson candidate is formed from the two highest p_T, opposite charge electrons and must have an invariant mass $m_{\ell^+\ell^-}$ between 70 and 110 GeV. The reconstructed $\not{E}_T$ also has to be smaller than 100 GeV to reject the $t\bar{t}$ background.

- **Trigger:** Electron triggers (Chapter 5.2.6.1)
- $\mathbf{p_T}$: at least two PF electrons with $p_T > 30$ GeV and 10 GeV for leading and sub-leading, respectively
- $\eta : |\eta_{SC}| < 2.5$
- **Electron Id:** both electrons identified with the *loose* working point (Table 5.13)
- **Electron Iso:** included in Id requirement
- **Z mass:** $70 \leq m_{e^+e^-} \leq 110$ GeV

Di-muon channel (2μ):

Similarly, in the 2μ category, events are required to have at least two isolate muons within the detector geometrical acceptance. Also, the p_T threshold is set to 30 GeV for the leading muon and to 10 GeV for the sub-leading muon. The Z boson candidate is formed from the two highest p_T, opposite charge

muons and must have an invariant mass $m_{\ell^+\ell^-}$ between 70 and 110 GeV. The reconstructed $\not{E}_T$ also has to be smaller than 100 GeV to reject the $t\bar{t}$ background.

- **Trigger:** Muon triggers (Chapter 5.2.6.4)
- $\mathbf{p_T}$: at least two muons with $p_T > 30$ GeV and 10 GeV for leading and sub-leading muon, respectively
- $\eta : |\eta| < 2.4$
- **Muon Id:** at least one muon identified as *tight*, the other with the *loose* Id (Table 5.14)
- **Muon Iso:** PFIso < 0.25
- **Z mass:** $70 \leq m_{\mu\mu} \leq 110$ GeV

5.6.2 Hadronic Selection

The selections of the hadronic part are exactly the same for all the three lepton categories, with the exception of the *jet Id* in the specific case of the 0ℓ category, for which a tighter cut is applied. The jets are considered to be ordered by decreasing values of the CSVv2 discriminator.

- $\mathbf{p_T}$: at least two AK4 PFJets with $p_T > 30$ GeV
- $\eta : |\eta| < 2.4$
- **Jet Id:** *loose* PFJet Id; *tight* PFJet Id and charged hadron fraction > 0.1 for the 0 lepton channel
- **Lepton cleaning:** minimal separation between jet and isolated leptons (including τ) $\Delta R_{jet-\ell^\pm} > 0.4$
- **b-tagging:** counting b-tagged jets passing the *medium* working point (Table 5.17)

5.6.3 Signal Regions

After the application of the selections described in the previous section and the cut on the multivariate discriminators, nine different signal regions are defined (1, 2, or 3 b-tags and 0ℓ, $2e$, 2μ). Signal region (SR) is defined as the optimised Higgs mass window (described in Chapter 5.4) between 100 and 140 GeV. Therefore, events with a di-jet invariant mass m_{jj} between 100 and 140 GeV enter the signal regions; otherwise, if $m_{jj} < 400$ GeV, they fall within the di-jet mass *sidebands*, which are used as Control Regions (CRs) to estimate the contributions of the main backgrounds as described in the next section.

5.6.3.1 1 B-TAG

In the 1 b-tag category, events with only one jet characterised as *medium* CSV selection are included in the signal region for the three leptonic categories (0ℓ, $2e$, 2μ). In this case, the SM Higgs candidate is reconstructed by one jet of which its CSV working point selection is definitely *Medium* and there is no constrain on the second jet. Table 5.27 reports the selections which are applied in this special category.

Variable	0ℓ	2ℓ
Pre-selection as described in Sec. 5.6.1		
$m_{\ell^+\ell^-}$ GeV	-	$70 < m_{\ell^+\ell^-} < 110$ GeV
Jet1 CSV	medium	
Jet2 CSV	!medium	
Jet3 CSV	!medium	
$m_{b\bar{b}}$ GeV	$100 < m_{b\bar{b}} < 140$ GeV	
$\not{E}_T$ GeV	> 200 GeV	< 100 GeV
Angular LD	-	> 0.5
Event LD	-	> 0.5

Table 5.27: Cuts for the 1 b-tag signal regions.

It is important to note that there is no constrain on CSV working point selection of the second and the third jet. This cut is applied for the three different leptonic categories (0ℓ, $2e$, 2μ). On the other hand, the angular and event shape discriminators are applied only on $2e$ and 2μ categories.

After applying the selections and cuts on the multivariate discriminators, the number of survived data and expected events are listed in Table 5.28 for the main SM processes in the 1 b-tag signal region. As shown, the data/background ratio is about 1.0079 for the zero-lepton category, 0.9866 for $2e$ category and the ratio for the 2μ category is 0.9733. Additionally, there is no contribution from DY samples including neutrinos as final states in the two lepton categories, as expected.

Figure 5.62 shows the m_A distribution for $2e$ and 2μ categories. Furthermore, five signal samples are randomly displayed on the plots. The data are well described by background sources for low and intermediate m_A for both lepton categories. However, a poor data/background agreement is noticeable at the highest masses of A boson due to low MC statistics.

Additionally, the p_T distributions of the Z boson and of the SM Higgs boson are shown in Fig. 5.63 and Fig. 5.64, respectively.

In the case of 0ℓ category, the transverse mass of A candidate is presented in Fig. 5.65 as well as the $\not{E}_T$ distribution.

	0ℓ	$2e$	2μ
Data	2124	4471	6047
DYJetsToLL-0b	3.38	2023.36	2694.69
DYJetsToLL-1b	0.79	1448.62	2020.9
DYJetsToLL-2b	0.56	700.55	987.74
DYJetsToNuNu-0b	666.25	0	0
DYJetsToNuNu-1b	138.6	0	0
DYJetsToNuNu-2b	115.83	0	0
ST	63.4	9.76	18.36
TTbarDL	29.66	260.04	363.56
TTbarSL	607	12.52	26.48
VV	70.79	75.53	98.27
WJetsToLNu	411.05	1.15	3.13
BkgSum	2107.32	4531.54	6213.13

Table 5.28: Number of data events and expected events for the various SM processes in the 1 b-tag signal regions.

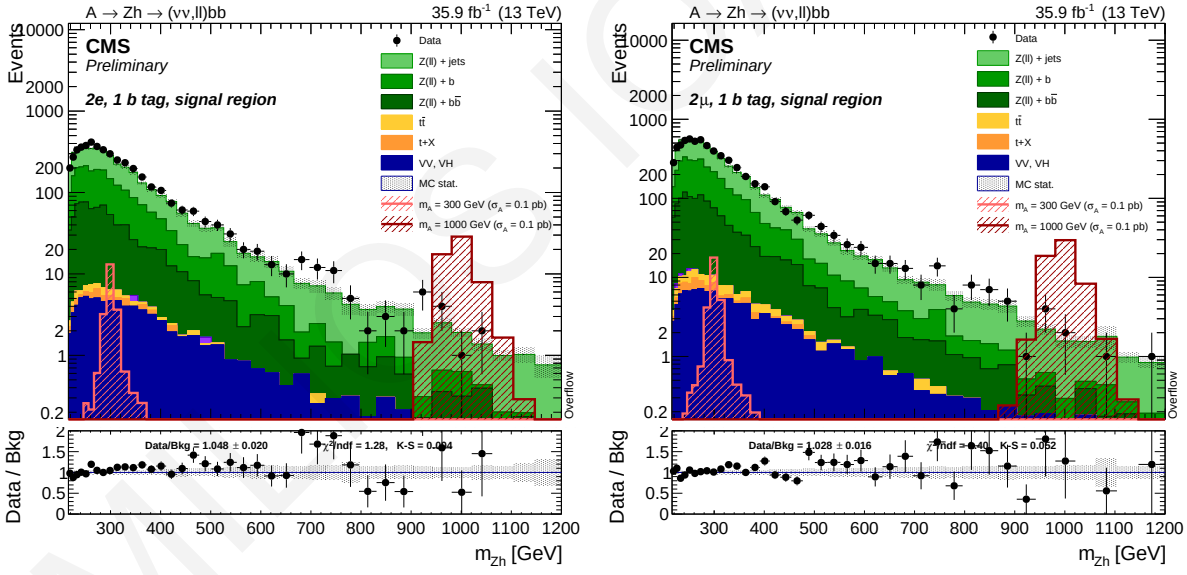

Figure 5.62: Four-body invariant mass after the kinematic constraints. The signal process is shown for the A masses ($m_A = 300,\ 1000$ GeV) with the total cross section of 0.1 pb.

The background of $Z(\nu\bar{\nu}) + jets$ is dominant in the 0ℓ category for the 1 b-tag signal region and a possible signal peak of A candidate may be overlapped. In addition, the p_T distribution of the pair of b-quarks is presented in Fig. 5.66 (left plot), where the kinematic cut on the transverse momentum of the Higgs candidate is observable at 200 GeV ($p^T_{b\bar{b}} > 200$ GeV). The angular separation between the two jets which reconstruct a SM Higgs candidate is also presented in Fig. 5.66. The angular separation

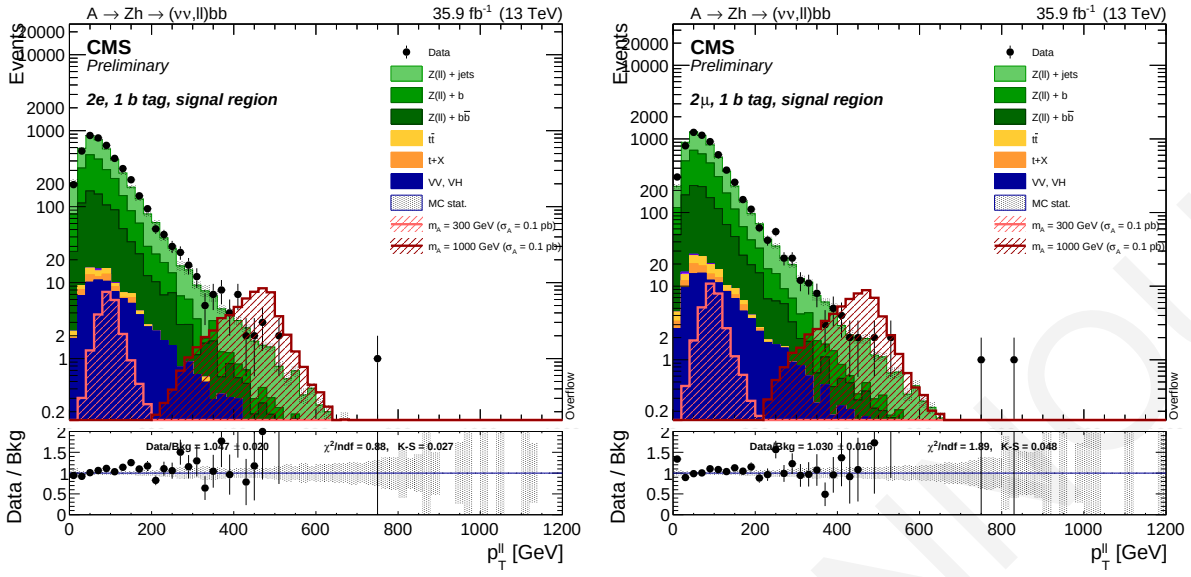

Figure 5.63: p_T distribution of the Z candidate. The signal process is shown for the A masses ($m_A = 300,\ 1000$ GeV) with the total cross section of 0.1 pb.

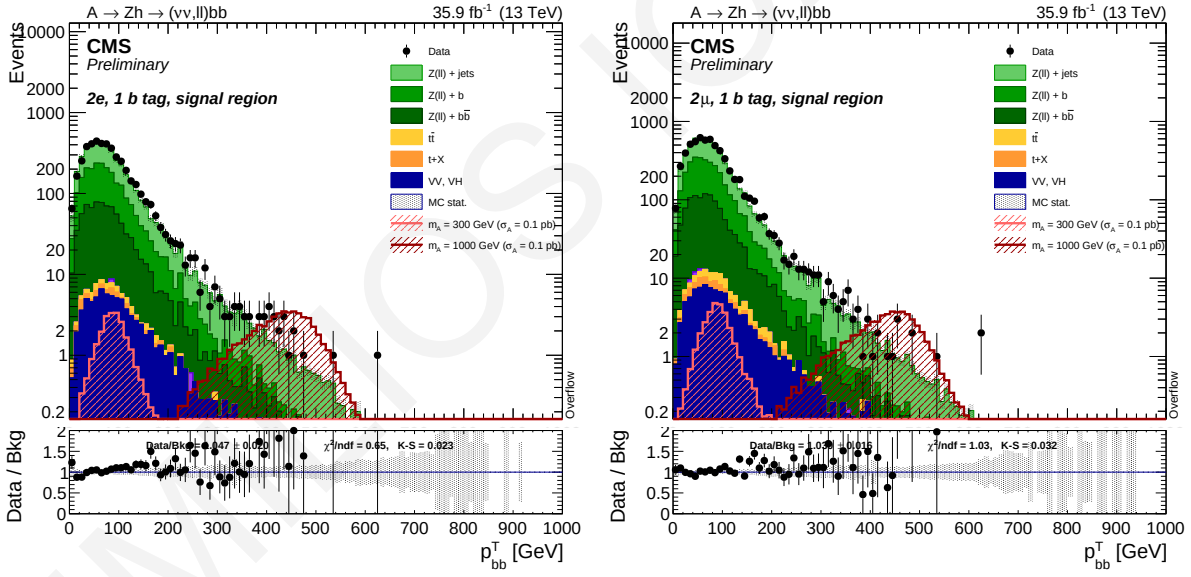

Figure 5.64: p_T distribution of the Higgs candidate. The signal process is shown for the A masses ($m_A = 300,\ 1000$ GeV) with the total cross section of 0.1 pb.

between the two jets ranges between 0.5 and 1.5, which means that the two jets are probably the decay products of the light CP-even Higgs candidate, h.

Finally, Fig. 5.67 presents the leading jet p_T distribution and the multiplicity of jets for the 0ℓ category in the signal region. The data/background agreement of the number of jets is remarkable as well as the

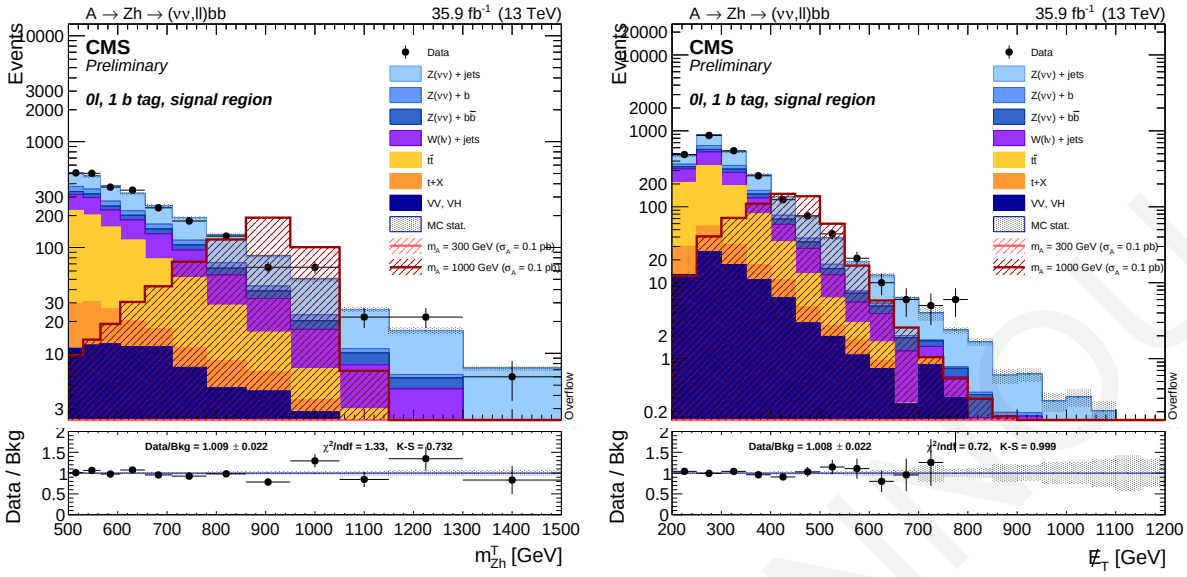

Figure 5.65: A candidate invariant transverse mass after the kinematic constraints on the dijet pair (left), and $\not{E}_T$ (right). The signal process is shown for the A masses ($m_A = 300,\ 1000$ GeV) with the total cross section of 0.1 pb.

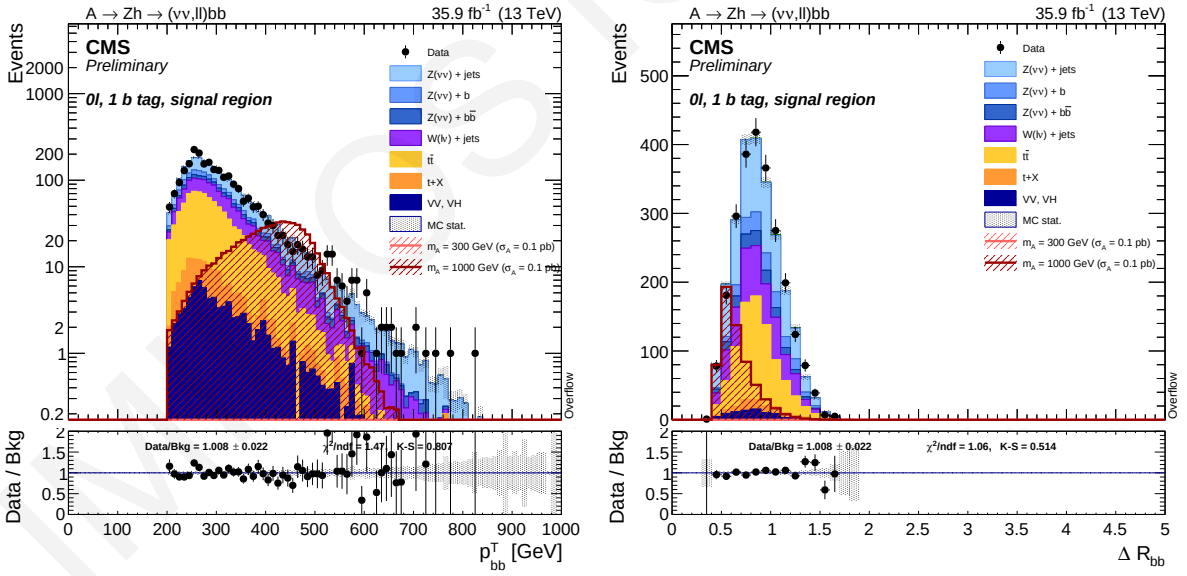

Figure 5.66: Higgs candidate p_T (left), angular separation between the two jets (right). The signal process is shown for the A masses ($m_A = 300,\ 1000$ GeV) with the total cross section of 0.1 pb.

high transverse momentum which characterises the leading jet in events.

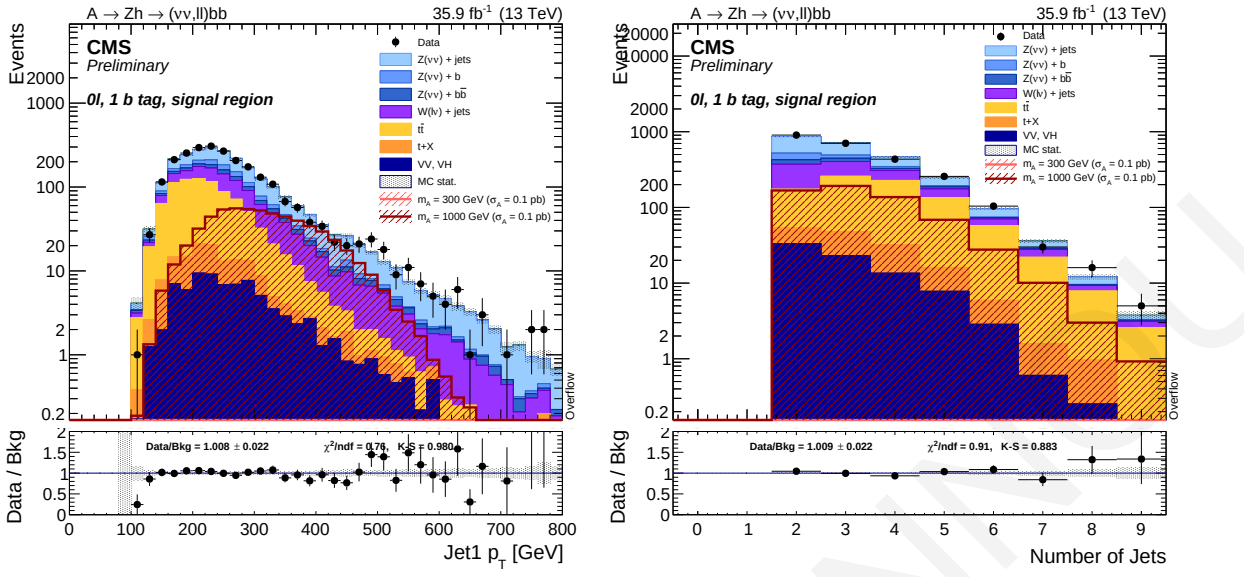

Figure 5.67: Leading jet p_T (left), jet multiplicity (right). The signal process is shown for the A masses ($m_A = 300,\ 1000$ GeV) with the total cross section of 0.1 pb.

5.6.3.2 2 B-TAG

The 2 b-tag category differs from the former 1 b-tag only on the constrain of the second CSV working point selection of the jet. In this category, the sub-leading jet must also have a medium CSV working point such as the leading jet. Table 5.29 records the various criteria which are applied in the 2 b-tag signal region. All the others remain the same as in the 1 b-tag signal region case.

Variable	0ℓ	2ℓ
Pre-selection as described in Sec. 5.6.1		
$m_{\ell^+\ell^-}$ (GeV)	-	$70 < m_{\ell^+\ell^-} < 110$ GeV
Jet1 CSV	medium	
Jet2 CSV	medium	
Jet3 CSV	!medium	
$m_{b\bar{b}}$ GeV	$100 < m_{b\bar{b}} < 140$ GeV	
$\not{E}_T$ GeV	> 200 GeV	< 100 GeV
Angular LD	-	> 0.5
Event LD	-	> 0.5

Table 5.29: Cuts for the 2 b-tag signal regions. The signal process is shown for the A masses ($m_A = 300,\ 1000$ GeV) with the total cross section of 0.1 pb.

Similarly, Table 5.30 lists the number of survived data and expected events after applying the selections and cuts on the multivariate discriminators for all background sources.

	0ℓ	$2e$	2μ
Data	323	894	1295
DYJetsToLL-0b	0.28	78.83	113.27
DYJetsToLL-1b	0.03	115.57	174.29
DYJetsToLL-2b	0.35	482.41	695.58
DYJetsToNuNu-0b	45.1	0	0
DYJetsToNuNu-1b	8.5	0	0
DYJetsToNuNu-2b	75.35	0	0
ST	14.29	4.31	6.6
TTbarDL	5.39	210.04	295.31
TTbarSL	106.65	2.89	5.11
VV	30.24	26.64	36.69
WJetsToLNu	57.26	0.91	0
BkgSum	343.44	921.6	1326.85

Table 5.30: Number of data events and expected events for the various SM processes in the 2 b-tag signal regions.

As shown from Tab. 5.30, there is no a big disagreement between the survived number of data and the number of MC background events.

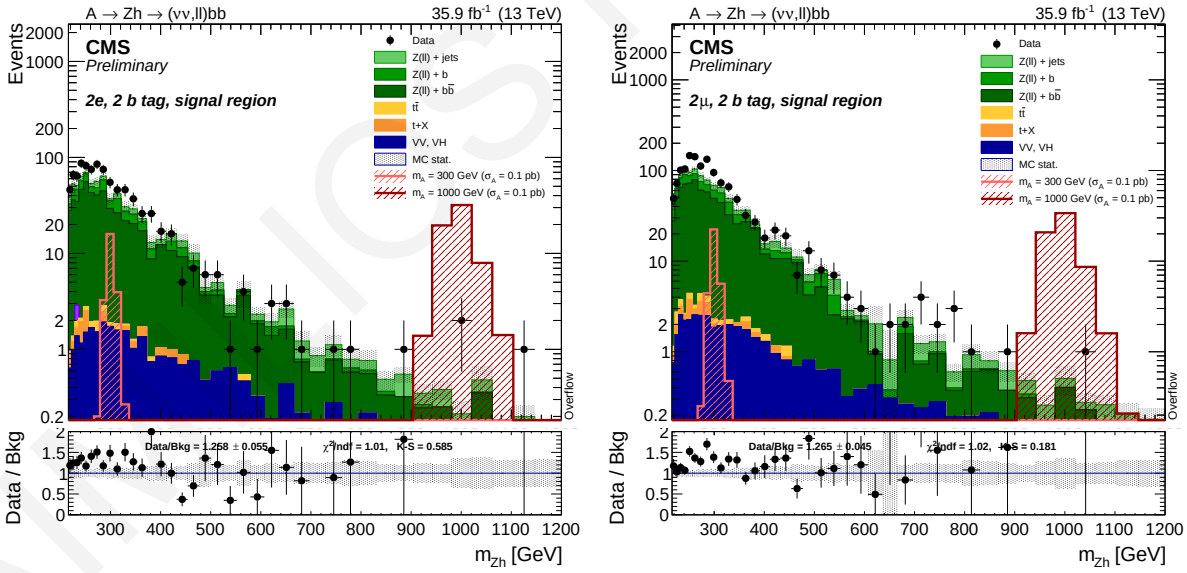

Figure 5.68: Four-body invariant mass after the kinematic constraints. The signal process is shown for the A masses ($m_A = 300,\ 1000$ GeV) with the total cross section of 0.1 pb.

Additionally, the mass distribution of the heavy pseudoscalar A boson is shown in Figure 5.68 for the $2e$ and 2μ categories. More signal events survive from the kinematical and topological criteria of the 2 b-tag categories because this signal region with these criteria perfectly simulate a possible real signal of

the A boson. A good data/background agreement is described in the 2 b-tag category for both leptonic decay modes. Furthermore, the p_T distribution for the Z boson is also displayed in Figure 5.69 for $2e$ (left) and 2μ (right) categories as well as the p_T of the SM Higgs boson's distribution in Fig. 5.70.

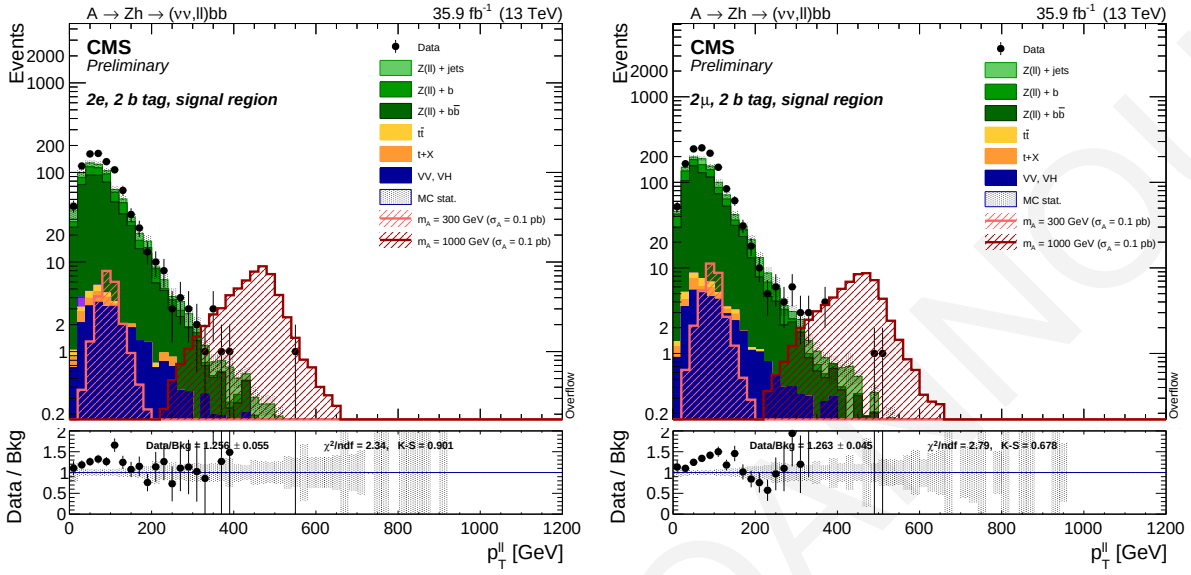

Figure 5.69: p_T of the Z candidate. The signal process is shown for the A masses (m_A = 300, 1000 GeV) with the total cross section of 0.1 pb.

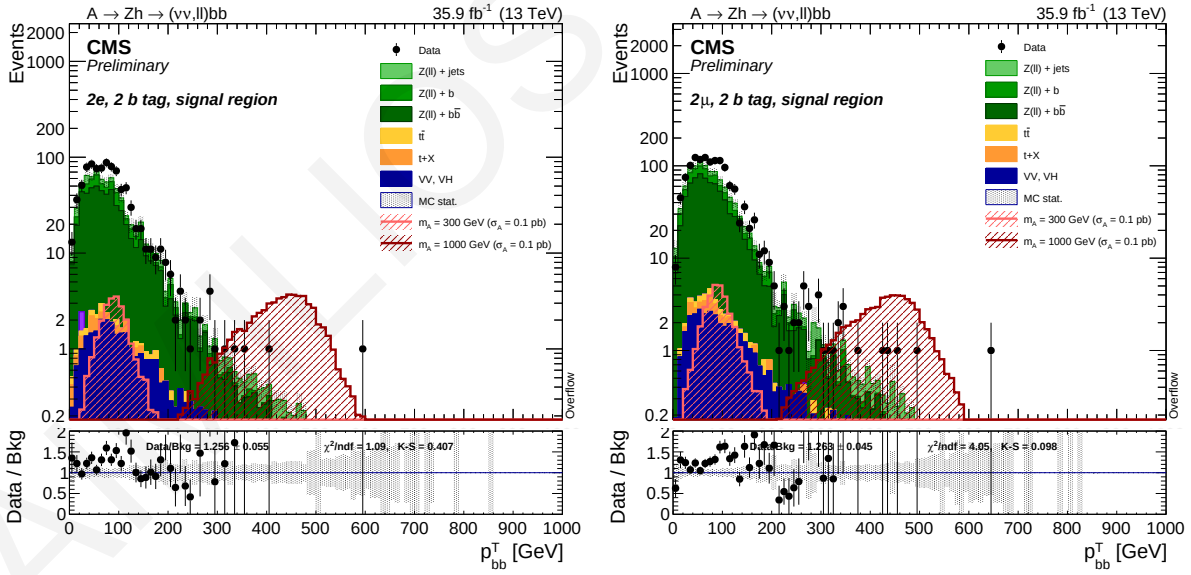

Figure 5.70: p_T of the Higgs candidate. The signal process is shown for the A masses (m_A = 300, 1000 GeV) with the total cross section of 0.1 pb.

Finally, the transverse invariant mass of the A candidate in 0ℓ category for the 2 b-tag signal region is presented in Figure 5.71 comparing it with the $\not{E}_T$ distribution. Higgs candidate's p_T and the angular

separation between the two jets, which are used for reconstructing the SM Higgs candidate, are presented in Figure 5.72. Similarly, the angular separation ranges from 0.5 to 1.5, which means that the two jets come from the Higgs decay mode because of the short distance between them.

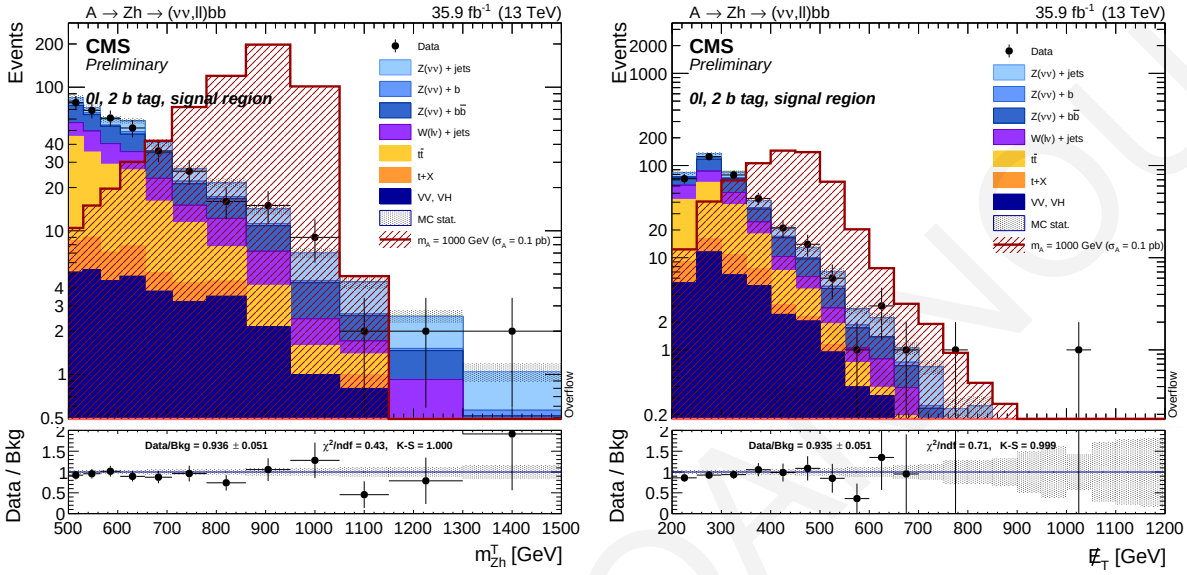

Figure 5.71: A candidate invariant transverse mass after the kinematic constraints on the di-jet pair (left), and $\not{E}_T$ (right). The signal process is shown for the A masses ($m_A = 300,\ 1000$ GeV) with the total cross section of 0.1 pb.

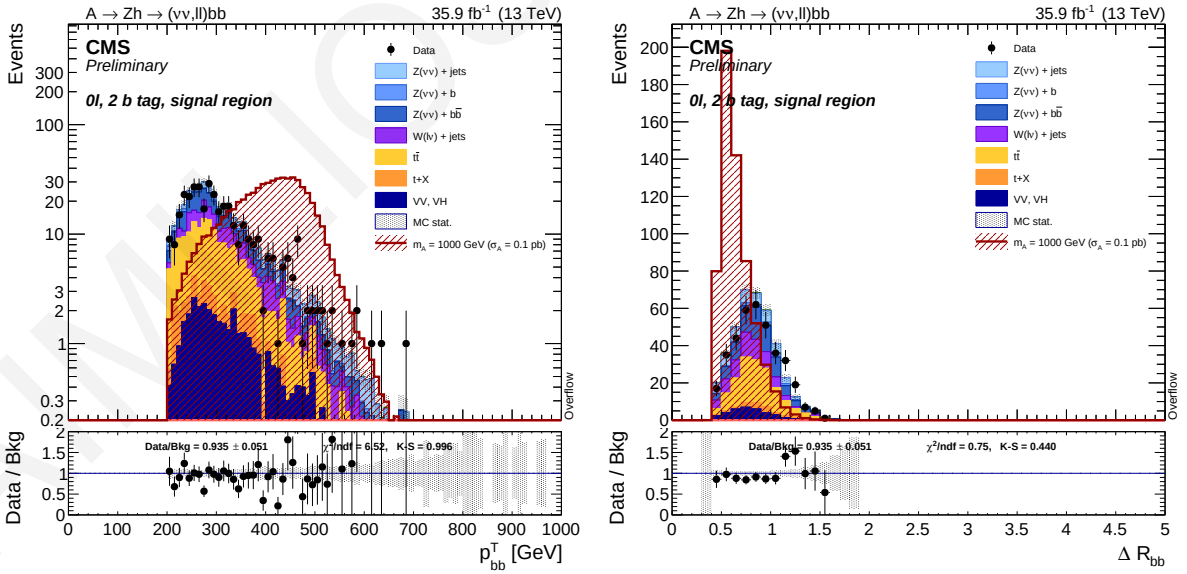

Figure 5.72: Higgs candidate p_T (left), angular separation between the two jets (right). The signal process is shown for the A masses ($m_A = 300,\ 1000$ GeV) with the total cross section of 0.1 pb.

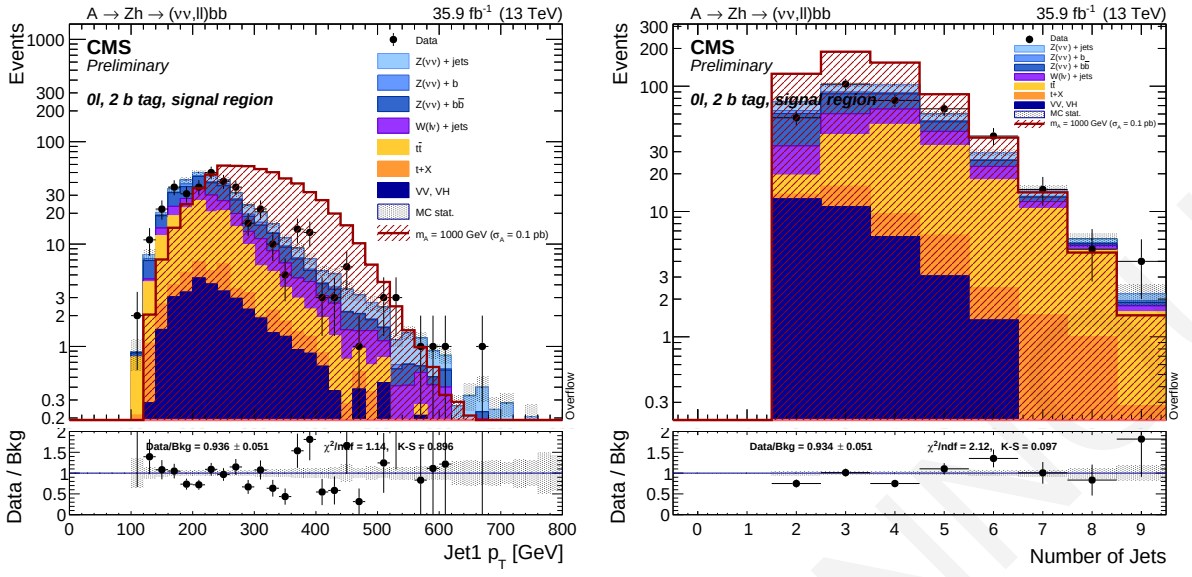

Figure 5.73: Leading jet p_T (left), jet multiplicity (right). The signal process is shown for the A masses ($m_A = 300,\ 1000$ GeV) with the total cross section of 0.1 pb.

Figure 5.73 shows the leading jet p_T distribution as well as the multiplicity of jets in data events, background, and signal samples. Overall, the data/background ratio is close to unit revealing a good description between data and MC samples for 0ℓ category in the 2 b-tag signal region.

5.6.3.3 3 B-TAG

The 3 b-tag signal region for all leptonic or non-leptonic categories is added to deal with a possible A boson signal from associated b-quark production mode. However, as shown in Chapter 5.2.1.2, a few signal events survive from detector acceptances (p_T and η), only 21% of the signal events, making difficult an observation of a heavy pseudoscalar A candidate signal peak. The situation is worsened when four b-tag signal region is required, only 2% of events could pass through geometrical acceptances and be investigated. Therefore, 4 b-tag signal region is not required in this analysis.

In the 3 b-tag signal region, due to the small statistics, the number of bins has been reduced by a factor 4, and the angular discriminator is not applied due to the large S/B ratio. In addition, a third jet CSV working point selection is required to be *medium*. All the others criteria remain the same at the rest signal regions. The requirements of the 3 b-tag signal region are reported in Table 5.31.

The remaining events after the implementation of all requirements are shown in Table 5.32. A few events reported in Table 5.32 are due to the 3 b-tag requirement as mentioned before.

Variable	0ℓ	2ℓ
Pre-selection as described in Sec. 5.6.1		
$m_{\ell^+\ell^-}$ (GeV)	-	$70 < m_{\ell^+\ell^-} < 110$ GeV
Jet1 CSV	medium	
Jet2 CSV	medium	
Jet3 CSV	medium	
$m_{b\bar{b}}$ GeV	$100 < m_{b\bar{b}} < 140$ GeV	
$\not{E}_T$ GeV	> 200 GeV	< 100 GeV
Angular LD	-	-
Event LD	-	> 0.5

Table 5.31: Cuts for the 3 b-tag signal regions.

	0ℓ	$2e$	2μ
Data	34	52	77
DYJetsToLL-0b	0	5.59	9.84
DYJetsToLL-1b	0	4.48	8.91
DYJetsToLL-2b	0	19.15	23.61
DYJetsToNuNu-0b	1.29	0	0
DYJetsToNuNu-1b	0.22	0	0
DYJetsToNuNu-2b	1.55	0	0
ST	1.99	0	0
TTbarDL	1.32	9.32	12.2
TTbarSL	17.19	0.34	0.81
VV	0.59	1.59	1.91
WJetsToLNu	1.45	0	0
BkgSum	25.6	40.48	57.27

Table 5.32: Number of data events and expected events for the various SM processes in the 3 b-tag signal regions.

Figure 5.74 shows the four-body invariant mass of A candidate after the kinematic constraints. Few events are highlighted in plots due to the small statistics.

Finally, the invariant transverse mass of A candidate after the kinematic constraints is displayed in Figure 5.75 as well as the $\not{E}_T$ distribution.

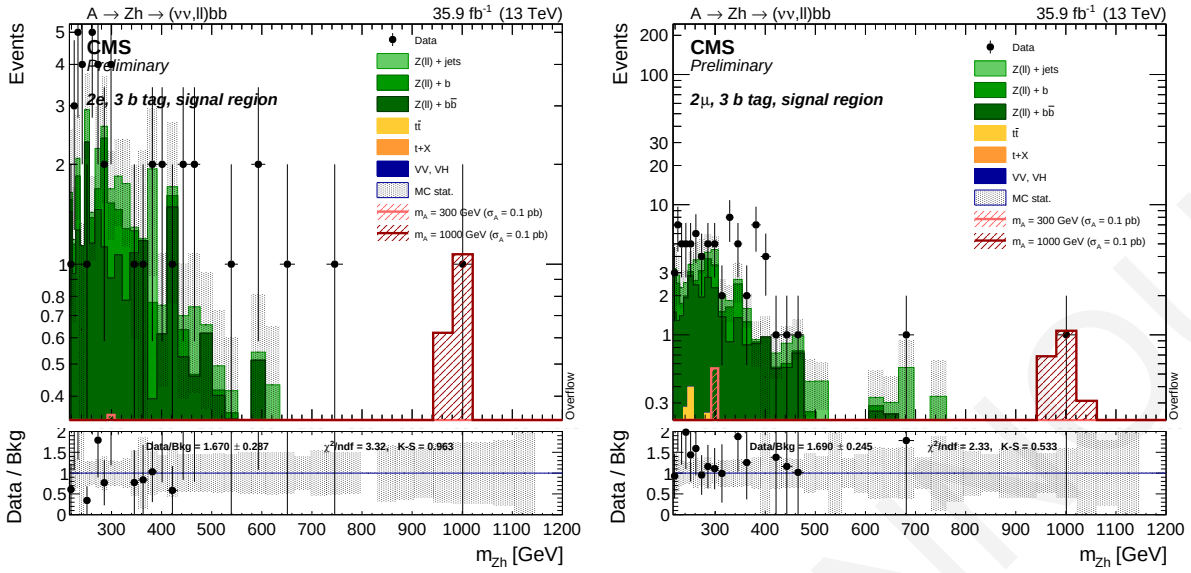

Figure 5.74: Four-body invariant mass after the kinematic constraints. The signal process is shown for the A masses ($m_A = 300,\ 1000$ GeV) with the total cross section of 0.1 pb.

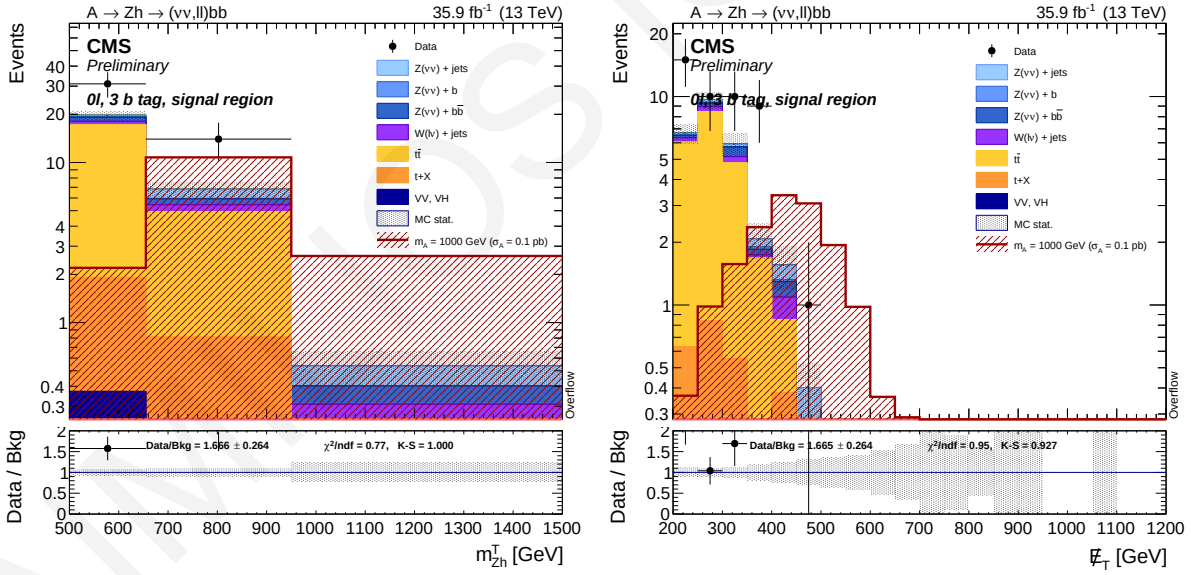

Figure 5.75: A candidate invariant transverse mass after the kinematic constraints on the di-jet pair (left), and $\not{E}_T$ (right). The signal process is shown for the A masses ($m_A = 300,\ 1000$ GeV) with the total cross section of 0.1 pb.

5.7 CONTROL REGIONS

As shown in the previous section, the most important background sources for the signal are: $Z + b\bar{b}$, $Z + b$, $Z + jets$ and $t\bar{t}$[2]. A control region for each of these background sources has been defined in order to check and validate the Monte Carlo prediction for both normalisation and shape. These control regions are used to constrain the main backgrounds normalisation in the final fit.

As mentioned, a control region is defined at the area where events fall in di-jet mass *sidebands* ($m_{b\bar{b}}$ < 100 GeV or $m_{b\bar{b}}$ > 140 GeV). Events with di-jet mass less than 100 GeV or greater than 140 GeV fall in sidebands, determining the control region.

5.7.1 Z+JETS

The contribution of Z plus light jets to the signal region is due to a mistag rate. Requiring two *Medium* b-tagged jets in the final state, the mistag probability is around $\approx 10^{-2} \cdot 10^{-2} \approx 10^{-4}$. However, the large cross section of Z plus light jets is such that some events survive in the signal region. Table 5.33 reports the kinematic cuts for the $Z + jets$ control region. As shown, the invariant mass of di-jets is required to be less than 100 GeV or greater than 140 GeV, ruling out the probability of events to fall in the signal region.

Variable	0ℓ	2ℓ
Pre-selection as described in Sec. 5.6.1		
$m_{\ell^+\ell^-}$ (GeV)	-	$70 < m_{\ell^+\ell^-} < 110$ GeV
Jet1 CSV	!medium	
Jet2 CSV	!medium	
$m_{b\bar{b}}$ (GeV)	$m_{b\bar{b}} < 100$, $m_{b\bar{b}} > 140$ GeV	
p_T^H (GeV)	> 200 GeV	-
$\not{E}_T$ (GeV)	> 200 GeV	< 100 GeV
Angular LD	-	> 0.5
Event LD	-	> 0.5

Table 5.33: Cuts for the Z+jets control region.

After applying the selections for Z+jets control region, survived events of data and background sources are recorded in Table 5.34. Data events are comparable with the sum of all background sources for each leptonic or non-leptonic category.

[2]In simulation, the number of b-jets is calculated after the reconstruction and selection of the two jets, by looking at flavour of the hadron associated to the jets via the $hadronFlavour()$ method.

	0ℓ	$2e$	2μ
Data	37828	142620	194085
DYJetsToLL-0b	140.17	142748.21	190369.17
DYJetsToLL-1b	0.26	3043.5	3902.77
DYJetsToLL-2b	0.43	870.44	1145.34
DYJetsToNuNu-0b	23397.57	0	0
DYJetsToNuNu-1b	214.1	0	0
DYJetsToNuNu-2b	81.47	0	0
ST	141.22	23.66	31.4
TTbarDL	34.42	285.75	376.82
TTbarSL	536.35	14.23	33.54
VV	1330.72	2105.96	2753.83
WJetsToLNu	11752.34	28.85	49.31
BkgSum	37629.05	149120.6	198662.18

Table 5.34: Number of data events and expected events for the various SM processes in the Z+jets control region.

Figure 5.76 displays the invariant (transverse) mass of A candidate and Figure 5.77 presents the spectrum of the transverse momentum of the Z boson candidate. Background samples describe perfectly the real data in the Z+jets control region for the three categories. As shown, the distribution is a smooth SM background continuum.

Figure 5.78 shows the mass distribution of the Z boson candidate for the $2e$ and 2μ categories. A good data/background agreement for both categories is observable, ensuring a perfect description of real data. It is important that background and data samples represent correctly the Z boson mass in order to build a confidence of correctness in the samples.

The absence of the signal area ($100 < m_{b\bar{b}} < 140$ GeV) is presented in Figure 5.79. The plots show the Higgs mass distribution where events with di-jet mass do not fall in the signal region.

Figure 5.81 presents the distance between two jets which are used to reconstruct the Higgs candidate. $\Delta\phi$ is shown on the left plots and ΔR variable is presented on the right plots. There is a peak in the SM background continuum at 0.5, which means that the distance between them is short.

Leading and/or sub-leading leptons' p_T, transverse momentum of jets for the 0ℓ and $2e$ or 2μ leptonic categories are shown in Fig. 5.82, 5.83, and 5.84.

Figure 5.85 shows the CSVv2 variable for the leading and sub-leading jet. As mentioned, there is no constrain on the CSVv2 variable in the Z+jet control region and jets can range from loose to tight working point selection as shown in the figure.

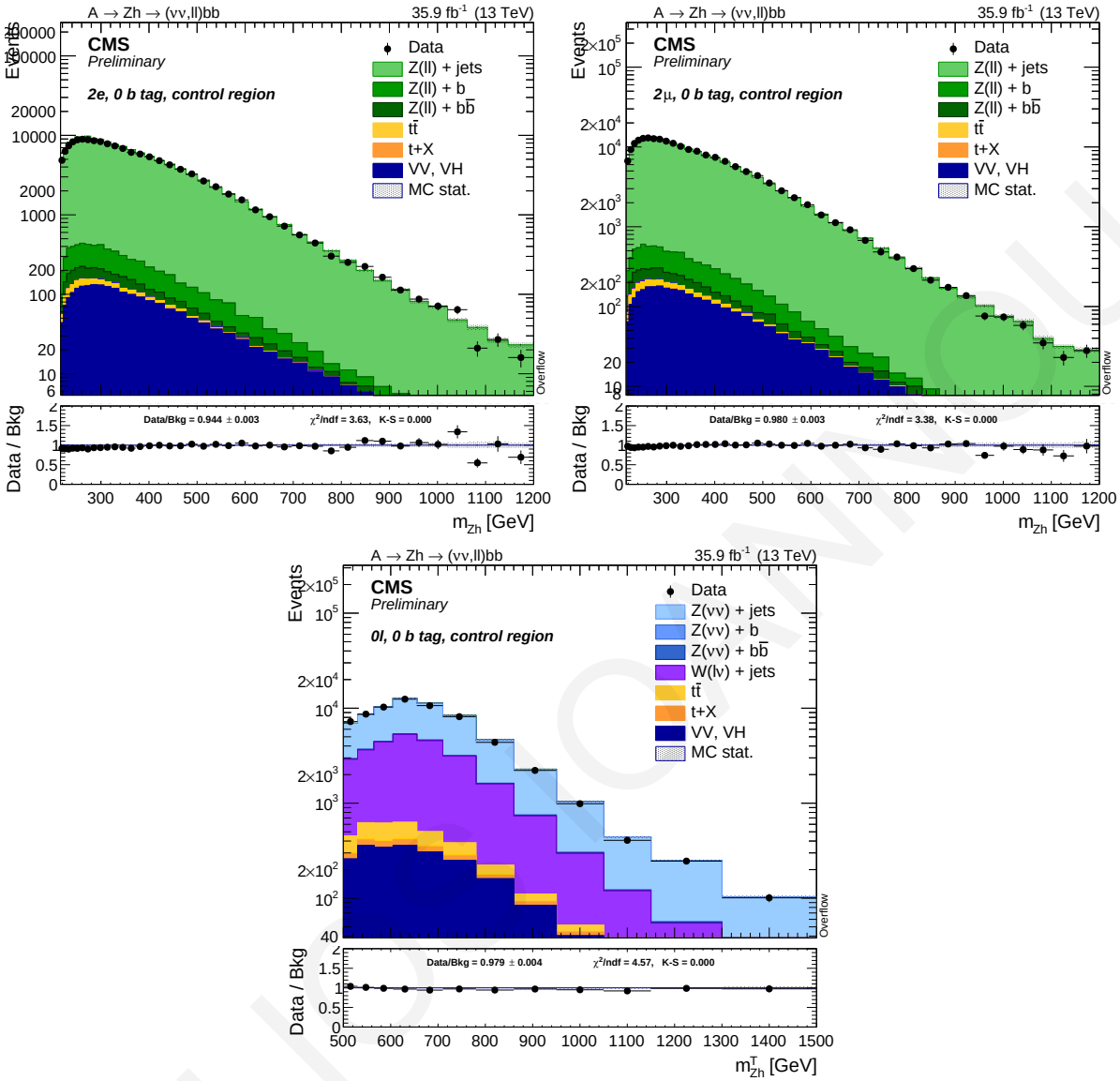

Figure 5.76: 4-body invariant (transverse) mass in the Z+jets control region for $2e$ (top left), for 2μ (top right), and for 0ℓ (bottom).

$\not{E}_T$ distribution is perfectly presented in Fig. 5.86 for 0ℓ, 2μ, and $2e$ categories. The leptonic categories ($2e$ and 2μ) are not described by a large MET as shown by their distributions, however, for the non-leptonic category (0ℓ) where the Z boson candidate decays into a pair of neutrinos, its events are described by very large $\not{E}_T$.

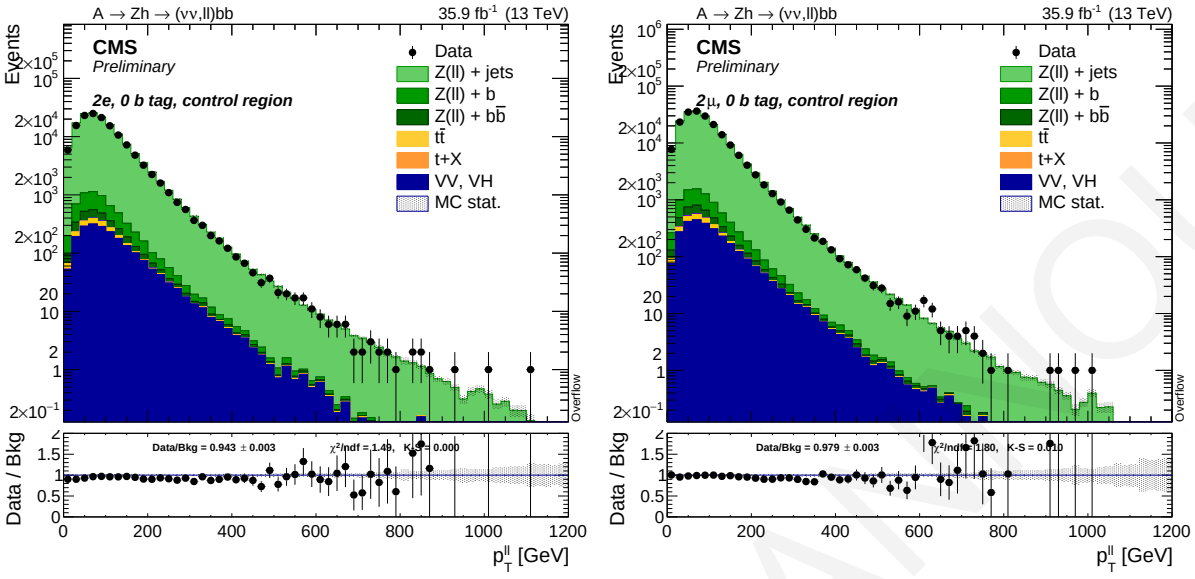

Figure 5.77: p_T spectrum of the Z boson candidate.

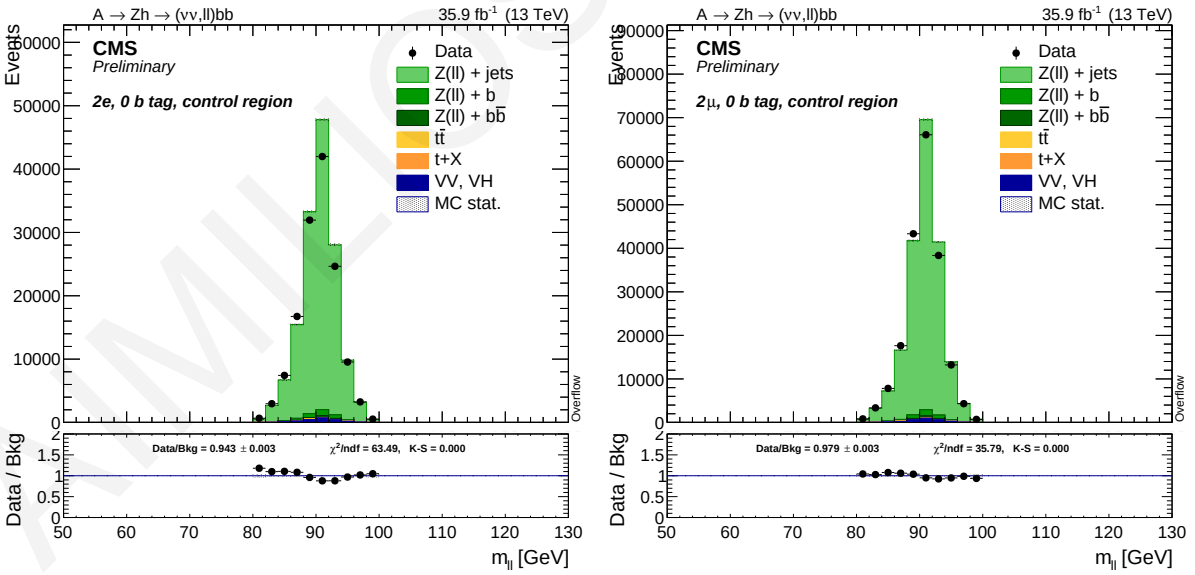

Figure 5.78: The distribution of the $Z \to e^+e^-$ (left) and $Z \to \mu^+\mu^-$ (right) mass.

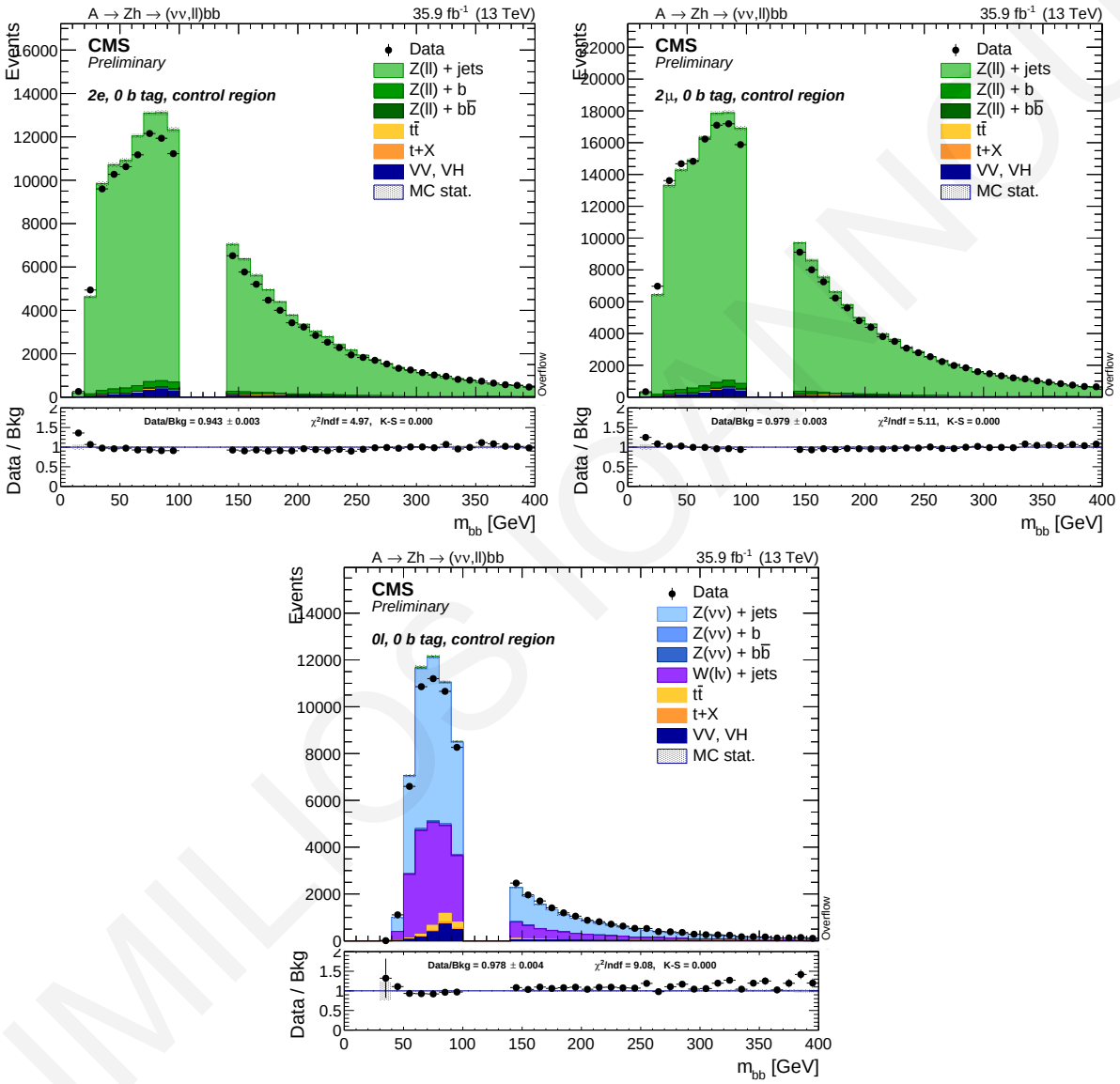

Figure 5.79: Mass of the Higgs boson candidate for the three categories.

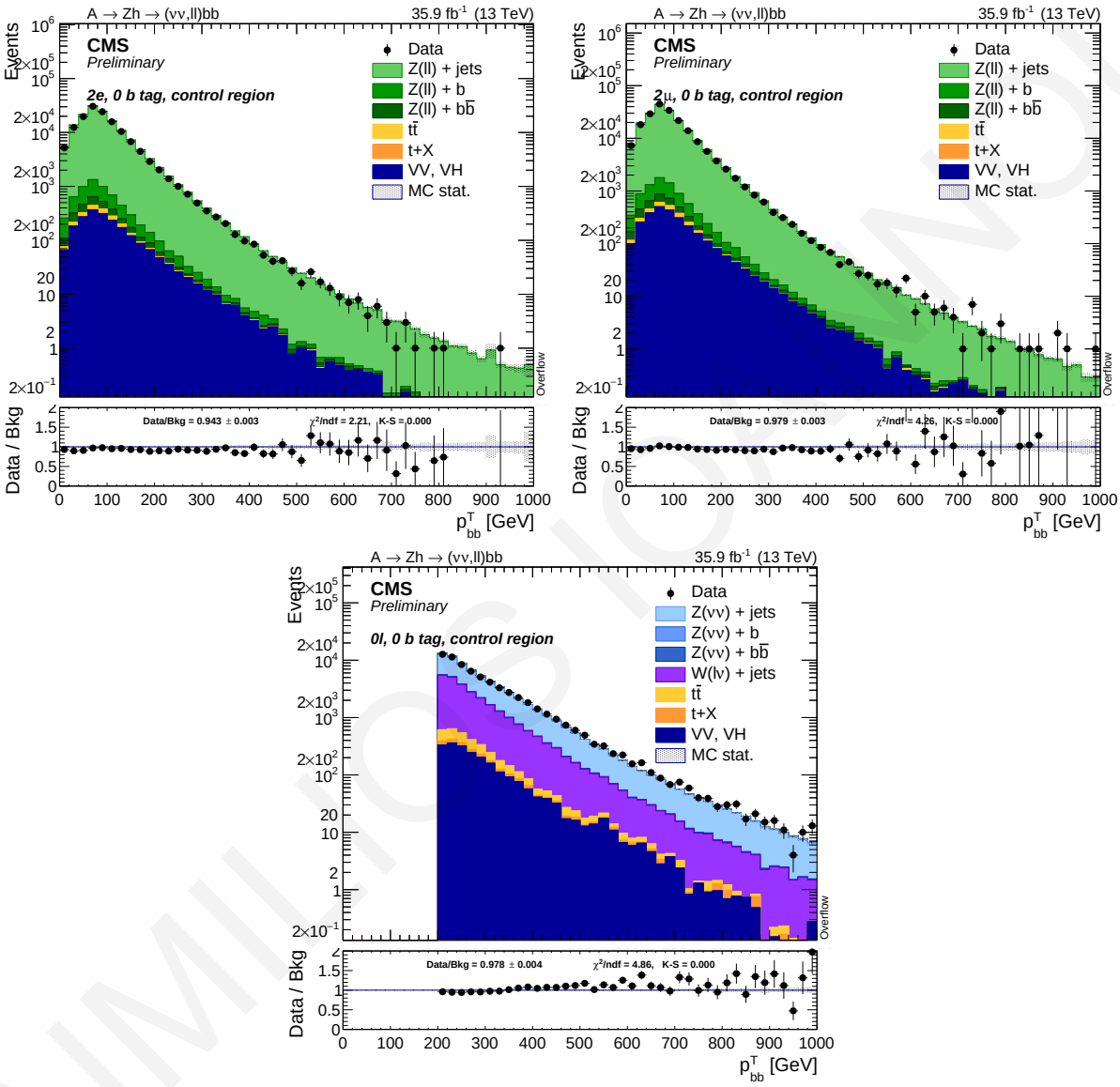

Figure 5.80: p_T of the Higgs boson candidate.

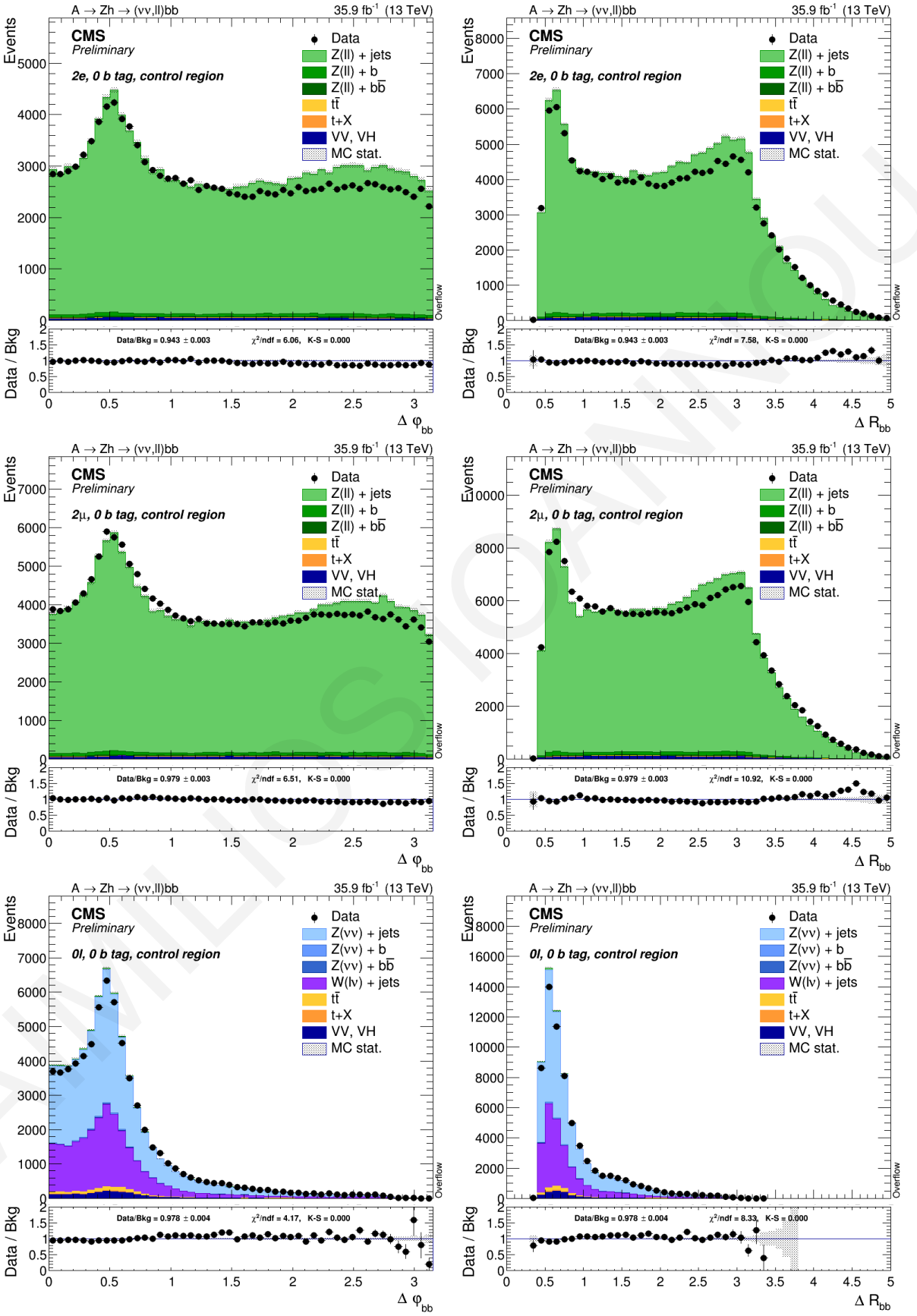

Figure 5.81: $\Delta\phi$ (left) and ΔR (right) between the two jets used to reconstruct the Higgs candidate.

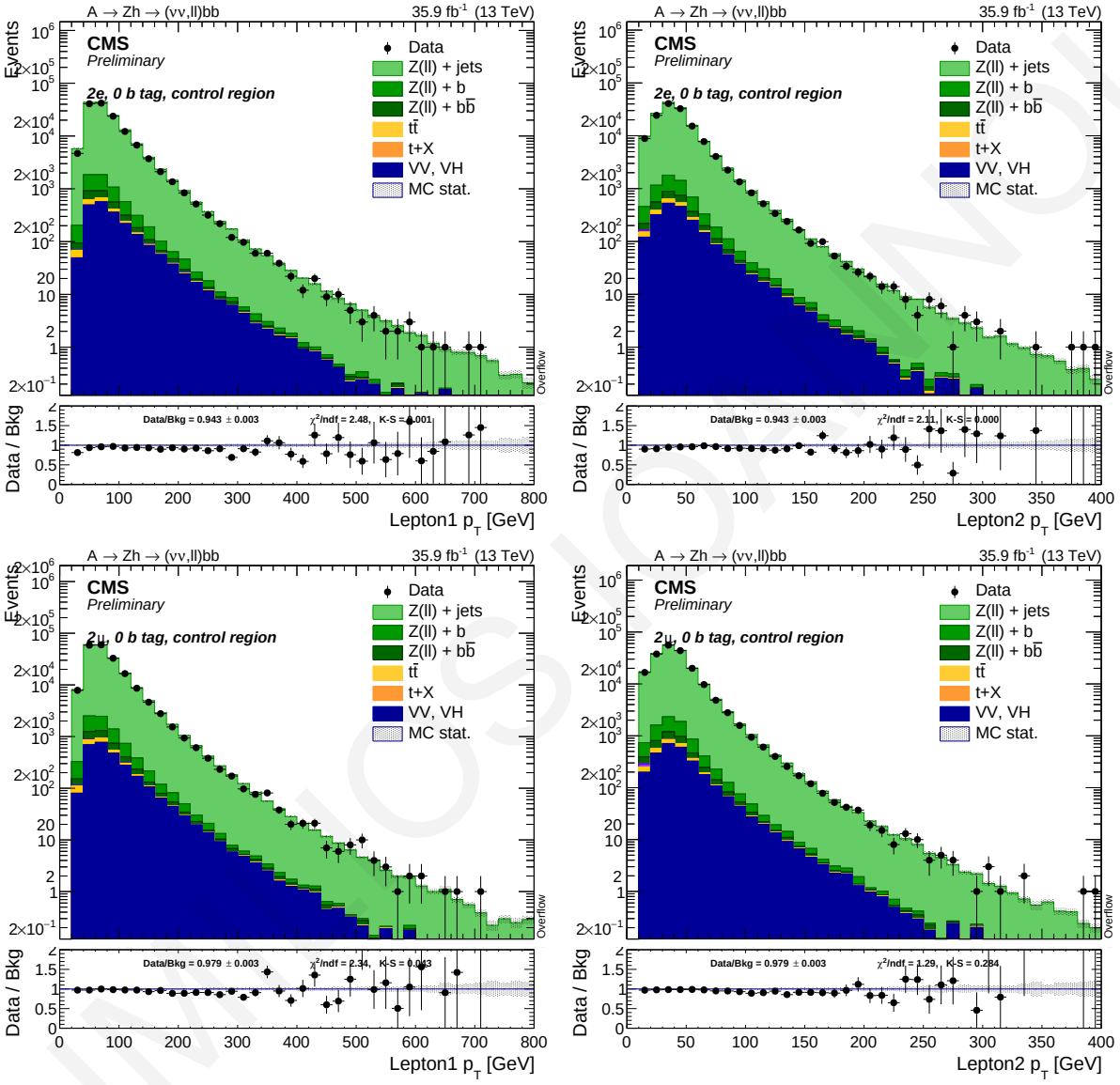

Figure 5.82: p_T distribution for the leading (left) and sub-leading (right) lepton in the event, for $Z \to e^+e^-$ (top) and $Z \to \mu^+\mu^-$ (bottom).

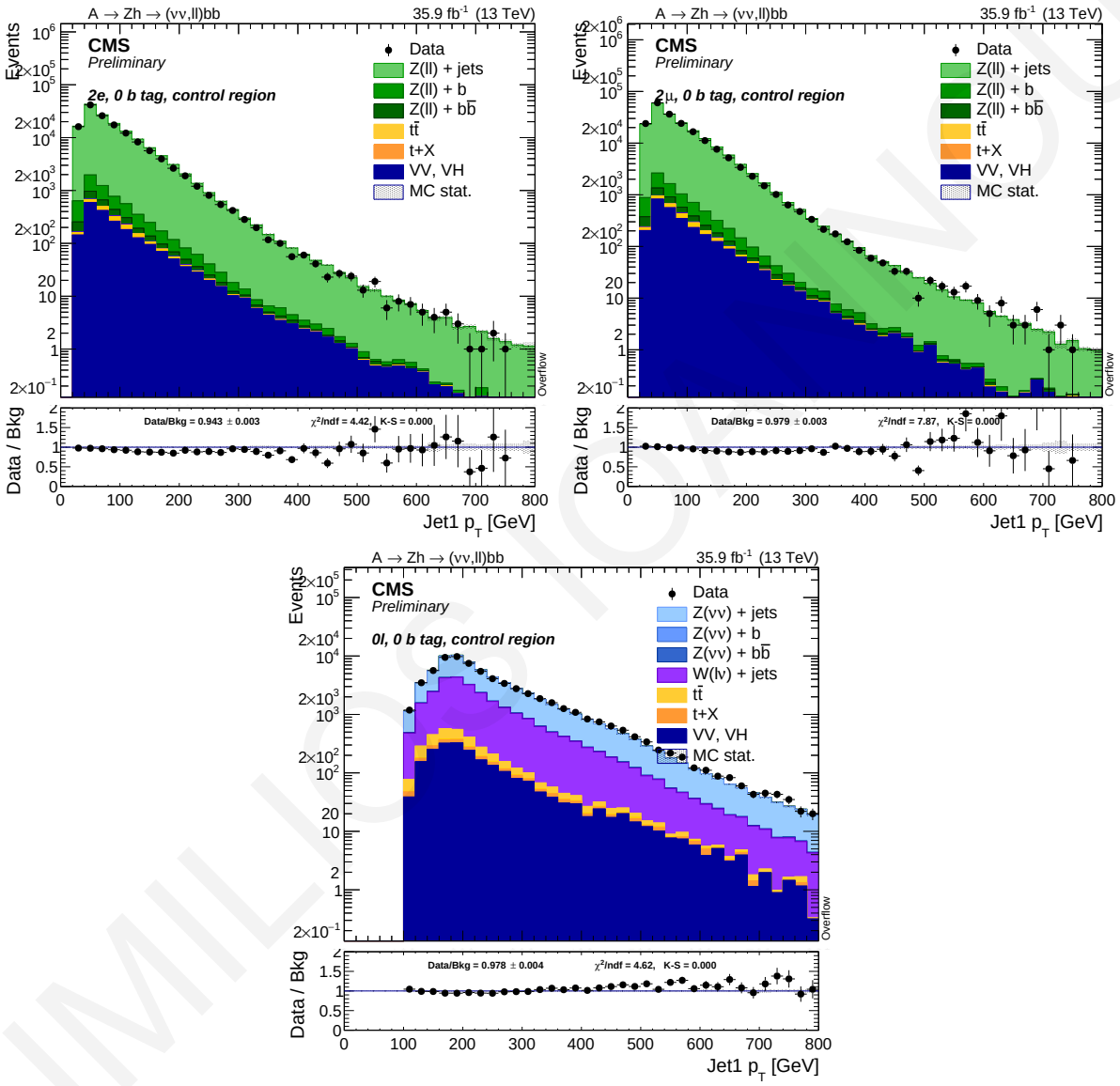

Figure 5.83: p_T distribution for the leading jet in the event.

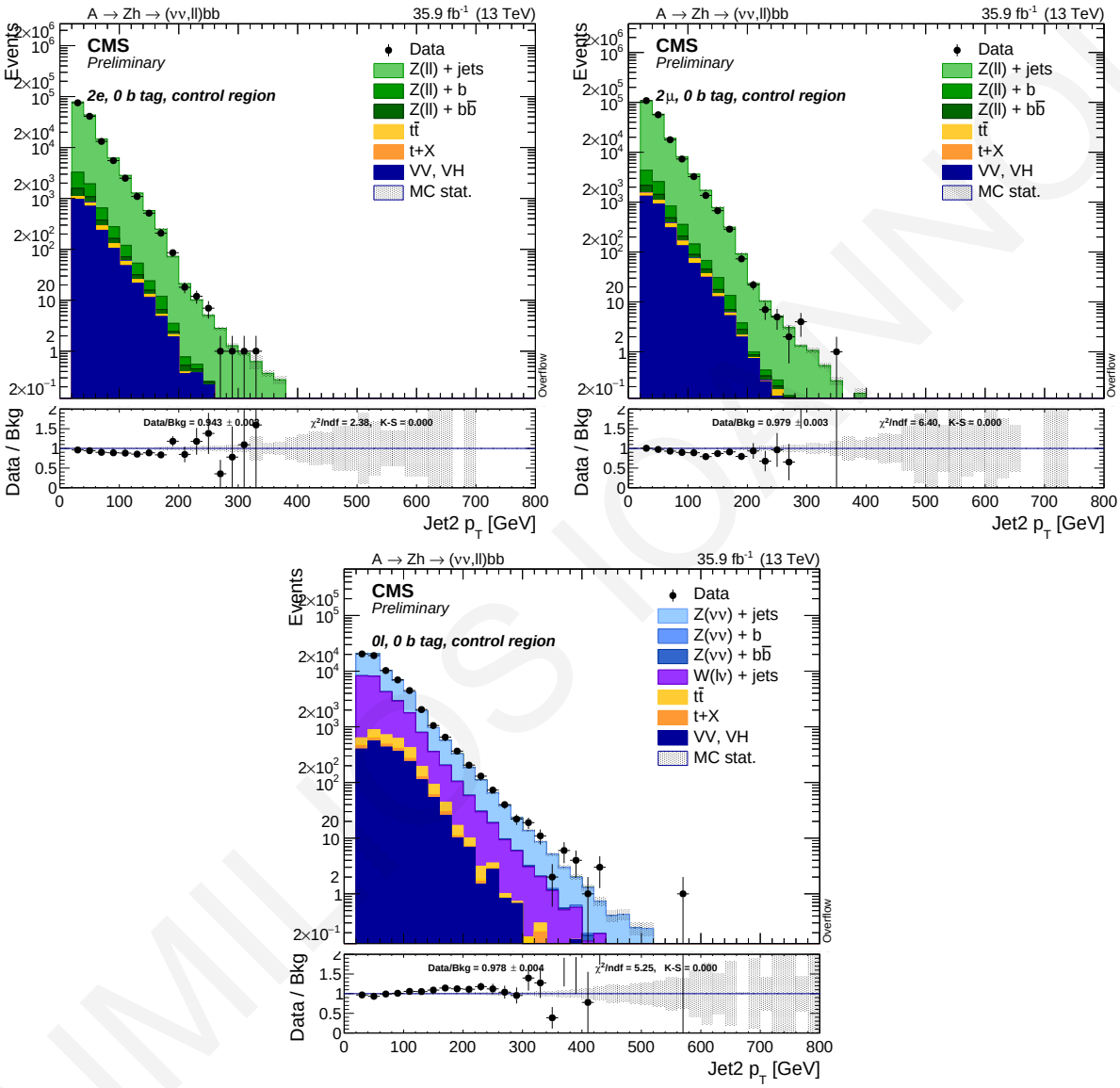

Figure 5.84: p_T distribution for the sub-leading jet in the event.

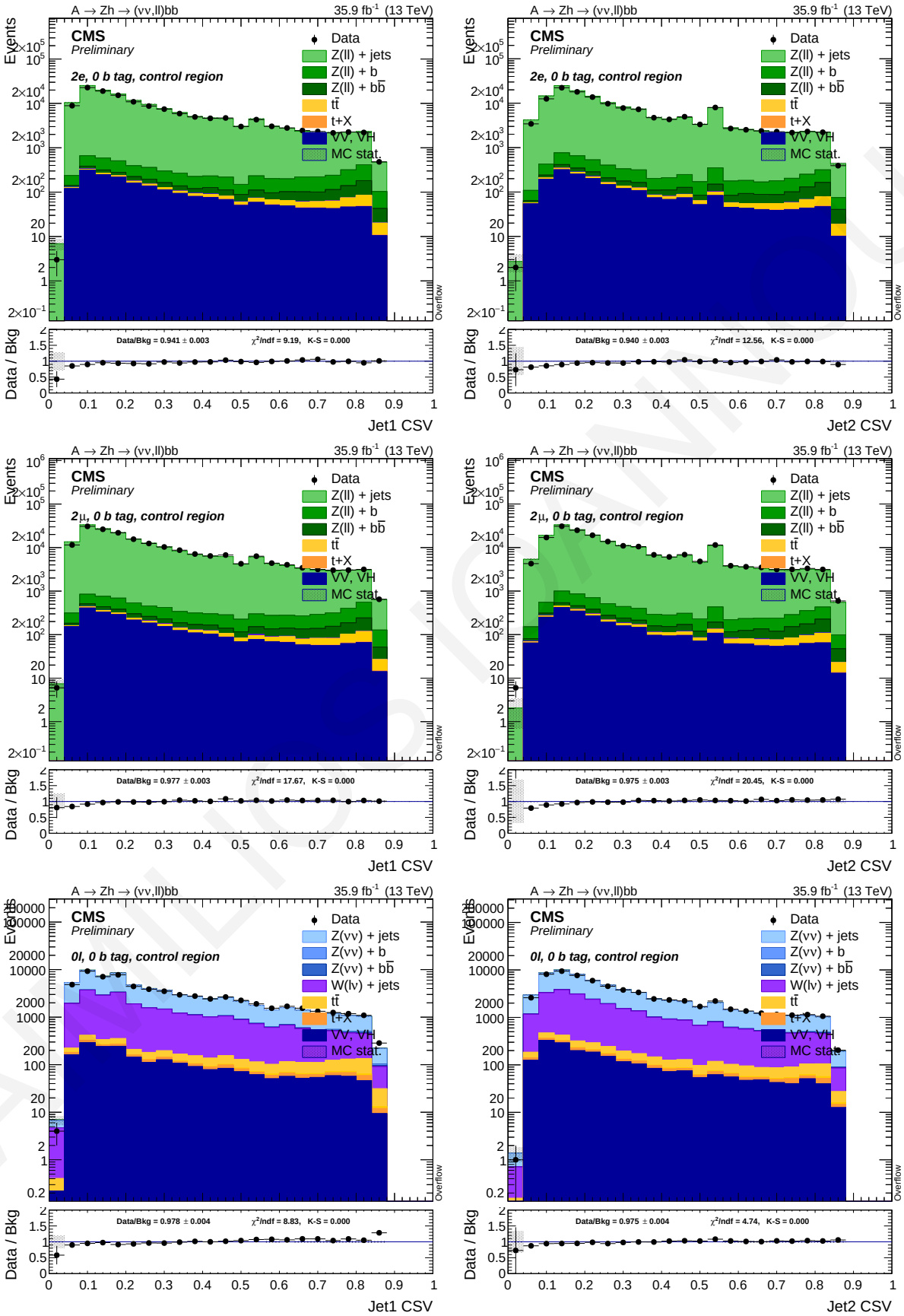

Figure 5.85: CSVv2 distribution for the leading (left) and sub-leading (right) jet in the event, for $Z \to e^+e^-$ (top), $Z \to \mu^+\mu^-$ (middle), and $Z \to \nu\bar{\nu}$ (bottom).

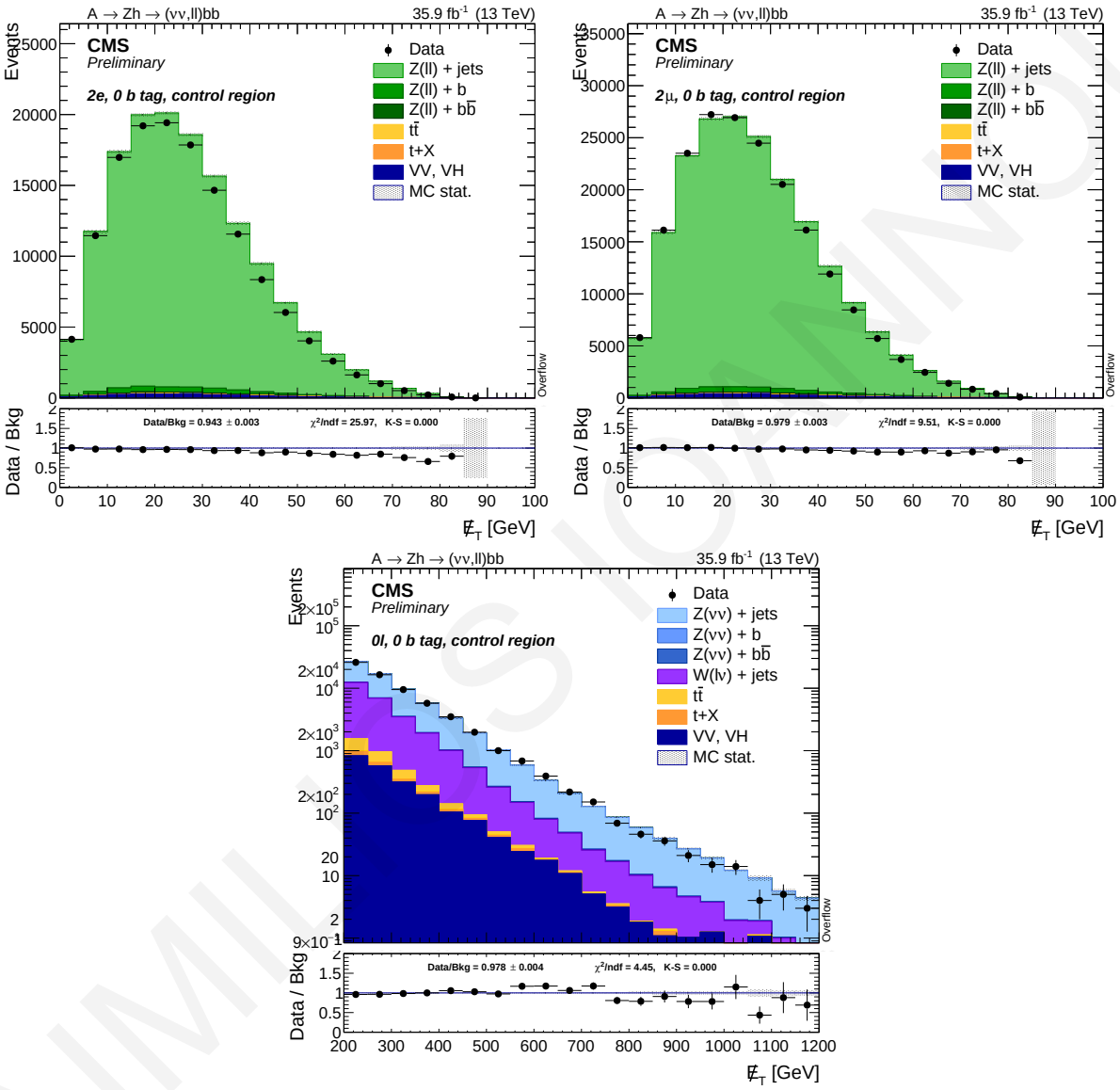

Figure 5.86: $\not{E}_T$ distribution for $2e$ (top left), 2μ (top right), and 0ℓ category (bottom) category.

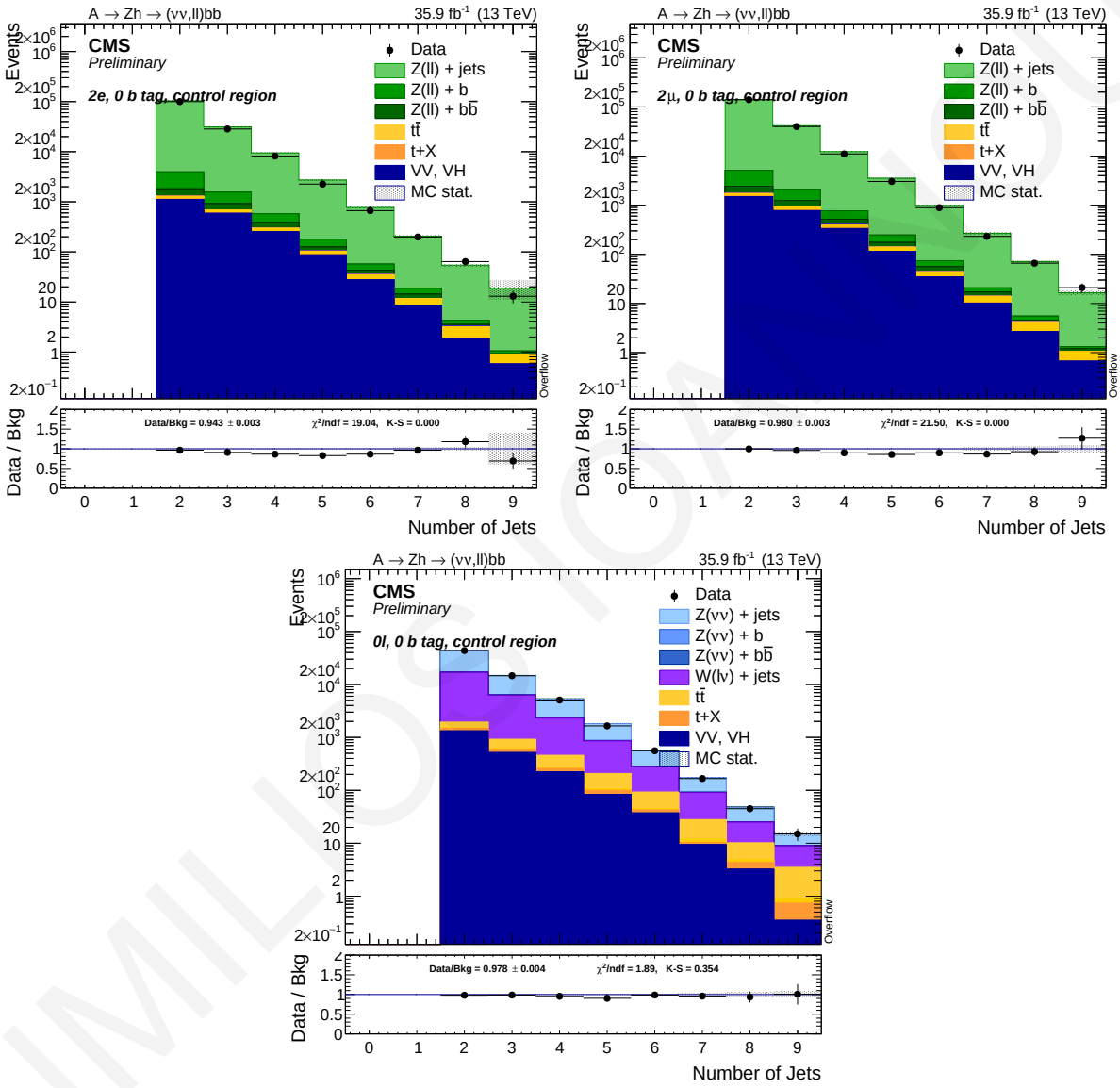

Figure 5.87: Number of jets with $p_T > 30$ GeV, regardless of the b-tagging status.

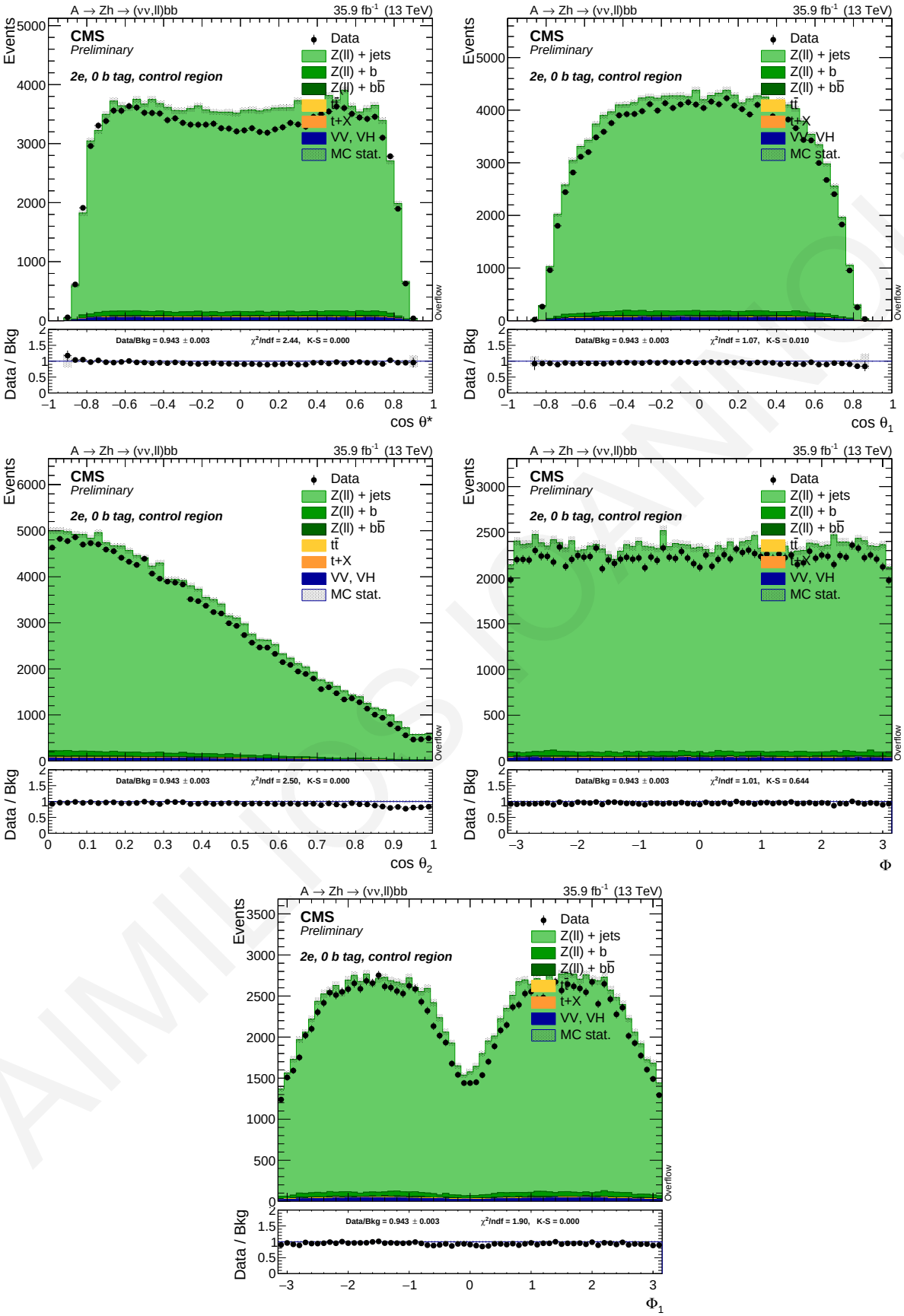

Figure 5.88: $\cos\theta^*$, $\cos\theta_1$, $cos\theta_2$, Φ, and Φ_1 distributions are shown for the $Z \to e^+e^-$ decay mode. These variables are described in Chapter 5.5.2.1.

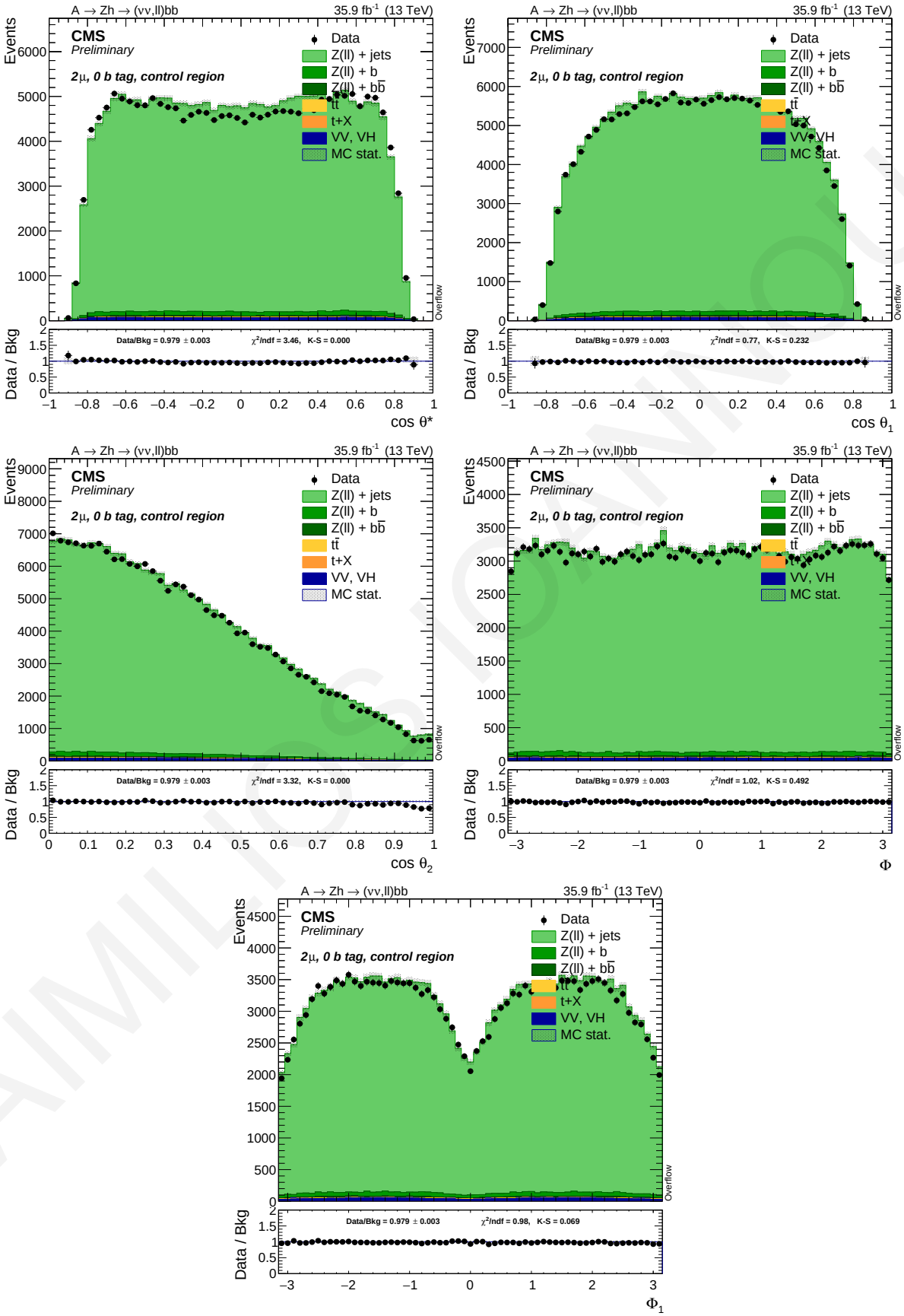

Figure 5.89: $\cos\theta^*$, $\cos\theta_1$, $cos\theta_2$, Φ, and Φ_1 distributions are shown for the $Z \to \mu^+\mu^-$ decay mode. These variables are described in Chapter 5.5.2.1.

5.7.2 Z+b

The second control region is meant to maximise the Z plus one b events. With respect to the Z+jets control region described before, there is the addition of the b-tagging requirement on the first jet; to make this region orthogonal with the $Z + b\bar{b}$ one, an anti b-tagging (*medium*) is applied to the second jet. Since with b-tagging the signal contamination in this region is no more negligible, a veto on the $m_{b\bar{b}}$ mass is applied, thus selecting events outside the Higgs mass window.

The data/MC agreement is shown for the A candidate (transverse) mass (Fig. 5.90), the Z p_T and mass (Fig. 5.91), $\not{E}_T$ (Fig. 5.92), Higgs candidate mass and p_T (Fig. 5.93), and the *Centrality* and jet multiplicity variables (Fig. 5.94).

Variable	0ℓ	2ℓ
Pre-selection as described in Sec. 5.6.1		
$m_{\ell^+\ell^-}$ (GeV)	-	$70 < m_{\ell^+\ell^-} < 110$ GeV
Jet1 CSV	medium	
Jet2 CSV	!medium	
$m_{b\bar{b}}$ (GeV)	$m_{b\bar{b}} < 100$, $m_{b\bar{b}} > 140$ GeV	
p_T^H (GeV)	> 200 GeV	-
$\not{E}_T$ (GeV)	> 200 GeV	< 100 GeV
Angular LD	-	> 0.5
Event LD	-	> 0.5

Table 5.35: Cuts for the Z+b control region.

This control region has more or less the same contribution from Z plus two b-partons, Z plus one b-parton and Z plus light partons, and a very small contamination of $t\bar{t}$.

	0ℓ	$2e$	2μ
Data	4818	17338	70955
DYJetsToLL-0b	8.79	7930.17	28721.38
DYJetsToLL-1b	1.7	5052.24	18215.13
DYJetsToLL-2b	0.88	2450.03	7560.06
DYJetsToNuNu-0b	1770.74	0	0
DYJetsToNuNu-1b	326.65	0	0
DYJetsToNuNu-2b	270.63	0	0
ST	108.75	38.94	528.04
TTbarDL	54.54	862.45	9575.14
TTbarSL	631.6	25.12	448.66
VV	205.69	321.92	1011.69
WJetsToLNu	1044.94	4.69	63.66
BkgSum	4424.91	16685.56	66123.76

Table 5.36: Number of data events and expected events for the various SM processes in the Z+b control region.

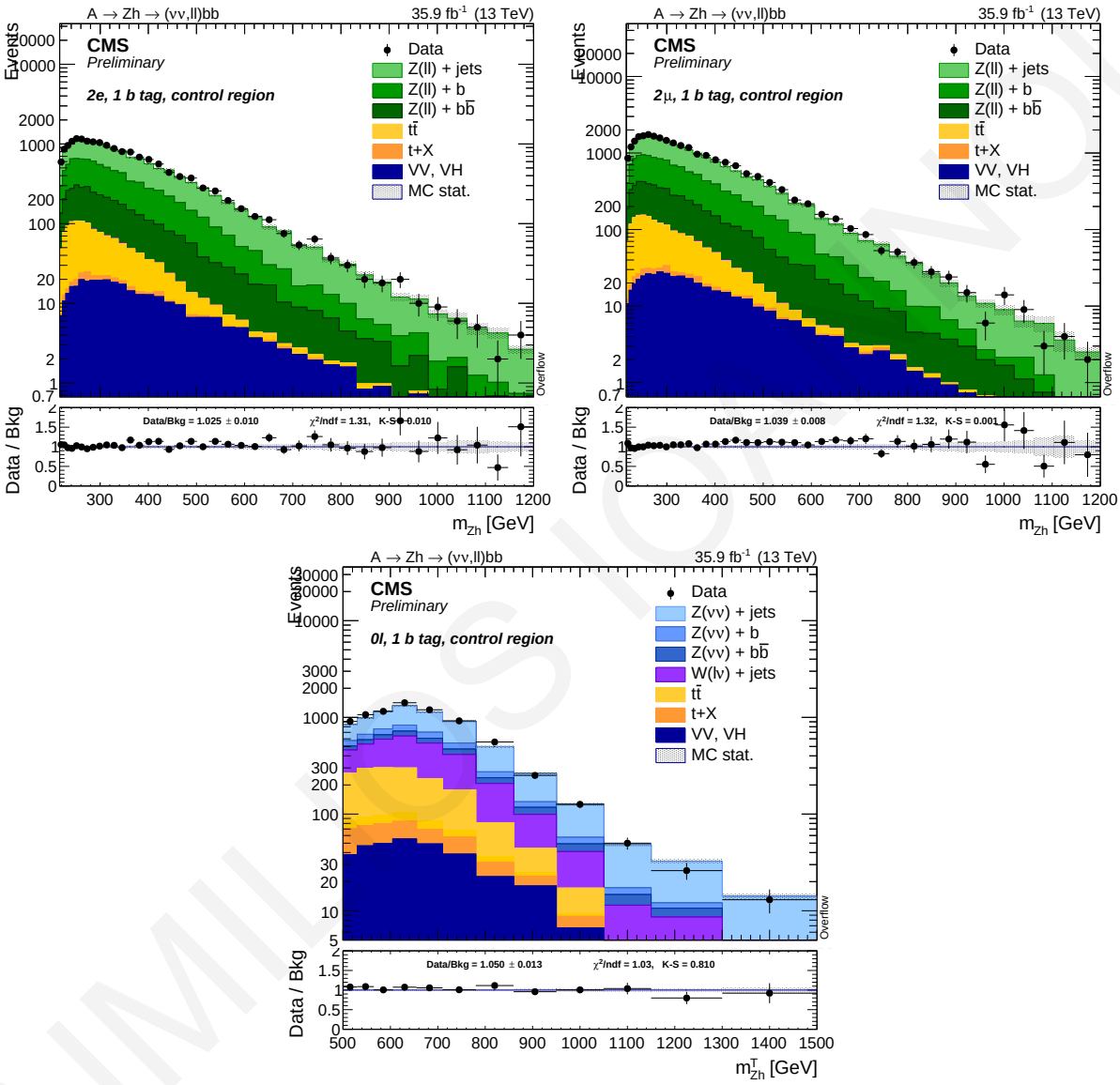

Figure 5.90: 4-body invariant (transverse) mass in the Z+b control region.

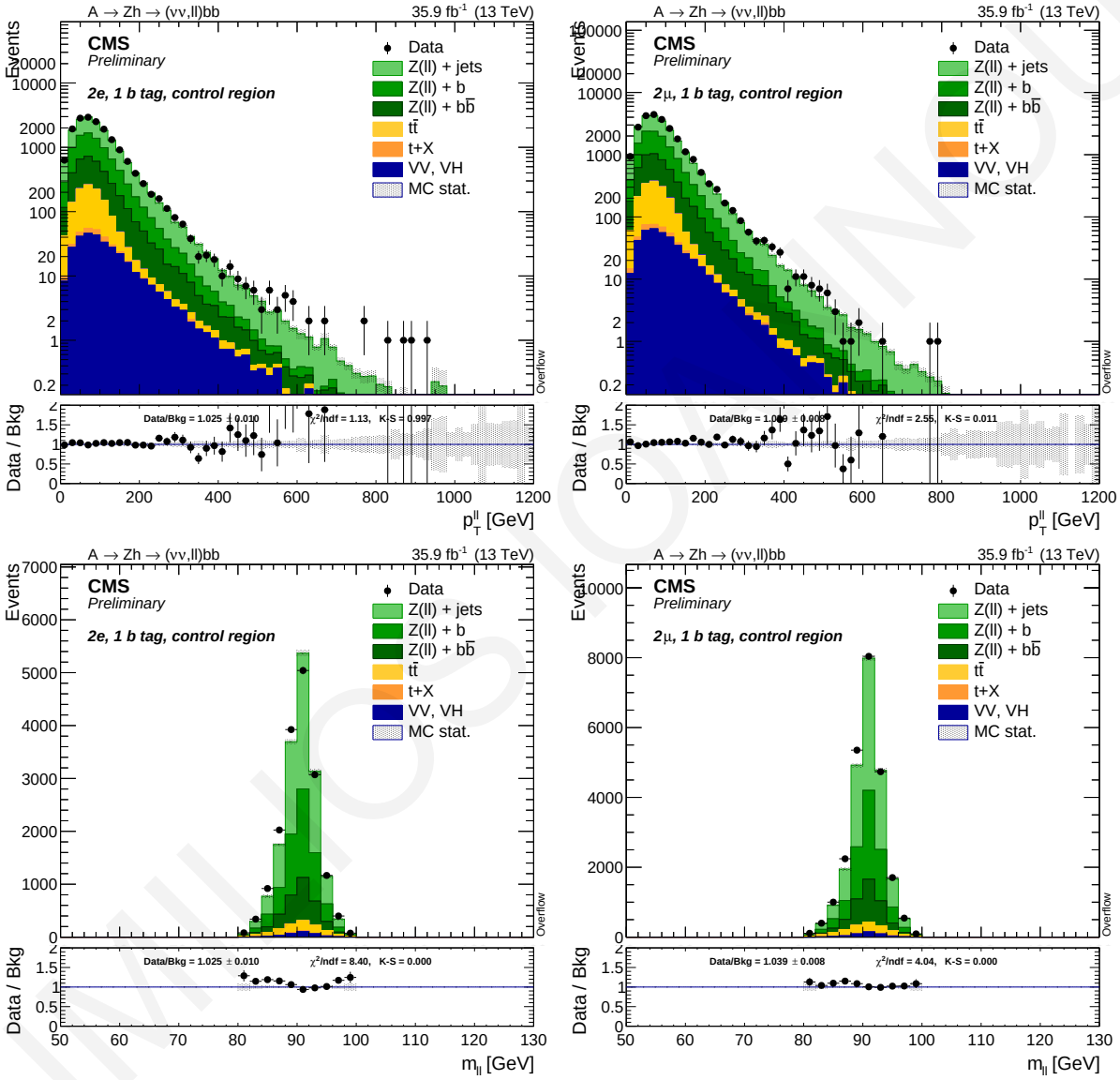

Figure 5.91: p_T spectrum (top) and mass (bottom) of the Z boson candidate.

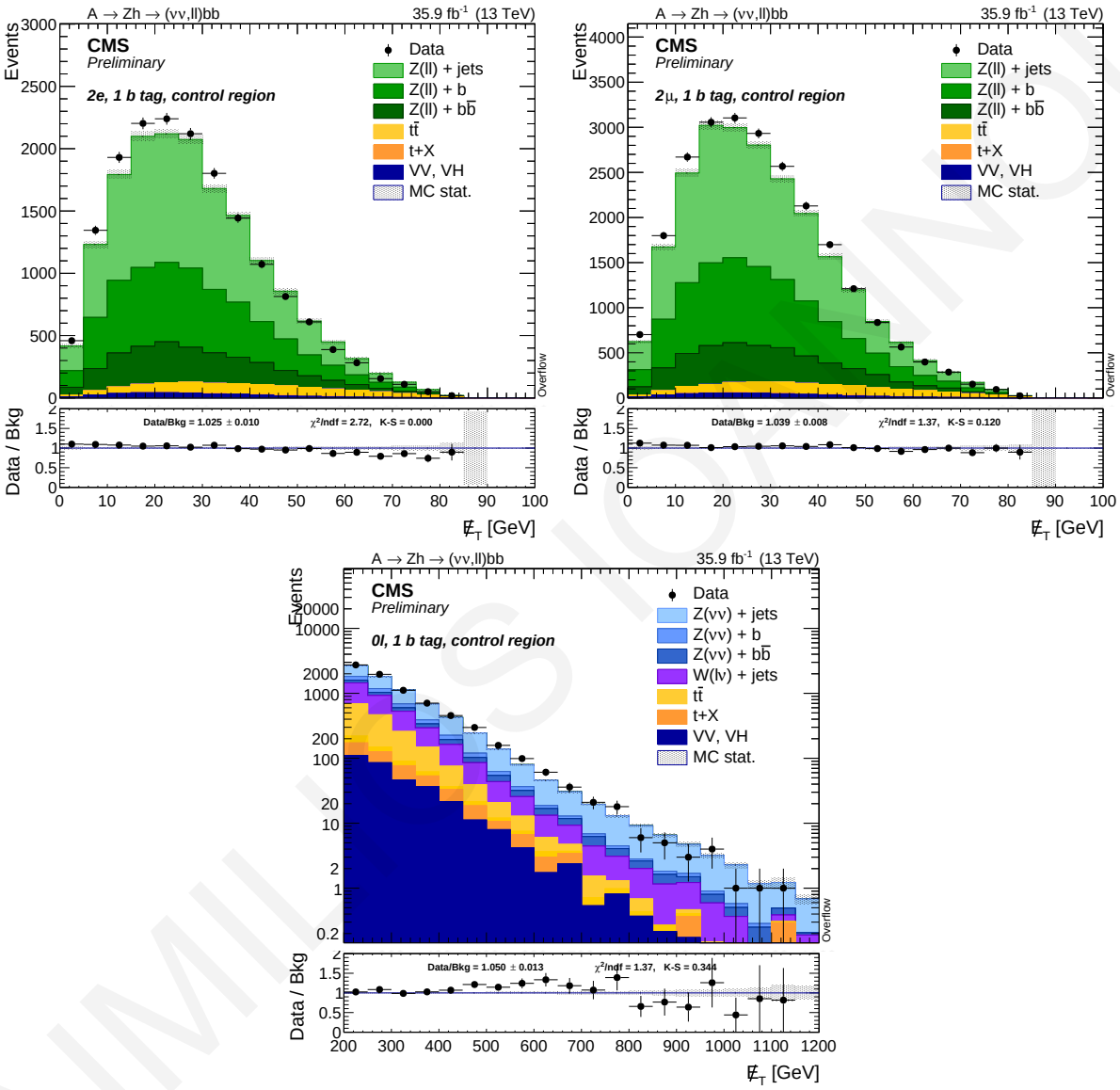

Figure 5.92: Missing energy spectra.

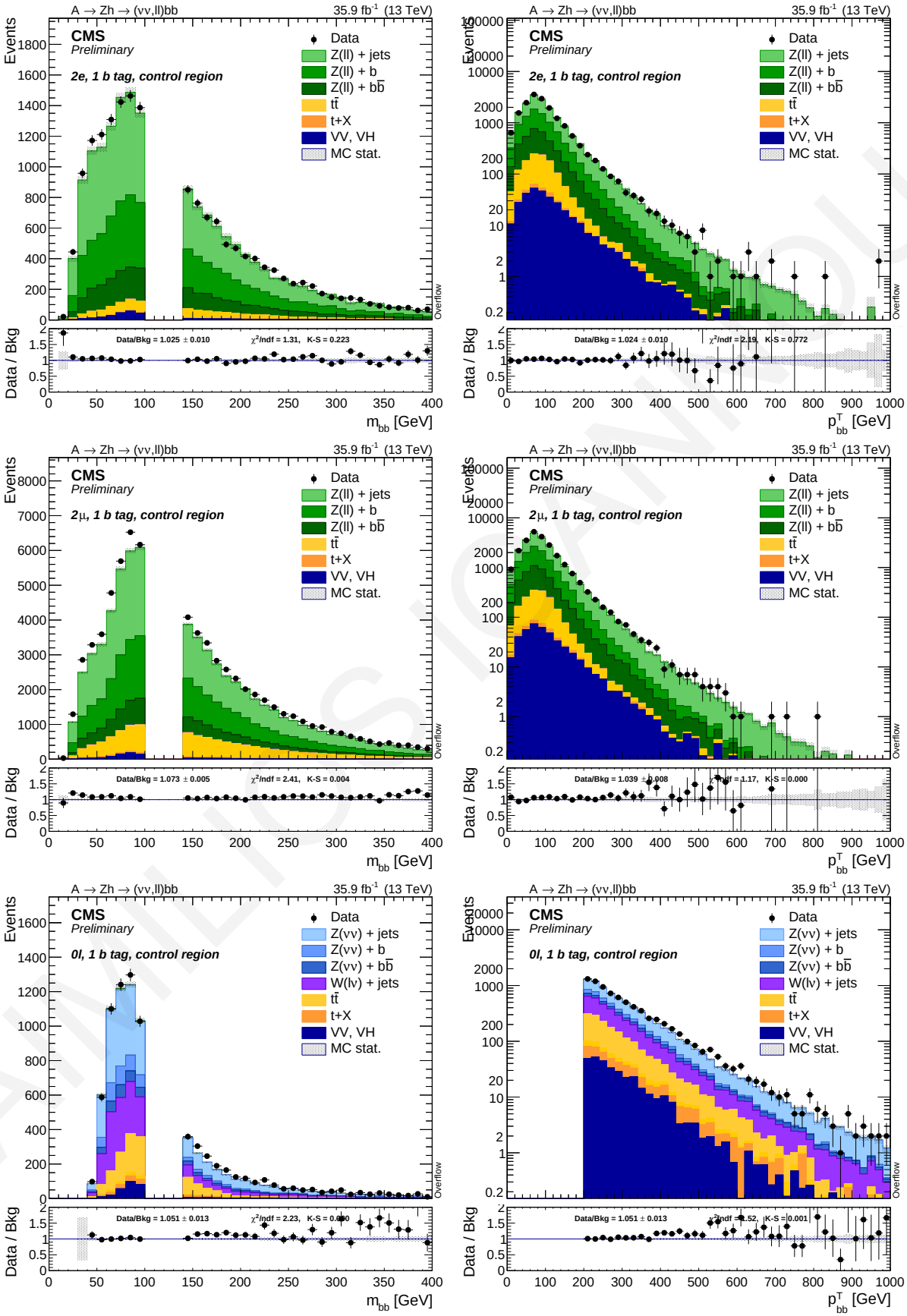

Figure 5.93: Mass (left) and p_T (right) of the Higgs boson candidate.

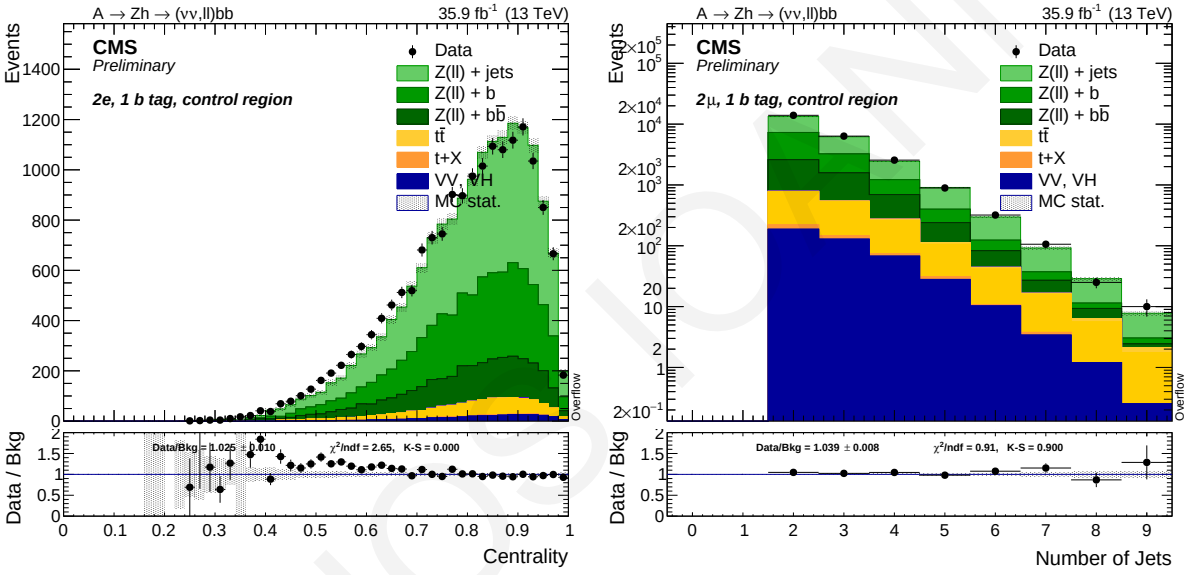

Figure 5.94: Centrality, defined as $\sum p_T/E_{vis}$ the sum of the p_T of all objects divided by the visible energy (left) and jet multiplicity (right).

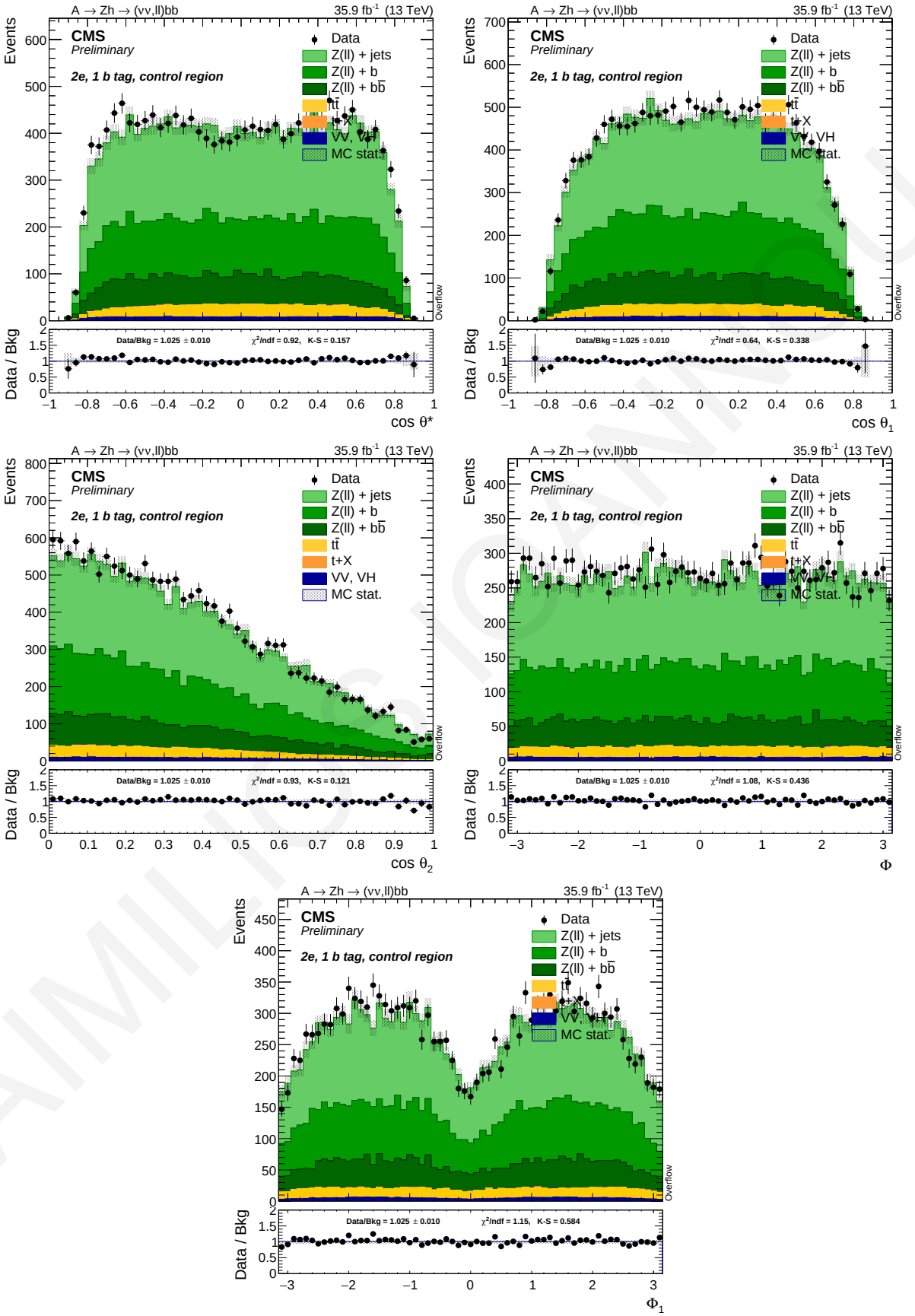

Figure 5.95: $\cos\theta^*$, $\cos\theta_1$, $cos\theta_2$, Φ, and Φ_1 distributions are shown for the $Z \to e^+e^-$ decay mode.

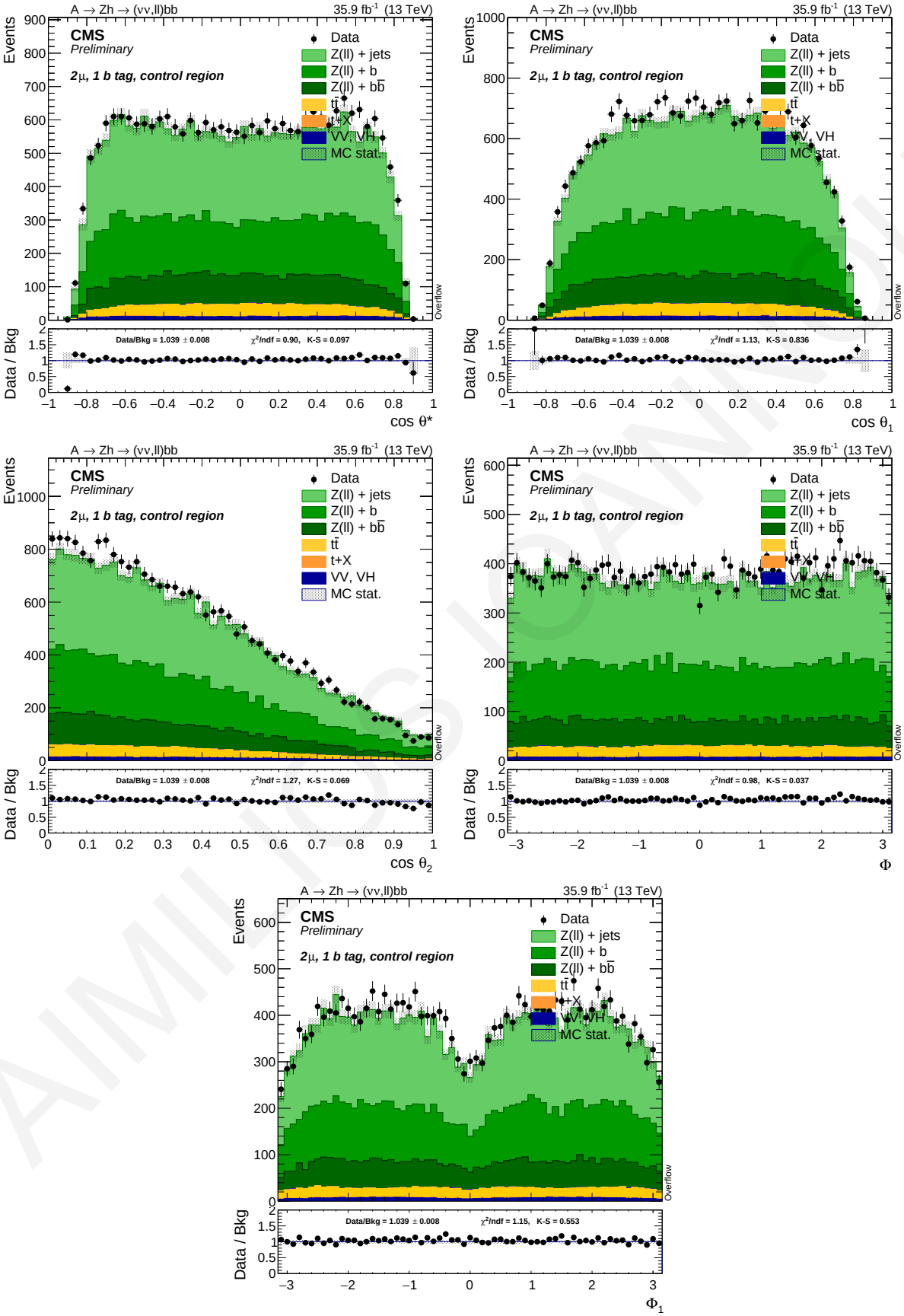

Figure 5.96: $\cos\theta^*$, $\cos\theta_1$, $cos\theta_2$, Φ, and Φ_1 distributions are shown the for $Z \to \mu^+\mu^-$ decay mode.

5.7.3 Z+$b\bar{b}$

The most important background source is the production of a Z boson plus two b-jets. This final state in this case is identical to that of the signal, the only difference is that the b-jets that reconstruct the Higgs mass are vetoed, as in the other control regions. The $Z + b\bar{b}$ control region is so defined by the following selections:

Variable	0ℓ	2ℓ
Pre-selection as described in Sec. 5.6.1		
$m_{\ell^+\ell^-}$ (GeV)	-	$70 < m_{\ell^+\ell^-} < 110$ GeV
Jet1 CSV	medium	
Jet2 CSV	medium	
$m_{b\bar{b}}$ (GeV)	$m_{b\bar{b}} < 100$, $m_{b\bar{b}} > 140$ GeV	
p_T^H (GeV)	> 200 GeV	-
$\not{E}_T$ (GeV)	> 200 GeV	< 100 GeV
Angular LD	-	> 0.5
Event LD	-	> 0.5

Table 5.37: Cuts for the $Z + b\bar{b}$ control region.

The selections are quite similar to the signal region ones described in Chapter 5.6, except for the inversion of the cut on m_h in order to have signal-depleted control region.

The $Z + b\bar{b}$ control region is mostly composed by true Z plus two b-partons events, with a small contamination of Z plus one or zero b-partons, where one or both of the light jets have been mistagged. A moderate contamination from $t\bar{t}$ is also present.

The data/MC agreement is shown for the A candidate (transverse) mass before applying the kinematic constraint (Fig. 5.97), and additionally the distribution of the A candidate (transverse) mass after the implementation of the kinematic constraint is presented in Fig. 5.98. The Z boson mass and its p_T are introduced in Fig. 5.99 and Fig. 5.100. The data/MC agreement is presented for the the Higgs candidate mass (Fig. 5.101) and its p_T (Fig. 5.102). The distribution of the leading and sub-leading for leptons and b-jets are also shown in Fig. 5.103, Fig. 5.104, Fig. 5.105, and Fig 5.106. Moreover, the $\not{E}_T$ variable and the minimum angular separation between the jets and the MET (only for the $Z \to \nu\bar{\nu}$ case) for the $Z \to \ell^+\ell^-$ and the $Z \to \nu\bar{\nu}$ decay channels are shown in Fig. 5.107 and Fig. 5.108, respectively. Finally, variables such as the *Centrality*, and jet multiplicity, are presented in Fig. 5.109 as well as the five helicity observables for the $2e$ (Fig. 5.110) and 2μ (Fig. 5.111) categories.

	0ℓ	$2e$	2μ
Data	710	3425	4640
DYJetsToLL-0b	1.1	374.04	498.67
DYJetsToLL-1b	0.01	396.78	569.65
DYJetsToLL-2b	1.43	1779.92	2414.29
DYJetsToNuNu-0b	124.97	0	0
DYJetsToNuNu-1b	23.08	0	0
DYJetsToNuNu-2b	165.34	0	0
ST	27.26	14.61	19.67
TTbarDL	15.19	701.27	969.98
TTbarSL	145.5	9.97	15.8
VV	53.93	92.14	123.73
WJetsToLNu	120.81	0	0.86
BkgSum	678.62	3368.73	4612.65

Table 5.38: Number of data events and expected events for the various SM processes in the $Z + b\bar{b}$ control region.

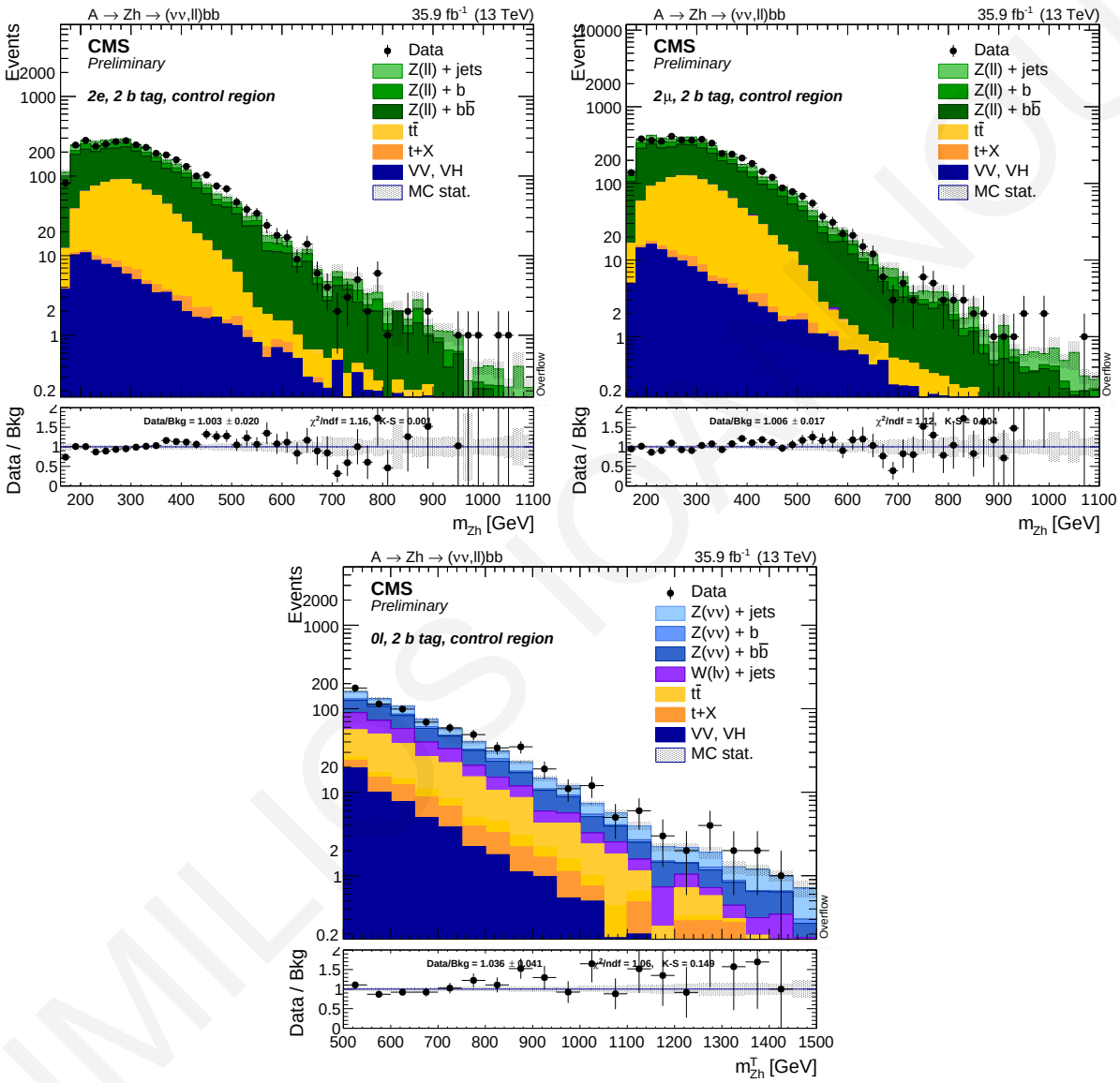

Figure 5.97: 4-body invariant (transverse) mass (before the kinematic constraint) in the $Z + b\bar{b}$ control region.

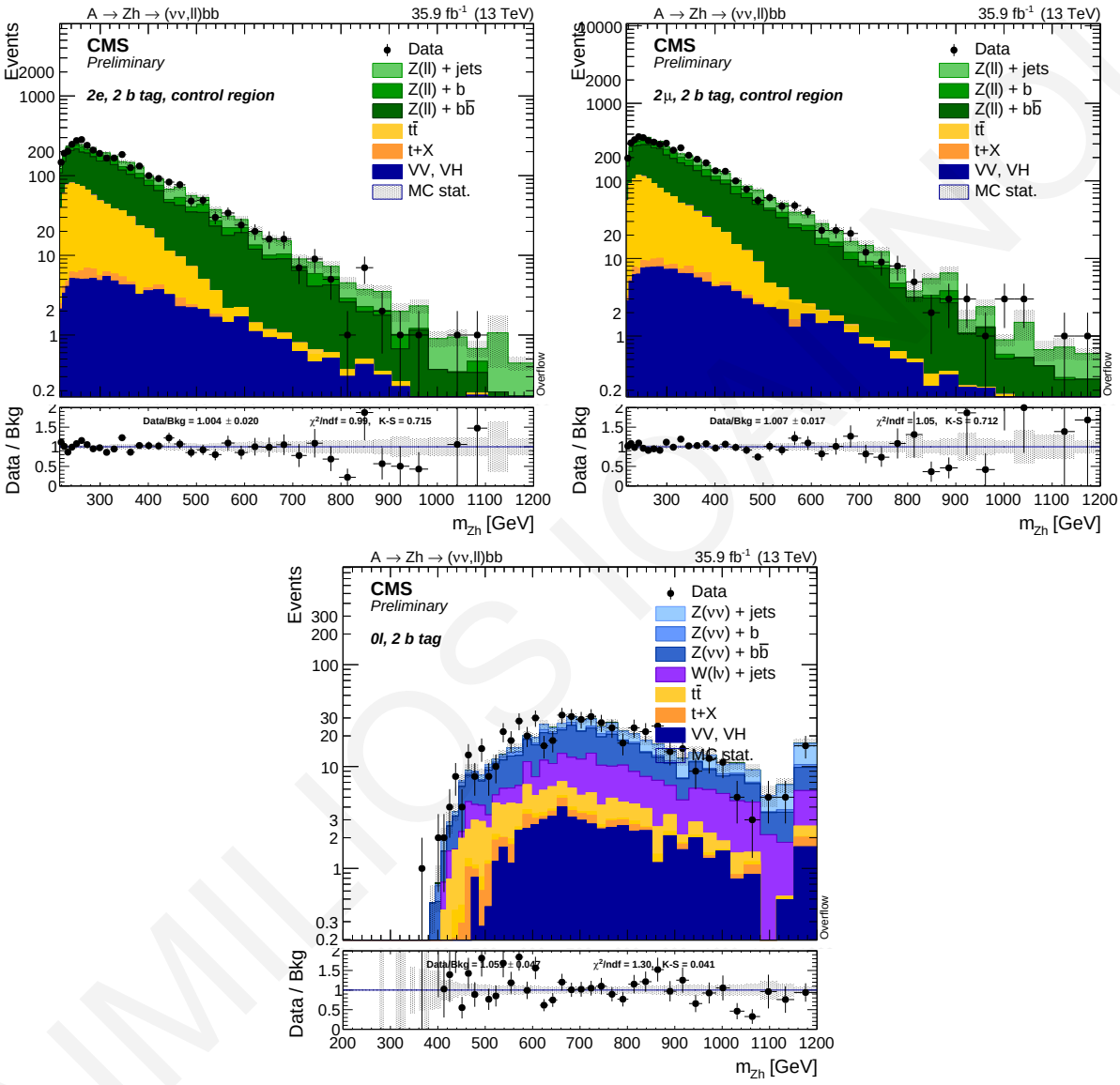

Figure 5.98: 4-body invariant (transverse) mass (after the kinematic constraint).

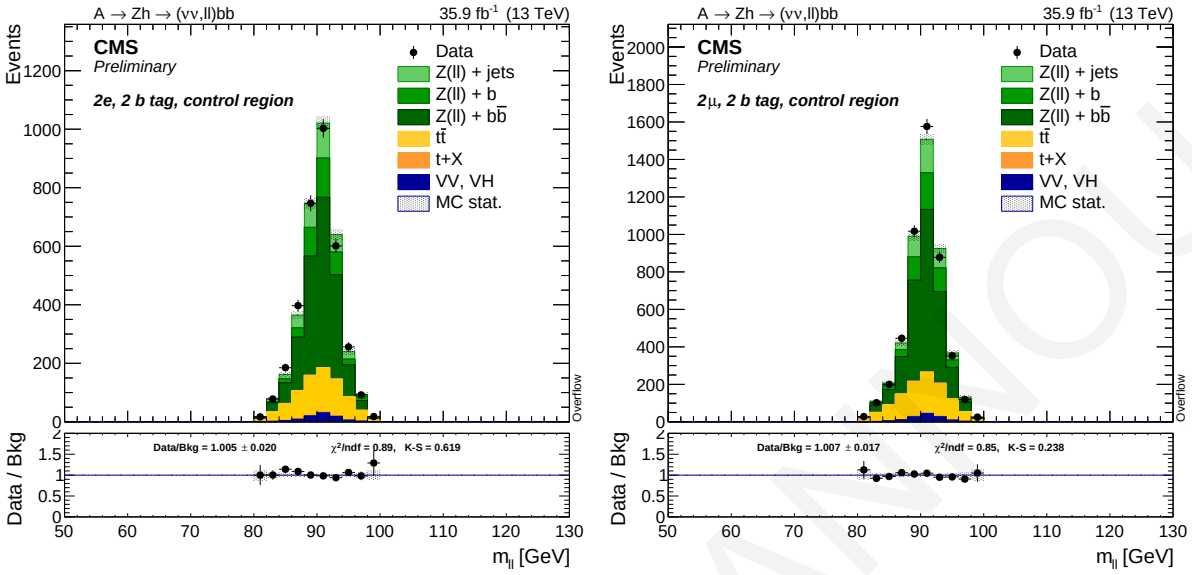

Figure 5.99: Dilepton invariant mass of the Z boson candidate.

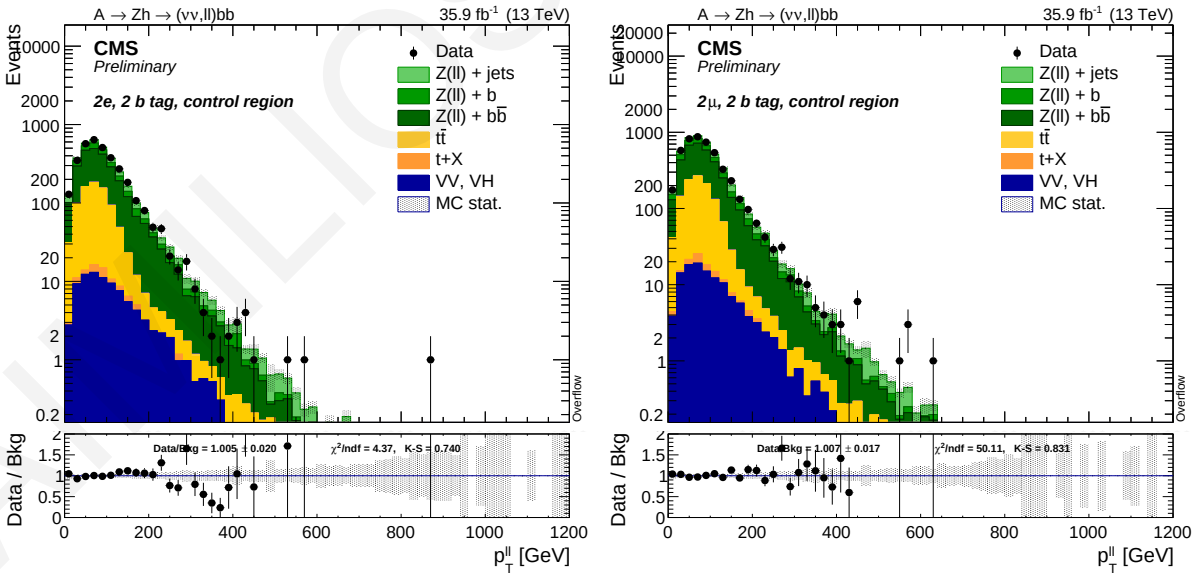

Figure 5.100: p_T spectrum of the Z boson candidate.

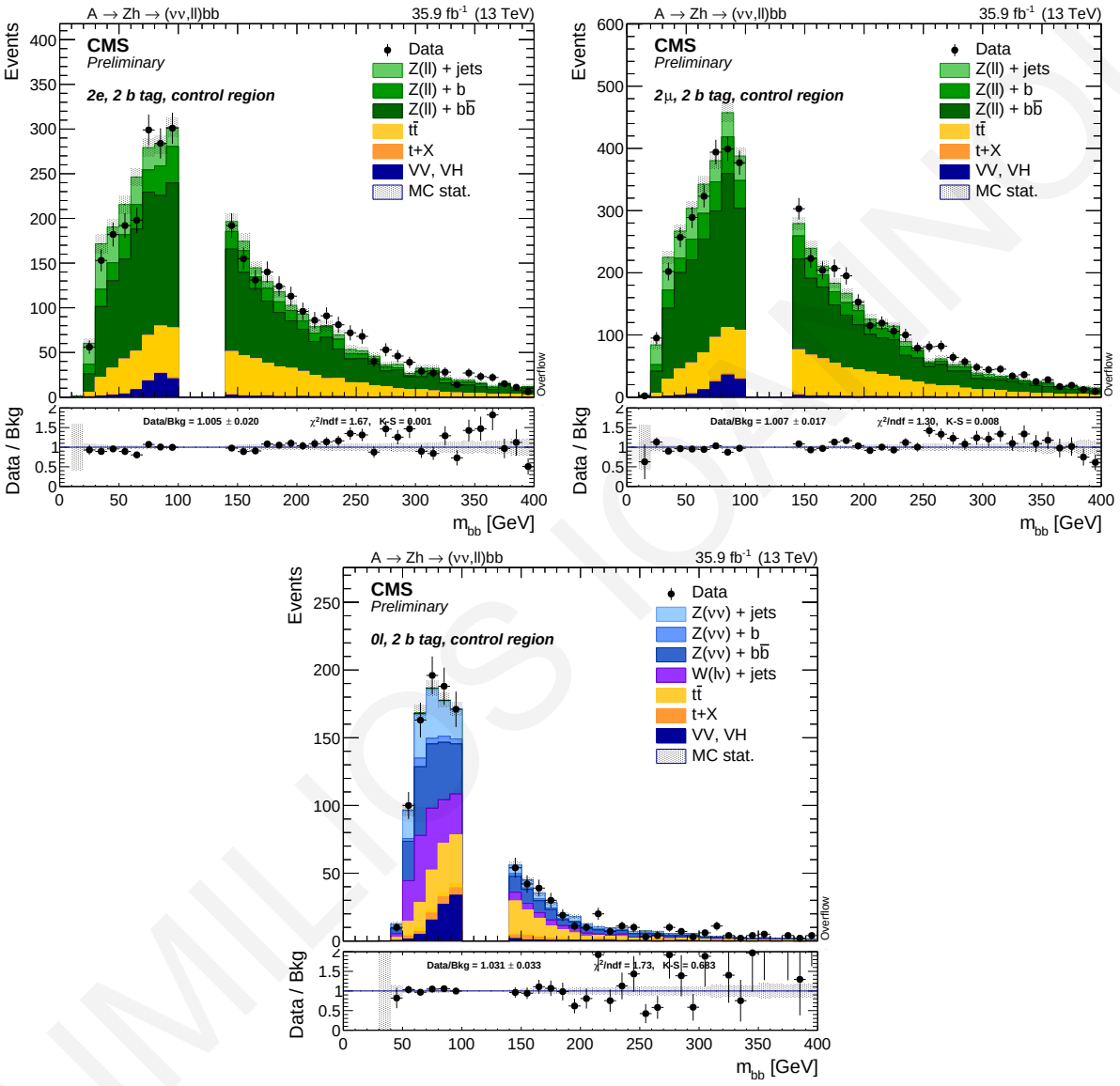

Figure 5.101: Mass of the Higgs boson candidate.

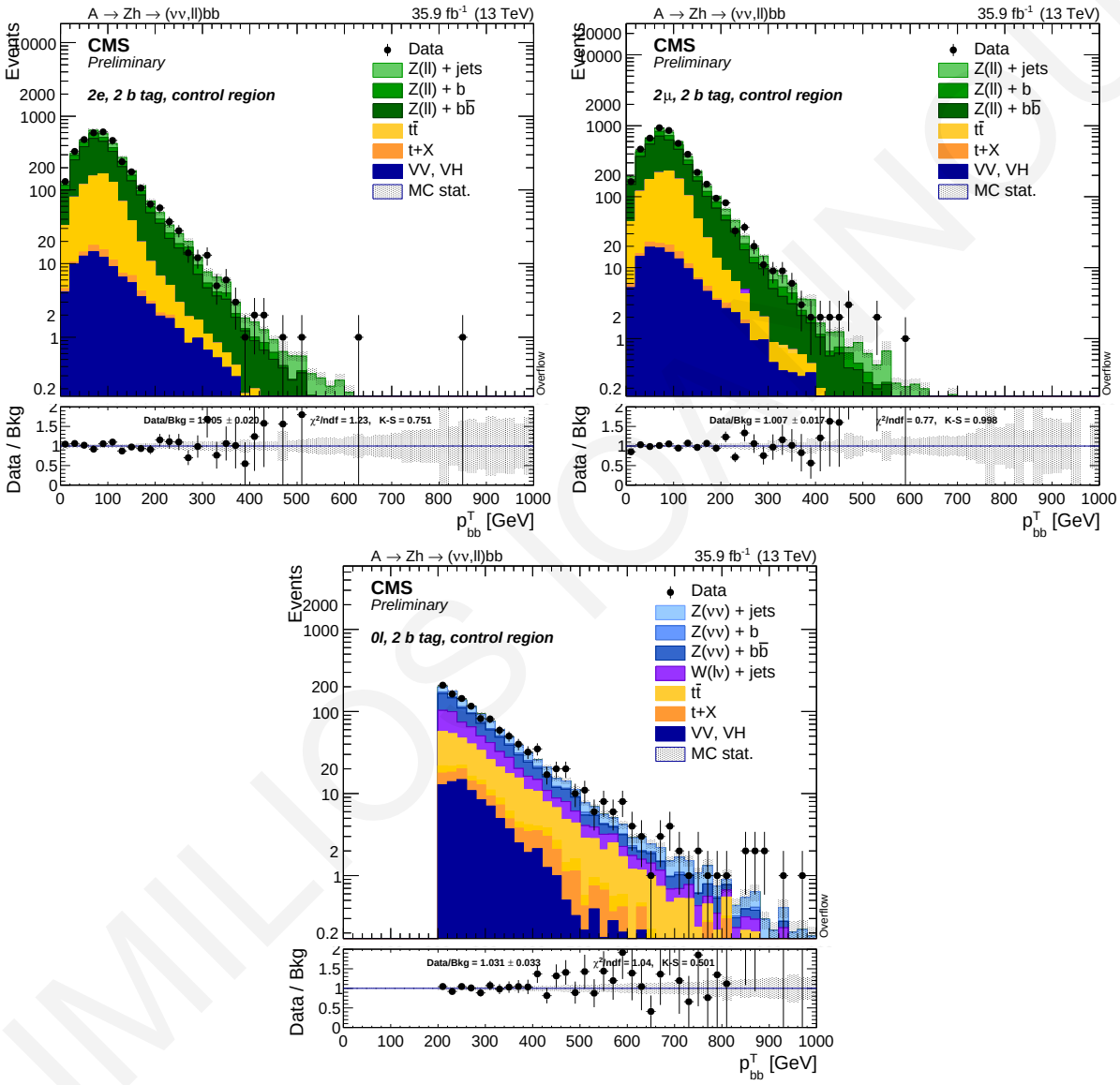

Figure 5.102: p_T of the Higgs boson candidate.

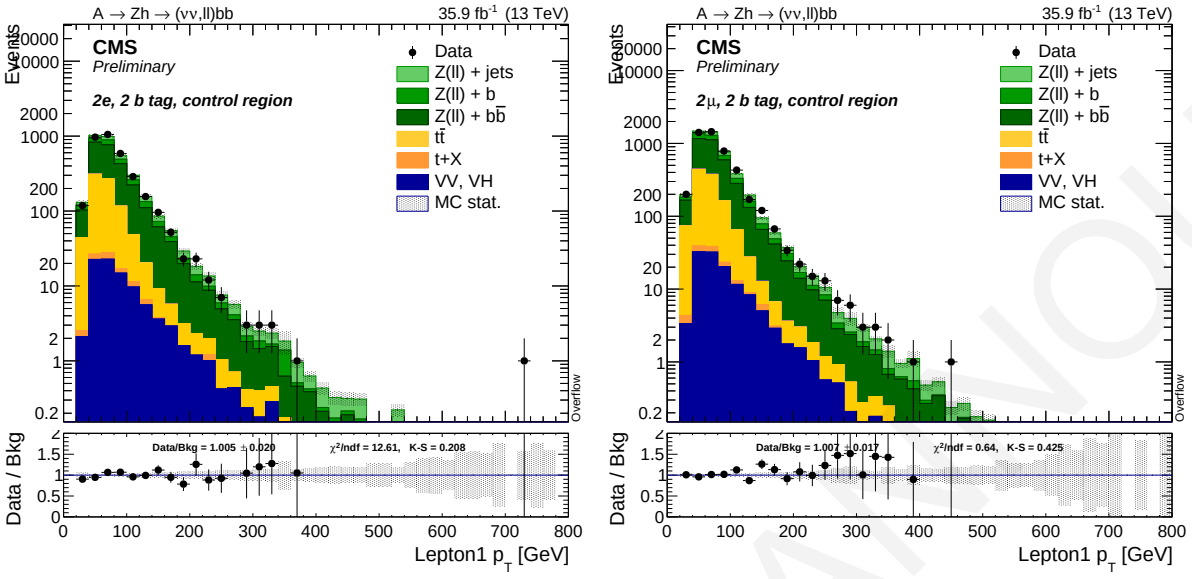

Figure 5.103: p_T distribution for the leading lepton in the event.

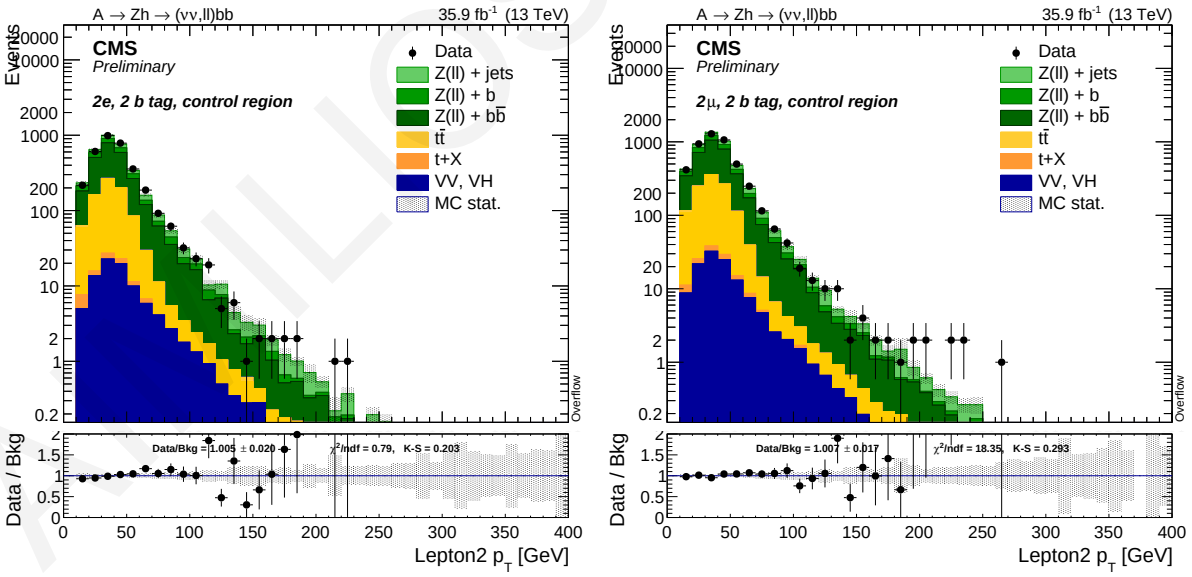

Figure 5.104: p_T distribution for the sub-leading lepton in the event.

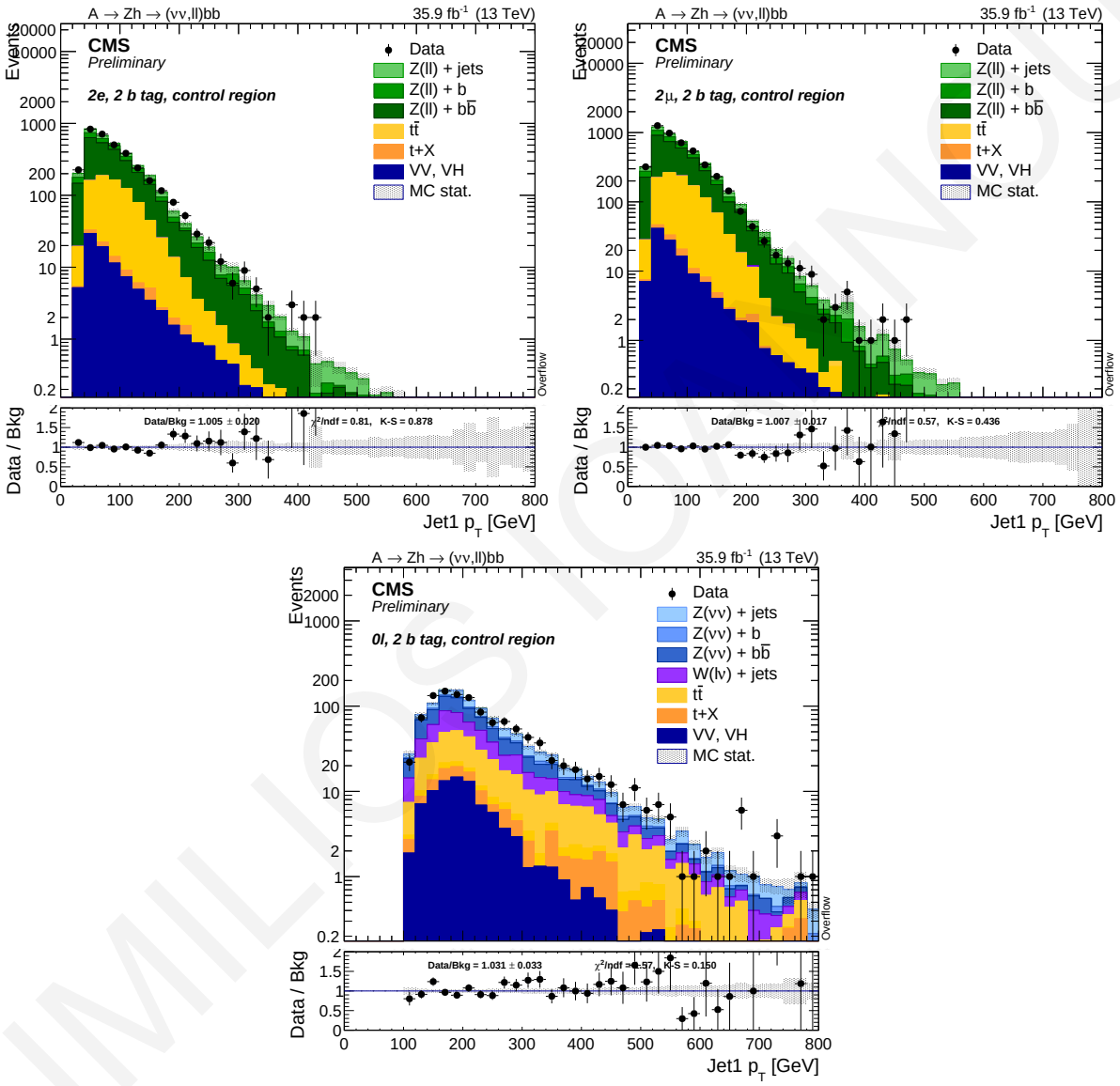

Figure 5.105: p_T distribution for the leading jet in the event.

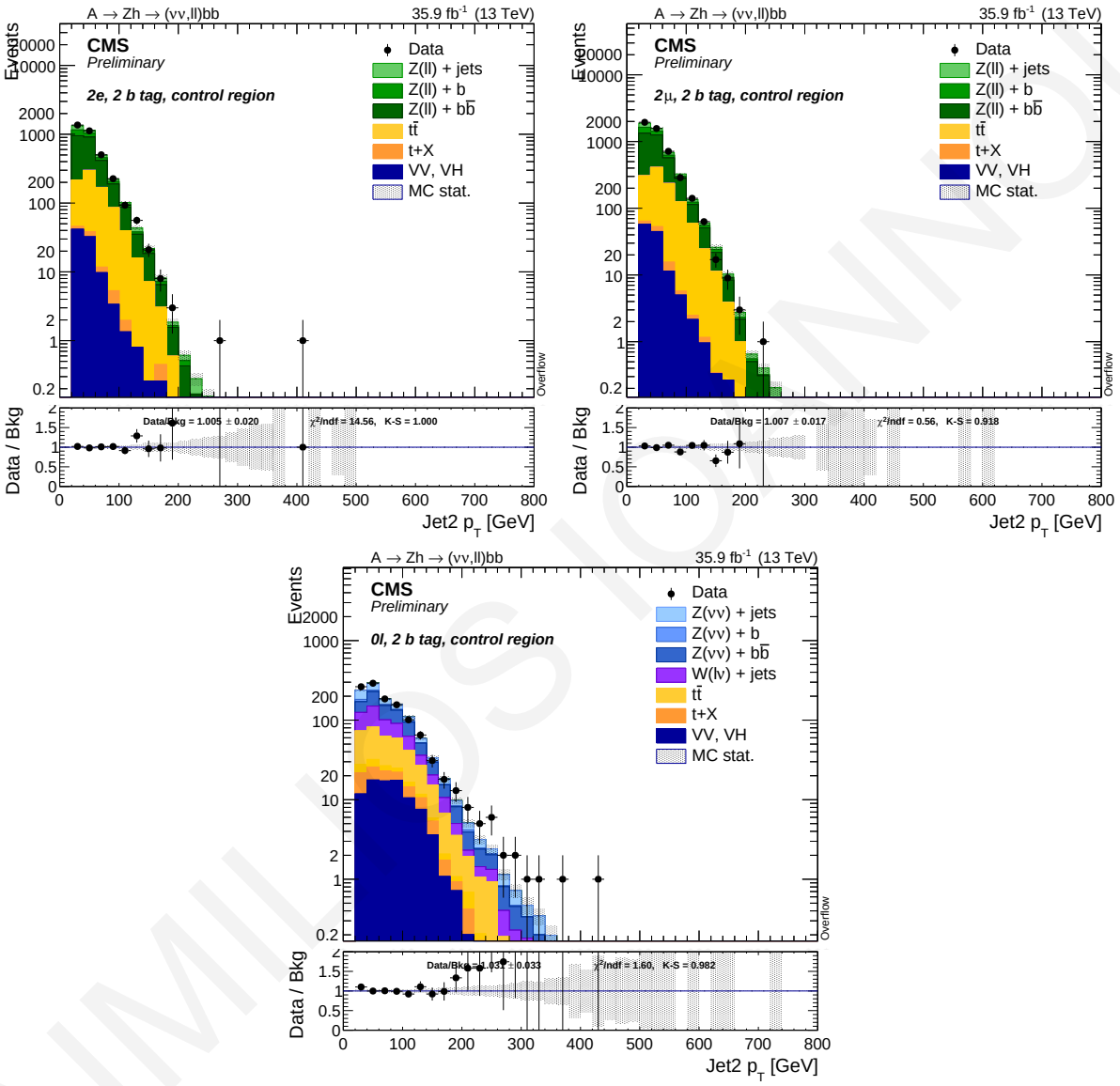

Figure 5.106: p_T distribution for the sub-leading jet in the event.

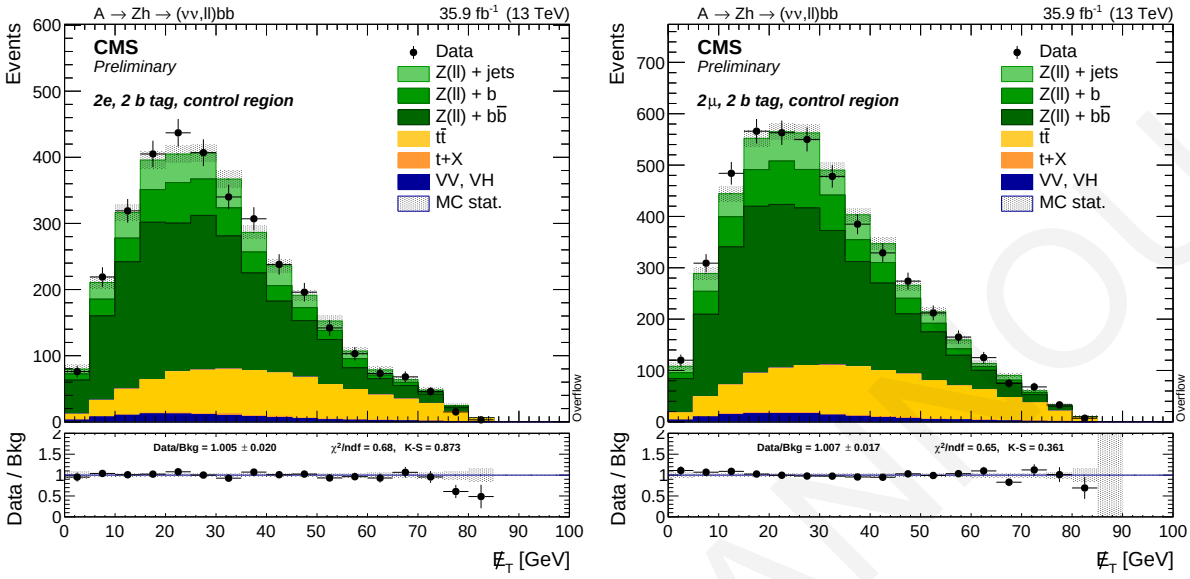

Figure 5.107: $\not{E}_T$ in the event.

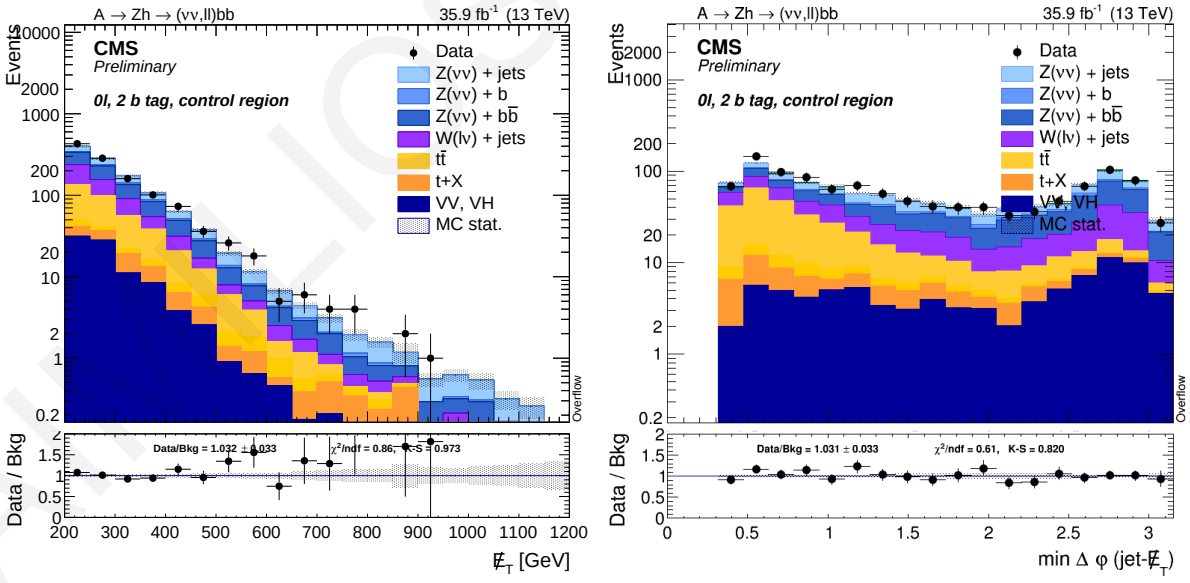

Figure 5.108: $\not{E}_T$ in the event (left) and minimum angular separation between the jets and the $\not{E}_T$ (right).

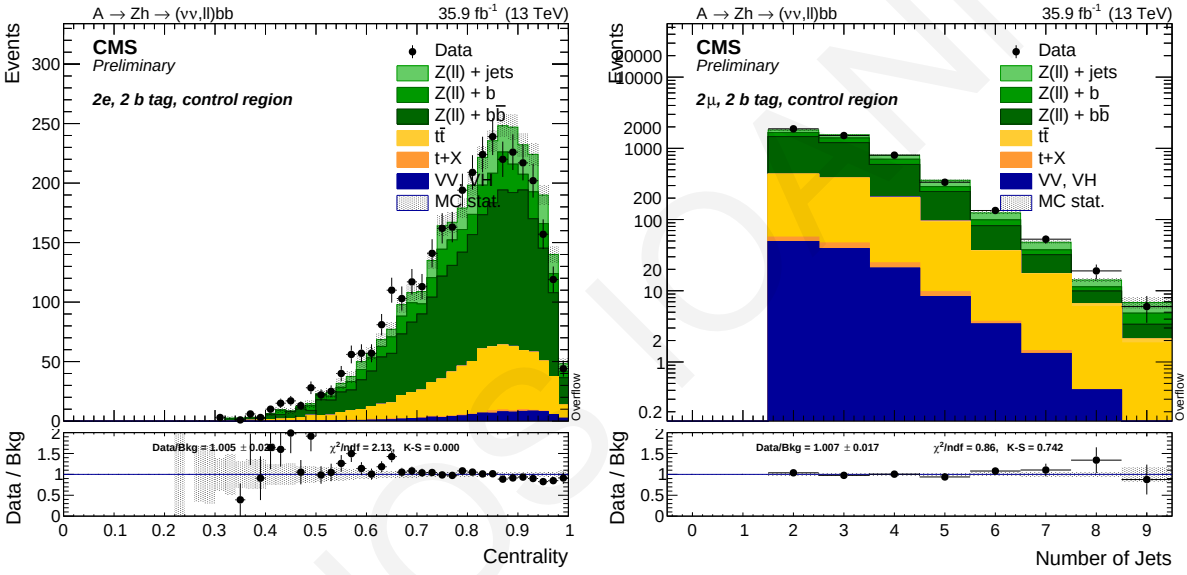

Figure 5.109: Centrality, defined as $\sum p_T/E_{vis}$ the sum of the p_T of all objects divided by the visible energy (left) and jet multiplicity (right).

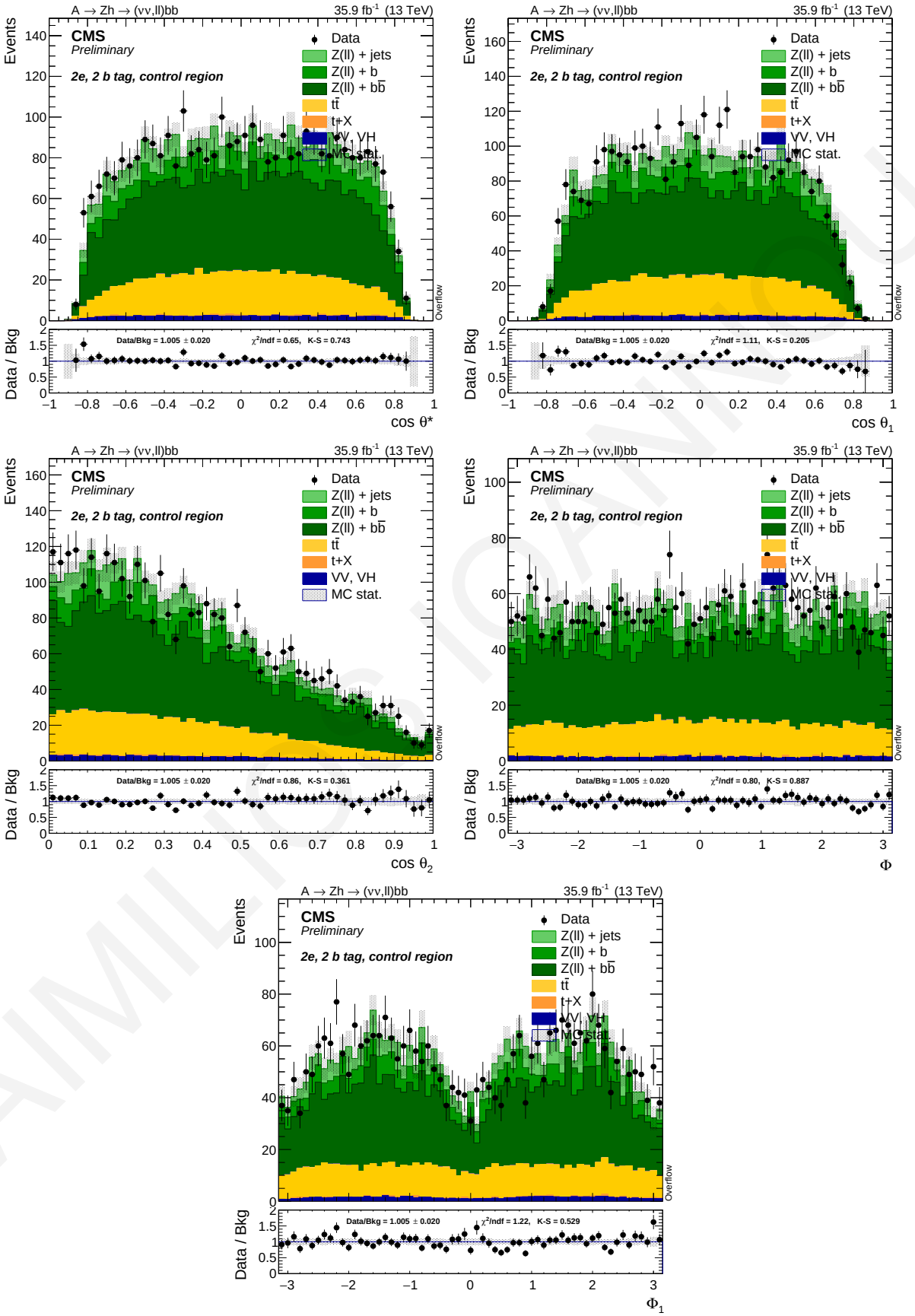

Figure 5.110: $\cos\theta^*$, $\cos\theta_1$, $cos\theta_2$, Φ, and Φ_1 distributions are shown for the $Z \to e^+e^-$ decay mode.

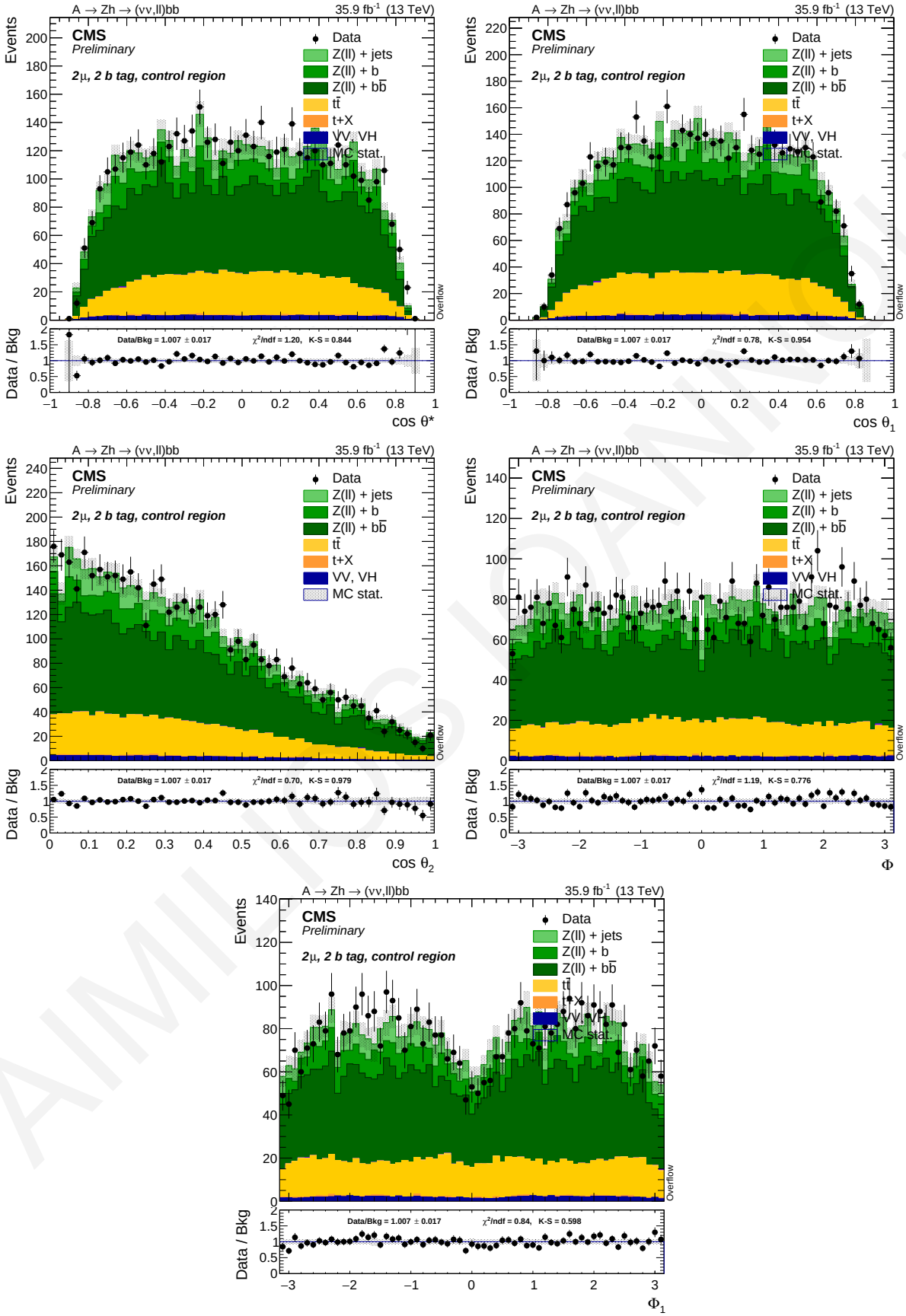

Figure 5.111: $\cos\theta^*$, $\cos\theta_1$, $cos\theta_2$, Φ, and Φ_1 distributions are shown for the $Z \to \mu^+\mu^-$ decay mode.

5.7.4 W+JETS

The W+jets control region is only useful for the 0ℓ final state because this background is negligible after the 2ℓ requirement. A dedicated W+jets control region is used to constrain this background, which composes up to 40% of the total background in the 0ℓ signal regions and cannot be disentangled from the dominant Z+jets otherwise. The W+jets events passing the 0ℓ selections have leptonically-decaying W bosons, and the lepton, usually a τ, is not identified or reconstructed in the detector, or is outside the geometrical acceptance. The W control regions reproduce the same selections as the 0ℓ signal regions, but require the presence of exactly one lepton:

- $1e$ exactly one electron, *tight* WP with $p_T > 30$ GeV
- 1μ exactly one muon, *tight* WP, *tight* PF isolation, with $p_T > 30$ GeV

The lepton four-momentum is subtracted from the $\not{E}_T$ computation to mimic the kinematics of the event when the lepton is lost. The resulting value, the hadronic recoil $\mathcal{U}$, is then used in place of the $\not{E}_T$. In order to discriminate against the $t\bar{t}$, which has a very similar signature of one isolated lepton and multiple jets, the events where any jet can be b-tagged with the *medium* working point is rejected. Events with a large jet multiplicity are also not taken into account.

Variable	$1e$	1μ
Pre-selection as described in Sec. 5.6.1		
leptons	$1e$ or 1μ	
$m_{\ell^+\ell^-}$ (GeV)	-	-
Jet1 CSV	!medium	
Jet2 CSV	!medium	
$m_{b\bar{b}}$ (GeV)	-	
p_T^H (GeV)	> 200 GeV	
$\not{E}_T/U$ (GeV)	> 200 GeV	
n of jets	≤ 3	
$m^T_{\nu\bar{\nu}b\bar{b}}$	> 500 GeV	
Angular LD	-	-
Event LD	-	-

Table 5.39: Cuts for the W+jets control region.

	$1e$	1μ
Data	8495	10645
DYJetsToLL-0b	126.77	129.15
DYJetsToLL-1b	0.74	1.27
DYJetsToLL-2b	0.23	0.55
DYJetsToNuNu-0b	1.4	0.07
DYJetsToNuNu-1b	0	0.07
DYJetsToNuNu-2b	0	0
ST	139.25	164.09
TTbarDL	39.94	42.51
TTbarSL	354.83	423.81
VV	344.03	423.29
WJetsToLNu	7835.7	9366.19
BkgSum	8842.88	10551

Table 5.40: Number of data events and expected events for the various SM processes in the W+jets control region.

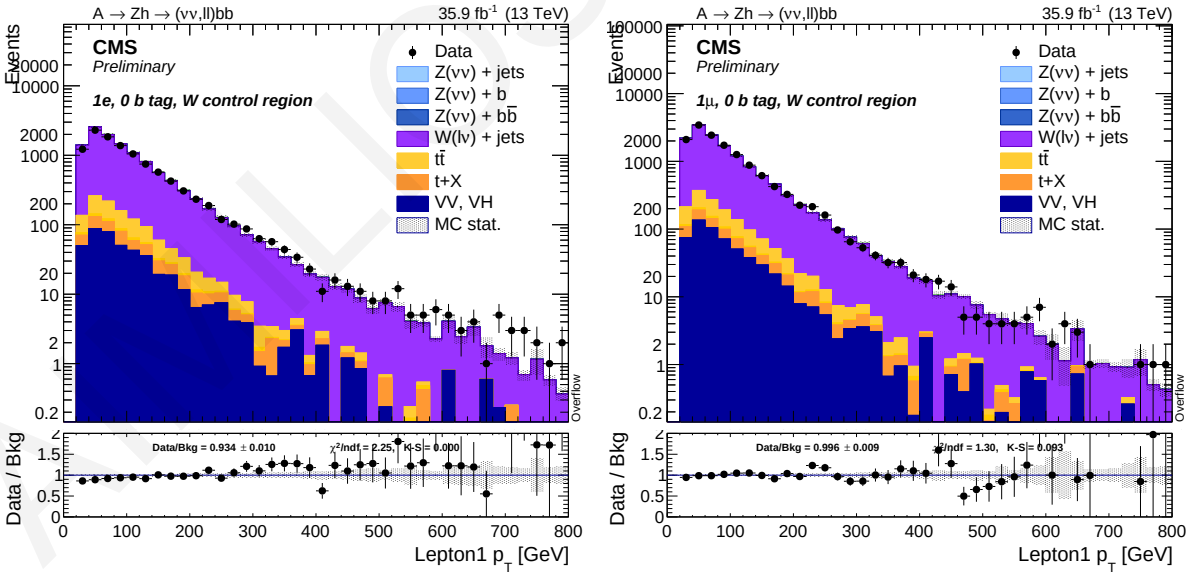

Figure 5.112: Leading lepton p_T.

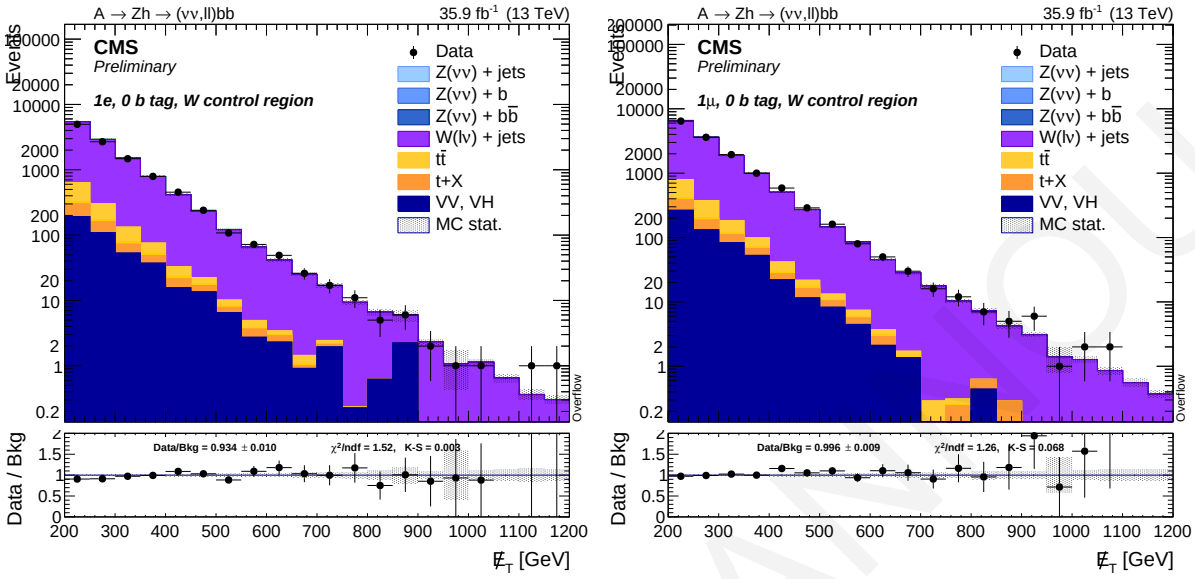

Figure 5.113: $\not{E}_T$ after the subtraction of the lepton momentum.

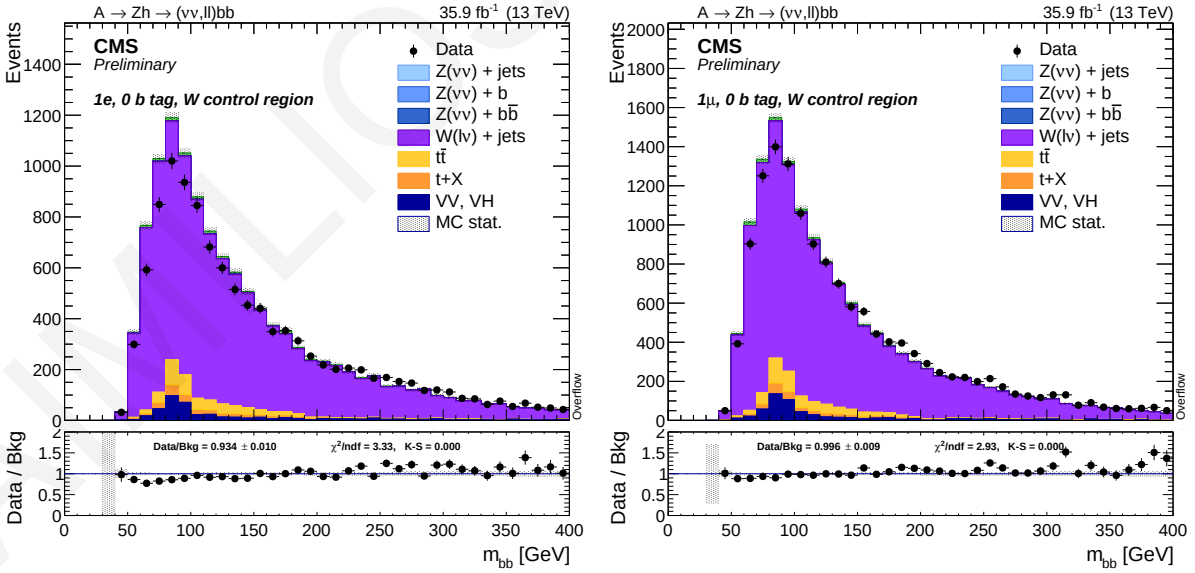

Figure 5.114: Higgs candidate mass.

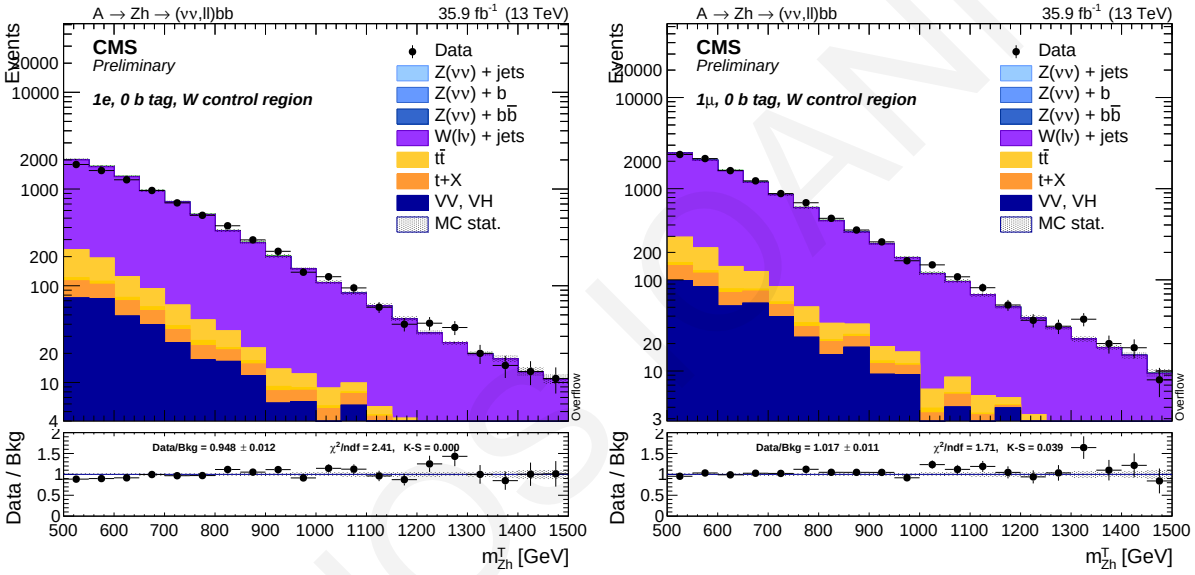

Figure 5.115: A boson candidate transverse mass (with the lepton momentum subtracted from the $\not{E}_T$).

5.7.5 TOP QUARK

The fourth control region is used to constrain $t\bar{t}$. MC samples belonging to this category are pair-produced $t\bar{t}$ in the semi-leptonic and full-leptonic channels; $t\bar{t}+Z$, $t\bar{t}+W$ and all single top samples are considered apart as independent, non data-driven backgrounds. Although the background is the same, there are a number of differences between the $t\bar{t}$ in the 0ℓ and 2ℓ categories:

- 0ℓ: in this final state (no leptons and large $\not{E}_T$), the all-hadronic decays are suppressed by the $\not{E}_T$ requirement. Most of the events passing the selections are semi-leptonic $t\bar{t}$ decays where one lepton (mostly τ leptons) is not reconstructed and identified, or it is outside the detector acceptance. In order to estimate this background, the events where the lepton is actually reconstructed are selected. The lepton is subtracted from the $\not{E}_T$ computation (constructing the hadronic recoil[3] U variable) to mimic the *lost lepton* signature and kinematics, and a similar cut is applied on U as on the $\not{E}_T$ in the 0ℓ regions. The requirements on the leptons are the same as the ones described in the W control regions. On the hadronic side, at least one b-tagged jet and at least 4 jets are required. These selections make the top control regions orthogonal to the W control regions.

- 2ℓ: the di-leptonic case is more straightforward, because it consists of events that pass the lepton and jet selections and have a di-lepton invariant mass sufficiently close to the Z nominal mass to be mis-identified as Z boson candidates. The $t\bar{t}$ control region is then selected by just inverting the Z mass requirement.

The selection for $t\bar{t}$ control region is the following:

Variable	$1e$	1μ	$2e$	2μ
Pre-selection as described in Sec. 5.6.1				
leptons	$1e$	1μ	$2e$	2μ
$m_{\ell^+\ell^-}$ (GeV)		-	$m_{\ell^+\ell^-} < 70, m_{\ell^+\ell^-} > 110$ GeV	
Jet1 CSV		medium		medium
Jet2 CSV		-		medium
$m_{b\bar{b}}$ (GeV)			-	
$\not{E}_T/U$ (GeV)		> 200 GeV		-
n of jets		≥ 4		-
$m^T_{\nu\bar{\nu}b\bar{b}}$		> 500 GeV		-
Angular LD	-	-		
Event LD	-	-		

Table 5.41: Cuts for the $t\bar{t}$ control region.

[3] It is defined as the vector sum of the transverse momenta of all particles except the vector boson

The resulting sample is almost pure $t\bar{t}$, with a smal contamination from single-top.

	$1e$	1μ	$2e$	2μ
Data	1670	1812	18567	25424
DYJetsToLL-0b	7.51	7.4	76.33	113.43
DYJetsToLL-1b	0.66	0.63	65.89	77.66
DYJetsToLL-2b	1.94	1.53	242.71	335.12
DYJetsToNuNu-0b	0.39	0	0	0
DYJetsToNuNu-1b	0.06	0	0	0
DYJetsToNuNu-2b	0.03	0.03	0	0
ST	291.17	301.92	615.44	797.54
TTbarDL	78.68	75.1	18308.43	24452.51
TTbarSL	954.74	997.34	261.04	323.39
VV	26.76	41.96	18.25	22.79
WJetsToLNu	431.6	467.44	13.2	11.35
BkgSum	1793.53	1893.37	19601.28	26133.78

Table 5.42: Number of data events and expected events for the various SM processes in the $t\bar{t}$ control region.

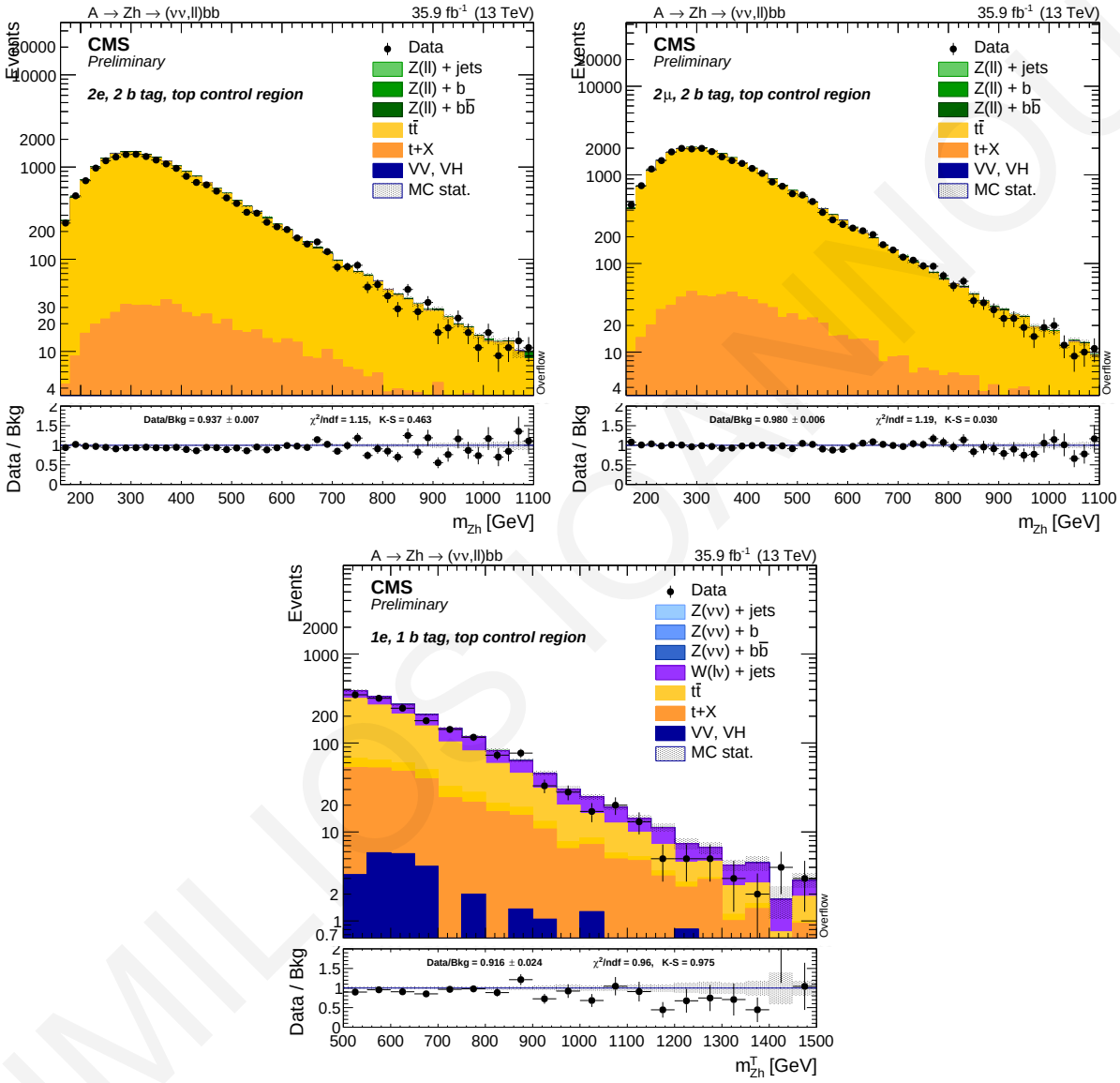

Figure 5.116: Invariant mass of the two electrons and two jets (top left), the two muons and two jets (top right), and transverse mass of the $\not{E}_T$ and the two jets (bottom) in the $t\bar{t}$ control region.

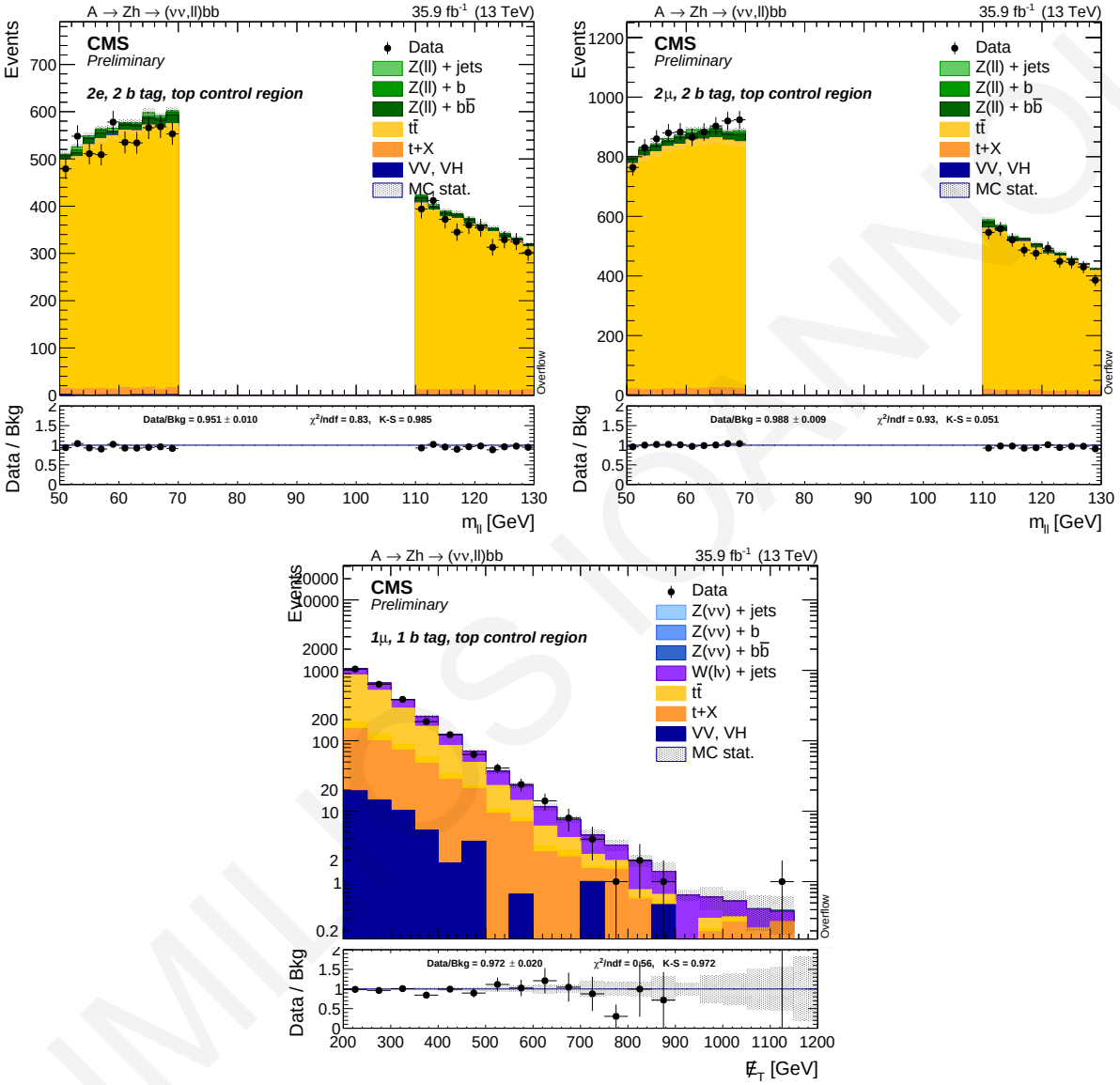

Figure 5.117: di-lepton invariant mass (left plot for $Z \to e^+e^-$, and right plot for $Z \to \mu^+\mu^-$ decay modes) and $\not{E}_T$ (bottom plot) in the $t\bar{t}$ control region.

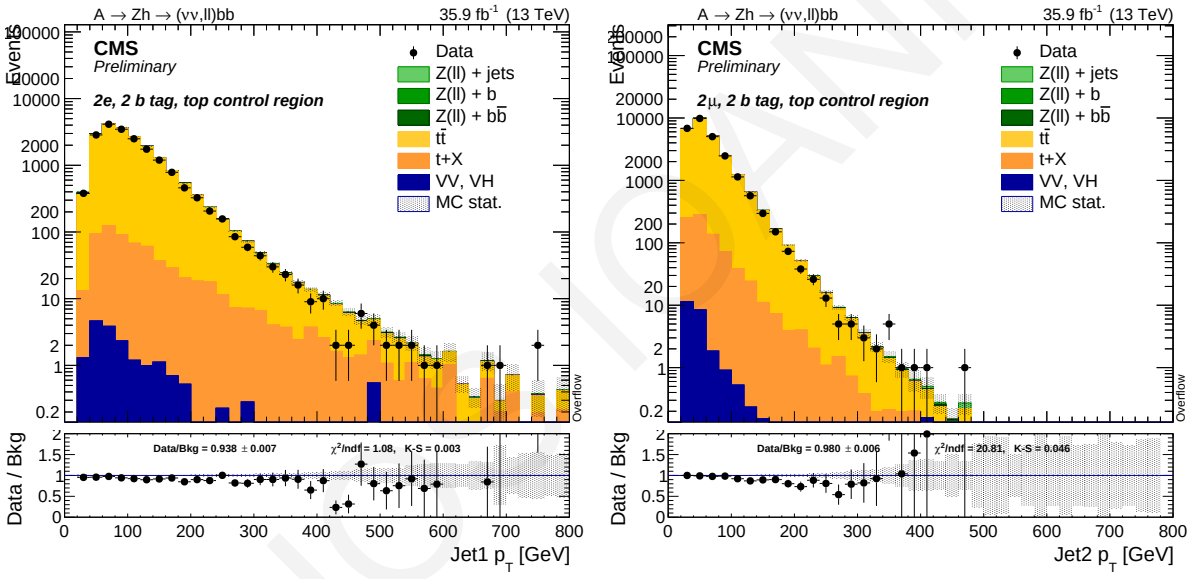

Figure 5.118: p_T distribution for the leading (left) and sub-leading (right) jet in the event.

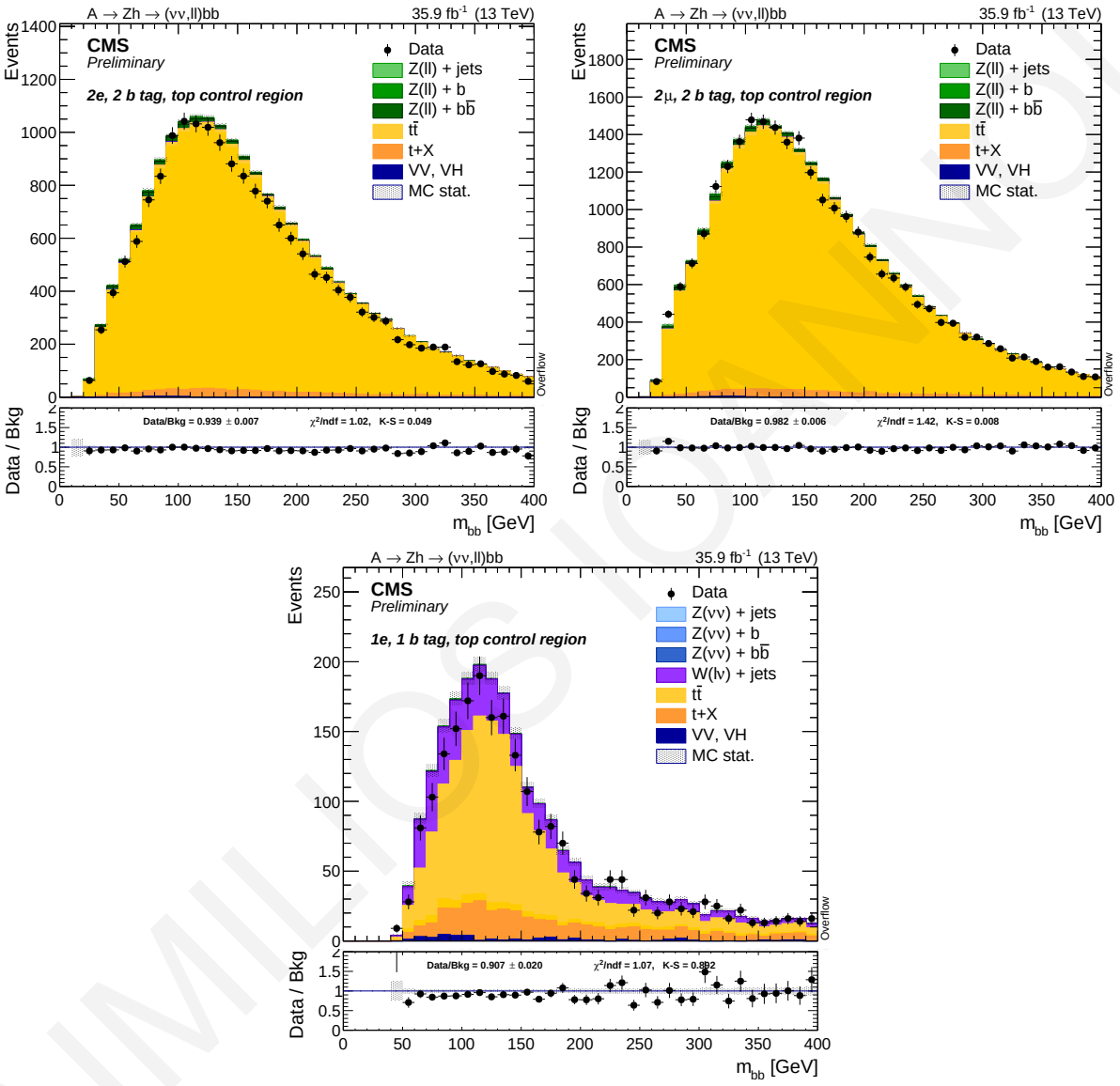

Figure 5.119: Mass of the Higgs boson candidate.

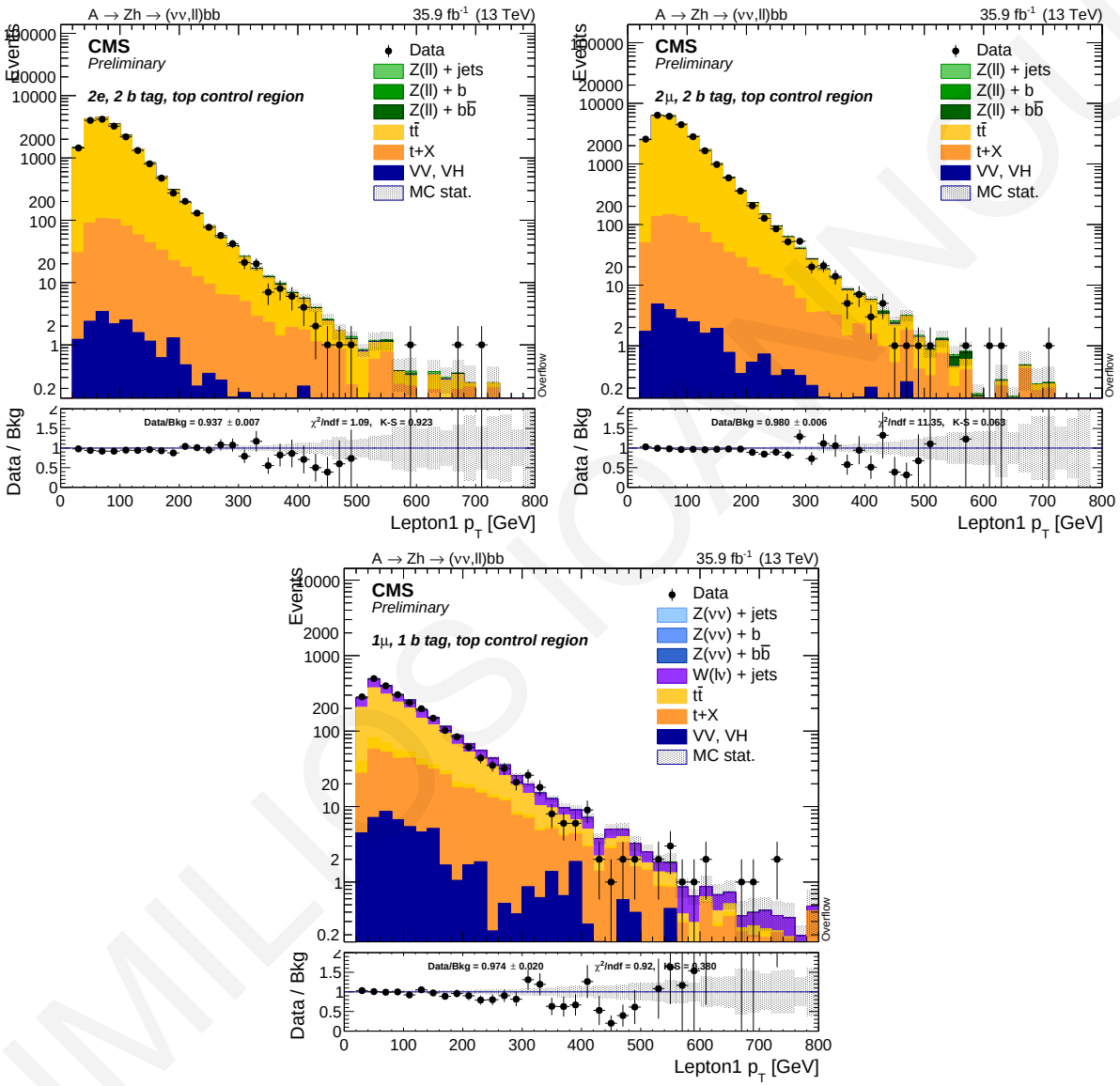

Figure 5.120: Leading lepton p_T for the $Z \to e^+e^-$ (top left), $Z \to \mu^+\mu^-$ (top right), and $Z \to \nu\bar{\nu}$ (bottom) decay modes.

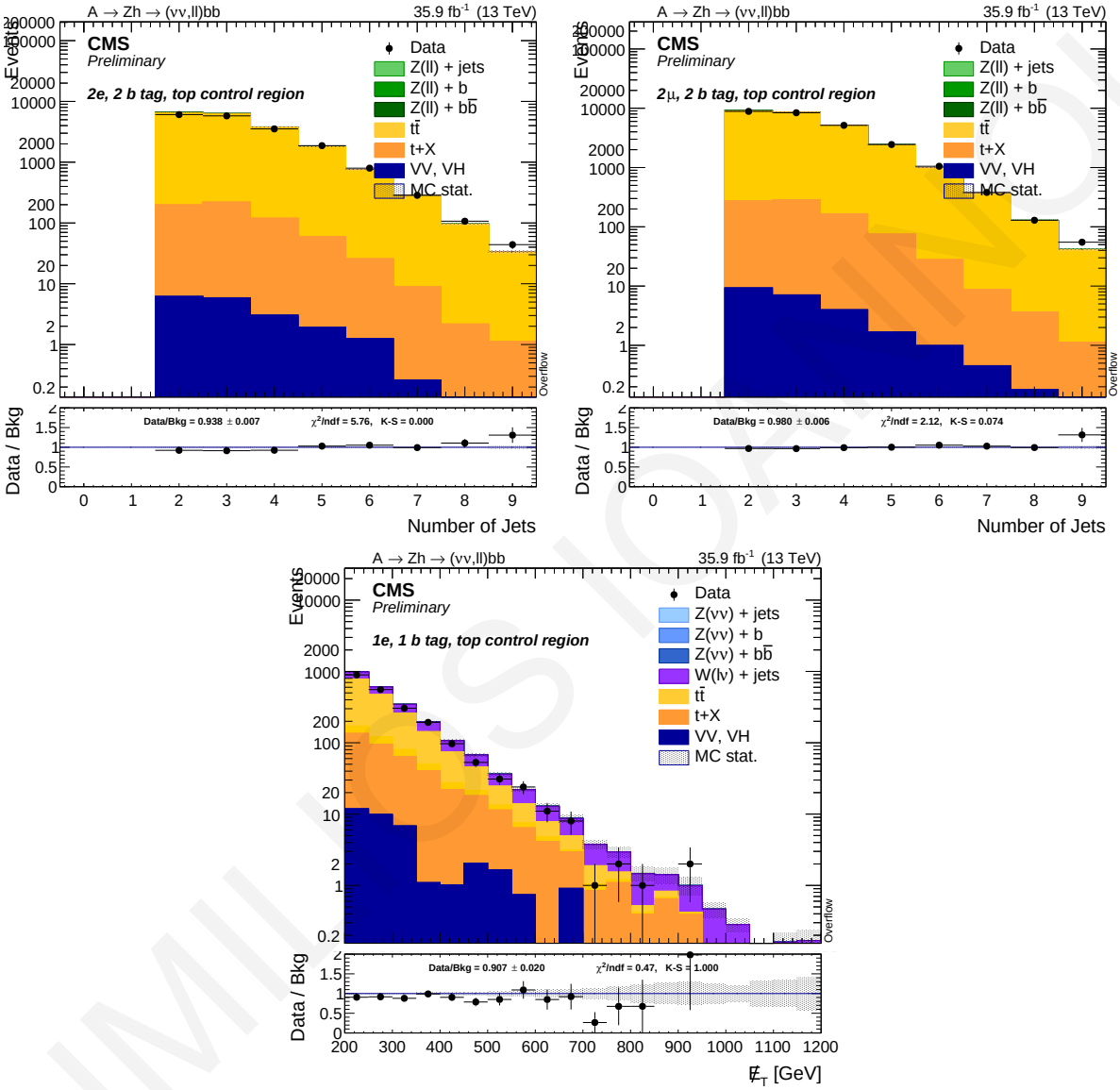

Figure 5.121: Number of jets with $p_T > 30$ GeV, regardless of the b-tagging status, for the $Z \to e^+e^-$ (top left) and $Z \to \mu^+\mu^-$ (top right) decay modes and the $\not{E}_T$ (bottom).

5.8 SYSTEMATIC UNCERTAINTIES

This section describes all systematic uncertainties which are found in this analysis. Systematic uncertainties are examined individually in the following sections.

5.8.1 BACKGROUND NORMALISATION

A crucial part of this analysis resides in the data-driven determination of the four most important backgrounds; this is done in appropriate control regions. The uncertainties on the background normalisation are determined by the fit itself, which also automatically accounts for the correlation between the different backgrounds.

The normalisation of the secondary backgrounds (single top, di-boson, and SM Z h production) is taken from simulation. The cross section uncertainties are taken from the dedicated *TWiki* [110], which come from the PDF and QCD scales. These values are added as normalisation uncertainties to the considered backgrounds, and are taken as correlated to the corresponding shape uncertainties.

5.8.2 INTERPOLATION TO THE SINGAL REGION

A dedicated systematic uncertainty has been studied to cover potential mis-modelings in the di-jet mass distribution, which may lead to a bias in the estimation of the normalisation in the SR (see Fig. 5.79, 5.93, 5.101). The systematic uncertainty is defined as the difference in the ratio between data and estimated background from simulation in the lower ($m_{jj} < 100$ GeV) and upper ($m_{jj} > 140$ GeV) sidebands, derived in the corresponding control regions. The relative differences are reported in Tab. 5.43. This uncertainty is applied only to the SR, and to all the backgrounds, and is taken as correlated between the different categories because of the assumption that the reason of this discrepancy (generator, MC tune, reconstruction) is the same regardless of the final state.

	1 b-tag	2 b-tag	3 b-tag
0ℓ	9.7%	3.4%	7.5%
$2e$	4.8%	10.8%	1.7%
2μ	8.1%	10.8%	5.6%

Table 5.43: Interpolation uncertainties from the m_{jj} sidebands to the signal regions. The uncertainty is the relative difference between the data/MC ratio in the m_{jj} lower and upper sidebands.

5.8.3 EXTRAPOLATION TO THE B-TAG SINGAL REGION

The statistics on the 3 b-tag control regions is not sufficient to treat these regions as independent, and furthermore the fraction of events with 3 real b-quarks is negligible, resulting in a region mostly populated by 2 genuine b-quarks and one mis-tagged jet. As a consequence, there is no floating parameter of the genuine Z+3 b-quarks background. However, requiring the third b-tag significantly reduces the backgrounds, and thus an appropriate systematic uncertainty has to be defined to cover potential mis-modelings in the extrapolation to the 3 b-tag region. This uncertainty is taken as the difference between the data/simulation ratio in the 3 b-tag control regions. These regions are never used in the analysis, and have the same selections as the corresponding 2 b-tag control regions (Chapter 5.7) but with 3 or more b-tags. The numerical values are reported in Tab. 5.44.

	3 b-tag
0ℓ	46.0%
$2e$	20.0%
2μ	34.7%

Table 5.44: Extrapolation uncertainties to the 3 b-tag signal regions. The uncertainty is the relative difference between the data/MC in the 3 b-tag control regions.

5.8.4 LEPTONS

Trigger uncertainty due to the limited statistics is evaluated by shifting by one standard deviation the trigger scale factors, as reported in Chapter 5.2.6. Additionally, a flat 2% systematic uncertainty is assigned for the electron trigger and 0.5% for the muon trigger as suggested by the corresponding POGs [92]. Identification and isolation systematics are evaluated by moving up and down the scale factors for tracking, reconstruction, identification, and isolation by their uncertainties (Chapter 5.3). For muons, additional flat uncertainties for identification and isolation, accounting for 1% and 1% respectively, are applied following the Muon POG prescription [92]. The numerical values are reported in Tab 5.45. These uncertainties do not depend on the mass of the resonance, and they are considered as flat. The uncertainties affecting different flavours are considered as uncorrelated, but those relative to a specific object (electrons or muons) are conservatively considered as correlated.

	Trigger	Id+Iso (1ℓ)	Id+Iso (2ℓ)
Electrons	0.9% (2%)	1.9%	3.6%
Muons	3% (0.2%)	1.0% (0.5%+0.2%)	1.9% (1.0%+0.4%)

Table 5.45: Summary of lepton normalization uncertainties. Number in parenthesis are systematic uncertainties.

Systematics for electrons and muons energy/momentum scale and resolution are evaluated by rescaling the energy or p_T of the leptons and counting the yield difference in the signal regions. After the kinematic constrain on the Z mass, the lepton energy scale and resolution is negligible, and not considered in the final limit.

5.8.5 JETS

Jets uncertainties are evaluated in the signal regions by moving up and down by one standard deviation the source of the uncertainty. The two sources are the uncertainty on the jet energy correction, also identified as jet energy scale (JES), and the uncertainty due to the different jet momentum resolution (JER). For the jet energy scale the p_T of the jets are shifted by the error value of the jet energy corrections, obtained using the full set of JESSources.

Since the jets are kinematically constrained to the Higgs mass, the procedure is repeated again for every variation of the jets' four momenta. After the kinematic constraint, the effect on the shape is essentially negligible. The remaining "threshold" effect, estimating the fraction of events with jets that pass or fail the kinematic thresholds, is estimated as a function of the signal jet mass, and is conservatively taken as 2-6% uncertainty for the JES and 1-2% for the JER. The same value, estimated for the secondary backgrounds, is taken as 5% for the JES and 2% for the JER.

5.8.6 B-TAGGING

The impact of b-tagging uncertainty is evaluated by varying the CSV by their scale factors, as recommended by the BTV POG [109]. An average systematic uncertainty of 6% per b-jet, 12% per c-jet, and 15% per fake tag (light quarks and gluons) are used; the exact value is assigned for each jet as a function of its p_T and η. Due to the dependence on the jet kinematics and flavour composition of the final state, the b-tagging systematics are taken as full shape uncertainties. Different templates are constructed as an effect of the variation of the scale factors, which translate to a different per-event weight. This approach naturally takes into account the full (anti-)correlation between different b-tagging categories. The signal normalisation variations are shown in Figure 5.122.

5.8.7 MISSING ENERGY

The $\not{E}_T$ is a composed object, built upon all the reconstructed particles in the detector. Therefore, it is affected by the energy scale and resolution of all the reconstructed objects, i.e. charged and neutral hadrons (clustered in jets and non-clustered), muons, electrons, photons and hadronic taus. Dedicated

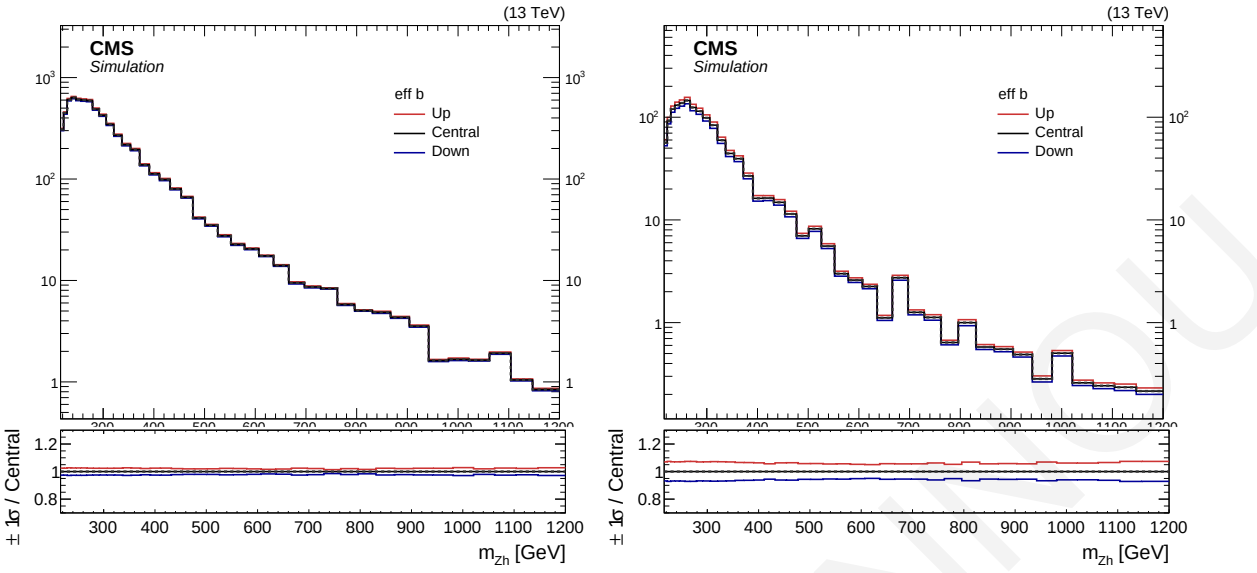

Figure 5.122: Signal normalisation variations obtained varying the b-tagging SF by one standard deviation in the 1 (left) and 2 (right) b-tags category.

uncertainties have been derived by propagating the original object scales and resolutions (JES and JER) to the $\not{E}_T$ itself. Additional variations, considered to be uncorrelated from the JES and JER effects, come from the unclustered $\not{E}_T$ in the event. The impact has been evaluated in the 0ℓ channel, and resulted in a systematic uncertainty of 1%.

5.8.8 PILE-UP

An additional source of systematic error is the limited knowledge of the total inelastic cross section at 13 TeV, used to get the expected primary vertices distribution used for pile-up reweighting. A 5% uncertainty is assumed for the default value of 69.2 mb [96], and the expected primary vertices distributions are varied accordingly. Changing the pileup weight varies also the MC normalisation in the signal regions, and the relative difference is estimated to be 0.1%. No shape uncertainties are considered for PU.

5.8.9 QCD RENORMALISATION AND FACTORISATION SCALE

Per-event weights are provided for a variation of the QCD renormalisation and factorisation scales by a factor 2. The two scales can be varied separately and independently, or together assuming 100% correlation. The largest exclusion in each event is then taken as the uncertainty. The weight is propagated up to the final distributions, accounting for both shape and normalisation uncertainties. The envelope

of all the considered variations is then considered as the template for the scale uncertainty, as shown in Fig. 5.123.

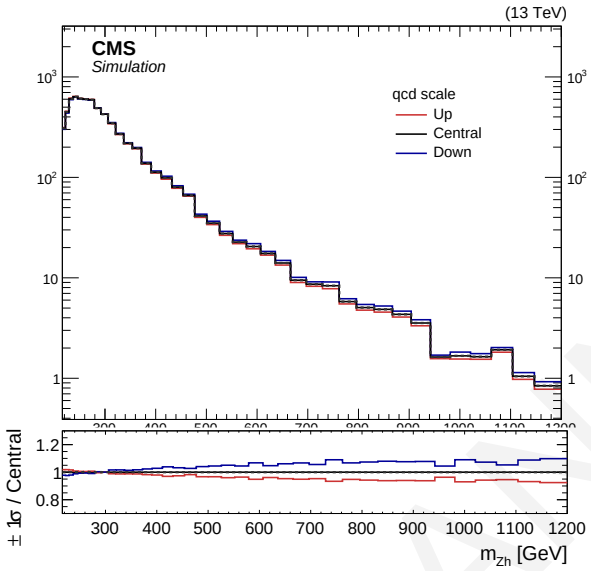

Figure 5.123: Normalisation variations due to the QCD scales.

5.8.10 Electroweak Corrections

Corrections to the Z+jets and W+jets p_T spectra due to NLO EWK contributions are estimated in Ref. [80], applied to the simulated processes, and the full difference of the correction is taken as systematic uncertainty. The corrections to the Z and W are considered as uncorrelated.

5.8.11 QCD Corrections

Corrections to the Z+jets and W+jets p_T spectra due to NLO QCD contributions are estimated as described in Chapter 5.2.2. Also in this case, the full difference of the correction is taken as systematic uncertainty. The corrections to the Z and W are considered as uncorrelated.

5.8.12 Top Momentum Reweighting

The top quark p_T is corrected in simulation to match the one observed in the data [88]. The systematic uncertainty is one-sided, and estimated by removing the weight from the event. This uncertainty affects both the normalisation and the shape of the $t\bar{t}$ background.

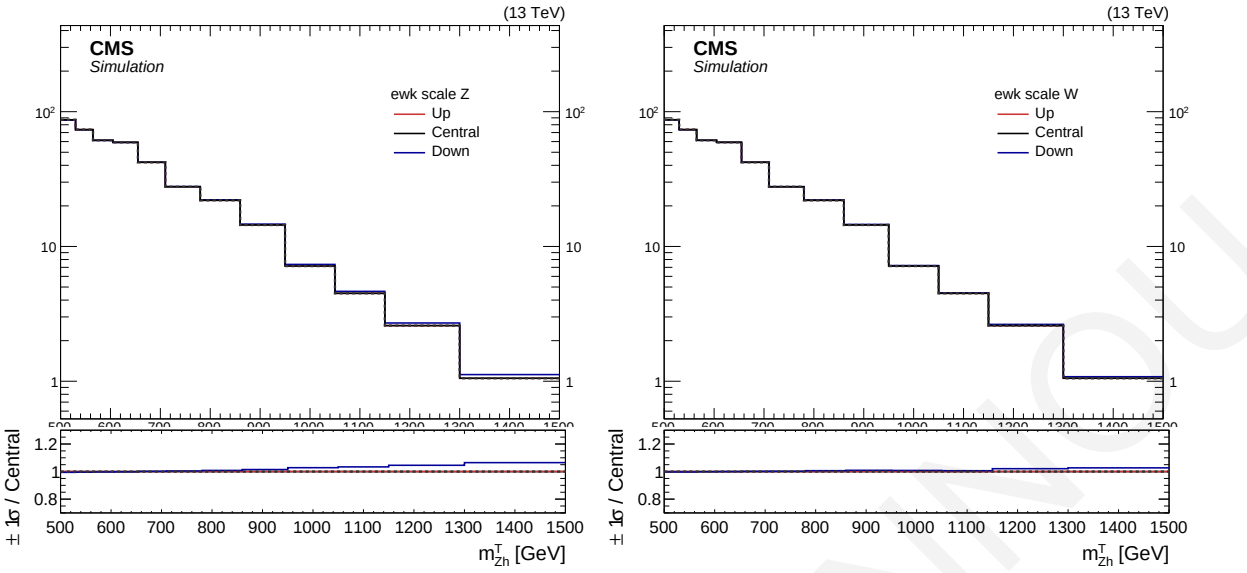

Figure 5.124: Shape variations due to the Z (left) and W (right) electroweak corrections in the 0ℓ category. Only the "down" variation is present.

5.8.13 FACTORISATION AND RENORMALISATION SCALE

Uncertainties on the acceptance due to the truncated perturbative series, the factorisation and renormalisation scale used for the event generation are varied in a correlated way by a factor of 1/2 and 2 around the central value. As per recommendations of the GEN group, the bin-by-bin largest variation of the two weights, between the two hypotheses of the two weights to be fully correlated or uncorrelated, is taken as shape uncertainty. The factorisation and renormalisation scales also affect the normalisation of both main and secondary backgrounds, and for the latter they cover potential differences when selecting events in the moderate boost regime.

5.8.14 PDF

Systematic uncertainties coming from PDF uncertainties have been considered in this analysis, according to the PDF4LHC prescriptions, and using the NNPDF3.0 set. The 100 weights have been considered together, by calculating the envelope of the weight distribution around the central value for each distribution, and propagated as a normalisation and shape uncertainty to the final distributions. The effect of the PDF uncertainty on the acceptance is found to be consistent between all the signal samples, and it is around 0.5%.

The PDF have an effect on the lepton acceptance. An average 3% uncertainty is assumed for each lepton. A different uncertainty is assumed for each main background (Z, W, $t\bar{t}$) in order to have uncorrelated

effects.

5.8.15 MONTE CARLO MODELING

An additional systematic error is added due to the non-perfect modeling of the simulation. This mismodeling is visible in many variables, but it is mostly notable in the Centrality (Fig. 5.125) of the event, defined as $\sum p_T/E_{vis}$ the sum of the p_T of all objects divided by the visible energy. From this discrepancy, a weight that linearly depends on the Centrality value is derived from the 2 b-tag control regions simultaneously for electrons and muons (since the results are compatible within fit uncertainties), and propagated to all the other variables, including m_{Zh}. The parameters of the reweight function are reported in Tab. 5.46. An uncertainty band is built by applying the weight. Fig. 5.126 shows the shape variations in the 1D projection on $m_{\ell^+\ell^-b\bar{b}}$. Unlike the Run-I analysis, the reweight is not applied by default, but rather added as a systematic uncertainty to cover potential mismodelings in the signal regions.

p_0	1.48 ± 0.03
p_1	-0.632 ± 0.041

Table 5.46: Parameters of the linear fit with a function $w = p_0 + p_1 \cdot x$, where x is the Centrality variable.

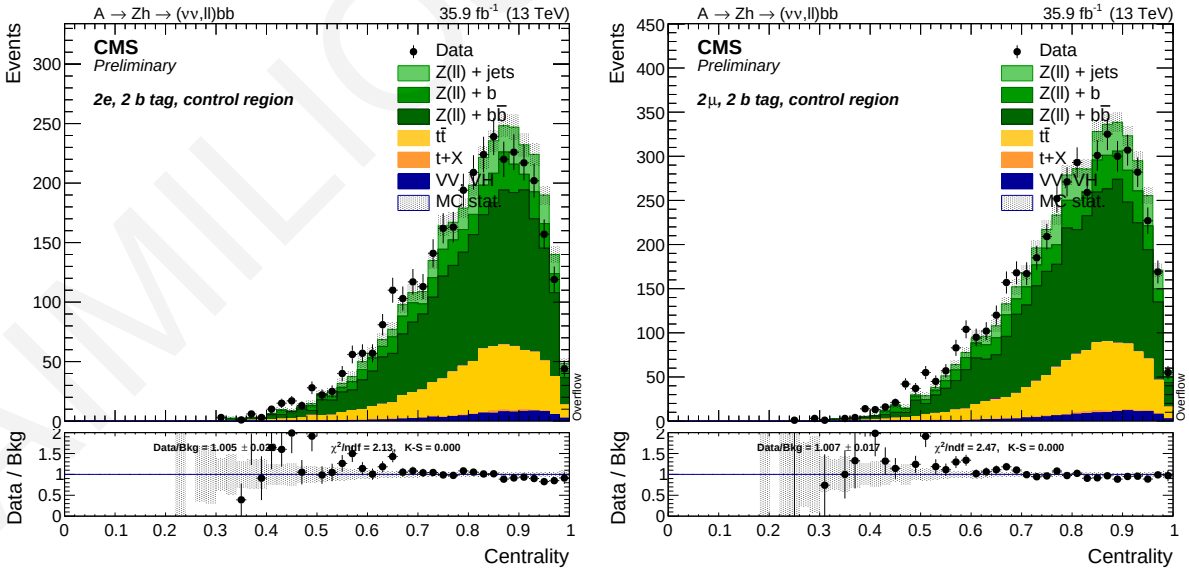

Figure 5.125: Centrality, defined as $\sum p_T/E_{vis}$ the sum of the p_T of all objects divided by the visible energy in the $2e$, 2 b-tag (left) and 2μ, 2 b-tag control regions (right).

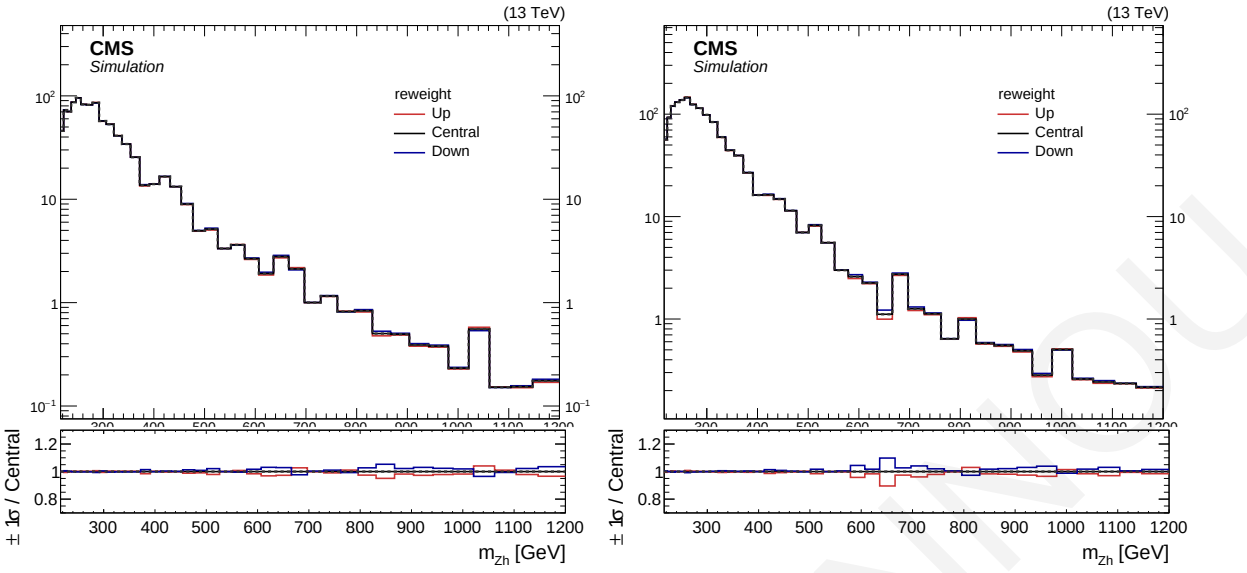

Figure 5.126: Projection of the reweighting variations on the 4-body invariant mass in the $2e$, 2 b-tag (left) and 2μ, 2 b-tag signal regions (right).

5.8.16 MONTE CARLO STATISTICS

The effect of the limited Monte Carlo statistics becomes non-negligible in the *Boosted Decision Trees (BDT)* bins closer to 1, where most of the signal sensitivity is expected. The BDT is used to construct the likelihood discriminators and could affect the sensitivity of the signal. This effect is accounted for by introducing additional coherent bin-by-bin shape uncertainties for each process and for each distribution [111]. Since the bin number is very high in the 2D analysis, only the 20 most significant bins (ordered by expected S/B) are used; we verified that adding more bins does not change the expected limit. Figure 5.127 shows the expected limit relative to that expected without considering the Monte Carlo statistics, as a function of the number of bins considered for the Monte Carlo statistics uncertainties. The larger contribution is for low mass ($m_A = 250$ GeV) and account for up to 20% increase in the expected limit.

5.8.17 SUMMARY OF UNCERTAINTIES

A summary of all systematic uncertainties is listed in Tab. 5.47.

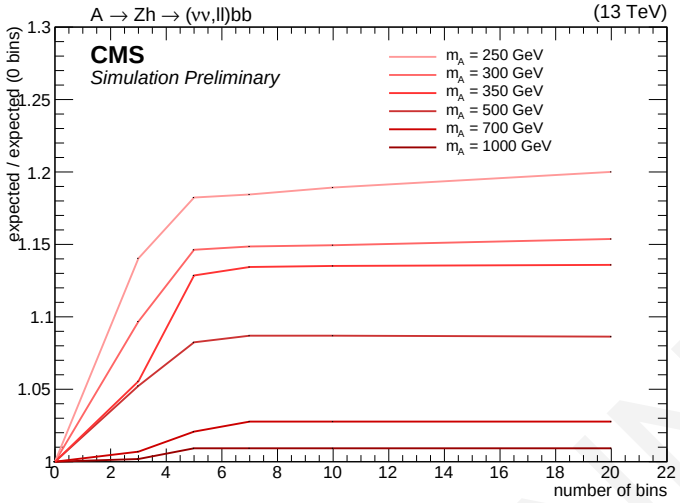

Figure 5.127: Expected limits as a function of the number of bins considered for the Monte-Carlo statistics systematic uncertainty, relative to the expected limit with no uncertainties, for different m_A values.

	Shape	Main backgrounds (Drell-Yan, $t\bar{t}$)	Other electroweak (single-top, VV, Vh)	Signal
Lepton and trigger efficiency	✓	-	2-3%	2-3%
Jet Energy Scale	✓	-	5%	2-6%
Jet Energy Resolution	✓	-	2%	1-2%
b-tagging	✓	-	4%	5-8%
Unclustered $\not{E}_T$	✓	-	1%	1%
Pile-up	✓	-	1%	1%
PDF	✓	-	3-5%	4-8%
top quark p_T (only $t\bar{t}$)	✓	8–15%	-	-
Factorization and renormalization scale	✓	2-6%		6-14%
Monte Carlo modeling	✓	1-15 %		-
Monte Carlo statistics	✓	1–20%		-
Interpolation to SR		2–10%		-
Extrapolation to 3 b-tag SR		20–46% (3 b-tag only)		-
Cross section		-	2-10%	-
Luminosity		-	2.5%	2.5%

Table 5.47: Summary of systematic uncertainties for backgrounds and signals.

5.9 RESULTS

The CL_s criterion (see Appendix A.1.7) is used to determine the 95% confidence-level limit on the signal contribution in the data, using the *RooStats* package [112]. In order to extract the limit on the production cross section times the branching ratios, the CMS standard *combine* tool [113] has been used. The *Asymptotic* method is used to calculate preliminary 95% C.L. upper limits with 1σ and 2σ bands using the CL_s frequentist calculation currently recommended by the LHC Higgs Combination Group [114]. The *ProfileLikelihood* method is used for significance and the background p-value; finally, the *MaxLikelihoodFit* method allows to get the signal *Best Fit Ratio*, the fit pulls and the pre/post fit distribution. The methods used to extract our results are described in Appendix A.1 in detail.

5.9.1 BACKGROUND SCALE FACTORS

Before testing the presence of the signal, a background-only fit is performed (including all systematic uncertainties described in Sec. 5.8) deriving the *background scale factors*. The numerical values and their post-fit uncertainties are reported in Tab. 5.48 and Tab. 5.49 and displayed in Fig. 5.128.

Overall, most of the scale factors are close to 1, however, the scale factor related to the $Z + 1b$ background process differs by 21% due to the difficulties in modeling the $Z+1b$ background. This difference is caused by the normalization for MadGraph 4-flavour scheme (4FS), which fails to describe simultaneously both the low- and high-p_T b-jet regions and its normalisation is underestimated by 20% [115].

Fig. 5.129 shows the distributions of the m_{Zh}^T and m_{Zh} for all categories. The grey dotted line represents the sum of the background before the fit; the shaded area represents the post-fit uncertainty. The ratio between data and SM background is given at the bottom of each panel.

background	scale factor
Z+0 b quark	0.993 ± 0.018
Z+1 b quark	1.214 ± 0.021
Z+2 b quark	1.007 ± 0.025
$t\bar{t}$	0.996 ± 0.014
W+jets	0.980 ± 0.023

Table 5.48: Background scale factors, as derived by the combined fit (with the signal regions blinded).

Signal region	0ℓ, 1 b tag	0ℓ, 2 b tags	0ℓ, 3 b tags	2ℓ, 1 b tag	2ℓ, 2 b tags	2ℓ, 3 b tags
Data	2452 ± 50	398 ± 20	45 ± 7	10512 ± 103	2188 ± 47	129 ± 11
Z+0 b quark	740 ± 12	48 ± 1	2.0 ± 0.2	4118 ± 15	175 ± 1	18 ± 1
Z+1 b quark	220 ± 6	13 ± 1	0.46 ± 0.06	4127 ± 18	365 ± 3	23 ± 1
Z+2 b quark	134 ± 3	86 ± 2	2.5 ± 0.3	1547 ± 11	1113 ± 7	51 ± 2
single top	74 ± 3	18 ± 1	3.0 ± 0.4	25 ± 0	10.0 ± 0.1	-
$t\bar{t}$	750 ± 12	143 ± 3	31 ± 3	592 ± 3	473 ± 3	26 ± 1
VV, Vh	76 ± 2	32 ± 1	0.93 ± 0.11	139 ± 1	53 ± 1	3.5 ± 0.1
W+jets	458 ± 13	65 ± 3	2.4 ± 0.3	3.7 ± 0.1	-	-
Total bkg.	2451 ± 26	405 ± 8	42 ± 5	10552 ± 35	2189 ± 12	121 ± 3
Pre-fit bkg.	2467 ± 26	427 ± 8	28 ± 5	$10\,740 \pm 35$	2250 ± 12	100 ± 3
$m_A = 300$ GeV	-	-	-	3.1 ± 0.2	3.3 ± 0.2	0.10 ± 0.01
$m_A = 1000$ GeV	27.3 ± 5.2	28.6 ± 5.4	3.5 ± 0.7	5.4 ± 1.0	6.1 ± 1.2	1.2 ± 0.2

Table 5.49: Expected and observed event yields after the fit in the signal regions. The di-electron and di-muon categories are summed together. The single dash symbol represents backgrounds with no simulated events passing the selections. The signal yields refer to pre-fit values corresponding to a cross section of 0.1 pb (gluon-gluon fusion for $m_A = 300$ GeV, and in association with b-quarks for $m_A = 1000$ GeV) multiplied by $Br(A \to Zh) \times Br(h \to b\bar{b})$. The uncertainties on the observed number of events reflect the statistics of the data events. The uncertainties on the total background take into account the correlation of systematic uncertainties among different background processes. The statistical and systematic uncertainties are combined for all samples except the data.

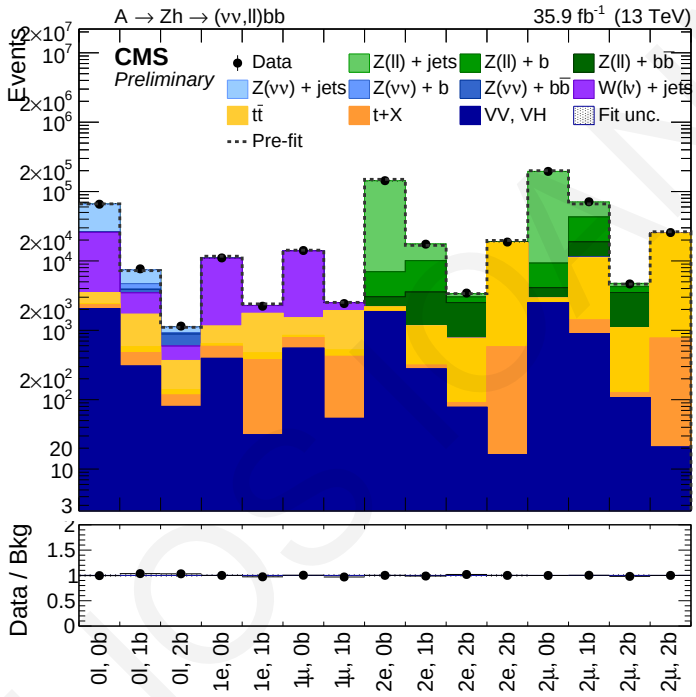

Figure 5.128: Pre- (dashed gray lines) and post-fit (stacked histograms) number of events in the different control regions used in the fit.

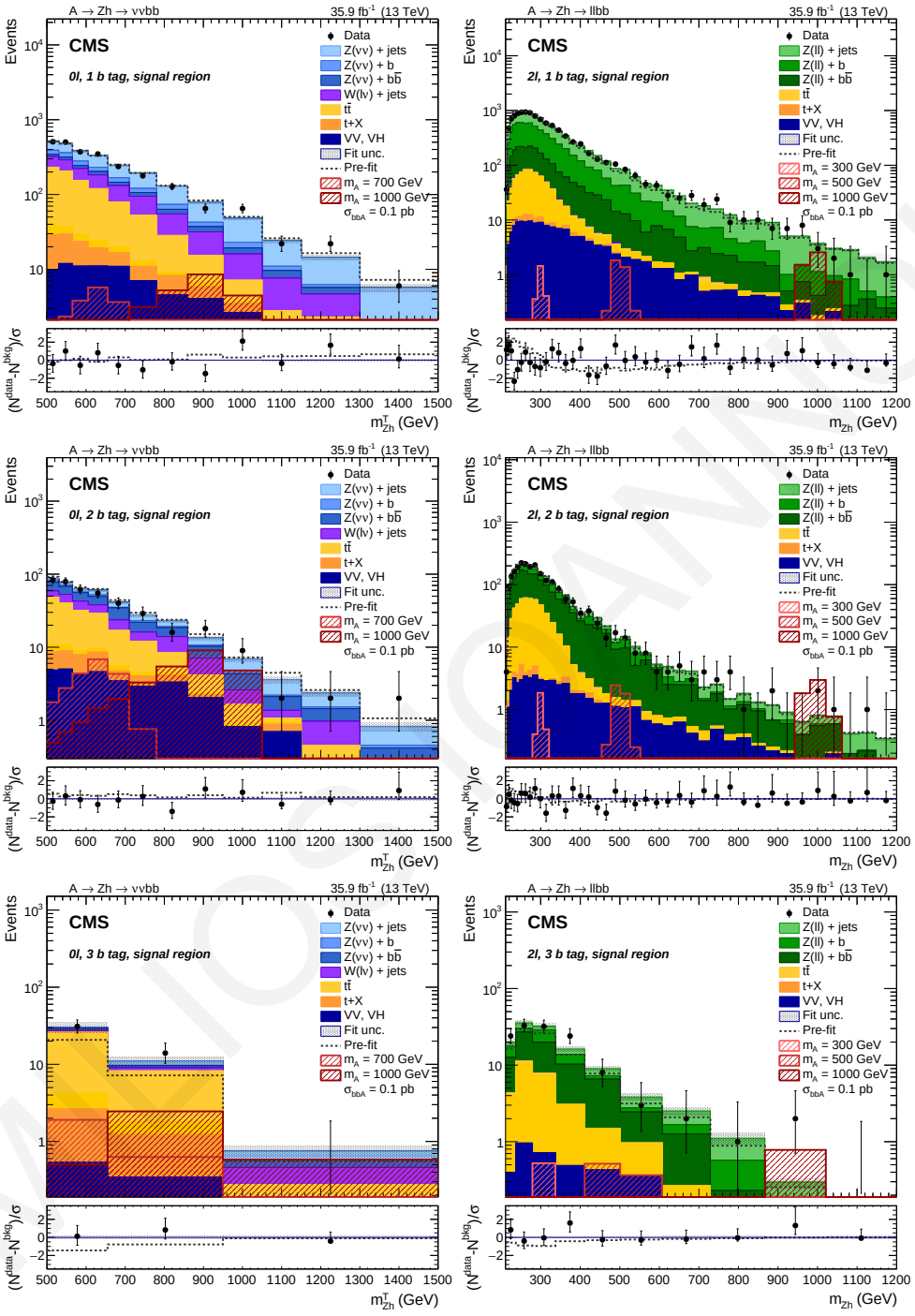

Figure 5.129: Distributions of the m_{Zh}^T variable in the 0ℓ categories (left) and m_{Zh} in the 2ℓ categories (right), in the 1 b tag (upper), 2 b tag (centre), and 3 b tag (lower) SR. In the 2ℓ categories, the contribution of the $2e$ and 2μ channels have been summed. The hatched red histograms represent signal produced corresponding to $\sigma_A \times Br(A \to Zh) \times Br(h \to b\bar{b}) = 0.1$ pb. The bottom panels depict the pulls in each bin, $(N^{data} - N^{bkg})/\sigma$, where σ is the statistical uncertainty in data.

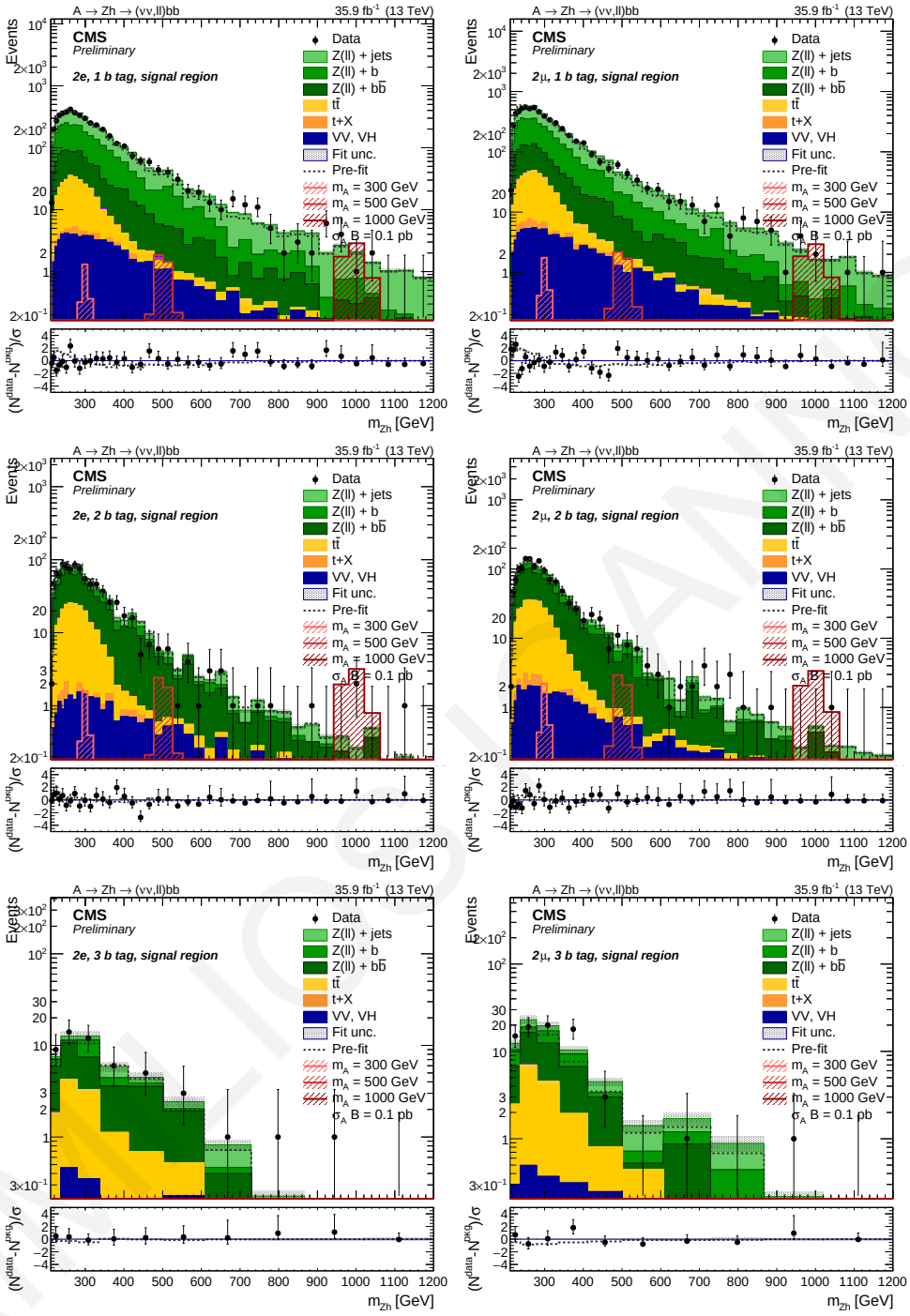

Figure 5.130: Distributions of the m_{Zh} variable in the $2e$ categories (left) and 2μ categories (right), in the 1 b tag (upper), 2 b tag (centre), and 3 b tag (lower) SR. The grey dotted line represent the sum of the background before the fit; the shaded area represents the post-fit uncertainty. The hatched red histograms represent signal produced corresponding to $\sigma_A \times Br(A \to Zh) \times Br(h \to b\bar{b}) = 0.1$ pb. The bottom panels depict the pulls in each bin, $(N^{data} - N^{bkg})/\sigma$, where σ is the statistical uncertainty in data.

5.9.2 EXPECTED LIMITS

Results are obtained from a combined signal and background fit to the unbinned m_{Vh} distribution, based on a profile likelihood defined as:

$$\mathcal{L} = \prod_i \frac{\mu_i^{n_i} \cdot e^{-\mu_i}}{n_i!} \qquad \text{with} \quad \mu_i = \sigma_i(S) + N_i(B) \tag{5.15}$$

where $N_i(S)$ and $N_i(B)$ are the signal and background events in the i-th bin, and σ is the signal strength modifier parameter. Systematic uncertainties are treated as nuisance parameters and are profiled (systematic uncertainties are incorporated in the profile likelihood) in the statistical interpretation. The background-only hypothesis is tested against the $A \to Zh$ signal in the ten categories, and with no evidence of significant deviations from background expectation, the asymptotic modified frequentist method is used to determine the limit at the 95% confidence level (CL) on the contribution from signal.

The observed upper limit on the resonance cross section times $Br(A \to Zh)$ times $Br(h \to b\bar{b})$, as well as the expected limit and its relative 68% and 95% uncertainty bands, are reported as a function of the resonance mass in Fig 5.131.

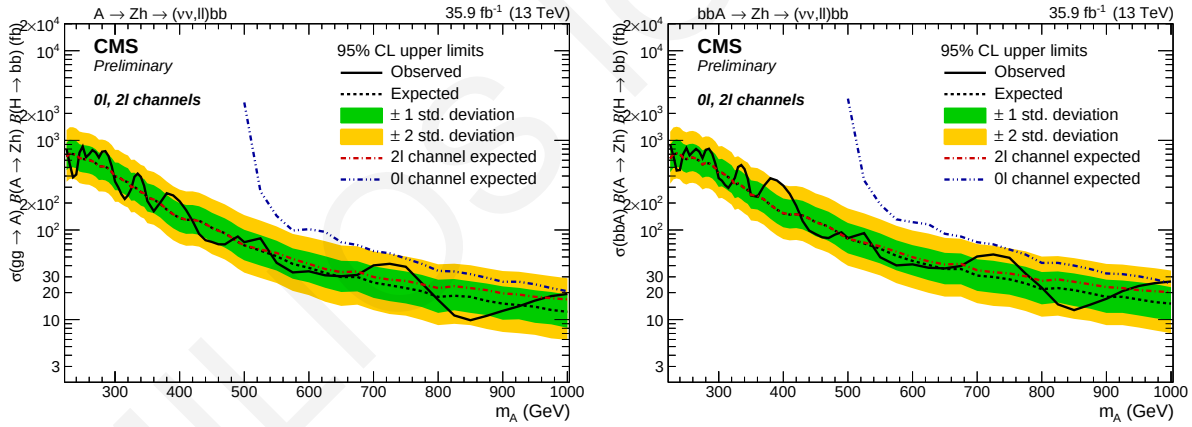

Figure 5.131: Observed and expected (with $\pm 1(2)\sigma$ band) 95%C.L. upper limit on $\sigma_A \times Br(A \to Zh)$ in the gluon fusion (left) and b-quark associated production (right), including all statistical and systematics uncertainties.

Figure 5.132 shows the observed and expected 95% C.L. upper limit on $\sigma_A \times Br(A \to Zh)$ in the gluon fusion and b-quark associated production in the non-leptonic channel only. No excess of data is observed in 0ℓ channel for both Higgs mechanism modes. Additionally, the expected limit in the leptonic channels ($2e$ and 2μ) in the gluon fusion and b-quark associated production is presented in Figure 5.133. There is no excess on data over the background prediction in the $2e$ and 2μ channels.

An upper limit at 95% CL on the number of signal events is set on $\sigma_A \times Br(A \to Zh) \times Br(h \to b\bar{b})$,

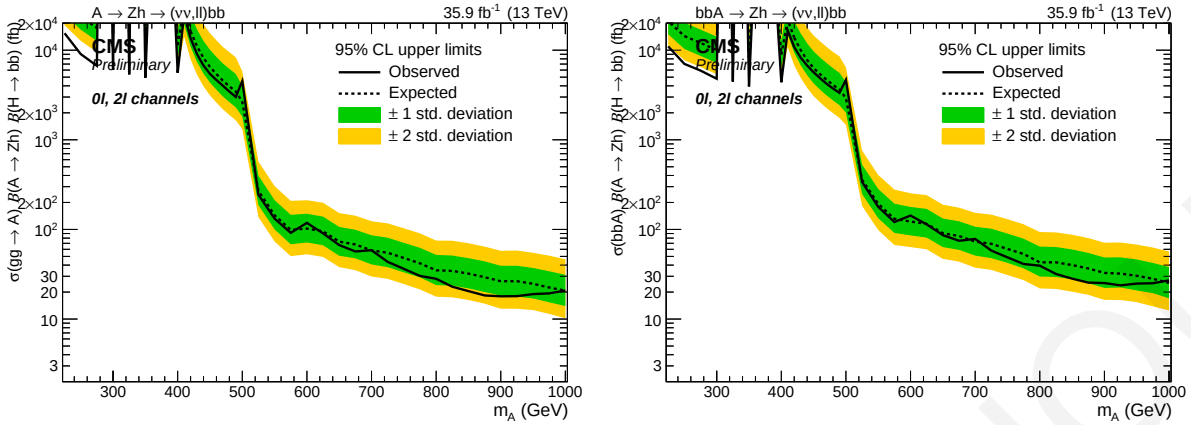

Figure 5.132: Observed and expected (with $\pm 1(2)\sigma$ band) 95%C.L. upper limit on $\sigma_A \times Br(A \to Zh)$ in the gluon fusion (left) and b-quark associated production (right) in the 0ℓ channel.

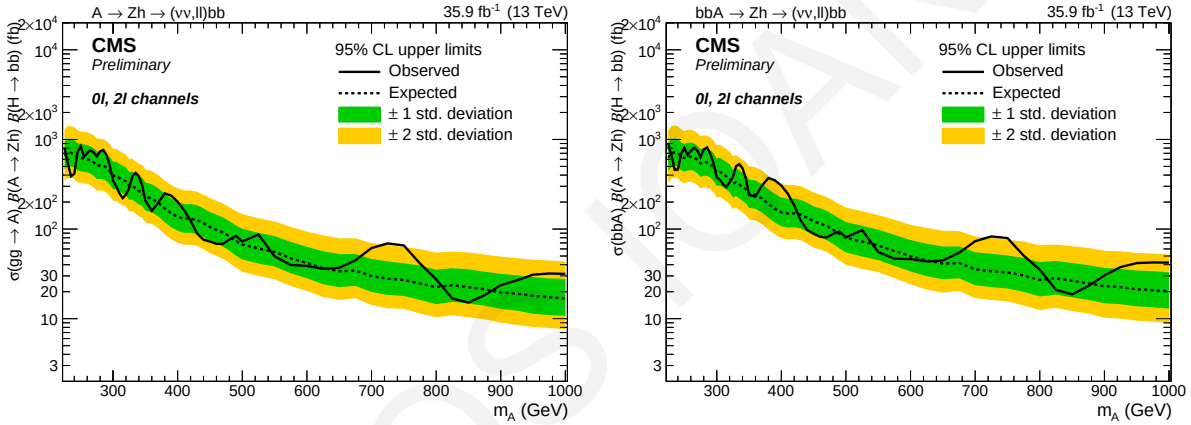

Figure 5.133: Observed and expected (with $\pm 1(2)\sigma$ band) 95%C.L. upper limit on $\sigma_A \times Br(A \to Zh)$ in the gluon fusion (left) and b-quark associated production (right) in the 2ℓ channel.

excluding above 1 pb for m_A near the kinematic threshold, ≈ 0.3 pb for $m_A \approx 2m_t$, and as low as 0.02 pb at the high end (1000 GeV) of the considered mass range. The sensitivity of the analysis is limited by the amount of data, and not by systematic uncertainties. These results extend the search for a 2HDM pseudo-scalar boson A for mass up to 1 TeV, which is a kinematic region previously unexplored by CMS in the 8 TeV data analysis.

The results are interpreted (as described in Chapter 5.9.5) in terms of Type-I, Type-II, Flipped, and Lepton-specific 2HDM formulations. In the scenario with $cos(\beta - \alpha) = 0.1$ and $tan\beta = 3$, as examined in Section 5.2.1, an A boson up to 380 and 350 GeV is excluded in 2HDM Type-I and Type-II, respectively, as illustrated in Fig. 5.134. These exclusion limits are used to constrain the two-dimensional plane of the 2HDM parameters $[cos(\beta - \alpha), tan\beta]$ (as reported in Sec. 5.9.5), with fixed $m_A = 300$ GeV in the range $0.1 \leq tan\beta \leq 100$ and $-1 \leq cos(\beta - \alpha) \leq 1$, using the convention $0 < \beta - \alpha < \pi$.

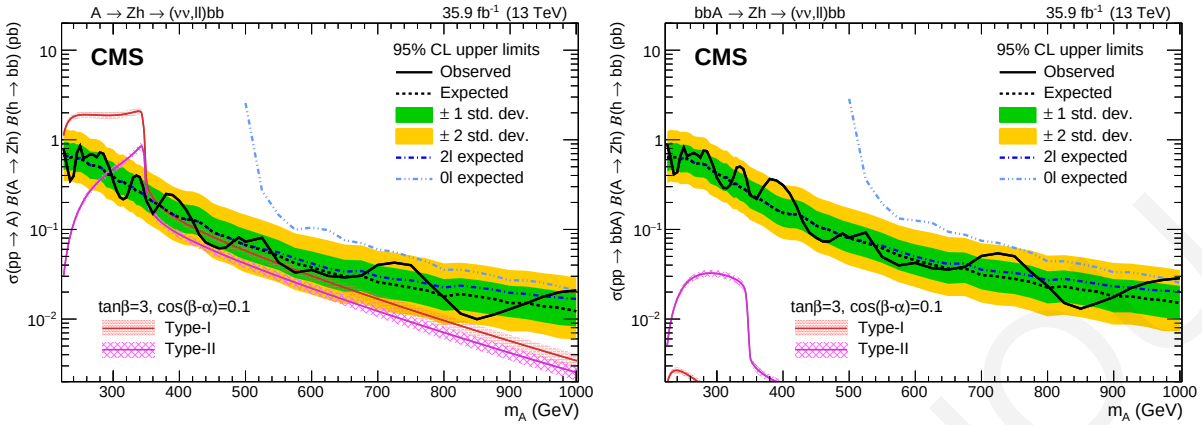

Figure 5.134: Observed (solid black) and expected (dotted black) 95% CL upper limits on $\sigma_A \times Br(A \to Zh) \times Br(h \to b\bar{b})$ for an A boson produced via gluon-gluon fusion (left) and in association with b-quarks (right) as a function of m_A. The blue dashed lines represent the expected limits of the 0ℓ and 2ℓ categories separately. The red and magenta solid curves and their shaded areas correspond to the product of the cross sections times the branching fractions and the relative uncertainties predicted by the 2HDM Type-I and Type-II for the arbitrary parameters $\tan\beta = 3$ and $\cos(\beta - \alpha) = 0.1$.

Because of the suppressed A boson cross section and $Br(A \to Zh)$, the region near $cos(\beta - \alpha) \approx 0$ is not accessible in this search.

To sum up, no excess of data over the background prediction is observed. Upper limits are set at 95% confidence level on the product of the A boson cross sections times the branching fractions $\sigma_A \times Br(A \to Zh) \times Br(h \to b\bar{b})$, which exclude 1 to 0.02 pb in the 225-1000 GeV mass range.

5.9.3 Fit Diagnostics

The signal extraction procedure described above allows the background to vary within the systematic uncertainties modifying the corresponding nuisance parameters. In this section these variations in the background are shown when the fit to the data is performed, both with the background-only and with the background plus signal hypothesis.

Prior to the data unblinding, the procedure is tested by setting the signal strength to zero (background-only fit), thus avoiding any information on the signal presence.

The pull fit is described in Appendix A.1.12. The fit results are presented as bars, where the value on the x-axis represents the pull values $\Delta x/\sigma_{in}$, and its error bar the fit constraining on the gaussian width of the nuisance parameter σ_{out}/σ_{in}, for both the background-only and the signal+background fit. The $(\hat{\theta} - \theta_0)\Delta\theta$ value on the y-axis represents the initial value of a nuisance parameter (θ_0) and the post-fit

value ($\hat{\theta}$) of the nuisance parameter and its uncertainty ($\Delta\theta$). The pull distributions are shown in Fig. 5.135.

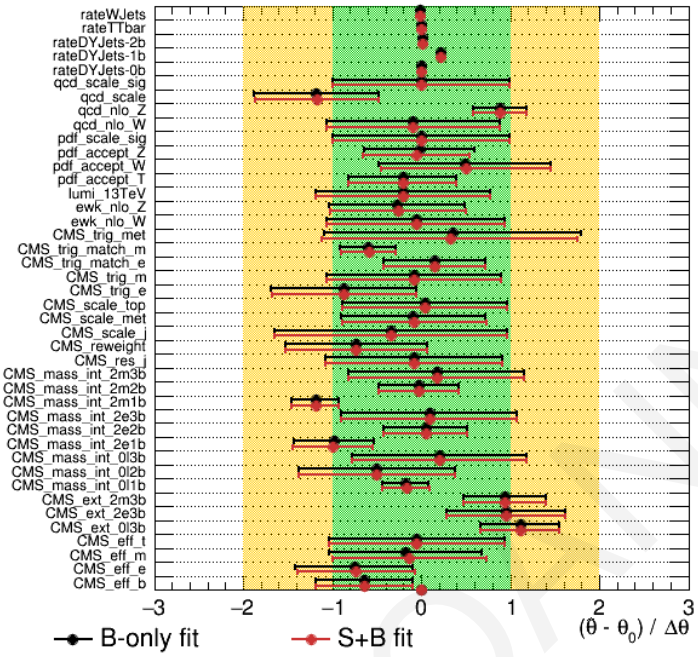

Figure 5.135: Pull values for the combination of all 0-, and 2-lepton channels in both the background-only and signal+background hypotheses. The considered signal is $m_A = 300$ GeV.

Some uncertainties are pulled by the fit, as expected. The QCD factorisation and renormalisation scales and the NLO QCD corrections are pulled (although in different directions) to accommodate the shape of the background in the medium and low mass regime. These pulls are dominated and constrained by the di-leptonic 1 b-tag signal regions, which have the largest discrepancy and statistics. A good agreement is observed instead in the 2 b-tag signal regions.

The mass interpolation uncertainties are compatible with the initial values by less than one standard deviation, but a couple of channels are close to this value. This is again observed in the high-statistics, poorly-modeled 1 b-tag di-leptonic regions. The simulation imperfect modeling typically affects the region with low m_{jj}, close to the Higgs mass window, and the normalisation based on the sidebands can be affected by these effects.

The uncertainties that determine the normalisation in the 3 b-tag SR are all pulled up by 1σ. This was expected already prior to the unblinding, as a similar effect was observed consistently in the 3 b-tag jet mass sidebands, and an appropriate systematic uncertainty was applied to account for this effect, which has been confirmed after the unblinding.

As a summary, the pulls in the background-only and signal+background fit do not show worrisome

features. A large fraction of uncertainties are within 1σ and not excessively pulled. A small tension is observed in some regions of the phase space, but these small discrepancies are well covered by the present set of systematic uncertainties.

5.9.4 IMPACTS

The signal extraction procedure described above allows the background to vary within the systematic uncertainties modifying the corresponding nuisance parameters. The plots report the impacts and the pulls of the fits (described in Section A.1.12), performed on data in the $m_A = 300,\ 500,$ and 1000 GeV signal hypothesis. Only the first thirty impacts and pulls are shown in the plots, for more details see Appendix E.5 which includes a full list of impacts for each mass point.

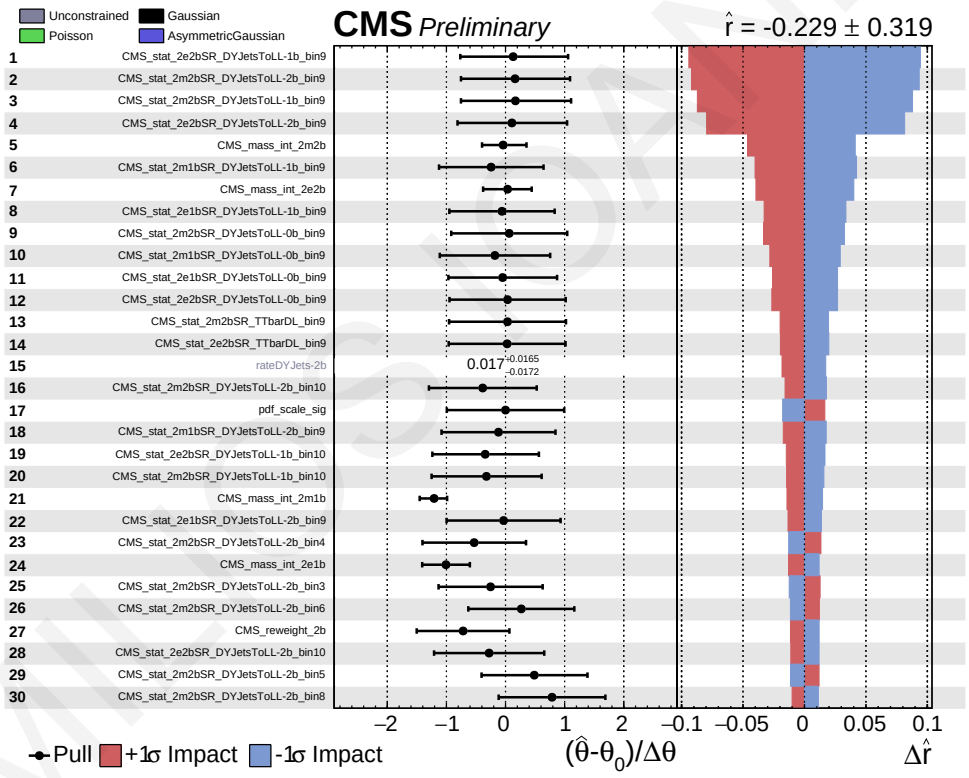

Figure 5.136: Impacts for the combination of all channels and the $m_A = 300$ GeV signal hypothesis.

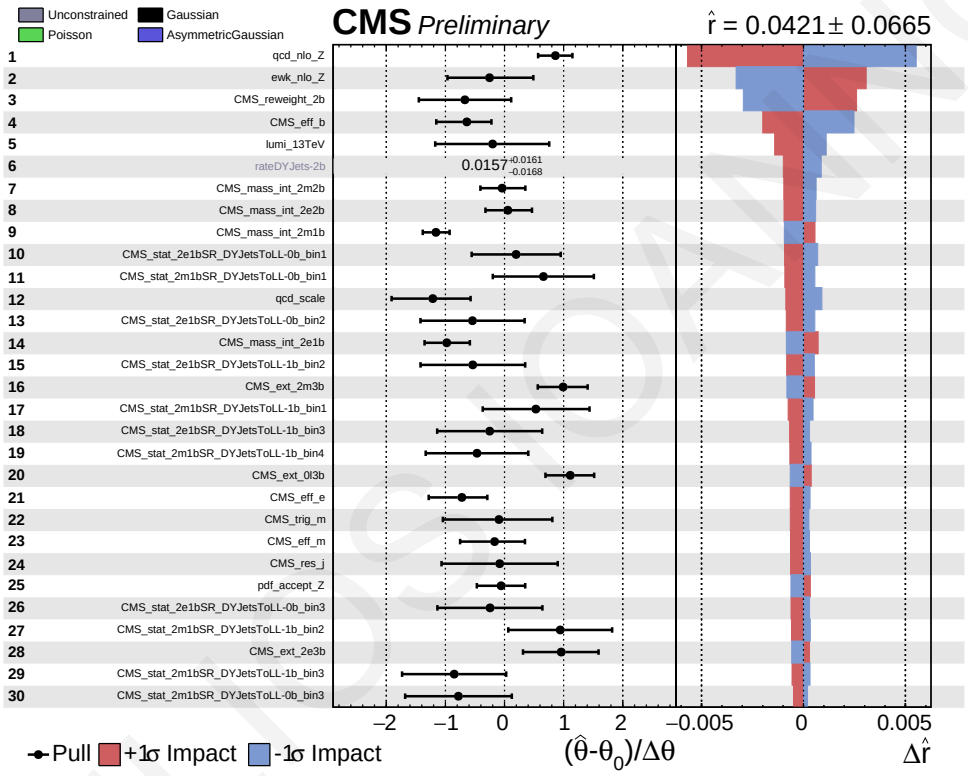

Figure 5.137: Impacts for the combination of all channels and the $m_A = 500$ GeV signal hypothesis.

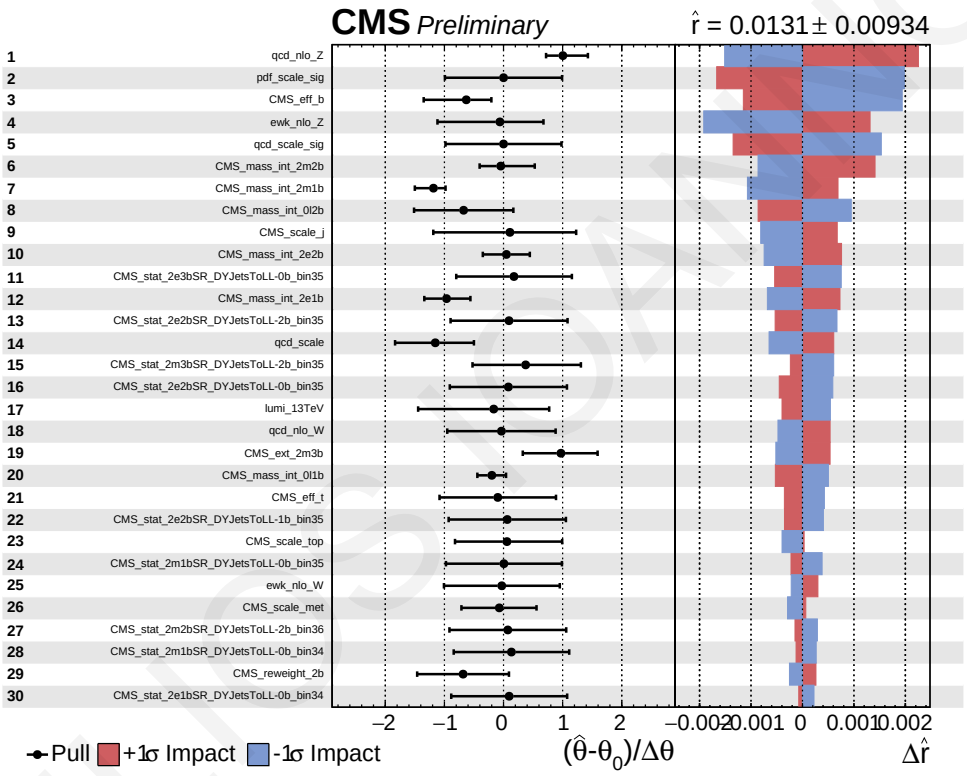

Figure 5.138: Impacts for the combination of all channels and the $m_A = 1000$ GeV signal hypothesis.

5.9.5 INTERPRETATION IN 2HDM

In this section, an interpretation of the results in terms of the Two Higgs Doublet Models (2HDM) is presented. In principle, 2HDM includes four different types which are separated by the coupling of the fermions to Higgs doublets (Φ_1 and Φ_2).

- **Type-I:** all fermions couple only to the Higgs field in the Φ_2 doublet.
- **Type-II:** up-type quarks couple to the Φ_2 doublet, while down-type quarks and charged leptons couple to the Higgs field in the Φ_1 doublet.
- **Flipped:** up-type quarks and charged leptons couple to the Φ_2 doublet and down-type quarks couple to Φ_1.
- **Lepton-specific:** all quarks couple to the Higgs field in the Φ_2 doublet and charged leptons couple to Φ_1.

In general, 2HDM has a large number of free parameters, which can be represented in different basis: For example, a set can be the following: $m_h,\ m_H\ , m_A,\ m_{H^\pm},\ m_{12},\ \beta,\ \alpha,\ \lambda_{6,7}$, where $m_{h,H,A,H^\pm}$ are the masses of the Higgs states, m_{12} is the coefficient of $[\Phi_1^+\Phi_2 + h.c.]$ operator in the 2HDM potential, α and β are mixing angles of the two Higgs doublet ($tan\beta$ is, as in the Minimal Supersymmetric Standard Model (MSSM), the ratio of the vev of the two doublets), and finally $\lambda_{6,7}$ are the coefficients of other dimension-4 operators in the Higgs potential as given in Eq. 2.6.

In order to reduce the number of free parameters, the following convention is applied, based on the Higgs Working Group prescriptions:

- the lightest Higgs is assumed to be the SM-line one discovered by LHC: $m_h \approx 125$ GeV;
- $m_H = m_{H^\pm} = m_A$, since A searches are not strongly dependent on m_H and $m_{H^\pm}$, and a large mass splitting would break the custodial symmetry and give large contribution to $\rho \neq 1$;
- $m_{12}^2 = m_A^2 \cdot \frac{tan\beta}{1+tan^2\beta}$, so the discrete $\mathbb{Z}_2$ symmetry is broken as in MSSM;
- $\lambda_{6,7} = 0$ to avoid CP-violation at the tree-level.

With these assumptions, the remaining parameters are one mass, m_A, and the two angles, α, and β. The results are presented as a given mass point m_A in the plane $tan\beta$ vs $cos(\beta - \alpha)$, as well as a given $cos(\beta - \alpha)$ point in the plane $tan\beta$ vs m_A. In the limit for $cos(\beta - \alpha) \to 0$, called *alignment limit* (described in Chapter 2.2.6), the light Higgs h behaves as the Standard Model one.

The cross sections have been computed via SuSHI 1.6.1 and the branching fractions via 2HDMC 1.7.0, both at next-to-next-leading order (NNLO), using the previous assumptions.

For each mass point (m_A = 225, 250, 275, 300, 325, 350, 400, 500, 600, 700, 800, 900, 1000 GeV) the cross section and branching fractions are computed for $0.1 \leq tan\beta \leq 100$ in variable step (finer at low $\tan\beta$) and $0 \leq cos(\beta - \alpha) \leq 1$ with step 0.02.

The cross sections for all type models do not depend on α, so their dependence on m_A and $tan\beta$ are shown in Fig. 5.139 for Type-I, in Fig. 5.140 for Type-II, in Fig. 5.141 for Flipped, and in Fig. 5.142 for Lepton-specific.

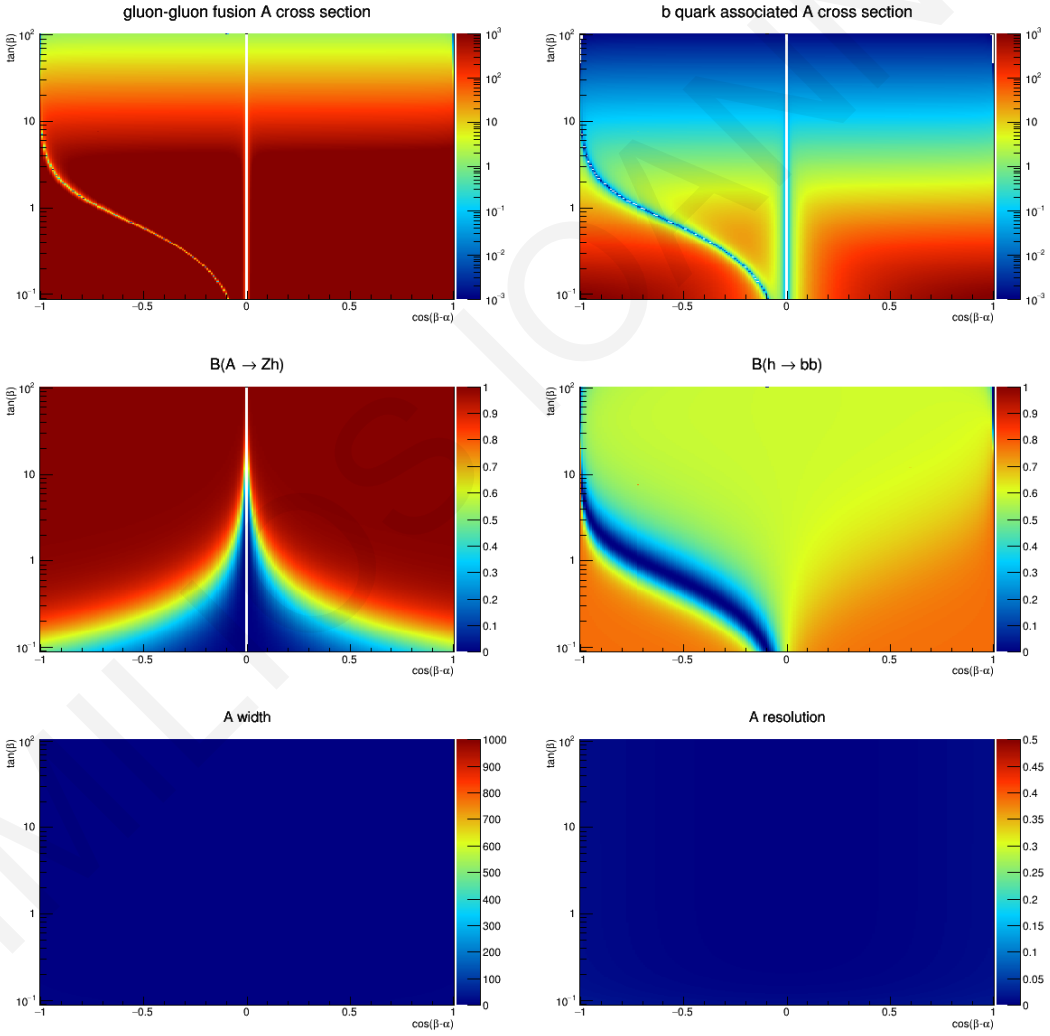

Figure 5.139: Cross sections and branching ratios for the Type-I 2HDM model. Top left: gluon fusion A cross section; top right: b-quark associated A cross section; center left: $Br(A \to Zh)$; center right: $Br(h \to b\bar{b})$; bottom left: A boson natural width; bottom right: A boson resolution.

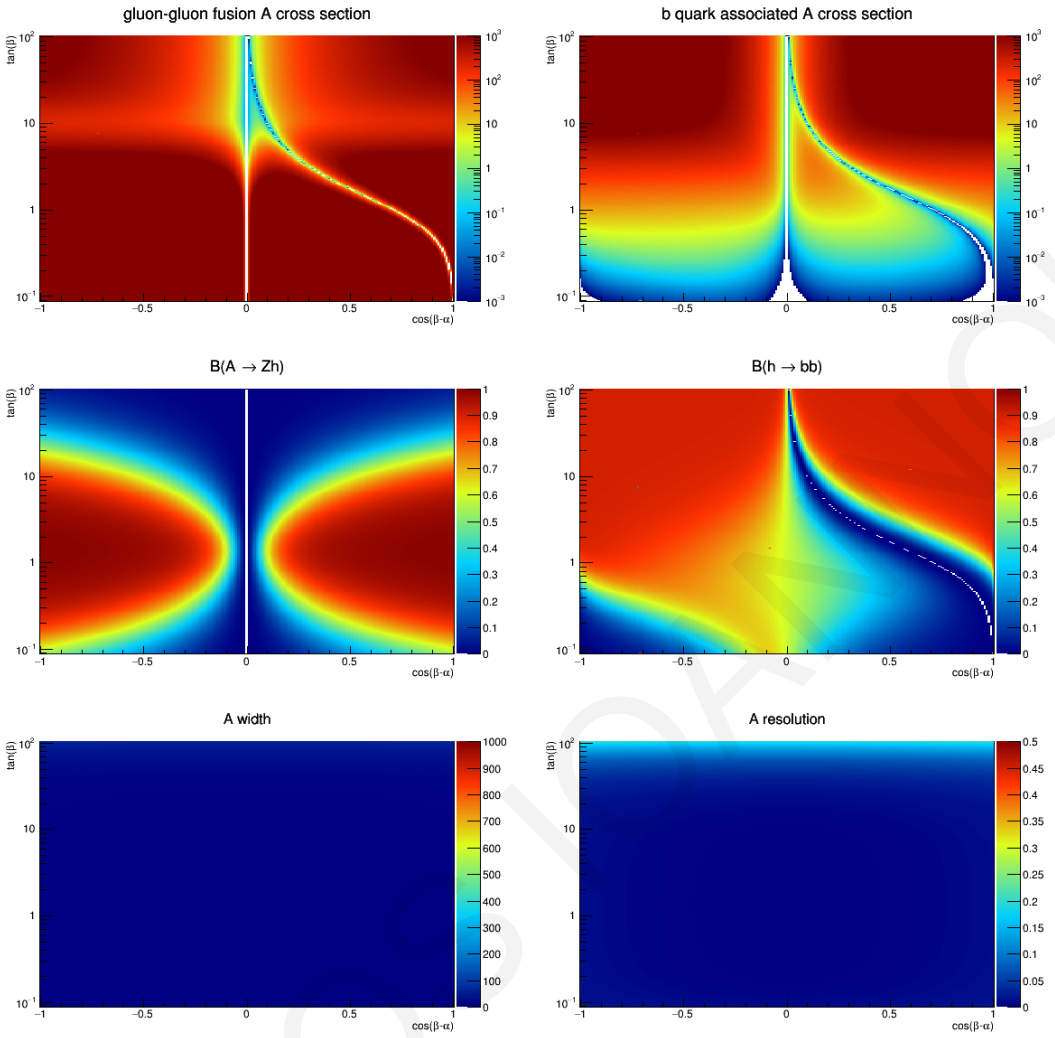

Figure 5.140: Cross sections and branching ratios for the Type-II 2HDM model. Top left: gluon fusion A cross section; top right: b-quark associated A cross section; center left: $Br(A \to Zh)$; center right: $Br(h \to b\bar{b})$; bottom left: A boson natural width; bottom right: A boson resolution.

Two channels can produce an A in the final state, as described in Chapter 2.2.8 and Chapter 5.2.1: gluon-gluon fusion (denoted as *ggA* in the plots) and associated production with b-quarks (denoted *bbA*). The first two cross sections are plotted separately for both Type-I and Type-II models. In the Type-I model, the bbA cross section is always negligible with respect to the ggA one, and both decrease with $tan\beta$. In the Type-II model, the ggA cross section decreases when the $tan\beta$ parameter increases, but in the case of the associated production with b-quarks the $b\bar{b}A$ cross section increases with $tan\beta$, and therefore for moderately large $tan\beta \sim 5$ it becomes comparable to the ggA one, and bigger afterwards. This is expected, since the relevant couplings for ggA and bbA are the ones of the up- and down-type quarks, respectively, and these are the same in Type-I (hence the same behaviour of the cross-section), while

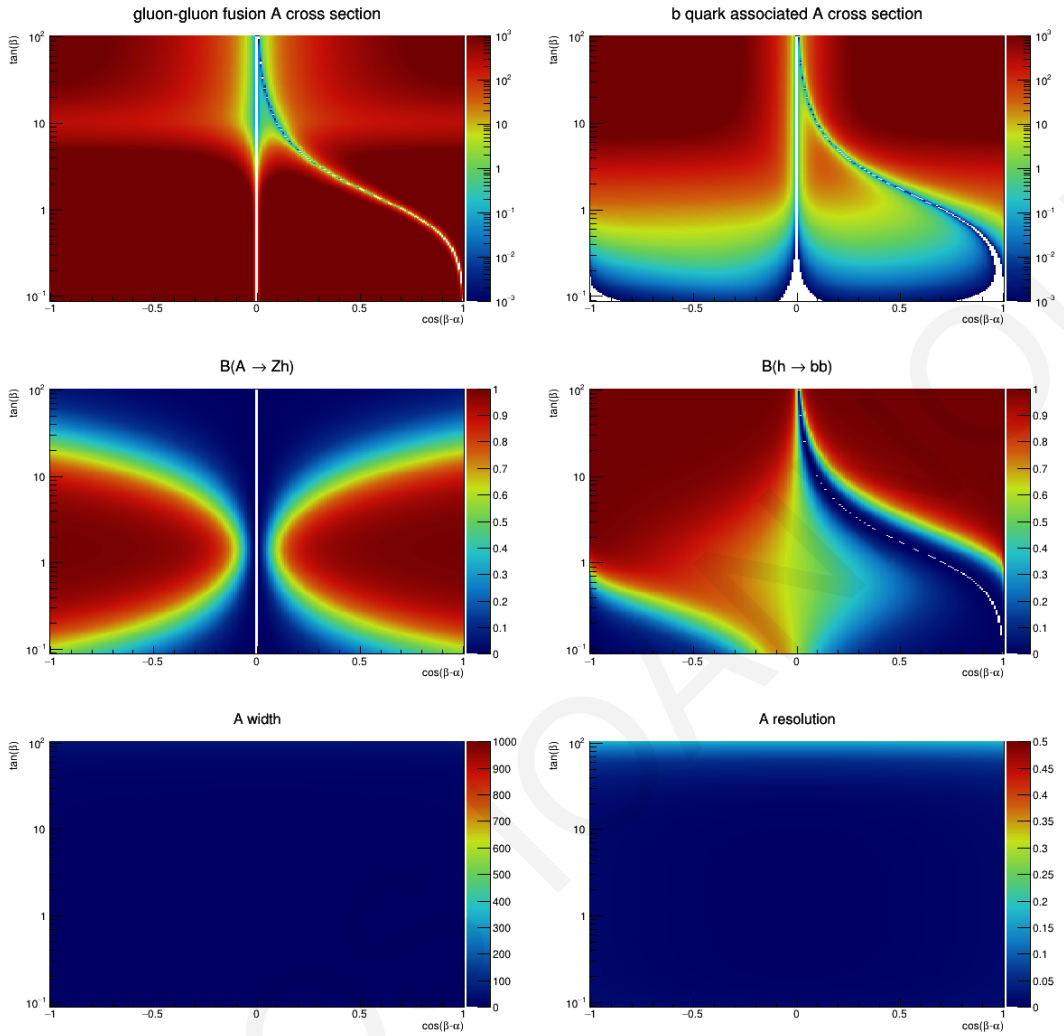

Figure 5.141: Cross sections and branching ratios for the Type-III or Flipped 2HDM model. Top left: gluon fusion A cross section; top right: b-quark associated A cross section; center left: $Br(A \to Zh)$; center right: $Br(h \to b\bar{b})$; bottom left: A boson natural width; bottom right: A boson resolution.

depend on $\tan\beta$ for Type-II, as in the MSSM case. The branching fraction of $A \to Zh$ channel vanishes in the alignment limit, as expected. In the case of the alignment limit, the 2HDM theory converges to the Standard Model where only one physical Higgs state, h, survives and the other four Higgs bosons disappear. The branching fraction of $h \to b\bar{b}$ is not the one predicted by the Standard Model in all 2HDM phase space: this is guaranteed only in the alignment limit, namely for $cos(\beta - \alpha) = 0$. The deep valley with $Br(h \to b\bar{b}) \sim 0$ present in Type-II is due to the coupling of the down-type quarks to the Higgs boson, which is proportional to $(-sin\alpha/cons\beta)$, vanishing for $a \sim 0$.

Moreover, the cross sections of Flipped and Lepton-specific models do not depend on the mixing angle

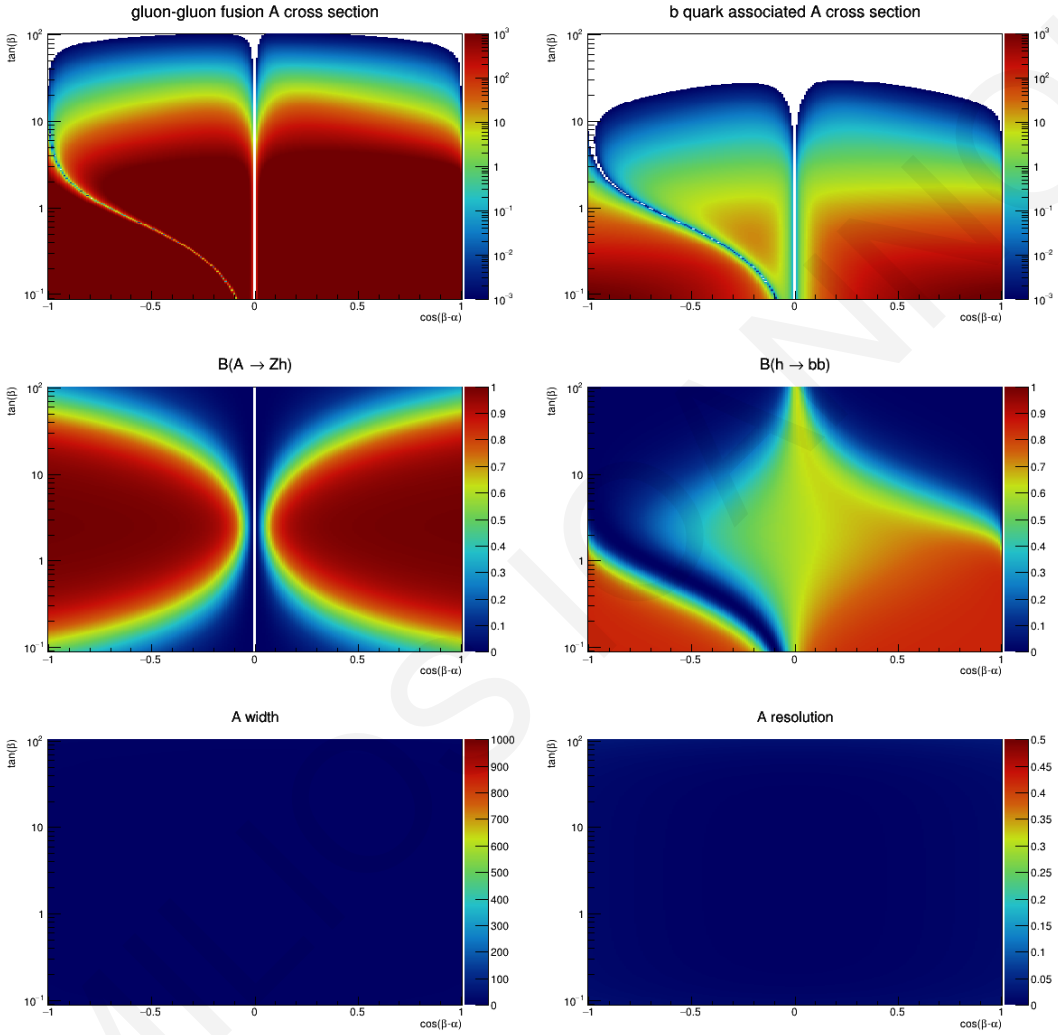

Figure 5.142: Cross sections and branching ratios for the Type-IV or Lepton-specific 2HDM model. Top left: gluon fusion A cross section; top right: b-quark associated A cross section; center left: $Br(A \to Zh)$; center right: $Br(h \to b\bar{b})$; bottom left: A boson natural width; bottom right: A boson resolution.

α as well, however, they have strong dependence on the mass of A boson and $\tan\beta$, as indicated in Fig. 5.141 and in Fig. 5.142. On the other hand, these two models behave differently when the value of $\tan\beta$ increases or decreases. For instance, in the Flipped 2HDM type, obviously, the cross section of the gluon-gluon function and the bbA cross section become strongly important when the value of $tan\beta$ increases. However, both cross sections increase sharply when $tan\beta$ takes lower values in the Lepton-specific 2HDM type. Additionally, it is important to note that the bbA cross section vanishes when $tan\beta$ is $tan\beta > 10$. Secondly, in the case of the Lepton-specific type, the $Br(h \to b\bar{b})$ increases for the lowest values of $tan\beta$, as it occurs in Type-I 2HDM, where the coupling of the Higgs boson to down-type quarks is proportional to $cos\alpha/sin\beta$.

Finally, the expected and observed limits for the $m_A = 300$ GeV mass point, in the plane $tan\beta$ vs. $cos(\beta - \alpha)$ are reported in Fig. 5.143. The gluon-gluon fusion and the b-quarks associated production cross section are considered separately, by imposing simultaneous constraints on the combination of the two production modes.

As shown from Fig. 5.143, the exclusion limits reach the value of $tan\beta$ equal to 10 (6) in the Type-I type (Lepton-specific type). Additionally, there is a large parameter space which is excluded from the observed and expected cross sections in Type-II and Flipped models.

Furthermore, the cross sections of the four 2HDM models are presented in the plane $tan\beta$ vs. m_A. Figure 5.144, Figure 5.145, Figure 5.146, and Figure 5.147 show the cross sections of the gluon-gluon fusion and b-quark associated production, the $Br(A \to Zh)$ and $Br(h \to b\bar{b})$ and the natural width of A boson, as well as the A boson resolution in the plane m_A vs. $tan\beta$ for a given $cos(\beta - \alpha) = 0.1$.

In the Type-I model (Fig. 5.144), the cross section of the ggA and bbA depend on the m_A and the value of $tan\beta$ due to the coupling's dependence on $cot\beta$. In addition, the $Br(A \to Zh)$ increases up to the mass of 350 GeV and then it decreases significantly due to the opening of the $A \to t\bar{t}$ channel. After that, the cross section increases again at higher masses of A boson. On the other hand, the $h \to b\bar{b}$ branching fraction is not affected by an increase of the m_A, but only by large values of $tan\beta$ due to the coupling of h boson to down-type quarks, which is proportional to $cos\alpha/sin\beta$. The $Br(h \to b\bar{b})$ is important only for the lowest values of $tan\beta$ and is negligible for higher values.

In Type-II (Fig. 5.145) the cross section of the gluon-gluon fusion becomes negligible for higher values of $tan\beta$, however, at lowest values, $tan\beta \leq 1$, it increases significantly. On the contrary, the b-quark associated production cross section has an important rise when $tan\beta$ takes large values. Moreover, the $A \to Zh$ branching fraction remains unaffected, comparing it to the Type-I's $Br(A \to Zh)$. But, the $Br(h \to b\bar{b})$ is zero when the value of $tan\beta$ is equal to 10, for all mass points. This occurs because the coupling of the light Higgs to b-quarks vanishes for given values of $cos(\beta - \alpha)$ ($cos(\beta - \alpha) = 0.1$) and $tan\beta$ ($tan\beta = 10$).

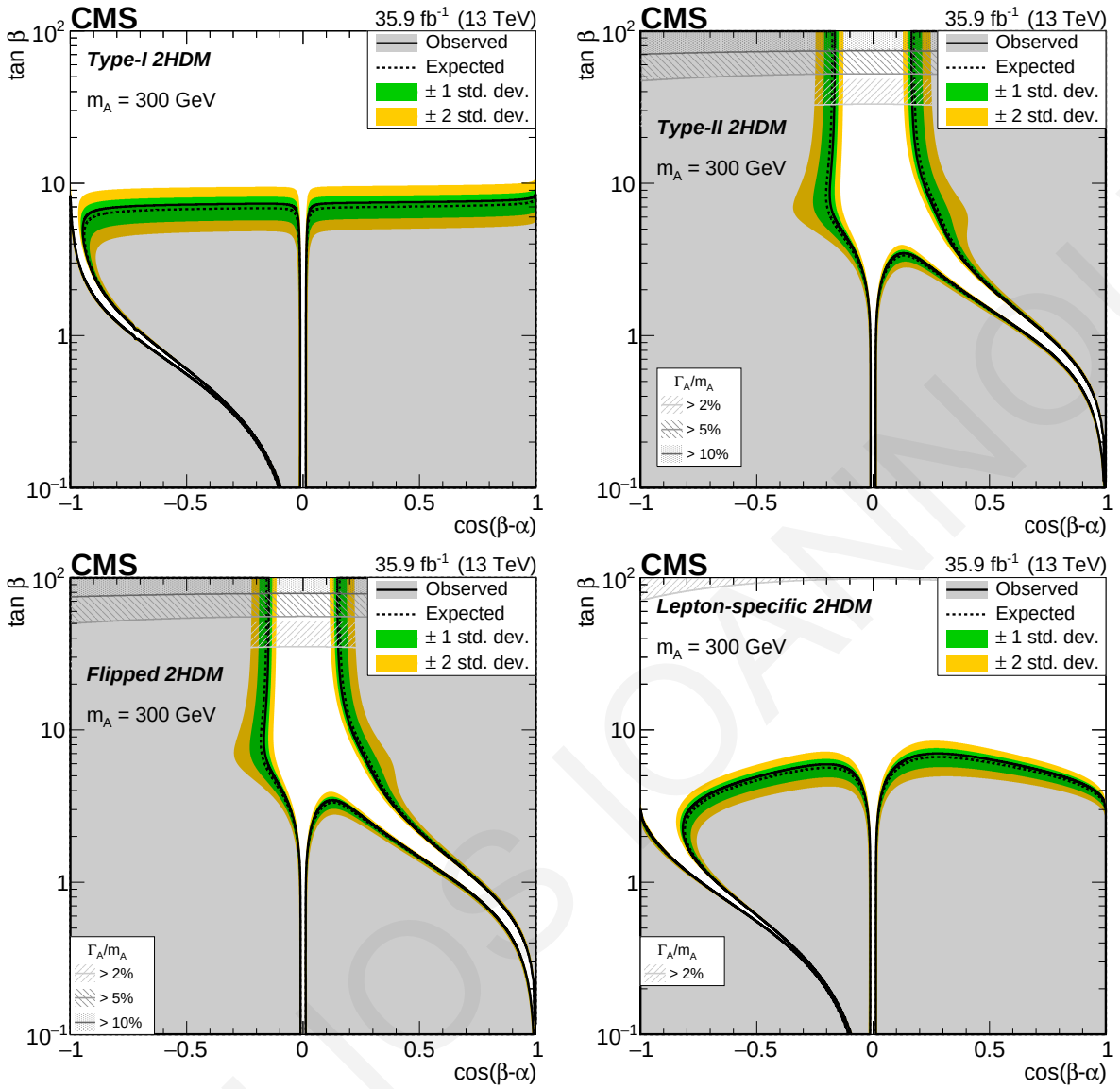

Figure 5.143: Observed and expected (together with $\pm 1, 2\sigma$ bands) exclusion limit for Type I (upper left), Type II (upper right) model, Flipped (lower left) model and Lepton-specific (lower right) model as a function of $tan\beta$ and $cos(\beta - \alpha)$, for $m_A = 300$ GeV. Contours are derived from the projection on the 2HDM parameter space for the $m_A = 300$ GeV signal hypothesis. The excluded region is represented by the shaded grey area. The regions of the parameter space where the natural width of the A boson Γ_A is comparable to the experimental resolution and thus the narrow width approximation is not valid are represented by the hatched grey areas.

The cross sections and branching ratios of the Flipped 2HDM model are presented in Fig. 5.146. This figure contains plots which behave similarly with the corresponding plots of the Type-II model. Couplings of the Flipped and Type-II models are similarly, however only the couplings of the charged leptons differ. As we know, the charged leptons couple to Φ_2 in the Flipped 2HDM type instead of Φ_1

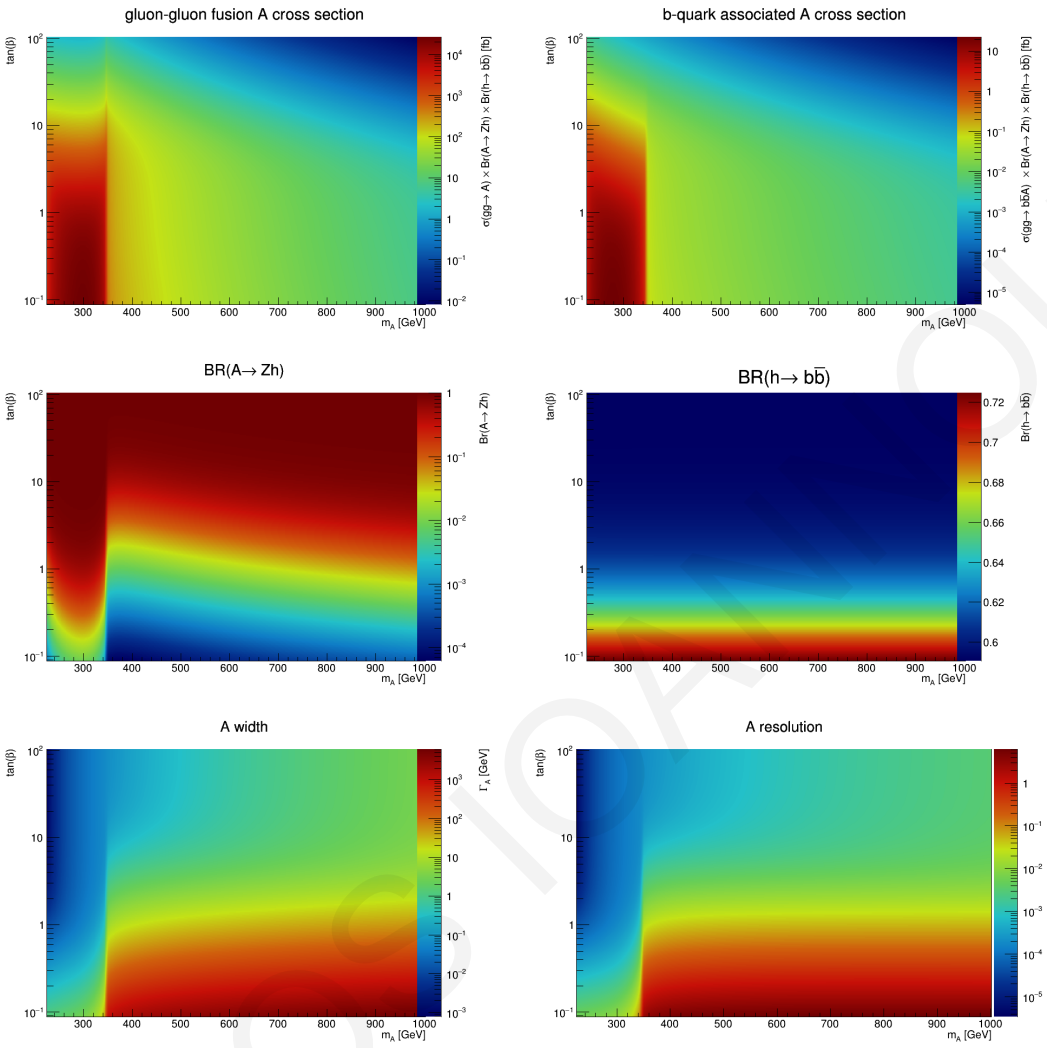

Figure 5.144: Cross sections and branching ratios for the Type-I in the plane m_A vs. $tan\beta$. Top left: gluon fusion A cross section; top right: b-quark associated A cross section; center left: $Br(A \to Zh)$; center right: $Br(h \to b\bar{b})$; bottom left: A boson natural width; bottom right: A boson resolution.

like in the Type-II type.

In the Lepton-specific type (Fig. 5.147), the cross sections of both processes decrease when $tan\beta$ and m_A increase significantly. They have a similar distribution such as the cross sections of Type-I. The $Br(A \to Zh)$ increases for some values of $tan\beta$ at A mass 350 GeV, in which it decreases sharply and then it increases again at higher masses. It is important to note that the branching fraction of the $h \to b\bar{b}$ decreases when $tan\beta$ takes higher values and is zero when $tan\beta$ is equal to hundred. Taking into account the values of $tan\beta$ and the value of $cos(\beta - \alpha)$ which are equal to 100 and 0.1, respectively, the coupling of the Higgs to b quarks vanishes again.

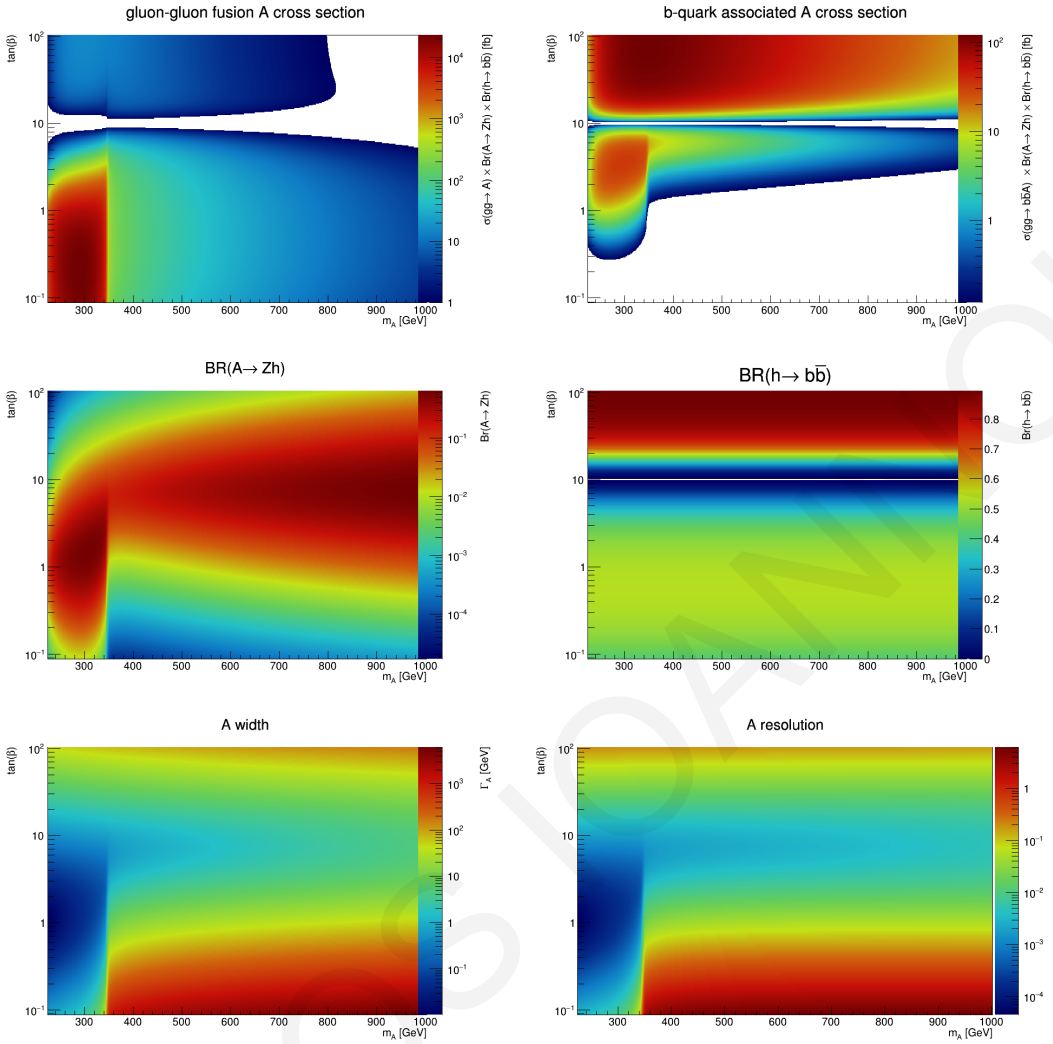

Figure 5.145: Cross sections and branching ratios for the Type-II in the plane m_A vs. $tan\beta$. Top left: gluon fusion A cross section; top right: b-quark associated A cross section; center left: $Br(A \to Zh)$; center right: $Br(h \to b\bar{b})$; bottom left: A boson natural width; bottom right: A boson resolution.

The parameter exclusion plot for the four 2HDM types in the plane $tan\beta$ vs. m_A, for a given $cos(\beta - \alpha) = 0.1$, is shown in Figure 5.148. As we can see, a significant parameter space is excluded for the four 2HDM types not only for the lower A boson masses but also for higher A masses up to 1000 GeV for the first time.

In Type-I (upper left plot in Fig. 5.148), the exclusion limit falls at the mass of 350 GeV where the $A \to Zh$ vanishes due to the opening of the $A \to t\bar{t}$ channel, and then it increases again at higher masses. A whole region is excluded up to $tan\beta \simeq 10$ and $m_A = 350$ GeV where the $A \to t\bar{t}$ channel is dominant and the branching ratio of $A \to Zh$ vanishes. In addition, there are three additional excluded

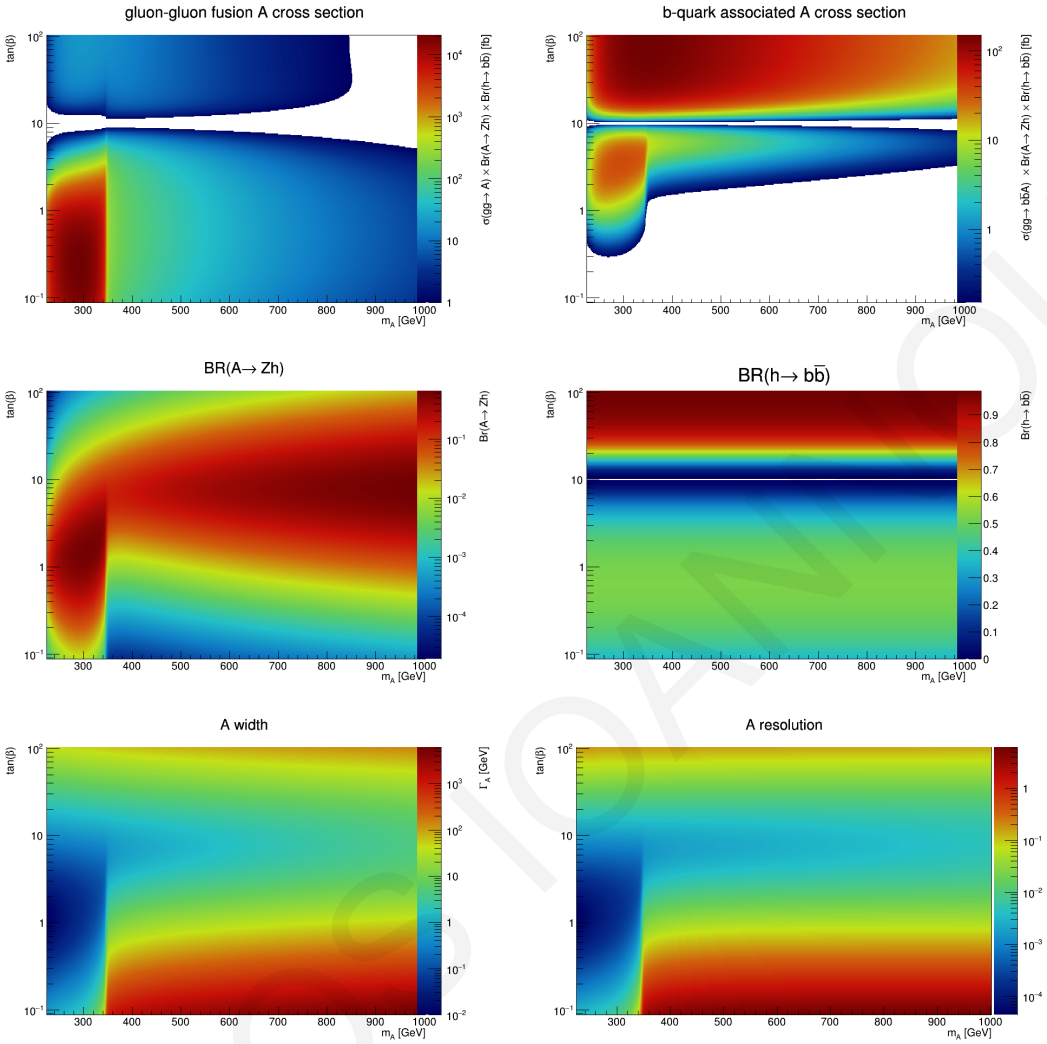

Figure 5.146: Cross sections and branching ratios for the Flipped in the plane m_A vs. $tan\beta$. Top left: gluon fusion A cross section; top right: b-quark associated A cross section; center left: $Br(A \to Zh)$; center right: $Br(h \to b\bar{b})$; bottom left: A boson natural width; bottom right: A boson resolution.

regions for higher masses between 400 GeV and 900 GeV and for lower values of $tan\beta$ up to 4.

In Type-II (upper right plot in Fig. 5.148), the shape of exclusion limit is similar with that of the Type-I model, however, the exclusion regions are smaller. The biggest exclusion region is for the values of $tan\beta$ up to 4 and for the A masses up to 350 GeV. There are three additional smaller excluded areas, "the small islands", for higher masses between 450 GeV and 850 GeV and for values of $tan\beta$ up to 2. Moreover, in the Type-II type, there is a parameter space which is excluded for the highest values of $tan\beta$ and A masses. This area ranges between the A masses 450 GeV and 1 TeV and for $tan\beta = 20$ up to 100.

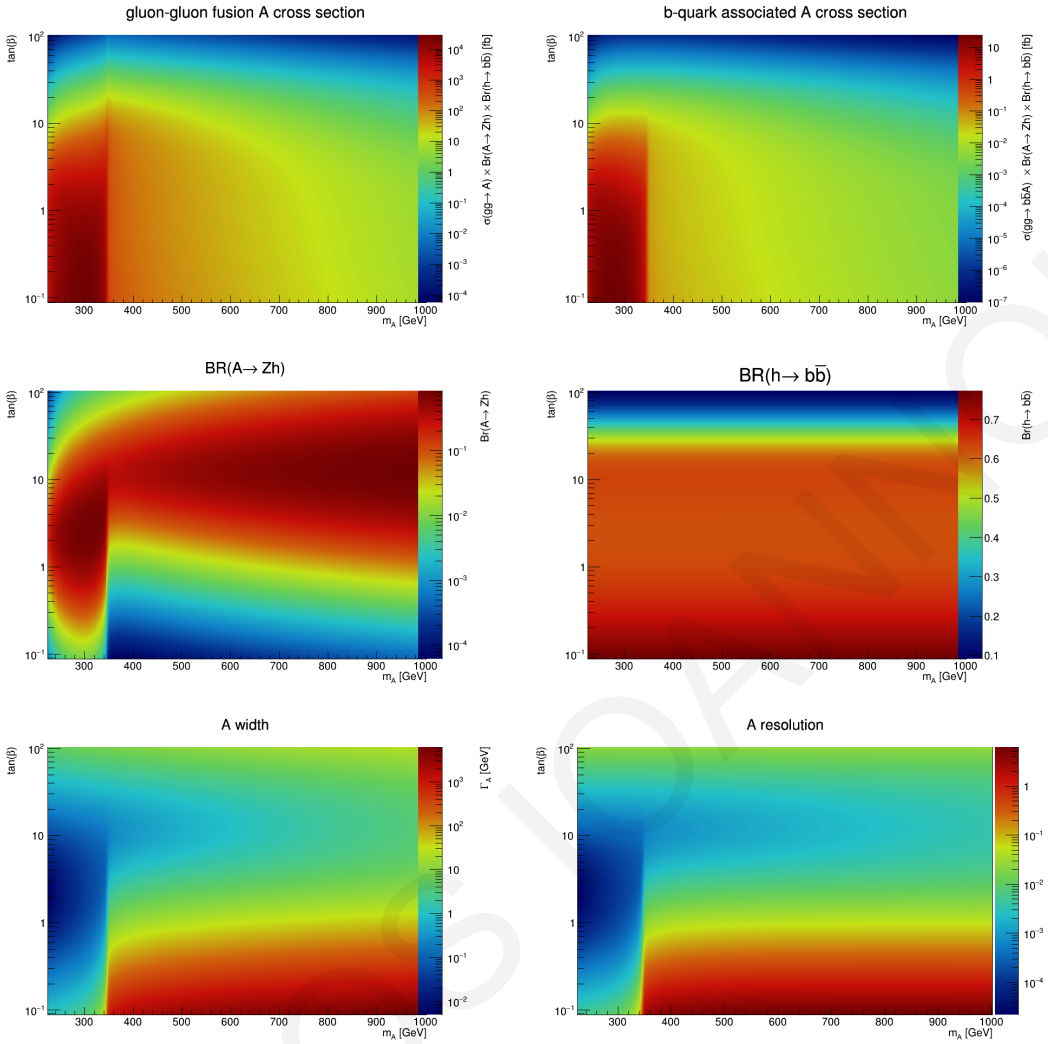

Figure 5.147: Cross sections and branching ratios for the Lepton-specific in the plane m_A vs. $tan\beta$. Top left: gluon fusion A cross section; top right: b-quark associated A cross section; center left: $Br(A \to Zh)$; center right: $Br(h \to b\bar{b})$; bottom left: A boson natural width; bottom right: A boson resolution.

The shape of exclusion limits for the Flipped type (bottom left plot in Fig. 5.148) is similar with the shape of the Type-II type as they have common features such as the same couplings of the quarks (up- and down-type quarks). The biggest exclusion region is between the A masses 225 GeV and 350 GeV for $tan\beta$ up to 4. There are also three additional smaller "islands" for higher A masses and for the values of $tan\beta$ up to 2. Similarly, A boson masses between 450 GeV and 1000 GeV for the values of $tan\beta \simeq 20$ up to 100 are excluded as shown in Fig. 5.148 (bottom left plot).

In the Lepton-specific 2HDM type, the biggest exclusion limits is for the A masses up to 350 GeV where the $A \to t\bar{t}$ decay channel becomes dominant and for the values of $tan\beta \lesssim 8$. Additionally, there are

three smaller exclusion regions for $tan\beta \lesssim 4$ and for A masses between 410 GeV and 890 GeV.

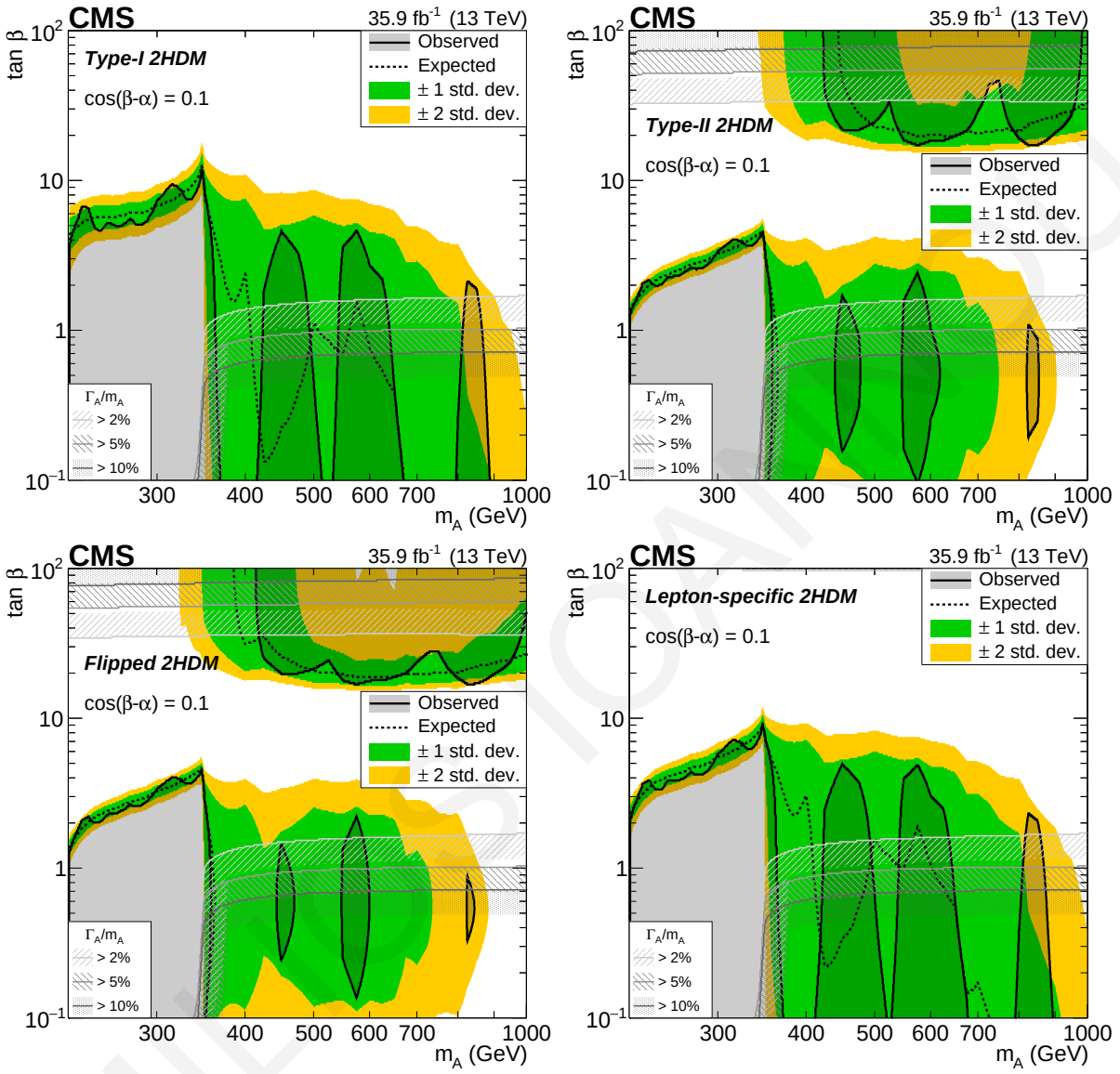

Figure 5.148: Observed and expected (with ± 1, ± 2 standard deviation bands) exclusion limits for Type-I (upper left), Type-II (upper right), flipped (lower left), lepton-specific (lower right) models, as a function of m_A and $tan\beta$, fixing $cos(\beta - \alpha) = 0.1$. The excluded region is represented by the shaded grey area. The regions of the parameter space where the natural width of the A boson Γ_A is comparable to the experimental resolution and thus the narrow width approximation is not valid are represented by the hatched grey areas.

In conclusion, the results (observed upper limit on the resonance cross section times $Br(A \to Zh)$ times $Br(h \to b\bar{b})$) were interpreted in terms of the four 2HDM types. The observed and expected exclusion limits for the four 2HDM types were presented in plane $cos(\beta - \alpha)$ versus $tan\beta$ and in plane m_A versus $tan\beta$ and a significant parameter space was excluded making the limits more restricted given

that many values of $tan\beta$, $cos(\beta - \alpha)$, and m_A have been excluded for the four 2HDM types.

Part IV

Conclusions And Future Plans

Chapter 6

Conclusions And Future Plans

In this section a brief summary of the current PhD Thesis is presented, highlighting the most important results of the $A \rightarrow Zh$ analysis. The events that were observed in the signal regions are perfectly consistent with the SM background prediction, revealing that there is currently no evidence for the pseudoscalar A boson in the 225-1000 GeV mass range, as shown in Table 6.1.

Signal region	0ℓ, 1 b tag	0ℓ, 2 b tags	0ℓ, 3 b tags	2ℓ, 1 b tag	2ℓ, 2 b tags	2ℓ, 3 b tags
Data	2452 ± 50	398 ± 20	45 ± 7	10512 ± 103	2188 ± 47	129 ± 11
Z+0 b quark	740 ± 12	48 ± 1	2.0 ± 0.2	4118 ± 15	175 ± 1	18 ± 1
Z+1 b quark	220 ± 6	13 ± 1	0.46 ± 0.06	4127 ± 18	365 ± 3	23 ± 1
Z+2 b quark	134 ± 3	86 ± 2	2.5 ± 0.3	1547 ± 11	1113 ± 7	51 ± 2
single top	74 ± 3	18 ± 1	3.0 ± 0.4	25 ± 0	10.0 ± 0.1	-
$t\bar{t}$	750 ± 12	143 ± 3	31 ± 3	592 ± 3	473 ± 3	26 ± 1
VV, Vh	76 ± 2	32 ± 1	0.93 ± 0.11	139 ± 1	53 ± 1	3.5 ± 0.1
W+jets	458 ± 13	65 ± 3	2.4 ± 0.3	3.7 ± 0.1	-	-
Total bkg.	2451 ± 26	405 ± 8	42 ± 5	10552 ± 35	2189 ± 12	121 ± 3

Table 6.1: Expected and observed event yields in the signal regions.

As we already reported, there is no excess of data over the background prediction and upper limits are set at 95% confidence level on the product of the A boson production cross sections times the branching fractions $\sigma_A \times Br(A \rightarrow Zh) \times Br(h \rightarrow b\bar{b})$. The upper limits on the total cross sections exclude 1 to 0.02 pb in the 225-1000 GeV mass range, as shown in Fig. 6.1.

Additionally, the cross sections of the scenario with $cos(\beta - \alpha) = 0.1$ and $tan\beta = 3$ are also presented in Fig. 6.1 and A masses up to 380 and 350 GeV are excluded for the 2HDM Type-I and Type-II, respectively. These results are used to constrain the 2HDM parameters as shown in Fig. 6.2.

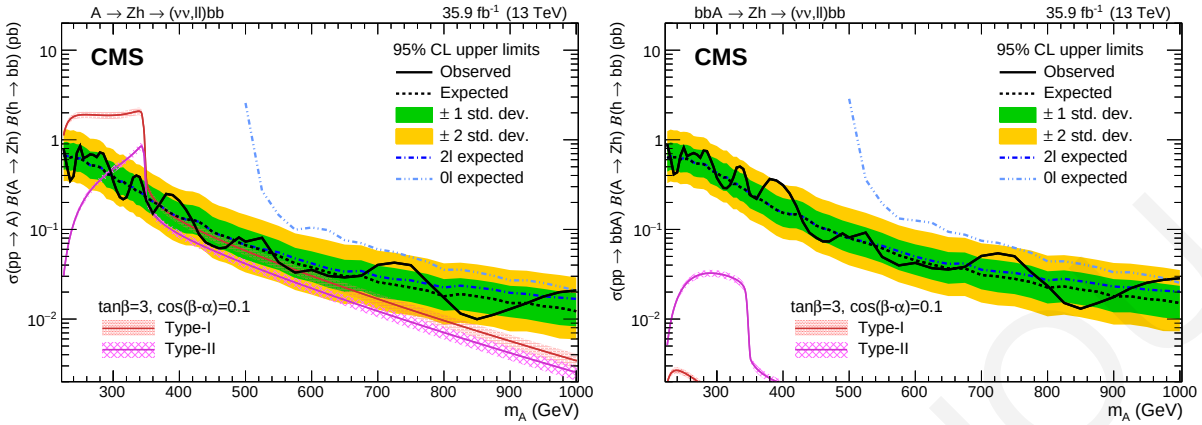

Figure 6.1: Observed (solid black) and expected (dotted black) 95% CL upper limits on $\sigma_A Br(A \to Zh) \times Br(h \to b\bar{b})$ for an A boson produced via gluon-gluon fusion (left) and in association with b-quarks (right) as a function of m_A.

The excluded two-dimensional plane of the 2HDM parameters $[cos(\beta - \alpha),\ tan\beta]$, with fixed $m_A = 300$ GeV, is plotted for the 2HDM Type-I and Type-II cases, as shown in Fig. 6.2 (upper plots). Moreover, the exclusion limits are used to constraint the two-dimensional plane of the 2HDM parameters $[m_A,\ tan\beta]$, fixing $cos(\beta - \alpha) = 0.1$ (lower plots). As we can see from Fig. 6.2, a large 2HDM parameter space can be constrained significantly by the findings of the $A \to Zh$ search making the limits more restricted.

The search of the $A \to Zh$ decay channel can be investigated further when Run-III starts operating in May 2021. As mentioned, the analysis is limited by the available amount of data and not by systematic uncertainties. For this reason, a large amount of data (implying better S/B ratio) will make the $A \to Zh$ channel much more sensitive and higher masses of A boson (up to 4 TeV) can be searched for with new CMS data, achieving better results.

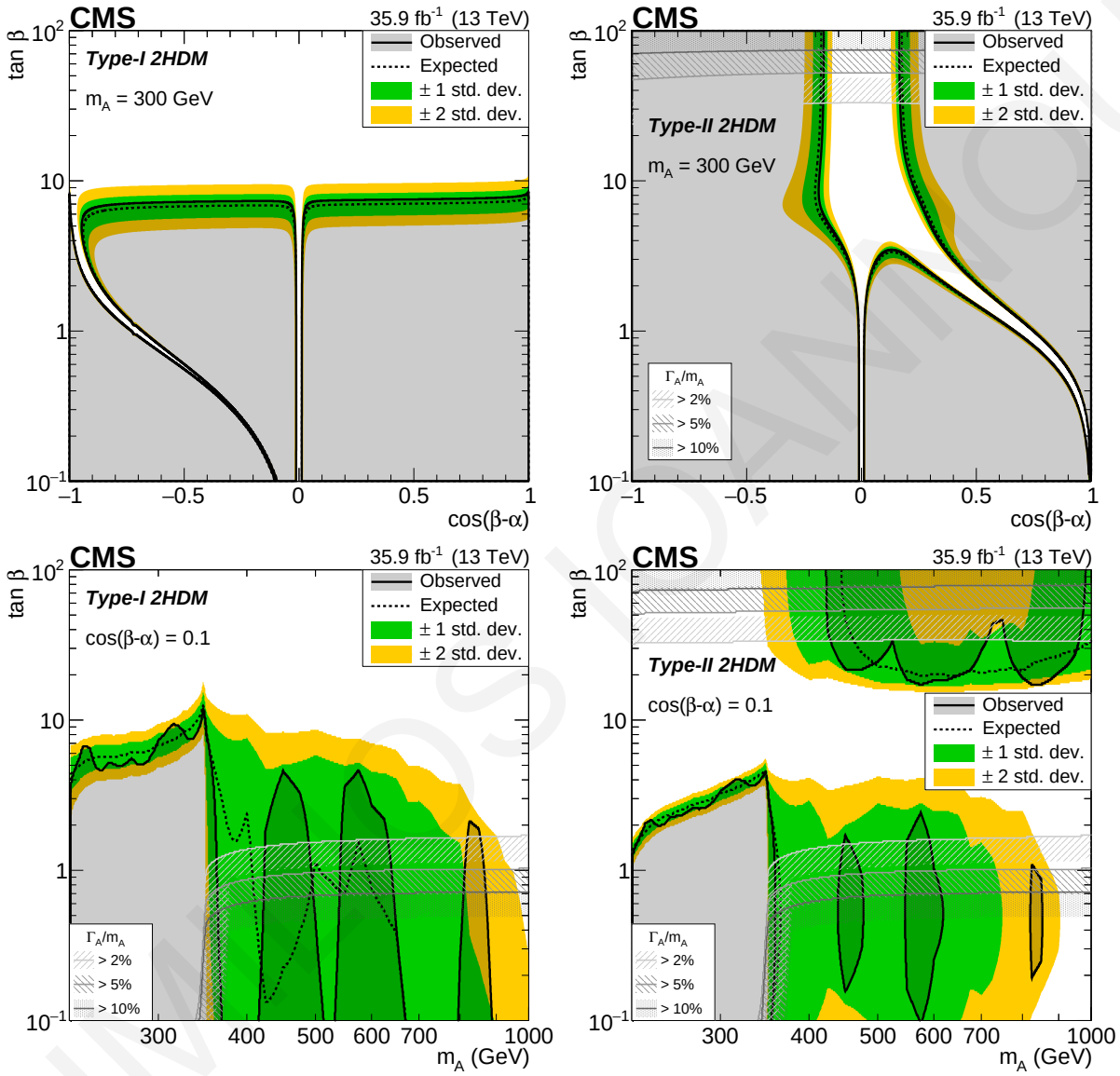

Figure 6.2: Observed and expected (with ±1, ±2 standard deviation bands) exclusion limits for Type-I, Type-II, as a function of $tan\beta$ and $cos(\beta - \alpha)$, for $m_A = 300$ GeV (upper plots) and as a function of m_A and $tan\beta$, fixing $cos(\beta - \alpha) = 0.1$ (lower plots).

Part V

Appendices And References

Appendices

A.1 Statistical Analysis In Particle Physics

A.1.1 Probability Density Functions

The *probability density function* (PDF) is a mathematical function which describes the probability prediction for a variable x. There are many PDFs which demonstrate results of random processes such as the *Gaussian* distribution and the *binomial* distribution. In High Energy Physics, the *Poisson* distribution is very common and widespread distribution, in particular for counting experiments.

Gaussian Distribution

The Gaussian distribution is given by:

$$f(x;\mu,\sigma) = \frac{1}{\sqrt{2\pi}\sigma} e^{\frac{-(x-\mu)^2}{2\sigma^2}} \tag{1}$$

There are two parameters describing the Gaussian distribution, μ which is the mean of the distribution and the scale parameter σ which denotes the standard deviation of the distribution. A general form of a gaussian distribution is shown in Fig. 3.

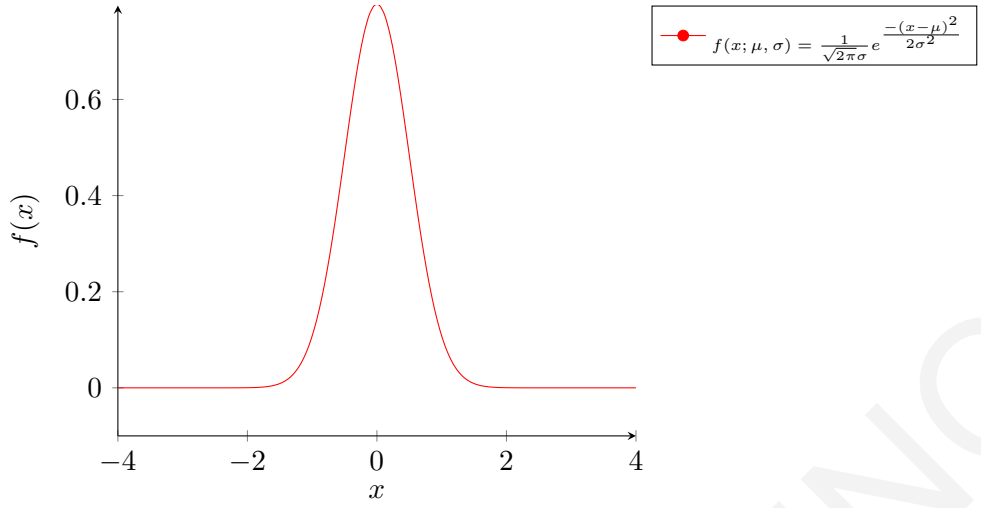

Figure 3: The Gaussian distribution.

The Binomial Distribution

The binomial distribution describes the probability for getting r successes from N trials.

$$f(r; N, p) = \frac{N!}{r!(N-r)!} p^r (1-p)^{n-r} \tag{2}$$

where p is a probability of a success on an individual trial.

The Poisson Distribution

The Poisson distribution is used in a counting experiment, which describes the probability to observe independent random events (r) that are occurring at a constant rate, such that the expected number of events is λ.

$$P = \frac{\lambda^r}{r!} e^{-\lambda} \tag{3}$$

In the case of Poisson distribution, it is important to ensure the independence of events. This means that the observation of one such event does not affect the observation of another event at any subsequent time in the interval. The statistical error is the basis of the well-known $\sigma = \sqrt{\lambda}$, where λ is the estimated quantity. Additionally, the Poisson can play the role of the limit of the binomial distribution. For large values of N and small p, the binomial distribution Eq. 2 looks like a Poisson function, where λ is equal to Np, and p is the probability of a success on an individual trial as in Eq. 2.

A.1.2 LIKELIHOOD

The *likelihood* function, $L(x;\theta)$, actually, is a cosmetic change of the probability of obtaining a result x given the value of a model parameter θ, $f(x,\theta)$. In principle, the likelihood $L(x;\theta)$ gives the probability that θ would lead to x.

In Particle Physics, and especially for a simple counting experiment where the only known information is the number of observed events, the likelihood function can be constructed by using the Poisson distribution, as follows:

$$L(n;s,b) = \frac{(s+b)^n}{n!}e^{-(s+b)} \tag{4}$$

$s+b$ is the expected total number of events, where s is the expected number of signal events and b the expected number of background events. The parameter n is the observed number of events.

In the real experiments either the data are binned in a histogram or are described by probability distribution functions (PDFs) of some observable x. When the data are binned in a histogram, the N bins can be considered as independent of each other. Consequently, the likelihood is given by the product of the likelihoods of every bin, as follows [116]:

$$L(n;s,b) = \prod_{i=1}^{N} \frac{(s_i+b_i)^{n_i}}{n_i!}e^{-(s_i+b_i)} \tag{5}$$

On the other hand, in the case where the likelihood is unbinned over k events in the data sample and the data are described by probability distribution functions (PDF), the likelihood is given by:

$$L(x;S,B,f_b(x),f_s(x)) = k^{-1}\prod_i (Sf_s(x_i)+Bf_b(x_i))e^{-(S+B)} \tag{6}$$

where $f_s(x)$ and $f_b(x)$ are *pdfs* of signal and background of some observables x, while S and B are the total event rates expected for signal and background.

$$S = \frac{s}{s+b} \tag{7}$$

$$B = \frac{b}{s+b} \tag{8}$$

A.1.3 THE METHOD OF MAXIMUM LIKELIHOOD

The likelihood function has already been discussed in Ap. A.1.2 and is an estimate method which is based on the construction of combined probability distribution of all measurements. After the con-

struction of the likelihood function, the next important step is an estimation of the central values of the parameters. The central values can be obtained by finding a parameter set $((\theta_1, ..., \theta_m))$ which corresponds to a value for which the likelihood is maximised. This technique is called *maximum likelihood method*.

Supposing the likelihood function as follows:

$$L(x;\theta) = \prod_{i=1}^{N} f(x_i;\theta) \tag{9}$$

where $\theta = (\theta_1, ..., \theta_m)$ is a set of m parameters with unknown values which have to be estimated. The maximum likelihood estimate (MLE) of the parameters θ are the values $\hat{\theta}$ for which the likelihood function $L(x;\theta)$ has its global maximum. The estimators can be given by the solutions of the equations,

$$\frac{\partial L}{\partial \theta_i} = 0, \qquad i = 1, ..., m \tag{10}$$

If there are more than one local maxima, the highest maximum of them is considered. The maximum likelihood method has many advantages such as the easy of use and the fact that no binning is mandatory.

A.1.4 PROFILE LIKELIHOOD RATIO

The profile likelihood ratio is given by the fraction below:

$$\lambda(\mu) = \frac{L(\mu, \hat{\hat{\theta}}(\mu))}{L(\hat{\mu}, \hat{\theta})} \tag{11}$$

The parameter μ is the signal strength defined as $\mu = \sigma/\sigma_{SM}$. The numerator is μ dependent and $\hat{\hat{\theta}}(\mu)$ corresponds to the θ value which maximises L for a specific μ. On the other hand, the denominator is not μ dependent. $\hat{\mu}$ and $\hat{\theta}$ parameters represent the best estimators obtained when no condition is required to the μ value. It is important to note that the presence of a signal produces only upward fluctuations of the background and only positive values of μ are taken into account in the statistical interpretation of the results, by using a modified likelihood ratio:

$$\bar{\lambda}(\mu) = \begin{cases} \frac{L(\mu, \hat{\hat{\theta}}(\mu))}{L(\hat{\mu}, \hat{\theta})} & \hat{\mu} \geq 0 \\ \frac{L(\mu, \hat{\hat{\theta}}(\mu))}{L(0, \hat{\hat{\theta}}(0))} & \hat{\mu} < 0 \end{cases} \tag{12}$$

A.1.5 KOLMOGOROV-SMIRNOV TEST

Another test which can be used to investigate that a data sample is compatible with a given distribution $f(x)$, is the *Kolmogorov-Smirnov test* thanks to Kolmogorov, Smirnov and Chakravarti [117, 118, 119]. In order to quantify the agreement of the data sample $(x_1, ..., x_n)$ with $f(x)$, the maximum distance between the two cumulative distributions $F_n(x)$ and $F(x)$ has to be determined as follows:

$$D_n = \sup_x |F_n(x) - F_m(y)| \tag{13}$$

The maximum distance (Eq. 13) asymptotically converges to zero as n and m are sufficiently large, if two investigating samples come from the same distribution.

In Chapter 5, several figures show a notation $K - S$ which corresponds to the *Kolmogorov-Smirnov* test. The Kolmogorov-Smirnov test has been performed for most of our results presented in our plots.

A.1.6 SYSTEMATIC UNCERTAINTIES

Systematic Uncertainties are measurement errors which are not due to statistical fluctuations in real or simulated data samples. They can be caused by the following sources:

1. badly known detector acceptances or trigger efficiencies
2. incorrect detector calibrations
3. detector resolutions
4. badly known background
5. uncertainties in the simulation or underlying theoretical models
6. uncertainties on input parameters, such as cross sections, branching ratios, lifetimes, the luminosity
7. computational and software errors
8. personal biases towards a specific outcome of an analysis
9. other usually unknown effects on the measurements

In other words, systematic uncertainties are nuisance parameters θ which affect the model but are not of direct interest in the decision. Nuisance parameters can be introduced by a probability density function

(PDF), $\rho(\theta)$ with some $\tilde{\theta}$ associated with the best estimate of the nuisance and some other parameters which describe the overall shape of the PDF and more specifically its width. Now, returning to the likelihood case, the nuisance parameters can be injected into the likelihood equation as a probability density function $\rho(\theta)$. By including the probability density function of nuisance parameters for binned histogram case, Eq. 5 is transformed like:

$$L(n;s,b) = \prod_{i=1}^{N} \frac{(s_i+b_i)^{n_i}}{n_i!} e^{-(s_i+b_i)} \prod_{j=1}^{L} \rho(\theta_j) \tag{14}$$

In the case of unbinned likelihood, the equation is given by:

$$L(x;S,B,f_b(x),f_s(x)) = k^{-1} \prod_{i} (Sf_s(x_i) + Bf_b(x_i)) e^{-(S+B)} \prod_{j=1}^{L} \rho(\theta_j) \tag{15}$$

The probability density function of the nuisance parameters can be assigned as flat PDF, if no constraint exists on a particular parameter. However, if there are constraints, a possible form of Gaussian PDF is chosen to describe uncertainties of parameters which can be both positive or negative:

$$\rho(\theta) = \frac{1}{\sqrt{2\pi}\sigma} e^{-\frac{(\theta-\tilde{\theta})^2}{2\sigma^2}} \tag{16}$$

On the other hand, the Gaussian distribution is not suitable for positive observables such as cross sections, efficiencies, luminosity, which are the most important quantities in *Experimental Particle Physics*. An alternative choice is the log-normal PDF which has a longer tail than normal Gaussian distribution for comparable uncertainties and it avoids negative values of observables like cross sections, luminosity, efficiencies etc. by converging to zero when parameter θ is null ($\theta = 0$).

$$\rho(\theta) = \frac{1}{\sqrt{2\pi} ln(\kappa)} e^{-\frac{(ln(\theta/\tilde{\theta})^2}{2(ln(\kappa))^2} \frac{1}{\theta}} \tag{17}$$

The parameter κ stands for the width of the log-normal PDF. This log-normal probability density function is chosen for all uncertainties. Fig. 4 shows log-normal distributions with different k values.

As shown in Fig. 4, for small uncertainties, the log-normal distribution is identified as a Gaussian distribution, in contrast to large uncertainties where the distribution behaves less appropriately.

In addition, there are cases where uncertainties originate from statistically limited number of events. In such cases, gamma distributions are utilised for describing statistical uncertainties associated with a number of Monte Carlo events or a number of observed events in a data sample. The gamma distribution is described by the formula:

$$\rho(n) = \frac{1}{\alpha} \frac{(n/\alpha)^N}{N!} e^{-n/\alpha} \tag{18}$$

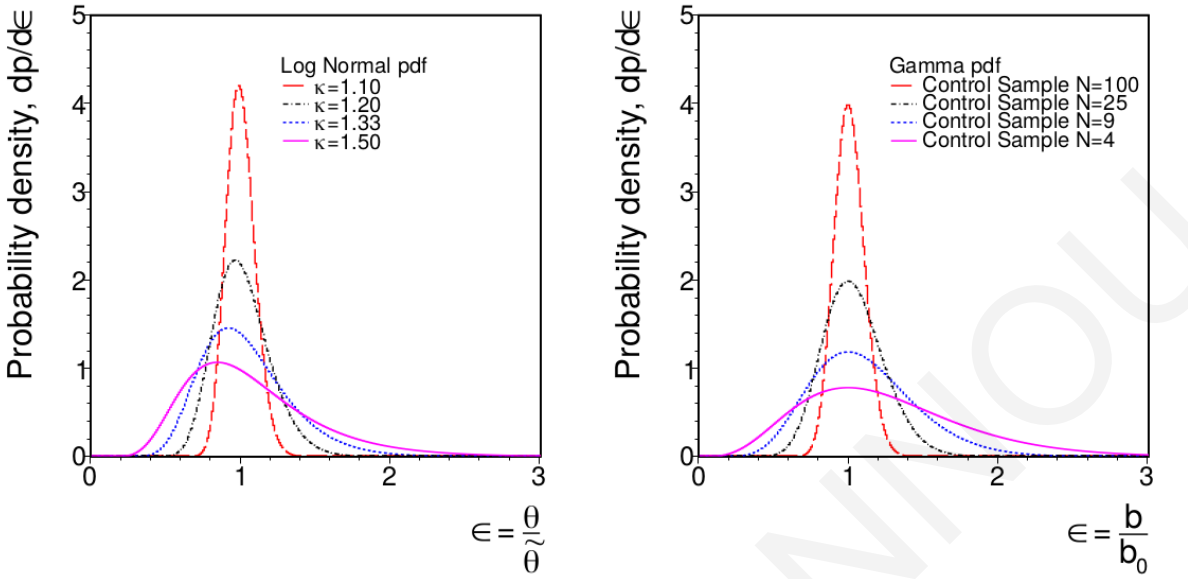

Figure 4: Left: Log-normal distributions with $k = 1.10,\ 1.20,\ 1.33$ and 1.50. Right: Gamma distribution with the number of events in a control sample $B = 100,\ 25,\ 9$ and 4. Taken from Ref. [116].

where n corresponds to the event rate in the signal region which can be related to the number of events N through the relation $n = \alpha N$. The gamma distribution can resemble with an exponential PDF for n, with the maximum at $n = 0$, mean=α and dispersion=α. Fig. 4 shows gamma distributions with different number of events.

A.1.7 Confidence Levels (CLs) Technique

In High Energy Physics, the *Bayesian* and the *classical frequentist* are statistical approaches which can characterise the absence of a signal. By using these methods one can quantify the agreement of data with a signal hypothesis which is expressed as a *confidence level* ($C.L.$). The confidence level method is used for computing exclusion limits. The signal is excluded when a 95% C.L. is required. The results usually are presented in a form of limits on $\sigma \times Br$ and any possible signal can be excluded at 95% C.L. when the 95% C.L. limit on μ drops to one, i.e. $\mu_{95\%CL} = 1$.

The computation of exclusion limits is based on the modified frequentist method which is called CL_s. The CL_s is simply defined as follows:

$$CL_s = \frac{CL_{s+b}}{CL_b} \tag{19}$$

where the confidence in the signal+background hypothesis, CL_{s+b}, is given by the probability that the

test-statistic, q_μ, is less than or equal to the value observed in an experiment, q_μ^{data} [120]:

$$CL_{s+b} = P(q_\mu \geq q_\mu^{data}|\mu s + b) \tag{20}$$

with

$$P(q_\mu \geq q_\mu^{data}|\mu s + b) = \int_{q_\mu^{data}}^{+\infty} \frac{dP_{s+b}}{dq} dq \tag{21}$$

where dP_{s+b}/dq is the probability distribution function of the test-statistic for signal+background experiment. The test-statistic, q_μ, can be derived from a fraction of likelihood functions, as follows [121]:

$$q_\mu = -2\ln\frac{L(data|\mu s + b)}{L(data|\hat{\mu} s + b)} \tag{22}$$

where $\hat{\mu}$ maximises the likelihood $L(data|\mu s+b)$. Similarly, the denominator of Eq. 19 is the confidence in the background hypothesis which is given by the probability:

$$CL_b = P(q_\mu \geq q_\mu^{data}|b) \tag{23}$$

with

$$P(q_\mu \geq q_\mu^{data}|b) = \int_{q_\mu^{data}}^{+\infty} \frac{dP_b}{dq} dq \tag{24}$$

where dP_b/dq is the PDF of the test-statistic for background only case. It is important to note that values of CL_b close to 1 imply incompatibility with the background hypothesis and agree with the signal+background hypothesis.

A.1.8 Exclusion Or Upper Limits

Many experiments have a primary target to search for new physics phenomena, however, sometimes, the outcomes of experiments are not so optimistic due to an insufficient number of observations which do not entail a discovery. In that case, where results cannot be published claiming a discovery, *exclusion limits* or *upper limits* can be set, allowing an exclusion of parameter sets of a new theory. Many analyses usually set upper limits on the production cross section of a hypothetical signal.

To extract exclusion limits on the production cross section, the test statistic, $\tilde{q}_\mu$, is constructed and based on the profile likelihood ratio, as follows:

$$\tilde{q}_\mu = -2\ln\frac{L(data|\mu, \hat{\theta}_\mu)}{L(data|\mu, \hat{\theta})} \quad 0 \leq \hat{\mu} \leq \mu \tag{25}$$

The test statistic is very useful tool for comparing the compatibility of the data with the background-only

and the signal+background hypotheses. The parameter $\hat{\theta}_\mu$ corresponds to the conditional maximum likelihood estimators of θ, given the signal strength parameter μ. By computing the test statistic equation (Eq. 25) for the given signal strength, μ, and defining values of the nuisance parameters $\hat{\theta}_0^{obs}$ and $\hat{\theta}_\mu^{obs}$ which describe the observed data for the background-only and signal+background hypotheses, probability density functions $f(\tilde{q}_\mu|\mu, \hat{\theta}_\mu^{obs})$ and $f(\tilde{q}_\mu|0, \hat{\theta}_0^{obs})$ can be constructed. The PDFs are generated by toy MC pseudo-data, assuming a signal strength μ in the signal+background hypothesis and for the background-only hypothesis the signal strength is set to be equal to zero ($\mu = 0$). Fig. 5 illustrates the PDF distributions as a function of test statistic $\tilde{q}_\mu$.

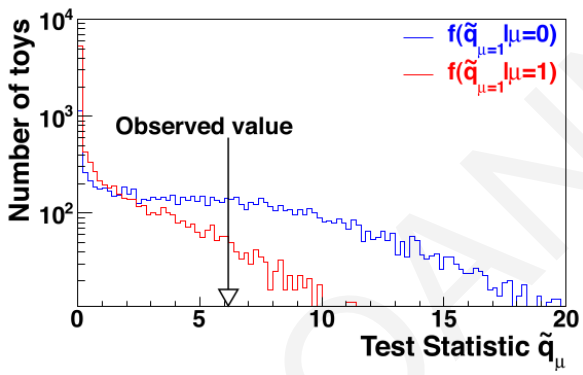

Figure 5: Test statistic distributions for signal+background and background-only hypotheses. Taken from Ref. [116].

Given that the PDF distributions have been constructed, two p-values have to be defined, p_μ and p_b, which are related to the probability of signal+background and background-only hypotheses, respectively:

$$p_\mu = P(\tilde{q}_\mu \geq \tilde{q}_\mu^{obs}|signal + background) = \int_{\tilde{q}_\mu^{obs}}^{\infty} f(\tilde{q}_\mu|\mu, \hat{\theta}_\mu^{obs}) d\tilde{q}_\mu \tag{26}$$

$$1 - p_b = P(\tilde{q}_\mu \geq \tilde{q}_\mu^{obs}|background - only) = \int_{\tilde{q}_0^{obs}}^{\infty} f(\tilde{q}_\mu|0, \hat{\theta}_0^{obs}) d\tilde{q}_\mu \tag{27}$$

Having constructed the probabilities for signal+background and background-only hypotheses, the $CL_s(\mu)$ can be calculated as a ratio of these probabilities (Eq. 26 and Eq. 27), as follows:

$$CL_s(\mu) = \frac{p_\mu}{1 - p_b} \tag{28}$$

A.1.9 Expected Limits

Before extracting any outcome or setting upper limits for new physics, expected limits are easily defined for the background-only hypothesis. The expected median upper limit and ± 1 and ± 2 standard

deviations can be considered, when a large set of background-only pseudo-data is generated and CL_s and $\mu^{95\%CL}$ are computed. Fig. 6 illustrates an example of differential distribution of possible limits on μ for the background-only hypothesis.

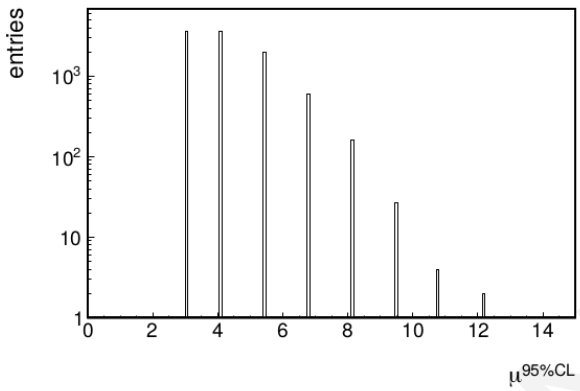

Figure 6: A differential distribution of possible limits on μ for the background-only case without systematic errors. Taken from Ref. [116].

The remaining step is the construction of a cumulative probability distribution of results. In order to build this kind of probability distribution, an integration procedure is mandatory from the side corresponding to low event yields. The cumulative probability distribution is shown in Fig. 7. When the probability crosses 50%, the value is considered as median expected value. Additionally, the ± 1 standard deviation (68%) occurs when the distribution ($\mu^{95\%CL}$) goes through the 16% and 84% quantiles (horizontal green lines in Fig. 7). The ± 2 standard deviation (95%) is defined when the probability crosses the point of 2.5% and 97.5% (horizontal light yellow lines in Fig. 7).

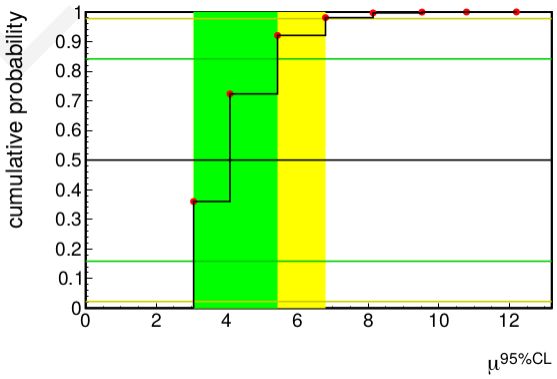

Figure 7: A differential distribution of possible limits on μ for the background-only case without systematic errors. Taken from Ref. [116].

A.1.10 THE $p-$VALUE AND SIGNIFICANCE

The previous sections explain the procedure that must be followed where no significant excess of data is observed on top of the expected background. However, when an excess of events is observed for claiming a discovery, it requires a determination of the sample which is sufficiently inconsistent with the background-only hypothesis presented in the data. A possible calculation of the test statistic, q_0, can be used for measuring the consistency or inconsistency of the observation with the background-only hypothesis.

$$q_0 = -2\ln\frac{L(data|0,\hat{\theta}_0)}{L(data|\hat{\mu},\hat{\theta})} \quad \hat{\mu} \geq 0 \tag{29}$$

Choosing the signal strength to be positive or equal to zero, $\hat{\mu} \geq 0$, the test statistic is placed to zero point for events with downward fluctuations. Moreover, the test statistic is used to define the probability p, *p-value*, as follows:

$$p_0 = P(q_0 \geq q_0^{obs}) = \int_{q_0^{obs}}^{\infty} f(q_0|0,\hat{\theta}_0^{obs})dq_0 \tag{30}$$

where $f(q_0|0,\hat{\theta}_0^{obs})$ is the distribution by generating pseudo-data for nuisance parameters around $\hat{\theta}_0^{obs}$. The *p-value* can be converted to the *significance*, Z, which is a quantitative measurement of the inconsistency with the background-only hypothesis. Eq. 31 is the conversion of the p-value to the significance:

$$p_0 = \int_{Z_0}^{\infty} \frac{1}{\sqrt{2\pi}} e^{-x^2/2} dx = \frac{1}{2} P_{x_1^2}(Z_0^2) \tag{31}$$

where $P_{x_1^2}$ corresponds to the survival function of χ^2 for one degree of freedom.

Additionally, the significance, Z, can be derived from the following equation:

$$Z_0 = \Phi^{-1}(1-p) \tag{32}$$

where Φ^{-1} is the quantile (inverse of the cumulative distribution) of the standard Gaussian. As a result of the above formula, the significance can be simply written with the test statistic according to the equation $Z_0 = \sqrt{q_0}$. The significance plays the role of Z standard deviations over its mean and as an upper-tail probability equal to p as illustrated in Fig. 8.

The most preferable way to present the p-value is not exactly the value of p, but, it is the equivalent number of standard deviations, $Z\sigma$. Table 2 shows a number of significance values expressed as $Z\sigma$ and their corresponding p-values.

Taking into account the Table 2 and its values, an observation of the signal can be reported when the significance is at least 3σ ($Z = 3$), which corresponds to a probability of background fluctuation (p-value) 1.35×10^{-3}. However, a discovery (the evidence of the signal) can be published in the case

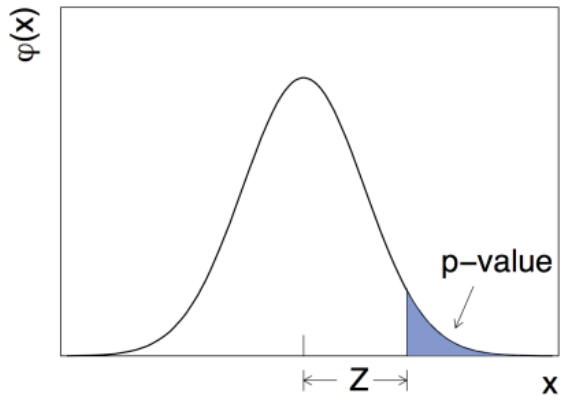

Figure 8: The relationship between p-value and significance of Zσ. Taken from Ref. [122].

$Z\sigma$	p-value
1.00	1.59×10^{-1}
1.28	1.00×10^{-1}
1.68	5.00×10^{-2}
2.00	2.28×10^{-2}
2.32	1.00×10^{-2}
3.00	1.35×10^{-3}
3.09	1.00×10^{-3}
3.71	1.00×10^{-4}
4.00	3.17×10^{-5}
5.00	2.87×10^{-7}
6.00	9.87×10^{-10}

Table 2: Significances expressed as $Z\sigma$ and corresponding p-values.

where the significance is at least 5σ ($Z = 5$), which corresponds to the p-value of 2.87×10^{-7}.

On the other hand, whether the test statistic, q_0, relies on the asymptotic behaviour of the likelihood ratio, the p-value can be obtained from the observed value q_0^{obs} without the need of a generation of pseudo-data:

$$p^{estimate} = \frac{1}{2}\left[1 - erf\left(\sqrt{q_0^{obs}/2}\right)\right] \tag{33}$$

The existence of the error function is remarkable from the equation above which is basically related to the cumulative Gaussian:

$$erf\left(\sqrt{q_0^{obs}/2}\right) = \frac{2}{\sqrt{\pi}} \int_0^{q_0^{obs}/2} e^{-x^2} dx \tag{34}$$

A.1.11 THE LOOK-ELSEWHERE EFFECT

The *look-elsewhere effect* is used for cases of experiments where the location of a possible peak is not known such as the case of the search of the Higgs boson or any search for new resonances. In these cases, the significance can be derived by using the p-value of the measured test statistic q, assuming a fixed value m_0 for the resonance mass. This significance is called *local significance* and can be written as:

$$p(m_0) = \int_{q_{obs(m_0)}}^{\infty} f(q(m_0)|\mu = 0)dq \tag{35}$$

The $f(q(m_0)|\mu = 0)$ is the PDF of the test statistic $q(m_0)$ for the signal strength equal to zero, $\mu = 0$. The *local significance* is a powerful statistical tool because it calculates the probability which corresponds to a background fluctuation at a fixed value of the mass m_0.

Moreover, there is also a *global p-value* which is the probability of the over-fluctuation of background at any mass value and it is larger than the local p-value. The global p-value can be computed by using the test statistic, as follows:

$$q_0(\hat{m_\theta}) = \max_{m_\theta} q_0(m_\theta) \tag{36}$$

where θ could be an unknown parameter, such as mass or width or other properties of a new signal. The global p-value can be determined by taking into account the look-elsewhere effect [123] which relies on the asymptotic behaviour of likelihood ratio and by using Davies' result [124]. The p-value of the global test statistic can be written:

$$p^{global} = P(q(\hat{m}) > u) \leq \langle N_u \rangle + \frac{1}{2}P(\chi^2 > u) \tag{37}$$

where $P(\chi^2 > u)$ is for an asymptotic approximation of the distribution of the local test statistic. The first term of Eq. 37, $\langle N_u \rangle$ is the average number of times the curve $q = q(m)$ goes through an horizontal line at a given level $q = u$ with a positive derivative. It is called as the average number of up-crossings. The up-crossings are illustrated in Fig. 9.

In addition, the average number of up-crossings at two levels u and u_0 can be given from the following formula:

$$\langle N_u \rangle = \langle N_{u_0} \rangle e^{-(u-u_0)/2} \tag{38}$$

$\langle N_{u_0} \rangle$ is referred to the average number of up-crossings at some lower reference level u_0, for example at level $u_0 = 1$. Sometimes, it is very useful to describe the look-elsewhere effect in terms of a *trial factor* which is the ratio of global to local p-value. Overall, the look-elsewhere effect is another comparison

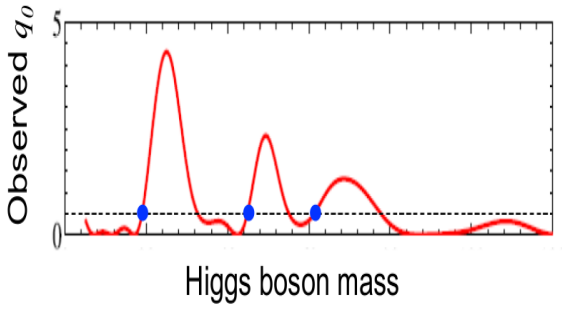

Figure 9: Visual illustration of up-crossings. Up-crossings for a given threshold value u are indicated by the blue points. Taken from Ref. [116].

tool when a possible peak of new signal can be anywhere in a wide mass range and, additionally, the magnitude of the effect depends on the mass resolution. When its magnitude is large, then the mass resolution gets worse.

A.1.12 Pull And Impact

Each analysis uses the notion of *pull* because the pull is an important formula which can quantify the difference of a nuisance parameter θ with an expected value of θ_0. The pull of a nuisance parameter, θ, is defined as:

$$pull(\theta) = \frac{\hat{\theta} - \theta_0}{\sigma_\theta} \tag{39}$$

A normal situation is when the pull average is zero with a standard deviation close to unit. If this does not happen, a further and deeper investigation is mandatory for fixing any possible issue.

Furthermore, it is reasonable in an analysis to check a measure of how much our parameter of interest differs as the nuisance parameter is changed. This measure is called *impact* and is given by:

$$impact(\theta) = \Delta\mu^{\pm} = \hat{\hat{\mu}}_{\theta_0 \pm \sigma_\theta} - \hat{\mu} \tag{40}$$

where $\hat{\hat{\mu}}_{\theta_0 \pm \sigma_\theta}$ is the *Maximum Likelihood Estimator* (MLE) of μ when every parameter is profiled by excluding the θ and setting the value of θ to its expectation value ± 1 standard deviation. The impact can be exploited for finding the most important nuisance parameters. Not all parameters are equally significant, hence, nuisance parameters which have a low impact can be neglected.

A.1.13 GOODNESS OF FIT

Goodness of fit is another important test which provides an evaluation of agreement between data sample and a function which is supposed to describe the data. In general, the g.o.f proves that the particular function describes reliably the data and any differences are just fluctuations. However, to extract such results, the data should deny the null hypothesis (background-only hypothesis or signal+background hypothesis) by finding the probability that fluctuations could have arisen by chance. If the probability is small, which means that the fluctuations are foreseen, the background-only hypothesis is then rejected and there is a discrepancy between the function and data where the fit is not good. On the other hand, if the probability is sufficiently large, the fit is accepted. This means that the fluctuations have really arisen by chance.

For the goodness of fit test, the model used to extract the agreement between data and function is a *saturated model* [125]. If the data can be described by Poisson distribution, the likelihood is:

$$L(n;y) = \prod_i \frac{y_i^{n_i}}{n_i!} e^{(-y_i)} \tag{41}$$

where y_i is equal to the signal and background relation with nuisance parameters, $\mu s_i(\vec{\theta}) + b_i(\vec{\theta})$. Consequently, the likelihood function of the saturated model is constructed when $y_i = n_i$, as follows:

$$L_{satur}(n;n) = \prod_i \frac{n_i^{n_i}}{n_i!} e^{(-n_i)} \tag{42}$$

The ratio of two likelihood functions in the saturated goodness of fit test is [126]:

$$\lambda_{satur} = \prod_i \left(\frac{y_i}{n_i}\right)^{n_i} e^{-y_i+n_i} \tag{43}$$

Finally, the test statistic in the saturated model is given by:

$$q_{satur} = -2\ln\left[\prod_i \left(\frac{y_i}{n_i}\right)^{n_i} e^{-y_i+n_i}\right] = 2\sum_i y_i - n_i + n_i \ln(\frac{n_i}{y_i}) \tag{44}$$

The observed value of the test statistic, q_{obs} can be derived, if Eq. 44 is minimised.

To derive the agreement or disagreement between data sample and the function which describes them, the observed value of the test statistic must be calculated in the saturated goodness of fit test. A good agreement between data and expectation is when the test statistic is placed under the bulk of the distribution. Otherwise, if the result of the test statistic is located in the tails of the distribution, the discrepancy between data and function is obvious. Fig. 10 shows two cases where a saturated goodness of fit test

was performed. The left plot of Fig. 10 illustrates the case where q_{obs} lies in the bulk of the distribution by declaring the agreement between data and the function. On the other hand, it is clear that the case where there is a discrepancy between data and the expectation value is the right plot. Undoubtedly, the test statistic is located in the tails of distribution by verifying the disagreement.

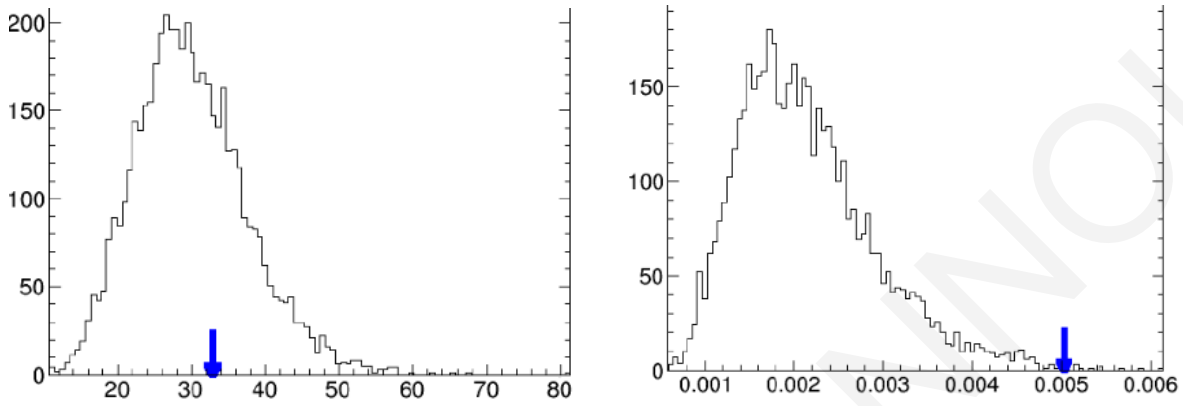

Figure 10: Examples of goodness of fit test. Entries as a function of test statistic. The blue arrow corresponds to the test statistic value, q_{obs}. Left: The test statistic lies in the bulk of the distribution and the agreement between data and expectation value is achievable. Right: The case where the discrepancy between data and function is noticeable due to the position of the test statistic which is located in the tails of the distribution.

A.1.14 Multivariate Analysis

Multivariate Analysis method (MVA) is a technique of event classification used in High Energy Physics. MVA is used to classify the signal events from background events, using the statistical distributions. In general, multivariate techniques combine the information of all observables of an event into one single variable y which can be used to distinguish signal events from background events. In order to achieve a remarkable separation, a cut on MVA variable must be applied. A suitable cut for MVA variable must be suitably chosen for rejecting as much as possible background, leaving the signal events unaffected, as illustrated in Fig. 11.

In this analysis, the *Likelihood Classifier* is used to discriminate the signal events from background events. The likelihood classifier or *Naive Bayes Classifier* uses the multi-dimensional PDF, which for each event i is the product of the one-dimensional PDFs, $p_{s(b),k}(x_k^{(i)})$. The product of probability densities is given by:

$$L_{s(b)}^{(i)} = \prod_{k=1}^{D} p_{s(b),k}\left(x_k^{(i)}\right) \tag{45}$$

where s stands for the signal and b corresponds to the case of the background events. D is for the

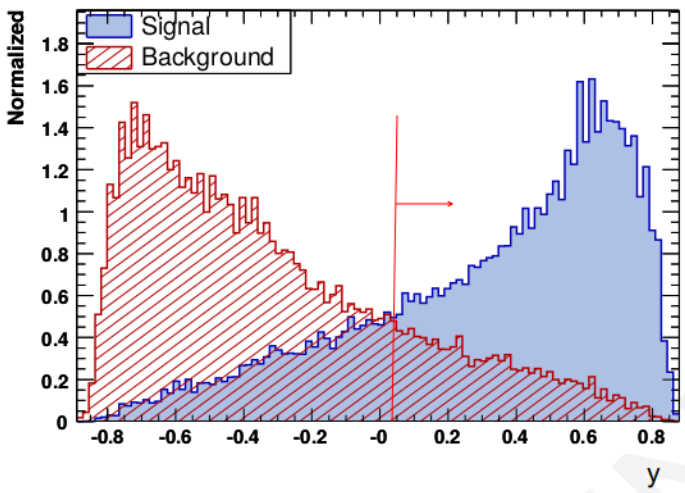

Figure 11: Example plot for signal and background distributions as a function of MVA variable y. The red line corresponds to the cut value of the MVA variable in which the best separation is achieved. Taken from Ref. [127].

dimension of the phase space. The MVA variable of the likelihood classifier is the likelihood ratio $y_L^{(i)}$ for event i, which is determined by:

$$y_L^{(i)} = \frac{L_s^{(i)}}{L_s^{(i)} + L_b^{(i)}} \tag{46}$$

To use the variable of likelihood classifier, $y_L^{(i)}$, the absence of correlations between the observables is required. This is the only disadvantage from other classifiers if one decides to use the MVA for distinguishing the signal from background events. Observables are the variables which will be used to construct the MVA variable, $y_L^{(i)}$, and they can be presented in a correlation matrix of observables as illustrated in Fig. 12.

As it can be shown from Fig. 12, the correlations between some observables are indeed zero, and if the classifier is constructed by these observables it will be close to an optimal choice because the PDF estimate from the events in one dimension is typically very accurate. However, it is forbidden to construct the likelihood classifier from correlated observables (observables where the correlations between them are not zero), because it will completely destroy a possible measure of a new particle mass.

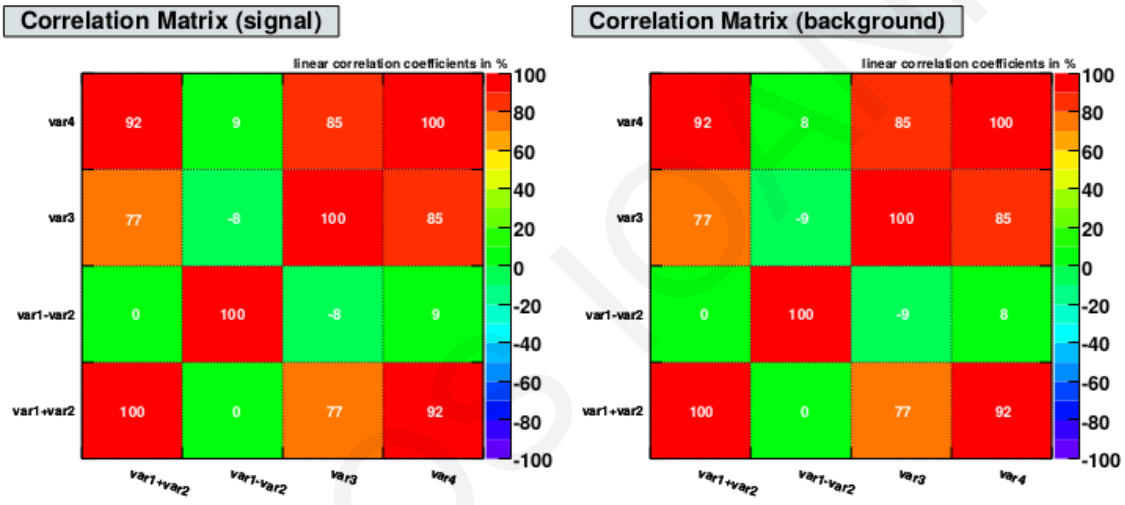

Figure 12: Linear correlation coefficients (observables) for the signal (left) and background (right) samples. Taken from Ref. [127].

B.2 Event Generation And Object Reconstruction

B.2.1 Monte Carlo Event Generation

When two opposite proton beams are collided at the LHC, six different processes occur before reconstructing the hits and signatures from the detectors as physical objects. The structure of a proton-proton collision is divided into the following processes, as follows:

1. Hard process,
2. Parton shower,
3. Hadronisation,
4. Underlying event,
5. Unstable particle decays (secondary decays), and
6. Pile-up.

A typical proton-proton collision at the LHC is illustrated in Fig. 13 where the processes built up by event generators, are pointed out.

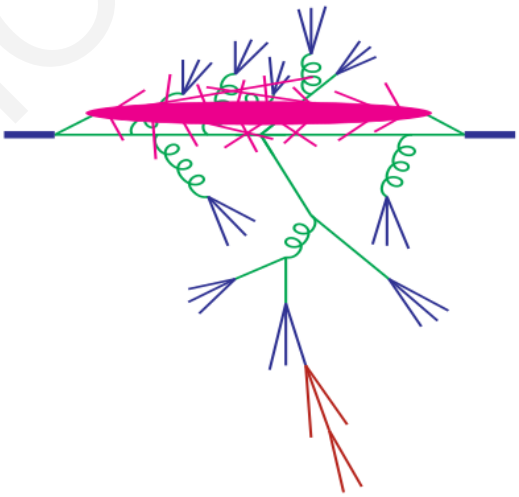

Figure 13: Diagram showing the structure of a proton-proton collision. Each colour corresponds to the different level involved in event generation. Green: parton shower, blue: hadronization, magenta: underlying event, brown: unstable particle decays. Taken from Ref. [128].

Firstly, an event generator starts the simulation at the heart of the collision by simulating the hard process. In fact, the simulation of the hard process is the calculation from perturbation theory of the probability distribution. The simulation is relatively trivial because PDFs describe partons involved in the process and the lowest order perturbation theory gives a probabilistic distribution of the outgoing partons.

Secondly, the parton shower is the second stage of the event generators. The partons involved in the hard collisions, are coloured particles, quarks and gluons. These quarks and gluons are radiated by scattered colour charges. The radiation of gluons occurs for partons on their way in and out of a collision. The gluons are coloured and an emitted gluon can trigger new radiation, leading to an extended shower. The parton shower starts from the hard process by growing gradually until the perturbation theory breaks down.

The next stage is the hadronisation which is the transition phase from partons to hadrons, which occurs in the detectors. To observe the hadronisation phenomenon, quarks and gluons must have low energies, below typically 1 GeV, where they cannot trigger a new radiation and cannot exist individually due to colour confinement.

Underlying events are the next process of the structure of a proton-proton collision. These are the final states of a typical proton-proton collision and typically consist of a small number of hadrons at low transverse momentum distributed across a wide range of rapidities. Actually, the underlying events are the events which do not come from the primary hard scattering (high energy, high momentum impact) process. They usually produce soft hadrons which cover and contaminate the interesting hard process.

Furthermore, another ingredient taken into account by an event generator, is the unstable hadrons particles which have a short lifetime and decay into stable particles. These hadrons are typically tau particles which will decay into muons or electrons as final states.

Finally, the last part of the event simulation at the LHC, is the Pile-up interactions. In general, the Pile-up interactions are soft inelastic collisions which are involved in the hard process. The Pile-up processes are treated by generating MC samples for a scenario with a higher number of vertices. The MC datasets are reweighed to match the real distribution of Pile-up interactions.

Many MC generators have been developed to simulate collision interactions at LHC. There are many choices about MC generators. However, some of them are specialised to Leading-Order (LO) or tree-level matrix elements and some others are specialised to Next-to-Leading-Order (NLO) matrix elements. Madgraph [129], Pythia [130, 67], Powheg [131], Herwig [132, 133], Sherpa [134], and aMC@NLO [135] are some generators which are frequently used and are preferable than others. The Powheg and aMC@NLO are generators which are able to compute NLO matrix elements, whereas the remaining

MC generators can just compute only LO matrix elements. The analysis presented in this thesis uses aMC@NLO to generate the hypothetical signal events. In addition, background samples are generated by using Pythia, Madgraph, Powheg and also aMC@NLO generators. The events (signal and background) are passed through Geant4 [70], which simulates interactions of particles with the detectors' material in the Experiment.

B.2.2 Object Reconstruction

When a particle passes through the detectors, it leaves hits in the tracker system and energy in the calorimeters. As a result, there is no way to identify what particle it is from these individual information and a need for a development of a sophisticated and reliable algorithm which links these signals from different detector systems is mandatory. Thus, CMS relies on the particle-flow (PF) algorithm [136, 137] to reconstruct particles such as electrons, photons, muons, charged and neutral hadrons and more complex objects such as taus, jets and missing transverse energy.

As mentioned before, information from each CMS detector are combined to reconstruct and identify stable particles by the particle-flow algorithm. In order to achieve high efficiency and low fake rate, the particle-flow algorithm adopts an iterative-tracking strategy. With this iterative technique, the particle-flow algorithm achieves a reconstruction of charged particles with as little as three hits and a fake rate of the order of a percent.

Moreover, the particle-flow algorithm takes advantage of a clustering algorithm in the calorimeters which is special for detecting and measuring the energy of stable neutral particles and neutral hadrons, distinguishing neutral particles from charged hadrons. Its purpose is to reconstruct and identify electrons and photons. The clustering algorithm has been developed to provide a high detection efficiency and a very good separation of close energy deposits.

Finally, the link algorithm [136] is used by particle-flow to connect PF elements in the various CMS sub-detectors. For instance, the link algorithm connects elements such as charged particle tracks, calorimeter clusters, muon tracks, to achieve a fully reconstructed single particle and at the same time, to get rid of any possible double counting from different detectors.

B.2.2.1 Tracks Reconstruction

Collecting the hits provided by the pixel and strip detectors (the CMS tracking system) tracks of particles can be reconstructed. Trajectories of charged particles are reconstructed by using the Combinatorial Track Finder (CTF) which is based on the combinatorial Kalman filter [138, 139]. The track reconstruc-

tion is based on the iterative tracking algorithm which is the procedure of multiple iterations of the CTF track reconstruction sequence. The ideal of CTF operation is to search for tracks with relatively large p_T and near the interaction region at the initial iterations. After each iteration, hits associated with tracks are removed by reducing the combinatorial complexity.

A typical iteration consists of four steps. First, the *seed generation* provides initial track using only a few hits and defines five parameters needed to describe the helical path of a charged particle in the quasi-uniform magnetic field of the tracker. The second step is the *track finding* based on a Kalman filter. The track finding extrapolates the seeded trajectory by adding hits from detector layers, building track candidates. Third, the *track-fitting* is used to reconstruct a track candidate given that all track candidate hits are collected. The track-fitting is the fit of reconstructed trajectory with a Kalman filter and smoother methods to accurately estimate the helix parameters. The last step of an iteration is the *track selection* in which "good" tracks are selected and "fake" tracks are discarded. In this stage, many quality flags are set in order to drop tracks which do not satisfy various criteria and are not associated with charged particles.

The performance of the CTF tracking algorithm is evaluated by using simulated events, plotting the tracking efficiency as a function of pseudorapidities and of the transverse momentum of charged particles, and rejecting the fake rate. The tracking efficiency is defined as the fraction of simulated charged particles that can be associated with corresponding reconstructed tracks, while the fake rate is defined as the fraction of reconstructed tracks that are not associated with any simulated particles.

Fig. 14 shows the efficiencies for muon (top plots) and electron (below plots) particles as a function of η (left) for $p_T = 1, 10,$ and 100 GeV, and of p_T for the three regions (barrel, transition, and endcap) of the CMS detectors. Muons are reconstructed better than the other charged particles in the whole tracker due to their interaction with the silicon detector through ionization of the medium. The efficiency of muon tracks reconstruction is greater than 99% for a transverse momentum range $1 < p_T < 100$ GeV, where the p_T-independent feature is validated. However, in the case of electron particles, the efficiency reaches at 98% only in the barrel region and depends on the p_T of the particles. In the endcap regions, the efficiency drops down around 94%, making the average efficiency of electrons worsen than muon's efficiency due to the significant energy loss through bremsstrahlung.

B.2.2.2 Primary Vertex Reconstruction

The primary-vertex reconstruction [140] aims to measure the location and the associated uncertainty of all interaction vertices in each event. The tracks included in the primary interaction region are selected based on the transverse impact parameter significance and must satisfy a minimum number of strip and pixel hits. After that, the selected tacks originating from the primary interaction region are clustered by

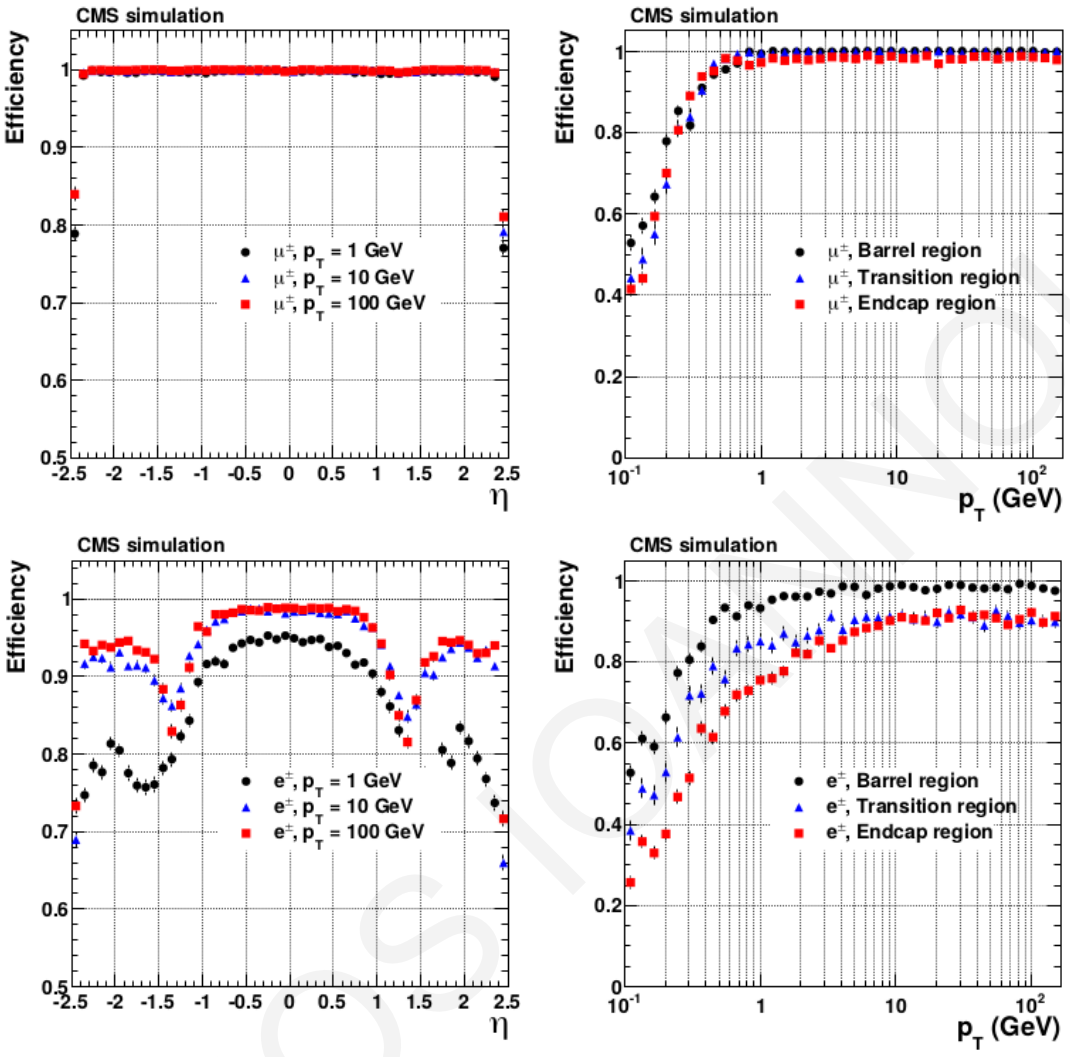

Figure 14: Track reconstruction efficiencies for muons and electrons as a function of η (left) and of p_T (right), fro $p_T = 1, 10,$ and 100 GeV. Taken from Ref. [56].

using a *deterministic annealing* (DA) algorithm [141] which selects tracks based on their z coordinates at the point of closest approach to the beam line. The last stage of primary-vertex reconstruction is the adaptive vertex fit [142] for candidates containing at least two tracks. The fitting process computes the best estimate of vertex parameters like position and covariance matrix, the number of degrees of freedom of the vertex and track weights of the tracks in the vertex. The number of degrees of freedom is crucial for selecting real proton-proton interactions because of its correlation with the number of tracks compatible with the primary interaction region. It is defined as follows:

$$n_{nof} = 2 \sum_{i=1}^{nTracks} w_i - 3 \tag{47}$$

where w_i is the weight of the i^{th} track.

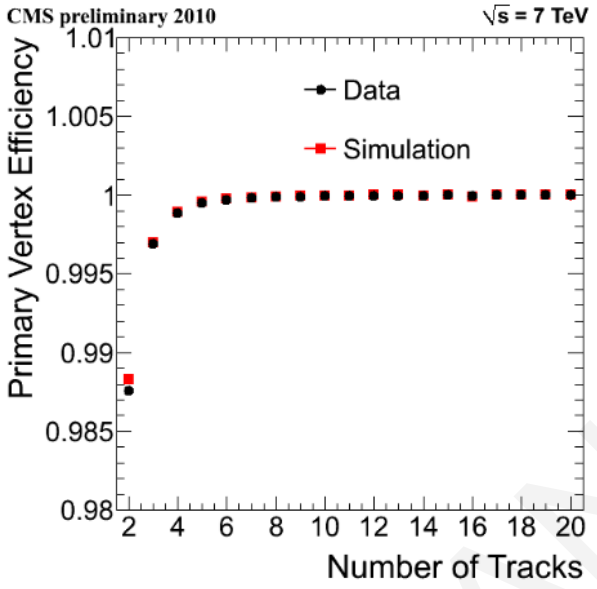

Figure 15: Primary vertex efficiency as a function of the number of tracks (data and simulated events). Taken from Ref. [143].

Fig. 15 shows the primary vertex efficiency as a function of the number of tracks. There is a good agreement between data and simulation and the primary vertex efficiency is estimated to be close to 100% if there are more than two tracks in the vertex.

B.2.2.3 Electron Reconstruction And Identification

Electrons are reconstructed by using information from the tracker and ECAL. The electron energy is collected by several crystals of the ECAL, however, some energy may not spread out over crystals due to the electron energy loss through bremsstrahlung effect. For example, an electron with energy 120 GeV deposits about 97% of its energy in a 5×5 crystal array. On the other hand, when electrons radiate photons due to the bremsstrahlung effect, its energy is differently distributed and its spread is quite smaller in the ECAL's clusters [144].

The initial energy of the electron is measured by collecting the energy of the radiated photons which spreads along the ϕ direction due to the bending of the electron trajectory in the magnetic field. Two different algorithms are used to measure the energy of electron. The *hybrid* algorithm is used to measure the energy in the barrel region, whereas the electron energy is collected by *multi*-5×5 algorithm in the endcap regions. The hybrid algorithm exploits the geometry of the ECAL barrel (EB), starting from a seed crystal which has the largest energy deposited in any considered region. The algorithm then adds

arrays of 5×1 crystals in η around the seed crystal, if their energies exceed a minimum threshold of $E_{array}^{min} = 0.1$ GeV. Arrays with energy greater than 0.35 GeV, are grouped into clusters in order to combine a final global cluster, called the supercluster (SC). As mentioned, the multi-5×5 algorithm is used in the ECAL endcaps (EE). Similarly, this algorithm starts collecting the seed crystals with local maximal energy relative to their four direct neighbours and have energy greater than 0.18 GeV. After that, around these seeds, the energy is collected in clusters of 5×5 crystals and they are then grouped into a SC if their energy is above 1 GeV, with a range in η of ± 0.07 and a range in ϕ of ± 0.3 rad. It is important to note that the SC energy is the sum of the energies of all its clusters and the SC position is calculated as the energy-weighted mean of the cluster positions.

Apart from this, electron information can be received from tracker system by reconstructing electron tracks with the standard Kalman filter (KF). Due to the large radiative losses for electrons in the tracker material, a dedicated tracking procedure is used for electrons, starting from the *seeding* as called the first step of the procedure. The seeding is performed by two complementary algorithms, the ECAL-based seeding and the tracker-based seeding. The ECAL-based seeding uses the SC energy and position to estimate the electron trajectory in the first layers of the tracker and it then selects electron seeds from all reconstructed seeds. The tracker-based seeding uses the tracks reconstructed by the general algorithm for charged particles and extrapolates these tracks to the ECAL and matches them to superclusters. The whole seeding step starts reconstructing tracks with the KF algorithm which works well in the absence of bremsstrahlung effects. However, when the bremsstrahlung is not negligible, the KF tracks with a small number of hits or a large χ^2_{KF}, are refitted using a dedicated *Gaussian Sum Filter* (GSF). The second step of the electron track reconstruction is the tracking step which uses the selected electrons' seeds to initiate electron-track building. The combinatorial KF method is used for the track building and a Bethe-Heitler function is applied for modeling the electron energy loss.

The electron candidates are constructed by associating the GSF track and a cluster in the ECAL. To associate the GSF track with the SC, a geometrical matching is required to be less than 0.003, such as:

$$|\Delta\eta| \times |\Delta\phi| = (|\eta_{SC} - \eta_{in}^{extrap}|) \times (\phi_{SC} - \phi_{in}^{extrap}|) < 0.02 \times 0.15 = 0.003 \qquad (48)$$

where η_{SC} is the SC energy-weighted position in η, and η_{in}^{extrap} corresponds to the track η extrapolated from the innermost track position and direction to the position of closest approach to the SC (analogous definitions for ϕ variable). The information on track observables, the electron PF cluster observables and the association between the two are combined by using a multivariate technique (MVA), reaching an overall efficiency of 93% for electrons from Z decay.

As mentioned, an important amount of electron energy loss is due to the bremsstrahlung process. The bremsstrahlung energy loss is estimated using the momentum at the point of closest approach to the

beam spot (p_{in}) and the momentum extrapolated to the surface of the ECAL from the track at the exit of the tracker (p_{out}), as follows:

$$f_{brem} = \frac{p_{in} - p_{out}}{p_{in}} \tag{49}$$

Similarly, electrons are classified by using the bremsstrahlung fraction in the ECAL.

$$f_{brem}^{ECAL} = \frac{E_{SC}^{PF} - E_{ele}^{PF}}{E_{SC}^{PF}} \tag{50}$$

where E_{SC}^{PF} and E_{ele}^{PF} are the SC energy and the electron-cluster energy measured with the PF algorithm. The number of clusters in the SC is used to classify electron candidates in the following categories:

- **Golden**: electrons with little bremsstrahlung effect ($f_{brem} < 0.5$).
- **Big-brem**: electrons with a large amount of bremsstrahlung radiated in a single step, either very early or very late along the electron trajectory ($f_{brem} > 0.5$).
- **Showering**: electrons with a large amount of bremsstrahlung radiated all along the electron trajectory.
- **crack**: electrons with the SC seed crystal adjacent to an η boundary between the modules of the ECAL barrel, or between the ECAL barrel and endcaps, or at the high $|\eta|$ edge of the endcaps.
- **bad track**: electrons with a significant bremsstrahlung fraction than the track bremsstrahlung fraction ($f_{brem}^{ECAL} - f_{brem} > 0.15$).

Electrons are identified by several strategies in CMS. Algorithms have been developed to identify prompt isolated electrons and to separate them from photons, jets misidentified as electrons or electrons from semi-leptonic decays of b and c quarks. In addition, more complex and sophisticated algorithms combine variables in multivariate analysis (MVA) to achieve better discrimination. The sensitivity of electron identification is maximised by using the *boosted decision tree* (BDT) algorithm [145]. Fig. 16 illustrates the results on the performance of the BDT algorithm and the sequential electron-identification algorithms for four selected working points for electrons with $p_T > 20$ GeV.

Furhtermore, Fig. 17 shows an example of dielectron invariant mass distribution from $Z \to e^+e^-$ events in data compared to simulation. There is a good agreement between data and simulation in the barrel and endcap regions.

Moreover, a better performance can be obtained when the information from all detectors is combined by using the PF techniques and following the PF isolation, defined as:

$$Iso_{PF} = \sum p_T^{charged} + max\left[0, \sum p_T^{neutral\ had} + \sum p_T^{\gamma} - p_T^{PU}\right] \tag{51}$$

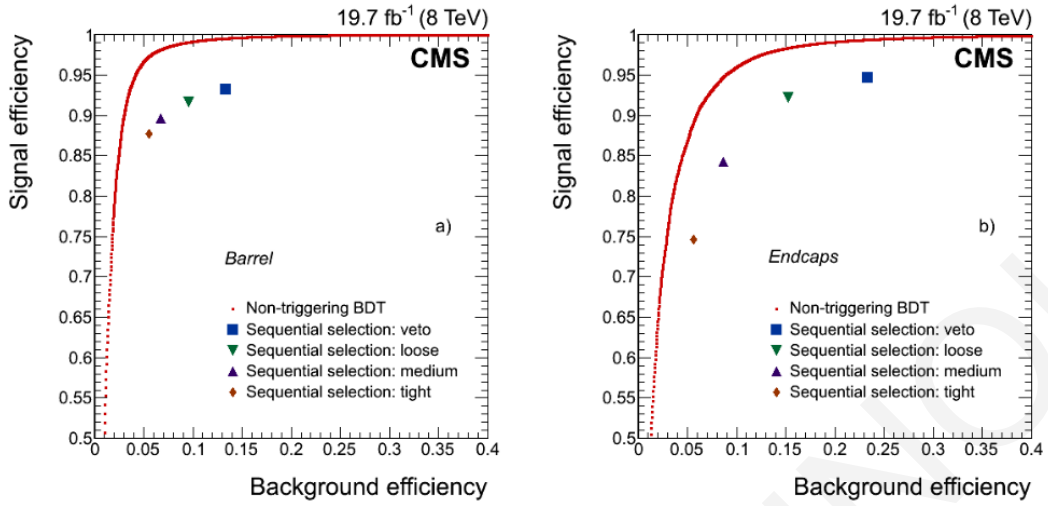

Figure 16: Performance of the electron BDT identification algorithm compared with results from working points of the sequential selection for barrel and endcap regions. Taken from Ref. [144].

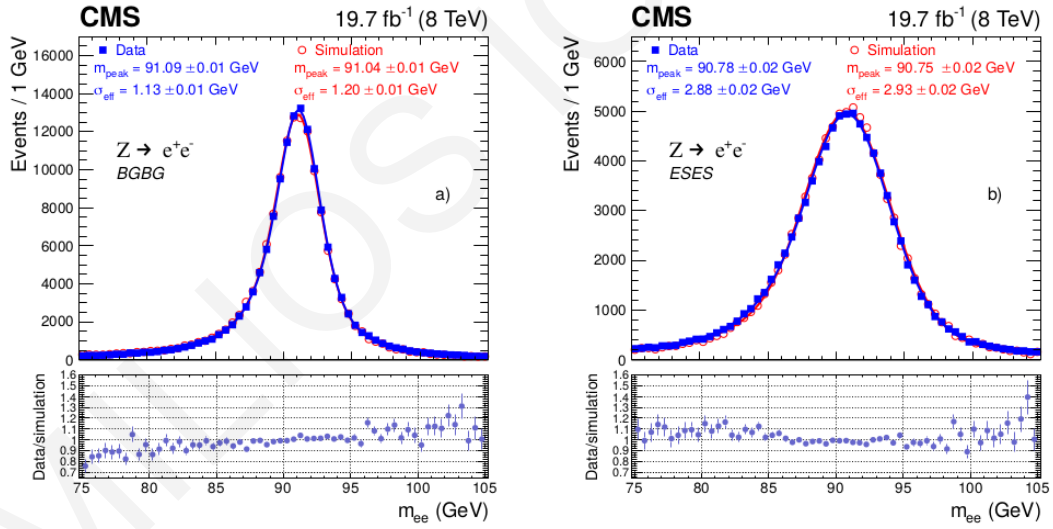

Figure 17: Invariant mass distribution of Z particle decayed into two electrons in data and simulation for barrel and endcap regions. Taken from Ref. [144].

where the sums run over the charged PF candidates, neutral hadrons and photons. Fig. 18 shows the performance of the detector-based isolation algorithm compared to that using the PF technique in the ECAL barrel and endcaps. By using the PF algorithm the performance is good, in particular in the endcaps, but a slightly better optimisation is observed in the barrel.

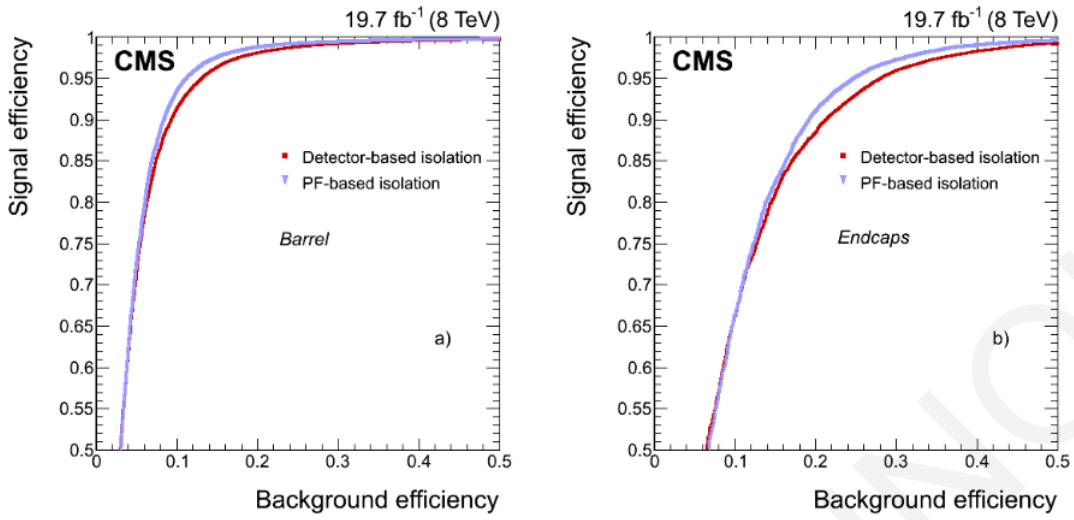

Figure 18: The comparison of performance between the detector-based isolation algorithm (red squares) and the PF algorithm (blue triangles) in the ECAL barrel (a) and endcaps (b). Taken from Ref. [144].

B.2.2.4 Muon Reconstruction And Identification

There are three kinds of muon reconstructions in the standard CMS software. Muons can be reconstructed from the tracks in the inner tracker (tracker track) and from the tracks in the muon system (standalone-muon track).

First, the *Standalone-muon tracks* are built by taking advantage of the information only from the muon subdetectors. Information from CSC, DT and RPC are gathered to build a muon trajectory using a Kalman-filter technique.

Second, the *Global Muon reconstruction* (outside-in) is the first type of reconstruction in which a matching of each standalone-muon track with a tracker track is performed, by comparing the parameters of the two tracks propagated onto a common surface. The Kalman-filter technique [139] is used to combine hits from the tracker track and the standalone-muon tracker by fitting *global-muon tracks*. The global-muon fit can dramatically improve the momentum resolution compared to the tracker-only fit at large transverse momenta, $p_T \gtrsim 200$ GeV/c.

Third, the *Tracker Muon reconstruction* (inside-out) considers possible muon candidates all tracker tracks with $p_T > 0.5$ GeV/c and total momentum $p > 2.5$ GeV/c. These tracker tracks are then extrapolated to the muon system, taking into account the magnetic field, the average expected energy losses, and multiple Coulomb scattering in the detector material. If at least one muon segment (DT or CSC hits) matches the extrapolated track, the corresponding tracker track qualifies as a Tracker Muon

[100].

Comparing the two types of muon reconstruction, the Tracker Muon is more efficient than the Global Muon at low momenta, $p_T \lesssim 5$ GeV/c, because it requires only a single muon segment in the muon system, while Global Muon is designed to have high efficiency for muons penetrating through more than one muon station and typically requires segments in at least two muon stations. However, global and tracker muons have high efficiency, about 99%, within the geometrical acceptance of the muon system.

To increase the efficiency of muon reconstruction, a particle-flow algorithm [94] is used for muon candidates. The PF algorithm combines information from all CMS sub-detectors to identify and reconstruct muons, by applying a set of selection criteria to candidates reconstructed with the standalone, global or tracker muon algorithms. The requirements are based on various quality parameters which identify the muons into various types, as follows:

- ***Loose muon identification (ID)*** identifies prompt muons coming from the primary vertex, light and heavy flavour decays. A loose muon is a muon selected by the PF algorithm that is also either a tracker or a global muon.

- ***Medium muon ID*** is a loose muon with a tracker track that uses hits from more than 80% of the inner tracker layers it traverses.

- ***Tight muon ID*** aims to suppress muons from decay in flight and from hadronic punch-through. A tight muon is a loose muon with a tracker track that uses hits from at least six layers of the inner tracker, including at least one pixel hit. The muon must be reconstructed as both a tracker muon and a global muon. The tracker muon must have sement matching in at least two of the muon stations. The global muon fit must have $\chi^2/dof < 10$ and include at least one hit from the muon system. A tight muon must be compatible with the primary vertex, having a transverse impact parameter $|dXY| < 0.2$ cm and a longitudinal impact parameter $|dx| < 0.5$ cm.

- ***Soft muon ID*** is a tracker muon with a tracker track that satisfies a high purity flag [56] and uses hits from at least six layers of the inner tracker, including at least one pixel hit. The tracker muon reconstruction must have tight segment matching, having pulls less than 3 both in local x and in local y. A soft muon is loosely compatible with the primary vertex, having $|dXY| < 0.3$ cm and $|dz| < 20$ cm.

- ***High momentum muon ID*** is reconstructed as both a tracker muon and a global muon. The requirements on the tracker track, the tracker muon, and the transverse and longitudinal impact parameters are the same as for a tight muon, as well as the requirement that there should be at least one hit from the muon system for the global muon.

Two strategies are developed to distinguish between prompt muons and those from weak decays within jets. The first one sums reconstructed tracks based on the isolation of a muon evaluated relative to its p_T by summing up the energy in the geometrical cone, $\Delta R = \sqrt{(\Delta\phi)^2 + (\Delta\eta)^2}$, surrounding the muon. The second technique uses charged hadrons and neutral particles coming from particle-flow (PF isolation). The PF isolation is performed by using the Eq. 51 as electron isolation.

Both strategies give a very high efficiency for all working points (loose, medium, tight etc.). In particular, tight and loose achieve efficiencies of 95% and 98%, respectively. They are tuned using simulated tight muons from $Z \to \mu^+\mu^-$ decays with $p_T > 20$ GeV.

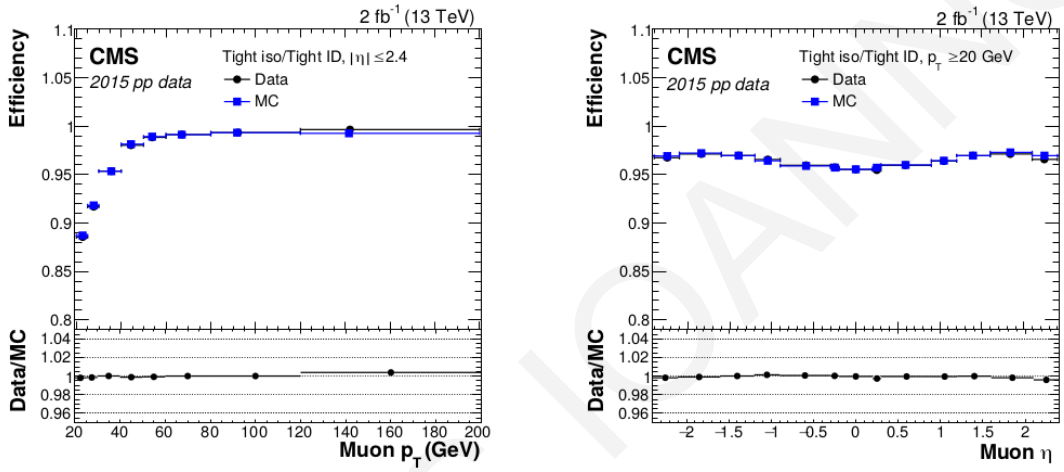

Figure 19: The efficiency of the tight PF isolation working point as a function of muon p_T for $|\eta|$ range below 2.4 (left) and as a function of η for muon with $p_T > 20$ GeV, using 2015 data and simulation. Taken from Ref. [100].

Fig. 19 shows the efficiency for the tight PF isolation working point which reaches over 95% when a muon candidate has p_T greater than 40 GeV in pseudorapidity range $|\eta| < 2.4$. In addition, the efficiency for the tight PF isolation working point for muons with $p_T > 20$ GeV is about 95% over all, over the pseudorapidity region.

B.2.2.5 Missing Transverse Energy

In principle, the missing transverse energy, $\vec{\not{E}}_T$, is the negative of the vector sum of the transverse momenta of all final-state particles reconstructed in the detector. $\vec{\not{E}}_T$ is equal to the total transverse momentum of all unobserved particles, such as neutrons or other weakly interacting objects.

$$\vec{\not{E}}^{raw} = -\sum_{i \in all} \vec{p_{T_i}} \tag{52}$$

The notation *"raw"* on the MET symbol is referred to the basic MET without corrections and is systematically different from true MET for many reasons, including the non-compensating nature of the calorimeters and detector misalignment. MET corrections will be applied to make MET a better estimate of true MET.

CMS has developed three sophisticated algorithms to reconstruct three different $\vec{\not{E}}_T$ which approach the true MET:

(a) PF $\vec{\not{E}}_T$, which is calculated using a complete particle-flow technique [136].

(b) Calo $\vec{\not{E}}_T$, which is based on calorimeter energies and the calorimeter tower geometry.

(c) TC $\vec{\not{E}}_T$, which corrects Calo MET by including tracks reconstructed in the inner tracker after correcting the expected energy deposition of tracks in the calorimeter.

The majority of CMS analyses use the PF MET because it is closer to the true MET than the other types of MET. The analysis described in this thesis uses PF $\vec{\not{E}}_T$. In order to estimate better the true MET, three different corrections are developed by CMS Collaboration:

The *Type-0 correction* is a mitigation for the degradation of the MET reconstruction due to the pileup interactions. In general, the Type-0 correction removes charged hadrons (originated from the vertices for pileup interactions) from MET calculations. In addition, the Type-0 correction removes an estimate of neutral pileup contributions. In the Type-0 correction the particles are classified as if they are produced in the hard scattering of interest (HS) or in pile-up interactions (PU):

$$\vec{\not{E}}_T^{raw} = -\sum_{i\in HS} \vec{p}_{T_i} - \sum_{i\in neuPU} \vec{p}_{T_i} - \sum_{i\in chPU} \vec{p}_{T_i} \tag{53}$$

The second sum runs over the pileup particles into neutral particles and the last sum is taken over the charged particles produced in the pileup interactions. The Type-0 MET can be derived from the raw MET above and the Type-0 corrections as follows:

$$\vec{\not{E}}_T^{Type-0} = \vec{\not{E}}_T^{raw} + \vec{C}_T^{Type-0} \tag{54}$$

where $\vec{C}_T^{Type-0} = (1 - R^0) \sum_{i\in chPU} \vec{p}_{T_i}$ is the Type-0 correction. R^0 is a function of the magnitude of $\sum_{i\in chPU} \vec{p}_{T_i}$ (sum of the charged particles produced in the pileup interactions).

The *Type-I correction* is a widespread MET correction in CMS Collaboration. This correction is a propagation of the jet energy corrections (JEC) [146] to MET. The Type-I correction replaces the vetor sum of transverse momenta of particles which can be clustered as jets with the vector sum of the transverse momenta of the jets to which JEC is applied. The raw MET can be derived from clustered jets or

unclustered jets:

$$\vec{\not{E}}_T^{raw} = -\sum_{i\in jets} \vec{p}_{T_i} - \sum_{i\in uncl} \vec{p}_{T_i} \tag{55}$$

The Type-I correction can be written as the difference between the vector sum of the transverse momenta of the jets where the JEC is not applied to and the vector sum of the transverse momenta of the jets where the JEC is applied to:

$$\vec{C}_T^{Type-I} = -\sum_{i\in jets} \vec{p}_{T_i} - \sum_{jet} \vec{p}_{T_{jet}}^{JEC} \tag{56}$$

Taking into account the Type-I correction and the raw MET, the Type-I MET can be written as follows:

$$\vec{\not{E}}_T^{Type-I} = \vec{\not{E}}_T^{raw} + \vec{C}_T^{Type-I} = -\sum_{jet} \vec{p}_{T_{jet}}^{JEC} - \sum_{i\in uncl} \vec{p}_{T_i} \tag{57}$$

The final correction of the MET object is the *Type-II correction* which was originally developed for Calo MET and is not used for the particle-flow MET. The Type-II correction corrects the $\vec{p}_T$ of unclustered particles by uniformly scaling it by a constant scale factor:

$$\vec{\not{E}}_T^{Type-II} = -\sum_{jet} \vec{p}_{T_{jet}}^{JEC} - C^{uncl} \sum_{i\in uncl} \vec{p}_{T_i} \tag{58}$$

In Fig. 20, the PF Type-I MET distribution has a very good agreement between simulated events and data which means that the Type-I correction can correct well the raw MET, approaching the true value of MET.

What is more, another significant variable is the $\vec{\not{E}}_T$ *significance*, or simply $\mathcal{S}$. This variable is important for analyses which use missing transverse energy variables because it has the ability to distinguish between events with spurious MET and those with genuine MET. Spurious $\vec{\not{E}}_T$ may originate from misreconstruction, finite detector resolution or detector noise and by using the MET significance variable, such events can be identified. The MET significance evaluates the p-value that the observed $\vec{\not{E}}_T$ is inconsistent with a null hypothesis, $\vec{\not{E}}_T = 0$, given the full event composition and resolution functions for each object in the event. A high value of $\mathcal{S}$ is an indication that the $\vec{\not{E}}_T$ observed in the event is not well explained by resolution smearing alone, suggesting that the event may contain unseen objects such as neutrinos or more exotic weakly interacting particles. The significance is defined as the log-likelihood ratio, as follows:

$$S \equiv 2\ln\left(\frac{\mathcal{L}(\vec{\epsilon} = \sum \vec{\epsilon}_i)}{\mathcal{L}(\vec{\epsilon} = 0)}\right) \tag{59}$$

The numerator expresses the likelihood of the hypothesis under test that the true value ($\vec{\epsilon}$) of the missing transverse energy is equal to the observed value ($\sum \vec{\epsilon}_i$), while the denominator expresses the likelihood of the *null hypothesis*, that the true missing transverse energy is actually zero. Under the null hypothesis, observation of any non-zero MET is attributed to resolution smearing.

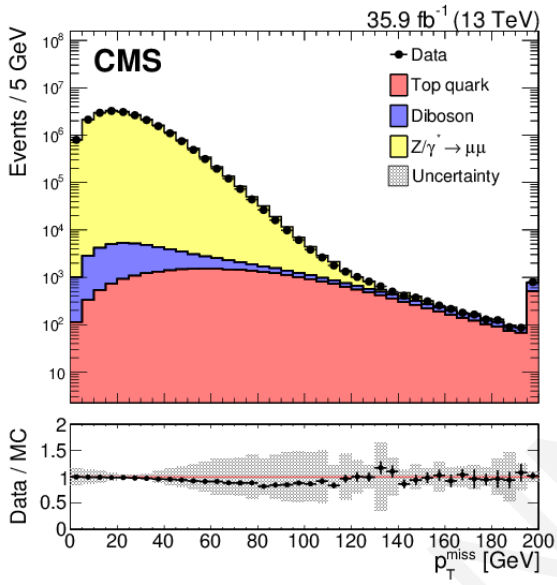

Figure 20: PF Type-I MET distribution after correcting the raw MET with Type-I correction. The last bin includes the overflow content. The systematic uncertainty due to the jet energy scale, jet energy resolution and variation on the unclustered energy is displayed with a grey band. Taken from Ref. [147].

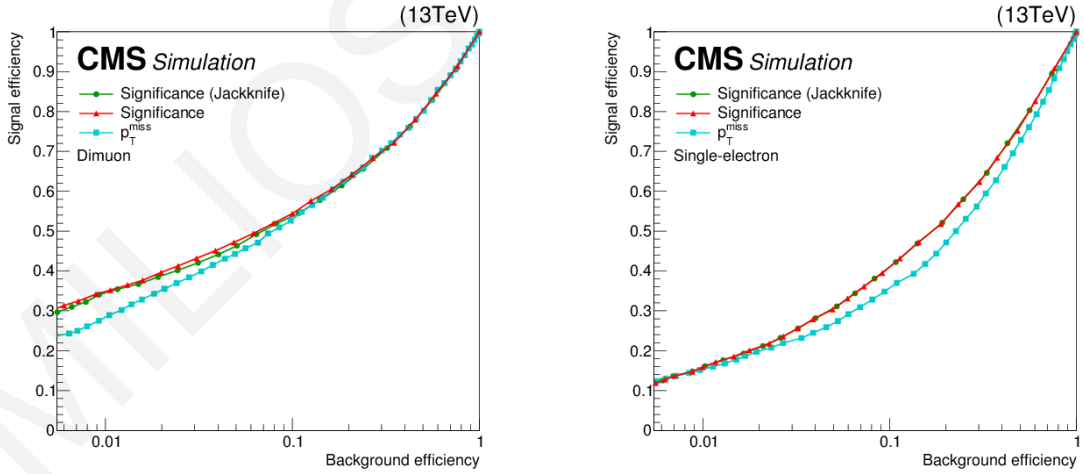

Figure 21: ROC (Receiver Operating Characteristic) curves comparing the signal versus background efficiency for the standard version of significance (red line), the Jackknife version [148] of S (yellow line) and MET (cyan line) using simulated di-muon events (left) and single-electron events (right). Taken from Ref. [147].

The discriminating power of the significance with respect to the $\vec{\not{E}}_T$ is shown in Fig. 21 for simulated

single-electron events and di-muon events. No significant difference between the two MET significance versions is observed. Both versions offer better signal to background separation compared to $\vec{\not{E}}_T$ only.

B.2.2.6 JET RECONSTRUCTION AND CORRECTION

In high-energy processes, many final states consist of quarks or gluons, however, these kind of states cannot be directly observed in the experimental life of LHC. Fortunately, sophisticated algorithms of CMS can identify such objects as *jets*. In general, jets are the experimental signatures of quarks and gluons produced in hard scattering of partons in proton-proton collisions. CMS has three different types of jet reconstruction: the *Calorimeter jets*, *Jet-Plus-Track jets* and the most popular jet reconstruction, the *Particle-Flow jets* [149]. The Calorimeter jets are reconstructed from energy deposits in the calorimeter towers and the Jet-Plus-Track jets are reconstructed by calorimeter jets whose energy response and resolution are improved by incorporating tracking information, according to the Jet-Plus-Track algorithm [150].

The last type of jet reconstruction used in the current analysis, is the Particle-Flow jets (PF jets). Jets are reconstructed by clustering particle candidates obtained using the particle flow (PF) algorithm. As mentioned in previous sections, the PF procedure identifies each particle-flow candidate through an optimized combination of all subdetectors' information. The PF candidates are clustered into jets using the anti-k_T algorithm [151]. The anti-k_T algorithm introduces distances d_{ij} between entities, particles (i) and pseudo-jets (j), and distances d_{iB} between particles and the beam (B).

$$d_{ij} = min(k_{ti}^{-2}, k_{tj}^{-2})\frac{\Delta_{ij}^2}{R^2} \tag{60a}$$

$$d_{iB} = k_{ti}^{-2} \tag{60b}$$

where $\Delta_{ij}^2 = (\phi_i - \phi_j)^2 + (\eta_i - \eta_j)^2$ and k_{ti}, y_i and ϕ_i are respectively the transverse momentum, rapidity and azimuth of particle i. In addition, R is a cone parameter chosen to be 0.4 in CMS Run-II. The clustering proceeds by identifying the smallest of the distances and if it is a d_{ij} recombining entities i and j, while if it is d_{iB} calling i a jet and removing it from the list of entities. The distances are recalculated and the procedure repeated until no entities are left.

Jets must be passed through several procedures for correcting their energies. The *charged hadron subtraction* (CHS) procedure is applied to clustered jets to reduce reconstruction biases such as pile-up interactions as well as particle candidates with a wrong primary vertex. These biases are removed by the CHS procedure. Furthermore, jet's energy is also affected by the non-linear response of the calorimeters, the detector segmentation, the presence of material in front of calorimeters, electronic noise, and noise due to additional interactions form the same bunch crossing. In order to mitigate these effects,

several levels of corrections, illustrated in Fig. 22, are applied to the raw jets.

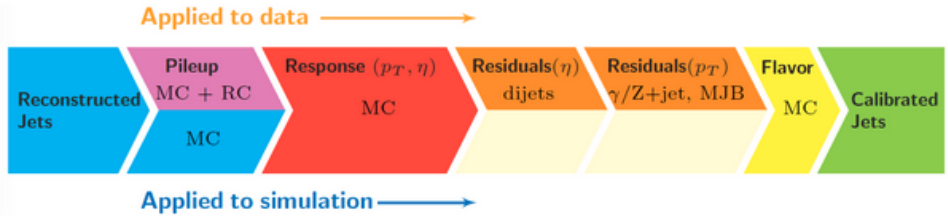

Figure 22: The various correction levels of reconstructed jets.

In the first level of correction, called *L1 Offset*, the pile-up and electronic noise effects are removed. The offset correction aims to estimate and subtract the energy not associated with the high-p_T scattering. By counting the number of good-quality primary vertices N_{PV} or by calculating the diffuse offset energy density ρ, the amount of pile-up removed by L1 offset can be estimated in the event.

After that, *L2L3 MC-truth corrections* are applied to the already corrected jets for pile-up offset. The old *L2Relative* and *L3Absolute* were replaced by L2L3 MC-truth corrections. The simulated jet response corrections are determined on a QCD di-jet sample, by comparing the reconstructed p_T to the particle-level jets which do not include energy from neutrino contributions. The corrections are derived as a function of jet p_T and η and make the response uniform over these two variables. In other words, the two old steps are now done in one step with MC-truth corrections.

The purpose of *L2L3Residuals* is to correct the remaining small differences within jet response in data and MC. The L2Residuals η-dependent corrections are determined with di-jet events, relative to a jet of similar p_T in the barrel reference region. These corrections include a p_T dependence of the *Jet Energy Scale (JES)* relative to the JES of the barrel jet. The L3Residuals correct the jet absolute scale (JES versus p_T). These corrections are determined using $Z + jet$, $photon + jet$ and multi-jet events for barrel jets.

The last level of jet's correction is the *L5 flavour corrections*. The L5 flavour corrections are optional corrections which are derived from MC simulation, using $Z + jet$ and $photon + jets$ simulated events. These corrections are provided for the $Z + jets$ and $photon + jets$ mixtures, and also for pure flavours. The L5 flavour corrections are optional for any CMS analysis, in contrast to the L1 offset and L2L3 MC-truth which are mandatory JECs at CMS for any CMS analysis using Monte Carlo samples. For real data, L1 offset, L2L3 MC-truth and L2L3Residuals must be applied for jet correction.

Fig. 23 shows the scale factor of the offset correction per additional pile-up interaction (μ) as a function of η for each type of PF particles. The three different data taking are presented with their scale factor. Additionally, Fig. 24 shows the relative correction scale factor as a function of η. The relative residual correction is well calibrated in the detector region of $|\eta| < 1.3$. Fig. 25 illustrates the jet energy scale for

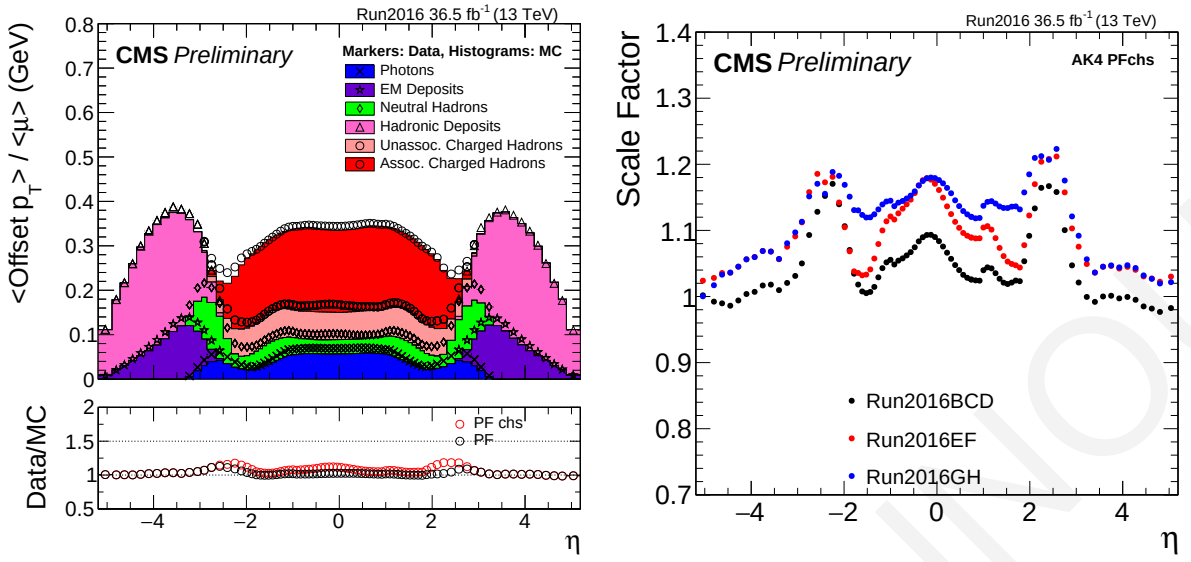

Figure 23: Left: The data/MC comparison for the average offset per additional pile-up interaction (μ) as a function of η for each type of PF particles. Right: The data/MC scale factors as a function of η for different data taking: Run2016BCD (beginning), Run2016EF (middle) and Run2016GH (end). Taken from Ref. [152].

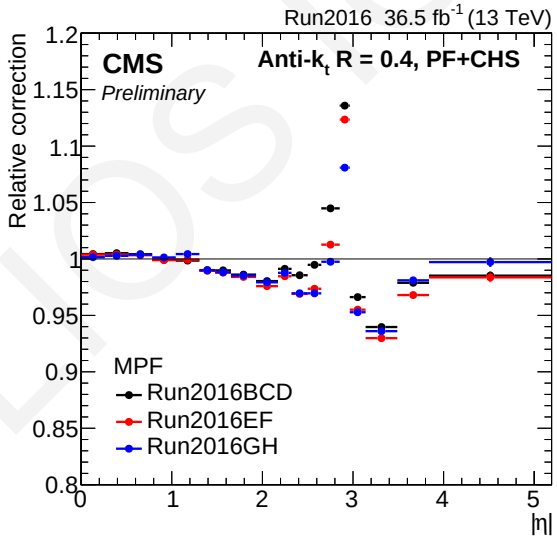

Figure 24: Relative residual correction value at average p_T in each η bin is shown for the three different data taking: Run2016BCD (beginning), Run2016EF (middle) and Run2016GH (end). Taken from Ref. [152].

absolute residual correction as a function of jet's transverse momentum. The large absolute correction is greater at the beginning and middle data taking, while a smaller absolute correction for the end data taking is obvious due to a fixed issue with strip tracker dynamic inefficiency. Finally, the jet energy

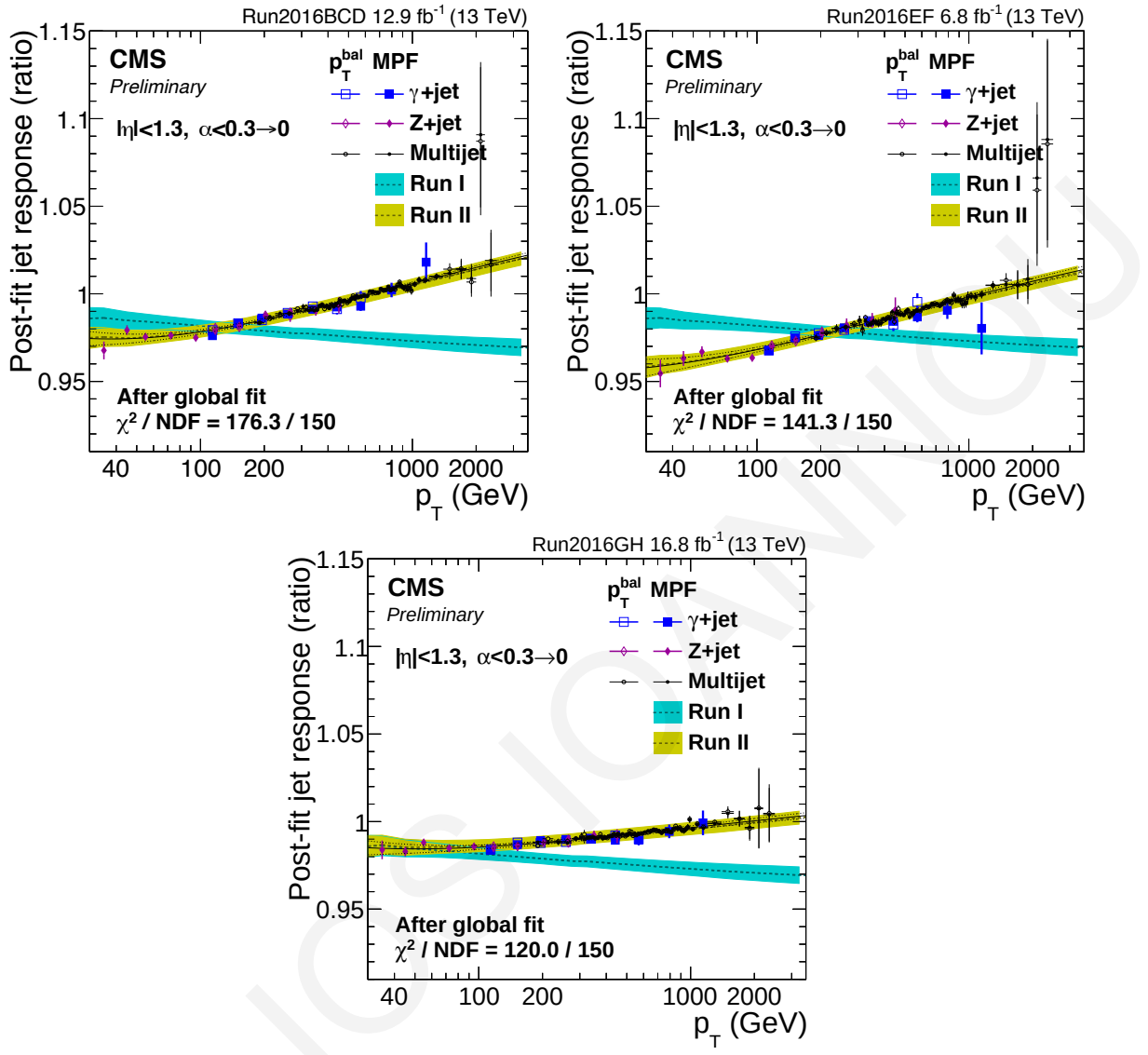

Figure 25: The data/MC comparison for absolute residual correction as a function of jet p_T for the three different data taking: Run2016BCD (left) Run2016EF (middle) Run2016GH (right). Taken from Ref. [152].

uncertainty as a function of jet p_T and η is shown in Fig. 26. The overall uncertainty on the jet energy scale for jets with $p_T = 30$ GeV is smaller than 3% in the barrel region and 6% up to $|\eta| \lesssim 4.5$. Moreover, the jet energy uncertainty decreases for large transverse momenta, reaching at 1%. For the lower transverse momenta, the uncertainty is up to 3% for all data taking in 2016.

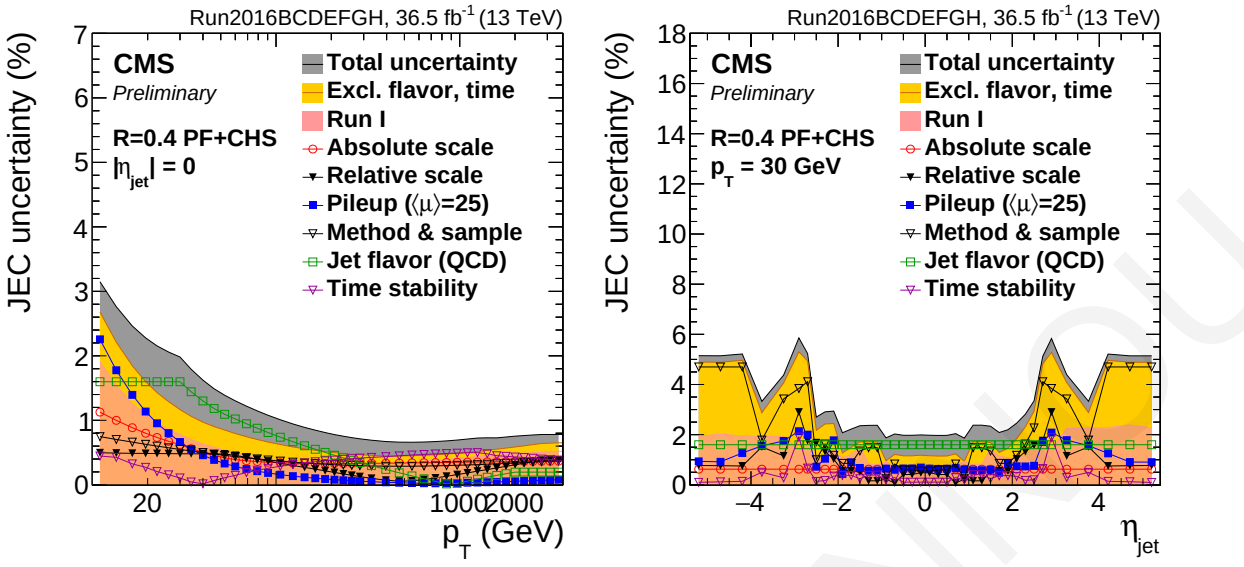

Figure 26: Jet energy uncertainty as a function of jet p_T (left) and as a function of η (right) for jet $p_T = 30$ GeV. Taken from Ref. [152].

B.2.2.7 B-JETS TAGGING

B-tagging algorithms are used to identify the b-jets in CMS when specific criteria for tracks are fulfilled. The b-tagging identifies jets as b-tagged jets using tracks with specific criteria, as follows:

- angular distance between track and jets axis $\Delta R < 0.3$;
- number of pixel hits equal or greater than two hits (≥ 2) and the number of tracker hits must be at least 8, including pixel (≥ 8);
- distance smaller than 0.2 cm (17 cm) in the transverse plane (along the beam axis) between the track and the primary vertex (PV) at the point of closest approach of the trajectory to the PV in the transverse plane;
- transverse momentum $p_T > 1$GeV/c;
- normalised $\chi^2 < 5$;
- distance to jet axis < 0.07 cm, defined as the spatial distance between the trajectory and the jet axis at their point of closest approach, where the jet axis is reconstructed with respect to the primary vertex;
- decay length < 5 cm, defined as the spatial distance between the PV and the point of closest approach between the track trajectory and the jet axis.

A very important quantity for b-tagging is the *impact parameter (IP)*, illustrated in Fig. 27, which is defined as the distance from the PV to the track at their point of closest approach in space. The IP is given the same sign as the scalar product of the jet axis direction with the vector pointing from the primary vertex to this point of closest approach [153]. The impact parameter can be used to estimate the mistagging performance of jets that do not come from b and c quarks if its value is negative. A negative impact parameter corresponds to a decay point behind the primary vertex and it arises mostly from the finite detector resolution which results in mis-measured track parameters.

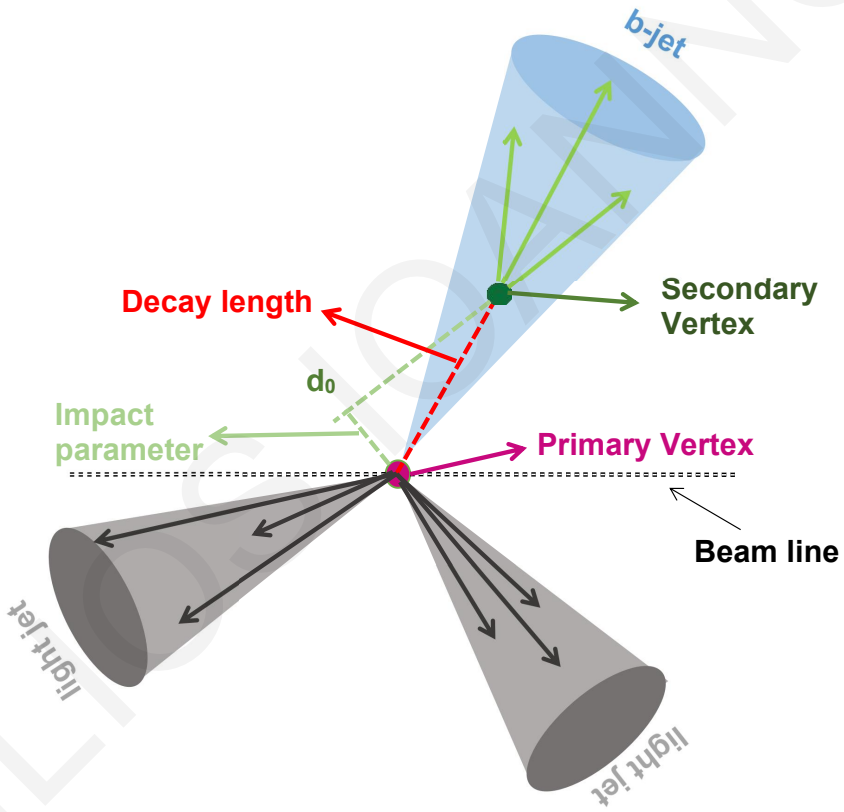

Figure 27: A sketch of a b-jet generation, a secondary vertex is also shown.

In addition, a *secondary vertex (SV)* is also shown in Fig. 27 and is reconstructed using the adaptive vertex fitter [154]. In order to identify long-lived particles, such as b-jets, the distance in space from the PV to the SV, and the flight distance are used. The flight direction of the candidate SV has to be within a cone $\Delta R < 0.5$ around the jet axis.

In the CMS Collaboration, five b-tagging algorithms [155] have been developed during the operation of

LHC. Three algorithms were used for the Run-I era:

- The *Track Counting High Purity (TCHP)* whose the discriminator value is defined as the impact parameter significance (IP/σ_{IP}, where σ_{IP} is the measurement uncertainty on the IP) of the track with the third highest impact parameter significance.
- The *Jet Probability (JP)* algorithm in which the jet is assigned a likelihood that all associated tracks come from the PV. The probability distribution of individual tracks is computed using the impact parameter significance of tracks with negative IP values, which are mostly produced in light-parton jets. This calibration is performed independently in data and simulation.
- The *Combined Secondary Vertex (CSV)* algorithm in which secondary vertices and track-based lifetime information are used to build a likelihood-based discriminator to distinguish between jets from b-quarks and those from charm or light quarks and gluons.

and two new b-tagging algorithms have been developed for Run-II analyses (the Combined Secondary Vertex Version2 and the DeepCSV). The *Combined Secondary Vertex Version 2 (CSVv2)* is based on the CSV algorithm and combines the information of displaced tracks with the information on secondary vertices associated with the jet using a multivariate technique. Two variants of the CSVv2 algorithm exist according to whether *inclusive vertex finding (IVF)* or *adaptive vertex reconstruction (AVR)* vertices are used. At least two tracks per jet are required and when algorithms calculate the values of the track variables, the tracks are required to have an angular distance with respect to the jet axis of $\Delta R < 0.3$. Beside, that any combination of two tracks compatible with the mass of the K^0_S meson in a window of 30 MeV is rejected. Jets that have neither a selected track nor a secondary vertex, are assigned a default output discriminator value of -1 [156]. The major differences between the CSV algorithm used for Run-I and the newer CSV algorithm (CSVv2) used for Run-II, are presented in Tab. 3.

In addition, taking advantage of the knowledge of deep machine learning [157], the identification of jets from heavy-flavour hadrons can be improved. The evolution of the CSVv2 algorithm is called *DeepCSV* and it was developed using a deep neural network with more hidden layers, more nodes per layer and a simultaneous training in all vertex categories and for all jet flavours. The only difference between the older and newer algorithm is that the track-based variables up to six tracks are used in the training of the DeepCSV. The training of the deep neural network is performed using jets with p_T between 20 GeV and 1 TeV, and within the tracker acceptance. It is performed using the KERAS deep learing library, interfaced with the TENSORFLOW library that is used for low-level operations, such as convolutions. The neural network uses four hidden layers that are fully connected, each one with 100 nodes. Each node in one of the hidden layers uses a rectified linear unit as its activation function to define the output of the node given the input values. For the nodes in the last layer, a normalized exponential function is

Input Variable	Run-I CSV	Run-II CSV (CSVv2)
SV 2D flight distance significance	✓	✓
Number of SV	×	✓
Track η_{rel}	✓	✓
Corrected SV mass	✓	✓
Number of tracks from SV	✓	✓
SV energy ration	✓	✓
$\Delta R(SV, jet)$	×	✓
3D IP significance of the first four tracks	✓	✓
Track $p_{T,rel}$	×	✓
$\Delta R(track, jet)$	×	✓
Track $p_{T,rel}$ ratio	×	✓
Track distance	×	✓
Track decay length	×	✓
Summed tracks E_T ratio	×	✓
$\Delta R(summed\ tracks, jet)$	×	✓
First track 2D IP significance above c threshold	×	✓
Number of selected tracks	×	✓
Jet p_T	×	✓
Jet η	×	✓

Table 3: Input variables used for the CSV and CSVv2 algorithms.

used for the activation to be able to interpret the output value as a probability for a certain jet flavour category, $P(f)$.

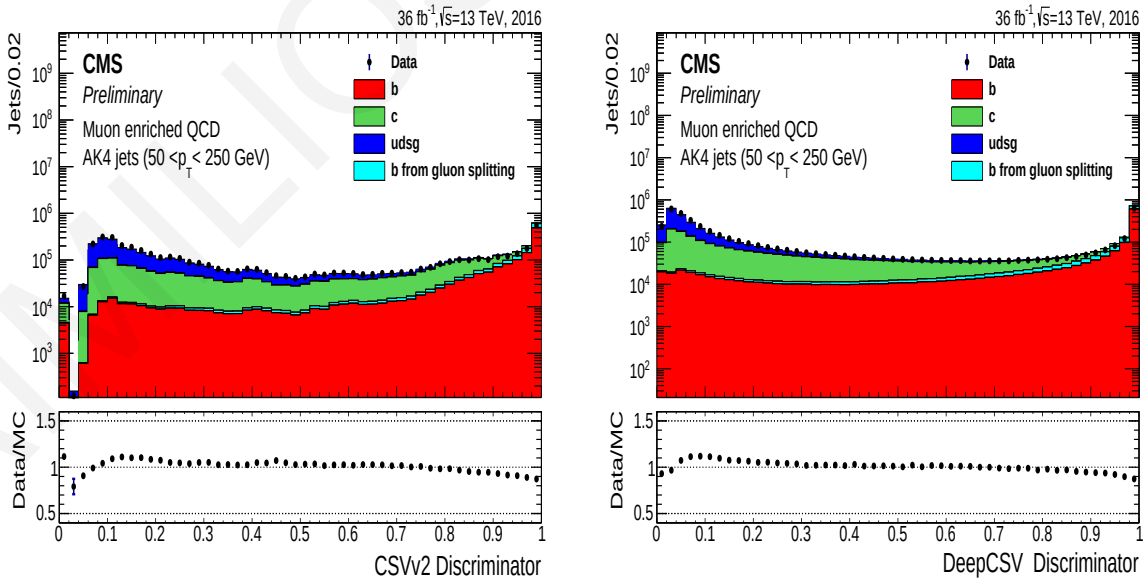

Figure 28: Reference distributions for the CSVv2 (left) and DeepCSV algorithms (right), for each flavour contribution. Taken from Ref. [158].

Despite the fact that the DeepCSV is a newer version of CSVv2 using deep machine learning techniques, the investigation of $A \to Zh$ channel presented in this thesis was performed using the CSVv2 algorithm to identify the b-jets because the DeepCSV technique was not realised to the CMS community in the period of the search. As it is shown in Fig. 28, differences between the two algorithms are minor and the results are not affected at all using either the older b-tagging technique or the newer.

C.3 SIGNAL SAMPLES

The signal samples generated by aMCNLO generator, are reported on Tab. 4 for gluon-gluon fusion production mode and on Tab. 5 for b-quark associated production mode. There are two investigated channels for each production mechanism. For the case of gluon-gluon fusion, samples for $A \to Zh \to \ell^+\ell^- b\bar{b}$ and $A \to Zh \to \nu\bar{\nu}b\bar{b}$ channels are included on the table list.

Sample name	$\sigma \times Br$ (pb)
GluGluToAToZhToNuNuBB_M-225_13TeV-madgraphMLM-pythia8	0.11648
GluGluToAToZhToNuNuBB_M-250_13TeV-madgraphMLM-pythia8	0.11648
GluGluToAToZhToNuNuBB_M-275_13TeV-madgraphMLM-pythia8	0.11648
GluGluToAToZhToNuNuBB_M-300_13TeV-madgraphMLM-pythia8	0.11648
GluGluToAToZhToNuNuBB_M-325_13TeV-madgraphMLM-pythia8	0.11648
GluGluToAToZhToNuNuBB_M-350_13TeV-madgraphMLM-pythia8	0.11648
GluGluToAToZhToNuNuBB_M-400_13TeV-madgraphMLM-pythia8	0.11648
GluGluToAToZhToNuNuBB_M-500_13TeV-madgraphMLM-pythia8	0.11648
GluGluToAToZhToNuNuBB_M-600_13TeV-madgraphMLM-pythia8	0.11648
GluGluToAToZhToNuNuBB_M-700_13TeV-madgraphMLM-pythia8	0.11648
GluGluToAToZhToNuNuBB_M-750_13TeV-madgraphMLM-pythia8	0.11648
GluGluToAToZhToNuNuBB_M-800_13TeV-madgraphMLM-pythia8	0.11648
GluGluToAToZhToNuNuBB_M-900_13TeV-madgraphMLM-pythia8	0.11648
GluGluToAToZhToNuNuBB_M-1000_13TeV-madgraphMLM-pythia8	0.11648
GluGluToAToZhToLLBB_M-225_13TeV-madgraphMLM-pythia8	0.05882
GluGluToAToZhToLLBB_M-250_13TeV-madgraphMLM-pythia8	0.05882
GluGluToAToZhToLLBB_M-275_13TeV-madgraphMLM-pythia8	0.05882
GluGluToAToZhToLLBB_M-300_13TeV-madgraphMLM-pythia8	0.05882
GluGluToAToZhToLLBB_M-325_13TeV-madgraphMLM-pythia8	0.05882
GluGluToAToZhToLLBB_M-350_13TeV-madgraphMLM-pythia8	0.05882
GluGluToAToZhToLLBB_M-400_13TeV-madgraphMLM-pythia8	0.05882
GluGluToAToZhToLLBB_M-500_13TeV-madgraphMLM-pythia8	0.05882
GluGluToAToZhToLLBB_M-600_13TeV-madgraphMLM-pythia8	0.05882
GluGluToAToZhToLLBB_M-700_13TeV-madgraphMLM-pythia8	0.05882
GluGluToAToZhToLLBB_M-750_13TeV-madgraphMLM-pythia8	0.05882
GluGluToAToZhToLLBB_M-800_13TeV-madgraphMLM-pythia8	0.05882
GluGluToAToZhToLLBB_M-900_13TeV-madgraphMLM-pythia8	0.05882
GluGluToAToZhToLLBB_M-1000_13TeV-madgraphMLM-pythia8	0.05882

Table 4: Signal samples in the gluon fusion production mode. The cross section for each relative sample is obtained by multiplying the production cross section by the vector boson branching fractions ($\mathcal{B}r(Z \to \ell\ell) = 0.101$, $\mathcal{B}r(Z \to \nu\nu) = 0.200$, $\mathcal{B}r(h \to b\bar{b}) = 0.5824$ [159]).

Additionally, events for the same processes are also generated for the b-quark associated production mechanism. In summary, two possible channels for each production mode are investigated for a signa-

ture of a heavy pseudo-scalar A boson. Each samples includes 100k events.

Sample name	$\sigma \times Br$ (pb)
BBAToZhToLLBB_M-225_13TeV-madgraph-pythia8	0.05882
BBAToZhToLLBB_M-250_13TeV-madgraph-pythia8	0.05882
BBAToZhToLLBB_M-275_13TeV-madgraph-pythia8	0.05882
BBAToZhToLLBB_M-300_13TeV-madgraph-pythia8	0.05882
BBAToZhToLLBB_M-325_13TeV-madgraph-pythia8	0.05882
BBAToZhToLLBB_M-350_13TeV-madgraph-pythia8	0.05882
BBAToZhToLLBB_M-400_13TeV-madgraph-pythia8	0.05882
BBAToZhToLLBB_M-500_13TeV-madgraph-pythia8	0.05882
BBAToZhToLLBB_M-600_13TeV-madgraph-pythia8	0.05882
BBAToZhToLLBB_M-700_13TeV-madgraph-pythia8	0.05882
BBAToZhToLLBB_M-750_13TeV-madgraph-pythia8	0.05882
BBAToZhToLLBB_M-800_13TeV-madgraph-pythia8	0.05882
BBAToZhToLLBB_M-900_13TeV-madgraph-pythia8	0.05882
BBAToZhToLLBB_M-1000_13TeV-madgraph-pythia8	0.05882
BBAToZhToNuNuBB_M-225_13TeV-madgraph-pythia8	0.11648
BBAToZhToNuNuBB_M-250_13TeV-madgraph-pythia8	0.11648
BBAToZhToNuNuBB_M-275_13TeV-madgraph-pythia8	0.11648
BBAToZhToNuNuBB_M-300_13TeV-madgraph-pythia8	0.11648
BBAToZhToNuNuBB_M-325_13TeV-madgraph-pythia8	0.11648
BBAToZhToNuNuBB_M-350_13TeV-madgraph-pythia8	0.11648
BBAToZhToNuNuBB_M-400_13TeV-madgraph-pythia8	0.11648
BBAToZhToNuNuBB_M-500_13TeV-madgraph-pythia8	0.11648
BBAToZhToNuNuBB_M-600_13TeV-madgraph-pythia8	0.11648
BBAToZhToNuNuBB_M-700_13TeV-madgraph-pythia8	0.11648
BBAToZhToNuNuBB_M-750_13TeV-madgraph-pythia8	0.11648
BBAToZhToNuNuBB_M-800_13TeV-madgraph-pythia8	0.11648
BBAToZhToNuNuBB_M-900_13TeV-madgraph-pythia8	0.11648
BBAToZhToNuNuBB_M-1000_13TeV-madgraph-pythia8	0.11648

Table 5: Signal samples in the b-quark associated production mode. The cross section for each relative sample is obtained by multiplying the production cross section by the vector boson branching fractions ($\mathcal{B}r(Z \to \ell\ell) = 0.101$, $\mathcal{B}r(Z \to \nu\nu) = 0.200$, $\mathcal{B}r(h \to b\bar{b}) = 0.5824$ [159]).

D.4 BACKGROUND SAMPLES

Dataset	$\sigma \times \mathcal{B}$ (pb)
DYJetsToLL_M-50_TuneCUETP8M1_13TeV-amcatnloFXFX-pythia8	5765.4
DYJetsToLL_M-50_TuneCUETP8M1_13TeV-madgraphMLM-pythia8	5765.4
DY1JetsToLL_M-50_TuneCUETP8M1_13TeV-madgraphMLM-pythia8	1016
DY2JetsToLL_M-50_TuneCUETP8M1_13TeV-madgraphMLM-pythia8	331.4
DY3JetsToLL_M-50_TuneCUETP8M1_13TeV-madgraphMLM-pythia8	96.36
DY4JetsToLL_M-50_TuneCUETP8M1_13TeV-madgraphMLM-pythia8	51.4
DYJetsToLL_M-50_HT-100to200_TuneCUETP8M1_13TeV-madgraphMLM-pythia8	147.4
DYJetsToLL_M-50_HT-200to400_TuneCUETP8M1_13TeV-madgraphMLM-pythia8	40.99
DYJetsToLL_M-50_HT-400to600_TuneCUETP8M1_13TeV-madgraphMLM-pythia8	5.678
DYJetsToLL_M-50_HT-600to800_TuneCUETP8M1_13TeV-madgraphMLM-pythia8	1.367
DYJetsToLL_M-50_HT-800to1200_TuneCUETP8M1_13TeV-madgraphMLM-pythia8	0.6304
DYJetsToLL_M-50_HT-1200to2500_TuneCUETP8M1_13TeV-madgraphMLM-pythia8	0.1514
DYJetsToLL_M-50_HT-2500toInf_TuneCUETP8M1_13TeV-madgraphMLM-pythia8	0.003565
ZJetsToNuNu_HT-100To200_13TeV-madgraph	280.35
ZJetsToNuNu_HT-200To400_13TeV-madgraph	77.67
ZJetsToNuNu_HT-400To600_13TeV-madgraph	10.73
ZJetsToNuNu_HT-600To800_13TeV-madgraph	3.221
ZJetsToNuNu_HT-800To1200_13TeV-madgraph	1.474
ZJetsToNuNu_HT-1200To2500_13TeV-madgraph	0.3586
ZJetsToNuNu_HT-2500ToInf_13TeV-madgraph	0.008203
WJetsToLNu_TuneCUETP8M1_13TeV-amcatnloFXFX-pythia8	61526.7
WJetsToLNu_TuneCUETP8M1_13TeV-madgraphMLM-pythia8	61526.7
WJetsToLNu_HT-100To200_TuneCUETP8M1_13TeV-madgraphMLM-pythia8	1345
WJetsToLNu_HT-200To400_TuneCUETP8M1_13TeV-madgraphMLM-pythia8	359.7
WJetsToLNu_HT-400To600_TuneCUETP8M1_13TeV-madgraphMLM-pythia8	48.91
WJetsToLNu_HT-600To800_TuneCUETP8M1_13TeV-madgraphMLM-pythia8	12.05
WJetsToLNu_HT-800To1200_TuneCUETP8M1_13TeV-madgraphMLM-pythia8	5.501
WJetsToLNu_HT-1200To2500_TuneCUETP8M1_13TeV-madgraphMLM-pythia8	1.329
WJetsToLNu_HT-2500ToInf_TuneCUETP8M1_13TeV-madgraphMLM-pythia8	0.03216

Table 6: Z, W+jets simulated samples. The cross section × branching ratio is shown in pb. SM boson branching fractions are taken from Ref. [159].

Dataset	$\sigma \times \mathcal{B}$ (pb)
TT_TuneCUETP8M2T4_13TeV-powheg-pythia8	831.76
TTWJetsToLNu_TuneCUETP8M1_13TeV-amcatnloFXFX-madspin-pythia8	0.2043
TTZToLLNuNu_M-10_TuneCUETP8M1_13TeV-amcatnlo-pythia8	0.2529
ST_s-channel_4f_leptonDecays_13TeV-amcatnlo-pythia8_TuneCUETP8M1	3.36
ST_t-channel_antitop_4f_leptonDecays_13TeV-powheg-pythia8_TuneCUETP8M1	26.38
ST_t-channel_top_4f_leptonDecays_13TeV-powheg-pythia8_TuneCUETP8M1	44.33
ST_tW_antitop_5f_inclusiveDecays_13TeV-powheg-pythia8_TuneCUETP8M1	35.85
ST_tW_top_5f_inclusiveDecays_13TeV-powheg-pythia8_TuneCUETP8M1	35.85
WWTo4Q_4f_13TeV_powheg_madspin_pythia8	51.723
WWTo2L2Nu_13TeV_powheg_madspin_pythia8	12.178
WWTo1L1Nu2Q_13TeV_amcatnloFXFX_madspin_pythia8	49.997
WZTo1L1Nu2Q_13TeV_amcatnloFXFX_madspin_pythia8	10.71
WZTo2L2Q_13TeV_powheg_madspin_pythia8	5.595
WZTo2Q2Nu_13TeV_amcatnloFXFX_madspin_pythia8	6.488
ZZTo2L2Q_13TeV_amcatnloFXFX_madspin_pythia8	3.22
ZZTo2L2Nu_13TeV_amcatnloFXFX_madspin_pythia8	3.22
ZZTo2Q2Nu_13TeV_amcatnloFXFX_madspin_pythia8	4.04
ZZTo2L2Q_13TeV_powheg_madspin_pythia8	0.564
ZZTo4L_13TeV_powheg_pythia8	1.212
ZZTo4Q_13TeV_amcatnloFXFX_madspin_pythia8	6.842
ZH_HToBB_ZToLL_M125_13TeV_amcatnloFXFX_madspin_pythia8	0.0507
WH_HToBB_WToLNu_M125_13TeV_amcatnloFXFX_madspin_pythia8	0.2580
ZH_HToBB_ZToNuNu_M125_13TeV_amcatnloFXFX_madspin_pythia8	0.1003
QCD_HT100to200_TuneCUETP8M1_13TeV-madgraphMLM-pythia8	27540000.0
QCD_HT200to300_TuneCUETP8M1_13TeV-madgraphMLM-pythia8	1735000.0
QCD_HT300to500_TuneCUETP8M1_13TeV-madgraphMLM-pythia8	366800.0
QCD_HT500to700_TuneCUETP8M1_13TeV-madgraphMLM-pythia8	29370.0
QCD_HT700to1000_TuneCUETP8M1_13TeV-madgraphMLM-pythia8	6524.0
QCD_HT1000to1500_TuneCUETP8M1_13TeV-madgraphMLM-pythia8	1064.0
QCD_HT1500to2000_TuneCUETP8M1_13TeV-madgraphMLM-pythia8	121.5
QCD_HT2000toInf_TuneCUETP8M1_13TeV-madgraphMLM-pythia8	25.42

Table 7: $t\bar{t}$, dibosons and multijet simulated samples. The cross section $\times$ branching ratio is shown in pb. SM boson branching fractions are taken from Ref. [159].

E.5 IMPACTS AND PULLS

The full list of impacts and pulls for $m_A = 300,\ 500$, and 1000 GeV are shown in the following figures:

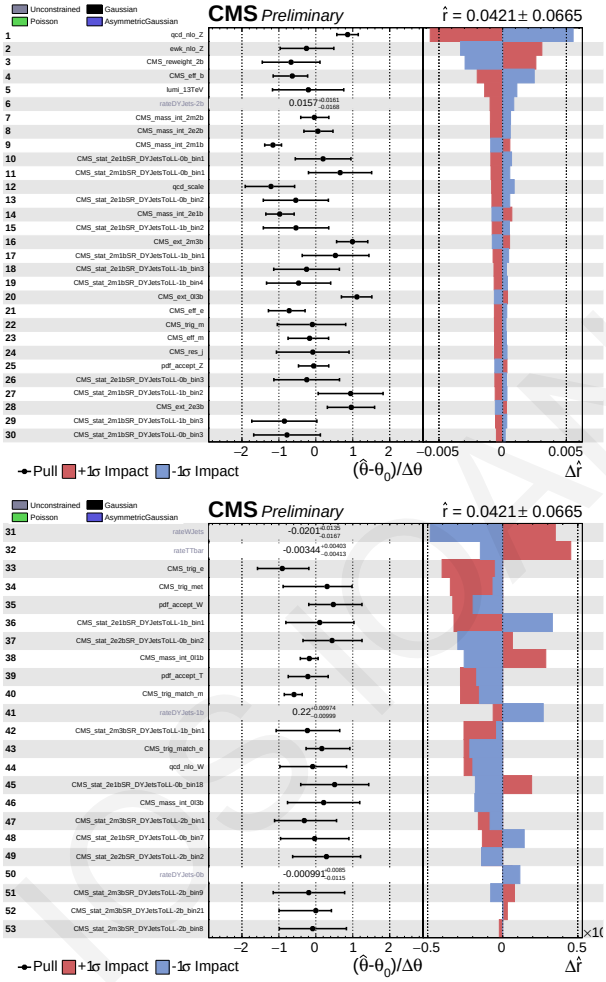

Figure 29: Impacts for the combination of all channels and the $m_A = 500$ GeV signal hypothesis.

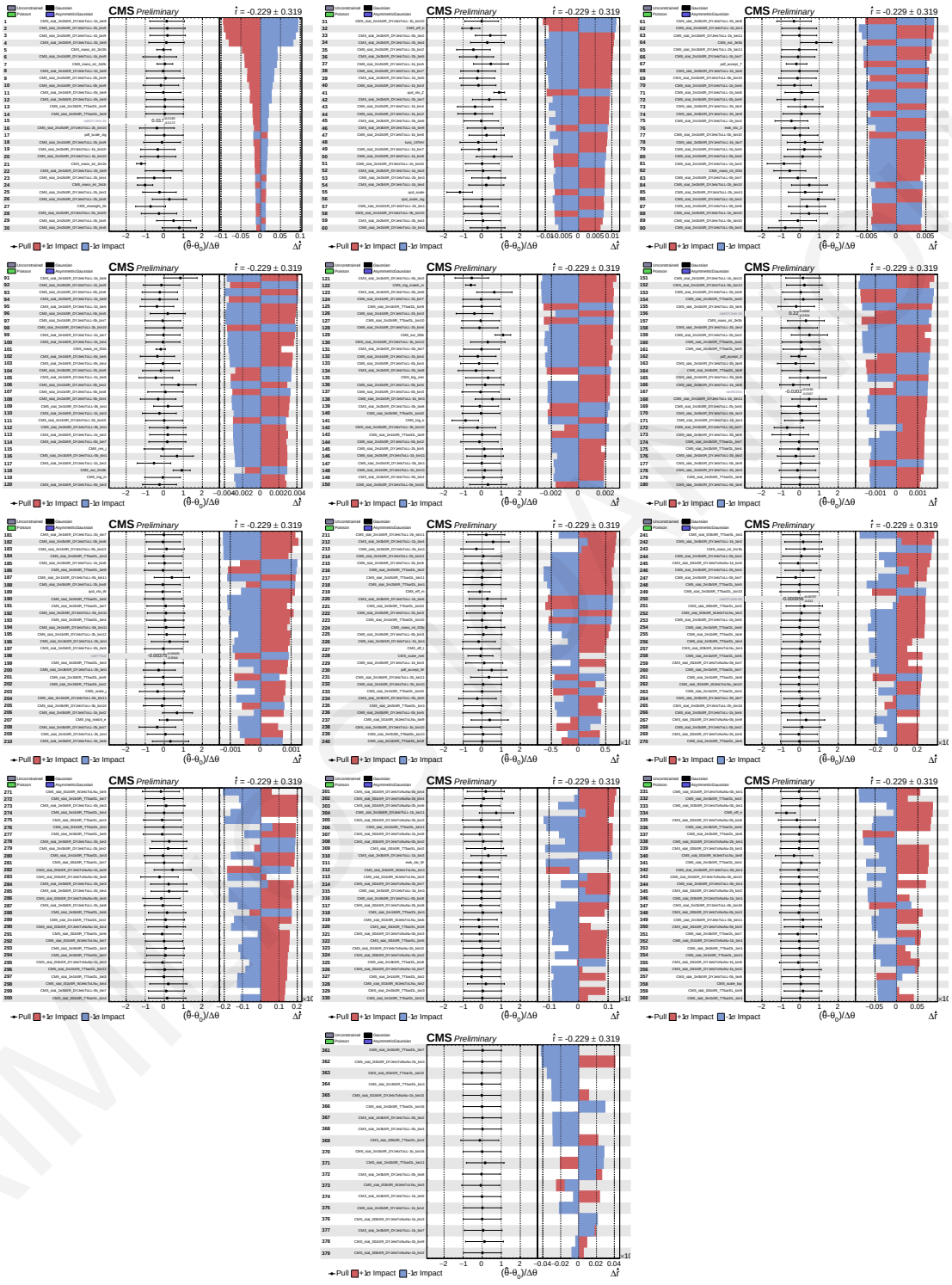

Figure 30: Impacts for the combination of all channels and the $m_A = 300$ GeV signal hypothesis.

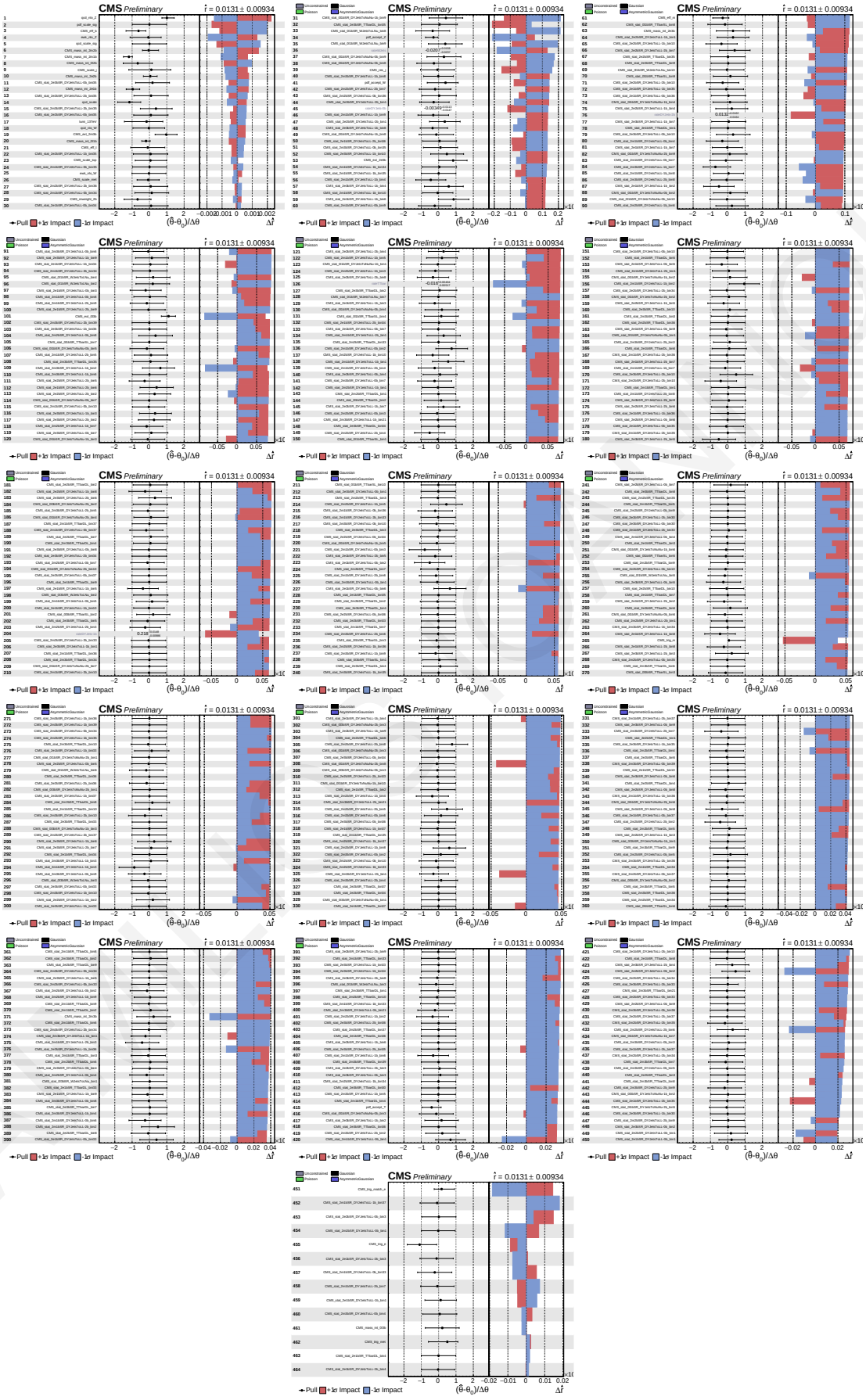

Figure 31: Impacts for the combination of all channels and the $m_A = 1000$ GeV signal hypothesis.

References

[1] G. C. Branco et al. "Theory and phenomenology of two-Higgs-doublet models". In: *Phys. Rept.* 516 (2012), pp. 1–102. DOI: 10.1016/j.physrep.2012.02.002. arXiv: 1106.0034 [hep-ph].

[2] Hyun Min Lee. "Lectures on Physics Beyond the Standard Model". In: July 2019. arXiv: 1907.12409 [hep-ph].

[3] Jihn E. Kim. "Light Pseudoscalars, Particle Physics and Cosmology". In: *Phys. Rept.* 150 (1987), pp. 1–177. DOI: 10.1016/0370-1573(87)90017-2.

[4] *Summary results of high mass BSM Higgs searches using CMS run-I data*. Tech. rep. CMS-PAS-HIG-16-007. Geneva: CERN, 2016. URL: https://cds.cern.ch/record/2142432.

[5] Christian Weiser. *A Combined Secondary Vertex Based B-Tagging Algorithm in CMS*. Tech. rep. CMS-NOTE-2006-014. Geneva: CERN, 2006. URL: http://cds.cern.ch/record/927399.

[6] S.L. Glashow. "Partial-symmetries of weak interactions". In: *Nuclear Physics* 22 (1961), pp. 579–588. DOI: 10.1016/0029-5582(61)90469-2.

[7] Abdus Salam. "Weak and Electromagnetic Interactions". In: *Conf. Proc.* C680519 (1968), pp. 367–377.

[8] Steven Weinberg. "A Model of Leptons". In: *Phys. Rev. Lett.* 19 (1967), pp. 1264–1266. DOI: 10.1103/PhysRevLett.19.1264.

[9] F. Halzen and Alan D. Martin. *QUARKS AND LEPTONS: AN INTRODUCTORY COURSE IN MODERN PARTICLE PHYSICS*. 1984. ISBN: 0471887412, 9780471887416.

[10] Alessandro Bettini. *Introduction to Elementary Particle Physics*. Cambridge University Press, 2008. DOI: 10.1017/CBO9780511809019.

[11] E. Noether. "Invariant Variation Problems". In: *Gott. Nachr.* 1918 (1918), pp. 235–257.

[12] S. L. Glashow, J. Iliopoulos, and L. Maiani. "Weak Interactions with lepton-Hadron Symmetry". In: *Phys. Rev. D 2* (1970), p. 1285. DOI: 10.1007/978-3-319-18512-5.

[13] P.M. Watkins. "DISCOVERY OF THE W AND Z BOSONS". In: *Contemp. Phys.* 27 (1986), pp. 291–324. DOI: 10.1080/00107518608211015.

[14] F. Englert and R. Brout. "Broken Symmetry and the Mass of Gauge Vector Mesons". In: *Phys. Rev. Lett.* 13 (1964). [,157(1964)], pp. 321–323. DOI: 10.1103/PhysRevLett.13.321.

[15] Peter W. Higgs. "Broken Symmetries and the Masses of Gauge Bosons". In: *Phys. Rev. Lett.* 13 (1964). [,160(1964)], pp. 508–509. DOI: 10.1103/PhysRevLett.13.508.

[16] D. B. Chitwood et al. "Improved measurement of the positive muon lifetime and determination of the Fermi constant". In: *Phys. Rev. Lett.* 99 (2007), p. 032001. DOI: 10.1103/PhysRevLett.99.032001. arXiv: 0704.1981 [hep-ex].

[17] *LHC Cross Section Working Group*. 2019. URL: https://twiki.cern.ch/twiki/bin/view/LHCPhysics/LHCHXSWG.

[18] Serguei Chatrchyan et al. "Observation of a new boson at a mass of 125 GeV with the CMS experiment at the LHC". In: *Phys. Lett.* B716 (2012), pp. 30–61. DOI: 10.1016/j.physletb.2012.08.021. arXiv: 1207.7235 [hep-ex].

[19] Serguei Chatrchyan et al. "Observation of a New Boson with Mass Near 125 GeV in pp Collisions at $\sqrt{s} = 7$ and 8 TeV". In: *JHEP* 06 (2013), p. 081. DOI: 10.1007/JHEP06(2013)081. arXiv: 1303.4571 [hep-ex].

[20] Georges Aad et al. "Observation of a new particle in the search for the Standard Model Higgs boson with the ATLAS detector at the LHC". In: *Phys. Lett.* B716 (2012), pp. 1–29. DOI: 10.1016/j.physletb.2012.08.020. arXiv: 1207.7214 [hep-ex].

[21] Vardan Khachatryan et al. "Observation of the diphoton decay of the Higgs boson and measurement of its properties". In: *Eur. Phys. J.* C74.10 (2014), p. 3076. DOI: 10.1140/epjc/s10052-014-3076-z. arXiv: 1407.0558 [hep-ex].

[22] Vardan Khachatryan et al. "Measurement of the properties of a Higgs boson in the four-lepton final state". In: *Phys. Rev. D* 89 (9 2014), p. 092007. DOI: 10.1103/PhysRevD.89.092007. URL: https://link.aps.org/doi/10.1103/PhysRevD.89.092007.

[23] Albert M Sirunyan et al. "Observation of the Higgs boson decay to a pair of τ leptons with the CMS detector". In: *Phys. Lett.* B779 (2018), pp. 283–316. DOI: 10.1016/j.physletb.2018.02.004. arXiv: 1708.00373 [hep-ex].

[24] Albert M Sirunyan et al. "Observation of $t\bar{t}H$ production". In: *Phys. Rev. Lett.* 120.23 (2018), p. 231801. DOI: 10.1103/PhysRevLett.120.231801. arXiv: 1804.02610 [hep-ex].

[25] A. M. Sirunyan et al. "Observation of Higgs boson decay to bottom quarks". In: *Phys. Rev. Lett.* 121.12 (2018), p. 121801. DOI: 10.1103/PhysRevLett.121.121801. arXiv: 1808.08242 [hep-ex].

[26] Gustavo Burdman. "New solutions to the hierarchy problem". en. In: *Brazilian Journal of Physics* 37 (July 2007), pp. 506 –513. ISSN: 0103-9733. URL: http://www.scielo.br/scielo.php?script=sci_arttext&pid=S0103-97332007000400006&nrm=iso.

[27] Y. Fukuda et al. "Evidence for oscillation of atmospheric neutrinos". In: *Phys. Rev. Lett.* 81 (1998), pp. 1562–1567. DOI: 10.1103/PhysRevLett.81.1562. arXiv: hep-ex/9807003 [hep-ex].

[28] A. Aguilar-Arevalo et al. "Evidence for neutrino oscillations from the observation of anti-neutrino(electron) appearance in a anti-neutrino(muon) beam". In: *Phys. Rev.* D64 (2001), p. 112007. DOI: 10.1103/PhysRevD.64.112007. arXiv: hep-ex/0104049 [hep-ex].

[29] Joan Elias-Miro et al. "Higgs mass implications on the stability of the electroweak vacuum". In: *Phys. Lett.* B709 (2012), pp. 222–228. DOI: 10.1016/j.physletb.2012.02.013. arXiv: 1112.3022 [hep-ph].

[30] Yong Tang. "Vacuum Stability in the Standard Model". In: *Mod. Phys. Lett.* A28 (2013), p. 1330002. DOI: 10.1142/S0217732313300024. arXiv: 1301.5812 [hep-ph].

[31] Michael Dine and Alexander Kusenko. "The Origin of the matter - antimatter asymmetry". In: *Rev. Mod. Phys.* 76 (2003), p. 1. DOI: 10.1103/RevModPhys.76.1. arXiv: hep-ph/0303065 [hep-ph].

[32] Sean Fraser, Ernest Ma, and Oleg Popov. "Scotogenic Inverse Seesaw Model of Neutrino Mass". In: *Phys. Lett.* B737 (2014), pp. 280–282. DOI: 10.1016/j.physletb.2014.08.069. arXiv: 1408.4785 [hep-ph].

[33] M. C. Gonzalez-Garcia and Michele Maltoni. "Phenomenology with Massive Neutrinos". In: *Phys. Rept.* 460 (2008), pp. 1–129. DOI: 10.1016/j.physrep.2007.12.004. arXiv: 0704.1800 [hep-ph].

[34] Mark Trodden. "Electroweak baryogenesis". In: *Rev. Mod. Phys.* 71 (1999), pp. 1463–1500. DOI: 10.1103/RevModPhys.71.1463. arXiv: hep-ph/9803479 [hep-ph].

[35] H.E. Haber and G.L. Kane. "The search for supersymmetry: Probing physics beyond the standard model". In: *Physics Reports* 117.2 (1985), pp. 75 –263. ISSN: 0370-1573. DOI: https://doi.org/10.1016/0370-1573(85)90051-1. URL: http://www.sciencedirect.com/science/article/pii/0370157385900511.

[36] Sheldon L. Glashow and Steven Weinberg. "Natural Conservation Laws for Neutral Currents". In: *Phys. Rev.* D15 (1977), p. 1958. DOI: 10.1103/PhysRevD.15.1958.

[37] Mayumi Aoki et al. "Models of Yukawa interaction in the two Higgs doublet model, and their collider phenomenology". In: *Phys. Rev.* D80 (2009), p. 015017. DOI: 10.1103/PhysRevD.80.015017. arXiv: 0902.4665 [hep-ph].

[38] John F. Gunion et al. "The Higgs Hunter's Guide". In: *Front. Phys.* 80 (2000), pp. 1–404.

[39] Nathaniel Craig, Jamison Galloway, and Scott Thomas. "Searching for Signs of the Second Higgs Doublet". In: (2013). arXiv: 1305.2424 [hep-ph].

[40] John F. Gunion and Howard E. Haber. "The CP conserving two Higgs doublet model: The Approach to the decoupling limit". In: *Phys. Rev.* D67 (2003), p. 075019. DOI: 10.1103/PhysRevD.67.075019. arXiv: hep-ph/0207010 [hep-ph].

[41] Jérémy Bernon et al. "Scrutinizing the alignment limit in two-Higgs-doublet models: m_h=125 GeV". In: *Phys. Rev.* D92.7 (2015), p. 075004. DOI: 10.1103/PhysRevD.92.075004. arXiv: 1507.00933 [hep-ph].

[42] P. M. Ferreira et al. "Probing wrong-sign Yukawa couplings at the LHC and a future linear collider". In: *Phys. Rev.* D89.11 (2014), p. 115003. DOI: 10.1103/PhysRevD.89.115003. arXiv: 1403.4736 [hep-ph].

[43] Stan Bentvelsen, E Laenen, and Patrick Motylinski. "Higgs production through gluon fusion at leading order". In: (Apr. 2019).

[44] Rudiger Voss and Amos Breskin, eds. *The CERN Large Hadron Collider, accelerator and experiments*. 2009. URL: http://www-spires.fnal.gov/spires/find/books/www?cl=QC787.P73C37::2009.

[45] CERN. *CERN*. 2008. URL: https://home.cern/.

[46] S. Chatrchyan et al. "The CMS Experiment at the CERN LHC". In: *JINST* 3 (2008), S08004. DOI: 10.1088/1748-0221/3/08/S08004.

[47] G. Aad et al. "The ATLAS Experiment at the CERN Large Hadron Collider". In: *JINST* 3 (2008), S08003. DOI: 10.1088/1748-0221/3/08/S08003.

[48] A. Augusto Alves Jr. et al. "The LHCb Detector at the LHC". In: *JINST* 3 (2008), S08005. DOI: 10.1088/1748-0221/3/08/S08005.

[49] K. Aamodt et al. "The ALICE experiment at the CERN LHC". In: *JINST* 3 (2008), S08002. DOI: 10.1088/1748-0221/3/08/S08002.

[50] Florian Pitters. "The CMS High-Granularity Calorimeter for Operation at the High-Luminosity LHC". In: *Springer Proc. Phys.* 213 (2018), pp. 7–11. DOI: 10.1007/978-981-13-1316-5_2. arXiv: 1802.05987 [physics.ins-det].

[51] Klaus Hanke et al. "The LHC Injectors Upgrade (LIU) Project at CERN: Proton Injector Chain". In: *Proceedings, 8th International Particle Accelerator Conference (IPAC 2017): Copenhagen, Denmark, May 14-19, 2017*. 2017, WEPVA036. DOI: 10.18429/JACoW-IPAC2017-WEPVA036.

[52] CMS Collaboration. *CMS-Luminosity*. 2019. URL: https://twiki.cern.ch/twiki/bin/view/CMSPublic/LumiPublicResults.

[53] *The CMS tracker system project: Technical Design Report*. Technical Design Report CMS. Geneva: CERN, 1997. URL: http://cds.cern.ch/record/368412.

[54] *The CMS tracker: addendum to the Technical Design Report*. Technical Design Report CMS. Geneva: CERN, 2000. URL: http://cds.cern.ch/record/490194.

[55] The CMS Collaboration. "The CMS experiment at the CERN LHC". In: *Journal of Instrumentation* 3.08 (2008), S08004–S08004. DOI: 10.1088/1748-0221/3/08/s08004. URL: https://doi.org/10.1088%2F1748-0221%2F3%2F08%2Fs08004.

[56] Serguei Chatrchyan et al. "Description and performance of track and primary-vertex reconstruction with the CMS tracker". In: *JINST* 9.10 (2014), P10009. DOI: 10.1088/1748-0221/9/10/P10009. arXiv: 1405.6569 [physics.ins-det].

[57] M Atac et al. "Beam test results of the US-CMS forward pixel detector". In: *Nuclear Instruments and Methods in Physics Research Section A: Accelerators, Spectrometers, Detectors and Associated Equipment* 488.1 (2002), pp. 271 –281. ISSN: 0168-9002. DOI: https://doi.org/10.1016/S0168-9002(02)00472-2. URL: http://www.sciencedirect.com/science/article/pii/S0168900202004722.

[58] Serguei Chatrchyan et al. "Energy Calibration and Resolution of the CMS Electromagnetic Calorimeter in pp Collisions at $\sqrt{s} = 7$ TeV". In: *JINST* 8 (2013). [JINST8,9009(2013)], P09009. DOI: 10.1088/1748-0221/8/09/P09009. arXiv: 1306.2016 [hep-ex].

[59] *The CMS electromagnetic calorimeter project: Technical Design Report*. Technical Design Report CMS. Geneva: CERN, 1997. URL: http://cds.cern.ch/record/349375.

[60] S. Baccaro et al. "Radiation damage effect on avalanche photodiodes". In: *Nuclear Instruments and Methods in Physics Research Section A: Accelerators, Spectrometers, Detectors and Associated Equipment* 426.1 (1999), pp. 206 –211. ISSN: 0168-9002. DOI: https://doi.org/10.1016/S0168-9002(98)01493-4. URL: http://www.sciencedirect.com/science/article/pii/S0168900298014934.

[61] K. W. Bell et al. "Vacuum phototriodes for the CMS electromagnetic calorimeter endcap". In: *IEEE Transactions on Nuclear Science* 51.5 (2004), pp. 2284–2287. ISSN: 0018-9499. DOI: 10.1109/TNS.2004.836053.

[62] Bayatian et al. *CMS Physics: Technical Design Report Volume 1: Detector Performance and Software*. Technical Design Report CMS. There is an error on cover due to a technical problem for some items. Geneva: CERN, 2006. URL: https://cds.cern.ch/record/922757.

[63] M.C Fouz. "The CMS muon system". In: *Nuclear Instruments and Methods in Physics Research Section A: Accelerators, Spectrometers, Detectors and Associated Equipment* 446.1 (2000), pp. 366 –372. ISSN: 0168-9002. DOI: https://doi.org/10.1016/S0168-9002(00)00082-6. URL: http://www.sciencedirect.com/science/article/pii/S0168900200000826.

[64] Bayatyan et al. *CMS TriDAS project: Technical Design Report, Volume 1: The Trigger Systems*. Technical Design Report CMS. URL: http://cds.cern.ch/record/706847.

[65] Sergio Cittolin, Attila Rácz, and Paris Sphicas. *CMS The TriDAS Project: Technical Design Report, Volume 2: Data Acquisition and High-Level Trigger. CMS trigger and data-acquisition project*. Technical Design Report CMS. Geneva: CERN, 2002. URL: http://cds.cern.ch/record/578006.

[66] Albert M Sirunyan et al. "Search for a heavy pseudoscalar boson decaying to a Z and a Higgs boson at $\sqrt{s} = 13$ TeV". In: *Eur. Phys. J.* C79.7 (2019), p. 564. DOI: 10.1140/epjc/s10052-019-7058-z. arXiv: 1903.00941 [hep-ex].

[67] Torbjörn Sjöstrand et al. "An Introduction to PYTHIA 8.2". In: *Comput. Phys. Commun.* 191 (2015), pp. 159–177. DOI: 10.1016/j.cpc.2015.01.024. arXiv: 1410.3012 [hep-ph].

[68] Peter Skands, Stefano Carrazza, and Juan Rojo. "Tuning PYTHIA 8.1: the Monash 2013 Tune". In: *Eur. Phys. J.* C74.8 (2014), p. 3024. DOI: 10.1140/epjc/s10052-014-3024-y. arXiv: 1404.5630 [hep-ph].

[69] Vardan Khachatryan et al. "Event generator tunes obtained from underlying event and multiparton scattering measurements". In: *Eur. Phys. J.* C76.3 (2016), p. 155. DOI: 10.1140/epjc/s10052-016-3988-x. arXiv: 1512.00815 [hep-ex].

[70] S. Agostinelli et al. "GEANT4: A Simulation toolkit". In: *Nucl. Instrum. Meth.* A506 (2003), pp. 250–303. DOI: 10.1016/S0168-9002(03)01368-8.

[71] CMS collaboration. *CMSSW User Manual*. 2019. URL: https://twiki.cern.ch/twiki/bin/view/CMSPublic/WorkBook.

[72] *Investigations of the impact of the parton shower tuning in Pythia 8 in the modelling of* $\mathrm{t\bar{t}}$ *at* $\sqrt{s} = 8$ *and 13 TeV*. Tech. rep. CMS-PAS-TOP-16-021. Geneva: CERN, 2016. URL: https://cds.cern.ch/record/2235192.

[73] Richard D. Ball et al. "Parton distributions for the LHC Run II". In: *JHEP* 04 (2015), p. 040. DOI: 10.1007/JHEP04(2015)040. arXiv: 1410.8849 [hep-ph].

[74] The Madgraph team. *The MadGraph team*. 2016. URL: http://feynrules.irmp.ucl.ac.be/attachment/wiki/2HDM/2HDMtII_NLO.tar.gz.

[75] Robert V. Harlander, Stefan Liebler, and Hendrik Mantler. "SusHi: A program for the calculation of Higgs production in gluon fusion and bottom-quark annihilation in the Standard Model and the MSSM". In: *Comput. Phys. Commun.* 184 (2013), pp. 1605–1617. DOI: 10.1016/j.cpc.2013.02.006. arXiv: 1212.3249 [hep-ph].

[76] David Eriksson, Johan Rathsman, and Oscar Stal. "2HDMC: Two-Higgs-Doublet Model Calculator Physics and Manual". In: *Comput. Phys. Commun.* 181 (2010), pp. 189–205. DOI: 10.1016/j.cpc.2009.09.011. arXiv: 0902.0851 [hep-ph].

[77] CMS Collaboration. *SummaryTable1G25ns*. 2018. URL: https://twiki.cern.ch/twiki/bin/viewauth/CMS/SummaryTable1G25ns.

[78] S. Dittmaier et al. "Handbook of LHC Higgs Cross Sections: 1. Inclusive Observables". In: (2011). DOI: 10.5170/CERN-2011-002. arXiv: 1101.0593 [hep-ph].

[79] Ye Li and Frank Petriello. "Combining QCD and electroweak corrections to dilepton production in FEWZ". In: *Phys. Rev.* D86 (2012), p. 094034. DOI: 10.1103/PhysRevD.86.094034. arXiv: 1208.5967 [hep-ph].

[80] J. M. Lindert et al. "Precise predictions for $V+$ jets dark matter backgrounds". In: *Eur. Phys. J.* C77.12 (2017), p. 829. DOI: 10.1140/epjc/s10052-017-5389-1. arXiv: 1705.04664 [hep-ph].

[81] Johan Alwall et al. "A Standard format for Les Houches event files". In: *Comput. Phys. Commun.* 176 (2007), pp. 300–304. DOI: 10.1016/j.cpc.2006.11.010. arXiv: hep-ph/0609017 [hep-ph].

[82] Paolo Nason. "A New method for combining NLO QCD with shower Monte Carlo algorithms". In: *JHEP* 11 (2004), p. 040. DOI: 10.1088/1126-6708/2004/11/040. arXiv: hep-ph/0409146 [hep-ph].

[83] Stefano Frixione, Paolo Nason, and Carlo Oleari. "Matching NLO QCD computations with Parton Shower simulations: the POWHEG method". In: *JHEP* 11 (2007), p. 070. DOI: 10.1088/1126-6708/2007/11/070. arXiv: 0709.2092 [hep-ph].

[84] Simone Alioli et al. "A general framework for implementing NLO calculations in shower Monte Carlo programs: the POWHEG BOX". In: *JHEP* 06 (2010), p. 043. DOI: 10.1007/JHEP06(2010)043. arXiv: 1002.2581 [hep-ph].

[85] Michal Czakon and Alexander Mitov. "Top++: A Program for the Calculation of the Top-Pair Cross-Section at Hadron Colliders". In: *Comput. Phys. Commun.* 185 (2014), p. 2930. DOI: 10.1016/j.cpc.2014.06.021. arXiv: 1112.5675 [hep-ph].

[86] Rikkert Frederix and Stefano Frixione. "Merging meets matching in MC@NLO". In: *JHEP* 12 (2012), p. 061. DOI: 10.1007/JHEP12(2012)061. arXiv: 1209.6215 [hep-ph].

[87] Alberto Zucchetta Lisa Benato et al. *Search for heavy resonances decaying into a vector boson and a Higgs boson in the ($\nu\nu$, $\ell\ell$) $b\bar{b}$ final state*. Tech. rep. CMS-NOTE-2015-186. Geneva: CERN, 2015.

[88] Vardan Khachatryan et al. "Measurement of differential cross sections for top quark pair production using the lepton+jets final state in proton-proton collisions at 13 TeV". In: *Phys. Rev.* D95.9 (2017), p. 092001. DOI: 10.1103/PhysRevD.95.092001. arXiv: 1610.04191 [hep-ex].

[89] N.Adam, J.Berryhill, V.Halyo, A.Hunt, K. Mishra. *Generic Tag and Probe Tool for Measuring Efficiency at CMS with Early Data*. Tech. rep. CMS-NOTE-2009-111. Geneva: CERN, 2009.

[90] CMS Collaboration. *EGamma POG-Cut based electron ID for Run2*. 2019. URL: https://twiki.cern.ch/twiki/bin/view/CMS/CutBasedElectronIdentificationRun2.

[91] CMS Collaboration. *HLT Trigger*. 2019. URL: https://twiki.cern.ch/twiki/bin/view/CMSPublic/SWGuideGlobalHLT.

[92] CMS Collaboration. *Reference muon id, isolation and trigger efficiencies for Run II*. 2019. URL: https://twiki.cern.ch/twiki/bin/view/CMS/MuonReferenceEffsRun2.

[93] CMS Collaboration. *Muon POG-Muon ID and Isolation for Run2*. 2019. URL: https://twiki.cern.ch/twiki/bin/view/CMS/SWGuideMuonIdRun2.

[94] A. M. Sirunyan et al. "Particle-flow reconstruction and global event description with the CMS detector". In: *JINST* 12.10 (2017), P10003. DOI: 10.1088/1748-0221/12/10/P10003. arXiv: 1706.04965 [physics.ins-det].

[95] P.Azzurri A.Rizzi S.Donato. "Primary vertex sorting". 2015. URL: https://indico.cern.ch/event/369417/contributions/1788757/attachments/734933/1008272/pv-sorting-xpog.pdf.

[96] CMS Collaboration. *Pileup Reweighting Procedure*. URL: https://twiki.cern.ch/twiki/bin/viewauth/CMS/PileupReweighting.

[97] CMS Collaboration. *Utilities for Accessing Pileup Information for Data*. URL: https://twiki.cern.ch/twiki/bin/view/CMS/PileupJSONFileforData.

[98] *CMS Tracker Operational Experience*. 2016. URL: https://indico.cern.ch/event/452781/contributions/2297531/attachments/1342796/2022894/CMS_Tracker_Operational_Experience_Fiori.pdf.

[99] W Adam et al. "Reconstruction of electrons with the Gaussian-sum filter in the CMS tracker at the LHC". In: *Journal of Physics G: Nuclear and Particle Physics* 31.9 (2005), N9–N20. DOI: 10.1088/0954-3899/31/9/n01. URL: https://doi.org/10.1088%2F0954-3899%2F31%2F9%2Fn01.

[100] A. M. Sirunyan et al. "Performance of the CMS muon detector and muon reconstruction with proton-proton collisions at $\sqrt{s} = 13$ TeV". In: *JINST* 13.06 (2018), P06015. DOI: 10.1088/1748-0221/13/06/P06015. arXiv: 1804.04528 [physics.ins-det].

[101] *TauID for 13 TeV run: recommendation from the Tau POG*. 2019. URL: https://twiki.cern.ch/twiki/bin/view/CMS/TauIDRecommendation13TeV#Cut_based.

[102] *Pileup Removal Algorithms*. Tech. rep. CMS-PAS-JME-14-001. Geneva: CERN, 2014. URL: https://cds.cern.ch/record/1751454.

[103] R. Salam. *Fastjet package*. CNRS. technical report. 2011.

[104] *Jet energy scale uncertainty sources*. 2019. URL: https://twiki.cern.ch/twiki/bin/view/CMS/JECUncertaintySources.

[105] CMS Collaboration. *JetMET POG - Jet ID for Run2*. 2019. URL: https://twiki.cern.ch/twiki/bin/view/CMS/JetID.

[106] CMS Collaboration. *Jet energy resolution smearing*. 2013. URL: https://twiki.cern.ch/twiki/bin/view/CMS/JetResolution.

[107] *b Tag and Vertexing Physics Object Group*. URL: https://twiki.cern.ch/twiki/bin/viewauth/CMS/BtagPOG.

[108] Serguei Chatrchyan et al. "Identification of b-Quark Jets with the CMS Experiment". In: *JINST* 8 (2013), P04013. DOI: 10.1088/1748-0221/8/04/P04013. arXiv: 1211.4462 [hep-ex].

[109] CMS Collaboration. *Methods to apply b-tagging efficiency scale factors*. 2013. URL: https://twiki.cern.ch/twiki/bin/view/CMS/BTagSFMethods.

[110] CMS Collaboration. *Standard Model Cross Sections*. 2018. URL: https://twiki.cern.ch/twiki/bin/viewauth/CMS/StandardModelCrossSectionsat13TeV.

[111] Roger Barlow and Christine Beeston. "Fitting using finite Monte Carlo samples". In: *Computer Physics Communications* 77.2 (1993), pp. 219 –228. ISSN: 0010-4655. DOI: https://doi.org/10.1016/0010-4655(93)90005-W. URL: http://www.sciencedirect.com/science/article/pii/001046559390005W.

[112] L. Moneta et al. "The RooStats project". In: *Proceedings of the 13th International Workshop on Advanced Computing and Analysis Techniques in Physics Research. February 22-27*. 2010, p. 57. arXiv: 1009.1003 [physics.data-an].

[113] CMS Collaboration. *Cms higgs combine tool*. 2013. URL: https://twiki.cern.ch/twiki/bin/viewauth/CMS/SWGuideHiggsAnalysisCombinedLimit.

[114] *SM Higgs Combination*. Tech. rep. CMS-PAS-HIG-11-011. Geneva: CERN, 2011. URL: http://cds.cern.ch/record/1370076.

[115] *Measurement of the associated production of a Z boson and b quarks in pp collision at 8 TeV*. Tech. rep. CMS-PAS-SMP-14-010. Geneva: CERN, 2015. URL: https://cds.cern.ch/record/2044919.

[116] *Procedure for the LHC Higgs boson search combination in Summer 2011*. Tech. rep. CMS-NOTE-2011-005. ATL-PHYS-PUB-2011-11. Geneva: CERN, 2011. URL: https://cds.cern.ch/record/1379837.

[117] A. KOLMOGOROV. "Sulla determinazione empirica di una lgge di distribuzione". In: *Inst. Ital. Attuari, Giorn.* 4 (1933), pp. 83–91. URL: https://ci.nii.ac.jp/naid/10010480527/en/.

[118] N. Smirnov. "Table for Estimating the Goodness of Fit of Empirical Distributions". In: *Ann. Math. Statist.* 19.2 (June 1948), pp. 279–281. DOI: 10.1214/aoms/1177730256. URL: https://doi.org/10.1214/aoms/1177730256.

[119] Marvin Karson. "Handbook of Methods of Applied Statistics. Volume I: Techniques of Computation Descriptive Methods, and Statistical Inference. Volume II: Planning of Surveys and Experiments. I. M. Chakravarti, R. G. Laha, and J. Roy, New York, John Wiley; 1967, $9.00." In: *Journal of the American Statistical Association* 63.323 (1968), pp. 1047–1049. DOI: 10.1080/01621459.1968.11009335. eprint: https://doi.org/10.1080/01621459.1968.11009335. URL: https://doi.org/10.1080/01621459.1968.11009335.

[120] Alexander L. Read. "Modified frequentist analysis of search results (The CL(s) method)". In: *Workshop on confidence limits, CERN, Geneva, Switzerland, 17-18 Jan 2000: Proceedings*. 2000, pp. 81–101. URL: http://weblib.cern.ch/abstract?CERN-OPEN-2000-205.

[121] Glen Cowan et al. "Asymptotic formulae for likelihood-based tests of new physics". In: *Eur. Phys. J.* C71 (2011). [Erratum: Eur. Phys. J.C73,2501(2013)], p. 1554. DOI: 10.1140/epjc/s10052-011-1554-0,10.1140/epjc/s10052-013-2501-z. arXiv: 1007.1727 [physics.data-an].

[122] Eilam Gross. "Practical Statistics for High Energy Physics". In: *CERN Yellow Reports: School Proceedings* 4.0 (2017), p. 165. ISSN: 2519-805X. URL: https://e-publishing.cern.ch/index.php/CYRSP/article/view/303.

[123] Eilam Gross and Ofer Vitells. "Trial factors for the look elsewhere effect in high energy physics". In: *Eur. Phys. J.* C70 (2010), pp. 525–530. DOI: 10.1140/epjc/s10052-010-1470-8. arXiv: 1005.1891 [physics.data-an].

[124] Robert B. Davies. "Hypothesis testing when a nuisance parameter is present only under the alternative". In: *Biometrika* 74 (1987), pp. 33–43. DOI: 10.1093/biomet/74.1.33.

[125] Robert D. Cousins. "Generalization of Chisquare Goodness-ofFit Test for Binned Data Using Saturated Models , with Application to Histograms". In: 2013.

[126] Steve Baker and Robert D. Cousins. "Clarification of the Use of Chi Square and Likelihood Functions in Fits to Histograms". In: *Nucl. Instrum. Meth.* 221 (1984), pp. 437–442. DOI: 10.1016/0167-5087(84)90016-4.

[127] Andreas Hoecker et al. "TMVA: Toolkit for Multivariate Data Analysis". In: *PoS* ACAT (2007), p. 040. arXiv: physics/0703039.

[128] Michael H. Seymour and Marilyn Marx. "Monte Carlo Event Generators". In: *Proceedings, 69th Scottish Universities Summer School in Physics : LHC Phenomenology (SUSSP69): St.Andrews, Scotland, August 19-September 1, 2012*. 2013, pp. 287–319. DOI: 10.1007/978-3-319-05362-2_8. arXiv: 1304.6677 [hep-ph].

[129] Fabio Maltoni and Tim Stelzer. "MadEvent: Automatic event generation with MadGraph". In: *JHEP* 02 (2003), p. 027. DOI: 10.1088/1126-6708/2003/02/027. arXiv: hep-ph/0208156 [hep-ph].

[130] Torbjorn Sjostrand, Stephen Mrenna, and Peter Z. Skands. "PYTHIA 6.4 Physics and Manual". In: *JHEP* 05 (2006), p. 026. DOI: 10.1088/1126-6708/2006/05/026. arXiv: hep-ph/0603175 [hep-ph].

[131] Carlo Oleari. "The POWHEG-BOX". In: *Nucl. Phys. Proc. Suppl.* 205-206 (2010), pp. 36–41. DOI: 10.1016/j.nuclphysbps.2010.08.016. arXiv: 1007.3893 [hep-ph].

[132] G. Corcella et al. "HERWIG 6: An Event generator for hadron emission reactions with interfering gluons (including supersymmetric processes)". In: *JHEP* 01 (2001), p. 010. DOI: 10.1088/1126-6708/2001/01/010. arXiv: hep-ph/0011363 [hep-ph].

[133] Johannes Bellm et al. "Herwig 7.0/Herwig++ 3.0 release note". In: *Eur. Phys. J.* C76.4 (2016), p. 196. DOI: 10.1140/epjc/s10052-016-4018-8. arXiv: 1512.01178 [hep-ph].

[134] T. Gleisberg et al. "Event generation with SHERPA 1.1". In: *JHEP* 02 (2009), p. 007. DOI: 10.1088/1126-6708/2009/02/007. arXiv: 0811.4622 [hep-ph].

[135] J. Alwall et al. "The automated computation of tree-level and next-to-leading order differential cross sections, and their matching to parton shower simulations". In: *JHEP* 07 (2014), p. 079. DOI: 10.1007/JHEP07(2014)079. arXiv: 1405.0301 [hep-ph].

[136] *Particle-Flow Event Reconstruction in CMS and Performance for Jets, Taus, and MET*. Tech. rep. CMS-PAS-PFT-09-001. Geneva: CERN, 2009. URL: http://cds.cern.ch/record/1194487.

[137] *Commissioning of the Particle-flow Event Reconstruction with the first LHC collisions recorded in the CMS detector*. Tech. rep. CMS-PAS-PFT-10-001. 2010. URL: http://cds.cern.ch/record/1247373.

[138] Pierre Billoir. "Progressive track recognition with a Kalman-like fitting procedure". In: *Computer Physics Communications* 57.1 (1989), pp. 390 –394. ISSN: 0010-4655. DOI: https://doi.org/10.1016/0010-4655(89)90249-X. URL: http://www.sciencedirect.com/science/article/pii/001046558990249X.

[139] R. Frühwirth. "Application of Kalman filtering to track and vertex fitting". In: *Nuclear Instruments and Methods in Physics Research Section A: Accelerators, Spectrometers, Detectors and Associated Equipment* 262.2 (1987), pp. 444 –450. ISSN: 0168-9002. DOI: https://doi.org/10.1016/0168-9002(87)90887-4. URL: http://www.sciencedirect.com/science/article/pii/0168900287908874.

[140] T. Speer et al. "Vertex fitting in the CMS tracker". In: (2006).

[141] K. Rose. "Deterministic annealing for clustering, compression, classification, regression, and related optimization problems". In: *Proceedings of the IEEE* 86.11 (1998), pp. 2210–2239. ISSN: 0018-9219. DOI: 10.1109/5.726788.

[142] R Frühwirth, Wolfgang Waltenberger, and Pascal Vanlaer. *Adaptive Vertex Fitting*. Tech. rep. CMS-NOTE-2007-008. Geneva: CERN, 2007. URL: https://cds.cern.ch/record/1027031.

[143] "Tracking and Primary Vertex Results in First 7 TeV Collisions". In: (2010).

[144] Vardan Khachatryan et al. "Performance of Electron Reconstruction and Selection with the CMS Detector in Proton-Proton Collisions at centre-of-mass energy of 8 TeV". In: *JINST* 10.06 (2015), P06005. DOI: 10.1088/1748-0221/10/06/P06005. arXiv: 1502.02701.

[145] A. Hoecker et al. "TMVA - Toolkit for Multivariate Data Analysis". In: *arXiv e-prints*, physics/0703039 (2007), physics/0703039. arXiv: physics/0703039 [physics.data-an].

[146] Vardan Khachatryan et al. "Jet energy scale and resolution in the CMS experiment in pp collisions at 8 TeV". In: *JINST* 12.02 (2017), P02014. DOI: 10.1088/1748-0221/12/02/P02014. arXiv: 1607.03663 [hep-ex].

[147] *Performance of missing transverse momentum in pp collisions at sqrt(s)=13 TeV using the CMS detector*. Tech. rep. CMS-PAS-JME-17-001. Geneva: CERN, 2018. URL: https://cds.cern.ch/record/2628600.

[148] M. H. Quenouille. "Approximate Tests of Correlation in Time-Series". In: *Journal of the Royal Statistical Society. Series B (Methodological)* 11.1 (1949), pp. 68–84. ISSN: 00359246. URL: http://www.jstor.org/stable/2983696.

[149] CMS Collaboration. "Determination of jet energy calibration and transverse momentum resolution in CMS". In: *Journal of Instrumentation* 6.11 (2011), p. 11002. DOI: 10.1088/1748-0221/6/11/P11002. arXiv: 1107.4277 [physics.ins-det].

[150] *The Jet Plus Tracks Algorithm for Calorimeter Jet Energy Corrections in CMS*. Tech. rep. CMS-PAS-JME-09-002. 2009. URL: http://cds.cern.ch/record/1190234.

[151] Matteo Cacciari, Gavin P. Salam, and Gregory Soyez. "The anti-k_t jet clustering algorithm". In: *JHEP* 04 (2008), p. 063. DOI: 10.1088/1126-6708/2008/04/063. arXiv: 0802.1189 [hep-ph].

[152] "Jet energy scale and resolution performance with 13 TeV data collected by CMS in 2016". In: (2018). URL: http://cds.cern.ch/record/2622157.

[153] *Performance of b tagging at sqrt(s)=8 TeV in multijet, ttbar and boosted topology events*. Tech. rep. CMS-PAS-BTV-13-001. Geneva: CERN, 2013. URL: http://cds.cern.ch/record/1581306.

[154] Wolfgang Waltenberger, Rudolf Frühwirth, and Pascal Vanlaer. "Adaptive vertex fitting". In: *Journal of Physics G: Nuclear and Particle Physics* 34.12 (2007), N343–N356. DOI: 10.1088/0954-3899/34/12/n01. URL: https://doi.org/10.1088%2F0954-3899%2F34%2F12%2Fn01.

[155] The CMS collaboration. "Identification of b-quark jets with the CMS experiment". In: *Journal of Instrumentation* 8.04 (2013), P04013–P04013. DOI: 10.1088/1748-0221/8/04/p04013. URL: https://doi.org/10.1088%2F1748-0221%2F8%2F04%2Fp04013.

[156] The CMS collaboration. "Identification of heavy-flavour jets with the CMS detector in pp collisions at 13 TeV". In: *Journal of Instrumentation* 13.05 (2018), P05011–P05011. DOI: 10.1088/1748-0221/13/05/p05011. URL: https://doi.org/10.1088%2F1748-0221%2F13%2F05%2Fp05011.

[157] Daniel Guest et al. "Jet flavor classification in high-energy physics with deep neural networks". In: *Phys. Rev. D* 94 (11 2016), p. 112002. DOI: 10.1103/PhysRevD.94.112002. URL: https://link.aps.org/doi/10.1103/PhysRevD.94.112002.

[158] "Heavy flavor identification at CMS with deep neural networks". In: (2017). URL: https://cds.cern.ch/record/2255736.

[159] Beringer et al. "Review of Particle Physics". In: *Phys. Rev. D* 86 (1 2012), p. 010001. DOI: 10.1103/PhysRevD.86.010001. URL: https://link.aps.org/doi/10.1103/PhysRevD.86.010001.